

THE PETROPHYSICAL PROPERTIES OF SHALE GAS RESERVOIRS

Thesis submitted for the degree of
Doctor of Philosophy
at the University of Leicester

by

David Anthony Hartigan M.Geol (Hons)

Department of Geology

University of Leicester

June 2014

Thesis abstract

A significant challenge to the petrophysical evaluation of shale gas systems can be attributed to the conductivity behaviour of clay minerals. This is compounded by centimetre to sub-millimetre vertical and lateral heterogeneity in formation geological and therefore petrophysical properties. Despite this however, we remain reliant on Archie based methods for determining water saturation (S_w), and hence the free gas saturation ($1-S_g$) in shale gas systems. There is however significant uncertainty in both how resistivity methods are applied and the saturation estimates they produce, due largely as Archie parameter inputs (e.g. a , m , n , and R_w) are difficult to determine in shale gas systems, where obtaining a water sample, or carrying out laboratory experiments on recovered core is often technically impractical.

This research assesses the geological implications for, and controls on, variations in pseudo Archie parameters in the Bossier and Haynesville Shale Formations in the northern Gulf of Mexico basin. Investigation has particularly focused on the numerical analysis and systematic modification of Archie parameter values to minimise the error between core S_w (Dean Stark analysis) and computed S_w values. Results show that the use of optimised Archie parameters can be effective in predicting S_w , particularly in the Haynesville formation, but identifies systematic bias in generated Archie parameters that precludes their accurate physical interpretation. Analysis also suggests that variability in the resistivity (R_t) log response is the principal source of error in S_w estimates in the Bossier Shale. Moreover, results suggest that where clay volume exceeds 28%, the resistivity response becomes increasingly variable and elevated, indicating an apparent clay associated 'excess resistivity'. This is explained by a geologically consistent model that links increasing clay volume to bulk pore water freshening, supported by empirical adaptations that allow for improved Archie parameter selection and a further reduction in the error of S_w estimates.

Acknowledgements

I would like to thank my supervisors, Mike Lovell and Sarah Davies, for giving me the opportunity to undertake this project, and for their guidance and feedback throughout. This project was jointly funded by University of Leicester, BG Group, and the London Petrophysical Society. I would also like to thank BG Group for providing access to the data.

Special thanks also go to Stewart Fishwick for his advice and guidance and for tolerating my many questions, particularly in areas regarding programming and statistics. I would also like to thank Joao Afonso for his friendship and advice throughout my time at the University of Leicester, and the department on the whole for creating a pleasant and vibrant research environment.

Above all, I am grateful to my inspirational wife Catherine and two daughters, lolana and Sienna, whose love, energy and enthusiasm, enriches, motivates and supports all aspects of my life. You guys are awesome!

Table of contents

Thesis abstract	i
Acknowledgements	ii
Table of contents.....	iii
List of tables	x
List of figures.....	xi
Notation index	xvi
Chapter 1 Introduction	1
1.1 Background.....	2
1.2 Aims and objectives	5
1.2.1 Additional work undertaken	6
1.3 Thesis structure	7
Chapter 2 The sedimentology, petrophysical properties and evaluation of shale gas reservoirs	9

2.1	The sedimentology of shale gas reservoirs	10
2.1.1	What is shale?	10
2.1.2	Composition and classification	11
2.1.3	Sediment fabric and depositional processes	13
2.1.4	Sequence stratigraphy	18
2.1.5	Organic matter: enrichment, type and maturity	22
2.2	Wireline log responses in shale gas reservoirs	26
2.2.1	Gamma ray tool response.....	26
2.2.2	Neutron tool response.....	29
2.2.3	Density tool response	33
2.2.4	Resistivity tool response	35
2.3	Core porosity and water saturation in shale gas reservoirs	40
2.3.1	Porosity and water saturation	40
2.3.2	Laboratory determination; porosity and water saturation	40
2.3.3	What does measured porosity and water saturation represent in shale?	41
2.3.3.1	Clay chemistry and cation exchange capacity.....	41
2.3.3.2	The origin of water extracted by Dean Stark methods	44
2.3.3.3	Organic matter porosity and pore fluids.....	45
2.3.4	Data reliability and uncertainty	46
2.3.5	Summary: a petrophysical model for shale gas reservoirs.....	48
2.4	Evaluating water saturation: Archie's equation	50
2.4.1	An introduction to Archie's equation	50
2.4.2	Archie parameters (a , m and n).....	53
2.4.2.1	The a multiplier (sometimes referred to as tortuosity)	53
2.4.2.2	The porosity exponent, m	55
2.4.2.3	The saturation exponent, n	57
2.4.3	Shaly sand concepts.....	59
2.4.4	Model uncertainties.....	63
2.5	Summary and conclusions.....	67

Chapter 3	The geological setting, mineralogy and petrophysical properties of the Bossier and Haynesville Shale Formations	68
3.1	The Bossier and Haynesville Shale Formations.....	69
3.1.1	Geological setting and stratigraphy.....	70
3.1.2	Palaeotopography.....	72
3.2	The Bossier and Haynesville datasets	75
3.2.1	Rationale for data selection.....	75
3.2.2	Data integration and quality control	77
3.2.3	Formation zoning.....	78
3.2.3.1	Additional core data	79
3.2.3.2	Additional information	79
3.2.3.3	Data corrections	80
3.3	BSR-HY mineralogical and petrophysical properties	82
3.3.1	Overview of XRD bulk mineralogy	82
3.3.2	Overview of core / wireline petrophysical properties.....	84
3.4	Compositional trends in the Bossier-Haynesville	85
3.4.1	Spatial and mineralogical relationships.....	85
3.4.2	Total organic content, pyrite and redox conditions	91
3.5	Petrophysical trends in Bossier-Haynesville	94
3.5.1	Wireline and core gamma ray response.....	94
3.5.2	Typical petrophysical trends in the Bossier-Haynesville	97
3.6	A note on kerogen density	102
3.7	Summary and conclusions.....	108
Chapter 4	Unconventional applications of Archie's equation: sensitivity and error analysis.....	110
4.1	Introduction	111
4.1.1	Chapter structure.....	112
4.2	Methodology.....	114

4.2.1	Least error optimisation	114
4.2.2	Grid search optimisation methodology	115
4.2.2.1	Parameter constraints	116
4.2.2.2	Parameter step increment	116
4.2.2.3	Grid search model variants.....	117
4.2.2.4	Model validation.....	118
4.3	Results: Overview.....	119
4.3.1	Archie water saturation (S_{wA}) results.....	119
4.3.2	Residual errors	122
4.3.3	Generated Archie parameters	125
4.3.4	Summary	127
4.3.4.1	S_{wA} results	127
4.3.4.2	Residual MAE	127
4.3.4.3	Generated Archie parameters.....	128
4.4	Results: 1D parameter optimisation	129
4.4.1	Sensitivity analysis	129
4.4.2	Parameter trade-offs	131
4.4.2.1	Model W1: Parameter trade-offs.....	132
4.4.2.2	Model W2: Parameter trade-offs.....	134
4.4.2.3	Model W1 and W2: Shifts in fixed parameter assumptions	135
4.4.3	Core sample parameter modelling.....	136
4.4.3.1	S_{wR} vs. S_{wA} (model W4)	139
4.4.4	Summary	226
4.4.4.1	Sensitivity analysis	226
4.4.4.2	Parameter trade-offs	226
4.4.4.3	Core sample parameter modelling.....	226
4.5	Results: 2D parameter optimisation	228
4.5.1	Sensitivity analysis	228
4.5.2	Parameter trade-offs	231
4.5.3	Core sample parameter modelling.....	232
4.5.4	Summary	235
4.5.4.1	Sensitivity analysis	235

4.5.4.2	Parameter trade-offs	235
4.5.4.3	Parameter modelling	235
4.6	Results: 3D parameter optimisation	236
4.6.1	Sensitivity analysis	236
4.6.2	Parameter trade-offs	240
4.6.3	Core sample parameter modelling	242
4.6.4	Summary	246
4.6.4.1	Sensitivity analysis	246
4.6.4.2	Parameter trade-offs	247
4.6.4.3	Parameter modelling	247
Chapter 5	Unconventional applications of Archie's equation: does geology matter?	248
5.1	Introduction	249
5.2	Formation heterogeneity	250
5.2.1	Heterogeneity in optimiser model response	250
5.2.2	Heterogeneity in mineralogical / petrophysical properties	251
5.2.3	Mineralogical controls on petrophysical heterogeneity	254
5.2.4	Summary and conclusions	258
5.3	Water, resistivity and clay relationships	260
5.3.1	Key core petrophysical relationships	261
5.3.2	Anomalously high resistivities in the BSR	264
5.3.3	A mechanism for clay mineral freshening	265
5.3.3.1	Changes in pore fluid chemistry and salinity with depth	265
5.3.4	A mechanism for increased pore-complexity	272
5.3.5	Summary and conclusions	274
5.4	Composite core data summary	276
5.4.1	Petrophysical and mineralogical relationships	276
5.4.2	Linking mineralogy and petrophysics to formation fabric	280
5.4.3	Summary and conclusions	283

5.5	Predicted pseudo-Archie parameters	285
5.5.1	Comparison with previous works	285
5.5.2	Optimiser models and parameter manipulation	287
5.5.2.1	One dimensional models (W1 and W2)	287
5.5.2.2	Two dimensional models (W3)	287
5.5.2.3	Three dimensional models (W4)	288
5.5.3	Summary and conclusions	289
Chapter 6	Conclusions and recommendations for further work	290
6.1	Research question I:	291
6.2	Research question II:	292
6.3	Research question III:	294
6.4	Research applications	296
6.5	Additional findings	297
6.6	Summary	297
6.7	Recommendations for further work	299
Appendices	301
Appendix A	GRI method and laboratory protocol	302
Appendix B	Grid search optimiser: example Python code optimiser model W4	304
Appendix C	Multi-sensory core logger: a summary of work undertaken	306
Appendix D	Example petrophysical workflow	308
Appendix E	Electronic thesis.....	310

References311

List of tables

Table 2.1. Average and range in mudstone compositions (wt. %)	13
Table 2.2. Kerogen type, origin and hydrocarbon potential	25
Table 3.1. Wireline data: minimum criteria for well inclusion within study	76
Table 3.2. Core data: minimum criteria for core sample inclusion within study	76
Table 3.3. Summary of selected wells	77
Table 3.4. Summary of additional data.....	79
Table 3.5. Tool information derived from tool mnemonic.....	80
Table 3.6. Summary of lower, upper and optimum mineral / kerogen densities	103
Table 3.7. Effect of variations in $\rho_{Kerogen}$ on estimated $V_{Kerogen}$	107
Table 4.1. Grid search parameter range	116
Table 4.2. Grid search optimisation model variants.....	117
Table 4.3. Change in MAE from model H1 to W4.....	120
Table 5.1: Mean residual MAE per optimisation model (Figure 4.4)	251
Table 5.2. Mean predicted Archie parameters + standard deviation	285

List of figures

Figure 2.1. Mudstone classification	12
Figure 2.2. Mudstone texture as determined by sedimentary and diagenetic processes	14
Figure 2.3. Example mudstone textures	15
Figure 2.4. Mudstone sedimentary structures and inferred processes	15
Figure 2.5. Examples of mudstone lamina structure	16
Figure 2.6. Stratigraphic profile and core gamma trends in the Barnett Shale.....	19
Figure 2.7. General sequence stratigraphic model for shale gas systems	20
Figure 2.8. Sediment accumulation rates in proximal to distal settings for the Mowry Shale.....	22
Figure 2.9. Van Krevelen diagram showing kerogen type and evolutionary path	24
Figure 2.10. Gamma ray emission spectra	27
Figure 2.11. TOC, Uranium and GR relationships	29
Figure 2.12. Theoretical distribution of clay minerals	29
Figure 2.13. Illustration of the slowing down length.....	30
Figure 2.14. Schematic neutron and density response	32

Figure 2.15. Logging tool response (count rate) vs. density.....	33
Figure 2.16. Relationship between TOC and density.....	35
Figure 2.17. Schematic deep resistivity response in various lithologies	36
Figure 2.18. Schematic current distribution from the Laterolog-3 device.....	37
Figure 2.19. Principle of the induction tool measurement	38
Figure 2.20. Schematic of clay mineral sheet structure	42
Figure 2.21. Electrical double layer.....	44
Figure 2.22. FIB/SEM image showing kerogen porosity in shale.....	46
Figure 2.23. Comparison of as-received core porosity results	48
Figure 2.24. Generalised petrophysical model for a shale gas system	49
Figure 2.25. A: Formation factor (F) vs. total porosity and B: Resistivity index vs. water saturation.....	52
Figure 2.26. Pickett plot summarising key Archie relationships.....	52
Figure 2.27. Formation factor (F) vs. total porosity for variable (left) and fixed $\alpha=1$ (right) values	56
Figure 2.28. Relationship between calculated S_w , R_o/R_t and n	58
Figure 2.29. Effect of shale on F, C_w relationships.....	61
Figure 2.30. Schematic relationship between C_o and C_w	62
Figure 3.1. Study area	70
Figure 3.2: Stratigraphic section	72
Figure 3.3: Palaeogeography at the time of HY deposition (Kimmeridgian).....	73
Figure 3.4. Gas shale joint industry project sampling methodology	76
Figure 3.5. Bulk volume correction of mineral volumes.....	81
Figure 3.6. Summary mineralogical composition	82
Figure 3.7. Summary of key core bulk volume XRD mineralogy.....	83
Figure 3.8. XRD clay fractions (<i>See caption for Figure 3.7.</i>).....	84

Figure 3.9. Summary of key core and wireline petrophysical properties (<i>See caption for Figure 3.7</i>).	84
Figure 3.10. Cross section A-A'	86
Figure 3.11. Cross section B-B'	87
Figure 3.12. Contour plot of principal HY mineralogical components	89
Figure 3.13. Contour plot of principal BSR mineralogical components.....	90
Figure 3.14. Mineralogical relationships	91
Figure 3.15. TOC vs. W_{Pyrite} for the HY	92
Figure 3.16. GR and GRC logplots for well 3 including V_{Clay} , $V_{illite+mica}$ and TOC	95
Figure 3.17. TOC (wt. %) vs. U (ppm) for the BSR (left) and HY (right).	97
Figure 3.18. Wireline response for Well 3: cored Section.	98
Figure 3.19. ϕ_{TC} vs. ρ_b	100
Figure 3.20. $V_{Kerogen}$ vs. TOC (left) and ρ_{ma} vs. ρ_{ma_CLB} (right)	103
Figure 3.21. $\rho_{Kerogen}$ vs. Ro	105
Figure 3.22. TOC vs. ρ_{ma} with $\rho_{Keorgen}$ overlay	106
Figure 4.1. Grid search vs. solver methods and MAE vs. $RMSE$	118
Figure 4.2. S_{WA} vs. S_{WC}	120
Figure 4.3. Tiled S_{WA} vs. S_{WC} scatter plot for model W4	121
Figure 4.4. Comparison of MAE for variable parameter selection methods.....	122
Figure 4.5. Normalised MAE for each optimisation model	123
Figure 4.6. Comparison of average MAE by optimisation model and formation.....	124
Figure 4.7. Predicted Archie parameters for each optimisation model	125
Figure 4.8. Predicted Archie parameters, V_{Clay} , and key petrophysical properties	126
Figure 4.9. Sensitivity analysis (model W1 and W2).....	130
Figure 4.10. Parameter trade-offs (model W1)	133
Figure 4.11. Parameter trade-offs (model W2)	134

Figure 4.12. Parameter trade-offs (model W2 and W2).....	135
Figure 4.13. R_{we} vs. R_t (A) and m^* vs. R_t (B).....	137
Figure 4.14. BSR and HY BVW distributions.....	137
Figure 4.15: m^* vs. R_t	138
Figure 4.16. S_{WR} compared against S_{WA} (W4) and S_{WC}	224
Figure 4.17. Comparison of MAE between S_{WA} (W4) and S_{WR}	225
Figure 4.18. % Change in MAE when using S_{WR} as opposed to S_{WA} (W4).....	225
Figure 4.19. Sensitivity analysis (Model W3).....	229
Figure 4.20. Parameter distributions, sensitivity analysis (model W3).....	230
Figure 4.21. Parameter trade-offs (model W3).....	231
Figure 4.22. Core sample optimised parameters (model W3).....	233
Figure 4.23. Optimised parameter distributions for S_{WA} within +/-5% of S_{WC} (model W3)	234
Figure 4.24. Totalled parameter distributions for S_{WA} estimates within +/-5% of S_{WC} (model W3).....	234
Figure 4.25. Sensitivity analysis (model W4).....	237
Figure 4.26. Parameter distributions, sensitivity analysis (model W4).....	239
Figure 4.27. Parameter trade-offs (model W4).....	240
Figure 4.28. Optimised BSR parameters (model W4).....	241
Figure 4.29. Optimised Haynesville parameters (model W4).....	242
Figure 4.30. Individual core sample optimised parameters (model W4).....	244
Figure 4.31. Optimised parameter distributions for S_{WA} within +/-5% of S_{WC} (model W4)	245
Figure 4.32. Totalled parameter distributions for S_{WA} estimates within +/-5% of S_{WC} (model W4).....	246
Figure 5.1. Comparison of mineralogical / petrophysical variability.....	252
Figure 5.2. Average residual MAE (model W4) vs. key petrophysical inputs.....	253
Figure 5.3. R_t vs. V_{Clay} and heteroskedasity.....	255

Figure 5.4. R_t vs. V_{Clay} and clay fractions	256
Figure 5.5. k vs. V_{Clay} and heteroskedasity	257
Figure 5.6. S_{wC} vs. ϕ_{tC}	258
Figure 5.7. BVW vs. ϕ_{tC}	261
Figure 5.8. Matrix permeability (k) vs. ϕ_{tC} (coloured by BVW).....	262
Figure 5.9: Matrix permeability (k) vs. ϕ_{tC} (coloured by chlorite)	262
Figure 5.10. BVW vs. R_t	263
Figure 5.11. Schematic illustration of the effects of compaction on pore fluid salinity	269
Figure 5.12. Key change in petrophysical behaviour with V_{Clay}	272
Figure 5.13. Composite core summary panels.	279
Figure 5.14. Summary of available thin section imagery	280
Figure 5.15. Thin section images: BSR well 10.....	282
Figure 5.16. Thin section images: HY well 8	283
Figure D.1. Example petrophysical workflow	309

Notation index

The following is a list of the symbols and abbreviations used in the text, including symbol\abbreviation, description and, where relevant, unit.

α	Multiplier in Archie's equation (often referred to as tortuosity)	unitless
AE	Absolute error	parent unit
BSR	Bossier Shale formation	-
BVW	Bulk volume water	vol. % or frac.
BVW_M	Bulk volume modelled from $\phi_{tC} - S_{wA}$ relationships	vol. % or frac.
CAL	Calliper tool	inches
CLB	Core Laboratories	-
CV	Co-efficient of variation	-
GIP	Gas in place	tcf
GOM	Gulf of Mexico	-
GR	Wireline gamma ray response	gAPI
GRC	Core spectral gamma response	gAPI
GRG	Generalised reduced gradient	-
HI	Hydrogen Index	-
HY	Haynesville Shale formation	-
IQR	Inter quartile range	parent unit
k	GRI core matrix permeability	mD
K	Potassium	wt. %
m	Porosity exponent	unitless
m^*	$m=n$	unitless

MAD	Mean absolute deviation	parent unit
MAE	Mean absolute error	parent unit
MFS	Maximum flooding surface	-
n	Saturation exponent	unitless
ϕ	Porosity	vol. % or frac.
ϕ_d	Porosity calculated from density tool response	vol. % or frac.
ϕ_{dClay}	The density porosity of clay	vol. % or frac.
PEF	Photoelectric factor	barns/cm ³
ϕ_g	Gas filled porosity	vol. % or frac.
ϕ_M	Porosity modelled from $\rho_b - \phi_{tC}$ relationships	vol. % or frac.
ϕ_n	Neutron porosity tool response	vol. % or frac.
ϕ_{nClay}	The neutron porosity of clay	vol. % or frac.
ϕ_{tC}	GRI core total porosity	vol. % or frac.
Q_1	Quarter 1; the 25 th percentile	parent unit
Q_3	Quarter 3; the 75 th percentile	parent unit
RAPID	Reservoirs applied petrophysical integrated data	-
R_{Clay}	Resistivity of a of clay	$\Omega.m$
RE	Residual error	parent uint
RMSE	Root mean squared error	parent unit
Ro	Measured vitrinite reflectance	%
R_o	Resistivity of a fully water saturated rock	$\Omega.m$
R_t	Resistivity tool response (deep/true)	$\Omega.m$
R_w	Fluid resistivity	$\Omega.m$
R_{we}	Bulk fluid resistivity	$\Omega.m$
S1	Free hydrocarbons	mg/mg
S2	Hydrocarbons generated by thermal cracking of kerogen	mg/mg
S3	CO ₂ produced during kerogen pyrolysis	mg/mg
S_g	Gas saturation	vol. % or frac.
S_{gC}	GRI core gas saturation	vol. % or frac.
S_{oC}	GRI core oil saturation	vol. % or frac.
S_w	Water saturation	vol. % or frac.
S_{wA}	Water saturation calculated from Archie's equation	vol. % or frac.
S_{wC}	GRI core water saturation	vol. % or frac.

S_{WR}	Water saturation modelled using regressed Archie exponents	vol. % or frac.
Th	Thorium	ppm
T_{max}	Max. temperature of hydrocarbon release from kerogen	°C
TOC	Total organic matter	wt. % or frac.
U	Uranium	ppm
u	Mean	parent unit
V_{Clay_GR}	Clay volume calculated from the gamma ray tool response	vol. % or frac.
V_{Clay_nd}	Clay volume calculated from neutron-density tool relationships	vol. % or frac.
$V_{Mineral}$	XRD mineral volume (V_{Clay} , $V_{Calcite}$)	vol. % or frac.
VOI	Volume of investigation	-
W1	One dimensional optimisation model; one parameter (R_{we}) in Archie's equation is optimised.	-
W2	One dimensional optimisation model; one parameter (m^*) in Archie's equation is optimised.	-
W3	Two dimensional optimisation model; two parameters (R_{we} and m^*) in Archie's equation is optimised.	-
W4	Three dimensional optimisation model; three parameters (R_{we} , m , and n) in Archie's equation is optimised.	-
$W_{Mineral}$	XRD mineral weight (W_{Clay} , $W_{Calcite}$)	wt. % or frac.
ρ_b	Density tool response	g/cc
ρ_{bc}	GRI core bulk density	g/cc
ρ_f	Fluid density	g/cc
$\rho_{Kerogen}$	Organic matter density	g/cc
ρ_{ma}	Matrix density	g/cc
ρ_{ma_CLB}	Matrix density calculated by CLB	g/cc
ρ_{maC}	GRI core matrix density	g/cc
$\rho_{Mineral}$	Mineral density	g/cc
σ	Standard deviation	parent unit

Chapter 1

Introduction

The following chapter introduces the thesis. It provides background information outlining the industry and academic interest in furthering our understanding of the petrophysical properties of shale gas reservoirs. It describes the key aims and objectives of the research undertaken and outlines the thesis chapter structure. This chapter is split into the following sections:

- 1.1 *Background*
- 1.2 *Aims and objectives*
- 1.3 *Thesis structure*

All scientific notation and mathematical symbols used in the thesis are summarised in the notation index (page x), with ancillary material located in the appendices.

1.1 Background

Over recent decades rising global energy demand and advances in our geological understanding and technical capability have fuelled increasing investment in 'unconventional' shale gas reservoirs. Improved accessibility, coupled with the globally widespread abundance of shale (also referred to as mudstone), which comprises 45 to 65% of the stratigraphic record (Macquaker and Adams, 2003; Wignall, 1994), has generated a surge in shale gas exploration, production and hopes for improved domestic energy security. Despite this however, the petrophysical properties of shale remain something of an enigma, and we are yet to fully understand how shale geological properties (mineralogy and fabric) influence shale petrophysics. This lack of understanding generates uncertainty in formation evaluation methods leading to inaccuracy in resource potential and gas in place (GIP) estimates. For instance, the British Geological Survey estimate the GIP for central Britain to be between 822 tcf to 2,281 tcf of technically recoverable reserves (Andrews, 2013). To place this in perspective, if just 0.1% of the upper GIP estimate is proven to be economically recoverable, it would equate to 2.3 years of domestic UK gas consumption (based on a 2009 estimate of UK gas consumption [100 bcm] (Yeo, 2011)). The economic drive to improve our petrophysical understanding of shale gas systems is therefore substantial.

One of the most significant challenges to the petrophysical evaluation of shale gas systems can be attributed to the conductivity behaviour of clay minerals and entrained clay bound waters. This is compounded by centimetre to sub-millimetre vertical and lateral heterogeneity in formation composition and structure, where despite major variation in formation geological and therefore petrophysical properties, we remain routinely reliant on conventional, so called 'shaly sand' resistivity methods for the determination of water saturation (S_w), and hence the free gas saturation (S_g) in shale gas plays. The application of resistivity based methods is the subject of continuing debate, and there is often significant uncertainty in both how they are applied and the saturation estimates they produce. This is partly a consequence of the historical view that *"the quantification of the behaviour of shale conductivity....has only limited*

geological significance" (Rider 1986). A view that has contributed to a separation in our geological understanding of shale gas systems and the petrophysical rationale and methods employed to evaluate them.

S_w is most commonly derived using wireline logs based on Archie's equation, which relates the electrical resistivity of a rock (R_t) and its saturating fluid (R_w) to its porosity (ϕ) and S_w as developed for clean, clay free, siliciclastic rocks (Archie 1942):

$$S_w = \left(\frac{aR_w}{\phi_t^m R_t} \right)^{\frac{1}{n}} \quad (1.1)$$

where m is the porosity exponent, n is the saturation exponent and a is the tortuosity exponent. In reservoirs containing a significant clay component, numerous derivatives of Archie's equation called 'shaly sand' methods have been developed, and attempt to compensate equation 1.1 for the electrical conductivity of shale (of which clay is a primary component), incorporating factors related to shale distribution and additional terms such as clay bound (R_{Clay}) and clay free fluid (R_w) resistivities. When applied in shale gas systems, shaly sand methods therefore incorporate additional assumptions (clay type/distribution style, R_{Clay} , R_w) within a highly complex and heterogeneous petrophysical system. In addition, Archie parameters (a , m , n), which can be routinely derived in conventional reservoirs, are also difficult to determine, as obtaining a water sample, or carrying out laboratory experiments on recovered core is often technically impractical (Bust et al., 2011). As a consequence, the efficacy of complex shaly sand evaluation methods is questionable, and petrophysicists increasingly rely on optimised approaches using Archie's Equation. Where, with little or no information driving the selection of Archie parameters (a , m , n and R_w), parameter selection is data led and reliant on pseudo-Archie parameters modified to generate Archie S_w estimates (S_{wA}) that provide a good match to 'as-received' Dean Stark core water saturations (S_{wC}) (Bust et al., 2011; D. S. Chen et al., 1995; H. C. Chen et al., 1995; Chen et al., 2002; Cluff, 2012; Maute et al., 1992; Worthington, 2011a, 2011b, 2009, 2007). In other words, Archie parameters in shale gas systems are typically determined by core-wireline integration and calibration, with limited understanding of the geological

implications and controls on variations in pseudo Archie parameters and formation petrophysical properties. This thesis aims to investigate the influence of geological factors, including formation composition, heterogeneity and structure on those petrophysical properties that contribute to S_{wA} estimation by electrical methods in shale gas systems.

1.2 Aims and objectives

The influence of geological factors, including formation composition, heterogeneity and structure, on those petrophysical properties that contribute to S_{wA} estimation by electrical methods in shale gas systems are poorly understood. Through developing this understanding, the overall aim of this study is to contribute towards a geologically reasoned and informed approach to Archie parameter selection, advancing our predictive capability where petrophysical properties may be linked to geological observations in the absence of core data.

This study focuses on core and wireline data for the Bossier (BSR) and Haynesville (HY) Shale Formations, commercial shale gas plays in the northern Gulf of Mexico (GOM) basin. The approach taken has been to develop a series of numerical models to optimise and test the response and variation in residual error between core S_w (S_{wC}) data and calculated S_{wA} values generated using a generalised Archie type equation (see section 4.1) for a wide range of Archie parameter inputs. The results of this analysis, in combination with the available core and wireline data, are then used to address the following research questions:

- I. The variability in optimiser model output must be linked to the heterogeneity and inter-relationships of the petrophysical inputs (ϕ_{tC} , R_t , S_{wC}). In turn, the petrophysical inputs are an expression of the interaction and distribution of formation mineral and fluid components as determined by depositional and diagenetic processes.
 - a. *How does variability in the error of S_w model outputs for BSR and HY data link to the variability in underlying formation mineralogical and petrophysical properties as represented within the wireline and core data?*
 - b. *What are the principle geological controls on model accuracy?*
- II. The modelled results are based on a modified Archie's equation (equation 4.1), for which the principal underlying petrophysical mechanism is the negative relationship between the volume of the saturating electrolyte and formation

resistivity (Archie, 1942). Clay minerals are known to affect this relationship by reducing the resistivity, or inversely, by providing a source of excess conductivity (Hill and Milburn, 1956; Patnode and Wyllie, 1950; Winsauer and McCardell, 1953; Wyllie and Southwick, 1954). If uncorrected, this can overestimate S_w and contribute to an undervaluation of the reservoir.

- a. *How does core data for clay volume and the volume of the saturating electrolyte (BVW) relate to measured R_t , what is the geological basis for these relationships, and are they reflected by predicted Archie parameters values (m , n and R_w)?*
- III. The efficacy of a core calibrated optimised Archie approach and thus the geological validity of the Archie parameter values generated has not been tested or been given a geological rationale in the literature.
- a. *What are the mechanics of an optimised Archie approach, what controls the value of generated Archie parameters, and what can we infer of their validity from sensitivity analyses and parameter trade-offs?*
 - b. *How do modelled Archie parameter values compare with those predicted by other studies?*

1.2.1 Additional work undertaken

Additional work undertaken as part of this project included limited use of Haynesville core material for a single well. Analysis included thin section imaging and the use of a multi-sensor core logger which generated petrophysical (density, magnetic susceptibility, natural gamma response and resistivity) and geochemical (infra-red spectrophotometry) data. This work is briefly discussed in Appendix C, but due to data quality issues, did not contribute to and is not included within the body of this thesis or conclusions.

1.3 Thesis structure

This thesis begins with a review of the pertinent literature in Chapter 2. Chapter 3 builds on this review and outlines Bossier (BSR) and Haynesville (HY) reservoir geology, mineralogical and petrophysical properties. The methodology and analytical results are presented in Chapter 4, followed by a discussion of the results and mineralogical / petrophysical relationships in Chapter 5. Finally, the conclusions, as linked to the original thesis objectives, are presented in Chapter 6, followed by suggestions for further work. A brief description of each chapter is provided below:

Chapter 2: *The sedimentology, petrophysical properties and evaluation of shale gas reservoirs.* This literature review is split into four parts. The first introduces key concepts in mudstone sedimentology, including composition, sediment fabric, depositional processes and sequence stratigraphy. The second and third sections outline key wireline and core measurements used in this study, with an emphasis placed on mudstone mineralogical influences on measured values. The fourth and final section presents the concepts, principles and uncertainties of Archie and shaly sand methods for deriving water saturation.

Chapter 3: *The geological setting, mineralogy and petrophysical properties of the Bossier and Haynesville Shale Formations.* This chapter introduces and characterises the data used for analysis. It provides a brief geological overview of the study formations, including stratigraphy and influence of paleotopography on deposition. In addition, it outlines the data available for study, the rationale for data selection, quality control, wireline-core integration, formation zoning and applied data corrections. It also outlines basin mineralogical and petrophysical trends, and builds on Chapter 2 by emphasising uncertainties in the petrophysical evaluation of shale gas reservoirs. Uncertainty in selected kerogen density and knock-on implications for XRD mineral volumes are also explored.

Chapter 4: *Unconventional applications of Archie's equation: sensitivity and error analysis.* This chapter outlines the analytical methodology for a series of numerical models and sensitivity analyses of an Archie type saturation equation. It describes the analytical results and is presented in order of model dimensionality, i.e., the results of a one dimensional model are presented first, followed by the results of a two dimensional and finally, by the results of a three dimensional model. In this context, the number of dimensions refers to the number of Archie parameters optimised within each of the numerical models.

Chapter 5: *Unconventional applications of Archie's equation: does geology matter?* This chapter discusses the results presented in chapter 4 and is split into four parts. The first discusses the impact of mineralogical heterogeneity on formation petrophysical properties and petrophysical model results. The second evaluates the relationships between formation water, formation resistivity and clay volume. The third summarises key data relationships and qualitatively links variations in formation fabric with model petrophysical results. The fourth and final section discusses model biases and the generated pseudo-Archie parameters.

Chapter 6: *Conclusions.* This chapter presents the conclusions of the previous chapters with regard to the original objectives and outlines the scope for additional work.

Chapter 2

The sedimentology, petrophysical properties and evaluation of shale gas reservoirs

This chapter provides a review of the pertinent literature and is divided into five sections:

- 2.1 *The sedimentology of shale gas reservoirs*: outlines the composition, classification, fabric, depositional processes and sequence stratigraphy of shale gas reservoirs.
- 2.2 *Wireline log responses in shale gas reservoirs*: outlines wireline tool physics (gamma ray, density, neutron porosity and resistivity) and their response in shale gas reservoirs.
- 2.3 *Core porosity and saturation in shale gas reservoirs*: outlines laboratory methodology for the determination of porosity and water saturation and shale/mudstone effects.
- 2.4 *The evaluation of water saturation from wireline logs in shale gas reservoirs*: outlines Archie and shaly sand evaluation concepts for S_w derivation including uncertainties in parameter selection and model validity.
- 2.5 *Summary and conclusions*.

2.1 The sedimentology of shale gas reservoirs

Shale gas reservoirs are a type of ‘unconventional resource,’ an umbrella term without a universally agreed definition that includes shale oil, coal bed methane, gas hydrates and tight gas reservoirs (Etherington and Ritter, 2007; Haskett and Brown, 2005). Etherington and McDonald (2004) define an unconventional resources as one ‘*that cannot be produced at economic flow rates without assistance from massive stimulation treatments.*’ Whereas Stabell (2005) describes unconventional resources as ‘*large single accumulations that cannot be counted and analysed as discrete entities.*’ Sondergeld et al. (2010) defines unconventional resource systems as ‘*those which have a sorbed gas component,*’ a definition that excludes tight gas reservoirs. These definitions each highlight problematic aspects of shale gas systems, formations which are challenging to evaluate petrophysically owing to significant heterogeneity, low matrix permeabilities and porosities, and relatively high clay bound water, kerogen and adsorbed gas contents (Bohacs et al., 2013; Singh et al., 2013; Wu and Aguilera, 2013; Yu et al., 2013). The following sections explore how shale composition and mineralogic distribution, as shaped by sedimentological processes, contribute to the genesis of shale gas systems and their petrophysical properties (Alpin and MacQuaker, 2010).

2.1.1 What is shale?

Shale is one of a number of terms, including mudrock and mudstone, used to describe abundant fine-grained sedimentary rocks that represent up to 70% of the stratigraphic record (Alpin and MacQuaker, 2010; Macquaker and Adams, 2003; Tucker, 1982; Wignall, 1994). The preferred umbrella term for these rocks is mudstone (Bohacs et al., 2013; Macquaker and Adams, 2003), where shale is commonly regarded as a dark, organic rich fissile variety (Tucker, 1982; Wignall, 1994). Despite the preferred nomenclature however, the terms shale and mudstone remain interchangeable in common vernacular and industry related articles, a trend continued in the following text.

2.1.2 Composition and classification

A shale, or mudstone, is defined as a clastic sedimentary rock where over 50% of the grains have a particle size below 62 μm , and are considered organic rich when the total organic carbon (TOC) content exceeds 2 wt.% (Alpin and MacQuaker, 2010; Craig, 2004; Gamero Diaz et al., 2013). Historically, despite their importance as both seal and source rocks for conventional reservoirs, attempts to develop a mineral based classification scheme for mudstones are relatively recent (Allix et al., 2010; Gamero Diaz et al., 2013; Macquaker and Adams, 2003). This in part reflects the homogenous appearance of mudstones at outcrop and a legacy of classification based on informal terms relating to colour and texture (Boggs, 2009; Tucker, 1982; Wignall, 1994). The relatively recent shale gas boom has however highlighted the complexity and heterogeneity of mudstone structure and composition. With studies highlighting significant vertical and lateral heterogeneity in mineralogic and organic components at a range of scales (often less than 10mm) within vertically continuous formations hundreds of meters thick (Bohacs et al., 2013, 2005; Macquaker et al., 2010b; Passey et al., 2010; Suarez-Rivera et al., 2006). The classification scheme (Figure 2.1) proposed by Macquaker and Adams (2003), was intended to aid the interpretation of 'apparently homogenous shales' by reducing our reliance on the use of characteristics such as fissility, TOC, and other proxy variables (Macquaker and Adams, 2003; Schieber and Sethi, 1998). This aims to utilise grain size, origin and mineralogy to help tie heterogeneity in mudstone structure and composition back to their depositional processes and environment, stacking patterns and a sequence stratigraphic framework (Abouelresh and Slatt, 2012; Bohacs et al., 2005; Gamero Diaz et al., 2013; Macquaker et al., 2007; Passey et al., 2010). This has been advanced recently by Gamero Diaz et al. (2013), where the limits expressed in Figure 2.1 are used to create a lithology log based on XRD calibrated geochemical wireline data to help identify productive shale zones.

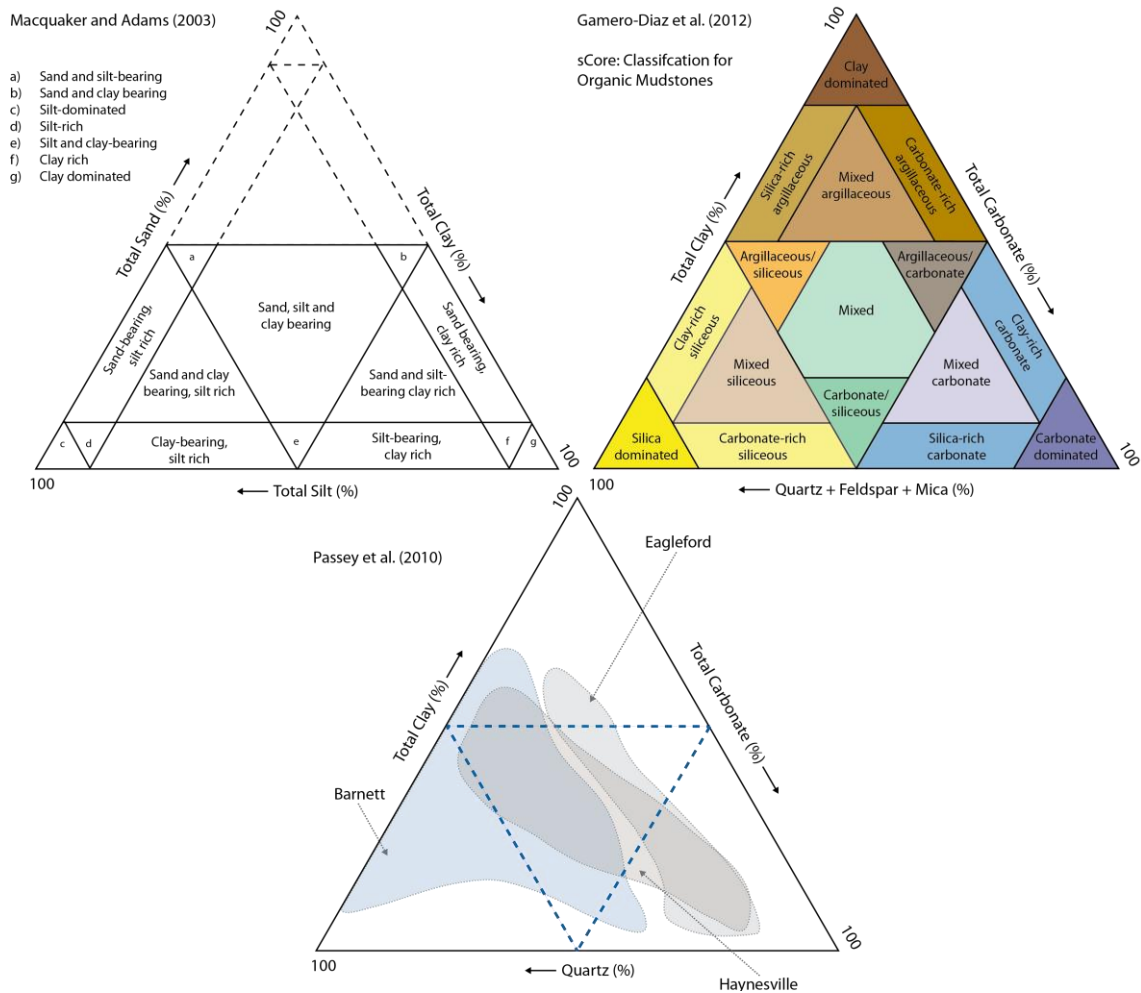


Figure 2.1. Mudstone classification

Mudstone classification schemes (adapted and redrawn from Gamero Diaz et al. (2013), Macquaker and Adams (2003) and Passey et al.(2010)

The classification system proposed by Gamero Diaz et al. (2013) permits stratigraphic correlation and parasequence identification with reduced reliance on the petrographic analysis of often limited core material. Though it remains to be seen as to whether uptake in industry or academia will be significant.

More commonly, the mineral components of a mudstone are represented in basic ternary plots (e.g. Adiguna, 2012; Chalmers et al., 2012; Gupta et al., 2012) so as to inform formation geomechanical models. This refers to the brittleness of shale formations, which are less plastic and more amenable to hydraulic fracture treatments when containing less than 50% clay (Adiguna, 2012; Glorioso and Rattia, 2012; Jarvie et al., 2007). This is reflected in Figure 2.1 and the USA generally, where most commercial shale plays fall below the 50% clay line (Passey et al., 2010). The determination of a formations brittleness index (BI) is part of typical petrophysical workflows, where

productive zones are defined based on petrophysical properties and modelled mineralogy (Adiguna, 2012; Popielski et al., 2012), with zones typically characterised by organic richness, log proxies, or structural features (Hammes, 2009; Loucks and Ruppel, 2007).

To give an indication of typical shale mineralogical composition, XRD data (in wt. %) is presented in Table 2.1 after Boggs (2009). These data are not specific to currently producing organic rich shales, and it should be noted that, as the defining characteristic of a mudstone is the predominance of grains below 62 μm and as commercially producing shales generally contain less than 50% clay, there is significant potential for compositional variation.

	Clay Minerals	Quartz	K feldspar	Plag feldspar	Calcite	Dolomite	Siderite	Pyrite	Other minerals	Organic carbon
<i>Min</i>	17.0	14.6	0.4	0.7	1.4	0.5	0.1	1.6	1.0	0.2
<i>Max</i>	57.2	53.5	12.4	11.9	14.6	7.9	5.1	10.9	4.0	10.9
<i>Mean</i>	39.7	37.5	3.0	4.3	5.4	2.5	1.1	3.2	0.4	3.5

Table 2.1. Average and range in mudstone compositions (wt. %)

Range in mudstone compositions based on XRD analysis of 125 samples of Quaternary to Ordovician age after Boggs (2009).

2.1.3 Sediment fabric and depositional processes

The fabric of a rock can be defined as the physical arrangement of its constituent particles and minerals and is the sum of its textural and structural features (Allaby, 2008; Schieber, 1978). Texture can be described as the size and shape of particles and their interrelationships, and structure refers to forms generated by sedimentary processes and contemporaneous biological activity (Allaby, 2008; Kearey, 2001). Preserved mudstone fabric therefore records the physical and chemical processes of mud deposition, bioturbation and burial history (Ghadeer and Macquaker, 2011; Schieber et al., 2007).

Texturally, mudstones are commonly associated with the preferred orientation of clay minerals that results from the compaction, dewatering and alignment of clay flakes (Tucker, 1982). The development of this characteristic texture occurs due to clay

physiochemical properties (see section 2.3.3.1) and in response to depositional processes and environmental conditions. Unlike larger granular particles of silt, which may be transported in suspension, sliding, rolling and saltation, clay and clay sized particles, which require minimal energy to remain in suspension, can be transported over long distances (Potter, 2005). These physical properties, combined with the tendency for clay minerals to have a negative surface charge, gives rise to clay attributes such as cohesion and plasticity that result in complex colloidal flocculation processes (Moon and Hurst, 1984; Smith, 1990). This refers to a process of clay particles moving randomly in suspension (Brownian motion), which, when in close proximity, become subject to attractive Van der Waals forces and repulsive electrostatic inter particle forces. The repulsive forces are generally eliminated in marine environments as sodium cations bind with and neutralise the negative clay mineral surface charge. This allows the attractive forces to precipitate the development of clay flocs (Boggs, 2009; Craig, 2004; Das, 2008; Leeder, 1999; Reeves et al., 2006a; Reynolds and Gorsline, 1992).

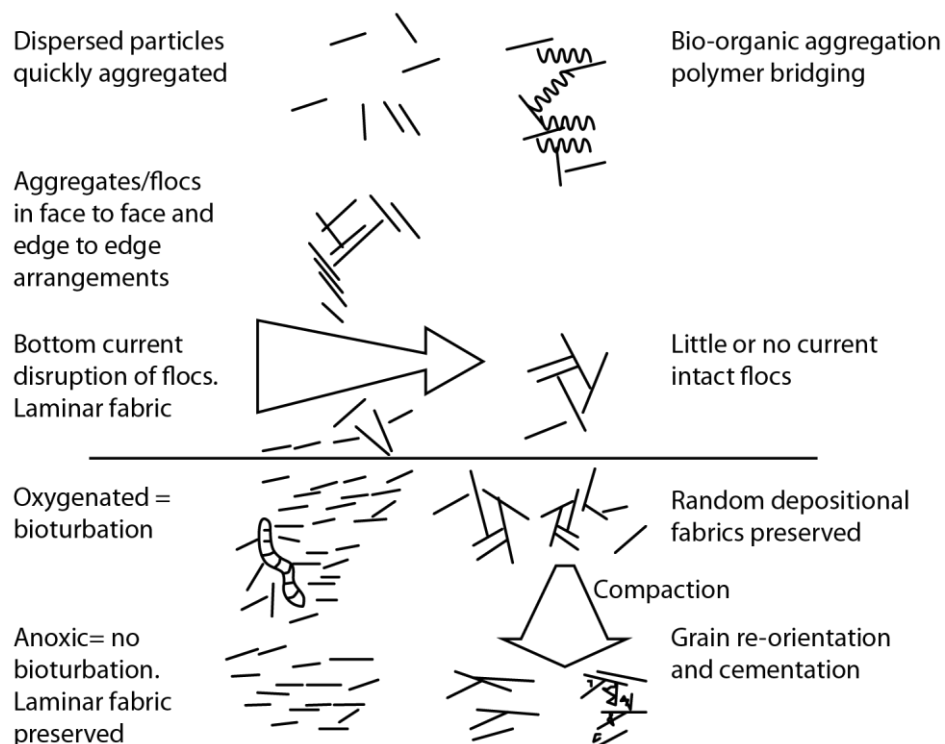


Figure 2.2. Mudstone texture as determined by sedimentary and diagenetic processes

Schematic representation of sedimentary and diagenetic influences on the development of mudstone texture (redrawn from Reeves et al., 2006b).

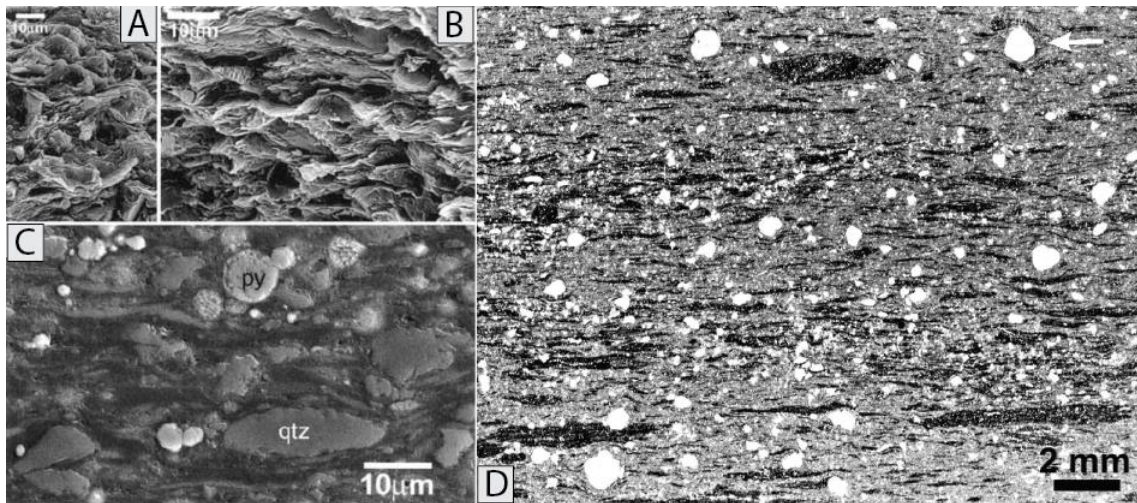


Figure 2.3. Example mudstone textures

(A) SEM image of bioturbated mudstone; (B) SEM image of aligned clay minerals; (C) BSE image of carbonaceous shale, note horizontal alignment of sediment grains (Schieber, 1978); (D) Shale with microbial-mat fragments (dark coloured deformed particles) and quartz grains (clear) in matrix of grey shale. Arrow indicates differential compaction around quartz grain (Schieber et al., 2010).

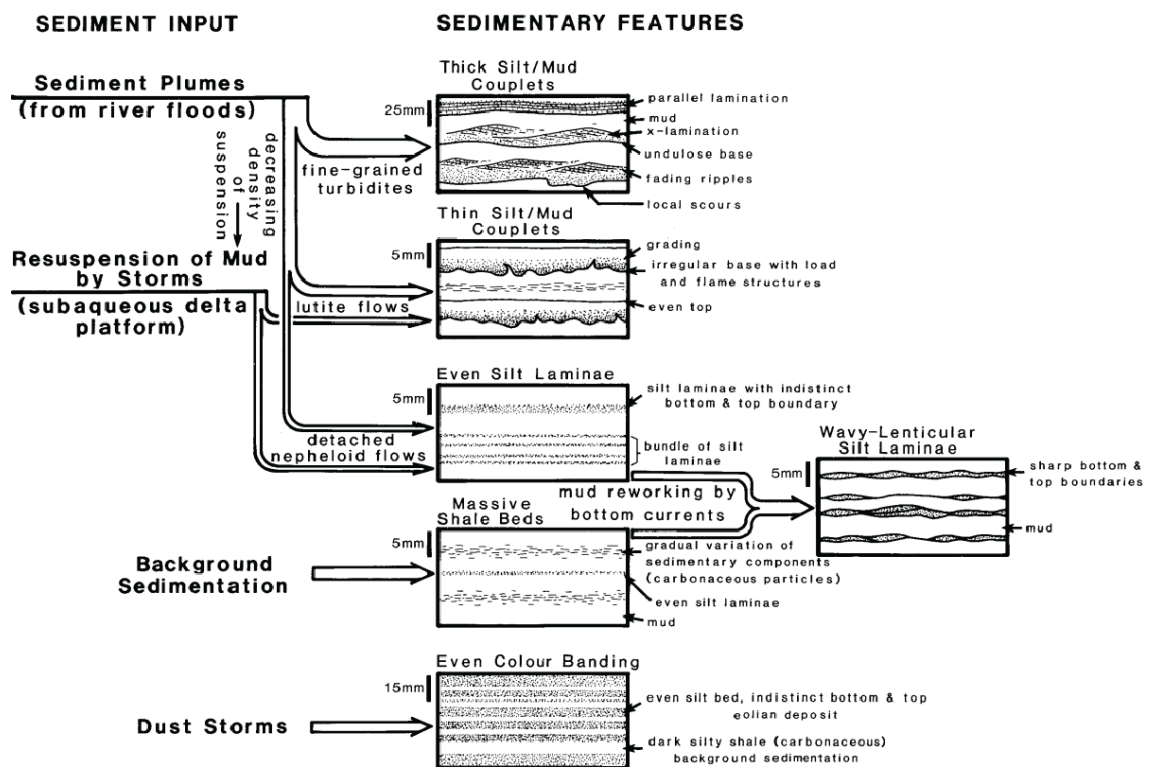


Figure 2.4. Mudstone sedimentary structures and inferred processes

Sedimentary structures and inferred depositional processes in fine-grained Precambrian Belt Series of Montana (Schieber, 1990).

In addition, the relative proportion of coarse (silt) to fine (clay) particles may exert a further control on sediment texture. For instance, silt grains are not compressible relative to the clay component, and during compaction reorient, sink into and deform

the surrounding clay matrix. With progressive burial this can distort and diminish any distinct clay flocculation style within muds at the water sediment interface (Reynolds and Gorsline, 1992). Where silt particles provide grain support, clay floccs may be preserved and anisotropy reduced (Fawad et al., 2010). In addition, the differential compaction of clay minerals around silt grains (Figure 2.3; image B) may enhance inter-particle porosity in the clay matrix adjacent to silt grains (Day-Stirrat et al., 2012; Schieber, 2010; Schieber et al., 2010).

The complexities of features inherent to mudstone fabric are often overlooked. This is largely due to the fine scale nature of mudstone structural sedimentary features, but is in part attributable to the general assumption that mud is deposited continuously, settling from suspension in quiet low energy bottom-water conditions to form characteristic parallel laminae (Macquaker and Bohacs, 2007). On closer inspection however, mudstones often reveal a wealth of sedimentary features and facies types that allow for an interpretation of their depositional environment (Schieber, 1990). Schieber (1978) lists a range of lamina styles (discontinuous, lenticular, wrinkled) that reflect either quiet settling, bottom-current re-working or the formation of microbial mats. In addition, internal lamina texture and structures can be quite variable including: grading, random and preferred clay orientation and sharp basal and top contacts. These fabrics (partly summarised in Figure 2.4) may have been generated by a variety of sedimentary processes including: event sedimentation (floods, storms, turbidity currents), flocculation, settling from suspension, current flow and erosion/reworking after deposition (Macquaker et al., 2007; Schieber, 1990, 1978).

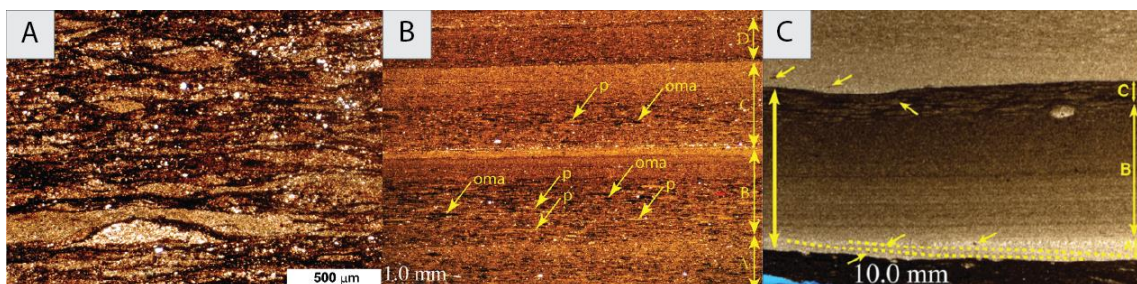


Figure 2.5. Examples of mudstone lamina structure

(A) Compacted rip up clasts; lenticular laminated Proterozoic shale that shows well defined compressed clasts which taper and pinch out laterally (Schieber et al., 2010, 2007). **(B)** Stacked succession of sharp-based, grading thin-bedded (labeled A to D) clay-size-rich mudstones collected from Ravenscar, containing 3.5% TOC. The basal lamina sets within the individual beds exhibit discontinuous wavy geometries and contain abundant

pellets (arrowed p) as well as organomineralic aggregates (arrowed oma). Gradationally overlying the basal laminaset are homogenised lamina. Note that bed C has a discontinuous silt lag at its base (Macquaker et al., 2010b). **(C)** Section collected from the Mowry Shale; stacked succession of normally graded thin beds, each with an erosional base. The basal laminaset (unit A) contain silt-sized clay-aggregate intraclasts (arrowed) and curved laminae (dotted lines) that lap down. This basal laminaset is abruptly overlain by thin intercalated lamina (unit B) composed of clay and silt that subtly grades upward and is capped by (unit C) a burrowed clay drape (Macquaker et al., 2010a).

Further investigation continues to expand the range of depositional processes that determine complex mudstone fabrics which are often simply considered as laminated. For instance, it has been demonstrated that a laminated appearance can be an artefact of bioturbation due to burrow compaction (Schieber, 1999). In addition, recent flume tank experiments have demonstrated higher than expected bedload transport velocities capable of transporting and depositing sand, with deposited clay flocs developing ripples that appear laminated following compaction (Schieber et al., 2007). Flume tank experiments (Schieber et al., 2010) have also reproduced typical lenticular mudstone fabrics, formed by eroding water rich muds to create centimetre sized 'rip up clasts' that can be transported for tens of kilometres before being deposited and compacted to produce a lenticular fabric. Additional structures in the Kimmeridge Clay Formation suggest episodic organic enrichment, where algal blooms and intense showers of marine snow are thought to have generated graded thin beds (<10mm thick) with erosional based (Figure 2.5 (B)) (Macquaker et al., 2010b). Graded thin beds (Figure 2.5 (C)) in the Mowry Shale have also been interpreted as resulting from wave-enhanced sediment-gravity flows (WESGF), which are believed to be widespread, suggesting higher energy mud transportation, re-working and deposition in deep water conditions (Aplin and Macquaker, 2011; Macquaker et al., 2010a).

It is clear that the detailed examination of mudstones continues to reveal significant variability and heterogeneity in fabric and mineralogy at very fine scales. An improved understanding of these processes is crucial, as formation fabric can exert significant control on physical properties such as porosity, permeability, stress/strain behaviour and therefore reservoir quality (Ambrose et al., 2010; Bustin et al., 2008; Dewhurst et al., 1999; Harrington and Horseman, 1999; Hart et al., 2013; Ozkan et al., 2011; Simm, 2007; Sondergeld et al., 2010). For instance, permeability, which strongly influences the production profile of shale gas wells, is thought to be largely dependent on formation fabric (Bustin et al., 2008). With higher permeability measured parallel to

and lower permeability measured orthogonal to laminar fabrics (Chalmers et al., 2012; Kwon et al., 2004). It has also been shown experimentally by mercury porosimetry and adsorption isotherm analysis, that whilst pore and pore throat sizes may be similar in anisotropic and massive shales alike, that anisotropic shales have significantly higher pore surface areas (Clarkson et al., 2012; Howard, 1991), with pores becoming elongated with increased vertical stress (Day-Stirrat et al., 2012). Studies of the Monterey shale have also linked bioturbation to enhanced permeability and reduced anisotropy, where high water contents and high permeability are suggestive of mobile water zones in bioturbated fabrics (Wood, 2012). This is supported by computer modelling of burrowed fabrics that suggest permeable burrow networks can connect otherwise hydraulically isolated strata and increase permeability (La Croix et al., 2012). As such, depositional fabrics can significantly influence later burial and diagenetic processes and thus permeability and porosity distributions (La Croix et al., 2012; Loucks et al., 2012; Ozkan et al., 2011), though burial diagenesis may overprint depositional fabrics (Bauluz et al., 2012). For instance, studies of the Barnett Shale have shown that compaction and diagenetic overprinting can often obscure any links between fabric, composition and petrophysical properties (Milliken et al., 2012). On balance however, it is clear that sediment fabric (primary or secondary) determines the intrinsic geometry of the pore-channels, forming a primary control on formation electrical properties (Lauer-Leredde et al., 1998; Winsauer and McCardell, 1953). An improved understanding of these processes is therefore crucial to the accurate interpretation of log properties.

2.1.4 Sequence stratigraphy

The sedimentary depositional processes discussed above are moderated by regional and global environmental factors (tides, storms, eutrophic events, regional and eustatic sea level change), depositing sediments that often stack systematically and vertically into larger packages that can be recognised laterally within a basin using sequence stratigraphic techniques (Abouelresh and Slatt, 2011; Aplin and MacQuaker, 2010; Macquaker et al., 2014; Passey et al., 2010; Slatt, 2011). These genetically related sequences are often recognisable in the wireline-log response, particularly in

response to the gamma ray tool (see section 2.2.1 for a discussion of the gamma response in shale systems). This typically manifests as a sequence with an upward increasing or decreasing gamma response, termed a ‘gamma ray parasequence’ (Slatt and Rodriguez, 2012), which is generally characterized by an overall gradation in grain size and bounded by correlative marine flooding surfaces (Abouelresh and Slatt, 2011; Leeder, 1999; Slatt, 2011; Wagoner et al., 1990). Such sequences are widely recognised in shale systems, including the Barnett Shale (Abouelresh and Slatt, 2011), the Woodford Shale (Romero and Philp, 2012), the Haynesville Shale (Hammes, 2012, 2009), the Bakken Shale (Angulo and Buatois, 2012) and many others.

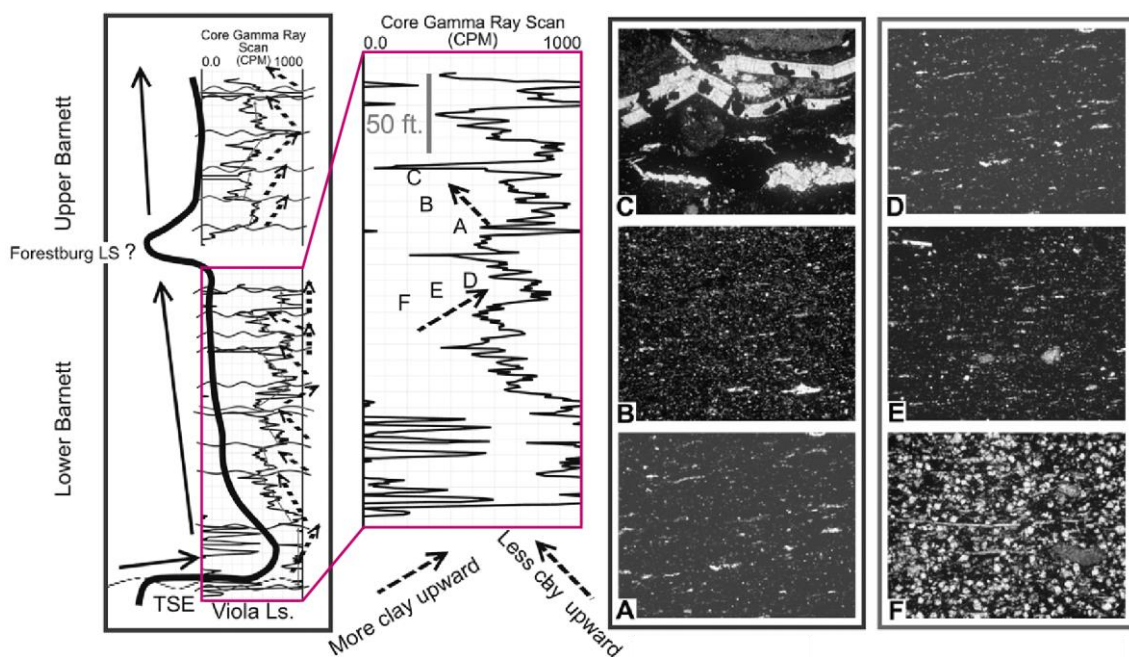


Figure 2.6. Stratigraphic profile and core gamma trends in the Barnett Shale

(Left) Complete core gamma-ray scan of the Barnett Shale in the northern Fort Worth Basin. The solid black curve and solid arrows correspond with a 2nd order stratigraphic sequence for the entire Barnett Shale. The smaller dashed arrows (to the right of the gamma ray curve) highlight several 3rd order sequences. (Centre) Expanded gamma ray scan highlighting two ‘gamma ray parasequences’ linked to thin section photomicrographs (Right), one decreasing up (A, B, C) and one increasing up (F, E, D). The decreasing up gamma sequence shows a progression from: (A) a lower clay-organic rich lithofacies to, (B) a more quartzose-clay lithofacie to, (C) a shelly-carbonate lithofacies. The decreasing up gamma sequence shows a progression from: (F) a lower dolomitic mudstone to, (E) a calcareous mudstone to, (D) a clay-organic rich lithofacies (adapted from Slatt and Rodriguez, 2012).

An example is given in Figure 2.6 after Slatt and Rodriguez (2012) for the Barnett Shale. This includes a core gamma ray response that corresponds with a 2nd order stratigraphic sequence overprinting ‘increasing up’ and ‘decreasing up’ 3rd order ‘gamma ray parasequences.’ The progressive change in fabric is depicted in the thin

section photomicrographs in Figure 2.6, where for the ‘increasing up’ gamma ray response (F, E, D), clay content increases. This is interpreted as shoreline retreat and is followed by a flooding surface and the onset of a ‘decreasing up’ gamma ray response (A, B, C) where the opposite progression is noted; clay content and the gamma response reduce as coarser grained clastics become more abundant as the shoreline advances.

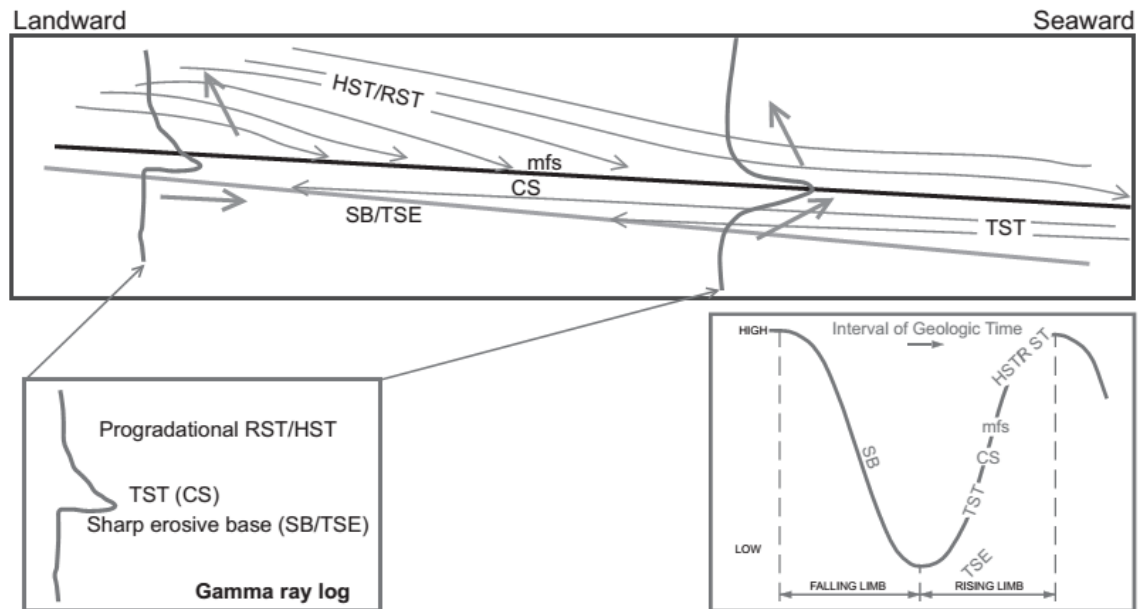


Figure 2.7. General sequence stratigraphic model for shale gas systems

The shale overlies a regional unconformity (SB/TSE), with a condensed organic rich layer (CS) at its base and a high gamma response, followed by an upward trend with a decreasing gamma response. This latter portion of this 2nd order sequence includes a number of thin 3rd order parasequences. The top of the CS is the maximum flooding surface (MFS) after which progradational (regressive), less organic-rich of the highstand systems tract downlap onto (Slatt and Rodriguez, 2012).

Interpreting the cyclical stacking of parasequences helps to build a stratigraphic framework that can act as the basis of regional mapping within a shale system, a practice that is now well established (e.g. Abouelresh and Slatt, 2012; Angulo and Buatois, 2012; Emery and Myers, 2009; Hammes and Frébourg, 2012; Hammes, 2009; Macquaker and Taylor, 1996; Schieber and Sethi, 1998; Slatt and Rodriguez, 2012; Slatt, 2011). Many productive shale plays (Barnett, Woodford, New Albany, Marcellus, Eagleford, Montney, Haynesville, Horn River and Caney) share a similar sequence stratigraphy (Slatt and Rodriguez, 2012) which can be represented by a generalised stratigraphic model (Figure 2.7).

In the model depicted in Figure 2.7, the shale overlies a regional unconformity (SB), with a condensed organic rich layer at its base and a high gamma response, followed by an upward decreasing gamma response. The latter portion of this 2nd order sequence includes a number of thin 3rd order parasequences (Figure 2.6). The integration of genetic beds within a sequence stratigraphic framework provides a basis for understanding and predicting the occurrence, distribution and character of prospective shale gas sequences at the basin scale (Passey et al., 2010). For instance, organic matter richness is a primary control on reservoir quality, where a shale succession is generally only considered as prospective if *TOC* exceeds 2 wt% (Sondergeld et al., 2010). The organic richness of shale is moderated by dilution (clastic input), organic matter production and accumulation, and is related to water depth and the distance to the shoreline (Bohacs et al., 2005; McClain et al., 2013; Passey et al., 2010). An example is given in Figure 2.8 for the Mowry Shale (Bohacs et al., 2005), highlighting increased clastic input, dilution and higher accumulation rates proximally. Moreover, the *TOC* accumulation rates depicted in Figure 2.8 are similar to the gamma ray trends suggested for the general stratigraphic model in Figure 2.7. Where, proximally, the most organic rich sediment accumulates in the transgressive systems tract (TST) just prior to the maximum flooding surface (MFDLS), and distally, the most organic rich sediments accumulate on or just after the MFDLS at the beginning of the highstand systems tract (HST). In other words, the basal organic rich layer in the general model (Figure 2.7) is likely to be diluted with clastic material proximal to the sediment source (landward), and increasingly sediment starved and condensed in distal locations of the basin. Trends which have been observed in the Haynesville Shale (Hammes and Frébourg, 2012), Marcellus Shale (McClain et al., 2013) and others. This predicative capability has recently been demonstrated by McClain et al. (2013), who utilised a stratigraphic model to predict the geographic and stratigraphic distribution of organic matter, silica and carbonate. These predictions were then used as a control on wireline mineral models and *TOC* estimates at local and basinal scales, and aided the recognition of engineering targets, horizontal well design and fracture stimulation strategies (McClain et al., 2013).

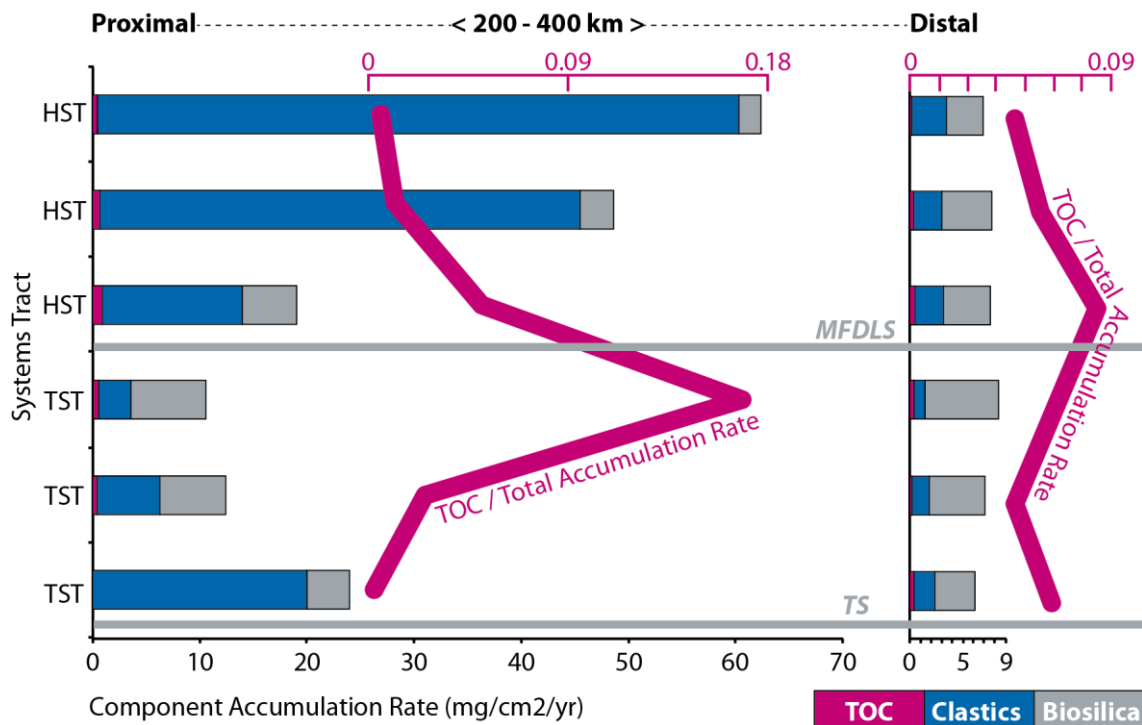


Figure 2.8. Sediment accumulation rates in proximal to distal settings for the Mowry Shale

Comparison of vertical and lateral changes in component accumulation rates for TOC, Clastics and Biosilica in the Mowry Shale. MFDLS indicates the stratigraphic position of the maximum flooding surface and TS indicates the transgressive surface. Note the high clastic dilution component proximally compared to the dominance of biosilica is distally (figure adapted from Bohacs et al., 2005 and Passey et al., 2010).

2.1.5 Organic matter: enrichment, type and maturity

Organic matter enrichment is typically linked to anoxic conditions resulting from a combination of poor water circulation, surface water biological productivity and the depletion of oxygen in the water column. In the absence of benthic fauna and the action of aerobic bacteria, organic matter destruction is restricted and its preservation enhanced (Canfield, 1994; Demaison and Moore, 1980; Ingall et al., 1993). While this general model is not disputed, recent studies suggest a far more complex series of interactions with higher energy currents and often less pervasive, more ephemeral anoxic bottom water conditions (Bohacs et al., 2005; Pedersen and Calvert, 1990; Schieber, 1999). This is reflected in the variety of mudstone fabrics discussed in section 2.1.3 (e.g, high energy bottom-water currents or organic enrichment related to episodic algal blooms; Macquaker et al., 2010a, 2010b).

A more holistic model of organic matter enrichment is described in a study by Bohacs et al. (2005), which relates organic matter enrichment to the interaction of three interdependent variables: production, destruction and dilution, generally expressed as:

$$\text{Organic matter enrichment} = \text{Production} - (\text{Destruction} + \text{Dilution}) \quad (2.1)$$

The study by Bohacs et al., (2005) finds that destruction rates, whilst dependant on oxygen levels, are also related to the access of limiting nutrients, production rates and burial rates (dilution). In combination with other studies (Passey et al., 2010), this identifies dilution as the dominant control on organic richness in proximal locations, whereas production is considered dominant in distal areas (see Figure 2.8). The implication of these factors is emphasised in section 2.1.4, where, when integrated within a stratigraphic model, they can aid in predicting the character and distribution of organic rich intervals.

In addition to the abundance or richness of organic matter within a formation (measured as *TOC*), organic matter type and maturity also acts to control the commercial viability of shale gas systems. Following sedimentation, the organic matter that evades destruction is subjected to increases in temperature and pressure as burial progresses. With time, the residual organic matter begins to cook and is transformed into kerogen, a mixture of insoluble organic compounds that make up the organic component in shale plays (Boyer et al, 2006). The type of kerogen depends on the nature of the organic matter and environment of deposition, and can be determined from carbon/oxygen and carbon/hydrogen ratios as depicted in Figure 2.9 (Boyer et al, 2006; Glorioso and Rattia, 2012; Seewald, 2003; Vandenbroucke and Largeau, 2007). The four types of kerogen (I, II, III, IV), their origin and hydrocarbon potential are summarised in Table 2.2 (Wu and Aguilera, 2013). The gas in most shale plays is typically generated by kerogen types II and III within the gas window (Figure 2.9), with a maturity of above 1.4 *Ro* (Heidari et al., 2011; Sondergeld et al., 2010; Weniger et al., 2010; Wu and Aguilera, 2013). Kerogen type II is largely generated in restricted deep marine settings, derived from the remains of algae and amorphous organic matter, whereas kerogen type III is largely derived from woody terrestrial plant debris

deposited in shallow to deep marine environments (Boyer et al., 2006; Passey et al., 2010).

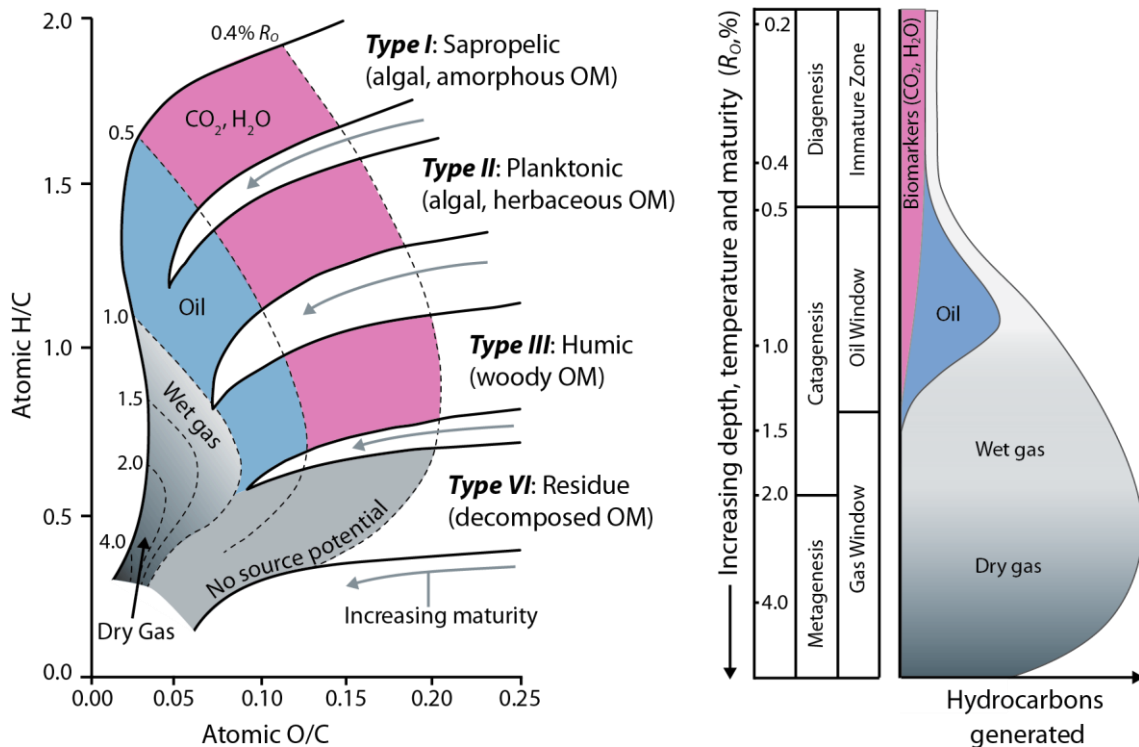


Figure 2.9. Van Krevelen diagram showing kerogen type and evolutionary path

Van Krevelen diagram (left) displays kerogen type and evolution with thermal maturity (R_o). The table and schematic model (right) show the timing and relative abundance gas generated with maturity (adapted from Boyer et al, 2006; Glorioso and Rattia, 2012; Mastalerz et al., 2013; Seewald, 2003).

Petrophysically, kerogen which has a low density of between 1.0 and 1.8 g/cc, is hydrogen dense (it has a high hydrogen index), is infinitely resistive, can be highly porous (depending on maturity) and can have a significant influence of wireline response (Bohacs et al., 2013; Bust et al., 2011; Schmoker, 1979). The impact of these attributes on formation petrophysical properties such as: resistivity, density, neutron porosity, gamma ray and core porosity and saturation are significant and discussed in section 2.2. Additionally, kerogen content may also impact sonic velocities, where a study by Prasad et al. (2009) suggests that high maturity shales can have a distinct relationship between acoustic impedance and kerogen content, indicating an increase in elastic impedance, velocity, and in some cases density with increasing shale maturity. Whilst the effects of gas, also positively associated with *TOC*, tend to negatively affect and slow the sonic and compressive velocities (Zhang et al., 2013). It should be noted that whilst the study by Prasad et al. (2009) suggests an increase in

kerogen density with maturity, kinetic models (Modica and Lapierre, 2012) suggest an increase in kerogen porosity with maturity. In other words, maturity may increase kerogen matrix density, but may also increase kerogen porosity, where the trade of between the two would determine kerogen bulk density. SEM studies by Curtis et al. (2011) in the Marcellus Shale find no relationship between thermal maturity and kerogen porosity. In other words, the effects of maturity on kerogen density/porosity are not certain. In addition, kerogen maturation and the effects of gas production may also impact formation pressure, the development of over-pressure, fracture development and fluid displacement and migration (Ramdhan and Goult, 2011; Tingay et al., 2013).

Environment	Kerogen type	Kerogen form	Origin
Aquatic	I	Alginite	Algal bodies
		Amorphous Kerogen	Structureless debris of algal origin
			Structureless planktonic material, primarily of marine origin
Terrestrial	II	Exinite	Skins of spores and pollen, cuticle of leaves and herbaceous plants
	III	Vitrinite	Fibrous and woody plant fragments and structureless, colloidal humic matter
	IV	Inertinite	Oxidised, recycled woody debris

Hydrocarbon potential	Oil	Gas	None
-----------------------	-----	-----	------

Table 2.2. Kerogen type, origin and hydrocarbon potential

Table adapted from Glorioso and Rattia (2012).

2.2 Wireline log responses in shale gas reservoirs

This section presents a review of the key wireline log responses available for analysis in Chapters 3, 4 and 5, including the gamma ray, density, neutron porosity and resistivity responses. These tools were included, as they were the only tools common to all wells within the study, e.g. sonic and other tools were only available for a select number of wells. Each tool is discussed in turn, including an outline of the tool physics followed by the typical log response in shale gas systems (for a detailed synopsis of wireline tool physics and responses, see Ellis and Singer (2007) and Rider and Kennedy (2011)).

2.2.1 Gamma ray tool response

The gamma ray (GR) log responds to the natural gamma radiation present within a formation. The source of radioactivity is largely related to the presence of shale, including clay minerals, and associated radioactive elements such as uranium (^{238}U), thorium (^{232}Th) and potassium (^{40}K) isotopes (Ellis and Singer, 2007; Heslop, 1974; Katahara, 1995; Rider, 1986). Though most rocks contain traces of radioactive material, shales and mudstones usually display the most gamma activity, and the GR log, often referred to as the 'shale log', is commonly used quantitatively as a shale indicator (Bhuyan and Passey, 1994; Heslop, 1974; Katahara, 1995).

The GR tool consists of a GR detector; a scintillator attached to a photomultiplier. As natural GRs emitted by K, Th and U isotopes within the formation pass through the scintillator they produce a flash of light which is converted into an electrical pulse by the photomultiplier and counted (Ellis and Singer, 2007; Rider, 1986; Lock and Hoyer, 1971). Simple GR tools (typically recorded in API [American Petroleum Institute] units) record the total natural radioactivity of the formation, whereas more sensitive spectral tools measure the energy of incident GRs. Which, as GR energy is proportional to the intensity of the flash generated as it passes through the scintillator (Hurst, 1990; Rider, 1986), allows for the identification of the source isotope (Figure 2.10), allowing their proportional abundance (U; ppm, Th; ppm and K; wt%) to be determined (Rider and Kennedy, 2011).

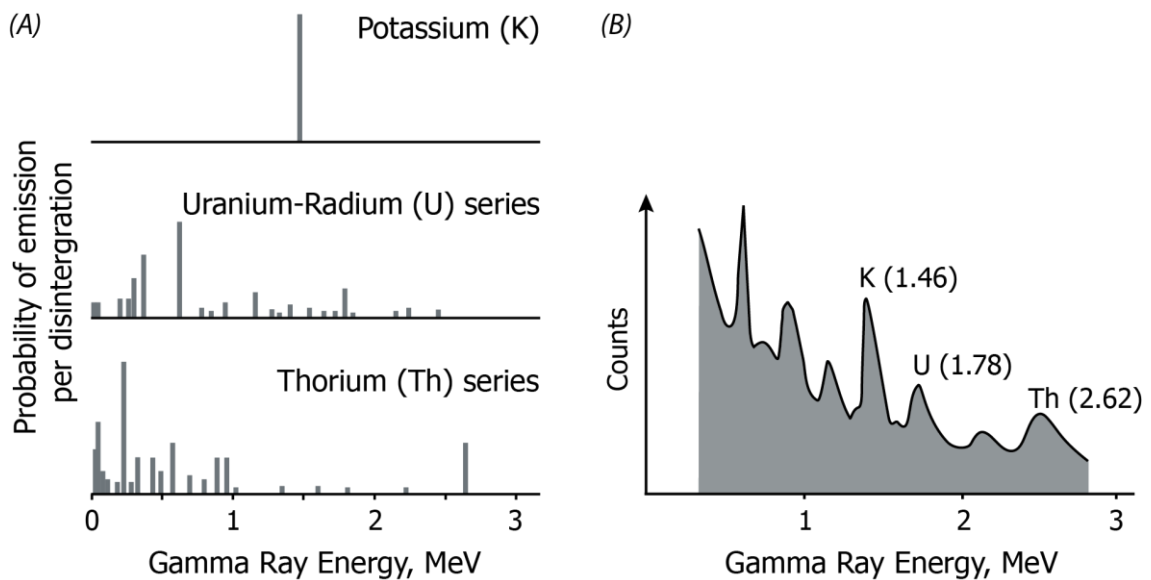


Figure 2.10. Gamma ray emission spectra

(A) The gamma ray spectra of K, U and Th and (B) the complex spectrum observed from a radioactive source containing K, U and Th (modified from Hurst, 1990).

The GR and spectral GR tools suffer minor environmental effects resulting from Compton scattering within the drilling fluid that can often be corrected using logging charts based on borehole diameter and mud weight. Larger more problematic effects, can result from borehole cave-ins, where the increased thickness of drilling fluid attenuates the energy of incoming GRs (Rider, 1986). Tool resolution and the volume of investigation (VOI) is also related to logging speed, where the likelihood backscattered GRs striking the detector decreases with increased logging speed. In general, the depth of investigation of GR tools is 10 to 25cm, with a vertical resolution of approximately 40cm, though in theory GRs may originate from anywhere within the formation (Ellis and Singer, 2007; Rider and Kennedy, 2011; Rider, 1986).

The GR tool is used both qualitatively as a lithology indicator (Hancock, 1992) and quantitatively to determine the shale or clay volume (Bhuyan and Passey, 1994; Heslop, 1974; Katahara, 1995; Passey et al., 2010). Qualitatively, the GR log is vital for differentiating lithological units and sequences within shale gas plays (Passey et al., 2010) and is widely utilised for core-log integration where core spectral GR data is available (Gupta et al., 2012). In addition, where shales are deposited in marine settings under reducing conditions, U is often associated with total organic content (TOC), and may be a useful indicator of organic richness (Alfred and Vernik, 2013;

Algeo and Maynard, 2004; Bohacs et al., 2005; Denham and Tieh, 1991; Guidry et al., 1996; Orlandi et al., 2011; Schmoker, 1979; Sullivan, 1985; Boyce and Carr, 2009). These relationships are depicted for the Barnett and Bakken Shales in Figure 2.11, though such relationships are sometimes limited, particularly in the presence of minerals containing radioactive material (Franquet et al., 2012; Jacobi et al., 2008; Sondergeld et al., 2010). In general however, the use of spectral GR tools is advantageous, as, in addition to empirical TOC-U relationships, clay type may also be inferred from Th and K cross plots and Th/K ratios (Glorioso and Rattia, 2012; Quirein et al., 1982) as highlighted on Figure 2.12. This oversimplified relationship is noted to work in some instances (Rider and Kennedy, 2011), but is generally used qualitatively, as, after Hurst (1990), it is widely considered that *'there is no theoretical, and negligible analytical basis for using Th/K cross-plots for mineral identification.'*

Quantitatively the GR tool is used to determine shale or clay volume using the following equation (Katahara, 1995):

$$V_{Sh} = \frac{GR - GR_{Clean}}{GR_{Sh} - GR_{Clean}} \quad (2.2)$$

where: V_{Sh} = Shale volume
 GR = GR log response
 GR_{Clean} = GR for a clean or clay free interval
 GR_{Sh} = GR for a pure shale

Though, where U enrichment is present, V_{Sh} or V_{Clay} estimates derived using equation 2.2 may be distorted. Moreover, reliance on GR log for V_{Sh} or V_{Clay} determination has generally been superseded by multi mineral solver models which combine, GR, neutron and density logs to estimate V_{Clay} (Adiguna, 2012; Eastwood and Hammes, 2011; Heidari et al., 2011; Singh et al., 2013). The links between organic matter and U and applications of GR and spectral GR tools are explored further in Chapter 3.

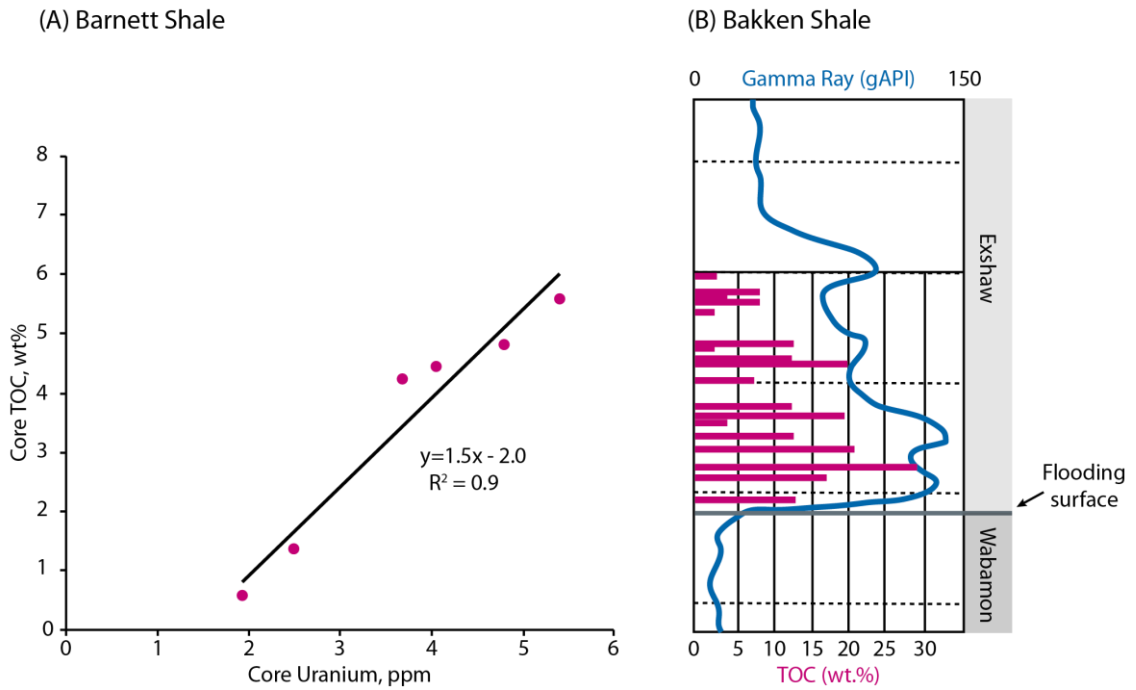


Figure 2.11. TOC, Uranium and GR relationships
 (A) Good TOC/Uranium relationship in the Barnett Shale (Jacobi et al., 2008). (B) TOC – GR relationships at the Exshaw flooding surface within the Alberta Bakken Shale (Passey et al., 2010)

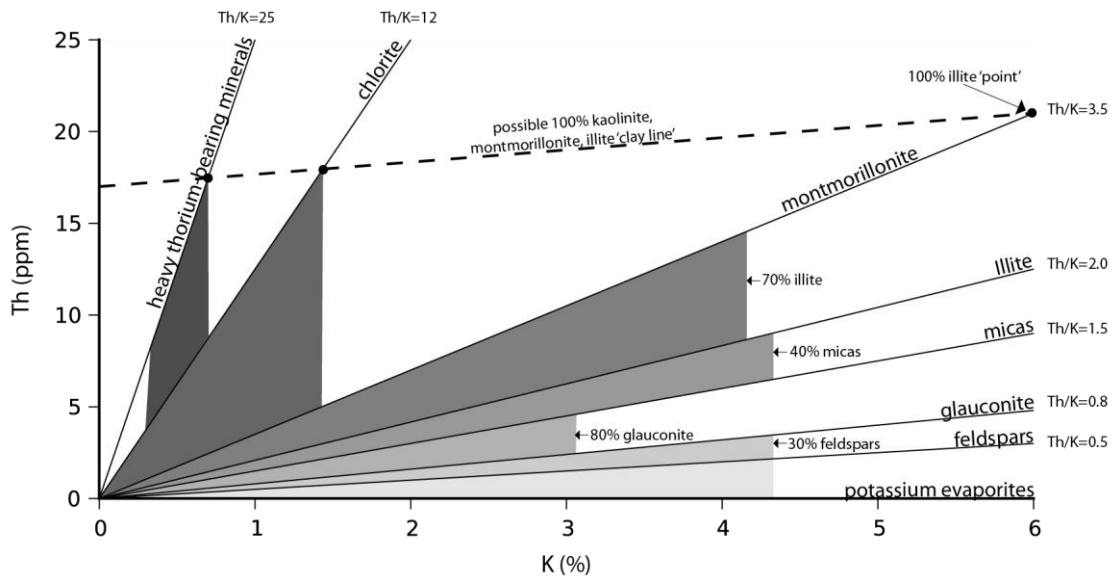


Figure 2.12. Theoretical distribution of clay minerals
 Th vs. K cross plot depicting the theoretical distribution of clay minerals and evaporites. (redrawn from Quirein et al., 1982 and Rider and Kennedy, 2011).

2.2.2 Neutron tool response

Neutron tools utilise a radioactive source (chemical or electrical) to measure a formations response to neutron bombardment (Ellis et al., 2004, 2003). It is synonymous with neutron porosity (ϕ_n), but the tool actually measures a formations

ability to attenuate emitted neutron energy, largely in response to their interaction with hydrogen in the formation (Ellis et al., 2004, 2003). Fast, high energy neutrons are emitted from the tool source and interact with atomic nuclei. With each subsequent interaction neutrons lose energy and speed, slowing to thermal energy levels where they are said to diffuse before being captured by formation nuclei in absorption reactions (Rider and Kennedy, 2011). The logging tool includes two or more detectors, one near and one far from the neutron source that record the small fraction of low energy neutrons that end up in their vicinity. The greater the ratio of the near to far counting rate, the more rapid the velocity loss within a formation, or, the shorter a neutrons slowing down length (Ellis et al., 2003).

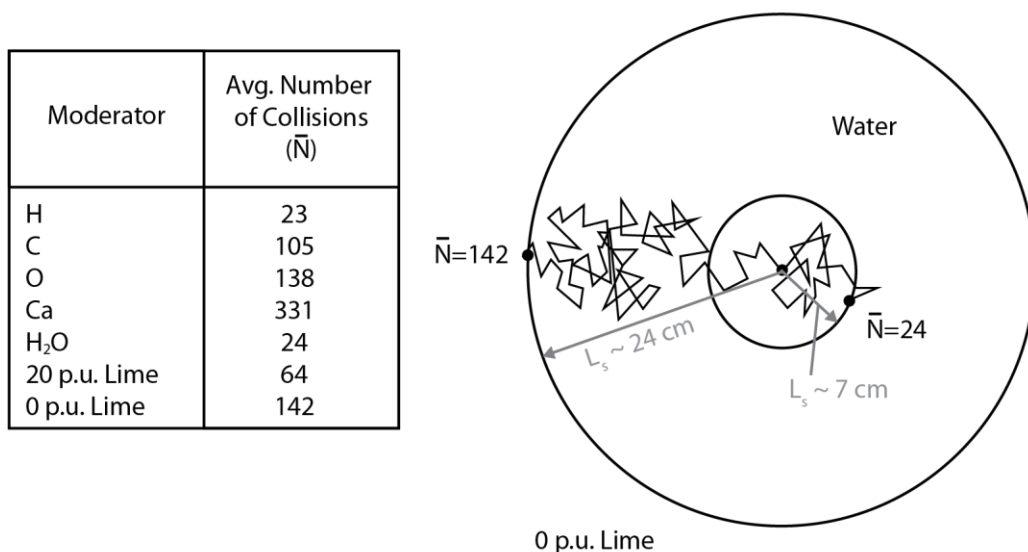


Figure 2.13. Illustration of the slowing down length

Illustration of the relationship between the number of collisions for slowing down and the slowing-down length in water and 0 p.u. limestone (taken from Ellis et al., 2003).

The scattering reactions which cause neutrons (particles with a mass similar to a proton) to lose energy are most efficient when colliding with particles of a similar mass, i.e. hydrogen (Figure 2.13). Neutron tool detectors take advantage of this, and, if the pore space is filled with hydrogen in the form of water or hydrocarbons, the response is related to porosity giving ϕ_n (Ellis and Singer, 2007; Ellis et al., 2004, 2003; Rider and Kennedy, 2011). It is implicit in this relationship that the distance a neutron can travel within a formation is largely moderated by a formation's hydrogen content or its hydrogen index (HI). For example, Chiamonte and Ellis (2000) demonstrated that the depth of investigation in a water filled limestone with a porosity of 20 % is

~15cm, whereas when the pore space is gas-filled (gas has a lower HI than water) this extended to ~25cm. Variation in hydrogen content is not however limited to formation fluids, and mineralogical variations can also impact neutron response. To compensate for this the neutron tool can be calibrated to limestone, sandstone or dolomite standards. In reality however, most neutron tools are calibrated to mineralogically simple limestone standards, particularly for compositionally complex formations such as shales, where the neutron log response must be considered less a response to porosity and more as the end product of a series of nuclear reactions (Rider and Kennedy, 2011).

As applied in shale gas systems, the neutron log response is dominated by the effects of gas, clay and TOC. Gas, which has a low HI compared to water, draws down the apparent ϕ_n . Whilst the effect of shale reflects the contribution of structural hydroxyl ions (-OH) within hydrous aluminium-silicates (clay minerals), which in addition to clay bound water, act to increase apparent ϕ_n (Boonen et al., 2010; Ellis et al., 2004; Parker et al., 2009; Sondergeld et al., 2010). This effect may be further exaggerated in TOC rich shales given the relatively high HI of organic matter (Glorioso and Rattia, 2012; Sondergeld et al., 2010), though ϕ_n is generally considered to be a poor indicator of organic matter richness (Passey et al., 2010). ϕ_n may also be distorted in shale by the increased abundance of elements with greater ability to absorb thermal neutrons (e.g. gadolinium, boron and chlorine) which act to further reduce the thermal neutron count (Gilchrist, 2009). As a consequence of these distortions, even with corrections applied, ϕ_n values are not considered an appropriate estimation of porosity (Wu and Aguilera, 2013). In practice the neutron log is almost always used in combination with the density porosity (ϕ_d) log, where the ϕ_n - ϕ_d overlay (Figure 2.14), and the character of their separation, can be a useful gas indicator (Passey et al., 2010). ϕ_n - ϕ_d combinations have also been used with good effect in the Barnett Shale and other North American shale plays for assessing kerogen maturity (Alfred and Vernik, 2013; Jacobi et al., 2008). Though more generally, the complex lithology and clay affiliated water in shale gas plays limits the use of the neutron tool and ϕ_n - ϕ_d overlay methods (Glorioso and Rattia, 2012). The ϕ_n - ϕ_d response to a variety of lithologies is depicted in Figure 2.14 displaying typical gas and shale cross-over effects. As a general rule, where

ϕ_n and ϕ_d stack or overlay, the formation is considered shale free (Parker et al., 2009). Neutron-density relationships and cross-plots remain in wide use in conventional and unconventional formations for the determination of lithology, clay properties and to find true porosities in shale free formations and effective porosity in shaly sands (Rider and Kennedy, 2011; Jacobi et al., 2008).

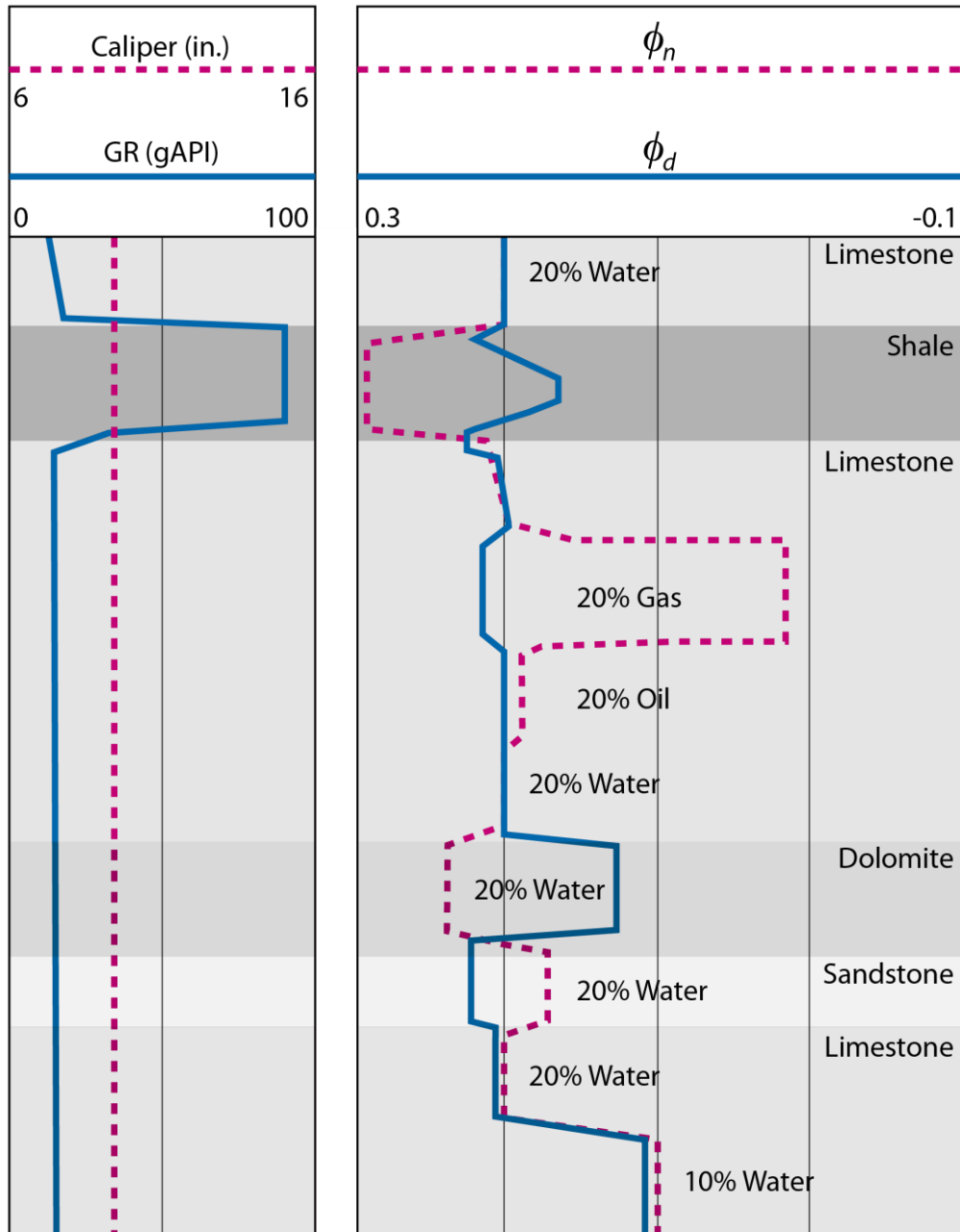


Figure 2.14. Schematic neutron and density response

Schematic neutron and density log response in 20% porosity lithologies with varying fluid content and borehole conditions (redrawn from Ellis et al., 2004).

2.2.3 Density tool response

The density log provides a continuous measurement of the combined solid rock matrix and pore fluid bulk density (ρ_b) in g/cc (Rider and Kennedy, 2011). A typical density tool utilises a radioactive source to emit a continuous beam of GRs into the formation. Similar to the GR tool, detectors (scintillators) located near and far from the source detect incident backscattered GRs following their interaction with the formation. Specifically, emitted GRs interact with electrons in the formation and lose energy via scattering interactions. GR energy attenuation is a function of electron density, which has a linear relationship with ρ_b (Figure 2.15), in other words the higher the count rate, the higher the formation density (Ellis and Singer, 2007; Rider and Kennedy, 2011).

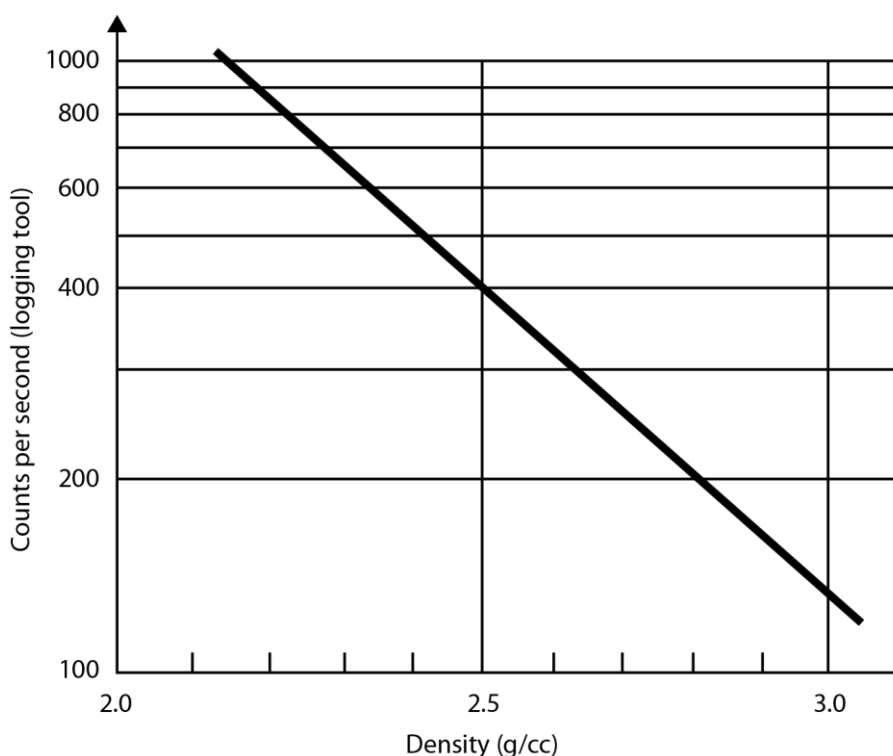


Figure 2.15. Logging tool response (count rate) vs. density

Correlation between the density tool radiation count rate and bulk density (taken from Rider and Kennedy, 2011).

Density tools are often utilised to measure the photoelectric factor (PEF) in addition to ρ_b . PEF refers to a lower energy interaction and transfer of energy from GRs to the bound electrons of atoms. Where, if the energy of the incident GR is sufficient, the electron is ejected from the atom and replaced by another, a process accompanied by the emission of a fluorescence X-ray with an energy signature dependant on the

atomic number of the material (Ellis and Singer, 2007). The PEF is used quantitatively as lithology indicator (Rider and Kennedy, 2011), though no PEF log data was available for study within this project and is not considered further.

Modern density tools are generally considered to have investigation depths of 5 to 10 cm at average formation densities, with the depth of investigation decreasing at higher density (lower porosity). Whereas vertical tool resolution is dependent on detector spacing, with some density tools able to resolve individual beds down to 10cm (Ellis and Singer, 2007; Rider and Kennedy, 2011). As a consequence of the shallow depth of investigation, the density tool is sensitive to rugose borehole conditions and requires interpretation in combination with the calliper log (Ellis and Singer, 2007).

As applied in shale gas plays, the density tool has a number of qualitative and quantitative roles. Quantitatively, ρ_b combined with knowledge of the matrix density (ρ_{ma}) can be used to determine the density porosity (ϕ_d) after the traditional relationship (taken from Zak and Smith, 1959):

$$\phi_d = \frac{\rho_{ma} - \rho_b}{\rho_{ma} - \rho_f} \quad (2.3)$$

where: ϕ_d = Density porosity
 ρ_b = Bulk density (log response)
 ρ_f = Fluid density
 ρ_{ma} = Matrix density

The use of equation (2.3) is however complicated in shale plays due to the presence of high density (siderite, pyrite) and low density (kerogen) components coupled with system heterogeneity and therefore inconsistency in ρ_{ma} , which is not likely to be adequately represented by core data (Sondergeld et al., 2010). Corrections exist, but are problematic in requiring knowledge of formation mineralogy, mineral and organic matter densities and water saturation. As a consequence, ϕ_d values, even with applied corrections, are not generally accepted for porosity evaluation (Murphy et al., 2013; Wu and Aguilera, 2013). More generally, the density tool's greatest utility is in its response to the low density of organic matter which often yields an empirical

correlation between density and core *TOC* values (Adiguna, 2012; Alfred and Vernik, 2013; Ambrose et al., 2010; Franquet et al., 2012; Glorioso and Rattia, 2012; Jacobi et al., 2008; Murphy et al., 2013; Passey et al., 2010; Wu and Aguilera, 2013; Zhang et al., 2013). This relationship is demonstrated in Figure 2.16, though it is again noted that this may be distorted in the presence of heavy minerals (Ambrose et al., 2010; Jacobi et al., 2008; Quirein et al., 2012) especially where *TOC* is frequently co-located with pyrite (Witkowsky et al., 2012).

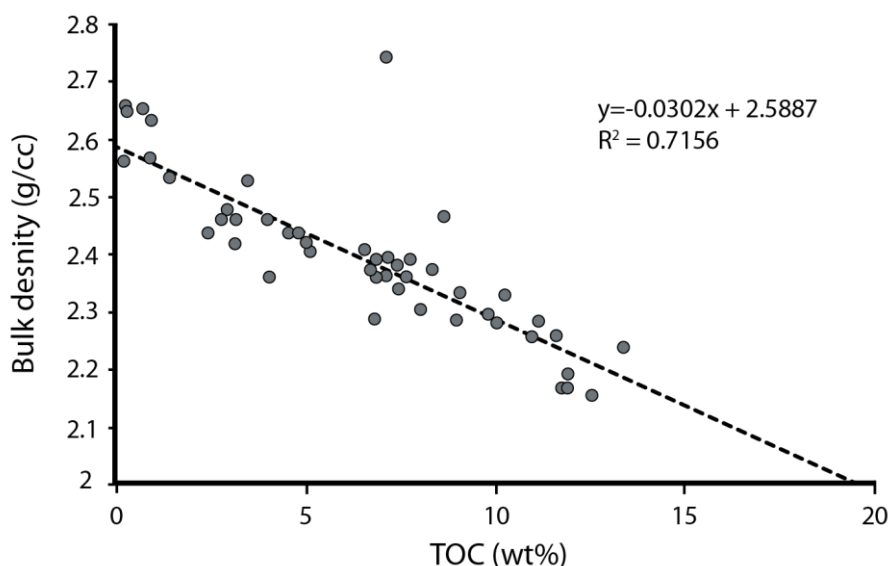


Figure 2.16. Relationship between *TOC* and density

Empirical correlation between density and *TOC* core data allows *TOC* log modelling from density tool (taken from Glorioso and Rattia, 2012).

The density tool response, as discussed in section 2.2.2, is also combined with neutron, sonic and resistivity logs within multi mineral models. It is also used qualitatively in combination with the neutron log, and can be a good indicator of lithology and gas and shale effects (Figure 2.14). Furthermore, the established increase in density with depth due to porosity reductions and diagenetic changes renders the density tool a key component of pore pressure prediction and compaction models in shale gas plays (Couzens-Schultz et al., 2013; Krushin, 2013).

2.2.4 Resistivity tool response

Resistivity is the measure of a materials ability to impede or resist the flow of an electrical current (measured in $\Omega.m$). The minerals that comprise most sedimentary

rocks have extremely high resistivities and act as electrical insulators, such that the resistivity tool response is almost completely dependent on the conductivity of fluid in the pore space and pore geometry/connectivity. Thus, where porosity and pore fluid salinity are known, formation resistivity can act as a pore fluid indicator, able to dissociate resistive hydrocarbons from conductive saline pore fluids (Figure 2.17). In other words, if hydrocarbons are present in sufficient quantity, they displace conductive pore fluid and elevate formation resistivity above that for the same formation when 100% saturated with conductive formation water (Edmundson, 1988a, 1988b; Rider and Kennedy, 2011).

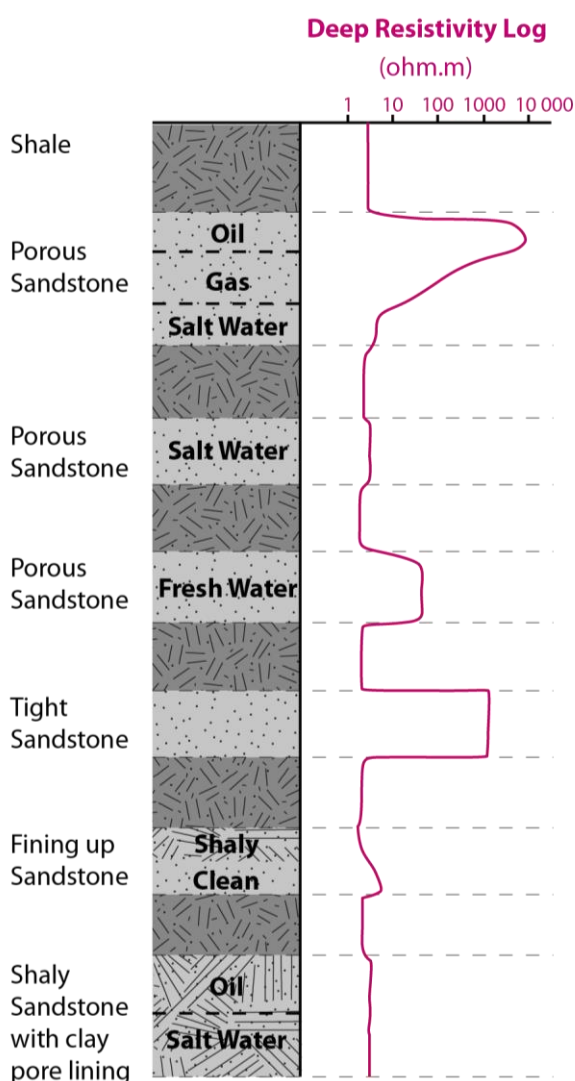


Figure 2.17. Schematic deep resistivity response in various lithologies

Resistivity response in various lithologies illustrating the effects of fluid salinity (oil, gas, fresh and saline water), permeability (tight sandstone) and clay (shaly/fining up sandstone), adapted from Rider, 1986.

Resistivity can be measured using a range of commercial tools, though the two most common group of tools are the laterolog and induction varieties. Laterolog tools utilise a direct electrical connection between the tool and formation with a laterally focused electrical current distribution. This is most easily envisaged using a three (LL3) electrode example which utilises guard currents (A_1 and A_1') to focus the emitted current of the centrally located electrode (A_0), though modern tools typically include 4 or more electrodes (Ellis and Singer, 2007; Rider and Kennedy, 2011).

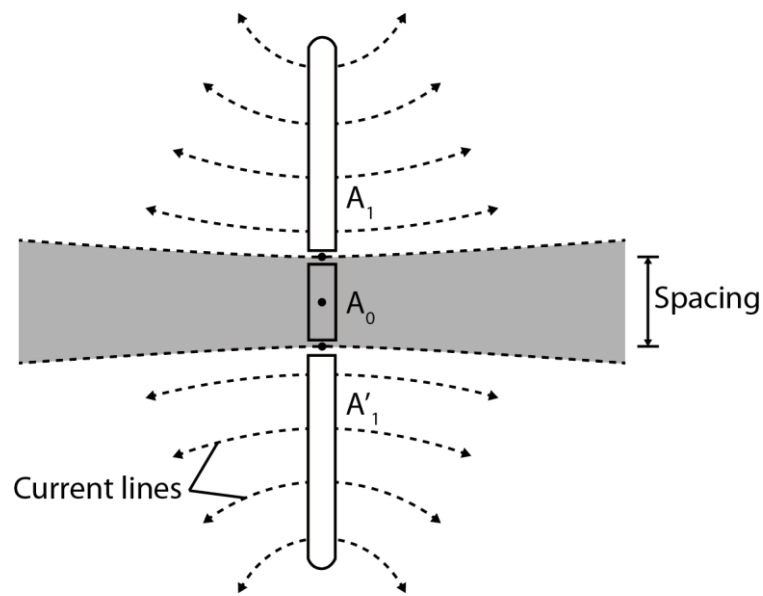


Figure 2.18. Schematic current distribution from the Laterolog-3 device

Schematic current distribution from the Laterolog-3 device in a homogenous formation with current focused (A_0) into the formation by guard electrodes (A_1 and A_1'). Taken from Ellis and Singer, 2007.

Laterolog resistivity is determined by monitoring the voltage drop between electrodes, and, as the tool requires direct electrical connection with the formation, are only effective in conductive water based muds. Modern tools record multiple simultaneous resistivities at depths of a few centimetres to a few meters with a typical vertical resolution of 60cm (Rider and Kennedy, 2011).

Unlike laterolog devices induction tools measure resistivity indirectly. The principle mechanism of the induction tool is depicted in Figure 2.19, where the transmitter produces an electromagnetic field in the formation that induces a current flow in a circular motion about the tool. The induced current creates a second electromagnetic field, which in turn generates an alternating current in the receiver coil, this can then be related to electrical properties of the formation allowing resistivity to be calculated

(Ellis and Singer, 2007). Commercial tools are more complicated, have more than the two coils depicted in Figure 2.19, and can measure resistivity at multiple depths of investigation of up to 600cm with a typical vertical resolution of 60cm. In addition, as induction tools require no direct electrical connection to the formation, they can operate in oil or water based muds, though as water based muds can distort the measurement, they are generally considered more accurate in oil based fluids (Ellis and Singer, 2007; Rider and Kennedy, 2011).

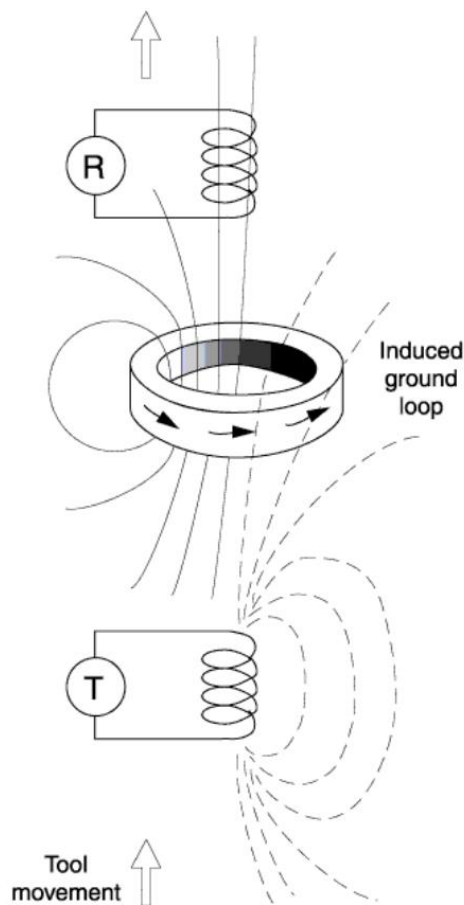


Figure 2.19. Principle of the induction tool measurement

Taken from Rider and Kennedy, 2011.

The schematic resistivity responses displayed in Figure 2.17 are for conventional reservoir systems, though they illustrate the role of pore fluid type, clay minerals and permeability on formation resistivity. The resistivity response is however more complicated in shale gas systems due to the competing influences of clay bound water, pore fluids, organic matter, conductive heavy minerals and also heterogeneous sediment fabric on the resistivity response. Shales may contain significant quantities of

clay, for which the associated and conductive clay bound waters tend to draw down formation resistivity (Adiguna, 2012; Kennedy and Herrick, 2012; Worthington, 2011a), though organic matter, which is infinitely resistive, will have the opposite effect (Passey et al., 1990). Conductive pyrite and other heavy minerals, which are often associated with organic matter, may also draw down resistivity. Though the impact of these components are likely to be highly dependent on formation structure and the connectedness of conductors and insulators, such that vertical and horizontal compositional and structural anisotropy are likely to be extremely important in moderating the resistivity response (Anderson et al., 2006; Corley et al., 2010; Le et al., 2011). In general, it is noted that *TOC* rich zones show an elevated resistivity response, though at very high maturities, conversion of organic matter to graphite and other mineralogical changes may act to reduce resistivity (Boyer et al, 2006).

The resistivity response has numerous quantitative and qualitative uses (see Rider and Kennedy, 2011 for a full discussion) and is frequently used quantitatively in combination with density or sonic log overlay methods for *TOC* prediction (Passey et al., 1990; Sondergeld et al., 2010; Spears and Jackson, 2009; Wu and Aguilera, 2013). The resistivity response is however most generally associated with the quantitative determination of water saturation based on Archie's equation, which is discussed further in section 2.4.

2.3 Core porosity and water saturation in shale gas reservoirs

The following section reviews key core laboratory data available for analysis in Chapters 3, 4 and 5, including total porosity and Dean Stark water saturation data. First porosity and water saturation are defined and laboratory protocols described, followed by a discussion of the fluid components that occupy the pore space, pore type and distribution, and factors that impact the interpretation of core porosity and saturation values in shale gas systems.

2.3.1 Porosity and water saturation

The porosity of a reservoir rock can be defined as the fractional volume of the reservoir that is not occupied by the solid framework of the reservoir (Donaldson and Tiab 2003):

$$\phi = \frac{V_b - V_{gr}}{V_b} \quad (2.4)$$

where: ϕ = Porosity fraction
 V_b = Bulk volume
 V_{gr} = Grain volume

The water saturation can simply be defined as that fraction of the pore space that is occupied by water, as represented by:

$$S_w = \frac{BVW}{\phi} \quad (2.5)$$

where: S_w = Water saturation
 BVW = The bulk volume of water

2.3.2 Laboratory determination; porosity and water saturation

The porosity and saturation data available for study within this thesis are provided by BG Group through Core Laboratories and utilises a crushed sample methodology (see

the full laboratory procedures in Appendix A) based on experiments performed at the Gas Research Institute on Devonian shales (Luffel and Guidry 1992). This method utilises a 300g sample taken from core material and weighed to $\pm 0.001\text{g}$, with sample V_b determined by mercury immersion to $\pm 0.01\text{cc}$. The sample is then processed in a mechanical rock crusher and sieved through 0.853 and 0.500 mm screens. A 100g sub-sample of crushed material collected on the 0.500 mm screen is then used for the determination of S_w by Dean Stark extraction. This utilises a vapour of solvent (usually toluene which is miscible with oil but not water) to rise through the sample and leach out oil and water in the pore space at 110°C (Handwerger et al., 2011). The water condenses out and is collected, whilst the solvent and oil is recirculated through the sample for one to two weeks. Following extraction the sample is dried in a vacuum oven at 110°C to remove the residual toluene until weight equilibrium is achieved with a minimum drying time of one week. By measuring V_g at ambient conditions using Boyle's Law double-cell technique with helium as the expansion gas, ϕ is then calculated from equation 2.4. S_w is calculated based on comparing the volume of water collected during Dean Stark extraction and the mass lost measured after drying.

2.3.3 What does measured porosity and water saturation represent in shale?

2.3.3.1 Clay chemistry and cation exchange capacity

As discussed above, the core samples are crushed, cleaned by solvent extraction and then oven heated. The resulting V_g is then measured and used to calculate ϕ from equation 2.4, though it is not fully understood what this measure actually represents. This uncertainty arises because clay minerals, sheet structured hydrous aluminosilicates, blur the distinction between the fluid filled porosity and the solid matrix, containing water in both liquid and solid phases. This includes non-liquid structural water as hydroxyl ions (OH^-) within the clay mineral lattice, bound water including adsorbed water at the mineral surface with more loosely attached diffuse double layer water, and capillary bound water in the interparticle porosity between clay grains (Handwerger et al., 2012, 2011; Passey et al., 1990; Reeves et al., 2006a).

The sheet structures that form clay minerals include layers of silica (Si^{4+}) coordinated tetrahedra with oxygen (O) and aluminium (Al^{3+}) coordinated octahedra with OH^- ions (Reeves et al., 2006a; Tucker, 1982). These sheets combine in stacked composite layers of alternating tetrahedral and octahedral sheets linked by common oxygen atoms (Tucker, 1982). This stacking arrangement determines clay mineral type and occurs in two varieties as summarised in Figure 2.20.

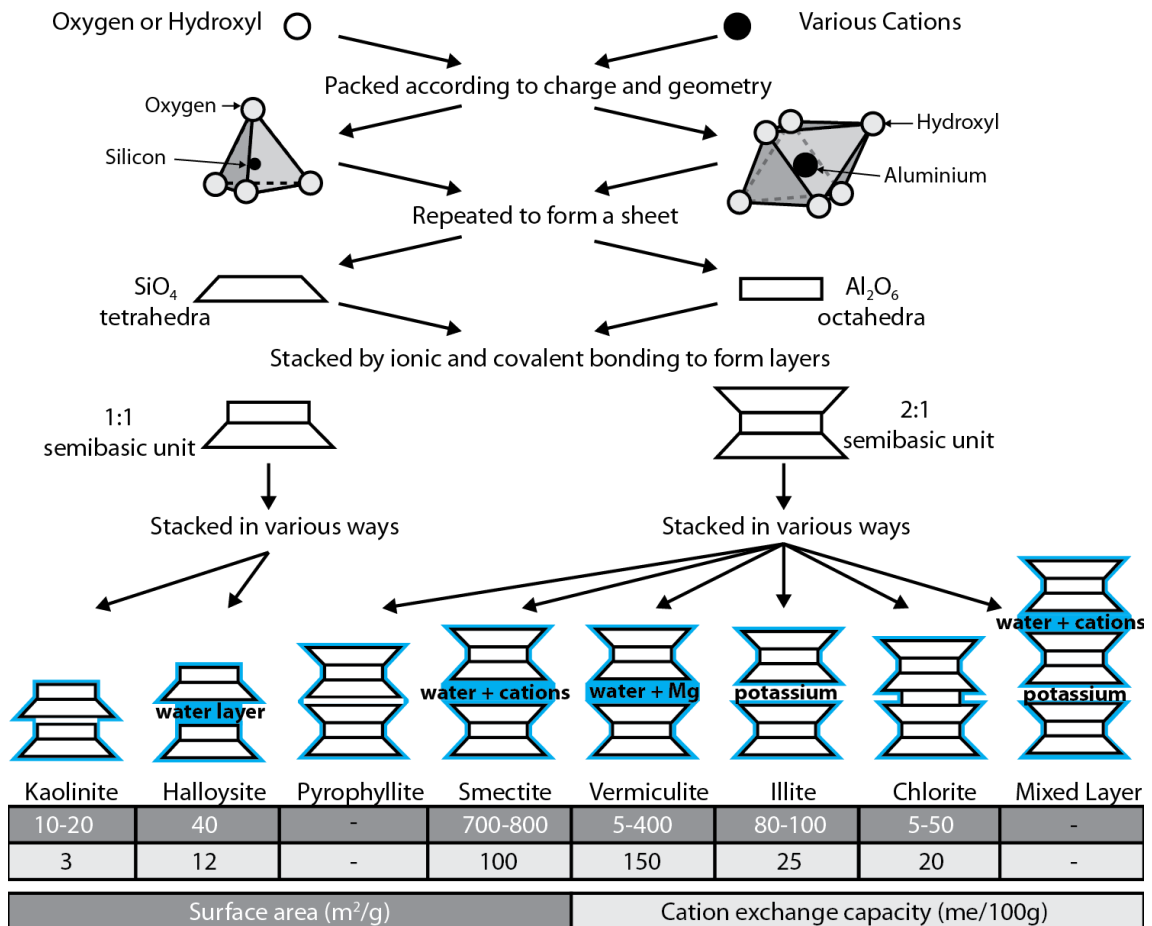


Figure 2.20. Schematic of clay mineral sheet structure

Schematic illustrating the stacking patterns and interlayer sites of clay minerals, blue shaded regions indicate water wet surfaces (modified from Das (2008) and Mitchell and Soga (2005)).

The structural water, in the form of non-conductive (Passey et al., 2010) OH^- ions, is part of the solid clay lattice associated with Al coordinated octahedra.. This is depicted in Figure 2.20 with absorbed water on the surface of the clay grains (in blue), highlighting internal and external clay mineral surfaces. The mechanisms that bind water to clay mineral surfaces are complex, though in general, it is understood that the cations which coordinate the structure of the tetrahedral and octahedral sheets are

subject to isomorphous substitution, particularly in 2:1 layer clay mineral varieties. This refers to the replacement of the coordinating cation (Si^{4+} or Al^{3+}) with an alternative cation of similar size and equal or lesser charge, without altering the crystal structure. For example, within tetrahedral sheets Si^{4+} may be replaced by Al^{3+} or Fe^{3+} and within the octahedral sheets Al^{3+} may be replaced by Fe^{3+} , Mg^{2+} or Fe^{2+} (Das, 2008; Reeves et al., 2006a; Tucker, 1982). The substitution of a cation with another of lesser charge leads to the development of a negative charge on the clay mineral surface that gives rise to the phenomenon of cation exchange. This refers to the ability a clay mineral to form an electrical double layer, and is the measure of a solid's ability to adsorb or exchange cations within a solution (Ellis and Singer, 2007). This is generally defined as cation exchange capacity (CEC) and represented as the amount of exchangeable ions (in milliequivalents) per 100g of dry clay (Das, 2008). This relationship and the presence of water and cations at or near clay mineral surface is expressed in Figure 2.21. This highlights an electrical double layer of water, with adsorbed water on the mineral surface, also known as the Stern layer, followed by a more loosely attached diffuse layer of cations attracted to the negative surface charge (Das, 2008). The higher the CEC, or the greater the surface charge imbalance and surface area of the clay mineral, then the higher the bound water content and water layer thickness (Krushin, 2013; Terzaghi, 1996). This is significant since, as the grain surface area increases exponentially with decreasing grain size, it follows, particularly in shales with a significant clay content, that the clay bound water volume will form an increasing proportion of the pore space. This is however moderated by clay type, and is depicted in the lower section of Figure 2.20, where it is evident from the stacking pattern of the clay minerals that there is variation in their surface area and CEC. In other words, less bound water is associated with lower CEC clay varieties and vice a versa.

In summary, clay minerals contain at least three water components: a) hydroxyls; which are included as porosity by neutron tools (see section 2.2.2) but are non-conductive and part of the solid matrix, b) clay bound water (external and internal), and c) capillary bound water. Where both the clay bound and capillary waters are measured by the neutron tool and are electrically conductive. This raises the following

question, which waters are measured by Dean Stark extraction or driven off by oven drying within the crushed sample method?

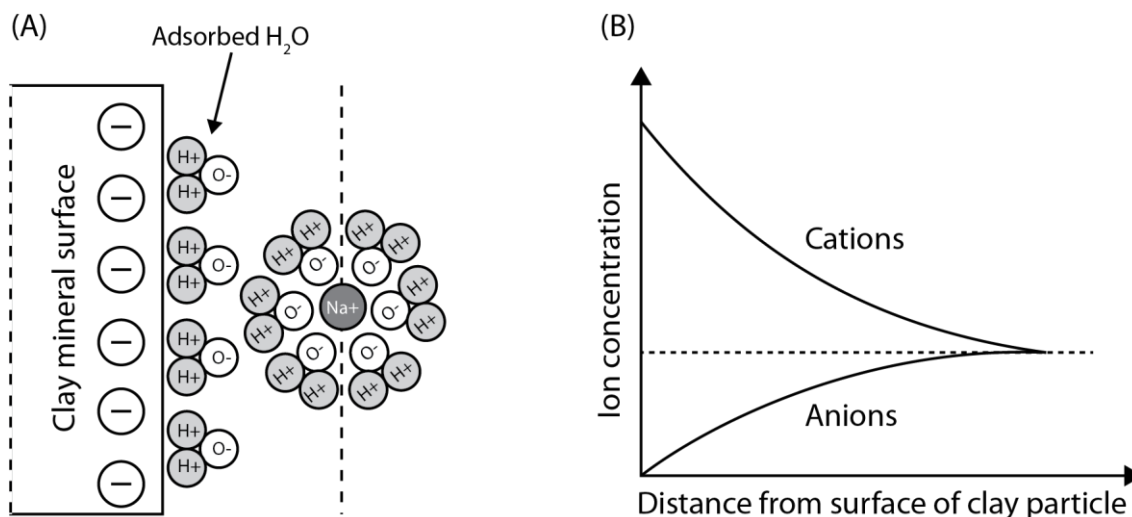


Figure 2.21. Electrical double layer

A) Schematic illustrating the electrical double layer, with adsorbed water at the mineral surface followed by a diffuse outer layer of water and cations (redrawn from Passey et al. (2010) and Ellis and Singer (2007)). B) Ion concentration with distance to the mineral surface (redrawn from Reeves et al., (2006a)).

2.3.3.2 The origin of water extracted by Dean Stark methods

An alternative to the determination of S_w by Dean Stark extraction is the retort method. This uses a programmed time series approach, where temperature is gradually increased in discrete steps and water driven off and collected. As the temperature increases more tightly bound water is liberated, with free water driven off at low temperatures, followed by bound water and eventually structural waters at higher temperatures. In general water is driven off continuously, with peaks in water loss (weight reduction) at various temperatures, though laboratories rarely publish the locations in this continuum at which they choose to classify water as either free, clay bound or structural (Handwerger et al., 2012, 2011). Thus the water sources by retort methods can arguably be defined, whereas fluid loss over time is not measured by Dean Stark extraction and so the waters origin is even more uncertain (Sondergeld et al., 2010). At relatively low temperatures (<110°C) it is generally considered that organic matter is not affected by either Dean Stark or retort methods, though there is limited evidence to suggest that sample crushing in labile less mature source rocks

may degrade the kerogen and confuse the porosity measurement (Modica and Lapierre, 2012). It is however widely observed that the total S_w derived by Dean Stark extraction (combined with oven drying) tends to be higher than that found by retort methods for the same sample (Handwerger et al., 2012, 2011; Michael et al., 2013; Sondergeld et al., 2010; Wu and Aguilera, 2013). Experiments by Derkowski and Bristow (2012) indicate that OH^- ions should only be removed at temperatures above 200°C , and that 90% of clay bound and capillary water is removed by drying to 110°C . This raises the question, why is there a difference in retort and Dean Stark water saturations at 110°C ? One explanation, based on experiments by Handwerger et al. (2012), suggests that the 'extra' Dean Stark water represents clay structural water that should not contribute to ϕ or S_w . Though the removal of OH^- requires far higher temperatures to be liberated, they suggest that solvent vapour wets the clay surface reducing the required temperature to break inter-molecular bonds and so release structural OH^- ions. This is however yet to be proven, and so the origin of waters extracted by the crushed methods described in section 2.3.2 remains unclear.

2.3.3.3 Organic matter porosity and pore fluids

The existence of an additional, variably connected pore system within the kerogen macerals of shales has been widely studied (see Figure 2.22), suggesting kerogen porosities (ϕ_{kerogen}) of up to 50% that significantly contribute to the total rock pore volume (Alfred and Vernik, 2013; Bohacs et al., 2013; Chalmers et al., 2012; Curtis et al., 2011, 2012; Heath et al., 2011; Loucks et al., 2012; Mastalerz et al., 2013; Modica and Lapierre, 2012; Murphy et al., 2013; Quirein et al., 2012; Zhang et al., 2013). Though in some shales, for example the Eagle Ford, weak correlations between *TOC* and porosity suggests a significant inorganic porosity (Murphy et al., 2013). The development of kerogen pores, typically at the nanoscale, is often linked to diagenetic processes and the conversion of organic matter to hydrocarbons (Ambrose et al., 2010), though there is limited evidence to suggest that ϕ_{kerogen} increases with maturity (see section 2.1.5). Moreover, it is widely believed that pores within the organic matrix contain only gas, with only water and minor amounts of gas located in the inorganic

porosity (Alfred and Vernik, 2013; Ambrose et al., 2010; Glorioso and Rattia, 2012; Modica and Lapierre, 2012; Ramirez et al., 2011; Wu and Aguilera, 2013).

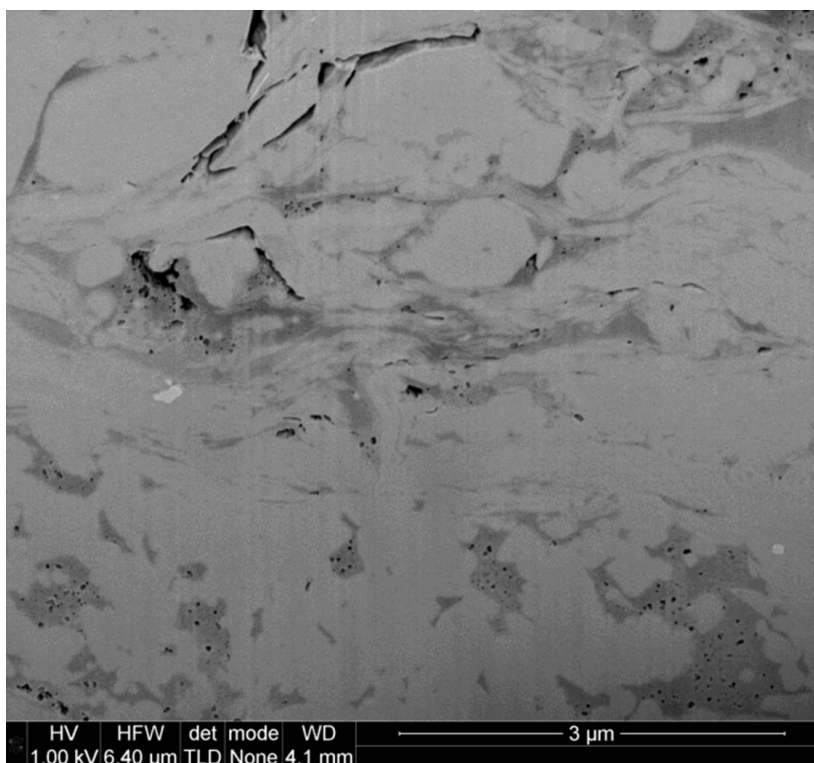


Figure 2.22. FIB/SEM image showing kerogen porosity in shale

The dark grey areas are kerogen macerals containing pores in black, with the light grey areas the clay and silica matrix (Ambrose et al., 2010).

The gas in the organic matter pores is held in two phases; a liquid like supercritical adsorbed phase on the kerogen pore walls and as free gas (Ambrose et al., 2010), with both gas phases removed by and included within the measure of ϕ generated by crushed rock analysis (Ambrose et al., 2010; Handwerger et al., 2012). Similar to clay bound and free water relationships, the ratio of free gas to sorbed gas is dependent on pore size. The smaller the organic pores, the greater volume of the pore space occupied by the adsorbed gas phase, though determining the pore size and distribution characteristics of kerogen, let alone applying such data to petrophysical models, remains challenging (Bohacs et al., 2013)

2.3.4 Data reliability and uncertainty

Studies by Profice et al. (2011) indicate that porosity estimation by crushed rock methods can be extremely sensitive to the accuracy of the crushed rock volume.

Though in general, crushed rock porosity estimates are considered robust, with repeatability studies showing excellent consistency (Luffel and Guidry, 1992). Moreover, recent work by Karastathis (2007), where the average sample grain size was reduced to 0.04 mm in combination with helium based standard Boyle's Law technique, also shows excellent agreement with commercial crushed rock analysis. So whilst it is considered that ϕ can be measured accurately and consistently by crushed rock methods, it must be noted that these experiments are not performed at effective stress conditions, and so measure a likely dilated, maximum total porosity (ϕ_t ; Sondergeld et al., 2010; Clarkson et al., 2012). Also, as pore surface area increases exponentially with decreasing grain size and as kerogen pores have particularly high absorptive capacities, the estimates of porosity based on Boyle's Law may be compromised (Cui et al., 2009; Sondergeld et al., 2010). This may occur if the hydrogen gas injected during analysis is absorbed into a liquid like state on organic and clay minerals surfaces, leading to an exaggerated porosity. Cui et al. (2009) also notes that shale acts like a molecular sieve, where smaller elements such as hydrogen are able to intrude further into the rock sample and so measure larger porosities, whilst the intrusion of larger particles like nitrogen may be restricted by narrow pore throats, though hydrogen is normally utilised for tight shale samples. Sondergeld et al. (2010) also notes that commercial laboratories often report consistently different porosity estimates. This is highlighted in Figure 2.23, which reveals a relatively consistent shift in reported porosity values between laboratories for the same samples. These relationships suggest systematic differences in sample preparation, handling and laboratory protocol may impact porosity estimates (Sondergeld et al., 2010). Thus, accepting that the derived values may be inexact, as crushed sample methods for porosity determination are considered robust and repeatable, analysis and evaluation should utilise the same laboratory for core analysis so as to minimise any error that may arise from differing laboratory procedures.

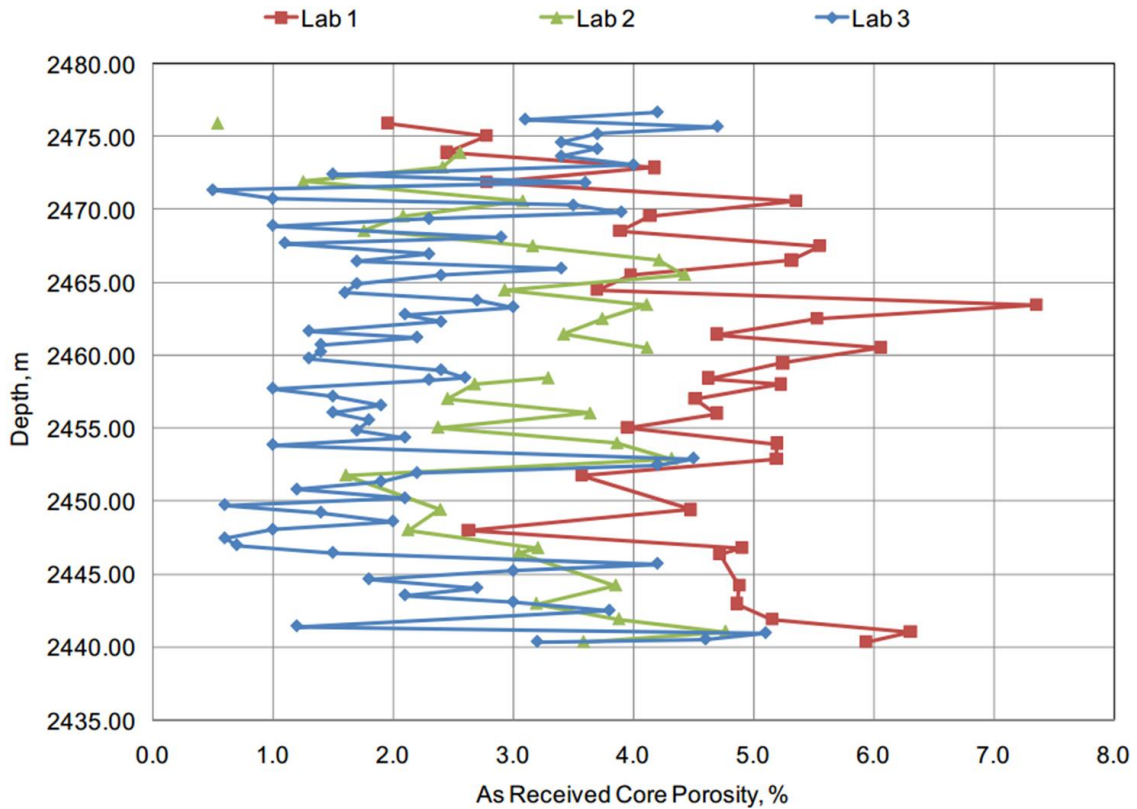


Figure 2.23. Comparison of as-received core porosity results

Labs 1 and 2 use crushed rock methods, but differ in crushing and sieving preparation methods. Lab 3 is based on measurements taken on a core cylinder (Sondergeld et al., 2010).

2.3.5 Summary: a petrophysical model for shale gas reservoirs

The preceding sections outline the rock volumes included within laboratory determinations of ϕ and S_w . This can be summarised in a simplified petrophysical model (Figure 2.24) as suggested by Bust et al. (2011). Whilst this does not include features related to fabric as determined by depositional and burial processes, it highlights the major mineral and organic components and their respective pore space/fluids. Principally, it highlights a dual porosity system: an organic porosity containing free and adsorbed gas, and an inorganic porosity containing clay bound and non-clay bound fluids. Whether or not the inorganic pore volume contains any adsorbed or free gas is yet to be conclusively determined, and though some authors suggest that the inorganic pore space contains no free gas (e.g. Alfred and Vernik, 2013) is likely to vary from reservoir to reservoir with the Alfred and Vernik model as an end member.

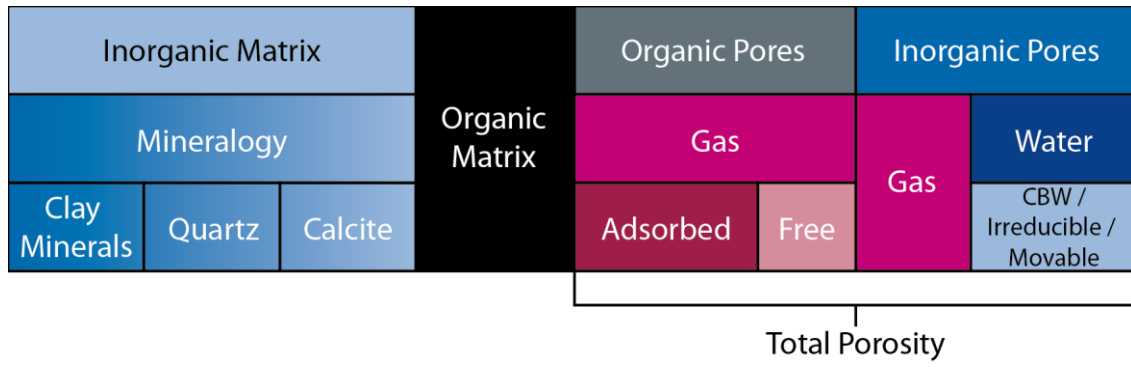


Figure 2.24. Generalised petrophysical model for a shale gas system
 Taken from Bust et al. (2011).

2.4 Evaluating water saturation: Archie's equation

The following section introduces Archie's equation and the determination of S_w using the resistivity log response. First Archie's equation is outlined with a brief discussion of the physical properties and value constraints of key Archie parameters. This is followed by a review of 'shaly sand' saturation models; adaptations of Archie's equation designed to compensate for the electrical properties of clay minerals, and a review of model uncertainties. It should be noted that deriving S_w by Archie methods is part of typical petrophysical workflows for shale gas systems. To give a sense of how determining S_w fits within the overall process of formation evaluation, an example workflow is presented in Appendix D.

2.4.1 An introduction to Archie's equation

In the 1930's and 40's Gus Archie undertook a series of experiments on core samples collected from Gulf Coast sandstone reservoirs and established a number of empirical relationships which have come to underpin resistivity based formation evaluation to the current day.

Archie's work stemmed from initial experiments undertaken on a variety of 100% brine saturated (20-100 g/l NaCl) sandstone core samples with a ϕ_t range of between 10 to 40%. He noted a linear relationship between sample resistivity at 100% brine saturation (R_o) and the resistivity of the saturating brine (R_w). He named the x coefficient for the linear trend the 'Formation Resistivity Factor' or F (Adisoemarta et al., 2000; Archie, 1942; Edmundson, 1988a). The relationship is generally written as:

$$F = R_o / R_w \quad (2.6)$$

Archie found that F was '*.. a function of the type and character of the formation, and varies, among other properties, with the porosity and permeability of the reservoir rock.*' Specifically, he noted that whilst ϕ_t varied significantly between formations, that

the character of the relationship between F and ϕ_t remained relatively consistent (Archie, 1942). The linear equation between F and ϕ_t is:

$$F = \frac{1}{\phi_t^m} \quad (2.7)$$

where: ϕ_t = Total porosity

m = The slope of the linear regression line defining the relationship between F and ϕ_t , known more simply as the **porosity exponent**

1 = The y intercept, commonly referred to the **α factor** or **tortuosity factor**

Archie found m to be specific to the pore geometry and depositional history of the formation under investigation and reported m values of between 1.8 and 2 for consolidated Gulf Coast sandstones and 1.3 for clean unconsolidated sands packed in the laboratory (Archie, 1942).

Archie developed these relationships further, and, drawing on previous studies relating to the resistivity of partially water saturated sands, suggested a second factor, the Resistivity Index or I , so as to increase sample resistivity when only partially saturated with an electrolytic fluid:

$$R_t = I * R_o \quad (2.8)$$

Combining existing literature and reported data, Archie noted the following relationship when plotted on a log: log scale:

$$I = \frac{1}{S_w^n} \quad (2.9)$$

where: n = Saturation exponent (found to be close to 2 (Archie, 1942))

By combining equations 2.7 and 2.9, the now termed Archie's equation expresses the relationship between ϕ_t , the fraction of ϕ_t saturated with conductive pore fluid (S_w) and the measured true resistivity (R_t) of the partially saturated clean sand:

$$S_w = \left(\frac{R_o}{R_t}\right)^{\frac{1}{n}} \text{ commonly written as: } S_w = \left(\frac{\alpha R_w}{\phi_t^m R_t}\right)^{\frac{1}{n}} \quad (2.10)$$

An idealised relationship for Archie parameters F , α , m , n and I with ϕ_t and S_w are displayed using artificially generated data in Figure 2.25.

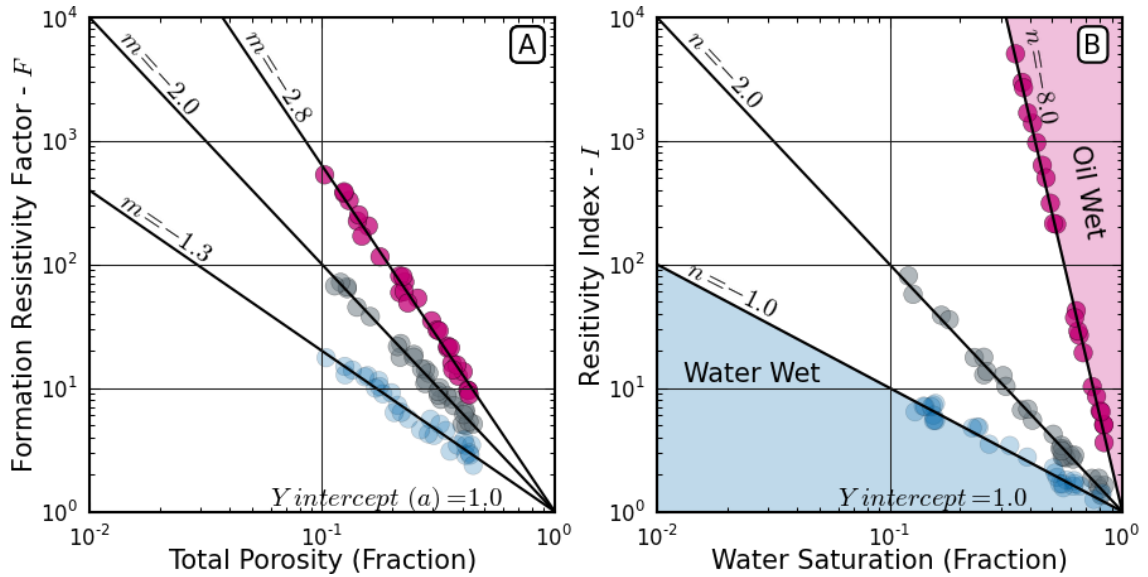


Figure 2.25. A: Formation factor (F) vs. total porosity and B: Resistivity index vs. water saturation
 Artificial data illustrating Archie relationships for F (A) and I (B). Based on figures in Edmundson (1988b).

Archie’s equation and the relationships between R_t , ϕ_t and S_w can be summarised in a Pickett plot (Figure 2.26) after (Pickett, 1966). This highlights a linear negative relationship between with ϕ_t and R_t ; the resistivity decreases as the conductive water filled pore volume increases. As S_w decreases, i.e, as the water filled pore volume is displaced by resistive hydrocarbons the, negative linear relationship between R_t and ϕ_t moves to the right.

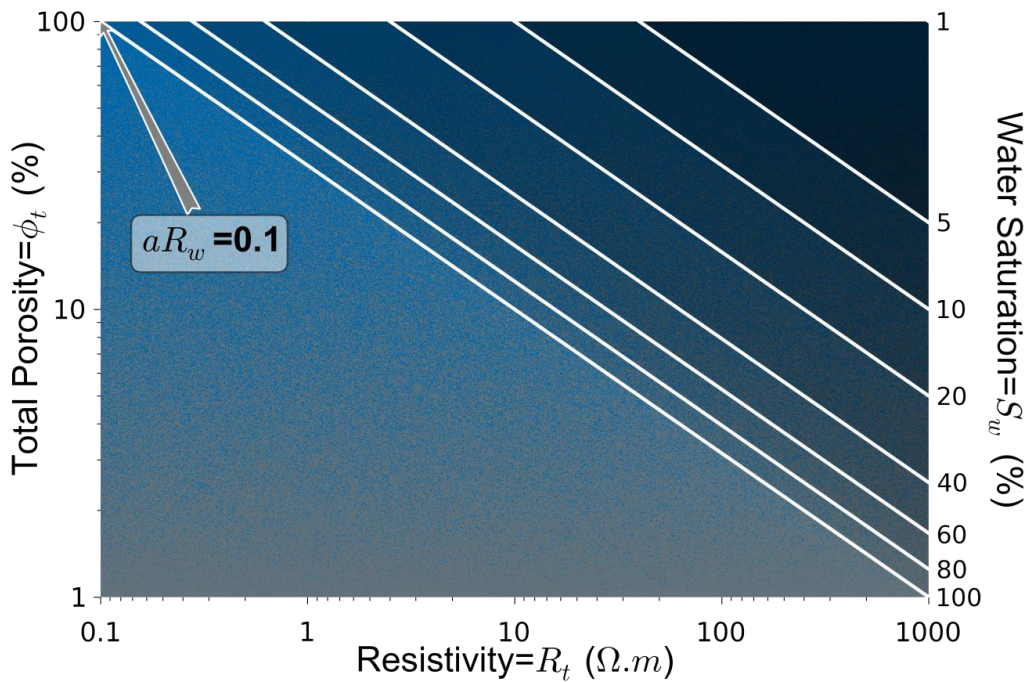


Figure 2.26. Pickett plot summarising key Archie relationships.

2.4.2 Archie parameters (a , m and n)

Archie (1942) noted an empirical link between F and variations in a rocks ϕ_t and permeability (k), suggesting a link between pore geometry and geological history. Over subsequent decades numerous studies have sought to explore those geological factors controlling the development and evolution of formation pore space, so as to better understand and select appropriate a , m and n exponent values. The following section explores the possible physical meaning and value range of Archie parameter values.

2.4.2.1 The a multiplier (sometimes referred to as tortuosity)

In Archie's original paper, the linear relationship between F and ϕ_t (equation 2.7) was explored with no physical interpretation given to the value of the y intercept (a). Moreover, despite the close association between ϕ_t and k , Archie utilised ϕ_t simply because he found it to be more reliable in predicting F than k . This empiricism, in combination with the limited geological definition of m given by Archie, led numerous researchers to seek a physically grounded model linking geometrical and textural parameters (pore tortuosity and surface area) to resistivity (Edmundson, 1988a). Wyllie and Rose (1950) suggested a model where the y intercept represents the physical relationship between ϕ_t and k , expressed as the tortuosity flow path of a fluid through the pore network. This can be visualised as a bundle of sinuous capillary tubes (Donaldson and Tiab, 2003; Salem and Chilingarian, 1999), where the tortuosity of the tube is represented by its deviation from a straight line across a sample after Carman (1937):

$$a = \left(\frac{L_a}{L} \right)^2 \quad (2.11)$$

where: L_a = Length of ionic flow path

L = Length of the porous medium traversed

Whilst this links a with ϕ_t , k and thus F , it is inherent within the capillary tube model that ions should flow along paths similar to the pore fluid. Such that $a = 1$ reflects both the shortest ionic and the shortest fluid flow path between two points and the values of $a > 1$ indicate increasingly inefficient or tortuous routes (Clennell, 1997). Whilst

simple and attractive however, linking ionic and fluid flow within a capillary tube model fails to reconcile the differences between the two, and more specifically, it fails to consider the possibility that the ionic flow medium may not be the free fluid. In other words, the shortest ionic flow path may not be the shortest fluid flow path (Clennell, 1997). This conceptual uncertainty is compounded by the limited agreement between laboratory and empirically derived relationships. For example, despite laboratory determined a values of between 1.37 and 3.3 for a number of sandstone samples, Winsauer (1952) found data for the Humble Formation to fit the following equation:

$$F = \frac{0.62}{\phi_t^{2.15}} \quad (2.12)$$

Where after Wyllie and Gregory (1953), the generally accepted notation of F became:

$$F = a/\phi_t^m \quad (2.13)$$

The observation that suitable empirical relationships can be found in the range of $a < 1$ or $a > 1$ (e.g. Worthington, 2011a, 2011b) makes it hard to accept a within the context of the above capillary tube analogy (where minimum theoretical value is $a = 1$). So what is a ? Numerous observations and studies link changes in a to k and ϕ_t , (Haro, 2009, 2008; Kurniawan and Bassiouni, 2007; Kurniawan et al., 2007; Rezaee et al., 2007; Worthington, 2011b). For instance, Rezaee et al. (2007) notes that increases in a are often linked to decreases in ϕ_t , and changes in grain size and sorting, but observes that a is independent from m and defines a as the tortuosity of the pore throats, whereas m relates to pore connectivity. Though it should be noted that a is dependent on m where determined from graphical relationships (e.g Figure 2.25). It is also noted (Kurniawan and Bassiouni, 2007) that a is linked to the thickness of the CBW layer and fluid salinity; at higher salinities abundant ions satisfy clay surface charge, minimising CBW thickness and thus dilating pore throats. Thus, whilst a , k , ϕ_t and therefore F may be intrinsically linked physically, their interplay electrically is far more complex, and, after decades of research, a still lacks an accepted physical definition. Where Ransom (2007) suggests that a simply has no physical relationship with pore geometry and m or their controlling factors such as grain shape, size, compaction, cementation or the

presence of clay grains. Instead, Ransom (2007) suggests that a is an intrinsic property of the resistivity relationship and F , and is proportionally related to secondary electrically conductive influences that affect ionic conduction, but not necessarily fluid flow.

As a consequence of the physical ambiguity that is a , a value of 1 is generally assumed (Awolusi et al., 2005; Heidari et al., 2011). Where in general, a is considered as a 'fudge' factor determined and 'tweaked' to optimise the relationship expressed for F , and is usually determined from the best fit line on a log plot of F against ϕ_t (e.g. Figure 2.25).

2.4.2.2 The porosity exponent, m

The porosity exponent (m) represents the slope of the best fit line for the correlation between F and ϕ_t (Figure 2.25). Where the steepness of m , and thus the log scale $F : \phi_t$ relationship, is related to the formation's geological history (Archie, 1942). This links m to those geological factors (depositional environment, burial history) that influence the evolution of pore geometry (Adisoemarta et al., 2000). The relationship between F , ϕ_t and m is depicted in Figure 2.25, where increases in m are generally related to greater grain cementation/consolidation or increased pore complexity.

Similar to models for a , basic conceptual models for m are likened to a porous medium composed of bundled capillary tubes (Donaldson and Tiab, 2003; Glover, 2009; Salem and Chilingarian, 1999). Though a value of $m=1$, which represents a series of capillary tubes crossing a sample in a straight line, is not considered feasible for real rocks. Whereas increases in m above unity indicate a reduced number of capillary tubes available, a narrowing of tubes, an increase in the number of dead ends within those tubes present, or any combination of factors which may influence capillary tube geometry and reduce pore connectivity (Salem and Chilingarian, 1999). This intrinsically links m with a and therefore pore connectivity and k (Glover, 2009). This relationship is depicted below in Figure 2.27, which contrasts the effects of a static selection of $a = 1$ versus a variable selection of a on the magnitude of m (Donaldson and Tiab, 2003). This effect can be significant, where as discussed in section 2.4.2.1, though a , k and ϕ_t are intrinsically linked, a is problematic to define, measure or

predict and so is generally assumed as equal to 1. Though making this assumption has however been shown to negatively affect the accuracy of S_w estimates in some studies (Adisoemarta et al., 2000; Rezaee et al., 2007). In addition to capillary tube analogies, Adisoemarta et al (2000) also links increases in m above 1 to an increasing contrast between the cross-sectional area of the pore and pore throat. Glover (2009) takes a similar view, interpreting m as representing the rate of change between porosity and pore space connectivity. Ransom (2007) describes m as an intrinsic property of the rock, related to the geometry of the electrically conductive water network as imposed by the pore walls or surfaces of solid insulating materials. Though perhaps as a function of the wide variety of formation properties which may govern and influence m values, such as: grain shape, size, orientation, surface rugosity, angularity, sphericity, structure, pore dimensions, pore isolation, pore throat size, authigenic mineral growth, and overburden pressure, there is no universally accepted definition of m (Donaldson and Tiab, 2003).

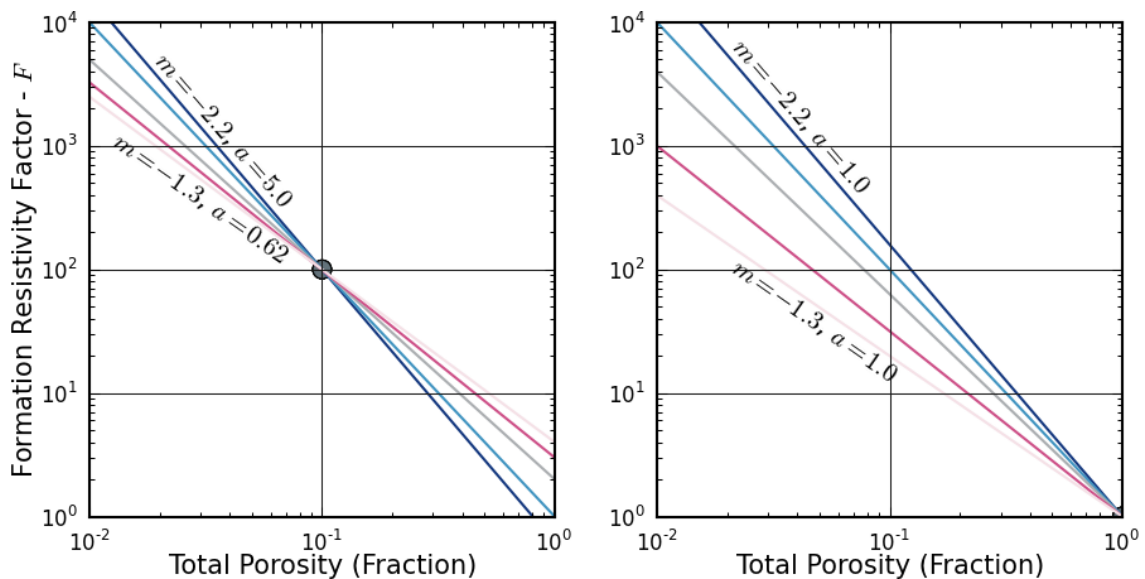


Figure 2.27. Formation factor (F) vs. total porosity for variable (left) and fixed $a=1$ (right) values
 F and ϕ_t relationships for variable (left) and fixed (right) a values (redrawn from Donaldson and Tiab (2003)).

Values of m have been shown to vary quite significantly for a range of rock types. For instance values of between $m=1.3$ and $m=2.0$ were found for unconsolidated sands and cemented sandstones respectively (Archie, 1942). Later experimental work has also demonstrated m for a number of different lithologies and materials packed in the laboratory including $m=1.3$ for a pack of perfectly spherical grains, $m=1.5$ for

unconsolidated sands, $m=5.5$ for vuggy carbonates, with values of around $m=2$ for mudstones and chinks (Edmundson, 1988b; Jackson, 1978). The limits placed on m value selection are therefore relatively well constrained, $m=1$ represents the theoretical minimum, $m=2$ is a standard value assumed if no other information is available (Awolusi et al., 2005; Knackstedt et al., 2007), and values of m increase above one in relation to relative pore geometrical complexity. Following Archie's equation for F , where a is known or assumed as equal to 1, m can also be calculated from Archie relationships (equation 2.14). Though m is more commonly derived graphically, resolved using a Pickett plot or plot of F against ϕ_t (Figure 2.25) for the formation in question.

$$m = \frac{\log(F/a)}{\log \phi_t} \quad (2.14)$$

2.4.2.3 The saturation exponent, n

In Archie's 1942 paper, n , later termed the saturation exponent, was given only cursory mention as a value that appeared to be close to 2 for both consolidated and unconsolidated sands (Archie, 1942). Based on this observation, Archie used $n=2$ as a constant, where, as expressed in his formula for the Resistivity Index (I), variations in S_w are solely responsible for altering a formation resistivity.

It is now accepted that many other factors such as fluid distribution, pore size distribution, wettability and fluid displacement history may also have a considerable effect on increases in formation resistivity relative to corresponding decreases in S_w (Edmundson, 1988b). These other factors can be represented by value changes in n , where n represents the degree to which the presence of hydrocarbons may interfere with ionic conduction as controlled by pore geometry and pore wall conditions. For instance, increasing n values can reflect a transition from water-wet to oil-wet rock systems as oil coated grain boundaries decrease formation conductivity (Donaldson & Siddiqui 1989). Where, in a water-wet pore system, as S_w decreases, n remains low as ionic conduction can be maintained along the water-wet pore walls. In an oil-wet pore system, as water S_w decreases, the remaining free water can become isolated, inhibiting conduction and leading to rapid increases in n (Adisoemarta et al., 2001).

Pore wall rugosity and micro-porosity have also been observed to impact n and the effects of hydrocarbon invasion on formation conductivity. Analyses undertaken by Diederix (1982) showed that n remained constant at a given S_w for a pack of smooth beads, whilst the same experiment using rough beads results in varying n values. SEM images also revealed the effects of clay micro-porosity on pore-wall surfaces and found that n values were low in sandstones at low S_w , as quartz grains had coatings of illite and kaolinite, and were higher, near $n=2$, at higher S_w where quartz grains had no grain coating. Diederix (1982) concluded ‘...that a rough surface will retain a relatively thick water layer through capillary forces, thus providing a favourable path for electrical conductance’.

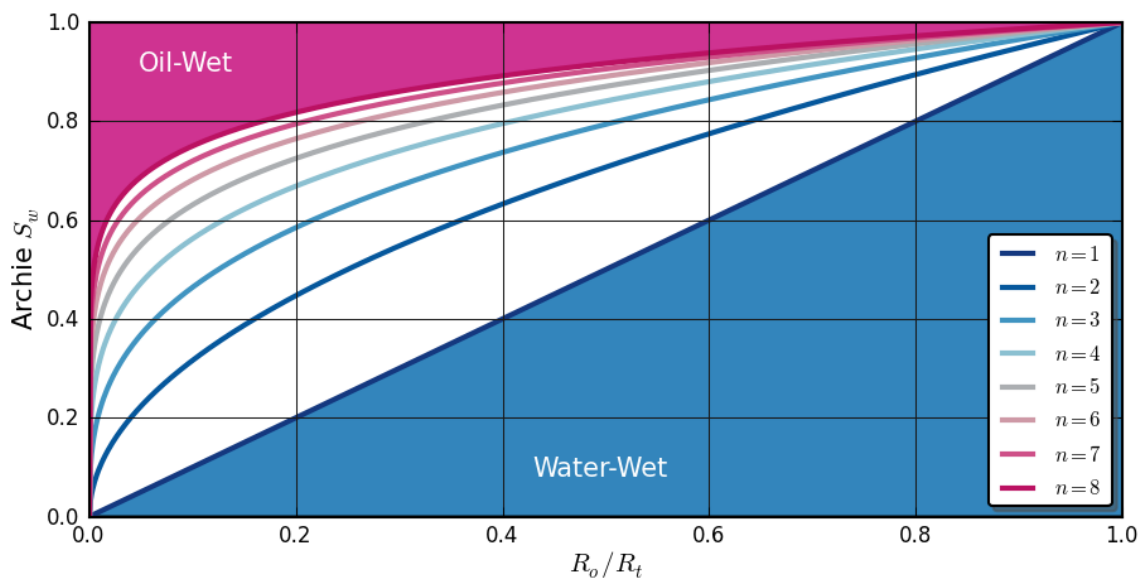


Figure 2.28. Relationship between calculated S_w , R_o/R_t and n

The effect of variable n values on calculated S_w (redrawn from Adisoemarta et al. (2001)).

The interplay of pore geometrical and surface conditions on n is generalised in a plot of I versus S_w in Figure 2.25, which displays an n range of $n=1$ to 8. At $n \geq 8$ the formation can be considered oil wet, whereas at the theoretical minimum ($n=1.0$) the formation can be considered as water wet. This is further generalised in Figure 2.28, which highlights the impact of variable n on S_w at low R_o/R_t values. Crucially it highlights that higher n values result in higher S_w values, such that an inappropriate selection of n may result in inaccurate S_w estimations, particularly at low S_w , where variations in n have the largest impact. It has also been shown that hydrocarbon invasion and saturation history can also affect n . Implying that invasion events may alter pore wall wettability,

or that different oil saturation distributions may result in varying impacts to ion conduction and n (Donaldson and Tiab, 2003; Edmundson, 1988b).

In summary, similar to m , the likelihood of n being constant for a formation is limited to only homogenous, clay free materials. This view is iterated by numerous authors who conclude that n is not a constant, but a product of S_w whose value is moderated by secondary factors relating pore geometry and pore wall conditions as described above (Adisoemarta et al., 2001; Donaldson and Tiab, 2003; Edmundson, 1988b; Haro, 2009; Stalheim and Eidesmo, 1995; Worthington, 2004). This suggests that in many respects n is similar to m (as n is related to pore geometry and pore wall conditions) such that n may be considered as essentially representing m following hydrocarbon migration into the formation (Ransom 2007). Under this rationale n cannot theoretically be less than m , a situation which would paradoxically require invading hydrocarbons to be more conductive than the displaced fluid. This suggests that whilst n cannot be less than m , neither should it possible for n to equal m at conditions other than 100% S_w . Where the presence of any hydrocarbons (S_w at less than 100%), would therefore require n to have at least a value greater than m , with n reaching a potential maximum value at irreducible S_w (Ransom, 2007). This view may however be considered contentious by some, after all, Archie's equation is based on observation, and m and n have no strict physical definition. As such, if it can be shown to be geologically justifiable, there are no grounds to dismiss n values lower than m . The selection of values for n can therefore be relatively well constrained, $n=1$ represents the theoretical minimum, $n=2$ is a standard value assumed if no other information is available, and values of n above one can be related to S_w , wettability and relative pore geometrical complexity. In common practice, n is derived graphically using a log plot of I against S_w , n is also commonly assumed as simply equal to m .

2.4.3 Shaly sand concepts

The previous section summarises Archie's Equation and associated parameters as developed for clay free sandstone reservoirs. In this context 'Archie' rocks can be defined as those which broadly adhere to the empirical relationships established by Archie (1942), and are free of 'non-Archie,' primarily clay effects. In other words, they

should display an ideal conductivity relationship where F remains constant for a 100% water saturated sample relative to changes in fluid resistivity. This is highlighted in Figure 2.29, where the 'clean sand' line depicts the ideal conductivity relationship for an 'Archie rock.' Figure 2.29 is plotted in terms of conductivity, where the Archie relationship for F is given as:

$$F = R_o / R_w = C_w / C_o \quad (2.15)$$

where: C_o and C_w are the reciprocal conductivity values of R_o and R_w respectively.

Following the development and application of Archie's equation to other formations, it was soon noted that F was not always constant for a given sample, but can decrease with C_w (Patnode and Wyllie, 1950; Worthington, 1985). Adapting Archie's equation to describe a wider variety of formations began with the understanding that unlike Archie rocks, the relationship between C_o and C_w is not linear, but curved in formations containing a significant clay content (Winsauer and McCardell, 1953). An observation attributed to the development of excess conductivity resulting from the accumulation of pore fluid ions within the double layer interface of clay minerals surfaces (see section 2.3.3.1). These ideas were further developed by Waxman and Smits (1968) who developed a relationship between the electrical conductivity of water-saturated shaly-sands to C_w and the CEC of the rock, which was later extended to include partially saturated conditions.

There are many formations with sufficient clay material that they cannot be classed as 'Archie rocks' as defined in Figure 2.29. The drive to compensate for the electrical behaviour attributed to the presence of clay minerals has resulted in the development of a plethora of 'shaly-sand' models. Within which the additional conductivity is generally incorporated into Archie's equation for F (equation 2.15) in the following form after (Worthington, 1985):

$$F = C_w / C_o + X \quad (2.16)$$

where: X = Composite shale conductivity term; approaches zero in 'Archie' rocks

The interrelationships between C_o , C_w and X are depicted in Figure 2.30, highlighting that the absolute value of X increases with C_o to some plateau and then remains constant as C_w continues to increase (Worthington, 2007, 1985). The clean sand line is expressed in the traditional Archie form as described by equation 2.13, whereas the shaly sand line is generally expressed as an Archie-type relation referred to as an ‘apparent or shaly-sand formation factor.’ The notations representing F and other Archie parameters can be confusing, but in non-Archie rocks the ‘apparent’ Archie parameters are generally denoted with an asterisk (*), i.e., in an Archie rock the porosity exponent is m whereas in a non-Archie rock the ‘apparent’ porosity exponent is m^* . This rule follows for F (F^*) and n (n^*).

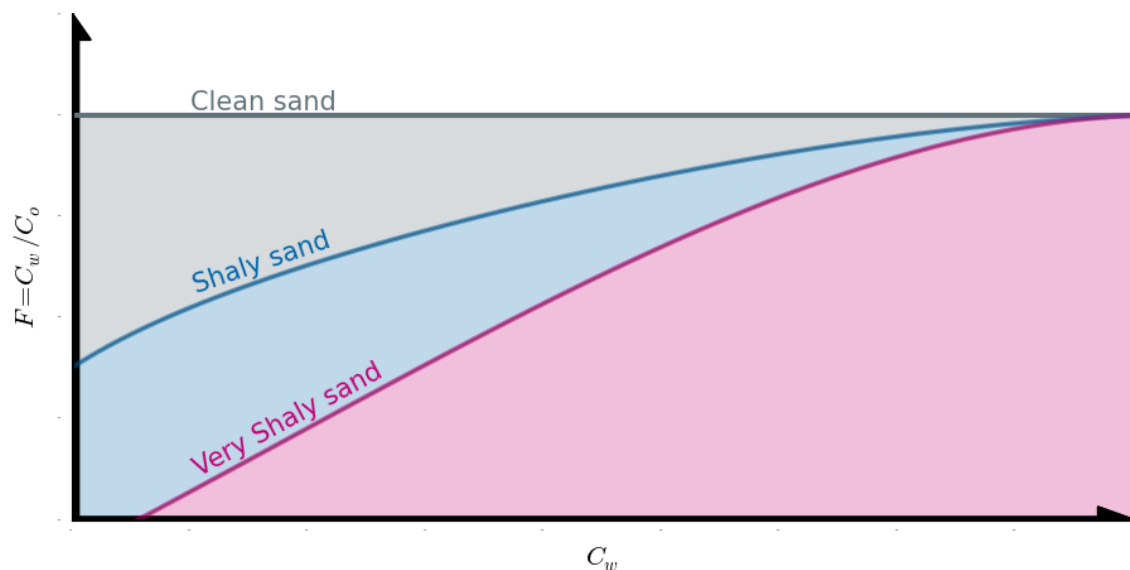


Figure 2.29. Effect of shale on F , C_w relationships

The effect of shale ‘excess conductivity’ and increasing C_o on conductivity relationships and F , note the departure of the shaly sand lines from the clean sand line, particularly at low C_o values (redrawn from Worthington (1985)).

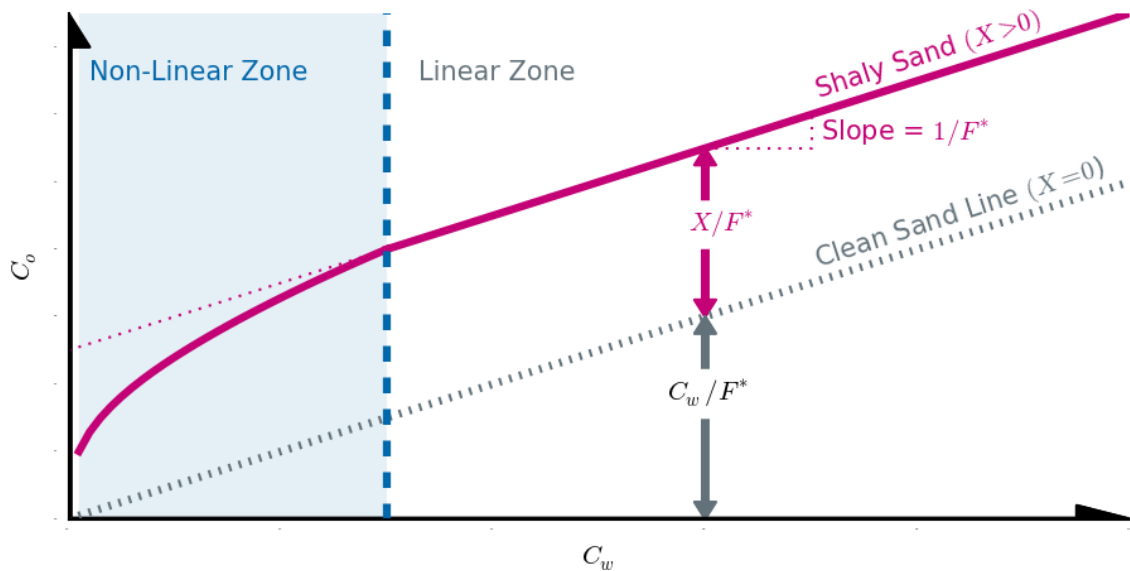


Figure 2.30. Schematic relationship between C_o and C_w

Relationship C_o and C_w illustrating the the effect of shale 'excess conductivity' (adapted from Juhasz (1981) and Worthington (2007)).

A large number of shaly-sand saturation models have been proposed to address problems associated with clay conductivity (e.g., Bardon and Pied, 1969; Clavier et al., 1984; Poupon and Leveaux, 1971; Waxman and Smits, 1968; Simandoux, 1963). All of these models, and many more, attempt to compensate for clay effects by partitioning formation resistivity between that associated with clay bound water (CBW) and free water. The approach taken by these models varies however, and can be categorised after Worthington (1985) into two distinct groups according to how the problem of clay excess conductivity is approached. These groups are categorised as a) ionic double layer models, and b) clay volume models, and are discussed briefly below:

- a) ***Ionic double layer models*** such as Clavier et al. (1984) and Waxman and Smits (1968) utilise clay minerals ability to form an ionic double layer that reflects their CEC; a measure of their ability to absorb or exchange cations within a solution (Ellis and Singer, 2007). A key advantage of shaly-sand methods based on the ionic double layer properties of clay is their ability to account for clay type and distribution within a formation (Worthington, 1985).
- b) ***Clay volume models*** such as Simandoux and Poupon and Leveaux (1971) can be classified as belonging to a group of methods based on clay volume (V_{clay}) fraction. Where V_{clay} can be defined as the volume of wetted clay per unit

volume of reservoir rock, and thus accounts for clay bound water as it relates to total porosity (Worthington, 1985). In this manner, the excess conductivity of the formation is managed volumetrically. Worthington (1985) describes this as a disadvantage for a number of reasons, but most significantly because the V_{clay} parameter does not take into account clay distribution or composition, such that variations in these factors may yield significant clay effects for the same V_{clay} fraction.

For reference, the equations for some common shaly sand models include (Brown, 1986; Worthington, 1985):

$$\begin{array}{l} \text{Normalised} \\ \text{Waxman} \\ \text{Smits} \end{array} \quad R_{we} = \frac{R_{wf} R_{wb} S_{wt}}{R_{wb} (S_{wt} - Q_{vn}) R_{wf} Q_{vn}} \quad S_{wt} = n^* \sqrt{\frac{R_{we}}{\phi_t^{m^*} R_t}} \quad (2.17)$$

$$\begin{array}{l} \text{Normalised} \\ \text{Dual Water} \end{array} \quad R_{we} = \frac{R_{wf} R_{wb} S_{wt}}{R_{wb} (S_{wt} - S_{wb}) R_{wf} S_{wb}} \quad S_{wt} = n^* \sqrt{\frac{R_{we}}{\phi_t^{m^*} R_t}} \quad (2.18)$$

$$\begin{array}{l} \text{Indonesia} \end{array} \quad \frac{1}{\sqrt{R_t}} = \left[\frac{V_{sh} \frac{1-V_{sh}}{2}}{\sqrt{R_{sh}}} + \frac{\phi_e^{m/2}}{\sqrt{\alpha R_w}} \right] S_{we}^{n/2} \quad (2.19)$$

$$\begin{array}{l} \text{Simandoux} \end{array} \quad \frac{1}{R_t} = \frac{\phi^m S_w^n}{\alpha R_w} + \frac{V_{sh} S_w}{R_{sh}} \quad (2.20)$$

where: equations 2.17) and 2.18) are ionic double layer models and equations 2.19) and 2.20) are V_{clay} based methods.

There are multiple shaly sand methods and a detailed review of their application is beyond the scope of this review. It is however recognised that of the many models available, that the CEC based models have the greatest scientific pedigree (Worthington, 1985), but require core in addition to log data .

2.4.4 Model uncertainties

Herrick and Kennedy (2009) describe Archie's equation as '*a good descriptor of the trends observed...*', but add that there are '*no physics inherent in the description. Consequently, the theory's parameters, m, n, and a, are a priori physically meaningless. Although it can be argued that these parameters must be functions of the distribution*

of the conducting phase...’ Though contentious, this view is reflected in the hundreds of papers seeking to adapt or physically link Archie parameter values to geological properties (e.g. Hill and Milburn, 1956; Khairy and Harith, 2011; Kumar et al., 2011; Mungan and Moore, 1968; Patnode and Wyllie, 1950; Ritch and Pennebaker, 1978; Winsauer, 1952; Wyllie and Gregory, 1953; Wyllie and Rose, 1950; Wyllie and Southwick, 1954) or those papers seeking to develop new, physically consistent conductivity models for porous media (e.g. Adisoemarta et al., 2001, 2000; Glover, 2009a, 2009b; Haro, 2008; Herrick and Kennedy, 2009; Iheanacho, 2013; Kurniawan and Bassiouni, 2007). For instance Iheanacho (2013) suggests that m and n are of the same origin and should be replaced by a single ‘*tortuosity*’ factor. Similarly, Kennedy and Herrick (2012) suggest a conductivity model with a single geometrical factor interpreted as the fraction of the porosity’s cross-sectional area participating in conduction. In spite of these efforts however, Archie based approaches remain the de facto method for determining S_w across a range of lithologies and the physical ambiguity of Archie parameters persists. Whilst physically exact definitions might not be applicable to Archie parameters, they have been indisputably shown to reflect pore geometrical and surface conditions (see section 2.4.2). Thus, in accepting that Archie’s empirical equation may have physical/conceptual limitations, the greatest uncertainty arises from its adaptation and application within complex heterogeneous reservoirs, where the selection of geologically meaningful Archie parameters becomes increasingly problematic. For instance, Worthington (2001) finds significant directional dependence on a and m parameters in sandstone reservoir rocks, highlighting non-systematic variations in parameter values of up to 200%. This demonstrates that Archie parameters can vary markedly even in relatively simple reservoir rocks, suggesting that the widespread use of assumed values (e.g. $a=1$, $m=n=2$: Adiguna, 2012; Awolusi et al., 2005; Han et al., 2008; Heidari et al., 2011; Knackstedt et al., 2007; Popielski et al., 2012; Ramirez et al., 2011) for lithologies ranging from clean sandstones to tight gas shales is likely to result in significant uncertainty in derived S_w estimates. This is especially true of shale gas systems, whose mineralogical and structural heterogeneity (see section 2.1) is not reflected by the vertical resolution of wireline data or core sampling frequency (see section 2.2), and so is not well

represented by models based on petrophysical homogeneity. Though empirical relationships suggest m values of between 1.45 to 1.85 in shale gas plays (Ramirez et al., 2011; Wu and Aguilera, 2013; Yu et al., 2013; Zhao et al., 2007), with m also linked to organic matter maturity in some shales (Wu and Aguilera, 2013). In general however, whilst they remain the de facto choice, the applicability of Archie based models in shale systems is widely questioned (Alfred and Vernik, 2013; Bust et al., 2011; Doveton, 2001; Glorioso and Rattia, 2012; Modica and Lapierre, 2012; Passey et al., 2010). Where a recognised failing of Archie and shaly sand method is the implicit assumption that the nature of the pore space and derivative electrical effects are consistent for all clay-bound and non-clay bound formation fluids alike (Haro, 2008; Herrick and Kennedy, 2009; Kurniawan and Bassiouni, 2007; Worthington, 1985). In other words, there is only a single set of pore geometrical factors (m, n), which assumes that all formation fluids exist in pores that share similar geometries, pore wall conditions and electrical properties. A situation which clearly contradicts the petrophysical model for a gas bearing mudstones (Figure 2.24), where multiple fluid phases are located in pore spaces hosted by a structurally and mineralogically heterogeneous organic rich matrix (Bust et al., 2011; Glorioso and Rattia, 2012; Passey et al., 2010; Quirein et al., 2010). These uncertainties are compounded by a lack of published experimental data examining Archie parameters in shale samples. Although some studies have examined shale dielectric and electrical petrophysical properties (e.g. Al-Marzoug et al., 2013; Clennell et al., 2006; Dewhurst et al., 2013, 2008), these have focused on examining relationships between CEC, depth, consolidation and compressive strength. This lack of data is likely attributable to a number of factors, firstly, connate fluid and resistivity data sampled from core material is scarce and unreliable due to the influence of flowback water, imbibed drilling fluids and free water in fractures that may not be representative of shale pore fluids (Bustin et al., 2008; Nieto et al., 2009). This is highlighted by questionably large variations in fluid salinity over short vertical distances measured in the Horn River Basin (Sondergeld et al., 2010). Moreover, special core analysis (which is not performed at reservoir conditions) is expensive and time consuming, and, for the determination of Archie parameters (where an understanding of fluid resistivity is both critical and lacking) core

scale structural heterogeneity and variation in S_w can yield large variations in n and m , which can in turn lead to inaccurate Archie log models (Bona et al., 2014; Clarkson et al., 2012; Nieto et al., 2009). As a consequence, special core analysis and the determination of F , l and thus m and n is not often included within petrophysical workflows (e.g. Bust et al., 2011; Pitcher et al., 2012, see Appendix D). Despite this, in the absence of alternative models, the application of Archie based log models to shale sequences is routine (e.g. Adiguna, 2012; Ahmad and Haghghi, 2012; Boyce and Carr, 2009; Glorioso and Rattia, 2012; Haghghi and Ahmad, 2013; Nieto et al., 2009; Popielski et al., 2012; Ramirez et al., 2011; Utley, 2005; Wu and Aguilera, 2013), where Archie parameter selection is often not mentioned, simply assumed, or data lead/fitted/optimised/calibrated/solved/selected to match benchmark/baseline core saturation (normally Dean Stark) data (Bust et al., 2011; D. S. Chen et al., 1995; H. C. Chen et al., 1995; Chen et al., 2002; Cluff, 2012; Maute et al., 1992; Worthington, 2011a, 2011b, 2009, 2007). For instance, in applying Archie's relationships to complex reservoirs (shale gas, tight gas, gas hydrates etc.) Worthington (2011a) states that so long as the interpretive problems related to unconventional resources are *'identified correctly, a petrophysical database can be tuned optimally so that it is fit for purpose.'* Though the efficacy of this approach, and any inherent geological relationships between the output Archie parameters and formation properties have yet to be investigated.

2.5 Summary and conclusions

This literature review highlights a significant volume of material relevant to the study of the petrophysical properties of shale gas systems. Firstly it is clear that depositional processes in shale systems impart significant control on sediment fabric and composition which in turn help determine porosity-permeability distributions and formation petrophysical properties. It is also apparent that the scale of variation and heterogeneity in fabric/composition is far below that which can be reconciled by wireline data, which have a typical vertical resolution of over 30cm. Moreover, the effects of important shale attributes, e.g., *TOC*, clay contents, on wireline data is also emphasised, whilst uncertainty in how these properties impact the determination of core properties such as ϕ_{tc} and S_{wc} are discussed, highlighting further uncertainty in defining an overall petrophysical model for shale gas systems. Finally, the concepts of Archie based methods and inherent uncertainties are discussed. In this final point it should be noted that shale gas systems are not significantly referred to. As, whilst numerous authors utilise Archie based methods for the determination of the free gas saturation in shale systems, to date, none explore the nature of its application, efficacy, or attempt to link model outcomes to the overriding geological controls on shale gas systems. These latter points form the focus of the following research.

Chapter 3

The geological setting, mineralogy and petrophysical properties of the Bossier and Haynesville Shale Formations

This chapter presents an overview of the geological setting of the Bossier (BSR) and Haynesville (HY) Shale Formations, outlines the rationale for the selection of wireline and core data and characterises the petrophysical and geological data selected for study. This chapter is divided into the following sections:

- 3.1 *The BSR and HY Shale Formations; geological setting and stratigraphy.*
- 3.2 *The BSR and HY Shale datasets: rationale for data selection, data quality control, formation zoning and data corrections.*
- 3.3 *BSR and HY core data mineralogical and petrophysical properties.*
- 3.4 *BSR-HY spatial and compositional relationships.*
- 3.5 *Petrophysical trends within the BSR-HY productive region.*
- 3.6 *A note on kerogen density; outlines key uncertainties in kerogen density values.*
- 3.7 *Summary and conclusions.*

3.1 The Bossier and Haynesville Shale Formations

The productive area of the Upper Jurassic Bossier (BSR) and Haynesville (HY) Shale Formations (defined by Hammes and Frébourg (2012) in Figure 3.1) is located in the region of the Sabine Uplift, an area straddling the Texas and Louisiana border in the northern Gulf of Mexico (GOM) Basin. The BSR-HY interval in this region is recognised as one of the most prolific and active shale-gas plays in North America, with recoverable reserves estimated in the hundreds of trillions of cubic feet (Hammes and Frébourg, 2012; Hammes et al., 2011). The HY is usually of special interest and has higher reservoir pore pressures and higher initial production and steeper decline rates than many contemporary North American analogues (Eagle Ford, Woodford, Fayetteville and Barnett; Baihly et al., 2010; Diaz De Souza et al., 2012; Fan et al., 2010; LeCompte et al., 2009; Parker et al., 2009). The following section provides an overview of the geological setting, stratigraphy and palaeotopographic influences on BSR-HY deposition.

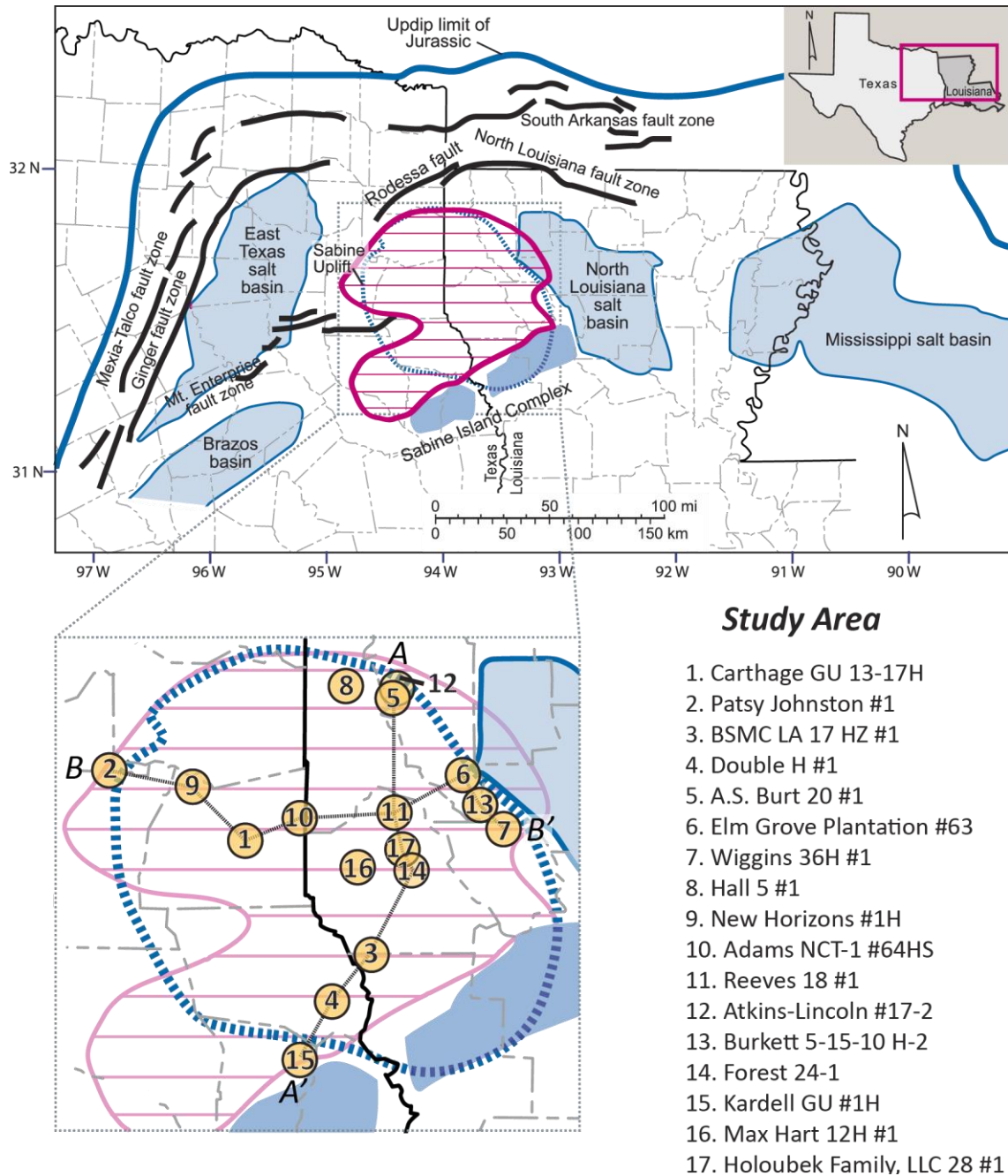


Figure 3.1. Study area

Map reproduced from Hammes and Frébourg, (2012) indicating the main structural features that influenced HY deposition: Salt Basins (green), fault zones (black) and the Sabine Island Complex (blue). The red area indicates the productive Haynesville region (2012 estimate). The expanded map indicates wells included within the study. Cross-sections A-A' and B-B' are shown in Figure 3.10 and Figure 3.11.

3.1.1 Geological setting and stratigraphy

Deposition of the BSR-HY interval began in the early Kimmeridgian (Figure 3.2) under the influence of basement structures related to the opening of the GOM basin (Hammes and Frébourg, 2012; Hammes et al., 2011; Mancini, 2010; Salvador, 1987).

GOM basin spreading began as part of the breakup of the Pangaea supercontinent in the Late Triassic (Rhaetian), with initial basin deposits including Upper Triassic and Lower Jurassic red beds, volcanic rocks and evaporites (Hudec et al., 2013b; Salvador, 1987; Stern and Dickinson, 2010). The latter evaporite deposits formed in response to intermittent flooding of sea water into the basin from the Pacific. Under arid conditions and with restricted intermittent communication with the ocean, hypersaline lakes and synsedimentary evaporites formed under the influence of structural highs and lows generated by basin extension (Salvador, 1987; Stern and Dickinson, 2010). These deposits form the widespread and fossil free Louann Salt, deposited over a poorly constrained period from the Toarcian to latest Callovian (180 to 161 Ma; Hudec et al., 2013b). Continued subsidence and the onset of sea floor spreading in the Oxfordian initiated a marine invasion from the Pacific (Salvador, 1987) and a reworking of continental deposits of the Norphlet Formation (Mancini, 2010). This was followed by the retrogradational deposition of the near shore Norphlet Sandstone Formation and the distal Smackover Limestone Formation, which initiated overburden induced movement and subsidence in the underlying Louann Salt (Hudec et al., 2013a, 2013b; Mancini, 2010; Mancini et al., 1985). Following maximum transgression in the late Oxfordian, reduced accommodation space led to the deposition of the prograding near shore Buckner Formation (sabkha deposits), with continued basinward deposition of Smackover limestones and deep basin mudstones (Hammes and Frébourg, 2012; Mancini, 2010). From the Oxfordian onward, progressive sediment loading increased salt mobility and induced a basin-ward tilting in the underlying Louann Salt (Dooley et al., 2013; Hudec et al., 2013a). Synsedimentary halokinesis (the sub-surface flow of salt) both influenced palaeotopography and the deposition of later sediments (Hammes and Frébourg, 2012), resulting in the development of numerous salt structures across the region (Condon et al., 2006). An increase in global sea level at the end of the Oxfordian marks the onset of HY (Kimmeridgian) deposition (the distal expression of the Lourak Group) which retrogrades over the proximal carbonate ramps and platforms of the Gilmer and Haynesville Lime Formations. A maximum flooding surface (MFS) at the end of the Kimmeridgian marks the BSR-HY boundary (Hammes and Frébourg, 2012) and the beginning of the progradational BSR deposition (the distal

expression of the coarser Cotton Valley clastics) in a period of rapid mechanical subsidence (Klein and Chaivre, 2003). BSR-HY stratigraphy is summarised in Figure 3.2.

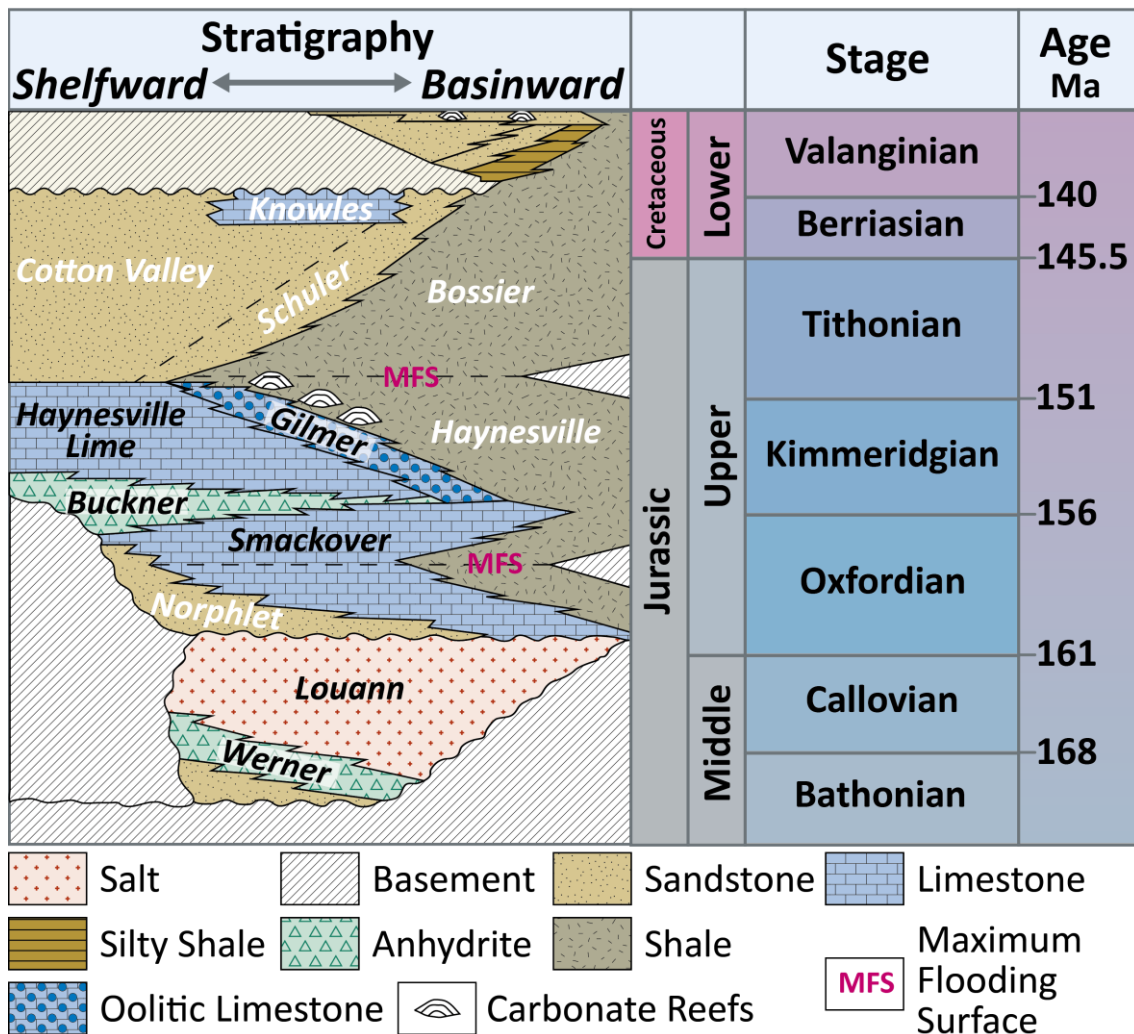


Figure 3.2: Stratigraphic section
Upper Jurassic stratigraphic section of East Texas modified after Hammes and Frébourg (2012).

3.1.2 Palaeotopography

The productive BSR-HY interval occurs in a generally shallower area of Jurassic sediments (Hammes et al., 2011) above the Sabine Uplift (Figure 3.1). A broad low relief basement arch with an elevated vertical relief that separates the East Texas basin from the North Louisiana Salt basin (Condon et al., 2006). The Sabine uplift is one of a number of basement highs in the northern GOM basin and was a positive feature throughout primary deposition in the Mid to Upper Jurassic (Adams, 2009; Condon et al., 2006). As a result of Sabine basement elevation during early GOM basin extension,

the area of BSR-HY shale-gas production (Figure 3.1) is characterised by thinner deposits of underlying Louann Salt (Adams, 2009; Hammes et al., 2011). Moreover, in addition to influencing initial sediment accumulation (Figure 3.3), foreland tectonics applied lateral compression in the middle to late Cretaceous (Laramide) resulting in a foreland fold pair; the Sabine Uplift and the North Louisiana Salt basin (Adams, 2009). This was the primary period of uplift and may have influenced heat flow, diagenetic processes and the maturation of organic matter (Condon et al., 2006; Hammes et al., 2011).

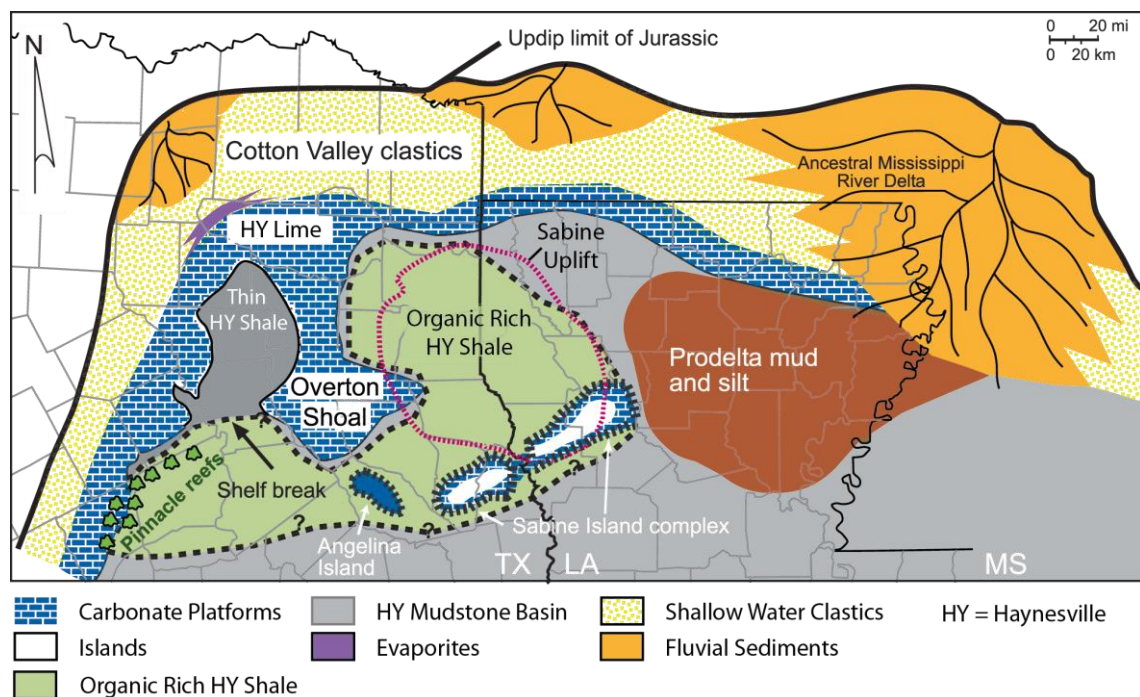


Figure 3.3: Palaeogeography at the time of HY deposition (Kimmeridgian)

Palaeogeography during Haynesville Deposition (Kimmeridgian) modified after Hammes et al., (2011).

Though the GOM is one of the most widely studied basins in the world, interest in the BSR-HY interval is relatively recent and has a correspondingly limited literature base (Hammes and Carr, 2009; Hammes and Frébourg, 2012; Hammes, 2012, 2009; Hammes et al., 2011). Key texts include Hammes and Frébourg (2012) and Hammes et al. (2011), which detail the influence of palaeotopography and the Sabine Uplift on the style of HY deposition in the Kimmeridgian (Figure 3.3). At that time, a series of carbonate banks and shoals ringed an area which would later become the East Texas Salt basin (Figure 3.1) west of the Sabine Uplift. Carbonate platforms also ringed the Sabine Uplift to the north and hugged the slopes of topographic highs and islands to

the south (Angelina Island and Sabine Island Complex). Siliciclastic input was constrained to parts of the basin east of the Sabine Uplift, an area which would later become the North Louisiana Salt basin, linked to sediments supplied by the Mississippi River Delta. As a consequence of the topographic highs and carbonate platforms to the north, west and south and due to the distance of the central and western areas of the basin to the sediment source in the east, clastic input was restricted. This led to the deposition of condensed carbonate and organic rich HY in a slope to basinal setting with storm related influxes of skeletal and carbonate material from regional highs (Hammes et al., 2011). Restriction to clastic input was compounded by an increase in global sea level throughout the Kimmeridgian and associated retreat of the sediment source. Where following maximum transgression, sea level decline marked the onset of clay rich, organic matter diluted BSR deposition, prograding westward from the Mississippi River Delta to eventually cover the area of the East Texas Salt basin (Steinhoff et al., 2011). In contrast to this, data for this study, discussed in section 3.4, indicate a predominantly northern origin to clastic sediments, though this may reflect local trends within the wider region. BSR sediments are generally characterised by higher detrital and lower organic matter contents. Though areas of BSR deposition in distal areas of the basin, which were again influenced by local topographic highs, were at times sufficiently sediment starved so as to preserve relatively high organic matter contents. This is particularly true of the unofficially termed mid-BSR, which locally preserves total organic carbon (*TOC*) of over 5% (Hammes and Frébourg, 2012).

3.2 The Bossier and Haynesville datasets

BSR-HY core and wireline data utilised in this study include 17 wells selected from the Core Laboratories (CLB) 'reservoirs applied petrophysical integrated data' (RAPID) database (access provided by BG Group). The database is part of a joint industry project to study the BSR-HY interval, which includes wireline, geological and production data for a total of 98 wells. All wireline and core data have been integrated, depth shifted and managed by CLB.

The following section outlines the rationale for the inclusion of the data within this study and describes data quality control, formation zoning and data corrections.

3.2.1 Rationale for data selection

Wells selected for inclusion within this study (and their associated core and wireline data) were required to meet two criteria:

1. Wells were selected to cover a wide geographical area within the productive HY region (Figure 3.1) with the aim of capturing basin wide variation in BSR-HY geological properties. Though the number of wells is insufficient for a comprehensive basin analysis, wells were selected along north-south (*A-A'*) and east-west (*B-B'*) transects so as to qualitatively identify geological / petrophysical BSR-HY trends.
2. Wells were screened for meeting minimum wireline (Table 2.1) and core data (Table 3.2) requirements. Only core data sampled according to the 'gas shale joint industry project sampling methodology' (Figure 3.4) were utilised. This ensured that measured core properties are both contiguous and available for all core samples included in the study.

The location, names and assigned reference numbers for wells included within this study are summarised in Figure 3.1 and Table 3.3.

Wireline data	Variable	Notation	Unit
	Gamma ray	GR	gAPI
	Neutron porosity	ϕ_n	fractional
	Density	ρ_b	g/cc
	Deep resistivity	R_t	$\Omega.m$

Table 3.1. Wireline data: minimum criteria for well inclusion within study

Gas research institute (GRI)			
Core data	Variable	Notation	Unit
	Bulk density	ρ_{bc}	g/cc
	Matrix density	ρ_{ma}	g/cc
	Total porosity	ϕ_{tC}	frac.
	Matrix permeability	k	mD
	Water saturation	S_{wC}	fractional
	Oil saturation	S_{oC}	fractional
	Gas saturation	S_{gC}	fractional
X-ray powder diffraction (XRD)			
	Calcite, dolomite, k-feldspar, kerogen (volume only), marcasite, plagioclase, pyrite, quartz, total clay (comprising Illite + mica, chlorite and mixed-layer clay fractions)	$W_{Mineral}$	wt. %
		$V_{Mineral}$	vol. %.
Geochemistry (includes total organic carbon)			
	Total organic carbon	TOC	wt. %
Core spectral gamma response (GRC)			
	Core spectral gamma response	GRC	gAPI
	Uranium, Thorium	U, Th	ppm
	Potassium	K	wt. %

Table 3.2. Core data: minimum criteria for core sample inclusion within study

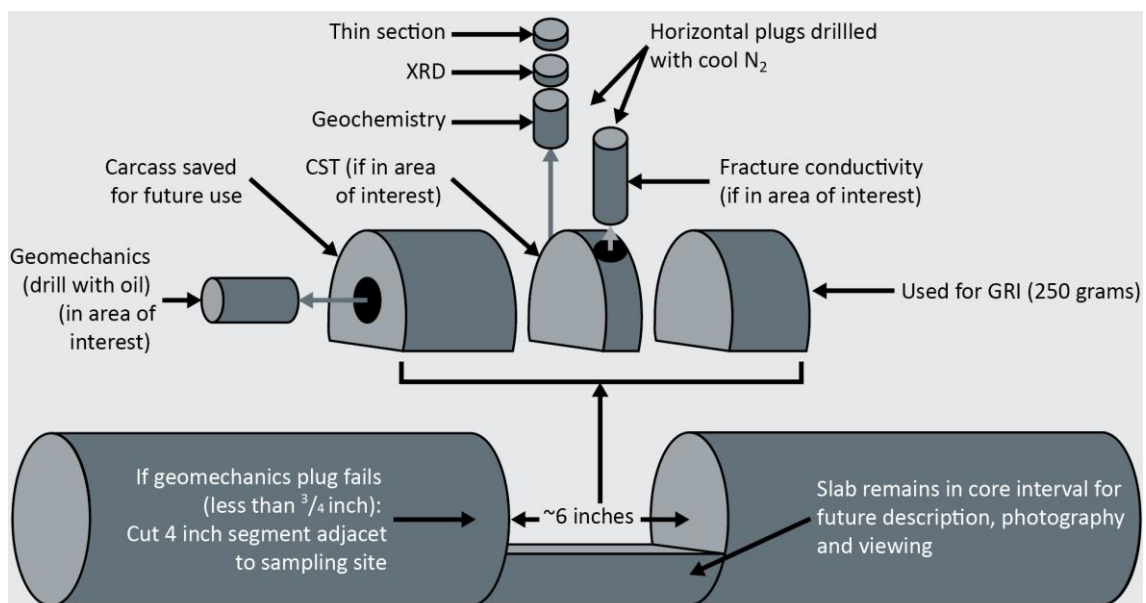


Figure 3.4. Gas shale joint industry project sampling methodology

Well ref.	Operator	Well name	Drilling fluid
1	BP America	Carthage GU 13-17H	WBM
2	EXCO	Patsy Johnston #1	WBM
3	Comstock Resources	BSMC LA 17 HZ #1	WBM
4	Marathon USA	USA Double H #1	WBM
5	Southern Star	A.S. Burt 20 #1	WBM
6	KCS Resources	Elm Grove Plantation #63	WBM
7	Questar	Wiggins 36H #1	WBM
8	Matador Resources	Hall 5 #1	WBM
9	XTO	New Horizons #1H	OBM
10	Chevron	T. C. Adams NCT-1 #64HS	OBM
11	EXCO	Reeves 18 #1	OBM
12	Southern Star	Atkins-Lincoln #17-2	WBM
13	QEP Resources	Burkett 5-15-10 H-2	Unknown
14	Shell	Sustainable Forest 24-1	OBM
15	Devon	S Kardell GU #1H	OBM
16	El Paso Corp.	Max Hart 12H #1	OBM
17	EXCO	Holoubek Family, LLC 28 #1	OBM

WBM: Water based mud

OBM: Oil based mud

Table 3.3. Summary of selected wells

3.2.2 Data integration and quality control

Following well selection, wireline and core data were integrated within the Schlumberger Techlog software platform. Core and wireline data had been previously integrated by CLB using wireline GR and core spectral GR (GRC) data, with core data corrected to wireline depths (ft.). This process was repeated to ensure an accurate depth shift and found good agreement with CLB interpretation, with only minor adjustments made to core depths. In general, the core data was satisfactorily ‘block’ shifted (i.e. core data depths were shifted by a fixed amount) to match wireline data using high relief gamma peaks as markers. Well 15 however, required intermittent stretching and shortening of GRC to match wireline GR. Whilst easily matched high relief GR peaks add a degree of confidence to core-wireline integration, intervening low relief GR zones can be challenging to match and increase uncertainty. As a consequence, though not excluded from the study, the accuracy of core to log integration and therefore the picked GR , ρ_b , R_t and ϕ_n values for well 15 should be viewed with caution.

In addition, the downloaded data were compared to data inventories provided on the RAPID database. This revealed minor inconsistencies in some wells related to duplicate GRI and XRD core results. All duplicate core data were removed.

3.2.3 Formation zoning

All data were zoned by formation (BSR and HY) according to depth information provided on the CLB RAPID database. In addition to wireline data, a total of 484 core samples were available for inclusion within the study, including 199 samples within the BSR and 285 samples within the HY. The stratigraphic boundaries for each well were determined by their respective operators based on wireline interpretation, sequence stratigraphic and biostratigraphic techniques and nannofossil events. In the absence of core however, stratigraphic boundaries could not be independently verified and were used as provided by CLB.

As discussed in section 3.1.2, within the BSR-HY interval the HY is generally the targeted zone of interest. This is apparent in the selected study wells (see cross sections; Figure 3.10, Figure 3.11) where cored sections largely target the HY. As a consequence, whilst the HY is comprehensively sampled, many of the BSR core samples are located near the BSR-HY boundary in the lowermost BSR. Furthermore, it should be noted that the HY ranges in thickness from 200 to 300 ft., (Hammes et al., 2011) and is relatively thin in comparison to the BSR, which has a thickness of between 250 to 2000 ft., (Condon et al., 2006). In other words, the BSR is comparatively under-sampled given its greater thickness. In addition, whilst many publications refer to the BSR as a single entity (e.g. Condon et al., 2006; Corley et al., 2010; Eastwood and Hammes, 2011), others divide the BSR into upper and lower or locally upper, middle and lower sections (Hammes and Frébourg, 2012; Steinhoff et al., 2011). Where locally, the lower (Zhang and Wieseneck, 2011) or middle (Hammes et al., 2011) BSR may be considered as being potentially more productive. In any case, when directly comparing BSR and HY data, the majority of publications present the BSR as undivided. Accordingly, as the BSR is relatively under-sampled and as BSR divisions are not uniformly available for each well, and as prospective BSR (middle or lower) zones are

related more to spatial disposition than age and depth, the BSR is also presented as undivided in the following study.

3.2.3.1 Additional core data

As outlined in Figure 3.4 the adopted CLB sampling methodology includes additional analyses that were not routinely available for each core sample, and were not considered critical to the petrophysical analysis undertaken in Chapter 4. A summary of additional core data that were (where available) integrated in Techlog as described in section 3.2.2 is provided in Table 3.4.

Core data	Geochemistry (includes pyrolysis and vitrinite reflectance)		
	<i>Variable (frequency)</i>	<i>Notation</i>	<i>Unit</i>
	Free hydrocarbons (450)	S1	mg/mg
	Hydrocarbons generated by thermal cracking of kerogen (450)	S2	mg/mg
	CO ₂ produced during kerogen pyrolysis (450)	S3	mg/mg
	Max. temperature of hydrocarbon release from kerogen (30)	T_{max}	°C
Measured vitrinite reflectance (98)	R_o	%	
Thin section imagery and petrographic descriptions			
Thin section images in plane and epifluorescent light at a variety of scales for each core sample (484) including brief petrographic descriptions.			
Langmuir adsorption isotherms			
Adsorption temperature (°F), langmuir pressure (psi), langmuir volume (scf/ton) (48)			

Table 3.4. Summary of additional data

3.2.3.2 Additional information

The laboratory protocol for the GRI analytical programme is included in Appendix A as provided by CLB RAPID database documentation. All GRI data analyses were performed and provided by CLB. Though requested, laboratory analytical methodologies for remaining core and thin section analyses indicated in Figure 3.4 were not provided. In addition, no information is available regarding wireline tool type. This information can usually be inferred from tool mnemonics using online technical

resources such as the '[Mnemonics Tool Search](#)' provided by the Society of Petrophysicists and Well Log Analysts (SPWLA). For instance, a search for the mnemonic 'LL3' on the SPWLA mnemonic tool search yields the following information:

Mnemonic Name	Company	Model	Gen Tool	Log System	Discipline	Description
LL3	baker atlas	-	-	-	-	LATEROLOG (3 ELECTRODE)
LL3	halliburton	LL3	RESISTIVITY	PLS2	-	LATEROLOG 3

Table 3.5. Tool information derived from tool mnemonic

CLB has however standardised all available downloadable wireline data, such that GR, ϕ_n , ρ_b , and R_t are simply denoted by CLB as GR, NPHI, RHOB and RT. As a consequence, no information regarding tool type is available and, though requested, no further information regarding tool type was provided. Although differences may exist between different vendors of downhole tools, it is assumed here that data may be compared and interpreted with minimal uncertainty.

3.2.3.3 Data corrections

All data and results retrieved from CLB were used 'as-received' and were not corrected or manipulated with the exception of XRD mineral data. XRD mineral data were bulk volume corrected to include GRI porosity values (ϕ_{tC}) such that the sum of the porous and mineral volumes is equal to one. CLB XRD mineral volumes, which are a dry volume percentage, were bulk volume corrected to include for GRI ϕ_{tC} by:

$$V_{Mineral_BVC} = (1 - \phi_{tC}) \cdot V_{Mineral} \quad (3.1)$$

where $V_{Mineral}$ is the CLB reported mineral volume (as a fraction) and $V_{Mineral_BVC}$ is the corrected mineral volume. This correction is applied so that the sum of all volumes reported for a given core sample equal 1.0.

There is however a potential inconsistency in this correction (equation 3.1). CLB reported ϕ_{tC} values (CLB GRI documentation is supplied in Appendix A) are oven-dried at 110°C until weight stabilised for at least a week. As a consequence, there may be a

discrepancy in the moisture loss between samples prepared for XRD (typically dried at 60°C) and ϕ_{TC} (dried at 110°C), with the latter likely to contain additional clay bound water and possibly some clay structural water (Handwerger et al., 2012, 2011). As CLB documentation available on the RAPID database typically includes bulk volume corrected XRD volume data however, it is assumed that XRD sample material is prepared and dried according to GRI methods, i.e. dried at 110 °C. If not, equation 3.1 would result in a slight reduction of all mineral volumes, an exaggeration of ϕ_{TC} and a duplication of bound water component integral to V_{Clay} . There may also be additional errors arising from the disparate sampling of XRD and GRI material (Figure 3.4), where ϕ_{TC} is measured on a sample a few centimetres away from the XRD sampling location.

Overall data correlations and trends do not however appear significantly affected. This is demonstrated in Figure 3.5 with the example V_{Clay_BVC} vs. V_{Clay} (as received from CLB), where the correlation coefficient (R^2) is 0.996 and was found to vary from 0.991 to 1 for the remaining mineral volumes. In summary, despite the potential discrepancy in moisture loss between XRD and GRI oven drying, the impact on mineral trends and relationships was not found to be significant.

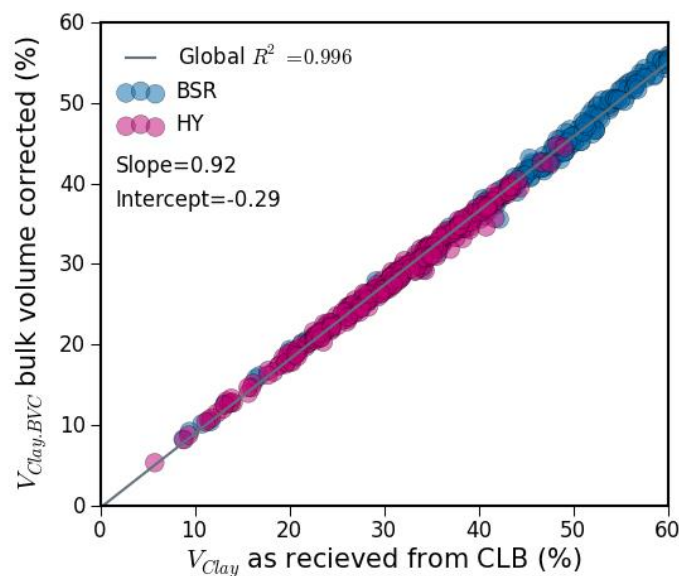


Figure 3.5. Bulk volume correction of mineral volumes

Scatter plot of bulk volume corrected V_{Clay} (V_{Clay_BVC}) vs. V_{Clay} as-received from Core Laboratories.

In the following sections and chapters, all reported mineral volumes are bulk volume corrected and are referred to simply as V_{Clay} , $V_{Calcite}$ etc. All remaining data were used as received from the CLB RAPID database.

3.3 BSR-HY mineralogical and petrophysical properties

This section provides a brief overview of the principal petrophysical and mineralogical core data listed in Table 2.1 and Table 3.2, including variable distributions and basic descriptive statistics such as the range, average value, and a measure of variability.

3.3.1 Overview of XRD bulk mineralogy

The mineralogy of the BSR-HY interval is summarised in Figure 3.6 using normalised XRD V_{Clay} , $V_{Carbonate}$ ($V_{Calcite} + V_{Dolomite}$) and V_{Quartz} values. For comparison, this includes shaded regions occupied by Barnett and Eagleford shale play data after Passey et al., 2010.

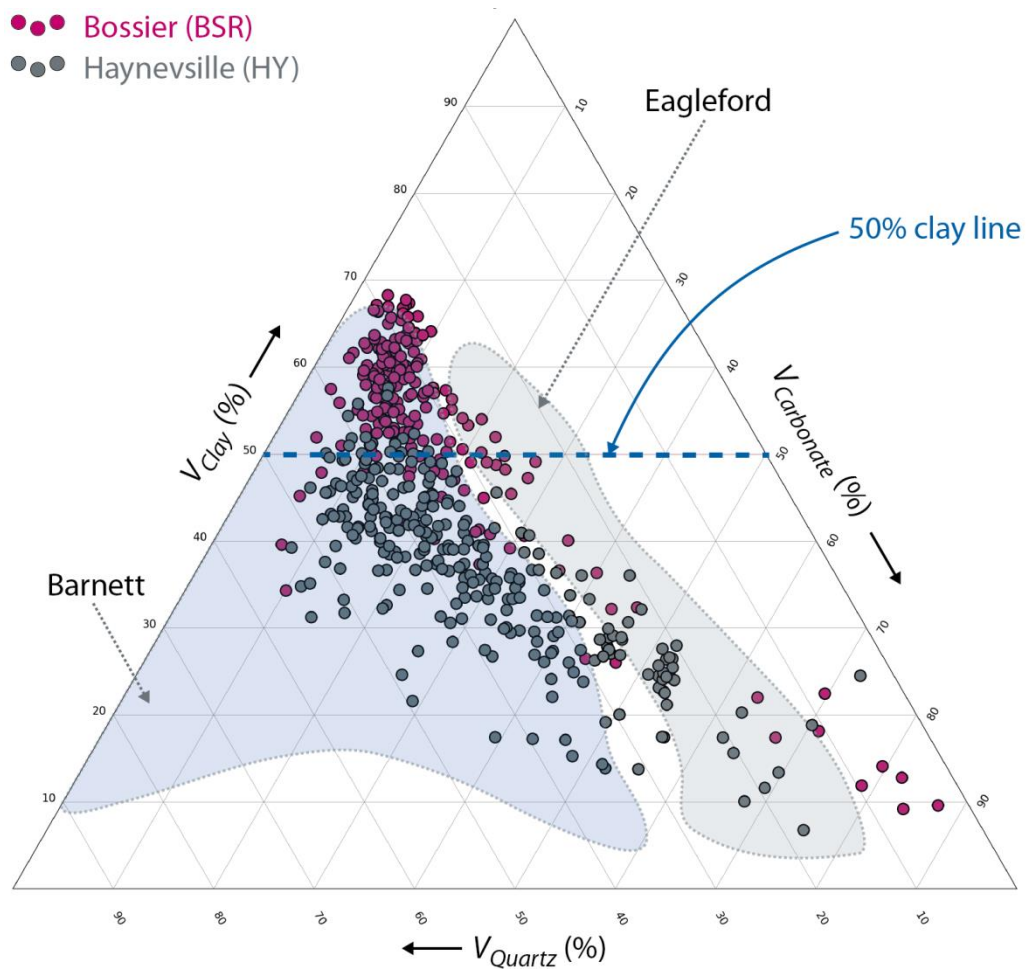


Figure 3.6. Summary mineralogical composition V_{Clay} , $V_{Carbonate}$ ($V_{Calcite} + V_{Dolomite}$) and V_{Quartz} ternary diagram. Includes shaded Barnett and Eagleford regions after Passey et al., (2010).

It is notable in Figure 3.6 that BSR-HY data occupies a broad compositional range with a significant body of BSR samples with over 50% V_{Clay} . The 50% V_{Clay} line forms a loose cut-off, above which clay plasticity is considered to impede reservoir stimulation practices. As a result, most currently producing shale gas plays contain less than 50% V_{Clay} , where the quartz and carbonate components add a brittle character that aids play development (Passey et al., 2010).

The key BSR-HY bulk volume XRD mineralogy is summarised in Figure 3.7, highlighting significantly lower V_{Clay} and higher V_{Quartz} , $V_{Calcite}$ and $V_{Kerogen}$ in the HY than in the BSR. Both formations have a similar V_{Pyrite} range and the BSR data includes seven compositionally distinct $V_{Dolomite}$ outliers above 50% volume.

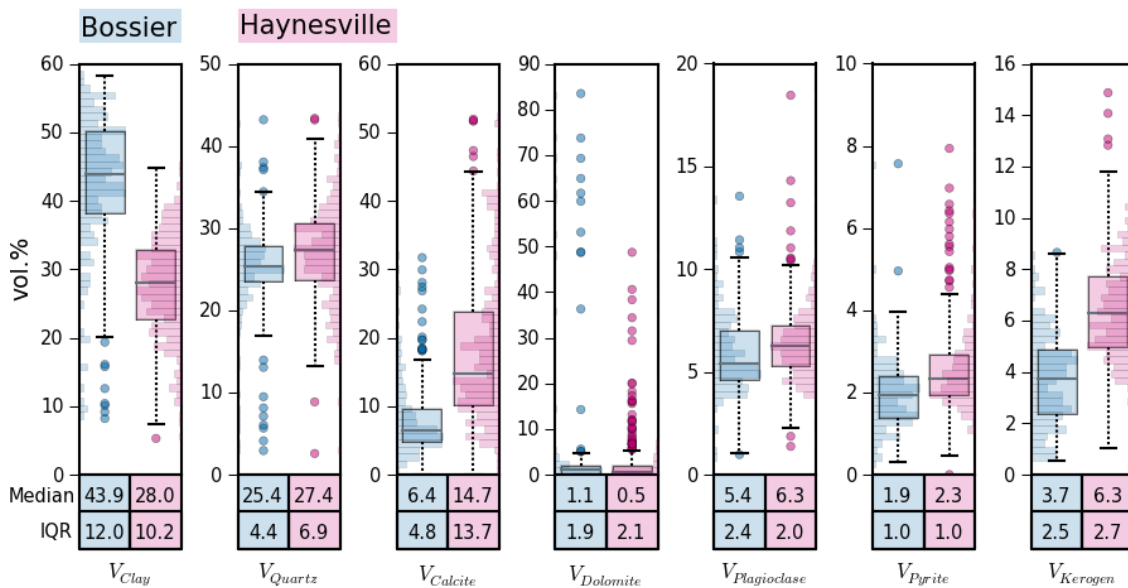


Figure 3.7. Summary of key core bulk volume XRD mineralogy

Box plot and distributions for XRD mineral volumes. The bold line in each box is the median value (also provided below each plot). The vertical extent of each box is the interquartile range (IQR= Q_3-Q_1) defined by the upper (Q_3) and lower (Q_1) quartiles. The whiskers (dotted lines) represent the range of data within 1.5 times the IQR. Core samples outside of the whiskers are classed as outliers (round markers). A histogram is included for illustrative purposes (no frequency scale is provided). Data for K-Feldspar and Marcasite are excluded. K-feldspar only registered a volume above 0% in 131 of 484 samples and ranged from 0.2 to 1.55 % for combined BSR and HY data with a median of 0.82%. Marcasite only registered a volume of above 0 % in 88 of 484 samples and ranged from 0.18 to 4.09 % for combined BSR and HY data with a median of 0.77%.

XRD analysis includes a measure of clay type as a fractional contribution to V_{Clay} , including chlorite, Illite+mica and mixed_layer clays and sum to 1.0 for a given sample (Figure 3.8). This highlights higher chlorite contributions to V_{Clay} in the BSR, whilst the HY has a lower, wider chlorite distribution. As a result, the Illite+mica and mixed_layer clay components form a larger fraction of V_{Clay} in the HY. It should be noted that where

the clay fractions are converted to a vol. % of V_{Clay} , the clay fraction volumes are denoted as $V_{Clay\ fraction}$ (eg. $V_{Chlorite}$, $V_{Illite+mica}$).

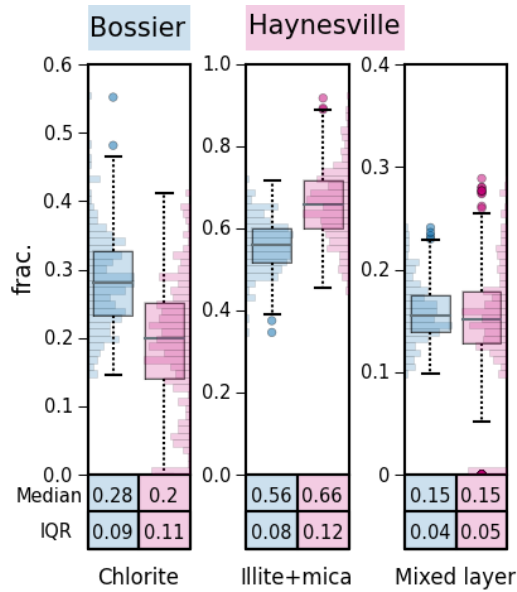


Figure 3.8. XRD clay fractions (See caption for Figure 3.7.)

3.3.2 Overview of core / wireline petrophysical properties

The principal petrophysical properties in Figure 3.9 highlight a similar range, distribution and average values for R_t , GR and ϕ_{tC} in both the BSR and HY. Differences include elevated ϕ_n , S_{wC} and ρ_{bC} in the BSR relative to the HY, with S_{wC} in particular having a wider and higher distribution. BSR samples also exhibit significantly lower k values than the HY.

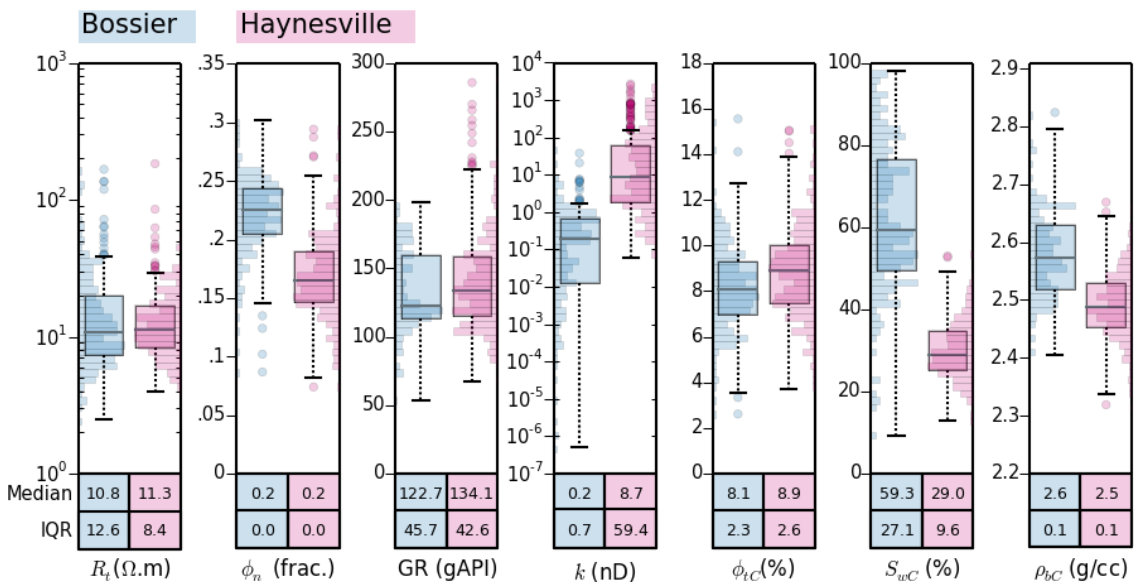


Figure 3.9. Summary of key core and wireline petrophysical properties (See caption for Figure 3.7.)

3.4 Compositional trends in the Bossier-Haynesville

A detailed study of the sequence stratigraphic framework within the BSR-HY interval was undertaken by Hammes and Frébourg (2012) based on the analysis of wireline and core data for ~200 wells, with further analysis of 10 well cores for which XRD, XRF, *TOC* and thin sections were sampled at 1ft intervals. Their study includes a series of excellent cross-sections detailing sequence stratigraphic correlations and a series of palaeogeographic reconstructions highlighting the influence of palaeotopography on formation deposition, much of which is discussed in section 3.1.2. Very little quantitative data is however provided, and spatial variations in formation composition are not mapped. Though this investigation includes far fewer wells and core data collected at a lower sampling rate (typical CLB core sampling interval is 10ft., as opposed to the 1ft. sampling interval used by Hammes and Frébourg (2012)), the following section outlines the spatial and mineralogical trends observed within the HY productive region (Figure 3.1).

3.4.1 Spatial and mineralogical relationships

The *A-A'* (north-south) and *B-B'* (east-west) cross sections are displayed in Figure 3.10 and Figure 3.11 respectively, highlighting the location and coverage of the core and wireline data. Cross-sections comprise wireline GR, core *TOC* and CLB stratigraphic boundaries.

Section 3.1.2 essentially describes the HY as a mixed siliciclastic / carbonate system where distal areas of the basin, or areas sheltered by local topographic highs, experienced reduced clastic input, resulting in locally condensed clastic poor, carbonate and *TOC* rich sediments. This is supported by cross-section *A-A'*, which depicts a reduction in HY thickness from north to south, with an associated increase in basal formation depth, that suggests a decrease in sediment load towards distal, deeper regions of the basin.

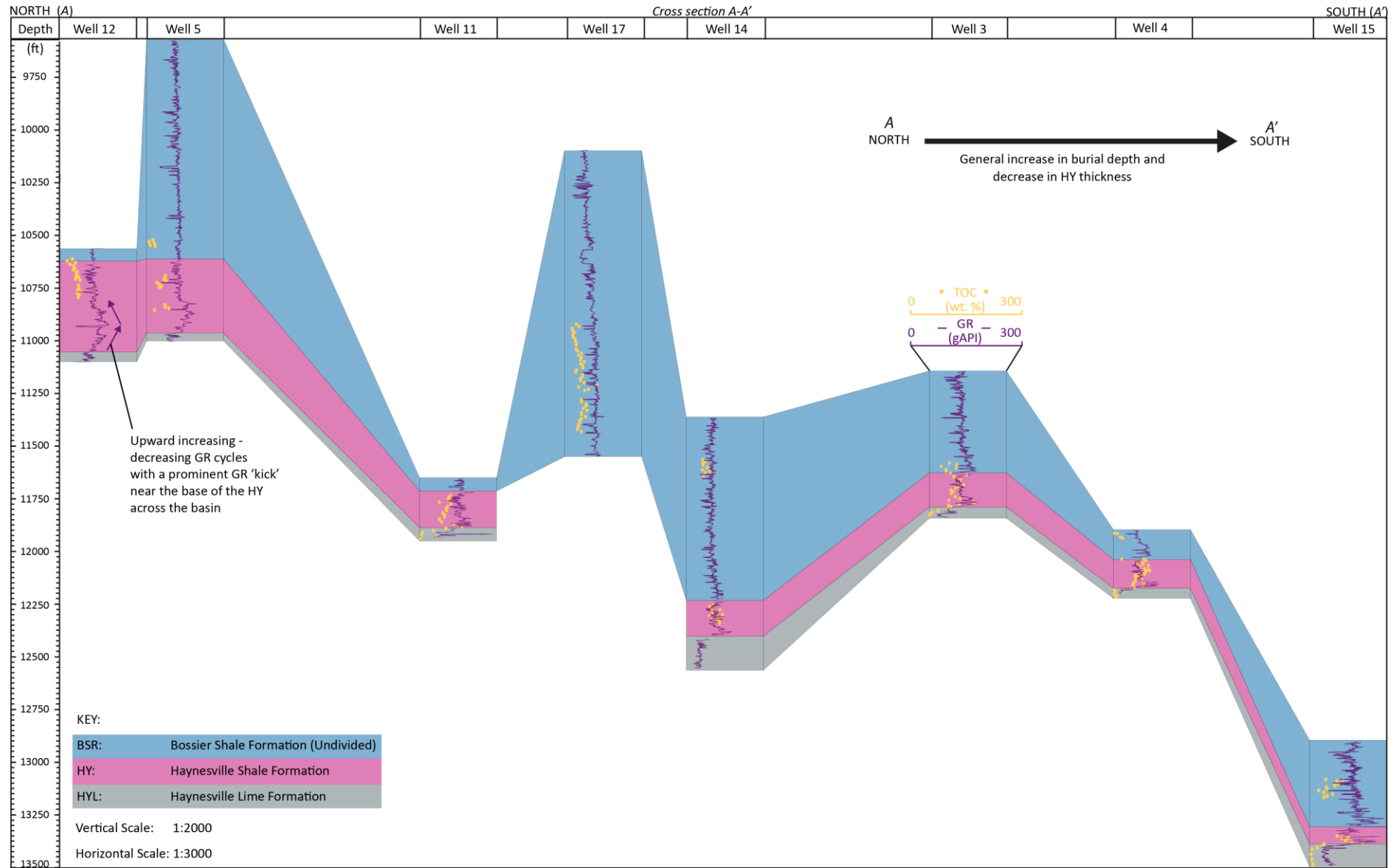


Figure 3.10. Cross section A-A'

Cross section A-A', north to south in the HY productive region (see Figure 3.1). Section includes GR and core TOC, indicative of cored and sampled intervals.

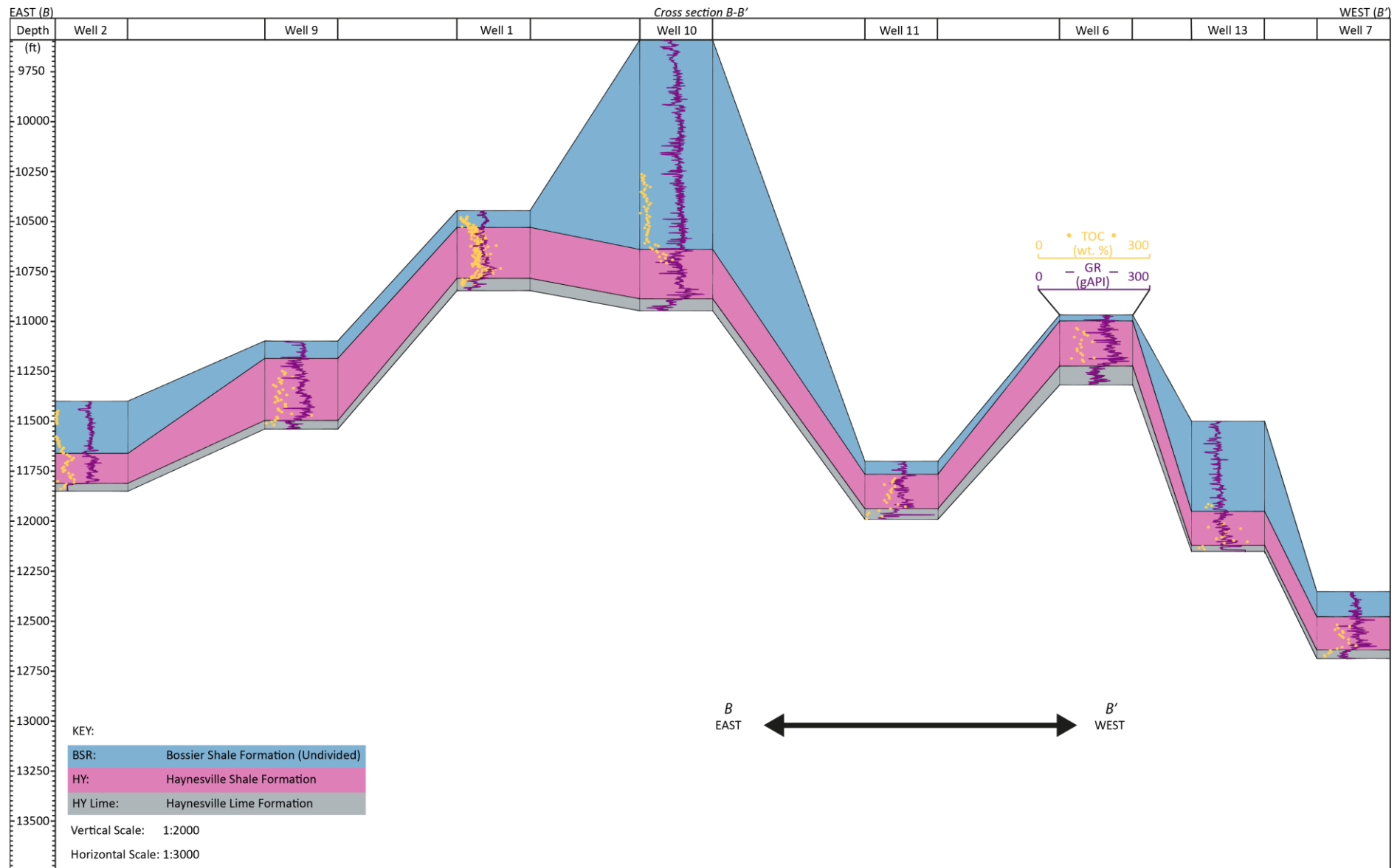


Figure 3.11. Cross section B-B'

Cross section B-B', east to west in the HY productive region (see Figure 3.1). Section includes GR and core TOC, indicative of cored and sampled intervals. Note, well 1 has a higher sampling rate for TOC only, remaining core analysis (GRI and XRD) are sampled at intervals similar to other wells.

This agrees with the palaeotopography presented in Figure 3.3 and discussions in section 3.1.2, where ancestral fluvial sources to the north may have acted in combination with near-shore re-sedimentation processes to supply sediment in this region. Moreover, the southernmost wells on section A-A' (wells 4 and 15) are both distally located and situated immediately to the north of the Sabine Island complex (Figure 3.3), which may have further restricted access to clastic input originating from the ancestral Mississippi River delta to the north-east. This is further illustrated by contour-plots in Figure 3.12, which highlight an increase in maximum depth, $V_{Carbonate}$ and $V_{Kerogen}$ and a decrease in V_{Quartz} , V_{Clay} and HY thickness to the south. Similar mineralogical trends are noted in the BSR (Figure 3.13), though as the upper stratigraphic boundary is unconstrained, an indication of thickness variation cannot be given. This data suggests a principally north to north westerly origin of clastic sediments within this region of the basin and is supported by stratigraphic relationships suggested by Dix et al. (2010). No clear trends are evident in cross-section B-B', though it is notable that the HY thickens towards the centre of the HY productive region, with the extreme western (well 2) and eastern (well 7) wells encountering relatively thin HY successions.

A composite plot of principal XRD mineralogical components (V_{Clay} , $V_{Calcite}$, $V_{Kerogen}$ and V_{Quartz}) is displayed in Figure 3.14. This highlights a negative linear relationship between V_{Clay} and $V_{Kerogen}$ indicative of organic matter dilution (Hammes and Frébourg, 2012) in northern proximal locations (Figure 3.12 and Figure 3.13). The clear negative trend between V_{Clay} and $V_{Calcite}$ also indicates a sharp reduction in calcite production above 30% V_{Clay} . This largely divides BSR and HY data, indicating that reduced carbonate production can be attributed to a change in environmental conditions linked to a rise in sea level and increased clastic input (Boggs, 2009; Hammes and Frébourg, 2012; Potter, 2005). It is also notable that there is no clear relationship between V_{Clay} and V_{Quartz} , perhaps indicative of a distinction in clastic sediment source. For instance, Hammes and Frébourg (2012) suggest an aeolian origin for detrital quartz, though they provide no supporting evidence.

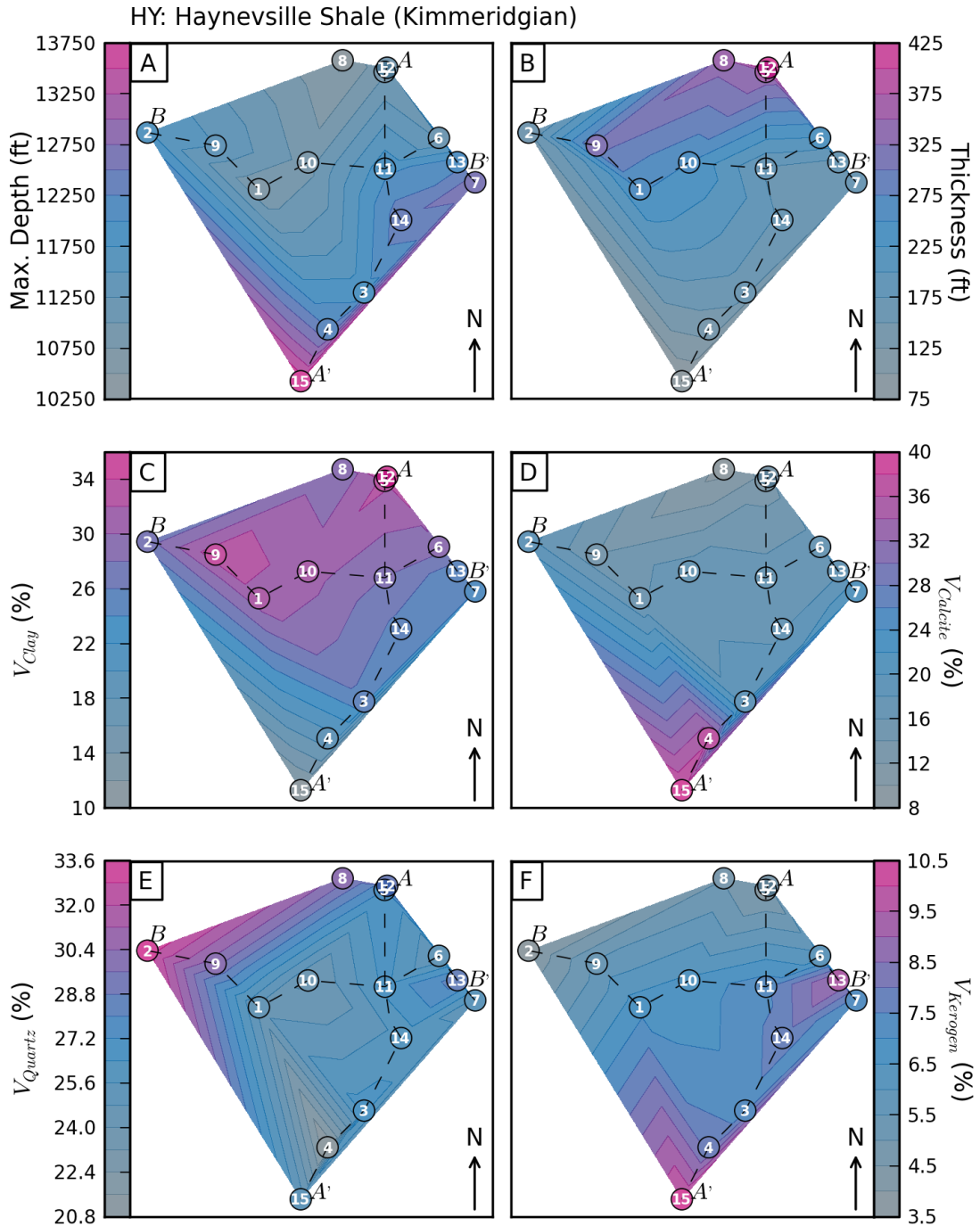


Figure 3.12. Contour plot of principal HY mineralogical components

Contour plots are generated using linear interpolation methods for average well values based on SciPy (scientific python) documentation (SciPy.org 2013). Note the increase in maximum depth, average $V_{Calcite}$ and $V_{Kerogen}$, and the decrease in average V_{Quartz} , V_{Clay} , and HY thickness to the south.

The suggestion of an aeolian origin for detrital quartz is not unreasonable, as the disintegration of Pangaea throughout the Oxfordian to Tithonian coincided with high CO_2 levels and a warm, dry climate (Moore et al., 1992), evidenced by evaporite and anhydrite deposits on the northern GOM shoreline (Figure 3.3) and continental aeolian

deposits within the Norphlet Formation (Mancini, 2010). In addition, continental aeolian deposits were widespread across the western interior of the USA, including the Entrada Formation in New Mexico and the extensive fossil rich Morrison Formation in western Texas, New Mexico, Colorado, Arizona, Utah and Nevada (Blakey et al., 1988; Tanner, 1965, Parrish et al., 2004).

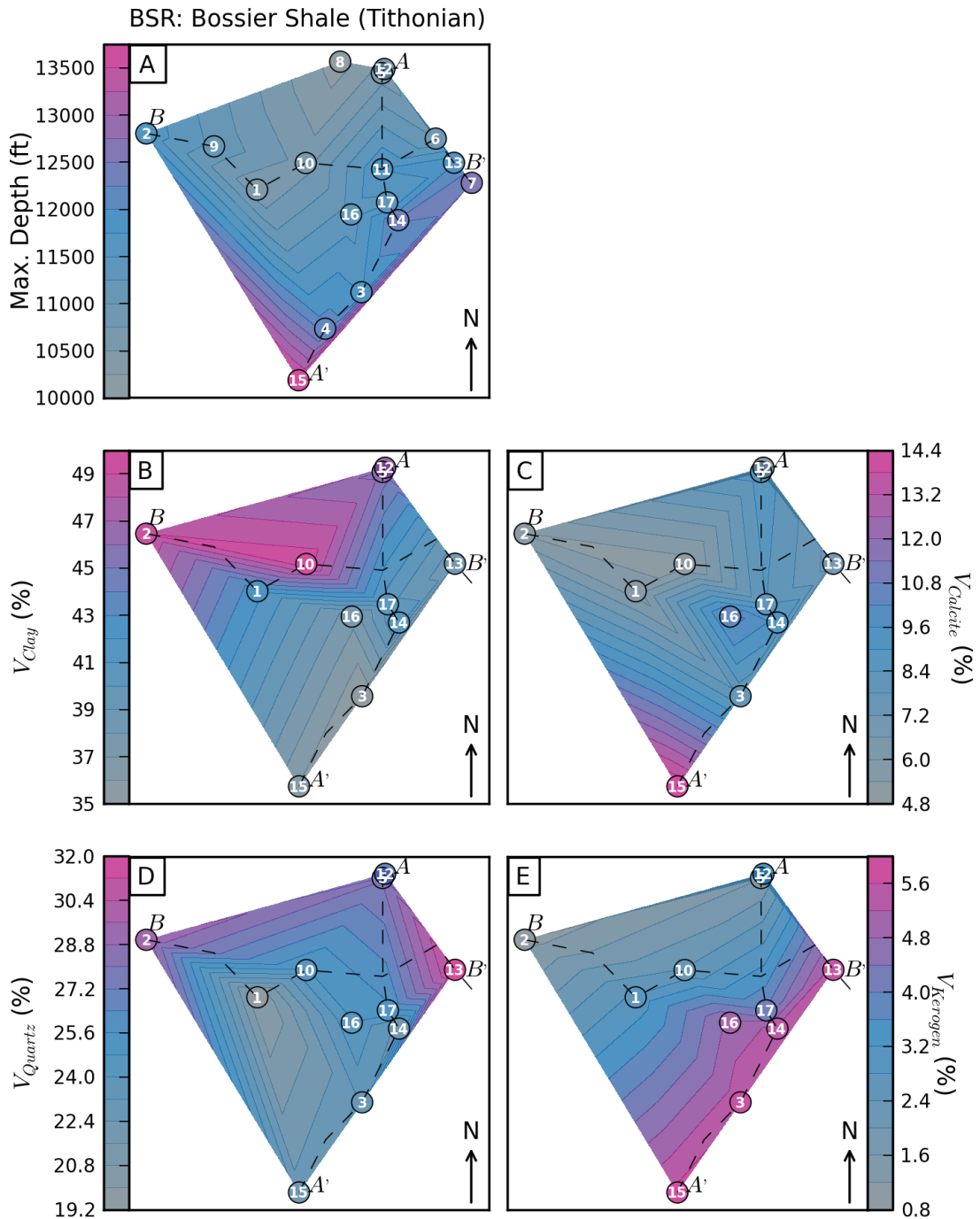


Figure 3.13. Contour plot of principal BSR mineralogical components

Contour plots are generated using linear interpolation methods for average well values based on SciPy (scientific python) documentation (Jones et al., 2001). Note the increase in maximum depth, average $V_{Calcite}$ and $V_{Kerogen}$ and the decrease in average V_{Quartz} and V_{Clay} in the BSR to the south and south east.

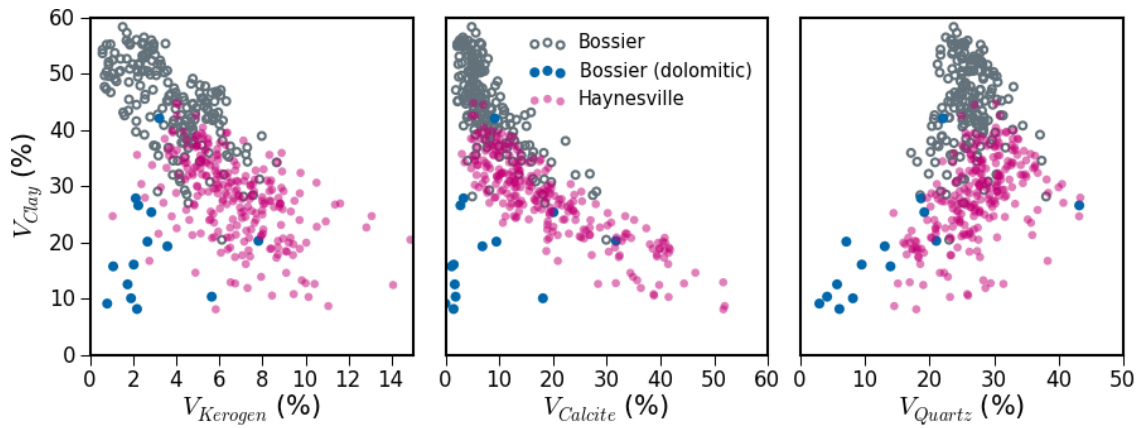


Figure 3.14. Mineralogical relationships

Scatter plot of principal BSR-HY mineralogical components. Note: a) the negative linear relationship between V_{Clay} and $V_{Kerogen}$, b) the negative linear relationship between V_{Clay} and $V_{Calcite}$, and c) the lack of any clear relationship between V_{Clay} and V_{Quartz} .

Conditions were therefore present for a significant windblown quartz component sourced to the north of the HY productive region. This may account for the relatively wide distribution of V_{Quartz} observed in the HY (Figure 3.14), but would require a consistent increase in aeolian quartz input to counter clay mineral dilution and maintain the narrow V_{Quartz} distribution observed for the BSR in Figure 3.14. This seems questionable, and whilst an aeolian quartz input may have been significant, any relationship between V_{Clay} and V_{Quartz} may have been distorted by differential diagenetic processes and the precipitation of biogenic silica and clay minerals in the BSR and HY.

3.4.2 Total organic content, pyrite and redox conditions

The restricted sediment input and high *TOC* contents found in the HY suggests an absence of the aerobic bacteria required to digest organic matter and thus an anoxic environment (Loucks and Ruppel, 2007; Potter, 2005). This is supported by the general absence of bioturbation, and by a positive co-dependant relationship between molybdenum and organic matter content in HY sediments (Hammes and Frébourg 2012). In addition, pyrite (Figure 3.7) which is typically present as small pyrite framboids (Hammes and Frébourg, 2012; Hammes et al., 2011), is the product of anaerobic sulphate-reducing bacteria suggestive of an anoxic, euxinic (sulfidic) environment (Hedges and Keil, 1995; Vandenbroucke and Largeau, 2007). The occurrence of framboidal pyrite is common in organic rich marine shale, where it is

often associated and co-located with kerogen (Macquaker et al., 2010; Sageman et al., 2003; Schieber, 2011; Taylor and Macquaker, 2011). This relationship was highlighted in a study by Witkowsky et al., (2012), which presents core data for nine wells in the HY that exhibit a positive linear trend between TOC and W_{Pyrite} . They utilise this relationship by plotting a regression line (forced through the origin) for the core TOC vs. W_{Pyrite} data, and then use the slope of regression to model TOC values from continuous W_{Pyrite} values estimated from a wireline mineral solver model. This relationship is tested in Figure 3.15 using data for wells 1 to 17 and (with the exception of wells 3, 4 and 15) covers a geographic area similar to wells within the Witkowsky et al., (2012) study.

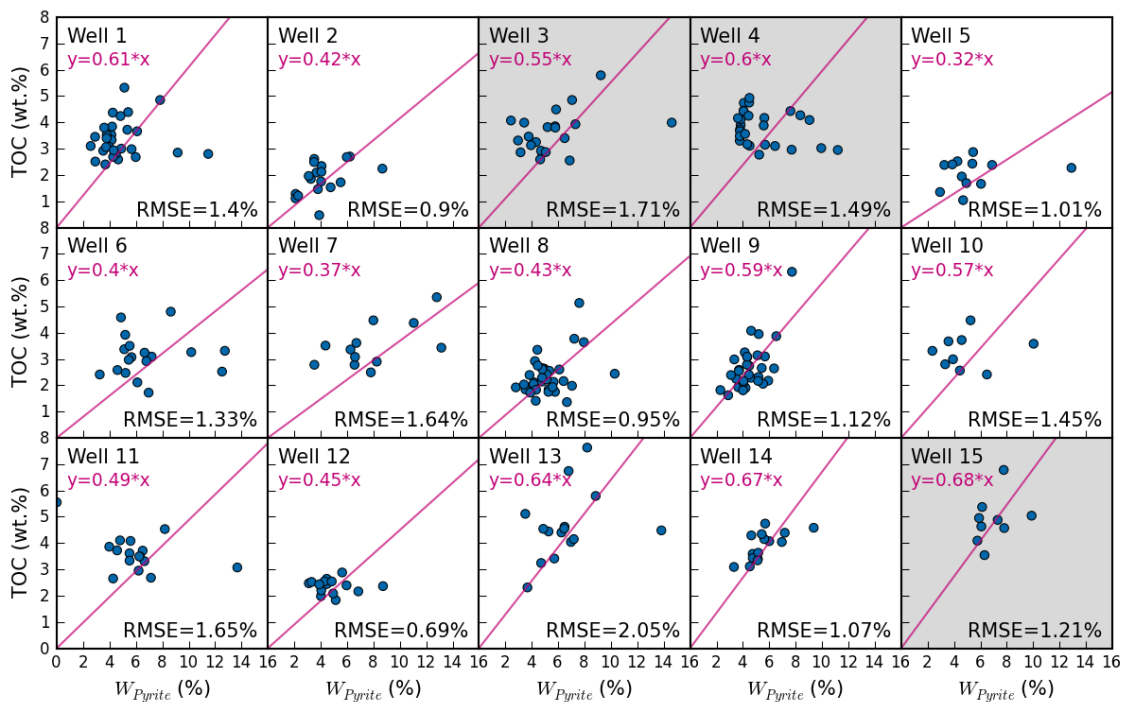


Figure 3.15. TOC vs. W_{Pyrite} for the HY

Matrix scatter plot of TOC vs. W_{Pyrite} for each HY well. Included are the trend line and line equations fitted through the origin and the root mean squared error (RMSE). Note: the correlations are generally poor and the errors are generally very high, in other words, W_{Pyrite} has limited utility in predicting TOC .

Figure 3.15 includes a least squared regression line forced through the origin as per Witkowsky et al., (2012) and the resulting linear equation. It is clear that little of the data plots near the regression line and that the relationship between TOC and W_{Pyrite} is poor. This is emphasised by the root mean squared error (RMSE), which represents the vertical misfit between the observed TOC values and those predicted by the equation of the fitted line. The RMSE (which is scaled after the parent unit; TOC wt.%) varies

from 0.69 to 2.05% with a mean of 1.31%. This is significant when considering the range in *TOC* values, which on average range from 2.15 to 5.01% for any one well. This equates to a relative or normalised error in the predicted *TOC* value of between $\pm 26.1\%$ and $\pm 60.99\%$. In other words, the linear relationship between *TOC* and W_{pyrite} is very poor and W_{pyrite} appears to have limited utility in predicting accurate *TOC* values in these wells. Given the similar geographic disposition of well data used in the Witkowsky et al., (2012) to those used in this study, it is not clear why there should be such a stark contrast in *TOC*- W_{pyrite} relationships. At the very least, it highlights either laboratory or reservoir inconsistencies that renders the application of empirical models problematic.

3.5 Petrophysical trends in Bossier-Haynesville

The petrophysical properties of gas bearing mudstones, and particularly the effects of clay and organic matter on petrophysical properties, are discussed in sections 2.2 and 2.3. The following section builds on this previous discussion and is intended to briefly illustrate key petrophysical trends within the BSR-HY interval. These trends are described using well 3, taken as a typical example of the BSR-HY data set, with composite cross-plots including all available core data where appropriate. First, as GR and core spectral GR (GRC) data are essential to accurate core-log integration (see section 3.2), a comparison of the wireline and core GR responses is presented with a brief examination of GR links to V_{Clay} and TOC . This is followed by a partial log evaluation for well 3 including V_{Clay} estimates, ϕ_n - ρ_b relationships and estimates of the bulk volume water (BVW) and total gas filled porosity (ϕ_g). A full analysis of the trends within all available petrophysical data is too expansive for inclusion, though summary statistical data for key petrophysical properties are presented in section 3.3. Moreover, a detailed examination of compositional-petrophysical relationships is presented in Chapter 7.

The following section includes:

- 3.5.1 An example of GR-GRC relationships and the influences of V_{Clay} and TOC on wireline and core GR.
- 3.5.2 A partial well evaluation utilising R_t , ϕ_n , ρ_b wireline responses, including modelled values for clay volume, total and gas filled porosity,

3.5.1 Wireline and core gamma ray response

The GR and GRC data available for the BSR-HY interval was utilised to integrate core and log data as discussed in section 3.2. An example of the integrated core-log data is given in Figure 3.16 for well 3, highlighting a good GR-GRC match.

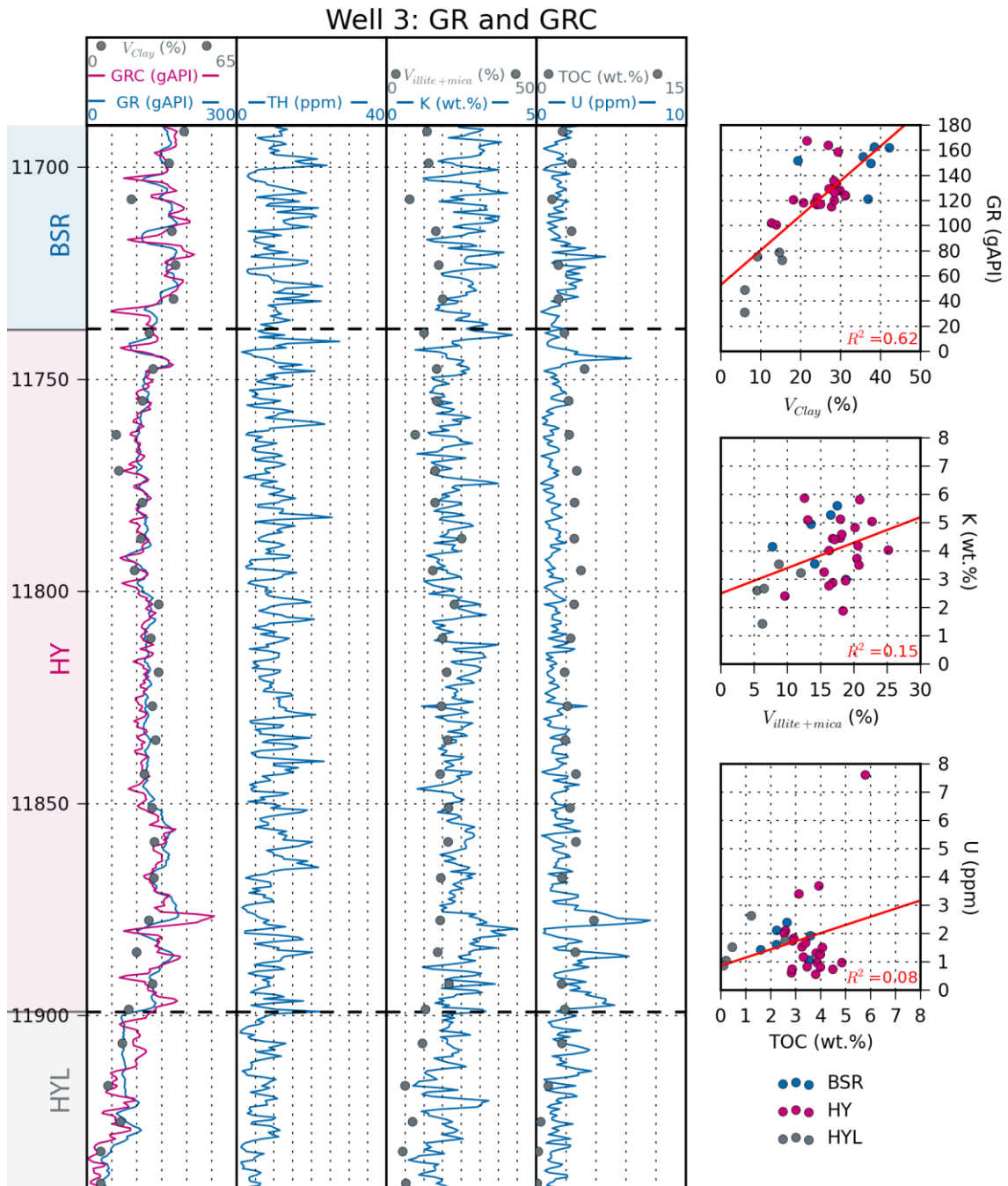


Figure 3.16. GR and GRC logplots for well 3 including V_{clay} , $V_{illite+mica}$ and TOC.

Log plots for GR and GRC for well 3 for the BSR (Bossier), HY (Haynesville) and HYL (Haynesville Lime) including V_{CLAY} , TH (thorium), K (potassium), VI+M ($V_{illite+mica}$), U (uranium) and TOC. Note the good agreement between GR, GRC and V_{clay} , the absence of any correlation between K and $V_{illite+mica}$ and the spike in TOC and U in the lowermost HY (though there is an absence of any linear correlation).

In addition, Figure 3.16 highlights a notable GR ‘kick’ (elevated GR) at the base of the HY and BSR. This ‘kick’ is widespread across the basin (see Figure 3.10 and Figure 3.11) in the HY with an additional GR kick at the base of the BSR in wells toward the south of the HY productive region (wells 3, 4 and 15). The regional correlation of these zones is evident on cross sections A-A’ and B-B’ (see Figure 3.10 and Figure 3.11), depicting a

series of basin wide upward-reducing and upward-increasing GR cycles in the HY. Unfortunately the coverage of cored intervals coupled with low intensity core sampling rates (discussed in section 3.4) precluded zoning the formation by upward-cleaning/decreasing cycles. A detailed study of these sub-divisions is however presented by Hammes and Frébourg (2012).

The GR and GRC tools respond to the combined uranium (U), thorium (Th) and potassium (K) content and are a measure of formation radioactivity. This radioactivity is generally associated with the volume of shale, principally clay, though organic matter is often linked with uranium (Alfred and Vernik, 2013; Algeo and Maynard, 2004; Schmoker, 1979), where equation 3.3 is often used to estimate shale or clay volume (Bhuyan and Passey, 1994; Ellis and Singer, 2007; Rider, 1986). In continuous shale sections however, without pure clay/shale free (GR_{Min} or GR_{Max}) end members, value selection and thus clay estimates can be inaccurate. Moreover, though it is necessary to quantify V_{Clay} and its related effects on formation resistivity and other petrophysical and geomechanical properties, the complex composition of shale requires that the effect of heavy minerals such as pyrite on ρ_b and R_t or TOC on ϕ_t and ρ_b must also be determined. As a consequence, multi-mineral models present a more commonly used and versatile option, combining the GR, with the ϕ_n and ρ_b logs to solve for the multiple mineral components including TOC and porosity (Adiguna, 2012; Eastwood and Hammes, 2011; Heidari et al., 2011; Singh et al., 2013). Nonetheless, Figure 3.16 highlights a reasonable ($R^2=0.62$) correlation between GR and V_{Clay} . In addition, though illite and mica generally contain higher levels of potassium (Doveton, 1994), there is no notable link between $V_{illite+mica}$ and K (Figure 3.16). Likewise, there is no notable linear correlation between U and TOC , though the TOC track in Figure 3.16 does spike at the base of the HY in association with GR, GRC and U.

The interplays between TOC , U, V_{Clay} and GR are displayed in Figure 3.17, a composite cross-plot including all core data and associated wireline responses for the BSR (left) and HY (right). As depicted, there are no clear trends and U varies across the entire spectrum of TOC , though BSR samples do link high V_{Clay} and GR to low TOC and U. In addition, there are a number of samples in the HY that link high U, TOC and GR with

low V_{Clay} , indicating localised TOC related U enrichment. This links to observations by Lüning and Kolonic (2003), who relate the strength of the TOC - U relationships to sedimentation rate and redox conditions. Where the BSR, which is bioturbated (i.e. at least partially oxic, or with limited periods of anoxia) and more rapidly deposited than the HY, has no observable TOC - U relationship. By contrast the restricted and more persistently anoxic conditions responsible for elevated TOC in the HY, are likely to have facilitated, at least locally, U preservation in the HY.

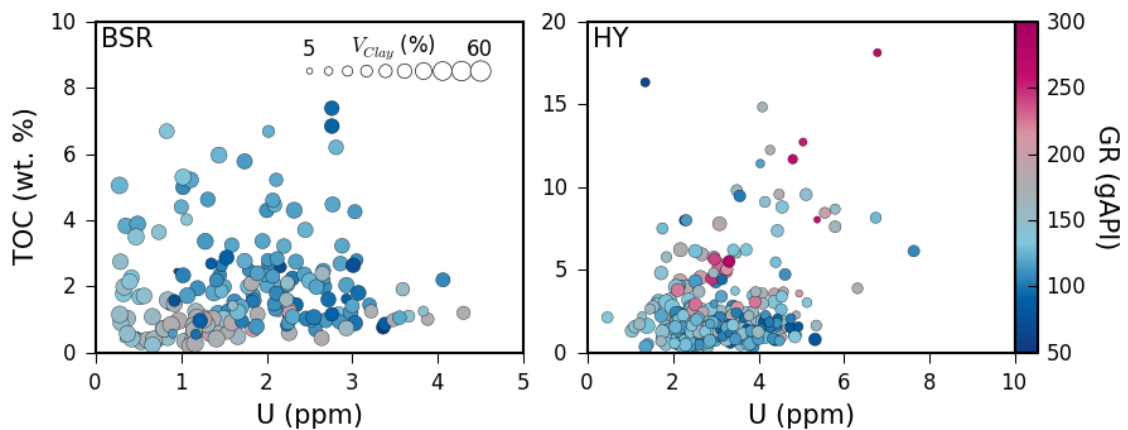


Figure 3.17. TOC (wt. %) vs. U (ppm) for the BSR (left) and HY (right).

Composite cross-plot of TOC vs. U for the BSR (left) and HY (right). Marker size is scaled against V_{Clay} and marker colour is scaled against GR . Note: there are no clear TOC - U trends, though there is a general increase in GR with V_{Clay} . It is also notable in the BSR that V_{Clay} and GR are elevated at low U and TOC . In the HY, though there is no clear overall trend, there are a number of high TOC , U and GR points with low V_{Clay} values that may indicate local TOC related U enrichment.

3.5.2 Typical petrophysical trends in the Bossier-Haynesville

A typical suite of log responses is given in Figure 3.18 for well 3, including calliper (CAL), GR , R_t , wireline data, ϕ_{tC} , V_{Clay} and S_{wC} core data and estimates for log modelled porosity, clay volume and ϕ_g . The following section discusses each track from left to right.

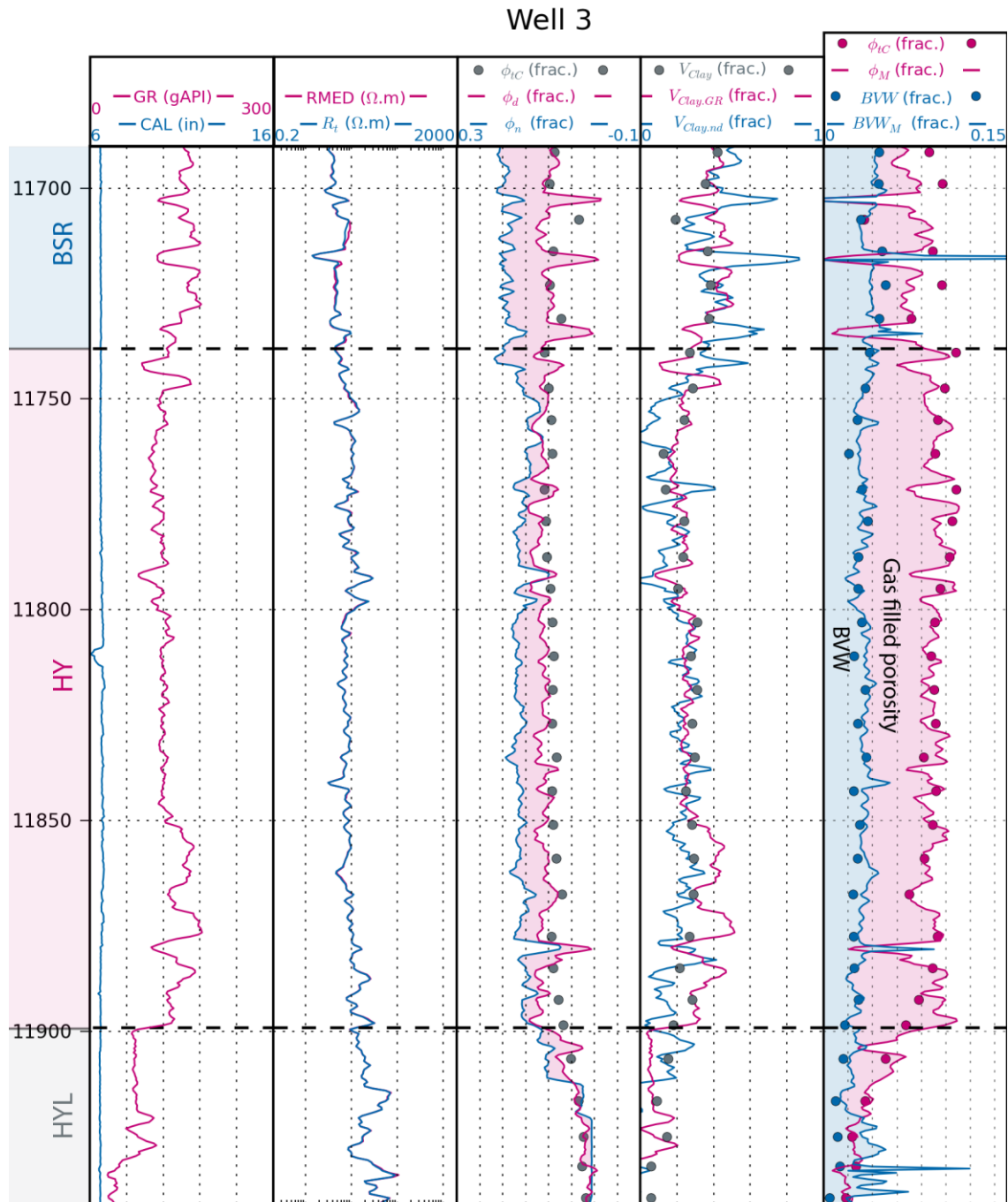


Figure 3.18. Wireline response for Well 3: cored Section.

Track 1 includes: GR (gamma response) and CAL (calliper). **Track 2** includes: R_t (deep resistivity) and RMED (shallow resistivity). **Track 3** includes: ϕ_{tc} , ϕ_d (density porosity computed from the ρ_b log) and ϕ_n . **Track 4** includes: V_{Clay} , $V_{Clay,GR}$ (clay volume calculated from GR) and $V_{Clay,nd}$ (clay volume calculated from neutron-density relationships). **Track 5** includes: ϕ_{tc} , ϕ_M (total porosity modelled from the ρ_b log), BVW (calculated from core ϕ_{tc} and S_{wc} values) and BVW_M (modelled using the Archie water saturation values multiplied by ϕ_M).

Track one includes wireline GR and calliper (CAL) readings, the latter indicating typically stable borehole conditions and no 'badhole' flagged intervals. Badhole refers to intervals with wider calliper readings indicative of borehole cave-ins, where

significant variations in borehole diameter can impair tool response. GR, discussed in section 3.5.1, is provided for reference.

Track two includes deep (R_t) and shallow (RMED) resistivity responses, which show limited separation, and therefore no gas or fluid invasion effects. Neither of which would be anticipated given the extremely low formation permeabilities described in Figure 3.9. It is notable however that R_t and RMED are slightly elevated in the TOC enriched lower HY.

Track three includes ϕ_{tC} , ϕ_n and ϕ_d calculated from the standard porosity density relationship (taken from Rider, 1986):

$$\phi_d = \frac{\rho_{ma} - \rho_b}{\rho_{ma} - \rho_f} \quad (3.2)$$

where: ϕ_d = density porosity
 ρ_{ma} = grain density (mean formation GRI ρ_{ma} used)
 ρ_f = fluid density (a value of 1 is assumed)
 ρ_b = bulk density (taken from the density log; ρ_b)

ϕ_n and ϕ_d highlight a typical neutron-density separation profile for the BSR-HY well data set, with a wide separation in the BSR due the effects of clay bound water on the neutron response and narrow separation in HY, reflecting reduced V_{Clay} and elevated $V_{kerogen}$ values.

Track four compares basic methods for V_{Clay} derivation including $V_{Clay.GR}$ and $V_{Clay.nd}$. $V_{Clay.GR}$ is calculated after (taken from Rider, 1986):

$$V_{Clay.GR} = \frac{GR - GR_{min}}{GR_{max} - GR_{min}} \quad (3.3)$$

where: $V_{Clay.GR}$ = Clay volume
 GR = GR log response
 GR_{min} = GR for a clean or clay free interval
 GR_{max} = GR for a pure clean or clay free interval

In the absence of adjacent beds with GR values reflecting clay free (GR_{min}) or pure clay (GR_{max}) end members, values were selected to optimise $V_{Clay.GR}$ output by minimising

the misfit between V_{Clay} (XRD) and $V_{Clay,GR}$, yielding: $GR_{min}=60$ and $GR_{max}=300$. Whereas $V_{Clay,nd}$ was calculated from the neutron density relationship (taken from Rider, 1986):

$$V_{Clay,nd} = \frac{\phi_n - \phi_D}{\phi_{nclay} - \phi_{Dclay}} \quad (3.4)$$

- where: $V_{Clay,nd}$ = Clay volume
 ϕ_n = ϕ_n log response
 ϕ_d = calculated density porosity (ϕ_d)
 ϕ_{nClay} = the neutron porosity of clay
 ϕ_{dClay} = the density porosity of clay

In the absence of ϕ_{nClay} and ϕ_{dClay} values for pure clay, the highest well ϕ_n value was taken as a response to clay, yielding $\phi_{nClay} = 0.3$, with the corresponding ϕ_d value yielding $\phi_{dClay} = 0.0882$. Both $V_{Clay,GR}$ and $V_{Clay,nd}$ curves reflect general XRD V_{Clay} trends, but highlight significant inaccuracy and emphasise the requirement for more sophisticated multi-mineral methods.

Track five includes two shaded regions: BVW (light blue) and ϕ_g (light red) defined by the BVW_M and ϕ_M curves respectively. ϕ_M refers to a total porosity modelled from the linear relationship between ϕ_{TC} and $\log \rho_b$ values depicted in Figure 3.19. As indicated on Figure 3.18, ϕ_M correlates reasonably with ϕ_{TC} calibration values, particularly in the HY.

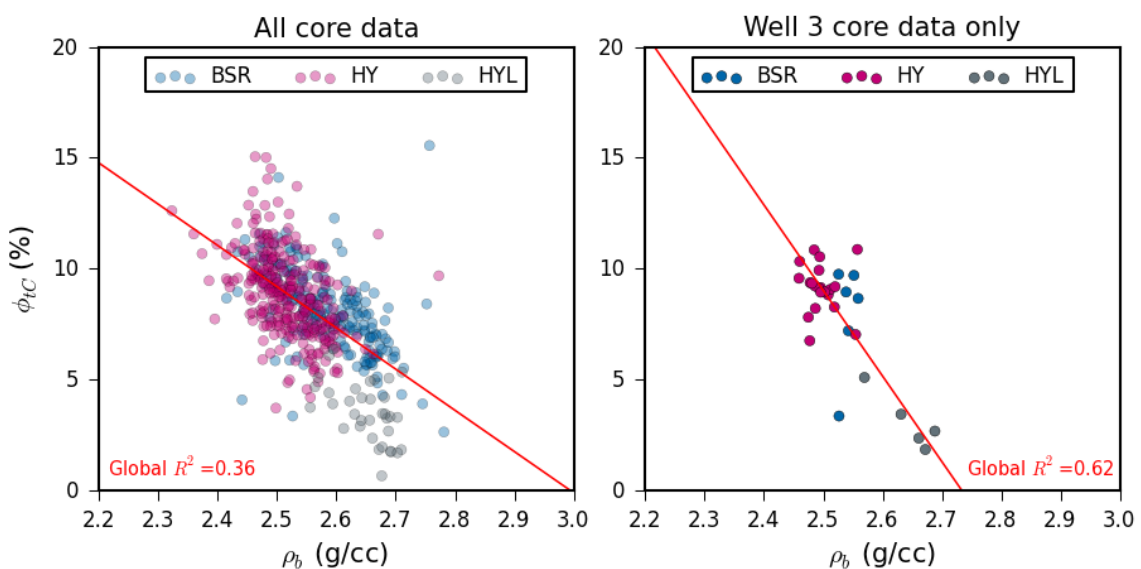


Figure 3.19. ϕ_{TC} vs. ρ_b . Cross plot of ϕ_{TC} vs. $\log \rho_b$ for all available core data (left) and for well 3 (right). ϕ_M is modelled from the linear relationship depicted in the plot for well 3 (right).

BVW_M refers to a modelled BVW . First an Archie water saturation (S_{wA}) is calculated based on Archie (1942):

$$S_{wA} = \left(\frac{\alpha R_w}{\phi_M^m R_t} \right)^{\frac{1}{n}} \quad (3.5)$$

where:

- ϕ_M = modelled total porosity
- R_t = Resistivity
- R_w = fluid resistivity (a value of 0.014 $\Omega \cdot m$ is assumed)
- α = tortuosity exponent (assumed as equal to 1)
- m = porosity exponent (assumed as equal to 2)
- n = saturation exponent (assumed as equal to 2)

S_{wA} is calculated from ϕ_M and R_t using typical industry assumptions for m , n and α values with an R_{we} of 0.014 $\Omega \cdot m$ (based on communications with BG Group). An analysis of applied Archie parameter selection is the focus of Chapter 4. BVW_M is then derived from:

$$BVW_M = S_{wA} * \phi_M \quad (3.6)$$

Accordingly, the blue shaded portion of track five represents the water filled porous volume (BVW_M) and the pink region represents the gas filled porosity (ϕ_g). It is notable that BVW (calculated using core GRI ϕ_{tC} and S_{wC} values after equation 3.6) correlates reasonably well with BVW_M and therefore S_{wA} in large sections of the HY. This log response is fairly typical of the BSR-HY well data set, with lower more accurately calculated S_{wA} values in the HY and higher more erroneous saturation values in the BSR. Also notable are three large spikes in ϕ_M in the BSR that correspond with spikes in ϕ_d , GR and R_t , reflecting the occurrence of dolomitic BSR bands. The ϕ_d peaks reflect the increased volume and density of dolomite and the inverted GR peaks most likely reflect a reduction in V_{Clay} , whilst the increased variability and positive and negative R_t peaks may reflect variations in pore type, connectivity and fluid within dolomitic BSR material.

3.6 A note on kerogen density

As indicated in Table 3.2, the XRD results retrieved from CLB include tabulated mineral wt. and vol. percentages. The vol. % mineral results also include a calculated grain density (g/cc). This is of interest as standard sample preparation for XRD analyses includes drying overnight to 60°C prior to grinding and analysis, such that the reported wt. % mineral data for a sample, which sum to 1, therefore excludes porosity (volume of moisture lost up to 60°C) and organic matter. The conversion of wt. % to vol. % must require assumed mineral densities ($\rho_{Mineral}$), hence the inclusion of a calculated grain density (g/cc) in the mineral vol. % results. Moreover, the vol. % results include $V_{kerogen}$ and notes that ‘kerogen contents are calculated using TOC and X-Ray diffraction data.’ That XRD kerogen volume was calculated from TOC is illustrated in Figure 3.20 (left), indicating that a constant kerogen density ($\rho_{Kerogen}$) was used. As $\rho_{Kerogen}$ is a far from certain parameter, understanding which value was used has a bearing on the uncertainty in reported kerogen and mineral volumes. A request was made to CLB and BG Group for documentation detailing XRD methodology and the conversion of wt.% to vol.%, but no response was received.

In the absence of a methodology however, the available wt.% mineral and calculated grain densities can be used to deduce (to within a high degree of certainty) the likely input $\rho_{Mineral}$ and $\rho_{Kerogen}$ values. Firstly the reported $W_{Mineral}$ values were converted to $V_{Mineral}$ in cubic centimetres (cc) by:

$$V_{Mineral} = \frac{\left(\frac{W_{Mineral}}{\sum W_{Mineral} + TOC} \right)}{\rho_{Mineral}} \quad (3.7)$$

where $\rho_{Mineral}$ is assumed and $W_{Mineral}$ is fractional. The assumed $\rho_{Mineral}$ values are provided in Table 3.6, where the ‘Lower bound’ values were initially used. The matrix density (ρ_{ma}) could then be calculated from:

$$\rho_{ma} = \frac{1}{\sum V_{Mineral}} \quad (3.8)$$

By comparing ρ_{ma} values with the calculated grain densities reported by CLB (ρ_{ma_CLB}) it was then possible to optimise the assumed input $\rho_{Mineral}$ values so as to minimise the misfit between ρ_{ma} and ρ_{ma_CLB} , where the ‘misfit’ was taken as the root mean squared error (RMSE). The Microsoft Excel Solver add-in was then used to globally optimise $\rho_{Mineral}$, with the freedom to optimise the assumed density values to an optimum within the upper and lower bound limits (Table 3.6). The returned optimal values are those which minimised the RMSE calculated between ρ_{ma} and ρ_{ma_CLB} .

The lower and upper bound density constraints and the optimised values are summarised in Table 3.6. In addition a scatter plot of ρ_{ma} and ρ_{ma_CLB} is given Figure 3.20 (right), highlighting their excellent agreement with a correlation coefficient (R^2) of 0.98.

$\rho_{Mineral}$	Calcite	Dolomite	Quartz	Pyrite	Plagioclase	K Feldspar	Total Clay	Marcasite	Kerogen
Lower bound	2.71	2.80	2.60	5.00	2.61	2.55	2	4.89	0.9
Upper bound	2.71	2.90	2.65	5.02	2.76	2.76	3	4.89	1.9
Optimum value	2.71	2.87	2.63	5.00	2.65	2.55	2.74	4.89	1.17

Note: Upper and lower mineral bound densities are taken from Gribble and Hall, (1992). Kerogen bounds were selected to encompass a range of values discussed in the literature.

Table 3.6. Summary of lower, upper and optimum mineral / kerogen densities

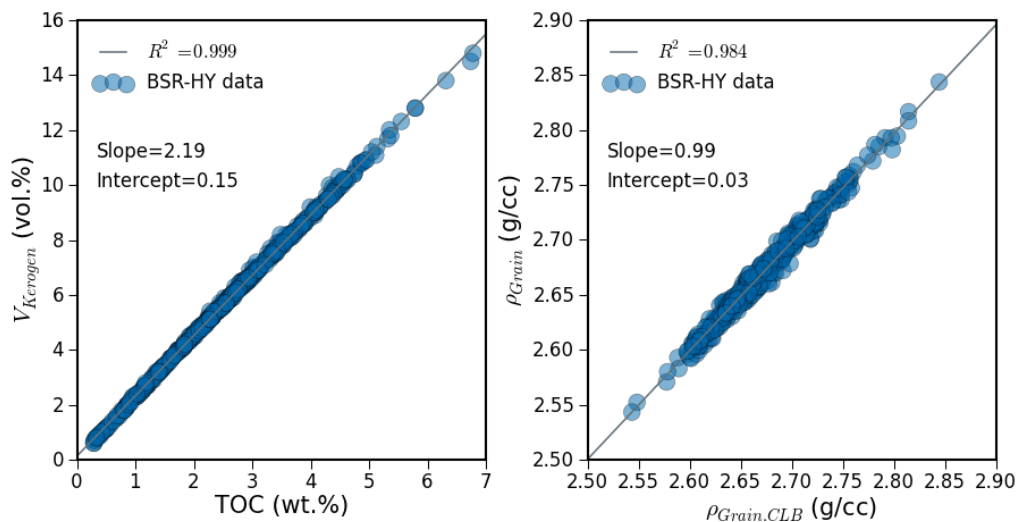


Figure 3.20. $V_{Kerogen}$ vs. TOC (left) and ρ_{ma} vs. ρ_{ma_CLB} (right)

Left: Cross-plot of $V_{Kerogen}$ vs. TOC as received from CLB. **Right:** ρ_{ma} calculated using optimised mineral / kerogen densities vs. ρ_{ma_CLB} . Note the good correlation.

It is clear from Figure 3.20 (left) that CLB uses density constants to derive $V_{kerogen}$ from TOC . Moreover, the excellent correlation between ρ_{ma} vs. ρ_{ma_CLB} (Figure 3.20; right) suggests that the optimised $\rho_{Mineral}$ and $\rho_{Kerogen}$ values given in Table 3.6 must be very similar to CLB values used for wt. to vol. conversion. This is supported by direct calculation of $\rho_{Kerogen}$ for each core sample:

$$\rho_{Kerogen} = \left(\frac{TOC \cdot \rho_{bC}}{V_{Kerogen}} \right) \quad (3.9)$$

where TOC is taken as a fraction and ρ_{bC} is the GRI core bulk density (g/cc). Using equation 3.9, the median $\rho_{Kerogen}$ for the BSR-HY data equals 1.12 g/cc and ranges from 1.02 to 1.25 g/cc. This variation most likely arises as, according to GRI methodology (Figure 3.4), ρ_{bC} and TOC values are derived from slightly different samples of core. Despite this however, the median value of 1.12 g/cc is fairly close to the optimised $\rho_{Kerogen}$ of 1.17 g/cc in Table 3.6 .

It is important to know the approximate values used for $\rho_{Kerogen}$, as whilst minerals densities can be narrowly constrained, $\rho_{Kerogen}$ varies widely in the literature as related to kerogen type and maturity (Bohacs et al., 2013). For instance, early work by Schmoker (1979) suggested a $\rho_{Kerogen}$ of 1.0 g/cc, though recent papers indicate a range of reasoned or assumed values of between 1.0 and 1.8 g/cc (Bust et al., 2011; Glorioso and Rattia, 2012; Handwerger et al., 2012, 2011; LeCompte et al., 2009; Popielski et al., 2012; Spears and Jackson, 2009). Moreover, it is recognised that $\rho_{Kerogen}$ can vary from shale to shale or from interpretation to interpretation, and where Ward (2010) suggests a $\rho_{Kerogen} = 1.53$ to 1.79 g/cc in the Marcellus, Jacobi et al. (2008) finds $\rho_{Kerogen} = 1.44$ g/cc in the Barnett, with Eastwood and Hammes (2011) estimating that $\rho_{Kerogen} = 1.45$ g/cc in the HY. Though Quirein et al. (2012), based on ρ_{ma} vs TOC relationships, suggests that $\rho_{Kerogen} = 1.12$ in the HY. Higher $\rho_{Kerogen}$ values in the HY are however supported by studies of field emission microscopy that indicate interparticle (inorganic) pores to be the dominant pore type in the HY, with kerogen hosted pores noted to be less abundant than in analogous US shale gas reservoirs (Curtis et al., 2010, 2012; Loucks et al., 2012; Milner et al., 2010). The Eastwood and Hammes (2011) example of $\rho_{Kerogen}$ in the HY was determined based on methods outlined by Guidry et

al., (1996) who defined a relationship between $\rho_{Kerogen}$ and vitrinite reflectance (R_o) as $\rho_{Kerogen} = 0.963 + 0.349 * R_o$. Using this relationship with available R_o data (Table 3.4) yields median $\rho_{Kerogen}$ values for the BSR and HY of 1.47 g/cc and 1.46 g/cc respectively, the results are depicted in Figure 3.21.

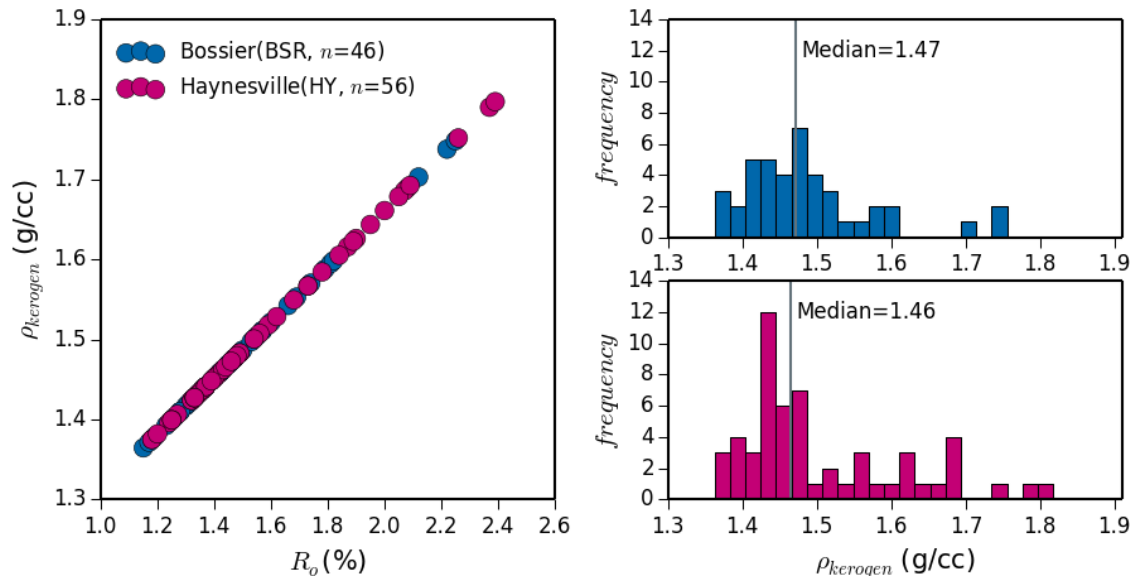


Figure 3.21. $\rho_{Kerogen}$ vs. R_o

Cross-plot of $\rho_{Kerogen}$ vs. R_o with histograms for $\rho_{Kerogen}$ (right) including BSR (blue) and HY (red) data.

$\rho_{Kerogen}$ can also be estimated from TOC and grain density (ρ_{ma}) relationships. This is depicted on Figure 3.22, where the $\rho_{Kerogen}$ is derived from:

$$\rho_{Kerogen} = \frac{TOC}{\left(\frac{1}{\rho_{ma_Min}}\right) - \left(\frac{1-TOC}{\rho_{ma_Max}}\right)} \quad (3.10)$$

where ρ_{ma_Min} and ρ_{ma_Max} refer to the x axis values for a selected line of best fit between TOC and ρ_{ma} .

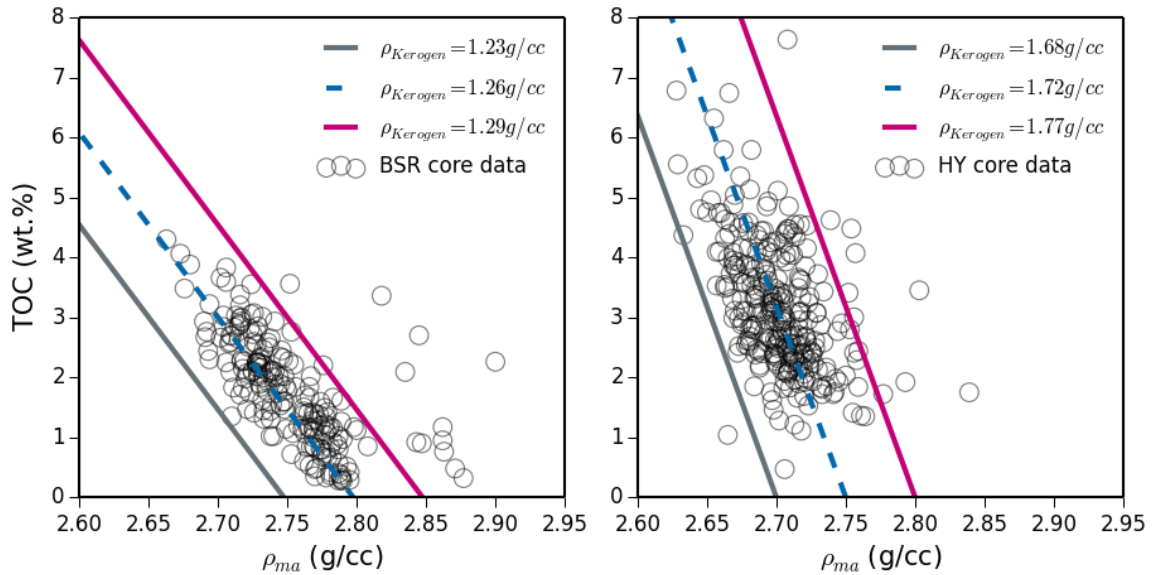


Figure 3.22. TOC vs. ρ_{ma} with $\rho_{Kerogen}$ overlay

Cross-plot of TOC and core matrix density (ρ_{ma}) with overlain TOC- ρ_{ma} relationships for $\rho_{Kerogen}$ values.

The $\rho_{Kerogen}$ values depicted in Figure 3.22 suggest markedly different values for the BSR and HY data with a combined $\rho_{Kerogen}$ envelope of 1.23 to 1.77 g/cc. This method of $\rho_{Kerogen}$ determination cannot be validated by published work (no similar method was observed in the literature), but is based on simple density, volume and mass relationships, and serves to highlight significant uncertainty and range in $\rho_{Kerogen}$ values. Moreover, the $\rho_{Kerogen}$ envelope suggested in Figure 3.22 is similar to the range of values derived using R_o relationships in Figure 3.21 and other published values discussed above. It should also be noted that Figure 3.21 infers that CLB assume a constant $\rho_{Kerogen}$ for both the BSR and HY, despite the very different ranges suggested by data in Figure 3.22.

The effect of using different $\rho_{Kerogen}$ values for deriving $V_{Kerogen}$ is displayed in Table 3.7. Here the solver model discussed above in Table 3.6 was repeated using a series of fixed $\rho_{Kerogen}$ values when converting from wt. to vol. %. As illustrated in Table 3.7, the optimised $\rho_{Kerogen}$ of 1.17 g/cc generates a median $V_{Kerogen}$ very close, to within 1.5%, of the reported CLB value. Increases or decreases from this optimum, result in significant change in estimated $V_{Kerogen}$, with subtle though consistent knock on effects for the remaining mineral volumes. This is critical, as reported CLB vol. % data are often the basis for the calibration of numerous petrophysical models. Though any errors arising

from inappropriate $\rho_{Kerogen}$ values are at least constant, and apply to all available core data.

Median CLB reported $V_{Kerogen}$ (vol.%) for the BSR-HY data = 5.70 %				
$\rho_{Kerogen}$ (g/cc)	1.00	1.17	1.45	1.80
Median solver $V_{Kerogen}$ values (vol.%)	6.50	5.62	4.54	3.70
Relative change (%)	+14.04%	-1.40%	-20.35%	-35.09%

Table 3.7. Effect of variations in $\rho_{Kerogen}$ on estimated $V_{Kerogen}$

In chapters 4 and 5, organic matter and mineral volumes are compared extensively to formation petrophysical properties and petrophysical modelling results. Thus, though not used directly in the calibration of any petrophysical models in this study, it remains important to outline uncertainties in the data, so as to help validate petrophysical-mineralogical relationships. Nevertheless, as this work and literature examples generally cite higher $\rho_{Kerogen}$ values of close to 1.45 g/cc, it is considered likely that $V_{Kerogen}$ estimates should be at least 20% lower than reported by CLB. Though without any means to verify an appropriate alternative $\rho_{Kerogen}$ value, and as the error is constant for all core data, mineral and kerogen volumes were used as provided by CLB.

3.7 Summary and conclusions

The BSR and HY data have distinct mineralogical properties and while the BSR is carbonate and *TOC* poor and clastic rich, the HY is clastic poor and *TOC* and carbonate rich. These mineralogical distinctions correspond with their petrophysical characteristics, with the HY having higher permeabilities, lower water saturations and a narrower neutron-density separation, indicative of high gas saturations and a reduced density response to *TOC*, than the BSR.

BSR-HY mineralogical and petrophysical properties are clearly influenced by palaeotopography as discussed in section 3.4.1 and largely support the findings of Hammes and Frébourg, 2012. Though the contour plots in Figure 3.12 and Figure 3.13 suggest a predominantly northern to north westerly origin of clastic sediments as opposed to the north-eastern ancestral Mississippi River delta source suggested by Hammes and Frébourg (2012). A north-westerly origin of clastic sediments is also supported by stratigraphic analysis undertaken by Dix et al. (2010). Though it is recognised that the Hammes and Frébourg (2012) study utilised a far larger data set covering a wider region, such that it is possible that data within this study identifies localised trends for sediment input within a wider region that may be dominated by sediment sourced to the north and east.

Empirical models developed in a near identical region of the BSR-HY for the prediction of *TOC* based on W_{Pyrite} are noted to be highly inaccurate and no consistent link between pyrite and organic matter is observed. This highlights either laboratory or reservoir inconsistencies that renders the application of empirical models problematic. Likewise, typical methods for the derivation of V_{Clay} are shown to be prone to significant uncertainty, emphasising the petrophysical complexity of shale gas reservoirs and the requirement for more sophisticated interpretation methods. In addition, it is noted that estimates of the gas filled porosity generated using Archie's equation for water saturation are reasonably accurate in some areas of the HY, despite the broad assumption made regarding the selection of petrophysical constants.

Uncertainty in XRD mineral volumes provided by CLB is evaluated and analysis indicates $\rho_{Kerogen}$ values for the BSR and HY data of between 1.23 to 1.77 g/cc. Far higher than constant value of $\rho_{Kerogen}=1.17$ g/cc thought to be used by Core Laboratories. This is likely to result in an overestimation of $V_{Kerogen}$ by approximately 20% when converted from wt. to vol. %, causing the remaining mineral volumes to be subtly overestimated. Any resulting error in the bulk volume corrected XRD mineral volumes are noted to be constant, and therefore, whilst there may be error in the absolute value of kerogen or mineral volumes, their trends and relationship with petrophysical properties should not be significantly affected.

Chapter 4

Unconventional applications of Archie's equation: sensitivity and error analysis

This chapter outlines the research rationale, analytical methodology and results. The results are split into four components; first an overview of the results is presented, followed by the analysis of data generated by a series of optimisation models in three further sections. The chapter is divided as follows:

- 4.1 *Introduction*: outlines rationale, aims and objectives.
- 4.2 *Methodology*.
- 4.3 *Results: Overview*.
- 4.4 *Results: 1D parameter optimisation*.
- 4.5 *Results: 2D parameter optimisation*.
- 4.6 *Results: 3D parameter optimisation*.

4.1 Introduction

Water saturation (S_w) in gas bearing mudstones is routinely derived using Archie based methods with little or no information driving the selection of Archie parameters (m , n and R_w). Instead parameter selection is often data led, using pseudo-Archie parameters (Bust et al., 2011; Chen et al., 1995; Chen et al., 1995; Maute et al., 1992; Worthington, 2011a, 2011b, 2009, 2007) modified to generate Archie S_w estimates (S_{wA}) that provide a good match to the 'as-received' Dean Stark core water saturations (S_{wC}) (Cluff, 2012).

This chapter utilises S_{wA} calculated using a generalised form of Archie's equation for a partially saturated formation (Archie, 1942; Brown, 1986; Juhasz, 1981):

$$S_{wA} = \left(\frac{R_{we}}{\phi_t^m R_t} \right)^{\frac{1}{n}} \quad (4.1)$$

where:	ϕ_t = Total porosity	<i>Core data (ϕ_{tC})</i>
	R_t = Resistivity (deep)	<i>Log data</i>
	R_{we} = Effective fluid resistivity	<i>Optimised</i>
	m = Porosity exponent	<i>Optimised</i>
	n = Saturation exponent	<i>Optimised</i>

The normalised equivalents of the Dual Water and Waxman Smits formulae equate to equation 4.1, with Archie's aR_w replaced with R_{we} , an effective fluid resistivity term inclusive of the electrical contributions of clay bound and non-clay bound formation fluids. The optimised output parameter R_{we} therefore encompasses those values which might be predicted by Archie (aR_w), Dual Water or Waxman Smits methodologies. This approach was selected as the latter two methods are based on the ion-exchange properties of clay minerals and have the least disputed scientific basis (Worthington, 1985). This approach is not without recognised failings however, as in applying the composite fluid resistivity term R_{we} is the implicit assumption that the nature of the pore space and derivative electrical effects are consistent for all clay-bound and non-clay bound formation fluids alike (Haro, 2008; Herrick and Kennedy, 2009; Kurniawan

and Bassiouni, 2007; Worthington, 1985). In other words, only a single set of pore geometrical factors (m,n) are applied to the numerator R_{we} , such that all formation fluids are assumed to exist in pores which share similar geometries, pore wall conditions and electrical properties. This assumption is in clear contradiction with the generalised petrophysical model for a gas bearing mudstone (see section 2.3.5) in which multiple fluid phases are located in pore spaces hosted by a structurally and mineralogically heterogeneous organic rich matrix (Bust et al., 2011; Glorioso and Rattia, 2012; Passey et al., 2010; Quirein et al., 2010). Nevertheless, in the absence of more appropriate tools, a better understanding of the failings, response and general efficacy of routinely applied formation evaluation methods is an appropriate beginning in the search for new and improved methodologies. This is of particular interest as the influence of geological factors, including formation structure, composition and heterogeneity on those petrophysical properties that contribute to S_{wA} estimation by electrical methods in gas bearing mudstones is poorly understood. This chapter aims to investigate the links between formation geological / petrophysical properties and the residual error derived from comparing optimised S_{wA} estimates with benchmark S_{wC} observations. The relative effectiveness, plausibility and range of Archie parameters generated in using deterministic grid search optimisation methods to minimise error will also be evaluated. In developing this understanding, the aim is to contribute towards a geologically reasoned and informed approach to parameter selection, advancing our predictive capability where petrophysical properties may be linked to geological observations in the absence of core data. The full aims and objectives of the research are detailed in section 1.2.

4.1.1 Chapter structure

This chapter is split into the following sections:

4.2 *Methodology.*

4.3 *Results overview:* This section presents a comparison of the S_{wA} estimates, their residual errors and associated generated Archie parameters for multiple optimiser model variants.

4.4 *1D, 2D and 3D parameter optimisation*: The number of dimensions refers to the number of Archie parameters optimised within the model. Each optimisation model is investigated independently in sections 4.4, 4.5, and 4.6, and each systematically detail:

- i. *The sensitivity of residual mean absolute error (MAE) to parameter change*. This aims to identify parameter relationships and the presence of any systematic bias so as to help validate the geological viability of the optimised parameter.
- ii. *The trade-offs between generated parameters and input variables*. Identifying the primary forcing variable, and other geological properties by which it is influenced, is key to determining how formation geology influences Archie relationships in gas bearing mudstones.
- iii. *Direct calculation of Archie parameters for each core sample*. Archie parameters are derived by direct calculation or iteration for each core sample. This aims to identify any useful systematic variations that may inform underlying geological controls.

4.2 Methodology

4.2.1 Least error optimisation

Least squares regression is an example of optimisation where the parameters m and c (the slope and intercept and thus the equation of a straight line; $y=mx+c$) are data driven. In other words, they are fitted (optimised) based on the relationship between observed x and y variables to define a line that minimises the sum of squared deviations between the observed data points and the line. Allowing for the prediction of y (\hat{y}) based on x (Size et al., 1987).

A least error approach to parameter optimisation is not limited to linear systems, and can be incorporated within iterative higher dimensional functions to derive multiple parameters. The measure of error can also be calculated in multiple forms. This investigation utilises two standard measures of error, the root mean squared error (*RMSE*, equation 4.2) and the mean absolute error (*MAE*, equation 4.3) (Hyndman and Koehler, 2006; Willmott and Matsuura, 2005). Both measures of error are dimensioned in the form of the parent unit, but are also provided as a normalised percentage value (equation 4.4) where practical.

$$RMSE = \sqrt{\frac{1}{n} \cdot \sum (y - \hat{y})^2} \quad (4.2)$$

$$MAE = \frac{1}{n} \cdot \sum |(y - \hat{y})| \quad (4.3)$$

$$Normalised\ Value = \frac{RMSE\ or\ MAE}{max(y) - min(y)} \quad (4.4)$$

MAE and *RMSE* have been used in combination in an attempt to compensate for the potential bias that each method implies. *RMSE*, whilst probably the most common approach observed in the literature, can weigh the calculation in favour of larger errors as opposed to smaller ones, skewing fitted parameters towards sample outliers (where present). Conversely, *MAE* could be argued to favour the bulk of, but not the full

variance of sample data in the absence of outliers. As a compromise, results by both measures of error have been fully investigated to help judge any significant separation, and thus identify the potential impact of population variance or the presence of sample outliers on fitted parameters.

Having selected a measure of error, probabilistic or deterministic algorithms can be used to optimise parameters to minimise the selected measure. These typically include Markov Chain Monte Carlo (MCMC) methods or optimisers such as Microsoft Excel's Solver add-in. The latter are probably more widely used given their routine availability, user simplicity, and speed of use. Nonetheless, optimisers typically yield only single optimised parameter values (in this case m , n and R_{we}) and provide no information regarding the variation in least error over the range of possible values or the trade-offs between parameter inputs.

A more simplistic solution, which can yield globally optimised parameters and return the possible solutions over an iterable range of inputs, is to perform a comprehensive grid-search of parameter space. To this end, a simple Python script was written to evaluate the input parameters within Archie's equation. The code (see example in Appendix B) returns the *MAE* and *RMSE* for a given sample population for every possible input parameter combination within set limits for R_{we} , m and n . For instance, consider the input parameters as x, y, z coordinates in 3D space where the python code iterates over the possible coordinates, evaluating and returning the residual error at each point. Probabilistic MCMC methods were considered for this application, but given the relative simplicity of Archie's equation and the ability to compute the parameter combinations to an adequately fine scale, a grid-search approach was considered to be the most robust method (Bergstra and Bengio, 2012).

4.2.2 Grid search optimisation methodology

The methodology employed follows a simple workflow:

- a) Well data for the Bossier Shale (BSR) and the Haynesville Shale (HY) Formations were downloaded from the Core Laboratories database and screened to ensure

accuracy in depth shifting between the down-hole gamma and core spectral gamma response (quality control methods are described in section 3.2).

- b) Core samples where the primary input variables ϕ_{tC} and S_{wC} were available, were ascribed a depth matched R_t value.
- c) Core samples were grouped by formation in each well (where more than one formation is available).
- d) S_{wA} was calculated for each sample, and MAE and $RMSE$ were calculated for n samples in each formation in each well. Only optimised Archie parameter combinations and S_{wA} data where MAE or $RMSE$ values were less than 100% S_w , were recorded. This process was repeated for every Archie parameter combination (m , n and R_{we}) within defined parameter constraints and at a set step increment.

4.2.2.1 Parameter constraints

The range and theoretical minimum values of the parameter inputs m and n are discussed in section 2.4.2. These limits are expanded somewhat arbitrarily in the grid search so as to aid the investigation of parameter relationships. The range in parameters used is given in Table 4.2:

<i>Conceptual Range</i>	<i>Grid-Search Range</i>	<i>Parameter</i>
$1.5 < m < 2.5$	$1.0 < m < 4.0$	<i>Porosity exponent</i>
$1.5 < n < 2.5$	$1.0 < n < 4.0$	<i>Saturation exponent</i>
$0.006 < R_{we} < 0.1$	$0.006 < R_{we} < 0.1$	<i>Effective fluid resistivity</i>

Note: the lower R_{we} value is based on the lowest value on Chart Gen-9, the Resistivity of NaCl Solutions by Schlumberger

Table 4.1. Grid search parameter range

4.2.2.2 Parameter step increment

The selected step increment controls the scale of the output data and was typically set at between 0.001 and 0.05 (log space increments were used for R_{we}). For instance, with a step increment of 0.05, S_{wA} for a given sample is calculated at $R_{we}=0.006$, then 0.006732, 0.007554.....etc., to $R_{we}=0.1$, whilst $n= 1.0$ and $m= 1.0$. The process is then

repeated through the range of n and then again through the range of m . A step increment of 0.05 results in 96,746 ($61 \times 61 \times 26$) iterations per sample, or a combined 46,825,064 iterations for all 484 samples each time the code is run.

4.2.2.3 Grid search model variants

A grid search approach to parameter optimisation can perform multiple functions:

- Locate those parameters associated with globally minimised error.
- Capture the variation in error across the potential range of parameter values.
- In varying the number of freely optimised parameter dimensions (i.e., by optimising for one, two or all three available parameters (m , n and R_{we})), variations in parameter sensitivity can be investigated.
- Variations in sample size, where samples may be optimised holistically (formation wide), or binned into smaller sample groups based on well number, can also give some indication as to the sensitivity of Archie's equation to the effects of sample heterogeneity.
- The use and choice of static parameters, which reflect common assumptions regarding Archie parameters (e.g. $m=n=2$), can be evaluated.

It should be noted, that within this thesis, where it is assumed that $m=n$, the two exponents (m and n) in Archie's equation have been replaced by a single parameter, m^* .

The following grid search optimisation models are defined and investigated:

<i>Model ref:</i>	<i>Optimised parameters</i>	<i>Fixed parameter assumptions</i>	<i>No. of sample populations</i>	<i>No. of parameter dimensions</i>
H1	m, n, R_{we}	N/A	2	3
W1	R_{we}	$m=n=2$	26	1
W2	m^*	$R_{we} = 0.014$	26	1
W3	m^*, R_{we}	$m=n$	26	2
W4	m, n, R_{we}	N/A	26	3

Table 4.2. Grid search optimisation model variants

4.2.2.4 Model validation

The *MAE* and *RMSE* results produced using a grid search approach were validated using the Generalised Reduced Gradient (GRG) optimisation algorithm (in multi-start mode) in Microsoft Excel. Generated *MAE* or *RMSE* using the GRG method were found to correspond to values generated using grid search techniques to within 10^{-3} . Likewise, GRG optimised Archie parameters match, to within the selected step value (e.g. 0.05), those derived using the grid search method. An example of the near exact agreement between grid search and GRG least *MAE*, calculated for all model varieties across as well data is depicted in Figure 4.1

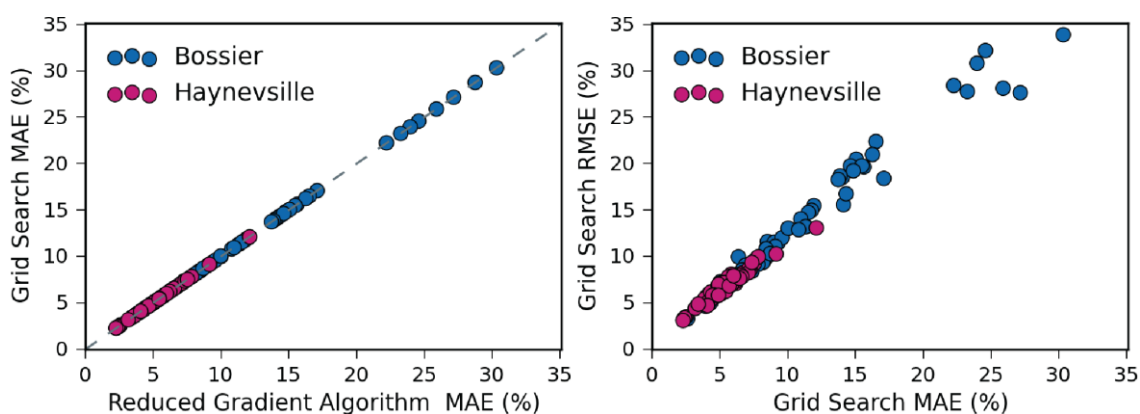


Figure 4.1. Grid search vs. solver methods and MAE vs. RMSE

Left: MAE (Grid Search) vs. MAE (Reduced Gradient Method). Right: RMSE vs. MAE. Data displayed for all data from optimisation models H1 and W1 to W4.

In addition, Figure 4.1 also plots grid search *RMSE* vs. *MAE*, and though there is some separation at higher error values they are in good agreement. The two different measures of error also produce minor variations in optimised parameters values, though the overall data trends and relationships were found to be near exact. As a consequence, though the data for both measures of error have been scrutinised, for clarity and consistency, only *MAE* data are presented in the following sections.

4.3 Results: Overview

This section presents an overview of the results generated by applying each of the grid search optimiser models to the core data and is divided as follows:

- 4.3.1 *S_{WA} results*: Presents *S_{WA}* estimates for optimiser models H1 and W4 (see Table 4.2).
- 4.3.2 *Residual errors*: Presents the residual error for each well and each optimiser model.
- 4.3.3 *Generated parameters*: Presents the generated Archie parameters for each optimiser model combined with bulk formation petrophysical/mineralogical properties.

4.3.1 Archie water saturation (*S_{WA}*) results

The combined results for BSR and HY optimised *S_{WA}* vs. *S_{WC}* are presented in Figure 4.2, which compares: model H1, a holistic basin wide approach that generates two sets of fitted parameters (one for each of the BSR and HY), and model W4, a well dependant approach that generates 26 sets of fitted parameters (one for each formation in each well). Models H1 and W4 are presented here as effective end members in optimiser flexibility/capability for minimising *MAE*.

Figure 4.2 shows a marked improvement in the correlation of *S_{WA}* vs. *S_{WC}* from model H1 to W4, with a significant reduction in *MAE* for both the HY and BSR. The *MAE*, normalised *MAE* and the percentage reduction in *MAE* are summarised in Table 4.3. Nonetheless, despite the significant reduction in *MAE* from model H1 to W4, *MAE* is still relatively high in the BSR at 10.13%. This is despite an increase from two to 26 optimised sample groups from model H1 and W4.

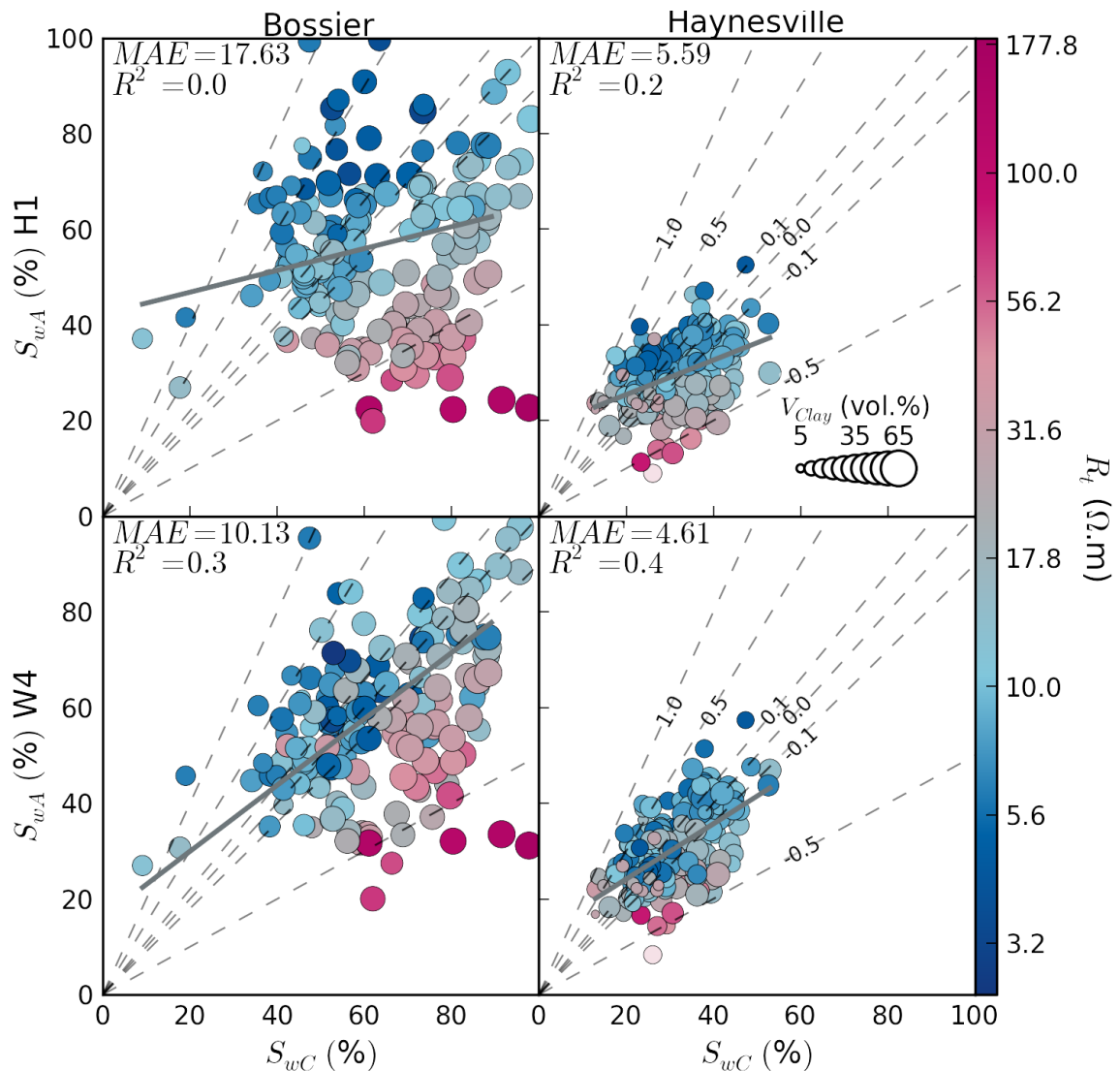


Figure 4.2. S_{wA} vs. S_{wC}

S_{wA} versus S_{wC} for the BSR (left), HY (right). Data is for model H1 (top) and W4 (bottom). Colour is a function of R_t and marker size is a function of bulk volume corrected V_{clay} . Dashed grey lines represent fractional relative error. Note: the increase in R_t and V_{clay} at low S_{wA} .

	MAE (%) H1	MAE (%) W4	% Relative Reduction in MAE (H1 to W4)
BSR	17.63	10.13	42.54
HY	5.59	4.65	16.81

Table 4.3. Change in MAE from model H1 to W4

Figure 4.2 also displays clear co-dependant relationships between R_t , V_{clay} and S_{wC} , particularly in the BSR, where the most resistive samples are also the most clay rich and water saturated. It is notable that this relationship typically results in significant S_w underestimates and generates large errors. These relationships, though less prominent, are also noted in the HY, which is notably less heterogeneous and more

constrained with regard to the distribution of all properties depicted in Figure 4.2 (R_t , V_{Clay} , S_{wC} and relative error).

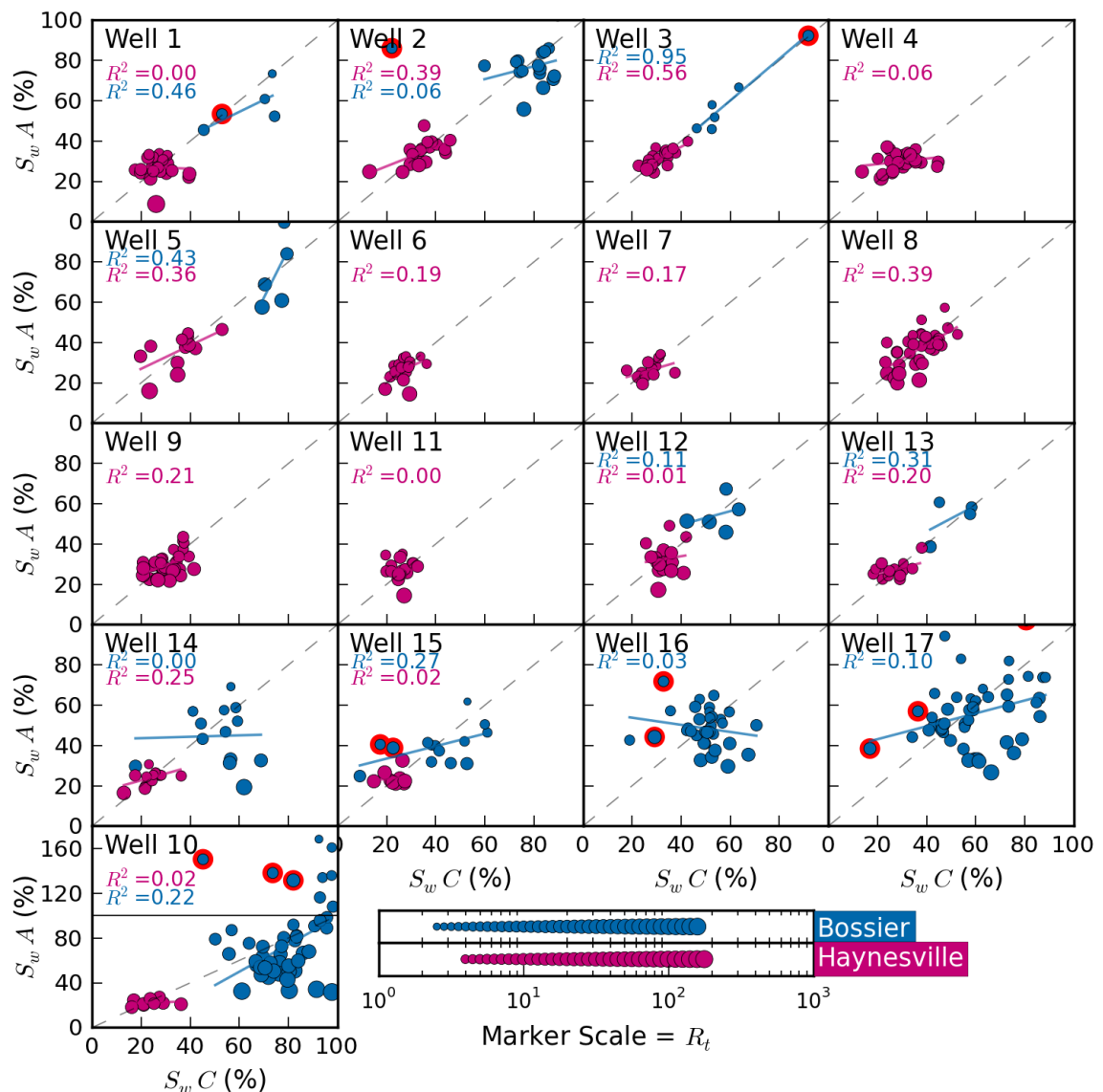


Figure 4.3. Tiled S_{wA} vs. S_{wC} scatter plot for model W4

S_{wA} versus S_{wC} for each well for model W4 (conceptual parameter limits applied). Marker size is a function of R_t . 14 BSR dolomitic outliers are highlighted in red and are excluded from R^2 calculation (an additional outlier plots off scale in well 17). Note: the larger markers (high R_t) tend to fall in the bottom right corner of the plot.

In addition to the composite results presented in Figure 4.2, optimised S_{wA} results for each well are provided in Figure 4.3, and again illustrate the apparent relationship between elevated R_t values and erroneous reductions in S_{wA} , particularly in well 10. It is again clear that this relationship is more prevalent in the BSR than the HY.

As discussed in Chapter 3, 14 core BSR samples are identified in Figure 3.7 as dolomitic outliers with $V_{Dolomite}$ over 4.67%. These dolomitic BSR samples are highlighted with a

red halo in Figure 4.3, and are uniformly distributed throughout the well data as discrete dolomitic bands. In the majority of wells they have little adverse effect in skewing minimised error and S_{wA} , but in wells 1, 2 and 10, they were noted to have an adverse effect on optimisation. As a consequence, the BSR dolomitic outliers, which are not representative of general reservoir lithology, were excluded from the optimisation process in Figure 4.3, and are excluded from all following analyses. As such, all future plots include data for 185 BSR and 285 HY core samples.

4.3.2 Residual errors

The optimisation models defined in Table 4.2 vary as a function of the available parameter dimensions (1D to 3D), the use of parameter constants (e.g. $m^*=2$), and number of population groups optimised (H1=2, W1-4=26). A comparison of the residual errors generated using each of the optimisation models (H1 and W1-W4) is given in Figure 4.4.

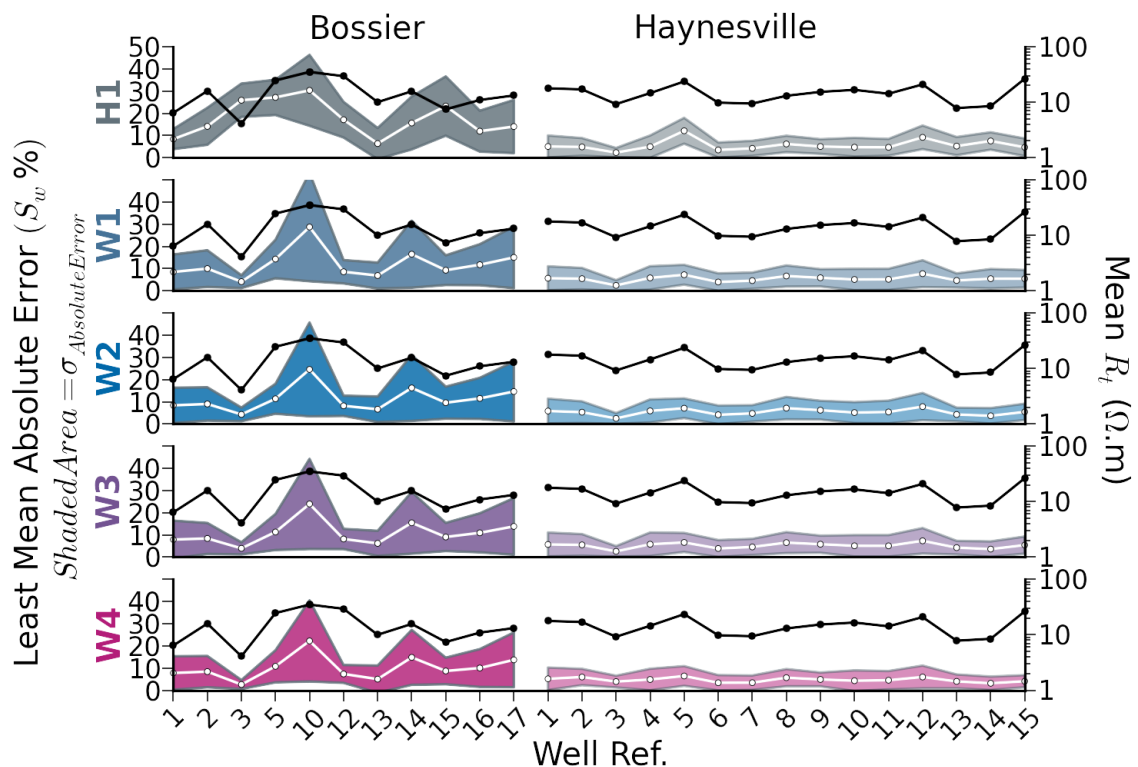


Figure 4.4. Comparison of MAE for variable parameter selection methods

Comparisons of least MAE (bold line) for each optimiser model (H1 and W1-W4). The shaded area is the standard deviation in absolute error (σ_{AE}) per well and the black line is mean R_t per sample group.

The residual error profiles displayed in Figure 4.4 show relatively little change between grid search models H1 to W4, despite alterations to the number of available parameter dimensions and sample binning. Also apparent are the consistently low residual errors reported for the HY, with markedly more varied error profiles for the BSR. Variations in least MAE are also shown to correlate well with the standard deviation in absolute error (σ_{AE} : shaded areas) and mean R_t . In other words, larger errors (least MAE) correspond with increased σ_{AE} and higher formation R_t . This may link to heterogeneity in formation compositional/petrophysical properties, where, as discussed in section 4.3.1 (Figure 4.2), the BSR exhibits wider V_{Clay} and S_{wC} distributions than the relatively constrained HY core data. In particular, the contrasting range and distribution in formation S_{wC} values for BSR and HY data may account for some of the difference in least MAE for the two formations. This is emphasised in comparing MAE in Figure 4.4 with normalised MAE in Figure 4.5, where the difference between the two formations becomes, with the exception of wells 2, 5 and 10, far less significant.

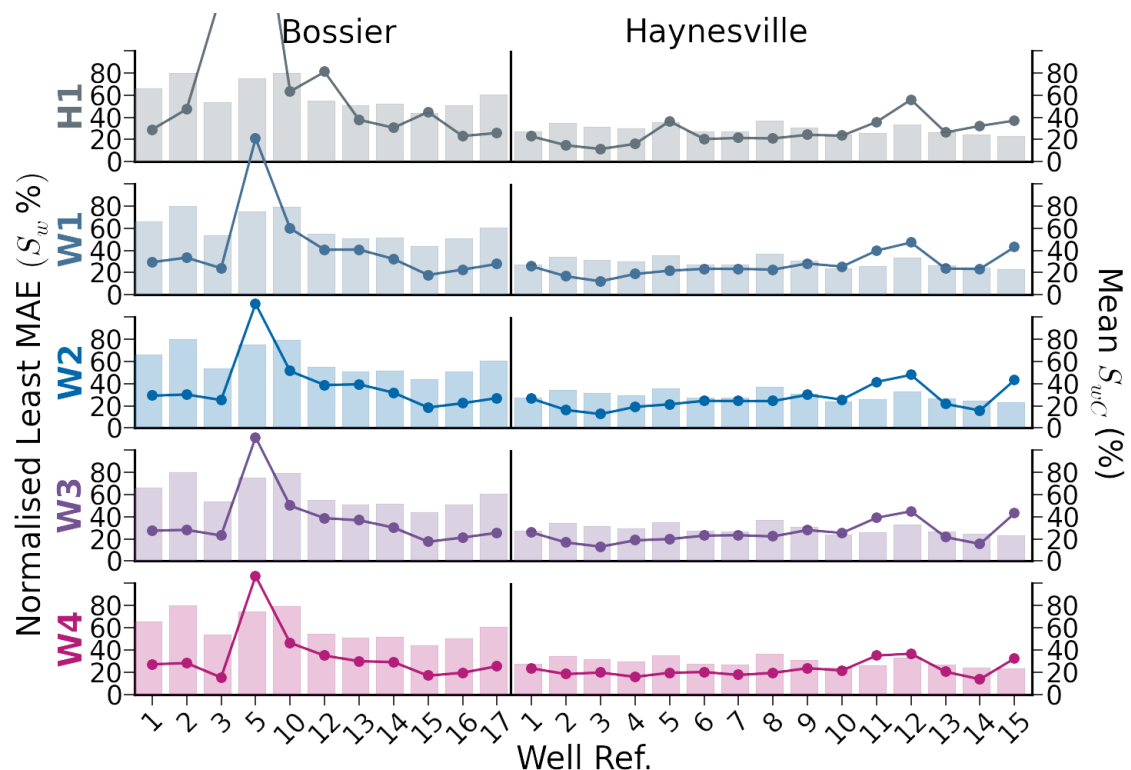


Figure 4.5. Normalised MAE for each optimisation model

Comparison of Normalised MAE (bold line) for each optimiser model (H1 and W1-W4). The bar chart is for mean S_{wC} per well. Note: the clipped MAE value for H1 well 5 is 267%. Also, higher S_{wC} values are noted in the BSR with normalised MAE values comparable to HY.

It is also evident in Figure 4.4 that the MAE for BSR well 3 falls sharply from model H1 to W1, indicating that heterogeneity in the BSR may be highly variable. In general

however, though there is an absence of any significant change in the error profiles between the optimisation models displayed in Figure 4.4, there is a general formation wide reduction in mean MAE with increasing optimiser model flexibility (H1, to W4). This change is highlighted in Figure 4.6 with an overall decline in error for the BSR and the HY equating to a relative reduction of 42.5% and 16.8% respectively (also see Table 4.3). For the HY, the decline in error between optimisation models is subtle, whereas for the BSR 31% of the 42.5% reduction in error occurs between model H1 and W1. It should be noted that model H1 holistically optimises all the BSR data within one sample population, whereas model W1 segregates the data into 11 sample populations. In other words, the most significant reduction in MAE in the BSR occurs when considering it as a heterogeneous (W1 to W4) as opposed to a homogenous (H1) system.

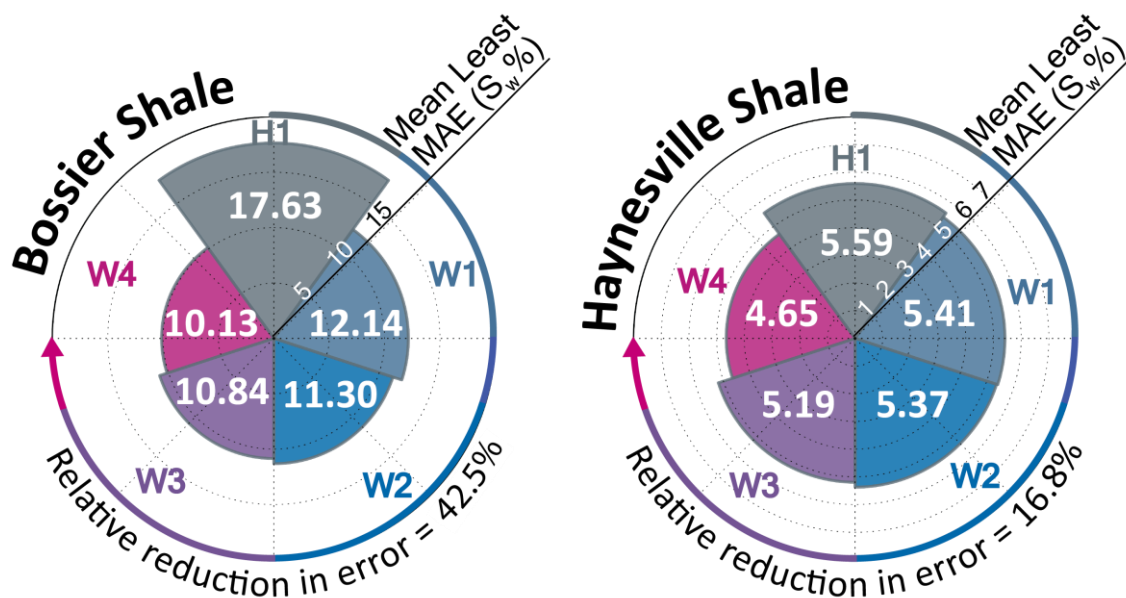


Figure 4.6. Comparison of average MAE by optimisation model and formation
 Note: the most significant reduction in error in the BSR is between model H1 and W1.

4.3.3 Generated Archie parameters

Archie parameters were optimised for each model (H1 and W1 to W4) over a range of parameter dimensions. The optimised least MAE parameters generated for each model are presented in Figure 4.7.

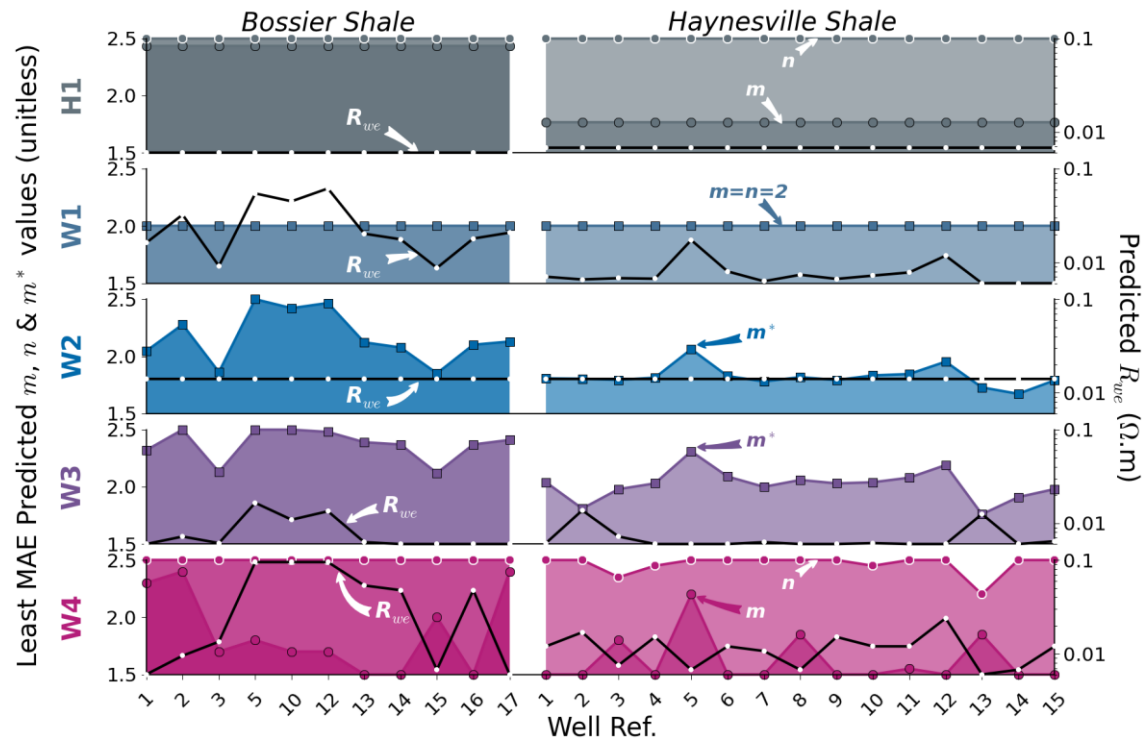


Figure 4.7. Predicted Archie parameters for each optimisation model

Note: in each model, optimisation tends to rely on modifying only a single parameter.

Figure 4.7 indicates a consistent stepped reduction in predicted parameter values from left (BSR) to right (HY) in all five subplots. It is also apparent that despite increases in parameter dimensions from 1D (W1 and W2) to 2D (W3) and 3D (W4), that the optimised solutions appear to remain generally reliant on modifying only a single parameter value. For example, predicted R_{we} values in W3 make only 7 modest excursions from the baseline position. This position is somewhat reversed in W4 with R_{we} having a more significantly variable profile, whereas values for n remain largely fixed at the maximum value constraint, and values for m make only sporadic movements from the minimum constraint. In any of the multidimensional models, that n should be consistently fixed at 2.5 or higher, or likewise that m or R_{we} might be constantly fixed at the minimum value appears peculiar and is discussed further in

section 4.4. Nevertheless, taking into account only the prominent, single parameter profiles from each model, it is clear that they are generally similar, with a consistent overall reduction in value from the BSR to the HY. The dominant parameter profile for each optimisation model (taken as H1: m , W1: R_{we} , W2 and W3: m^* , and W4: R_{we}) are compared directly in a composite log plot in Figure 4.8 with a number of bulk formation compositional and petrophysical properties.

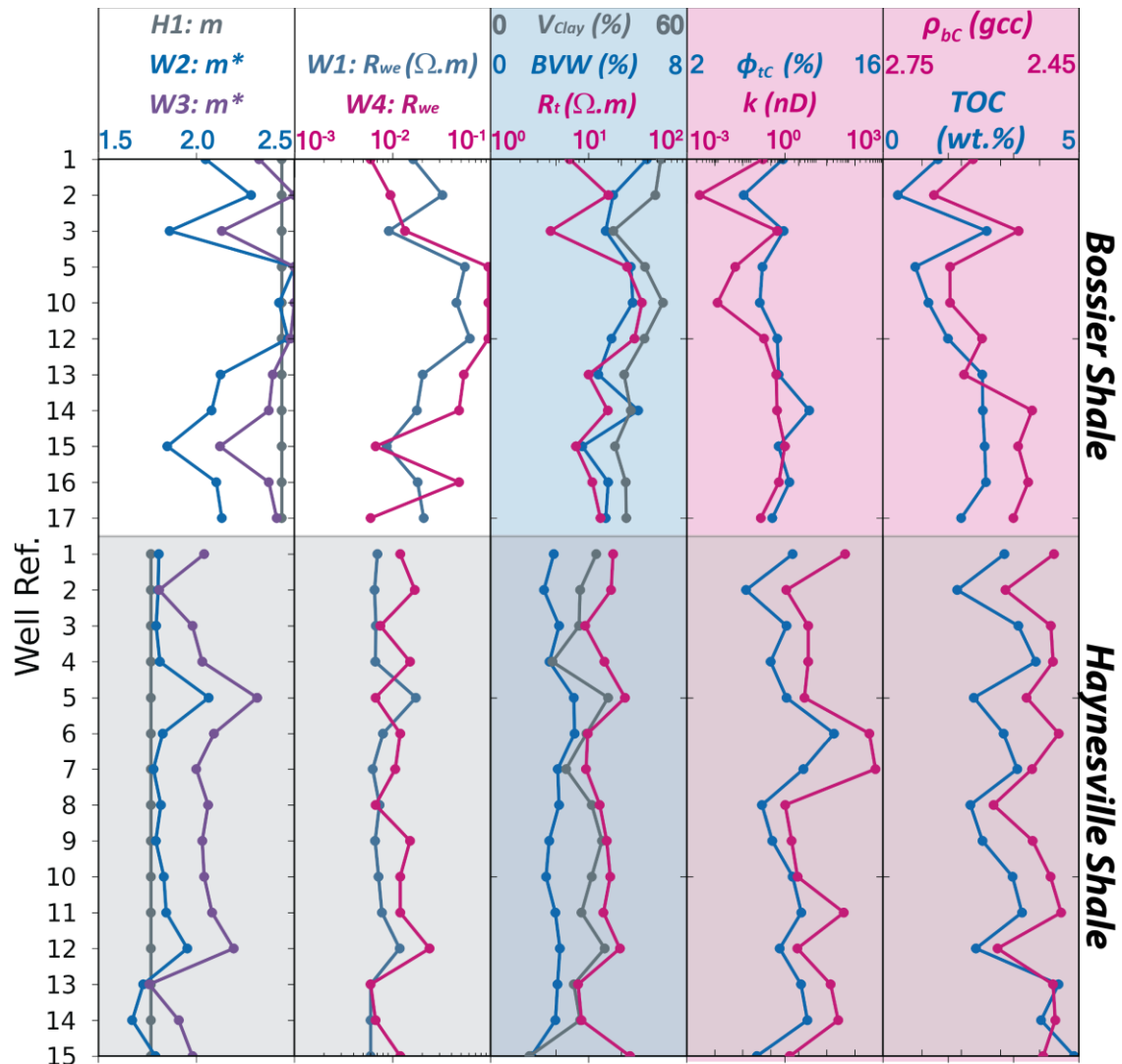


Figure 4.8. Predicted Archie parameters, V_{clay} , and key petrophysical properties

Optimised parameters and average formation properties for each sample group. This includes: V_{clay} , core matrix permeability (k), ϕ_{tc} , total organic carbon (TOC), bulk density (ρ_{bc}) and R_t .

The primary observations from Figure 4.8 include the similarity in trends between m^* for models W2 and W3 and R_{we} for models W1 and W4. These trends appear (Figure 4.8) to correlate well with R_t , bulk volume water (BVW see equation 4.7) and V_{clay} . By contrast, matrix permeability (k), ϕ_{tc} , total organic carbon (TOC) and core bulk density

(ρ_{bc}) have been included to show, in addition to the matching trends observed for the four variables, an absence of any apparent primary control over derived Archie parameters. Whilst evidence of overall parameter forcing from these properties (k , ϕ_{tC} , TOC and ρ_{bc}) is limited, local excursions such as the sharp drop in parameter values for well 3, do correspond with distinct spikes in k , ϕ_{tC} , TOC and ρ_{bc} .

Similar to Figure 4.2, the relationships depicted in Figure 4.8 link increasing BVW with elevated R_t and V_{Clay} . Furthermore, the noted correlation of bulk formation properties with V_{Clay} infers additional formation compositional trends that arise from the negative linear association between V_{Clay} and $V_{Carbonate}$ content noted in Figure 3.14.

4.3.4 Summary

4.3.4.1 S_{wA} results

- S_{wA} underestimates are routinely linked to high V_{Clay} and high R_t (Figure 4.2).
- BSR S_{wA} estimates are less accurate and S_{wC} , R_t and V_{Clay} variables are noted to have wider distributions than those for the HY (Figure 4.2).
- Overall there is a reduction in MAE from model H1 to W4, though the residual MAE remains significant (Figure 4.2).

4.3.4.2 Residual MAE

- Residual MAE and σ_{AE} are relatively low and consistent in the HY and between optimiser models. The reduction in MAE from model H1 to W1 is relatively low suggesting that HY data is not particularly sensitive to the style of sample binning (Figure 4.4).
- Residual MAE and σ_{AE} are highly variable in the BSR and between optimiser models. The largest reduction in MAE is between model H1 and W1, suggesting that BSR data is relatively sensitive to the style of sample binning (Figure 4.4).
- In both formations, varying the number of parameter dimensions in the optimiser model appears to have limited impact on error distribution from W1 to

W4, suggesting that the data is not particularly sensitive to parameter change in Archie's equation (Figure 4.4) within the optimisation model.

- Residual MAE and σ_{AE} correlate with mean R_t (Figure 4.4).

4.3.4.3 Generated Archie parameters

- Generated Archie parameters show limited variation between the optimiser models. In addition, optimisation appears to generally rely on the modification of only a single parameter, with additional parameters commonly fixed at either their upper or lower bound (Figure 4.7).
- A comparison of bulk formation properties with predicted Archie parameters associates an increase in parameter value contemporaneous with increases in BVW , R_t and V_{Clay} (Figure 4.8).
- k , ϕ_{TC} , ρ_{bc} and TOC appear to have little direct influence over parameter selection (Figure 4.8).

The following sections present a systematic analysis of each of the optimisation models and are intended to define the mechanics underpinning parameter selection.

4.4 Results: 1D parameter optimisation

This section details the analysis of 1D optimisation models (W1 and W2) and aims to highlight the nature of any model limitations, parameter interactions, parameter forcing linked to geological/petrophysical properties, and any predictive capabilities the investigation of these relationships might reveal.

The following sections include:

- 4.4.1 The sensitivity of *MAE* across the range of possible parameter values.
- 4.4.2 The trade-offs between parameters and input variables in Archie's equation.
- 4.4.3 The range of parameters produced by direct optimisation for each core sample.

4.4.1 Sensitivity analysis

Sensitivity, taken here as the effect of a change in parameter R_{we} (W1) or m^* (W2) on *MAE*, is investigated by comparing the full range of possible Archie parameters against the generated *MAE* as depicted in Figure 4.9. This produces a sensitivity curve for each well, for which the lowest point on the curve (lowest *MAE* on the y-axis) equates to the optimum parameter value on the x-axis. That these are termed sensitivity 'curves' indicates that sensitivity is not constant over the range of parameter values. For the purposes of overall comparison however, Figure 4.9 does include a tornado plot that provides a measure of sensitivity given as the % change in *MAE* for a 5% shift in parameter value above and below the optimal *MAE*.

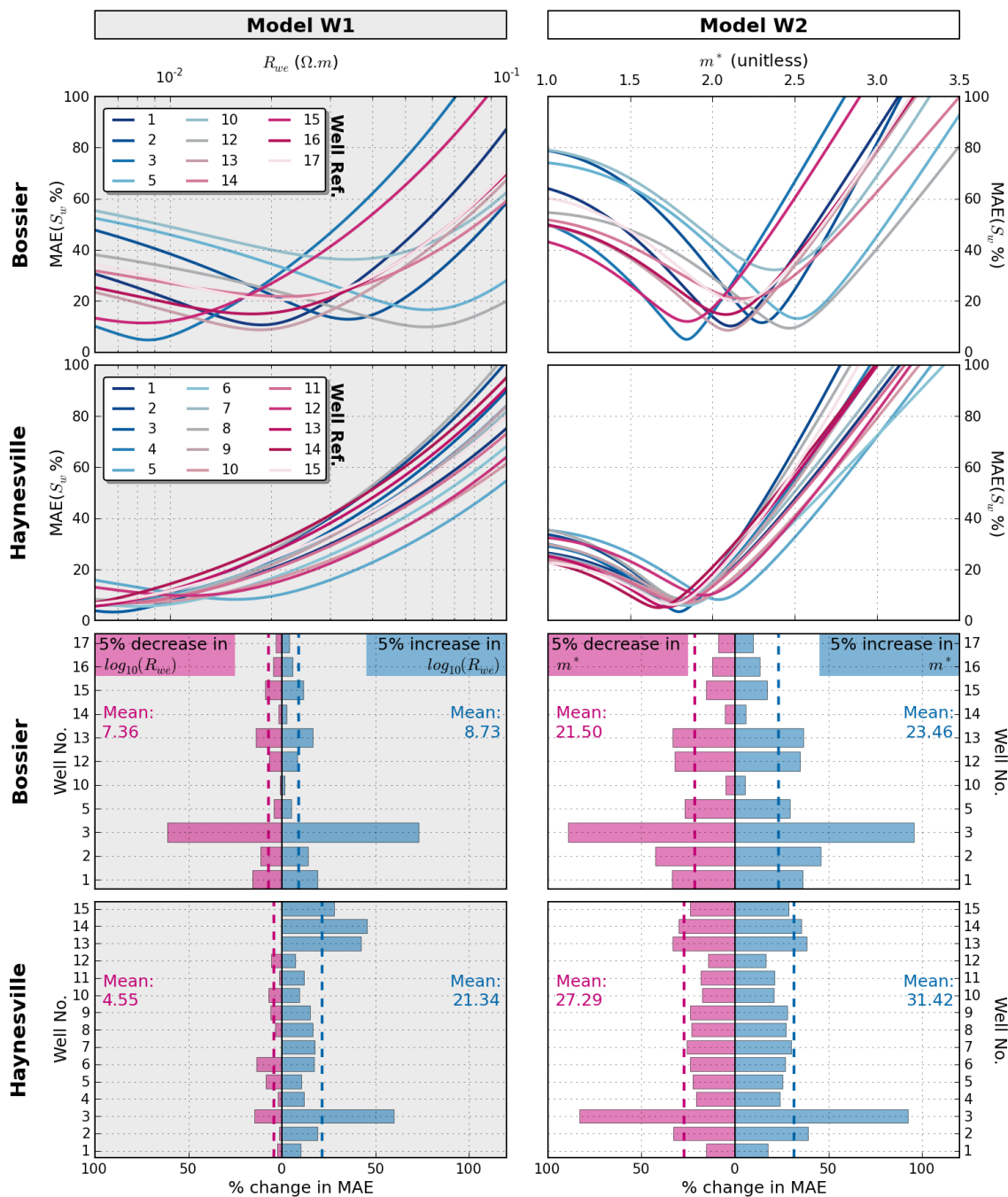


Figure 4.9. Sensitivity analysis (model W1 and W2)

Plots (left): Model W1. Plots (right): Model W2. Upper Four Plots : MAE (S_w %) vs. parameter value. Lower Four Plots: The relative change (%) in MAE for a 5% increase in parameter value above (blue) and below (pink) the optimum. Note: Well 3 has a relatively low residual error and high sensitivity and has therefore been excluded from the calculation of the reported mean values so as to prevent distortion.

Comparing the results from model W1 (Figure 4.9: Left) with W2 (Figure 4.9: Right), the MAE vs. m^* sensitivity plots (right) are more tightly and more steeply inclined than for R_{we} (left), indicating that Archie’s equation is more sensitive to value changes in m^* than R_{we} . This is reflected in comparisons of the tornado plots which show: a) that

error is more sensitive to changes in m^* than R_{we} and b), that MAE in the HY is more sensitive to parameter change than in the BSR. It is also apparent in Figure 4.9 that all HY data plot in a well constrained area with a relatively consistent sensitivity to parameter change. By contrast, the BSR sample groups display greater variation in sensitivity with optimal lows occupying a wider though generally higher range in either R_{we} or m^* values.

In the tornado plots for both models W1 and W2 (Figure 4.9), well 3 stands out as having particularly high parameter sensitivity. This occurs as samples from well 3 optimise to the lowest reported MAE and are more than three times as sensitive to a 5% parameter change. This highlights a general trend, where the curvature at the optimal base of each sensitivity curve generally becomes tighter and more steeply inclined at lower MAE values, thus yielding higher sensitivities. Though this is a trend and not a rule, and some wells (Figure 4.9), particularly in the BSR, show greater variations in basal curvature with reductions in MAE .

4.4.2 Parameter trade-offs

In order to investigate the controls on optimised parameter values and their trade-offs with the input variables ϕ_{tC} , R_t and S_{wC} , R_{we} and m^* can be directly back calculated from Archie's equation (equation 4.5 and equation 4.6) for a range of input variable combinations representative of the BSR and HY.

$$R_{we} = S_{wC}^{m^*} \cdot \phi_{tC}^{m^*} \cdot R_t \quad (4.5)$$

$$m^* = \frac{\log\left(\frac{R_{we}}{R_t}\right)}{\log(\phi_{tC}^{m^*} S_{wC})} \quad (4.6)$$

Where m^* indicates $m=n$. This assumption is made for both models W1 and W2 such that equation 4.5 and equation 4.6 can be simplified to solve for BVW :

$$BVW = S_{wC} \cdot \phi_{tC} \quad (4.7)$$

$$R_{we} = BVW^{m^*} \cdot R_t \quad (4.8)$$

$$m^* = \frac{\log\left(\frac{R_{we}}{R_t}\right)}{\log(BVW)} \quad (4.9)$$

The parameter trade-offs for models W1 and W2 were investigated using the same approach:

- W1) R_{we} was calculated (equation 4.8) for all input combinations across a representative range of R_t and BVW values at $m^*=2$,
- W2) similarly, m^* was calculated (equation 4.9) for an identical range of R_t and BVW values at $R_{we}=0.014 \Omega.m$ (R_{we} value based on personal communication with BG Group).

The resulting parameter trade-offs for Models W1 and W2 are presented in the following two sections.

4.4.2.1 Model W1: Parameter trade-offs

The parameter trade-offs effective within model W1 are illustrated in Figure 4.10 as R_{we} vs. R_t , where the large shaded area represents all possible R_{we} values within R_t and BVW parameter space. This depicts a positive linear trend between R_{we} and R_t for a given BVW , with increases in BVW acting to increase the $R_{we}: R_t$ ratio. Overlain on Figure 4.10 are the W1 MAE optimised R_{we} values for each well coloured by mean BVW . This demonstrates that the BSR and HY samples plot according to their bulk formation properties (i.e., in the centre of each respective BVW range), with marker colour giving a loose match to the directly calculated background data.

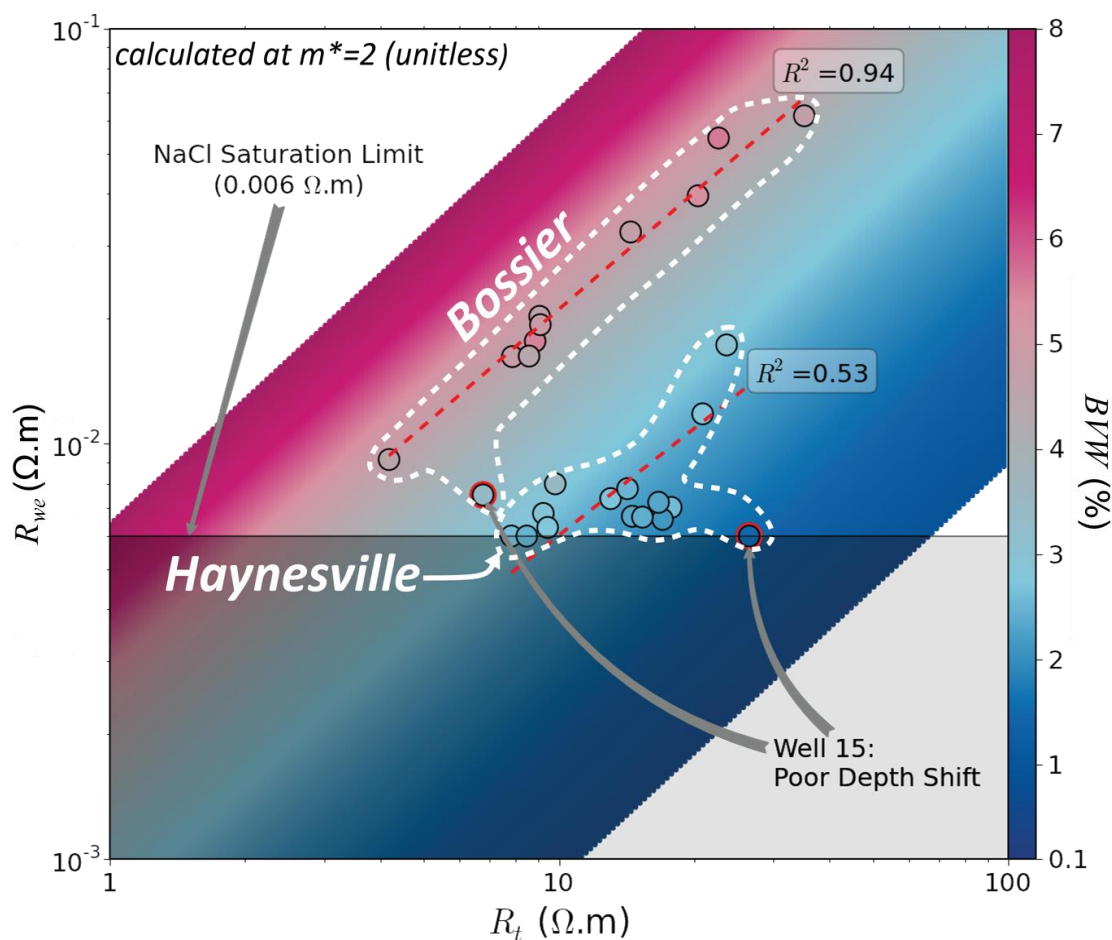


Figure 4.10. Parameter trade-offs (model W1)

R_{we} calculated at $m^*=2$ (Equation 4.8) vs. R_t for a BVW range (based on Equation 4.7) representative of BSR and HY core data. Overlain are W1 optimised R_{we} ($m^*=2$) vs. mean R_t values for each well, with marker colour a function of average well BVW scaled against the colour bar (right).

Although the overlain MAE optimised data lay in an appropriate BVW region, marker colour does not exactly match the calculated BVW background and there is limited deviation across the BVW range. This, combined with the linear trend for optimised R_{we} vs. R_t , suggests that optimised parameters are primarily responding to R_t and not BVW . The exception to this observation is the highlighted points for well 15, which exhibits unreliable depth-matched R_t parameters (see section 3.2.2) and is excluded from the calculation of R^2 . The optimised R_{we} values for the HY wells also plot in the appropriate BVW range, but appear limited by, and fall close to the saline saturation limit ($0.006 \Omega.m$), though the spread of the data across the BVW range suggests reduced forcing from R_t .

4.4.2.2 Model W2: Parameter trade-offs

The parameter trade-offs effective within model W2 are illustrated in Figure 4.11 as m^* vs. R_t and are similar to those for W1, with m^* displaying a linear trend with R_t , where the $m^*:R_t$ ratio is controlled by variations in BVW . It is also apparent, that the viable range in m^* expands (sensitivity decreases) as R_t increases, such that a small change in m^* at low R_t can accommodate larger shifts in BVW than at higher R_t values.

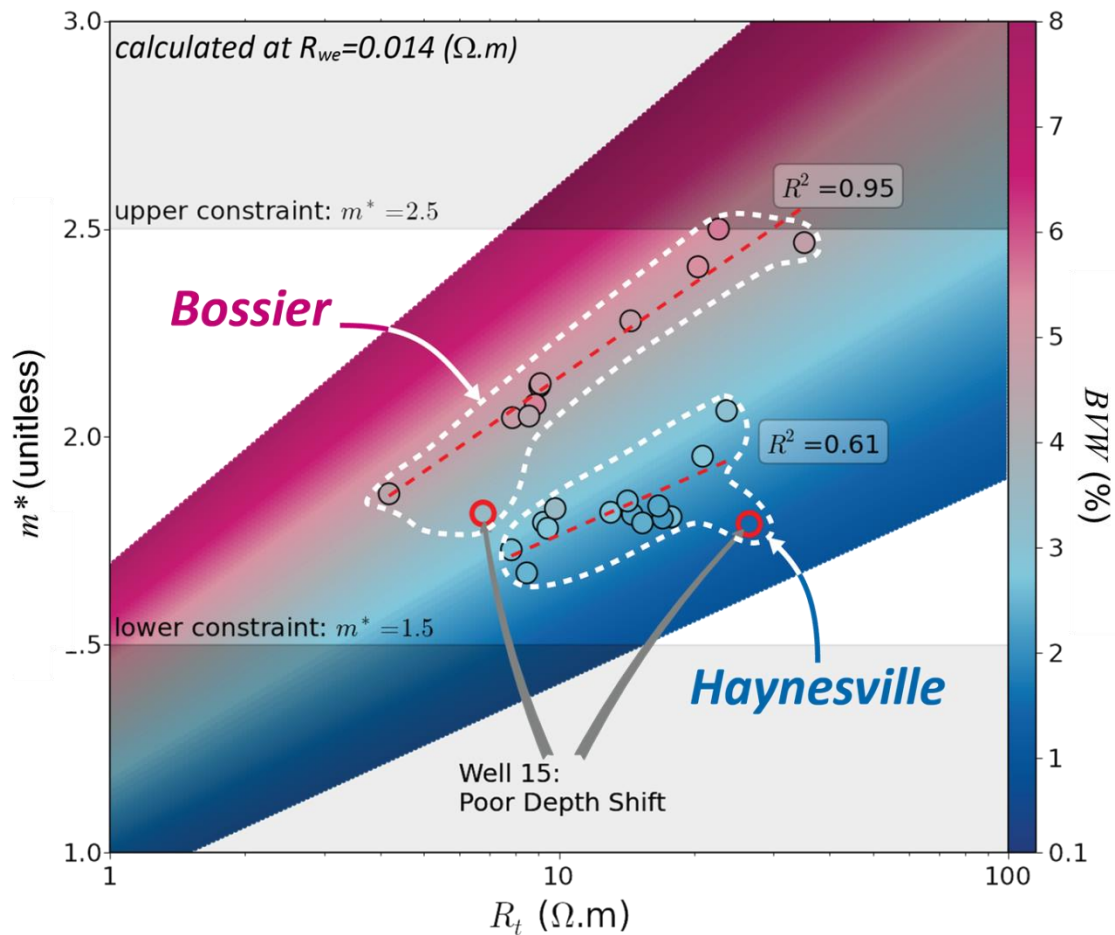


Figure 4.11. Parameter trade-offs (model W2)

m^* calculated at $R_{we}=0.014$ (Equation 4.9) vs. R_t for a BVW range (Equation 4.7) representative of HY and BSR core data. Overlain are W2 optimised m^* ($R_{we}=0.014$) vs. mean R_t values for each well, with marker colour a function of mean well BVW scaled against the colour bar (right).

Overlain on Figure 4.11 are the W2 optimised m^* values for each well plotted against mean R_t and coloured by mean BVW . As discussed previously, highlighted sample groups from well 15, were not included in the calculation of R^2 . It is again suggestive, particularly for the BSR, that R_t is the primary parameter forcing m^* selection within the optimisation model. The same is true for the HY, though the increased spread of

points across the BVW range again suggests that ϕ_{TC} and S_{wC} play a greater role in parameter forcing.

4.4.2.3 Model W1 and W2: Shifts in fixed parameter assumptions

Optimisation models W1 and W2 use fixed parameter assumptions ($m^*=2$ and $R_{we}=0.014$ respectively), the effects of modifying these parameters are illustrated in Figure 4.12. Plot A depicts the effects of decreasing m^* from 2 to 1.5 (model W1), which results in a narrower band of higher R_{we} values for the same BVW range and therefore an increase in the sensitivity of R_{we} . For samples with low R_t , this shifts the BVW range away from the saline saturation limit yielding increased choice in R_{we} selection. Plot B depicts the effect of a decrease in R_{we} from 0.014 to 0.006 $\Omega.m$ (model W2), which results in a very slightly wider band of higher m^* values for the same BVW range and thus a slight decrease in the sensitivity of m^* . Whilst the sensitivity of m^* is slightly reduced, the range of possible m^* values that can be selected is therefore slightly increased.

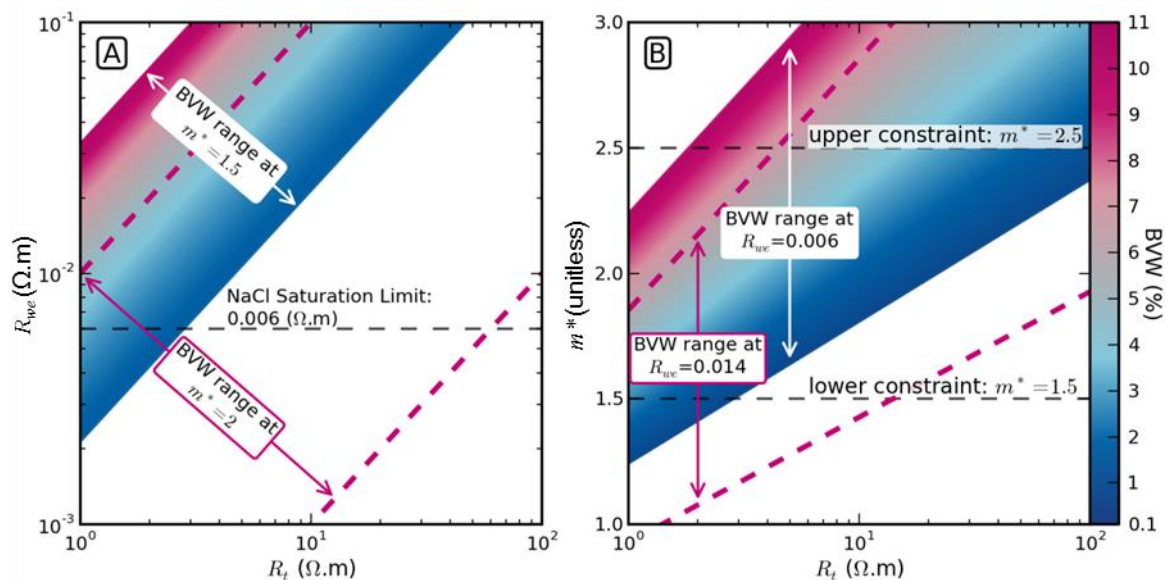


Figure 4.12. Parameter trade-offs (model W2 and W2)

Plot (A): R_{we} (Equation 4.8) versus R_t calculated at $m^*=2$ and 1.5 (model W1). Plot (B): m^* (Equation 4.9) versus R_t calculated at $R_{we}=0.014$ and 0.006 $\Omega.m$ (model W2). The range in input parameters ϕ_{TC} and S_{wC} (BVW , Equation 4.7) reflect BSR core data. Changes in the linear trend between R_{we} or m^* and R_t with variations in BVW are scaled by the colour bar (right). Note: plot (A), decreasing m^* increases R_{we} sensitivity and shifts the BVW interval away from the saline saturation limit. Plot (b), decreasing R_{we} results in a very slight decrease in the sensitivity of m^* with an associated increase in the range of m^* values.

It is indicated by both models W1 and W2, that reductions in the fixed assumptions ($m^*=2$ or $R_{we}=0.014$) act to modify the relative sensitivity of the calculated parameter by changing the range in parameter values over the same BVW interval. For model W1, decreases in m^* substantially increases R_{we} sensitivity, whilst for model W2, decreases in R_{we} very subtly decrease the sensitivity and thus increases the parameter range for m^* , implying that increasing either fixed parameter will have the opposite effect.

4.4.3 Core sample parameter modelling

As discussed in section 4.2, the approach taken in this chapter is to optimise Archie parameters for all the core data in each formation for each well. This implies an unrealistic homogeneity in formation geological and petrophysical properties uncharacteristic of heterogeneous fine grained formations. As such, the optimised Archie parameter values are synonymous with bulk averaged formation properties. In other words, the generated parameter values may be broadly appropriate for some core samples, but cannot fully represent the range of formation pore geometrical and fluid properties expressed in the core data.

Unique Archie parameter values can however be directly solved (equation 4.8 and 4.9) for each core sample using model W1 and W2 static parameter assumptions ($m^*=2$ and $R_{we} = 0.014$). This allows for further exploration of the range in parameter values and any links they might have with geological\petrophysical properties.

R_{we} and m^* values are calculated for each core sample (Figure 4.13), and broadly replicate relationships depicted for optimised model W1 and W2 parameters (Figure 4.10 and Figure 4.11). The linear relationships between R_{we} vs. R_t (Figure 4.13: A) and m^* vs. R_t (Figure 4.13: B) are also broadly similar. The data points in Figure 4.13 (A) and (B) are also scaled by V_{clay} , where increased marker size (higher clay contents) can be linked to BVW and either a relative increase in fluid resistivity (R_{we}) or to an increase in relative pore geometrical complexity (m^*).

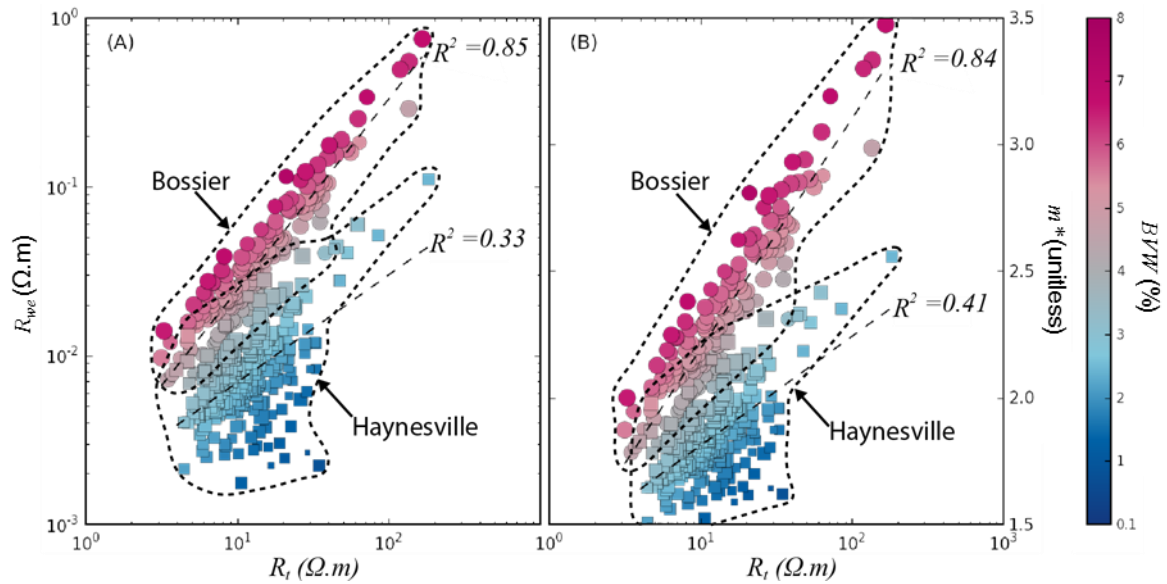


Figure 4.13. R_{we} vs. R_t (A) and m^* vs. R_t (B)

Plot (A): calculated R_{we} (Equation 4.8) vs. R_t for each core sample at $m^*=2$. Plot (B): calculated m^* (Equation 4.9) vs. R_t at $R_{we} = 0.014 \Omega.m$ for each core sample. Marker colour is a function of bulk volume water (BVW, Equation 4.7) and marker size is a function of V_{clay} . Note: Good linear R_t - R_{we} relationship for the BSR, with limited change in R_t with BVW, the reverse is true of the HY.

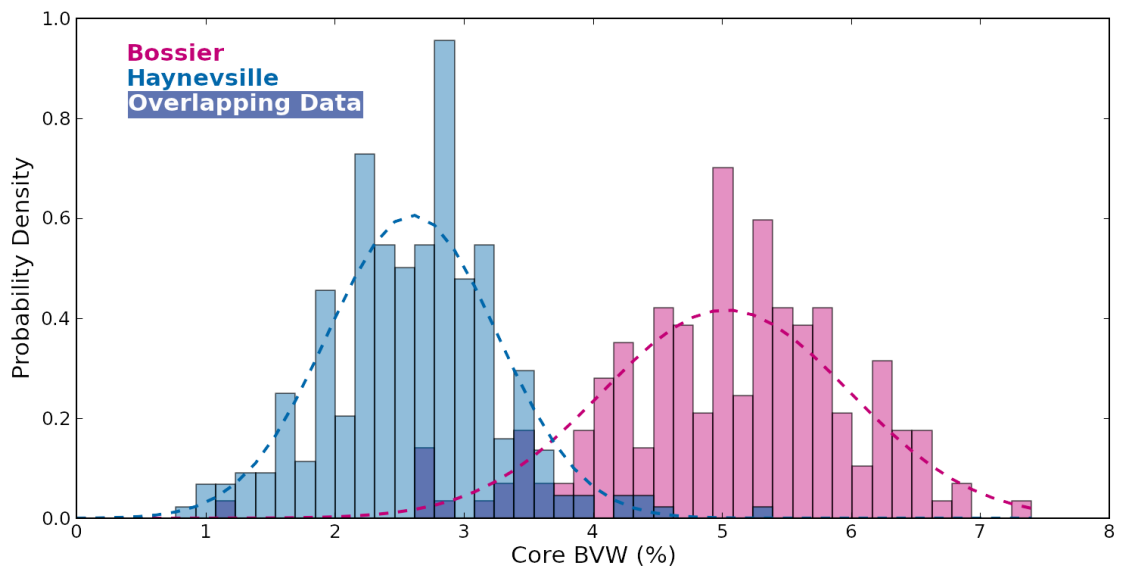


Figure 4.14. BSR and HY BVW distributions

BSR and HY probability density plots for BVW. Core BVW is calculated after equation 4.7.

An additional observation in Figure 4.13 is the limited overlap between HY and BSR data. This is highlighted in the BVW probability density distributions (Figure 4.14), where it is clear that the BSR and HY data exhibit a relatively disparate range in BVW values. It is also notable that, whilst the BSR BVW data has a larger range in BVW values (Figure 4.14), the individual core calculated parameter values (Figure 4.13) plot in a narrow linear band, such that only a minor shift in the ratio (parameter : R_t) can

express a large change in BVW . In other words, BSR core data does not appear to be sensitive to BVW conditions, implying that either highly variable BVW salinity/pore complexity or other geological factors must be influencing R_t . By contrast, though the HY has a narrower range in BVW (Figure 4.14), individual core calculated parameter values show a much greater sensitivity to BVW values, i.e. there is a large change in parameter values from high to low BVW (Figure 4.13).

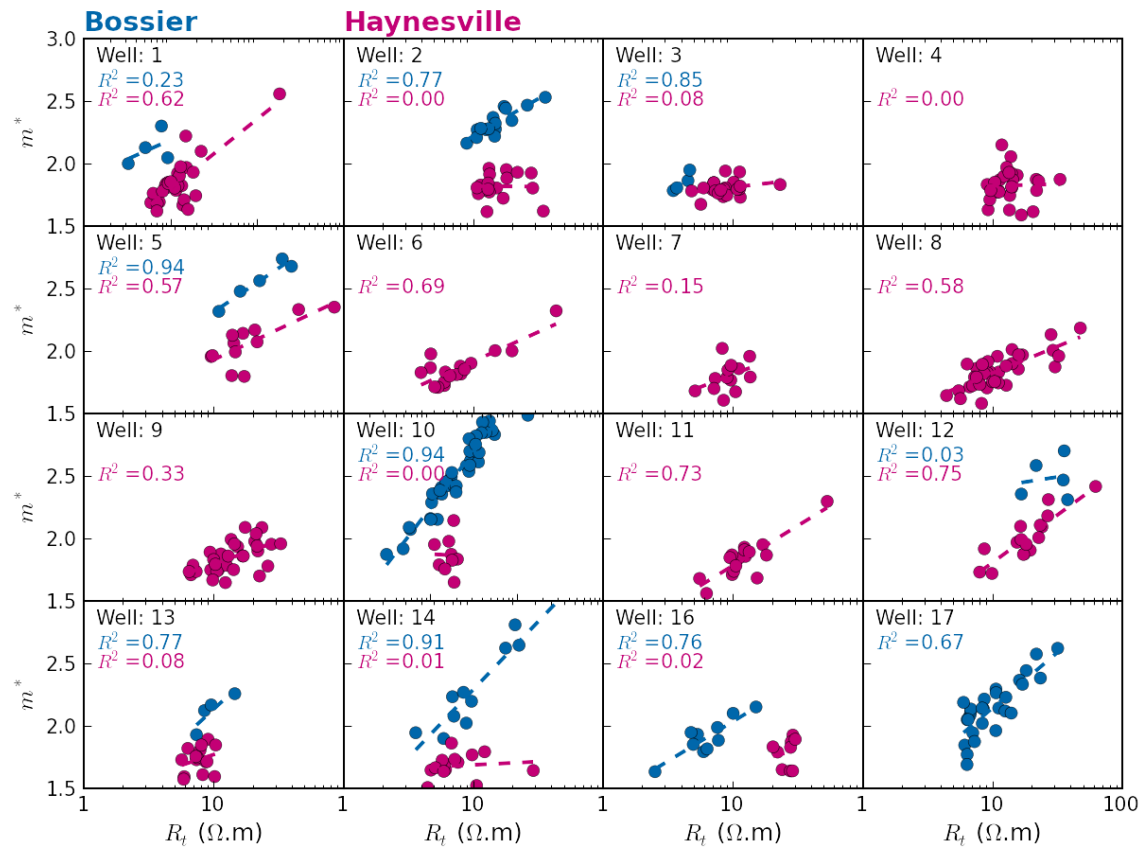


Figure 4.15: m^* vs. R_t .

Tiled scatter plot of m^* vs. R_t for each BSR (blue) and HY (red) well calculated at $R_{we}=0.014$ ($\Omega.m$). Well 15, noted to be of poor depth shift quality with unreliable depth matched R_t values, is not included. Dolomitic BSR samples ($\geq 5\%$ $V_{Dolomite}$) have also been excluded. Note the frequently linear m^*-R_t relationship.

The linear relationship between the calculated parameter (R_{we} or m^*) vs. R_t (Figure 4.13) allows for direct prediction of Archie parameters from R_t using least squared regression. This is illustrated in Figure 4.15, for m^* calculated for each core sample (equation 4.9) plotted against R_t for each well, demonstrating a common positive linear association (calculating for R_{we} using equation 4.8 gives near identical results). Using the regression coefficients derived from these relationships (Figure 4.15) to estimate m^* directly from R_t , saturation can then be estimated using Archie's equation as per

model W2, with R_{we} fixed at 0.014 Ω .m. This measure of S_w using regressed m^* exponents is termed S_{WR} . This approach has the advantage of avoiding the assumption of homogeneity implicit in an optimised solution (model W1 to W4), and allows for a greater expression of formation heterogeneity.

4.4.3.1 S_{WR} vs. S_{WA} (model W4)

The regression derived saturation S_{WR} is compared against S_{WA} derived from model W4 (the most accurate optimised S_w estimate available) and S_{WC} (the benchmark core values) for all wells in .

Comparison of MAE between S_{WA} (W4) and S_{WR}

Comparison of MAE (S_w %) between S_{WA} (W4) and S_{WR} estimates.

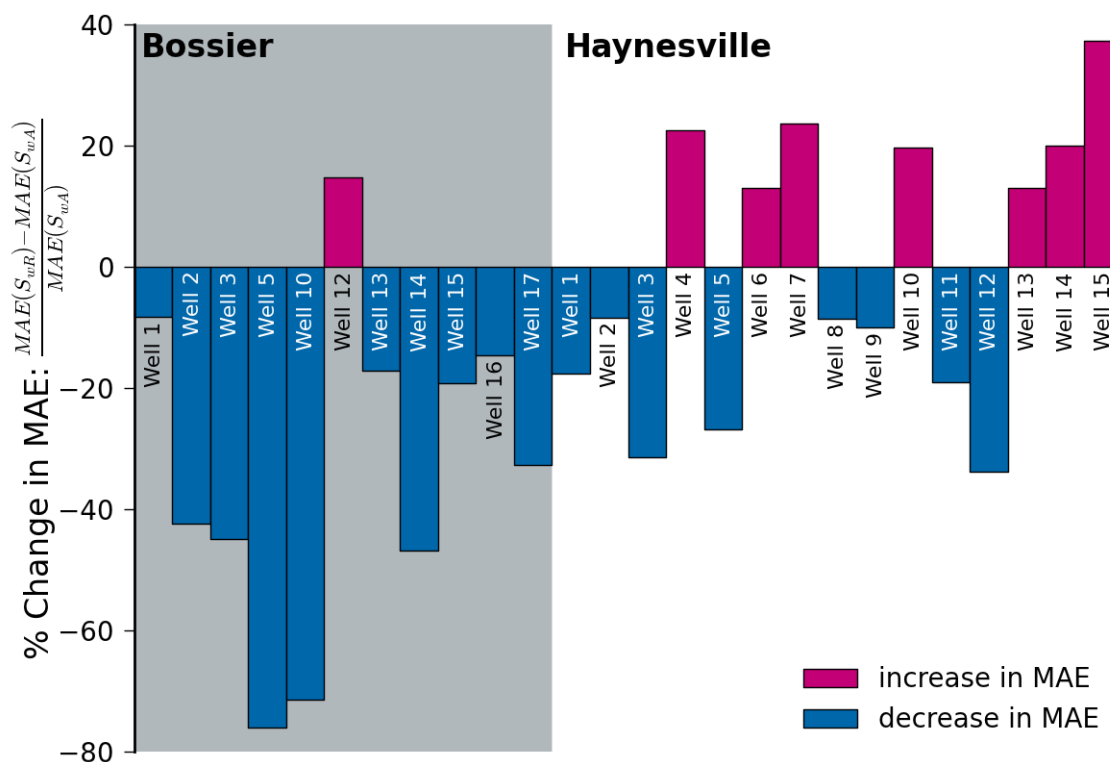


Figure 0.3. % Change in MAE when using S_{WR} as opposed to S_{WA} (W4)

The % change in MAE when using S_{WR} as opposed to S_{WA} (W4) for the BSR and HY data.

4.4.4 Summary

4.4.4.1 Sensitivity analysis

- Residual MAE is more sensitive to changes in m^* than R_{we} (Figure 4.9).

- The HY displays relatively consistent and higher sensitivity profiles. In contrast the BSR data displays a wider variety of parameter values and sensitivities suggestive of a more petrophysically heterogeneous formation (Figure 4.9).

4.4.4.2 Parameter trade-offs

- It is suggested that the primary variable forcing parameter selection in both models W1 and W2 is R_t . This effect is shown to be more dominant in the BSR, where data indicates that sample *BVW* exerts lesser control on parameter forcing. By contrast, variation in HY *BVW* appears to exert a larger impact on optimised parameter values (Figure 4.10 and Figure 4.11).
- The effects of changing static model assumptions for W1 ($R_{we}=0.014$) and W2 ($m^*=2$) are demonstrated:
 - model W1; reducing m^* increases the sensitivity of R_{we} and shifts the *BVW* range away from the saline saturation limit,
 - model W2; reducing R_{we} slightly decreases the sensitivity of m^* , thus increasing the range of possible m^* values (Figure 4.12).

4.4.4.3 Core sample parameter modelling

- The HY displays relatively consistent and higher sensitivity profiles. In contrast the BSR data displays a wider variety of parameter values and sensitivities suggestive of a more petrophysically heterogeneous formation (Figure 4.9).
- Directly solving for parameter values suggests that the BSR is far less sensitive to variations in *BVW* than the HY (Figure 4.13).
- The correlation between R_t and the calculated parameter (m^* or R_{we}) allows for parameter prediction using standard regression analysis (Figure 4.13). For a large number of wells the resulting S_{wR} estimates demonstrate a significant improvement over optimised S_{wA} (W4), with reductions in error as high as 78% in the BSR and 36% in the HY (**Error! Not a valid bookmark self-reference.**, Figure 0.2 and Figure 0.3).

4.5 Results: 2D parameter optimisation

This section details the analysis of the 2D optimisation model (W3) and aims to highlight the nature of any model limitations, parameter interactions, parameter forcing linked to geological/petrophysical properties, and any predictive capabilities the investigation of these relationships might reveal.

The following sections include:

- 4.5.1 The sensitivity of *MAE* across the range of possible parameter values.
- 4.5.2 The trade-offs between parameters and input variables in Archie's equation.
- 4.5.3 The range of parameters produced by direct optimisation for each core sample.

4.5.1 Sensitivity analysis

The sensitivity data for model W3 is displayed in Figure 0.4 and plots the change in *MAE* between S_{wA} and S_{wC} for every R_{we} and m^* parameter combination. Wells 3 and 10 are displayed as examples of characteristic BSR and HY relationships, highlighting a typical linear association between m^* and R_{we} . That m^* is a power function is also evident, such that *MAE* is more sensitive to increases rather than decreases in m^* from the optimum value. It also highlights, as in Figure 4.4, the tendency for R_{we} values to remain at or very near to the lowest bound. This is a compensatory effect, where reductions in R_{we} act to reduce the sensitivity of and thus expand the range of possible m^* values and so generate a preferred least error solution, though this reduction in parameter sensitivity is most likely linked to an increase in model error. In other words, high R_{we} increases the sensitivity of *MAE* to small changes in m^* . It should be noted that the reference to model error refers to the least error optimisation modelling approach, not specific *MAE* values.

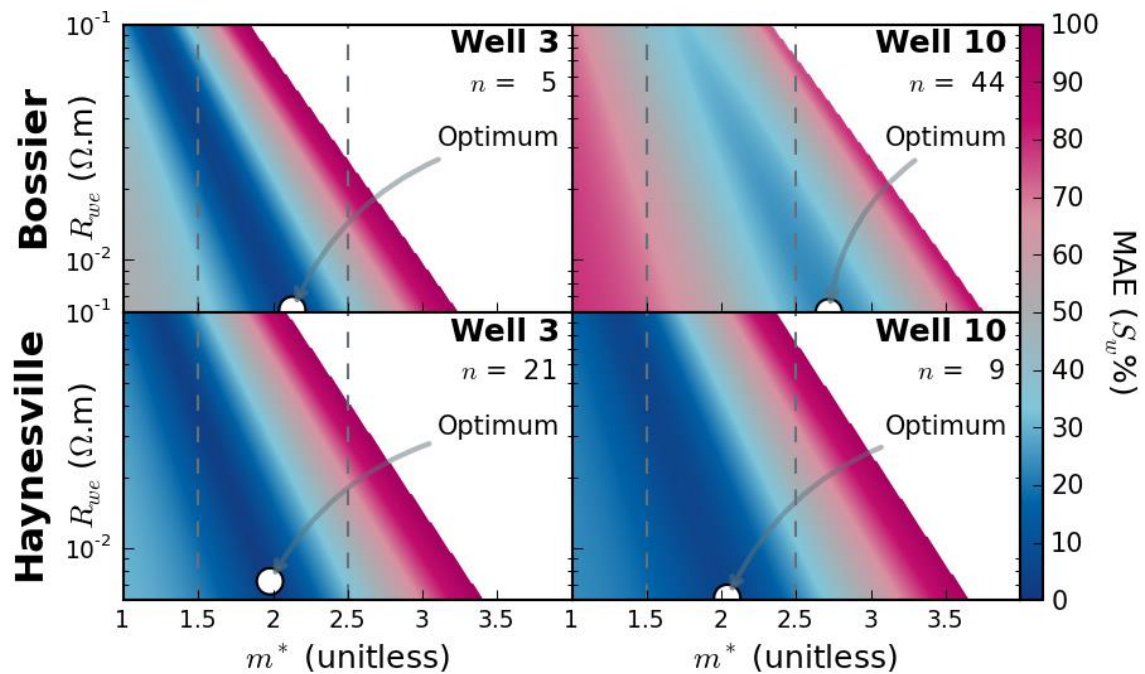


Figure 0.4. Sensitivity analysis (Model W3)

MAE sensitivity plot for model W3: R_{we} vs. m^ for the BSR (top) and HY (bottom). Two representative wells are displayed for each formation. The optimum values (white marker), corresponds with the least MAE, n refers to the number of samples within the optimised well. Note the decrease in m^* sensitivity as R_{we} decreases.*

The R_{we} , m^* relationships discussed above (Figure 0.4) are summarised for all wells (1 to 17) in Figure 0.5. This displays the parameter distributions for the lowest 5% of MAE values for each well, highlighting the optimum parameter values associated with global least MAE. Here, the R_{we} distributions show an increase in the number of low error solutions available at low R_{we} values. In all but three instances (HY wells 2, 3 and 13) the optimal R_{we} value is at or very close to the lower bound.

The m^* distributions depicted in Figure 0.5, whilst showing variation in parameter range, show a consistent distribution style. As discussed, MAE is more sensitive to higher m^* as opposed to lower values (m^* is a power function), as such each distribution is skewed with fewer high error solutions available to the right of the modal value than to the left. It should also be noted that the optimal m^* value rarely coincides with, and usually occurs to the right of the modal value. Those instances where the optimal m^* is to the left of the modal value also coincides with optimal R_{we} values that are above the lower bound (HY wells 2, 3 and 13).

Whilst these observations may reflect genuinely high fluid salinities (low R_{we}), it is clearly implied for the majority of wells, that optimiser model W3 simply minimises R_{we}

so as to refine m^* value selection, thus rendering the optimised values highly questionable in physical terms. The only exceptions to this trend are for HY wells 2, 3 and 13, whose optimal parameters may be of greater geological/physical significance.

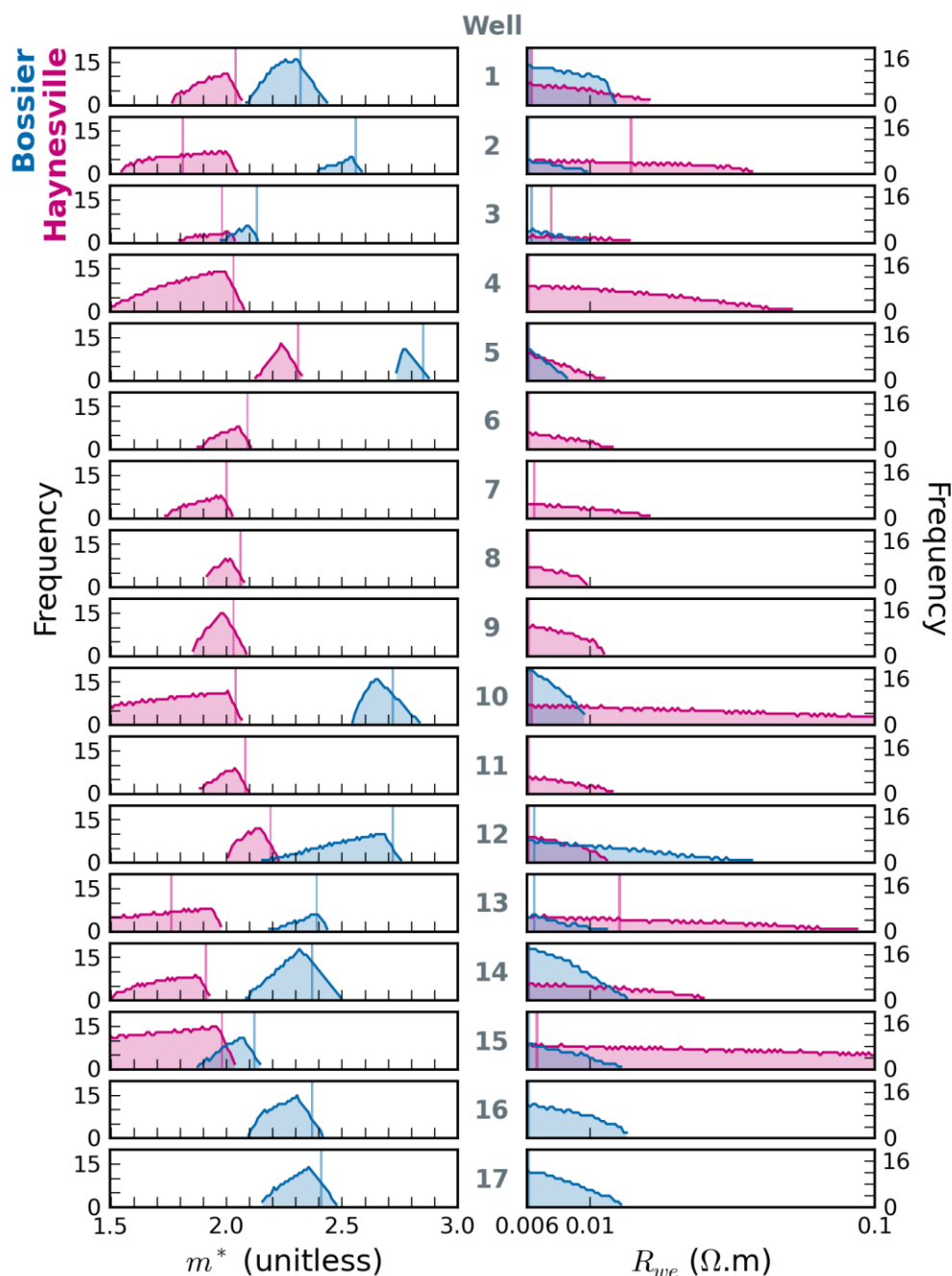


Figure 0.5. Parameter distributions, sensitivity analysis (model W3)

Plot of BSR (blue) HY (red) model W3 parameter distributions for the lowest 5% of MAE values. The faded bars indicate the optimal parameter value for each well and formation.

4.5.2 Parameter trade-offs

The parameter trade-offs in optimiser model W3 were modelled using equation 4.9 in the same manner as those for model W2. The approach was however modified to reflect the optimised R_{we} values reported in Figure 4.7, where 19 of 26 R_{we} values equal 0.006 $\Omega.m$. The R_{we} constant was therefore changed from 0.014 to 0.006 $\Omega.m$.

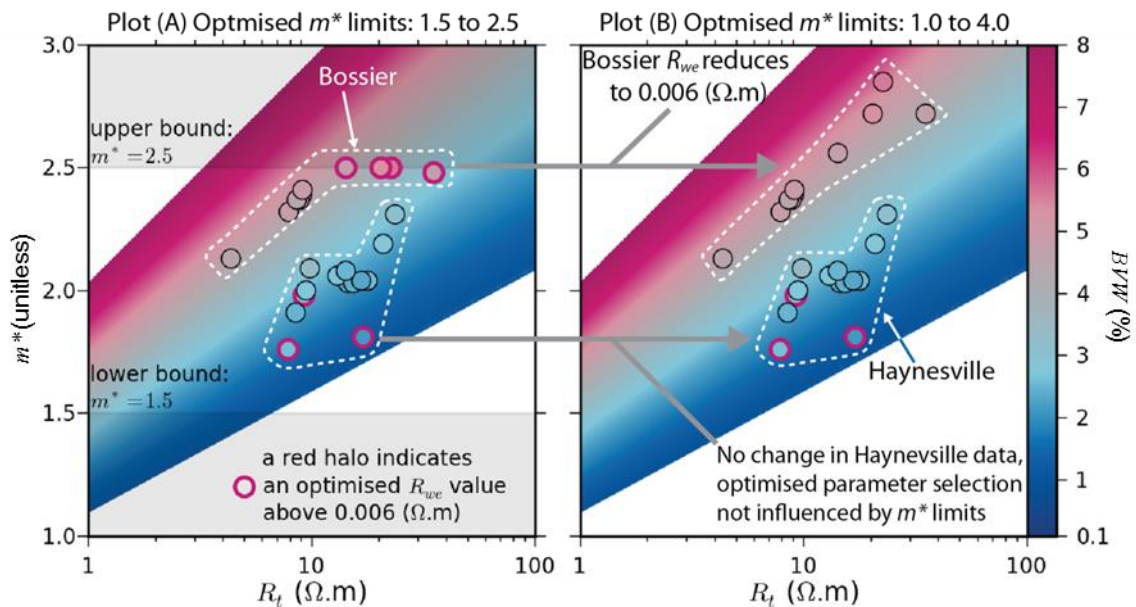


Figure 0.6. Parameter trade-offs (model W3)

Calculated m^* (at $R_{we}=0.006$, Equation 4.9) vs. average R_t for a BVW range (colour bar) representative of HY and BSR core data (Equation 4.7). Overlain are W3 optimised m^* vs. mean R_t values for each well, with marker colour a function of mean well BVW (colour bar right). Plot (A) shows overlain W3 optimised values where m^* is limited between 1.5 and 2.5 (conceptual limits). Plot (B) overlays W3 optimised data with expanded m^* limits of 1.0 to 4.0. *Note: consistent minimisation of R_{we} and good linear relationship for BSR data in plot (B).*

The parameter trade-offs depicted in Figure 0.6 are very similar in character to those described for model W2 (section 4.4.2.2), with a clear linear trend between optimised m^* vs. R_t values. The only exceptions to this linear relationship are the highlighted markers, representing wells whose R_{we} values optimise to in excess of 0.006 $\Omega.m$, for the BSR core data, these highlighted wells plot on the m^* upper bound ($m^*=2.5$). If the optimiser is allowed to exceed the m^* upper bound (as depicted), this results in slightly higher m^* values and R_{we} values of 0.006 $\Omega.m$, and a much improved linear $m^* : R_t$ relationship. In other words, as discussed in the sensitivity analysis, R_{we} appears to be simply modified so as to exploit a preferred range in m^* . The same is not however true for the HY data, where R_{we} values exceed 0.006 $\Omega.m$ for three wells (2, 3 and 13). This

reiterates previous observations that *BVW* in the BSR may not be the dominant factor in controlling R_t , the primary variable forcing optimised parameter selection.

4.5.3 Core sample parameter modelling

R_{we} and m^* values were generated iteratively for each core sample to further explore any parameter forcing. This was achieved using the Grid Search methodology outlined in section 4.2.2, applied to each individual core sample with a parameter step increment of 0.01.

The optimum parameter combinations generated for each core sample are given in Figure 0.7. Here the results are displayed as R_{we} vs. m^* for both the BSR (left) and HY (right), with marker colour and size as a function of R_t and *BVW* respectively. This plot indicates a linear trend between R_{we} and m^* , which can be further linked to perpendicular relationships with both *BVW* and R_t , such that R_t and *BVW* increase with increases in R_{we} and m^* . The distributions of the optimum parameters are also plotted alongside each axis, indicating a near uniform distribution in R_{we} for both formations, though there is a slight increase in frequency for the lowermost R_{we} values. By contrast, both formations have more normally distributed m^* parameters (Figure 0.7) of similar distribution and range to those calculated for model W2. That there should be a uniform distribution across the entire range of R_{we} in both formations is dubious, and similar to previous findings, it is probable that R_{we} values are selected principally to allow for a preferred selection of m^* .

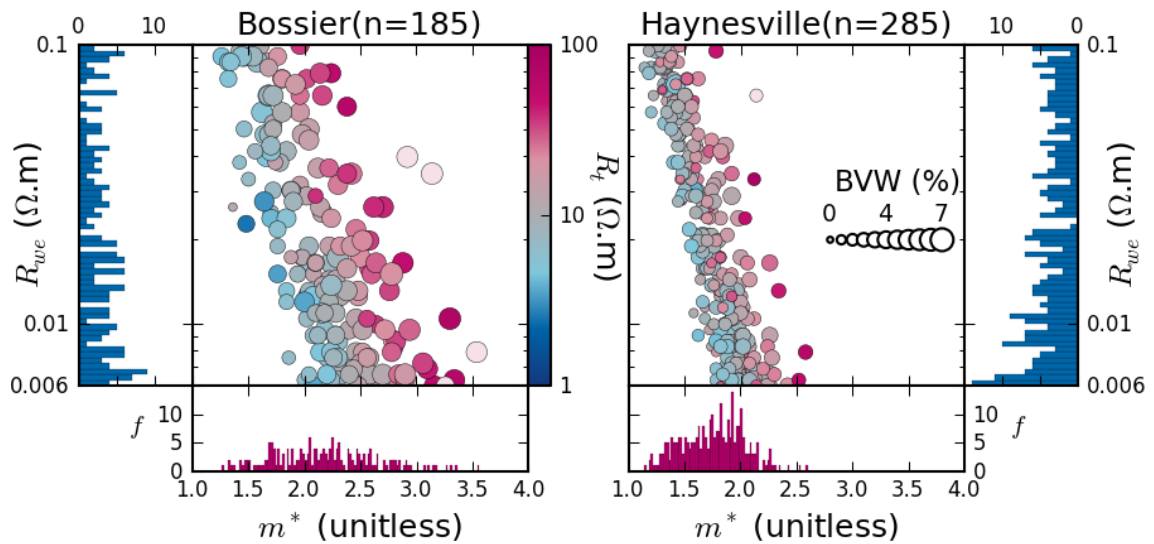


Figure 0.7. Core sample optimised parameters (model W3)

Grid search optimised R_{we} and m^* parameters for BSR and HY data. Marker colour and size are a function of R_t and BVW . Parameter distributions are provided on axis. Note linear R_{we} - m^* relationship with perpendicular R_t trend. In the BSR, and to a reduced extent in the HY, trends in R_t are linked to BVW .

The optimal parameters generated for each core sample and displayed in Figure 0.7 have least MAE values varying from between 0.000023% to 0.16% for the 470 BSR and HY core samples. These are however ‘least’ MAE solutions, with between 377 to 1487 alternative solutions within $\pm 5\%$ error of S_{wC} benchmark values for each core sample (at a 0.01 parameter spacing). Furthermore, given that the experimental error in core data measurements are poorly constrained (see section 2.3), what error bounds are appropriate: 5%, 10%, 15%, or more? If there is a geologically meaningful parameter combination, is it possible to identify it without tighter parameter constraints? This problem is explored in Figure 0.8 which displays the parameter distributions for S_{wA} estimates within $\pm 5\%$ of the benchmark S_{wC} values.

Figure 0.8, similar to previous results, depicts a relatively tight series of m^* distributions for the HY with a much wider and variable range in sample m^* distributions for the BSR. For both formations the range in m^* can be linked to BVW , with parameter distributions moving to lower m^* values at lower BVW . Furthermore, there is a consistent uniform though inclined distribution of near identical character for R_{we} in all core samples. This demonstrates a general increase in the availability of low error solutions at lower R_{we} values but ultimately fails to define a probabilistic value range. This suggests that identifying R_{we} by optimiser methods may not be

feasible and that a constant R_{we} may be more suitable. These results are summarised in Figure 0.9 by totalling the frequency in occurrence of each parameter for each formation. This highlights: a) the contrast in m^* parameter distributions, and b) identical distributions in R_{we} for the BSR and HY.

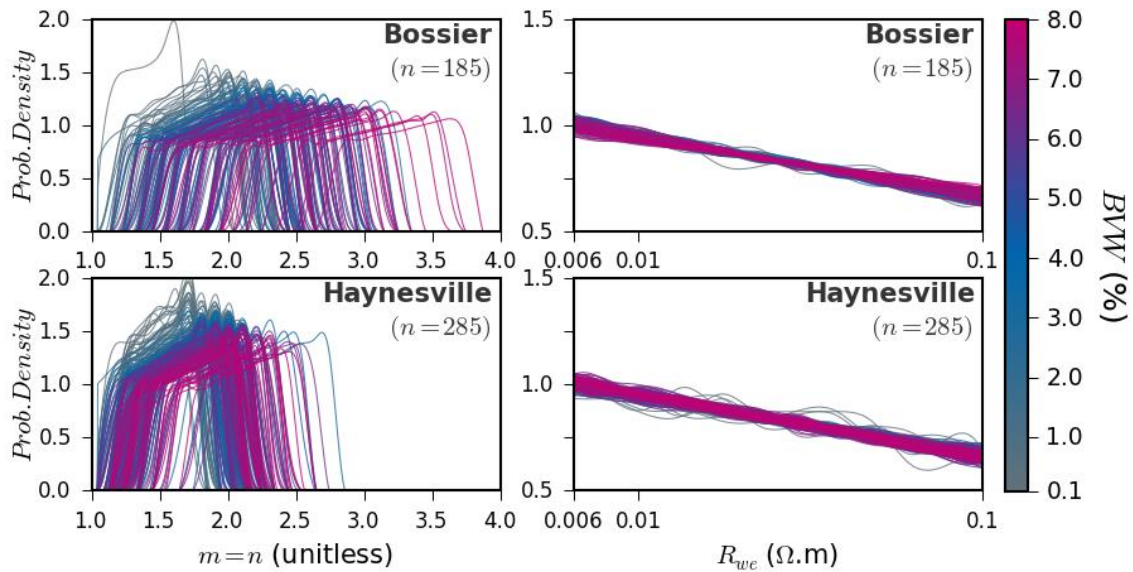


Figure 0.8. Optimised parameter distributions for S_{wA} within +/-5% of S_{wc} (model W3)

Grid search optimised R_{we} and m^* parameters distributions for S_{wA} estimates within +/- 5% of benchmark S_{wc} values for BSR (top) and HY (bottom) data. Line colour is a function of sample BVW.

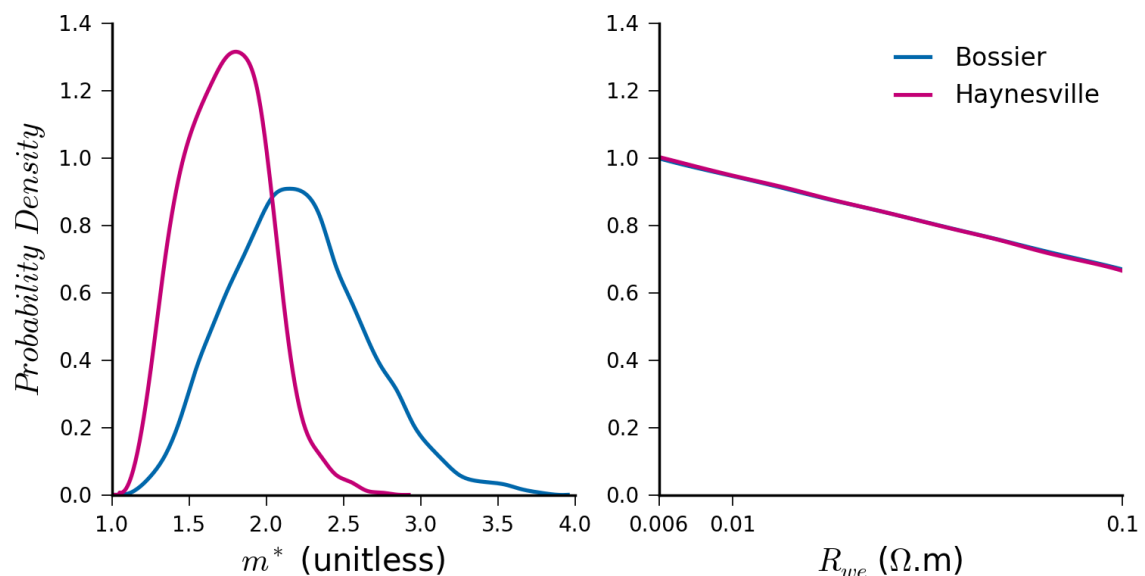


Figure 0.9. Totalled parameter distributions for S_{wA} estimates within +/-5% of S_{wc} (model W3)

Grid search optimised m^* (left) and R_{we} (right) parameter distributions for S_{wA} estimates within +/- 5% of benchmark S_{wc} values for BSR and HY data. Probability density is calculated from the total frequency of all core samples at each parameter value at a parameter spacing of 0.01.

4.5.4 Summary

4.5.4.1 Sensitivity analysis

- Results are demonstrated to favour minimised R_{we} values that reduce the sensitivity of, and expands the viable range of m^* values, therefore allowing for a preferred least error solution though at the expense of a likely increase in model error. The consistent manipulation of R_{we} values prevents a reasoned geological interpretation of the optimised value (Figure 0.4).

4.5.4.2 Parameter trade-offs

- Similar to the 1D models considered, analysis of the 2D model indicates a linear relationship between the optimised parameters and R_t , suggesting that BVW is of limited importance in forcing parameter selection (Figure 0.6).

4.5.4.3 Parameter modelling

- Model W2 predicted m^* and R_{we} can be shown to consistently relate to R_t and BVW (Figure 0.7).
- Results show consistent parameter distributions for the HY with diverse and heterogeneous distributions in the BSR (Figure 0.8).
- Distributions for m^* are noted to be consistent with those generated for 1D models.
- The lack of any parameter distribution for R_{we} stresses the tendency for this parameter to be minimised so as to increase the frequency of low error solutions (Figure 0.9).

4.6 Results: 3D parameter optimisation

This section details the analysis of 3D optimisation model (W4) and aims to highlight the nature of any model limitations, parameter interactions, parameter forcing linked to geological/petrophysical properties, and any predictive capabilities the investigation of these relationships might reveal.

The following sections investigate:

- 4.6.1 The sensitivity of *MAE* across the range of possible parameter values.
- 4.6.2 The trade-offs between parameters and input variables in Archie's equation.
- 4.6.3 The range of parameters produced by direct optimisation for each core sample.

4.6.1 Sensitivity analysis

The sensitivity data for model W4 is displayed in Figure 0.10, illustrating characteristic relationships between parameter modifications and their effects on *MAE* for wells 3 and 10 of the HY and BSR respectively. The plots on the left of Figure 0.10 present all the available data where *MAE* is less than 100%, with plots on the right presenting only those parameters for the lowest 5% of *MAE* values.

All plots in Figure 0.10 depict steep linear relationships between R_{we} and m and between m and n , with a shallower linear trend between R_{we} and n for both wells 3 and 10. The combination of these trends creates a distinct least error plane which remains broadly similar between all wells. As per model W3, it is evident that changing certain parameter values can be beneficial in modifying the sensitivity and effective value range of another. For instance, in BSR well 10, maximising n to $n=4$ decreases the sensitivity of both R_{we} and m , increasing the precision with which the later parameter can be selected.

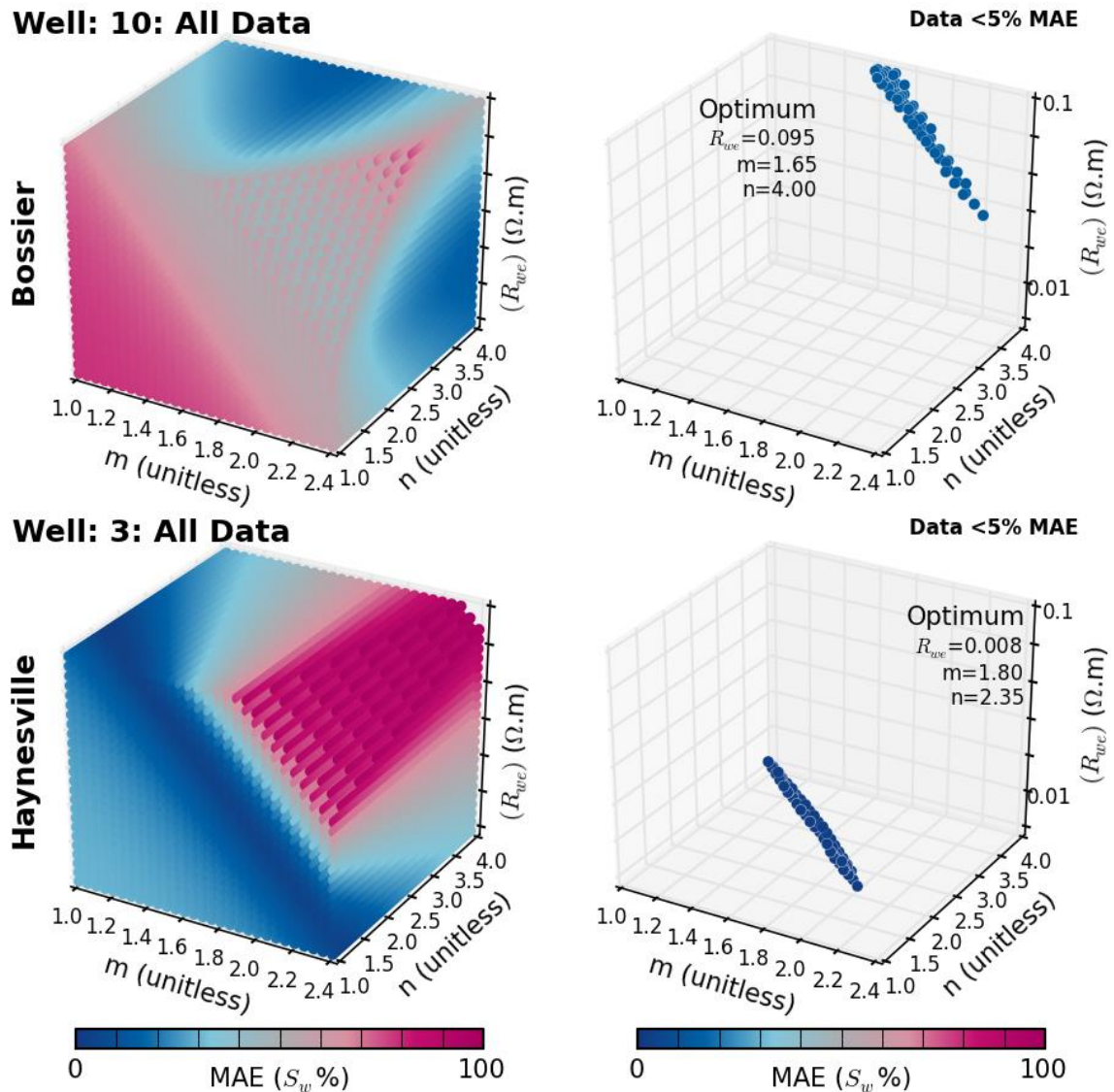


Figure 0.10. Sensitivity analysis (model W4)

MAE sensitivity plot for model W4: R_{we} vs. m and n for BSR (top) and HY (bottom) data. Plots Left: Parameter values for MAE $\leq 100\%$. Plots right: parameter values for the lowest 5% of MAE values.

Unlike well 10 however, HY well 3 is one of few wells where all of the generated parameters sit away from an upper or lower bound. Well 3 also has the best (least error) S_{wA} vs. S_{wC} correlation of any well. Though this may be linked to geological forcing, this cannot be confirmed, and it remains possible that R_{we} is only so low as to maximise the choice and selection of m and n .

The parameter relationships depicted in Figure 0.10 are summarised in Figure 0.11, which depicts parameter distributions for the lowest 5% of MAE values for each well in the BSR and HY. Here, with the exception of well 3 and 13, every well has at least one, often two, globally optimised parameters fixed at an upper or lower bound. The fixed

parameters are often minimum bound R_{we} or m or maximum bound n values, a feature coincident with an inclined parameter distribution.

Individual parameter distributions in Figure 0.10 are broadly similar to those described for model W3, though with some important distinctions. In model W3, m^* distributions for both formations are generally similar in form. Though where m^* is partitioned into individual optimised m and n parameters, it is clear that they each play a different role within the BSR and HY:

- In the BSR, which has relatively low gas saturations (Figure 4.5), m has a dominant role, exhibits a relatively normal distribution, and has optimal values which sit away from the parameter bound. This is coincident with n and R_{we} distributions that are generally inclined to their respective upper and lower bounds.
- In the HY, which has relatively high gas saturations (Figure 4.5), n has a dominant role, exhibits a relatively normal distribution, and has optimal values which sit away from the parameter bounds. This is coincident with m and R_{we} distributions that are generally inclined to their respective lower bounds.

The sensitivity analysis also highlights the impact of changing parameter bounds on the generated parameters. For instance, in Figure 4.7, model W4 optimised parameters were limited to conceptual upper and lower bounds (m and $n=1.5-2.5$) and appear reliant on modifying R_{we} values with m and n often fixed at their minimum and maximum respective bounds. Here, with m and n parameter bounds expanded to between 1 and 4, HY optimisation appears reliant on modifying n , showing little consistency between the two sets of optimised parameters.

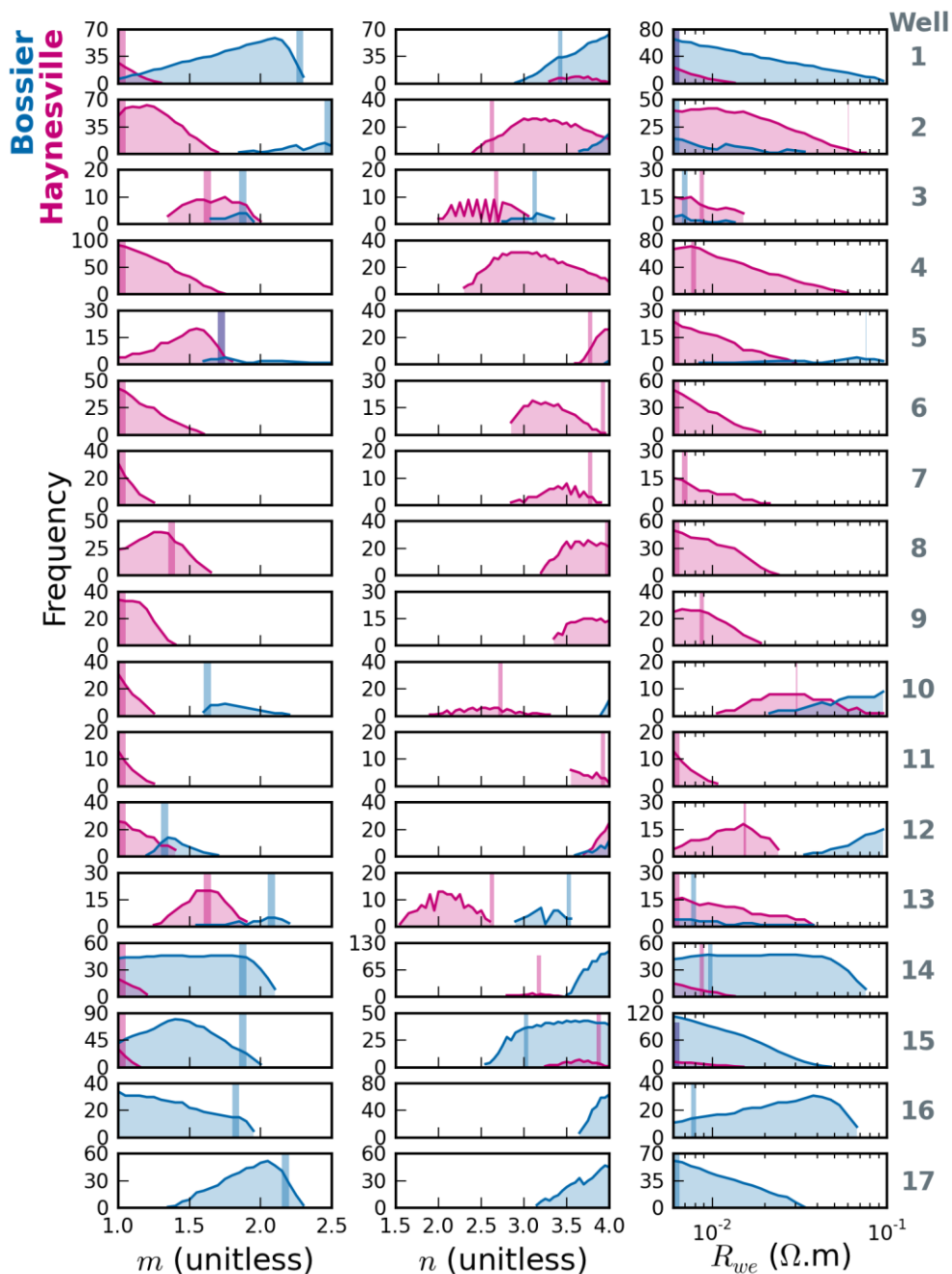


Figure 0.11. Parameter distributions, sensitivity analysis (model W4)

Plot of Haynesville model W4 parameter distributions for the lowest 5% of MAE values. Only parameter combinations which yield MAE values \leq (optimum MAE + (optimum MAE*0.05)). The faded red (HY) and blue (BSR) bars indicate the optimal parameter value for each well.

Furthermore, sensitivity data for model W3 demonstrate a clear tendency for R_{we} values to be manipulated so as to achieve a greater flexibility in m^* selection. Model W4 shows similar though more varied evidence of parameter manipulation, which, without a much improved understanding of the pore network and fluid salinity conditions, cannot be dissociated from the optimisation process. As a result, 3D optimised parameters offer limited prospect of accurate geological interpretation.

4.6.2 Parameter trade-offs

The parameter trade-offs in model W4 are illustrated in Figure 0.12 using equation 4.8 at $n=1$ (left) and $n=4$ (right) for a representative range of R_t , ϕ_{tc} and S_{wc} variables across the parameter range for m and R_{we} . This confirms prior observations that higher n values decrease the sensitivity of m and R_{we} , but also reveals a reduction in the sensitivity of all other input variables (R_t and BVW). It is therefore preferable for any optimised solution to favour higher n values and a reduced sensitivity and an increase in the possible range of other equation inputs.

Derived using: $R_{we} = R_t \cdot \phi_t^m \cdot S_w^n$

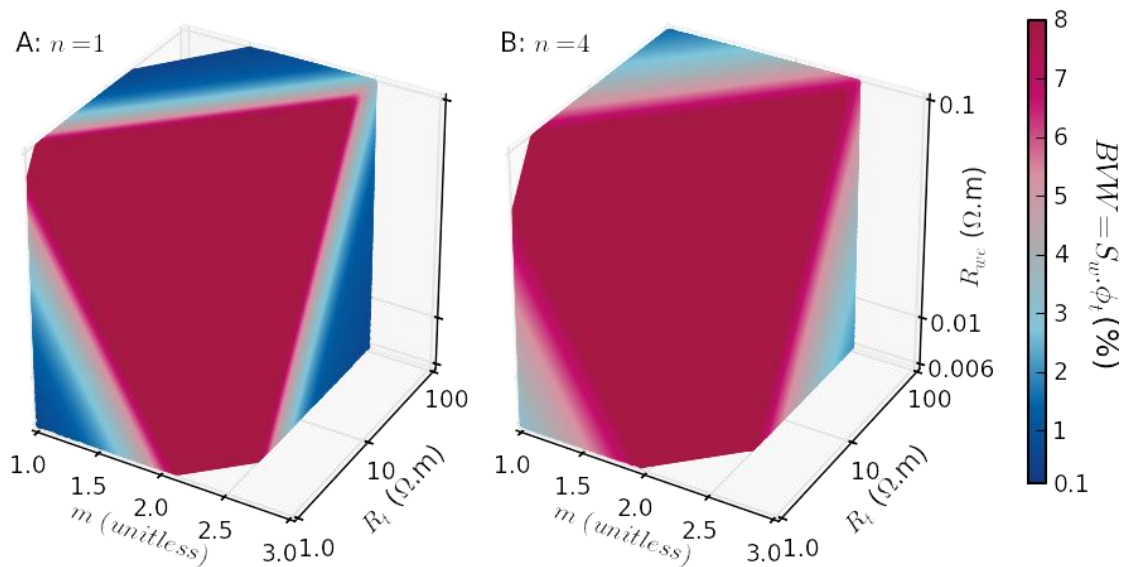


Figure 0.12. Parameter trade-offs (model W4)

Calculated R_{we} at $n=1$ (left) and $n=4$ (right) for a range of m , R_{we} , ϕ_{tc} and R_t values.

The relationship between model W4 optimised parameters and the parameter trade-offs are illustrated in Figure 0.13 for the BSR and in Figure 0.14 for the HY. In the BSR, the optimised parameters (all with n values of 2.5) sit on a plane. This is made clear on the rotated insert, with all points plotting on a plane equivalent to a near constant BVW of 3% (Figure 0.13).

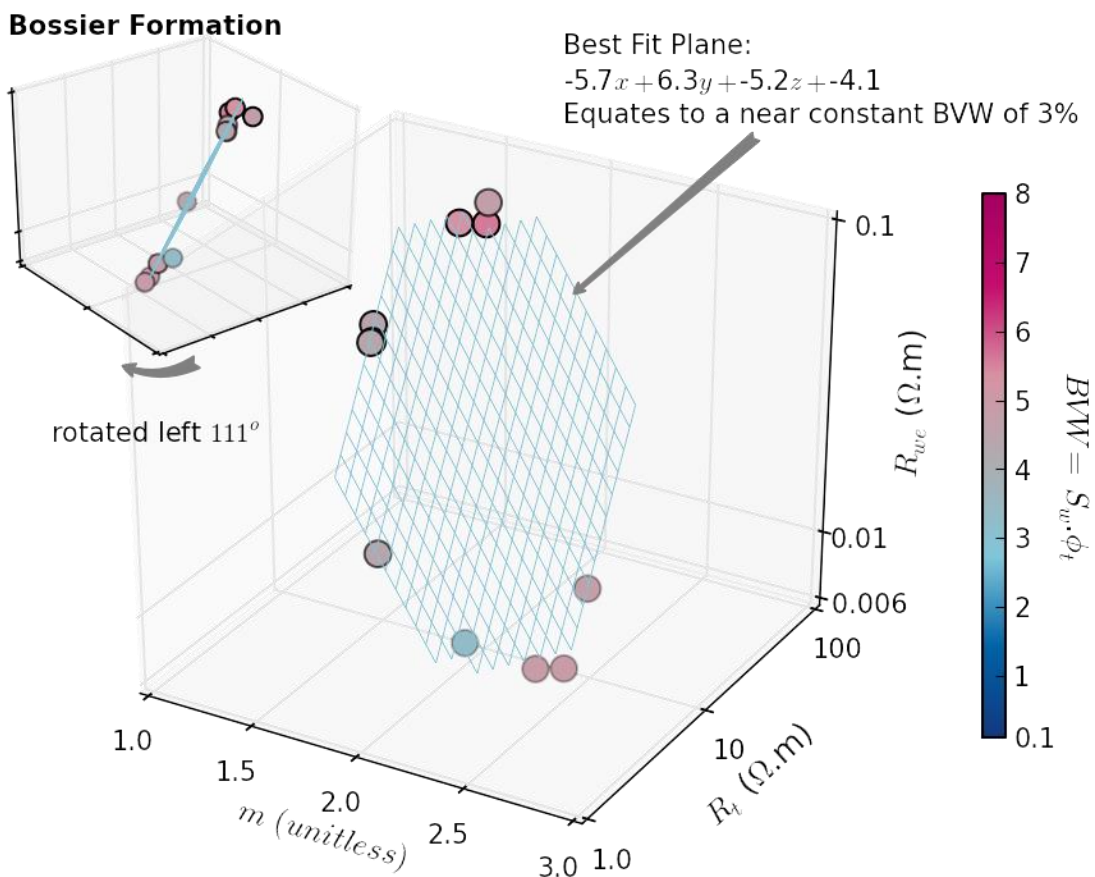


Figure 0.13. Optimised BSR parameters (model W4)

Model W4 optimised parameters and mean R_t and BVW values for all wells.

Similarly, the HY (Figure 0.14) optimised parameters also fit a plane highlighted by the rotated insert. This plane also indicates a near constant BVW of 1%, though not all HY wells optimise to $n=2.5$ (highlighted in red).

Haynesville Formation

Best Fit Plane:

$$-5.4x + 7.6y + -9.1z + -17.$$

Equates to a near constant BVW of ~1%

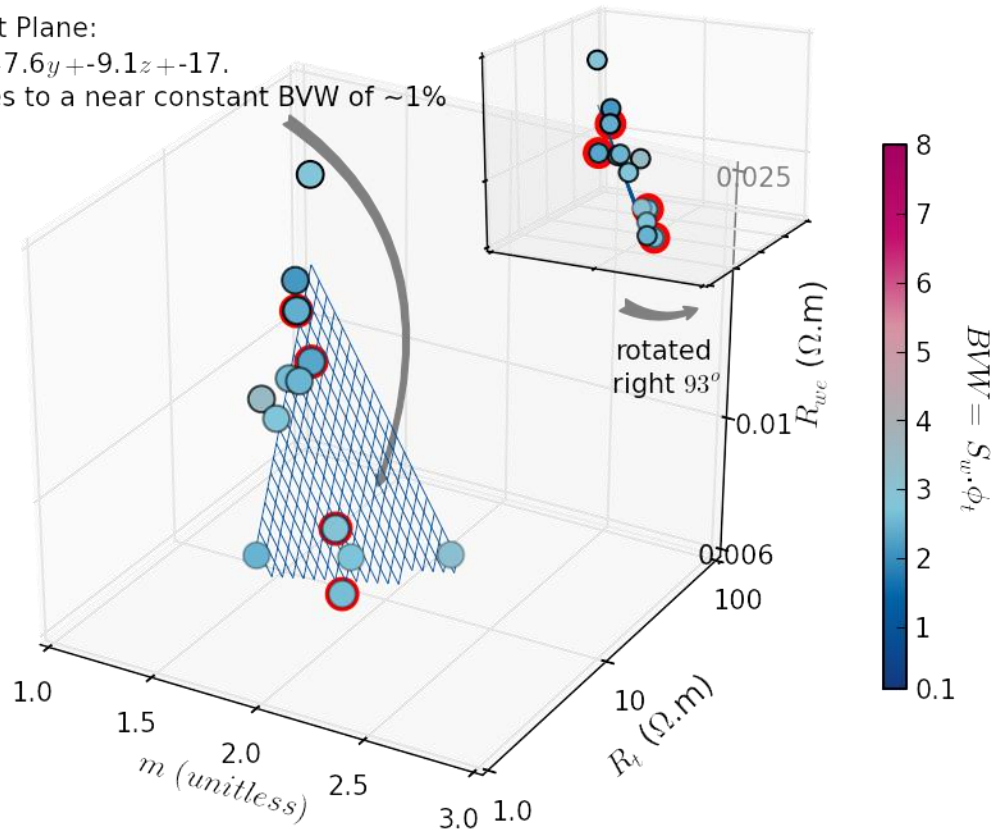


Figure 0.14. Optimised Haynesville parameters (model W4)

Model W4 optimised parameters and mean R_t and BVW values for all wells.

As with observations for models W2 and W3, the optimised W4 parameters are consistent in fitting to a specific BVW plane with limited movement across the BVW range. This combined with a good linear relationship with R_t , again suggests that pore water volume (BVW) is of secondary importance in forcing parameter selection. For the volume of fluid to have reduced importance, then either the fluid salinity or electrical properties must be highly variable, or other geological factors must be influencing R_t .

4.6.3 Core sample parameter modelling

R_{we} , m and n parameters were modelled with a parameter grid spacing of 0.05 using the same method outlined for model W3. The optimum parameter combinations generated are displayed in Figure 0.15 with marker colour controlled by n (y axis), so as to help judge depth within each 3D plot. For both the BSR and HY, no clear links could

be established between the generated parameters and wider formation mineralogical/petrophysical properties.

Both 3D scatter plots in Figure 0.15 are orientated 'edge on' to a plane defined by the optimum parameters. For the BSR, this plane is weakly defined by data with near uniform distributions, though there is a slight increase in the frequency of high n values linked to a decrease in m , with R_{we} remaining more or less uniform. By contrast, the HY occupies a distinctive plane in parameter space, with a distinct increase in the frequency of low R_{we} and m values, and n values that remain relatively uniform. These results support previous observations that the HY has a more constrained range of optimal Archie parameters than the BSR. Furthermore, the lack of defined parameter distributions in both formations combined with unreasonably oil wet (high n) or low salinity (high R_{we}) suggests that the generated parameters are 'not' geologically representative, and it was not possible to link observed parameters with wider geological/petrophysical data.

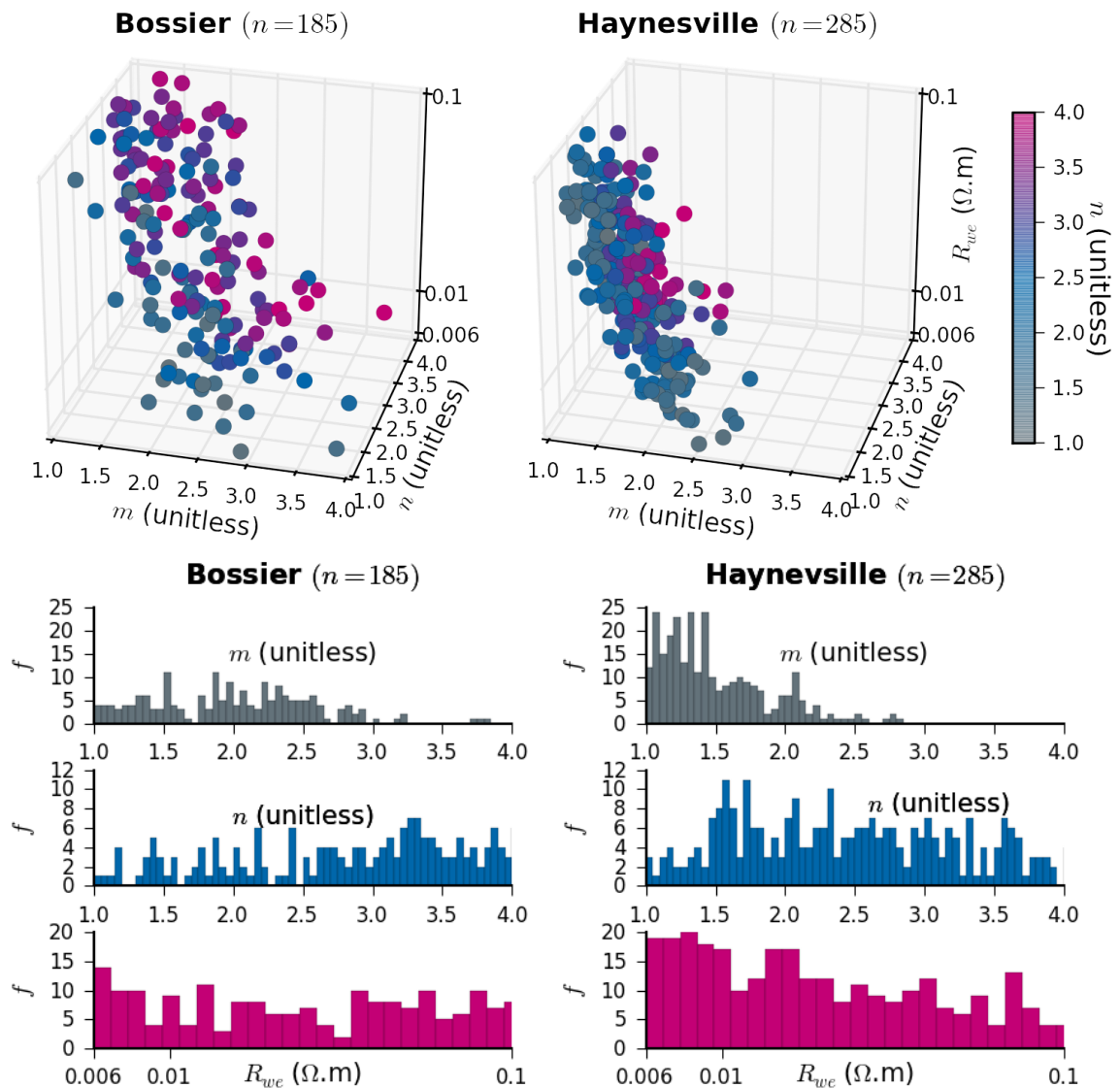


Figure 0.15. Individual core sample optimised parameters (model W4)

Grid search optimised R_{we} , m and n parameters for the BSR (left) and HY (right). Parameter distributions are included.

As with model W3, numerous alternative parameter combinations exist within a 5% MAE margin of benchmark S_{WC} values. The parameter distributions within $\pm 5\%$ error are displayed in Figure 0.16.

The BSR in Figure 0.16 shows significant variation in m , with an increase in m values at higher BVW. In addition, the n value distributions are consistently sloped, indicating a larger number of viable S_{WA} solutions at higher n values. Whilst the R_{we} values remain near uniform for the majority of samples, but similar to n , also indicate an increase in the number of viable solutions at low R_{we} for some low BVW values. Both R_{we} and n fail to define probabilistic parameter value ranges, representing solely least MAE solutions

with limited geological merit. By contrast the wide variations in m , which are significantly more variable than those observed for the HY, are analogous to variations observed for m^* in models W2 and W3 and may be linked to a greater degree of formation heterogeneity in BSR data.

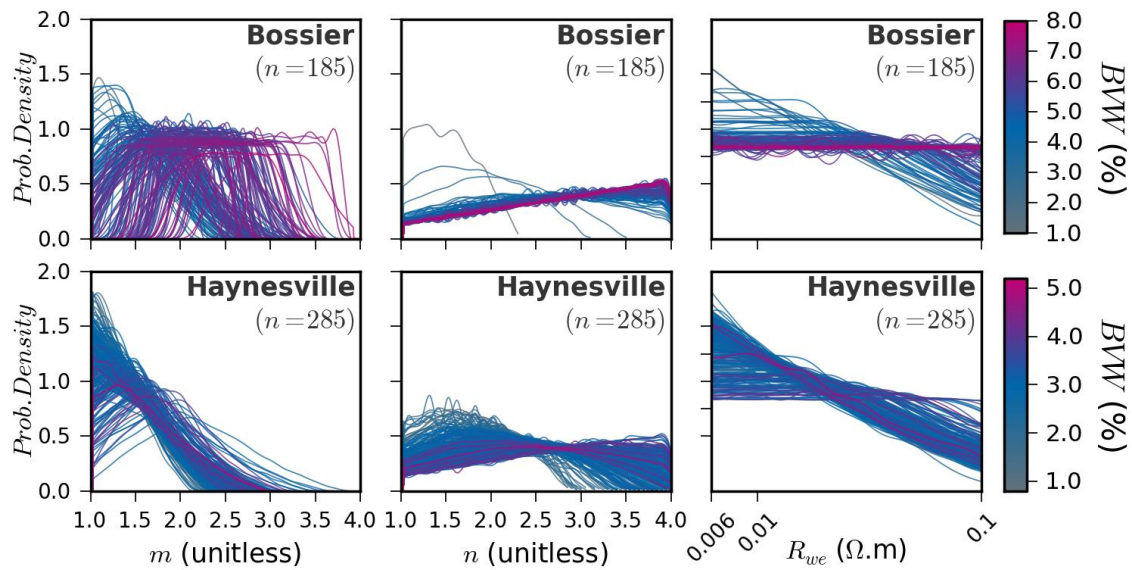


Figure 0.16. Optimised parameter distributions for S_{wa} within +/-5% of S_{wc} (model W4)

Grid search optimised R_{we} and m and n parameter distributions for S_{wa} estimates within +/- 5% of benchmark S_{wc} values for the BSR (top) and HY (bottom). Line colour is a function of sample BVW .

The parameter distributions generated for the HY differ significantly from those described for the BSR. Firstly, similar to m^* in model W3 and W2, m is consistently constrained to a relatively low value range. Secondly, there is significantly more character in n distributions which can be linked to BVW , i.e. higher BVW links to higher n values and vice a versa. Thirdly, though R_{we} distributions are broadly similar to those for the BSR, there is no apparent link to BVW .

These results are summarised in Figure 0.17 by totalling the frequency in occurrence of each parameter for each formation. Taken into consideration with Figure 0.16, this has a number of implications:

- a) the contrast in m parameter distributions may be representative of greater heterogeneity in formation petrophysical properties in the BSR as opposed to the HY,

- b) for the BSR, porosity and m is far more significant in controlling Archie's equation than formation fluid/pore wall interactions and n .
- c) for the HY, which has a far lower BVW range and a higher gas filled porosity, it suggests that formation fluid/pore wall interactions and hence n is a more significant factor in Archie's equation.
- d) for both formations, data generated for R_{we} provides little information that can be placed within a geological context, revealing only that lower values carry an increased chance of a low MAE solution.

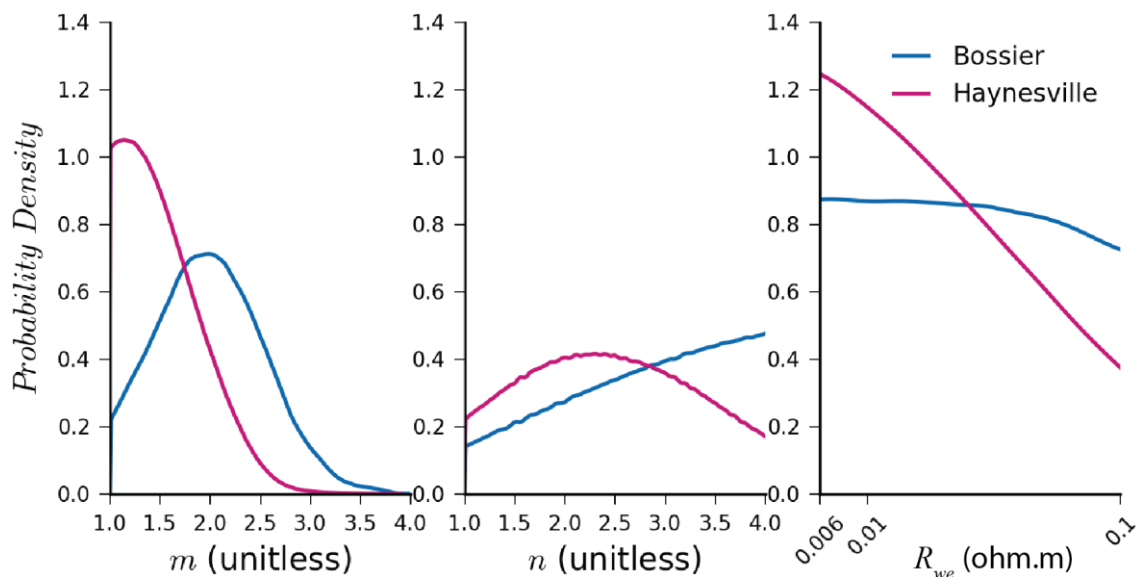


Figure 0.17. Totalled parameter distributions for S_{wA} estimates within $\pm 5\%$ of S_{wC} (model W4)
Grid search optimised R_{we} and m and n parameter distributions for S_{wA} estimates within $\pm 5\%$ of benchmark S_{wC} values for the BSR (top) and HY (bottom). Line colour is a function of sample BVW .

4.6.4 Summary

4.6.4.1 Sensitivity analysis

- In the BSR, n is routinely maximised and R_{we} minimised so as to reduce the sensitivity and increase the range in possible m values. This allows for a least MAE solution, but at the likely expense of an increase in model error (Figure 0.11).
- In the BSR, n is routinely maximised and R_{we} minimised so as to reduce the sensitivity and increase the range in possible m values. This allows for a least

MAE solution, but at the likely expense of an increase in model error (Figure 0.11).

4.6.4.2 Parameter trade-offs

- Analysis indicates, similar to the 1D and 2D models, a linear relationship between the optimised parameters and R_t , suggesting that *BVW* is of limited importance in forcing parameter selection (Figure 0.12).

4.6.4.3 Parameter modelling

- Similar to model W3, it is notable that parameter distributions in the BSR are notably more constrained than in the HY.
- m and n parameters are shown to have different roles in the BSR and HY (Figure 0.16 and Figure 0.17):
 - The BSR, which generally has low gas saturations and high V_{Clay} and CBW volume, demonstrates inclined uniform n distribution and appears reliant on optimising m .
 - The HY, which has relatively high gas saturations, has very low m values and distributions and appears reliant on optimising n .

Chapter 5

Unconventional applications of Archie's equation: does geology matter?

This chapter incorporates the results of the error analysis in Chapter 4 with log and core geological/petrophysical data presented in Chapter 3. This aims to provide a geological interpretation and rationale for optimised Archie parameters and associated petrophysical and mineralogical relationships and is broadly divided into four sections:

- 5.1 *Formation heterogeneity*: explores the links between mineralogical and petrophysical heterogeneity, and effects on optimiser model and Archie parameter outputs.
- 5.2 *BVW, R_t and V_{clay} relationships*: these relationships are explored and a model accounting for their behaviour proposed.
- 5.3 *Composite core data summary*: key core data are presented, highlighting mineralogical / petrophysical trends linked to variations in formation fabric.
- 5.4 *Predicted pseudo-Archie parameters*: the range and behaviour of predicted Archie parameters are discussed and compared with values reported in the literature.

5.1 Introduction

Following Archie's seminal 1942 paper, the terms 'Archie rock', 'Archie like' or 'non-Archie' (Herrick and Kennedy, 1996) have come to prominent use as describing 'clean' (clay free) formations with regular pore geometries described by petrophysical constants within Archie's equation. Nevertheless, though the BSR and HY might be considered to fail in meeting this 'clean' criterion (Glorioso and Rattia, 2012; Worthington, 2011b), results (Chapter 4) indicate that a modified Archie equation can work satisfactorily in some wells, particularly in the HY, despite significant mineralogical/petrophysical complexity. Understanding the geological controls on the accuracy and validity of Archie-based methods for a given shale gas prospect is therefore critical to the informed use of existing resistivity based methods and for the development of novel saturation modelling techniques.

5.2 Formation heterogeneity

The analysis of multiple optimisation models (sections 4.3 to 6.9) indicate that their residual *MAEs*, generated parameters and parameter sensitivities, are consistently more heterogeneous in the BSR than in the HY. The term heterogeneity is used here synonymously with variability, and variability in model outputs must be linked to the heterogeneity and inter-relationships of the petrophysical inputs (ϕ_{tC} , R_t , S_{wC}). In turn, the petrophysical inputs express the interaction and distribution of formation mineralogy and fluid components as determined by depositional and diagenetic processes. This section aims to link the separation of BSR and HY results to wider underlying formation geological properties as represented within the log and core data discussed in Chapter 3.

5.2.1 Heterogeneity in optimiser model response

Residual *MAEs* for the HY wells are both consistently low and of limited variability when compared to those for the BSR. This is depicted in Figure 4.4 and Figure 4.6 and summarised in Table 7.1, where the substantially higher range and variability in BSR *MAE* suggests that optimised Archie parameter constants are less able to characterise a wider range in BSR core sample characteristics. This is supported by the large reduction in mean BSR *MAE* between optimiser model H1 to W1 (Figure 4.6, Table 7.1), equivalent to a relative reduction in *MAE* of 31%. This constitutes the single largest decrease in *MAE* between optimiser models in the BSR and is accompanied by an increase in the number of optimised sample populations from one in H1 to 11 in W1. In other words, the largest reduction in *MAE* for the BSR is attained in considering it as a heterogeneous as opposed to homogenous petrophysical system. By contrast, reductions in mean *MAE* in the HY between H1 to W1 are slight, and equivalent to a relative reduction in *MAE* of 3%. In other words, the HY is not particularly sensitive to changes in the style of sample binning and can be adequately represented as an homogenous petrophysical system. This assertion is supported by Popielski et al., (2012), whose study of rock typing using k-means cluster analysis of conventional well

data suggested a 'vertically-homogenous Haynesville Formation' in their study well, which corresponded with low variability in petrophysical log and core properties (R_t , ρ_b , ϕ_n , S_{wc} , TOC , and ϕ_{tc}).

MAE (S_w %)	H1	W1	W2	W3	W4
BSR	17.64 ± 7.92	12.15 ± 6.62	11.31 ± 5.56	10.84 ± 5.44	10.14 ± 5.32
HY	5.59 ± 2.40	5.42 ± 1.28	5.37 ± 1.40	5.19 ± 1.25	4.66 ± 1.03

Table 7.1: Mean residual MAE per optimisation model (Figure 4.4)

Mean MAE taken as the mean of the residual MAE per Well (Figure 4.4) ± the average standard deviation in residual MAE.

Contrasts in the heterogeneity of residual MAE between the BSR and HY are mirrored by similar differences in modelled parameter sensitivity. Figure 4.9 (models W1 and W2) is a good example, where the sensitivity of MAE to changes in R_{we} and m^* is on average 30% lower and more variable in the BSR than in the HY, which displays very tight and consistent sensitivity curves. In addition, the optimised BSR parameters occupy a wider more variable m^* range (2.175±0.233) compared to more constrained HY m^* values (1.822±0.089). This trend is again emphasised for modelled core sample parameters, and is succinctly displayed in Figure 0.9 for model W3. Where the probability distribution in BSR m^* values is significantly wider than that for the HY data, equating to mean core modelled m^* values of 2.187±0.441 for the BSR and $m^*=1.735±0.273$ for the HY. It should be noted that generated core parameters are displayed to three decimal places to avoid rounding.

5.2.2 Heterogeneity in mineralogical / petrophysical properties

The mineralogical/petrophysical log and core data for the BSR and HY are characterised in Chapter 3. This includes plots of variable distributions highlighting key descriptive statistics, but does not explicitly attempt to categorise one formation as being petrophysically or mineralogically more heterogeneous than the other. This is in part because there is no universally accepted measure of variability that allows for direct comparison of variables with multiple parent units and underlying normal, log-normal and non-normal distributions. For example, σ provides a measure of the dispersion about the mean (μ), and is therefore ideally suited to normal or log-normal

distributions. For skewed distributions, where the mean may be influenced by extreme values, the interquartile range ($IQR=Q_3-Q_1$) may be a more suitable measure of variability. Other measures of variability such as median or mean absolute deviation (MAD), or normalised measures of error such as the co-efficient of variation ($CV=(\sigma/u)*100$) are equally dependant on assumptions regarding the underlying variable distribution. It is however, not the intention of this section to present a detailed review of the statistical measures of variability/heterogeneity, only to emphasise that it is a nontrivial and sometimes inexact process which should not be dissociated from the underlying distribution. With this in mind, a comparison of variability calculated simply as σ and IQR is presented for principal mineralogical/petrophysical components in Figure 7.1, though the reader is encouraged to refer back to the variable distributions presented in Chapter 3.

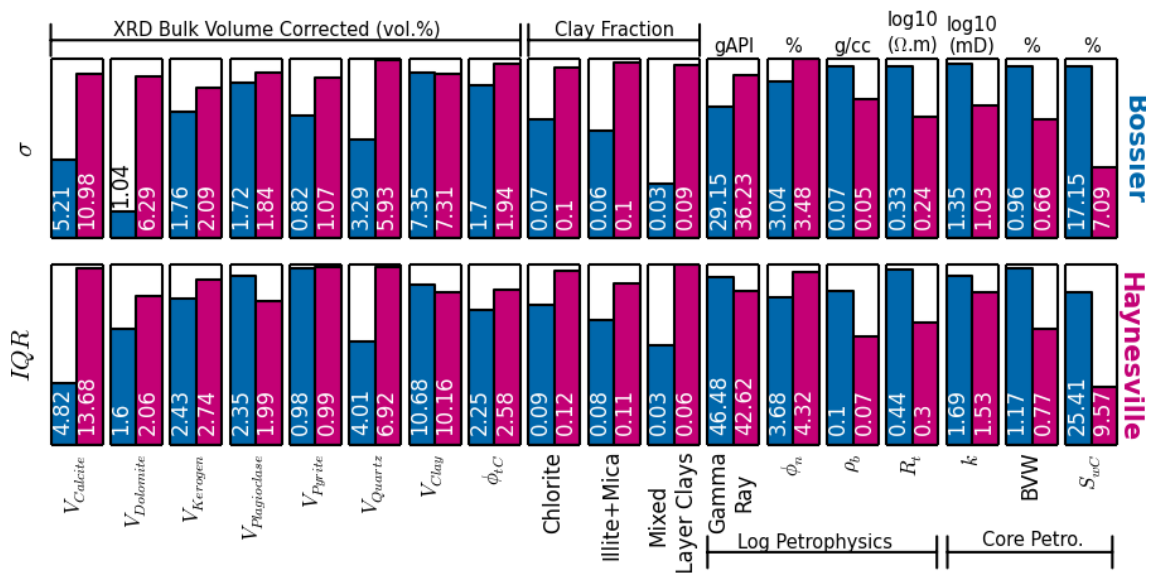


Figure 7.1. Comparison of mineralogical / petrophysical variability

σ (standard deviation) and IQR (interquartile range) calculated for bulk volume corrected XRD volumes and petrophysical log and core data.

Both measures of variability displayed in Figure 7.1 are in general agreement, though there are some variations, most notably for GR and $V_{Dolomite}$ and $V_{Plagioclase}$. In general however, two broad trends are evident: a) the HY is mineralogically more heterogeneous than the BSR, particularly with regard to $V_{Calcite}$, $V_{Dolomite}$ and V_{Quartz} , and b) the BSR is petrophysically more heterogeneous than the HY, with the exception of ϕ_{tC} , GR and ϕ_n .

Of the three principal input parameters (R_t , S_{wC} , and ϕ_{tC}) in an optimised Archie model, R_t , S_{wC} (and therefore BVW) are significantly more heterogeneous in the BSR. It therefore follows that the optimiser response (residual MAE , generated parameters and parameter sensitivities) should mirror this heterogeneity. In plotting mean residual MAE vs. σ for each of the three principal variables R_t , S_{wC} , and ϕ_{tC} , it is possible to further define which of the three variable inputs is most influential in determining the degree of variation and magnitude in MAE (Figure 7.2). Figure 7.2 indicates that as much as 94% of the variation in BSR residual MAE can be attributed to variability in formation resistivity, with little impact from S_{wC} and even less from ϕ_{tC} . This is supported by Wu and Aguilera (2012) who also suggest that saturation estimates are more sensitive to R_t than ϕ_{tC} . In contrast, HY residual MAE (model W4) is only weakly linked to R_t , with variability in S_{wC} and ϕ_{tC} playing a greater role in determining MAE . In other words, heterogeneity in BSR R_t , which is paradoxically not clearly linked to either porosity or saturation (i.e. ϕ_{tC} and/or S_{wC} often increase at higher resistivities), accounts for the observed variation in residual MAE and thus selected parameters and their sensitivity. For the HY, which exhibits low residual MAE s of limited variability, the source of error cannot be attributed to one, but a combination of all three inputs.

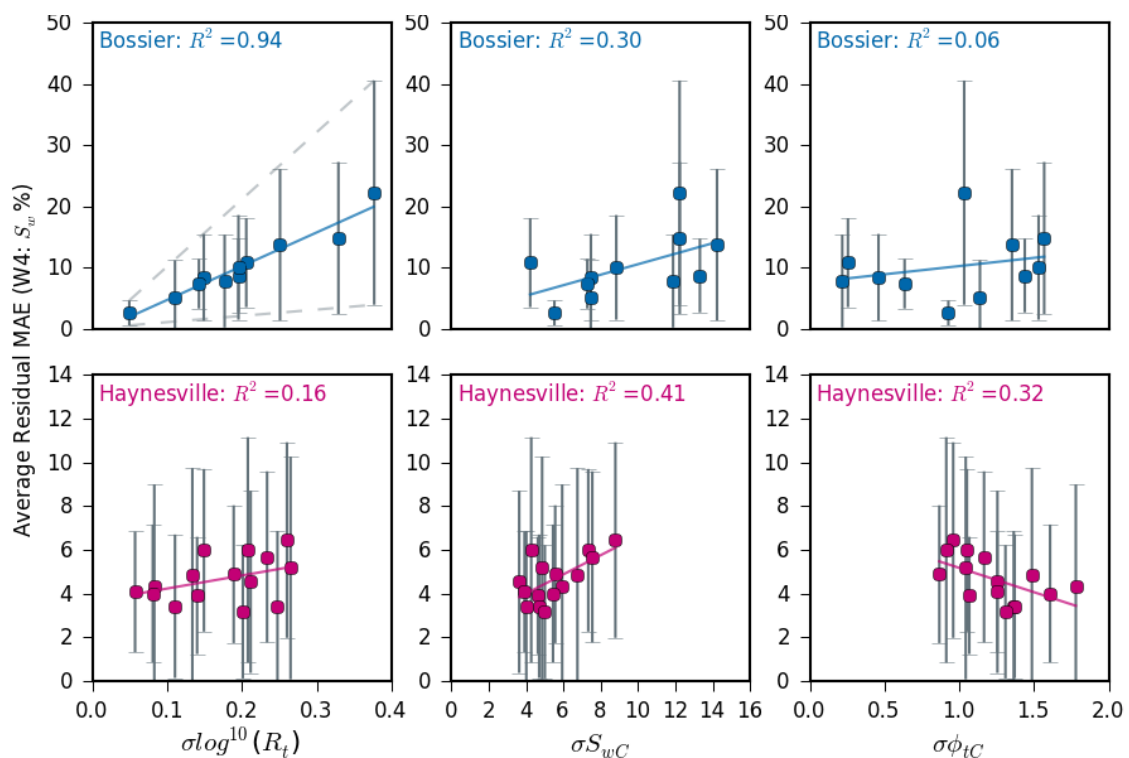


Figure 7.2. Average residual MAE (model W4) vs. key petrophysical inputs

Average residual MAE for each well vs. σ (standard deviation) in: R_t (left), S_{wC} (middle) and ϕ_{tC} (right). Average taken as the sample mean, limited difference found between median and mean MAE values.

The observation that R_t is the primary variable controlling error and the generated Archie parameters is supported by the results of the parameter trade-offs for models W1 to W4 (Figure 4.10, Figure 4.11, Figure 0.6, Figure 0.12), where, for each model, the predicted Archie parameters for the BSR increase linearly with R_t , with limited deviation attributable to BVW ($S_{wc} * \phi_{tc}$). By contrast parameter trade-offs analysed for the HY, show that parameters are selected in response to both R_t and BVW (Figure 7.2).

5.2.3 Mineralogical controls on petrophysical heterogeneity

That variability in mineralogical composition does not coincide with petrophysical heterogeneity (Figure 7.1) is not surprising. Complex textural effects, variations in mineral distributions and other factors (e.g. depositional style and environment) are likely to play a significant role in determining petrophysical variability in mudstones. Whilst there are undoubtedly multivariate textural/mineralogical relationships controlling the petrophysical properties, a significant portion of the observed variability can be linked to the presence and effects of clay minerals (see section 2.3.3.1). This is supported in comparing XRD mineral volumes with petrophysical properties, where V_{clay} consistently stands out as displaying heteroskedastic tendencies (heteroskedasticity refers to a systematic inconsistency in variance, where variance is not homogenous (Schwartzman, 1994)). An example is given as R_t vs. V_{clay} in Figure 7.3, where σR_t increases with increasing V_{clay} in the BSR. In other words, heterogeneity in R_t increases in core samples with higher V_{clay} .

That elevated R_t and/or σR_t should be linked to increased V_{clay} contradicts the long held consensus that clay effects typically act to reduce resistivity, or inversely, provide a source of excess conductivity (Hill and Milburn, 1956; Patnode and Wyllie, 1950; Winsauer and McCardell, 1953; Wyllie and Southwick, 1954). This relationship is absent in the HY (Figure 7.3), where there is no consistent relationship between R_t and V_{clay} .

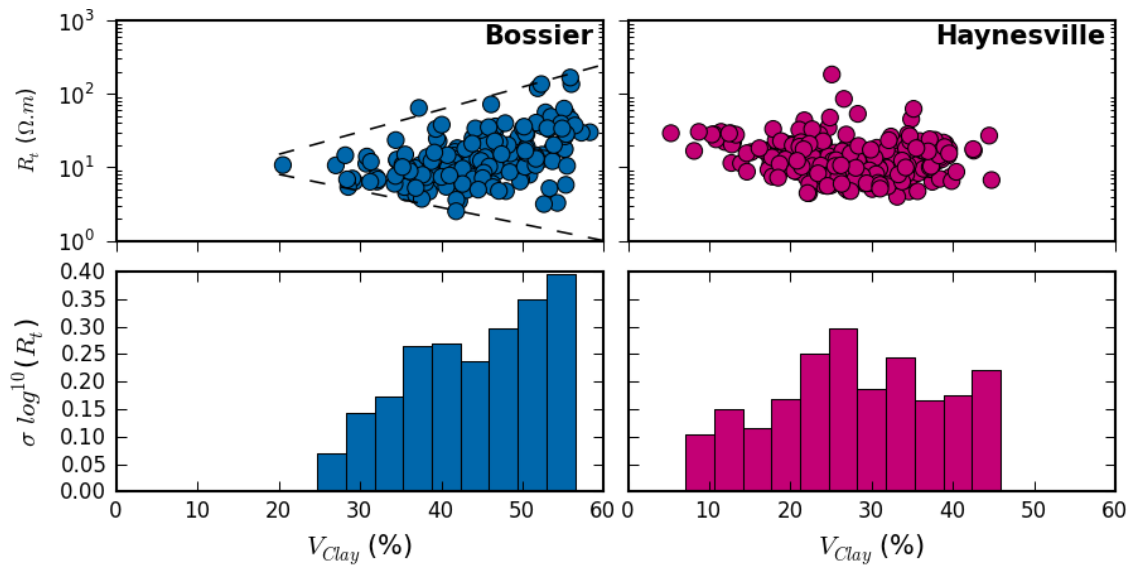


Figure 7.3. R_t vs. V_{clay} and heteroskedasity

R_t vs. V_{clay} cross-plots (top) for the BSR and HY coupled with bar charts of the $\sigma \log^{10}(R_t)$ for binned V_{clay} intervals (bottom).

It is notable however, that in combining HY and BSR data (Figure 7.4) a continuum is formed where R_t is shown to initially decline to a V_{clay} of $\sim 28\%$, and then increases with σR_t . This observation can be linked to clay mineralogy for which the following trends are noted:

- the chlorite fraction increases with increases in R_t and variability in R_t (σR_t) in the BSR,
- high variability in the chlorite fraction coincides with high σR_t in the HY,
- the illite+mica fraction increases at higher V_{clay} in parallel with increased σR_t ,
- the mixed-layer clay fraction shows little variability in the BSR, but significant variability in the HY where σR_t is more pronounced,

Taken together, the mixed-layer clays appear to have the least impact and the chlorite fraction the most impact on σR_t , with the illite+mica fraction (the dominant clay type) sitting somewhere in between. Significant control over electrical character can therefore be linked to the chlorite fraction or variations in other structural/mineralogical components concurrent with higher chlorite volumes.

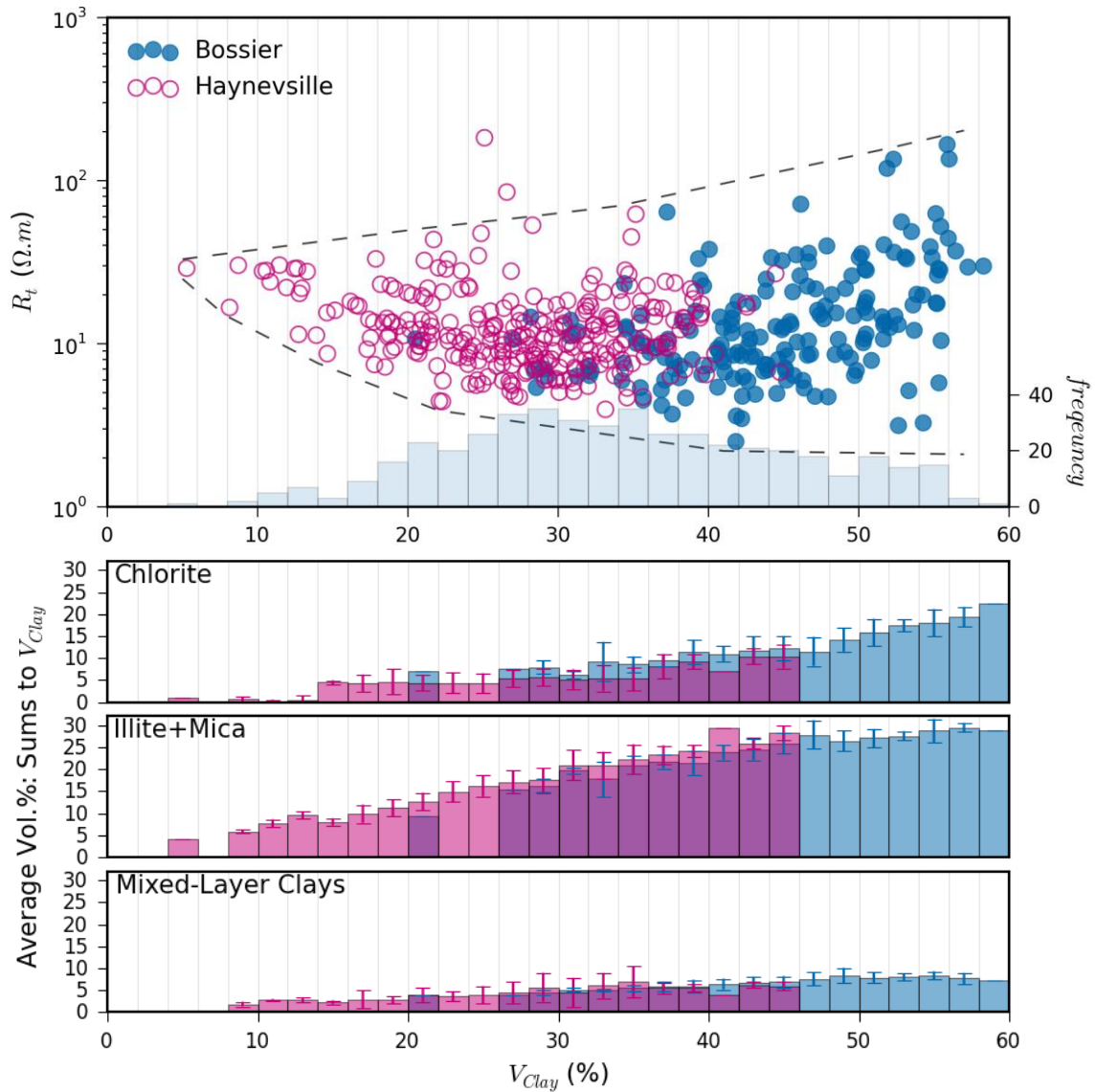


Figure 7.4. R_t vs. V_{Clay} and clay fractions

R_t vs. V_{Clay} cross-plot (top) for the combined BSR and HY data with integrated histogram. V_{Clay} represents the total of the chlorite, illite+mica and mixed-layer clay volumes, given here as a fraction of V_{Clay} which sum to 1 for every 2% V_{Clay} interval. Y axis error bars are a function of the standard deviation.

Just as an increase in V_{Clay} can be shown to coincide with an increase in σR_t , similar heteroskedastic relationships are noted in the BSR for V_{Clay} vs. σk (Figure 7.5) and fluid distribution (S_{wC} and ϕ_{tC}) in Figure 7.6. For k , elevated V_{Clay} is associated with an increase in σk at low matrix permeabilities. For S_{wC} and ϕ_{tC} , it is evident that high V_{Clay} is generally associated with low ϕ_{tC} and high S_{wC} and that $\sigma \phi_{tC}$ increases with decreases in V_{Clay} . Or put another way, σS_{wC} increases at higher porosities coincident with a decrease in V_{Clay} . Despite relatively high clay volumes (average = 44%), no such relationships are however observed in the HY.

These observations have the following implications:

- i. that V_{Clay} plays a dominant role in controlling fluid distribution and poro-perm relationships, and their respective heterogeneities in the BSR,
- ii. that the wide variability in k or R_t at a given high V_{Clay} value in the BSR, necessitates either a highly variable fluid chemistry or a difference in texture / grain partitioning and thus a potentially observable litho-facies distinction.
- iii. that clay minerals play a reduced role in controlling fluid distributions in the HY,
- iv. that V_{Clay} has a consistently limited impact on petrophysical variability in the HY suggests either a) homogeneity in clay distribution and/or pore fluid chemistry, or b) that clay volumes of below 28% are insufficiently high to dominate formation petrophysical properties.

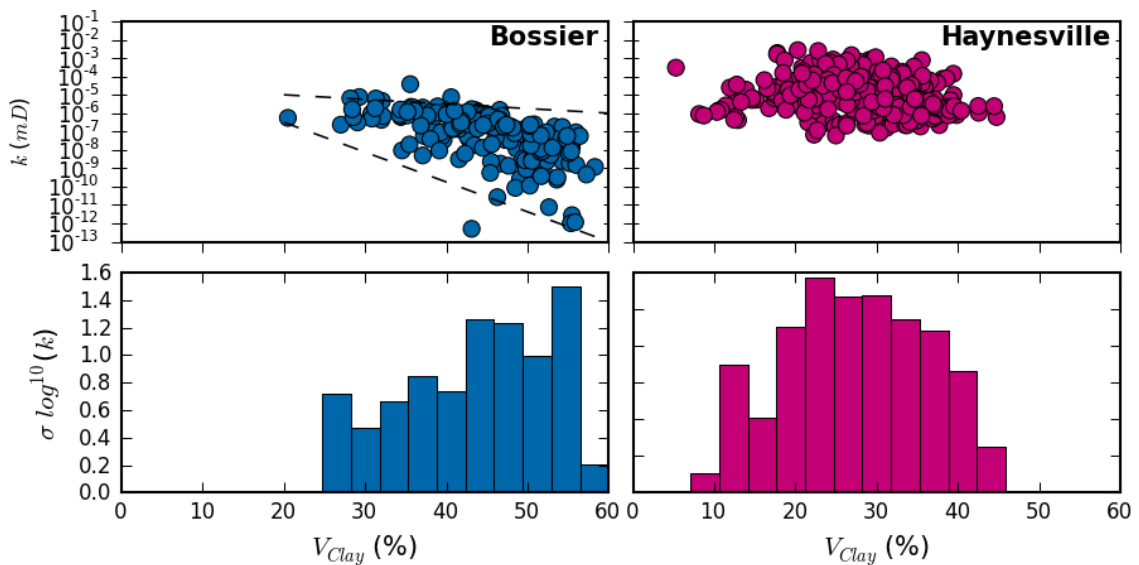


Figure 7.5. k vs. V_{Clay} and heteroskedasticity

k vs. V_{Clay} cross-plots (top) for the BSR and HY coupled with bar charts of the $\sigma \log^{10}(k)$ for binned V_{Clay} intervals (bottom).

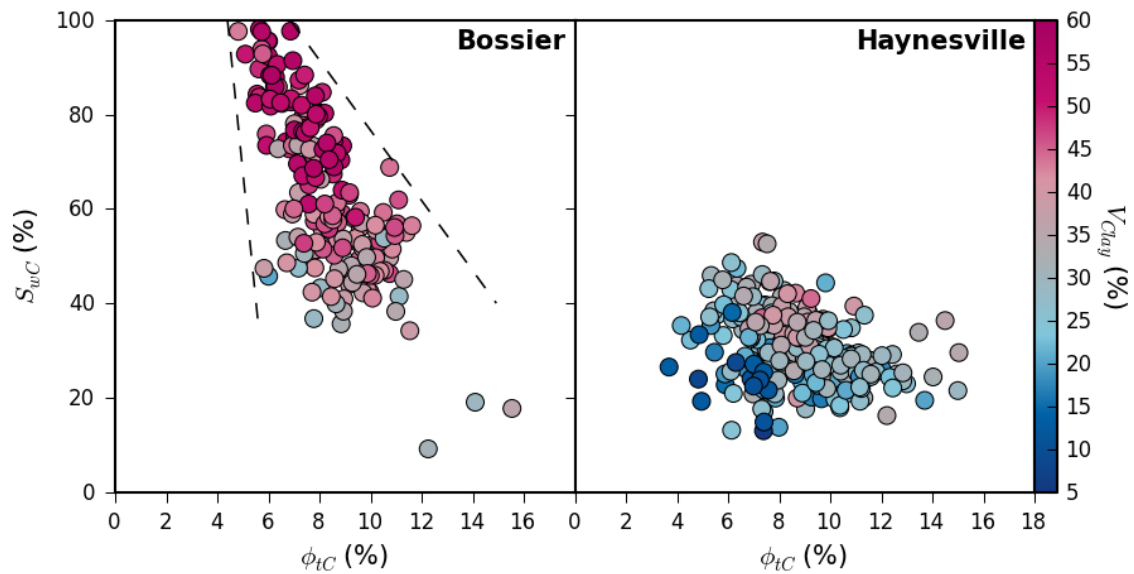


Figure 7.6. S_{wc} vs. ϕ_{tc}

S_{wc} vs. ϕ_{tc} cross-plots for the BSR (left) and HY (right), markers coloured by V_{clay} .

5.2.4 Summary and conclusions

- Though mineralogically heterogeneous, the HY is relatively homogenous petrophysically, resulting in low, well constrained residual MAE and well constrained Archie generated parameters and sensitivities.
- The BSR is homogenous mineralogically when compared to the HY, but is petrophysically heterogeneous.
- Elevated V_{clay} and in particular the chlorite clay fraction are associated with increased variability in R_t in the BSR.
- The role of clay minerals, their interaction with formation pore space and their influence over formation electrical properties varies significantly between the BSR and HY.
- Despite highly variable fluid distribution characteristics (BVW and S_{wc}) it is variability in R_t which is principally responsible for determining heterogeneity in MAE . As a consequence, generated Archie parameters for the BSR have a positive linear relationship with average R_t for all optimisation models considered. Thus, for porosity-fluid relationships to be the primary mechanism determining formation electrical properties, then R_{we} , m and n parameters are required to be extremely variable. Or, additional mineral or other textural

relationships must contribute to electrical characteristics, undermining and limiting the use of traditional Archie approaches to saturation modelling.

The relationships underlying the disparity in BSR-HY petrophysical heterogeneity and its links to error in S_w estimation are explored in the following section.

5.3 Water, resistivity and clay relationships

The negative relationship between the volume of the saturating electrolyte (BVW) and formation resistivity (Archie, 1942) is the principal petrophysical mechanism underlying Archie's equation. In the presence of a saline pore fluid, clay minerals and their electrical properties are considered detrimental to this relationship by contributing 'excess conductivity,' which if not corrected for, may result in reservoir undervaluation (Hardwick, 1989). Despite well documented clay effects (Hamada et al., 2001; Worthington, 2000), the results of the error analysis (sections 4.3 to 6.9) and core data petrophysical relationships (Figure 7.4), repeatedly highlight an unexpected and positive co-dependency between BVW , V_{clay} and R_t (Figure 4.8, Figure 0.7), but with very different trends for the BSR and HY. In effect, contrary to providing 'excess conductivity,' high clay volumes are coincident with an 'excess resistivity' and an overestimation of reservoir potential (Figure 4.2). As a consequence, unlike 'low resistivity pay' reservoirs where clay effects often require a compensatory **decrease** in m and n parameter values (Durand et al., 2001), the BSR-HY core modelled (e.g. Figure 4.13 or Figure 0.7) and optimised (e.g. Figure 0.6) R_{we} , m or n parameters are required to **increase** so as to compensate for the anomalously high BVW and R_t . The following section aims to elucidate key core petrophysical relationships and attempts to rationalise these observations within a geological framework. This discussion is divided into three parts:

- i. A review of the key core petrophysical relationships, their links with clay mineralogy and impact on Archie based saturation models.
- ii. A brief review of literature documenting and attempting to account for the unusually high resistivities observed in the BSR.
- iii. A proposed mechanism that integrates mineralogical and petrophysical relationships with burial and diagenetic processes, that can both account for the unusually high resistivities and the trends in optimised Archie parameters.

5.3.1 Key core petrophysical relationships

Clay minerals, their grain size and grain shape, are key factors in defining fabric and form a primary control on pore size distribution, fluid flow and thus permeability (Dewhurst et al., 1999). In addition, pore lining clay minerals can contribute significant microporosity and are often associated with high water saturations (Hamada et al., 2001; Herrick and Kennedy, 1996). These relationships are clearly observed in the BSR (Figure 4.2, Figure 7.7 and Figure 7.8), with BSR core samples exhibiting a quintuple association of increasing V_{Clay} linked to high S_{wC} , BVW , and low ϕ_{tC} and K . In other words, BSR poro-perm relationships and fluid distribution appears to be linked to, or even controlled by V_{Clay} . By contrast, the HY displays an even distribution of V_{Clay} from low to high ϕ_{tC} (Figure 7.7), inferring that V_{Clay} has limited impact on fluid distribution, though it is still observed to negatively impact k (Figure 7.8).

The effects of clay minerals on fluid distribution and poro-perm relationships can in part be attributed to the chlorite clay fraction, where, if authigenic in origin, and occurring predominantly in the style of grain coatings or interstitial growths, is likely to impact ϕ_{tC} and k (Rushing et al., 2008). This assertion is supported by the negative impact of chlorite on K and ϕ_{tC} depicted in Figure 7.9. Where chlorite contributes to microporosity (hence the BSR has a similar ϕ_{tC} range to the HY) but acts to narrow the pore-throats resulting in a lower k range (Figure 7.9).

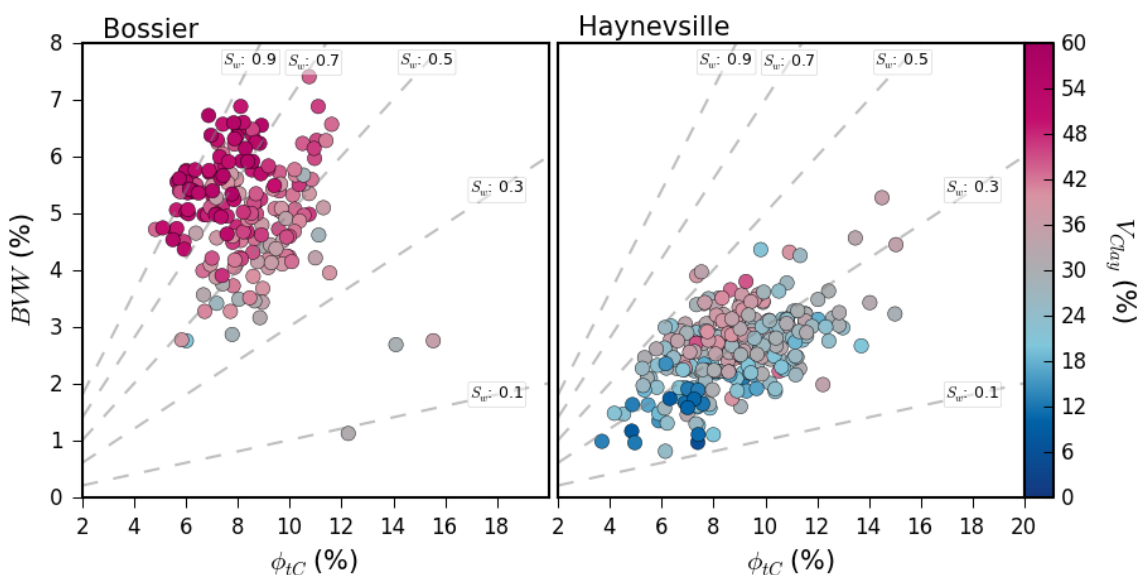


Figure 7.7. BVW vs. ϕ_{tC}
 BVW vs. ϕ_{tC} for the BSR (left) and HY (right). Marker colour is a function of V_{Clay} . Dashed grey lines depict S_w based on BVW / ϕ_{tC} .

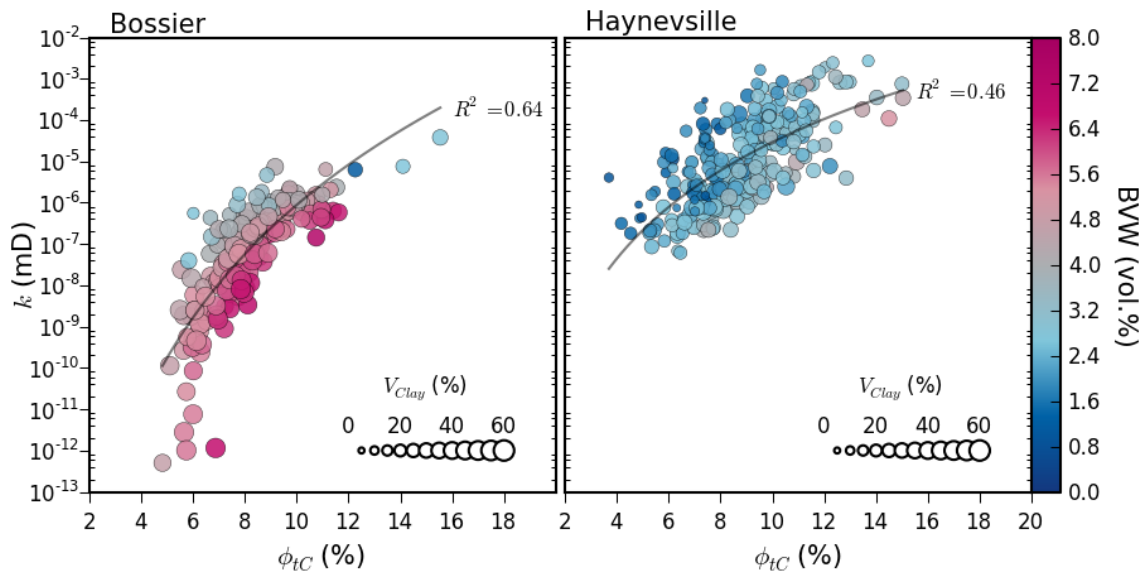


Figure 7.8. Matrix permeability (k) vs. ϕ_{tc} (coloured by BVW)

Matrix permeability (k) vs. ϕ_{tc} for the BSR (left) and HY (right) Formations. Marker colour is a function of $V_{Chlorite}$ and marker size a function of V_{Clay} .

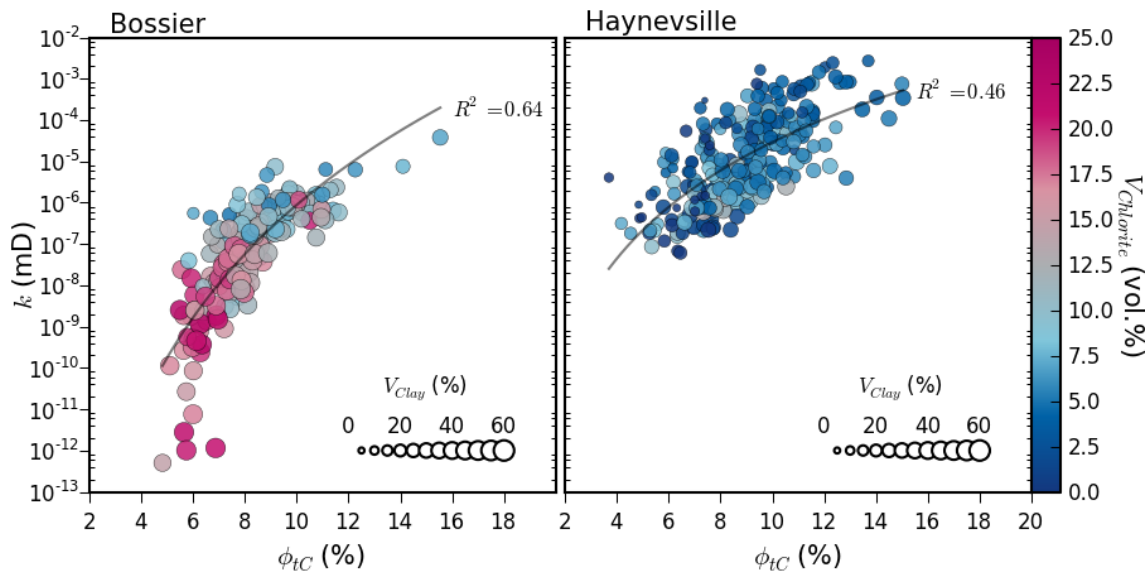


Figure 7.9: Matrix permeability (k) vs. ϕ_{tc} (coloured by chlorite)

Matrix permeability (k) vs. ϕ_{tc} for the BSR (left) and HY (right). Marker colour is a function of $V_{Chlorite}$ and marker size a function of V_{Clay} .

As a consequence of the impact of clay minerals on formation poro-perm and fluid distributional relationships, it follows that V_{Clay} should also impact formation electrical properties, where, as discussed, clay minerals are typically expected to increase rock conductivity by increasing the conductivity of bulk water in the pore spaces (Hamada 2001). Thus BVW might be expected to form a negative relationship with R_t , though Figure 7.10 shows that this is not entirely evident. So whilst the HY broadly complies with Archie's equation (a negative $BVW : R_t$ relationship) the BSR shows a significant

departure and an increase in R_t coincident with an increase in V_{Clay} . In addition, overlain on Figure 7.10 are the calculated R_t values for either fixed m^* (left) or fixed R_{we} (right). The BSR plot (left), shows good agreement between calculated R_t (at $m^*=2$) and V_{Clay} with incremental increases in R_{we} . Likewise, the HY plot (right) shows good agreement between calculated R_t (at $R_{we}=0.014$) and V_{Clay} with incremental increases in m^* . This demonstrates that either parameter (an increase in either fluid conductivity or pore complexity) can be utilised to compensate for the observed increase in R_t with V_{Clay} . This observation is identical to that made for W1 and W2 modelled core parameters (Figure 4.13), where either R_{we} or m^* can be directly regressed from R_t relationships, allowing for a significant reduction in MAE for S_{wR} estimates (Figure 0.3).

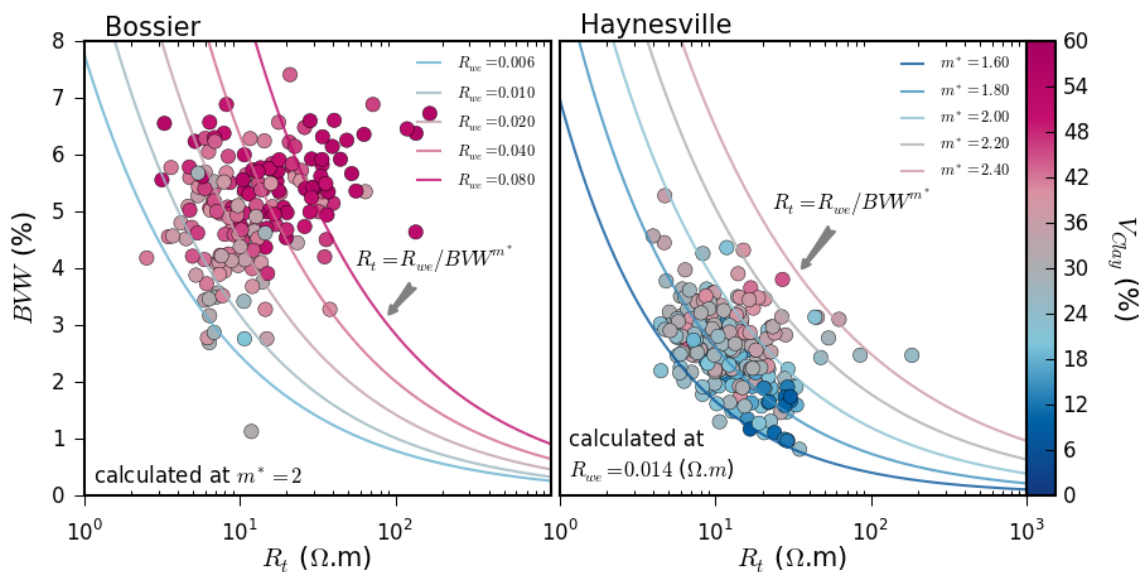


Figure 7.10. BVW vs. R_t
 BVW vs. R_t for the BSR (left) and HY (right). Marker colour is a function of V_{Clay} .

These observations suggest that V_{Clay} controls fluid distribution and formation electrical properties in the BSR and implies that free and capillary fluids contribute minimally to BVW. In addition, Figure 7.10 suggests that CBW is a net contributor to electrical resistance, either by a consequence of CEC effects and/or pore geometrical complexity. Similar observations are made for the HY, though in tandem with significantly lower V_{Clay} , far less influence over fluid distribution is observed. This raises the question: *what mechanism(s) might allow for clay minerals to add to bulk fluid resistivity and/or pore complexity, and so contribute to formation resistivity?*

5.3.2 Anomalously high resistivities in the BSR

Unexpectedly high resistivity tool responses have been previously reported in the BSR (Corley et al., 2010; Le et al., 2011) and in other northern Gulf of Mexico shales (Anderson et al., 2006). The unusual response manifests as both generally high deep resistivities and an unexpected separation in resistivity profiles with depth of investigation. This observation might normally be indicative of invasion by conductive fluids, but in this instance the extremely low BSR permeabilities (Figure 7.9), which show a similar response in oil or water based muds, make such an explanation physically untenable (Corley et al., 2010). In addition, the response does not correlate with organic content or gas production (e.g. high S_w and V_{Clay} in Figure 7.7) and neither are they unique to resistivity tool type (Corley et al., 2010).

These unusual effects were first noted on array induction logs in Oklahoma and Texas in the 1980's and were recently re-examined by Anderson et al., (2006), whose study suggests that the petrophysical complexity of shale microstructure might cause large dielectric permittivity resulting from a large internal polarisation due to the size and structure of clay minerals combined with disseminated pyrite. This mechanism requires that some dielectric permittivity be generated by the polarisation of the counter-ions in the double layer surrounding clay minerals, with the bulk of the permittivity generated by surface oxidation-reduction reactions on the surface of pyrite grains. Further investigation was undertaken by Corley et al.,(2010) using multiple tools with varying array spacings and frequencies of between 30 Hz to 200 MHz. This later study demonstrated a similar curve separation with depth of investigation for all tool types, but noted that the model proposed by Anderson et al (2006) (i.e., high dielectric permittivity caused by clay and pyrite and a single set of resistivity and dielectric permittivity parameters), could not reconcile the response for multiple tool types. In addition, the parameters were required to vary in X, Y and Z directions, and suggested exceptionally high horizontal resistivity anisotropy with exceptionally low (less than 1) vertical resistivity anisotropy. These conditions were felt to be physically unrealistic by Corley et al., (2010), who suggests that dielectric effects in isolation fail to account for the unusual log response. In order to explain the log

response Corley et al., (2010) suggests that a hypothetical series of vertical fractures filled with resistive material could satisfy the required conditions. This suggestion was tested by Le et al., (2011), who concludes that a series of vertical fractures filled with resistive material coupled with ultra-high permittivity parallel to bedding is required to explain the unusual log responses. Though in the absence of any geological evidence to support the presence of a series of vertical resistive fractures, a geological explanation remains enigmatic.

5.3.3 A mechanism for clay mineral freshening

In this study, anomalously high resistivities are highlighted as the cause of significant underestimation of S_{wA} (Figure 4.2). This is coincident with elevated V_{Clay} (Figure 4.2) and can be demonstrably corrected (**Error! Not a valid bookmark self-reference.**) by compensatory increases in either m^* or R_{we} (Figure 4.15). Furthermore, as depicted in Figure 7.10, increases in V_{Clay} correspond well with calculated R_t over a range of potential R_{we} values, implying an effective freshening of bulk formation fluid with increasing clay content. It can therefore be argued that the higher than expected resistivity response in the BSR may be a result of high V_{Clay} and clay dilution effects. Where, if BVW is principally formed from CBW , ions in addition to those required to satisfy the clay mineral surface charge will migrate away by diffusion along electrochemical gradients. In order to develop this hypothesis, it is first necessary to review the mechanisms related to changes in pore fluid chemistry and salinity with depth.

5.3.3.1 Changes in pore fluid chemistry and salinity with depth

The BSR-HY have a combined average porosity of 8%. Recently deposited clay rich muds have porosities as high as 90% (Velde, 1996), requiring the expulsion of large volumes of pore fluid over their burial history. The decline in porosity with burial and depth is well established (Hedberg, 1936; Mackey and Bridge, 1995). During this process, the sediment undergoes significant physical change (e.g. porosity, permeability, density) related to increased vertical stress, and chemical change (e.g.,

re-mineralisation reactions and thermal maturation of organic matter) in response to temperature and diagenetic processes (Boggs, 2009; Potter, 2005; Wignall, 1994). As a consequence, the pore water chemistry and its electrical resistivity also evolve typically from that of sea water at the time of deposition, to the saturating pore fluid present at the time of investigation. It is also generally accepted that pore fluid salinity increases with depth (Chilingar et al., 2002; Rieke and Chilingarian, 1974), and in the case of the Gulf of Mexico Basin, depth-salinity relationships are both well established and linked to formation overpressure (Fertl and Timko, 1971; Fowler Jr, 1970; Overton and Zanier, 1970; Sharp et al., 2001; Smith, 1977).

The effects of compaction on the pore fluid chemistry of clay rich muds and pure clays was widely investigated in the 1960's and 70's. Von Engelhardt and Gaida (1963) studied the effects of compaction on the pore solution chemistry on montmorillonite and kaolinite clay over a pressure range of 440 psi to 47,027 psi (*BSR-HY core were sampled at 10,000 ft. to 14,000 ft., equating to an approximate pressure range of 15,000 psi to 20,000 psi based on pore and overburden pressures from Rocha and Bourgoyne, (1996)*). This experiment applied instantaneous loads to clays saturated in a saline solution. Compaction was demonstrated to have no effect on the pore water chemistry of kaolinite clays, which have a near neutral surface charge and low CECs of 2-5 meq/100g (Ellis and Singer, 2007). Whilst the montmorillonite clays, which have high CECs of 5 to 40 meq/100g (Ellis and Singer, 2007), showed an decrease in pore fluid salinity up to pressures of 11,756 psi, after which salinity was noted to increase.

Later investigations by Chilingar et al., (1969) applied gradual loads to 'marine muds' from the Santa Cruz Basin (off-shore southern California), observing a decrease in the salinity of expelled fluids with increasing over-burden pressure. Implying both an increase in the salinity of the residual pore fluid, and that compaction rates can significantly impact pore fluid evolution. From these experiments Chilingar et al., (1969) concludes (A) that the salinity of expelled fluid decreases with increasing overburden pressure and (B), that the salinity of shale pore fluids should be lower than those of associated sandstones. The latter conclusion was reasoned on the basis of work by Fowler (1968), who found a correlation between high salinity and abnormally

high overpressures in the Bayou Field, Texas, where the salinity of produced water decreased with time. From this, as the freshest water was found in sands (which received their water from associated over-pressured shales) it was concluded that shale fluid salinity must be less than that of the associated sands. This was validated by Fertl and Timko, (1971), who found that the pore water chlorinity (indicative of salinity) of sands was consistently higher than that of associated shale's at similar depth. In addition, field examples presented by Overton and Zanier, (1970), Fertl and Timko, (1971) and Fowler Jr, (1970) highlight a decrease in shale resistivity with an increase in formation overpressure and a decrease in fluid salinity at approximately 10,000 ft., 11,300 ft. and 12,000 ft. respectively. In all three instances these observations can be explained by shale compaction models suggested by Powers, (1967) and modified by Burst, (1969). This advocates the release of structural pure water into the pore space during the remineralisation of smectite to illite at 3,200 to 16,000 ft., resulting in an increase in pore pressure (leading to formation overpressure) and a decrease in interstitial fluid salinity. Moreover, Krushin (2013), notes a loss in CEC (exchangeable ions and thus bound water salinity) with smectite to illite conversion, which correspond with observations by Dewhurst et al. (2008) and Dewhurst et al. (2013) that shale CEC decreases within increased compressive strength, consolidation and dewatering. It should however be noted, that whilst illitisation reactions may account for observed salinity changes and overpressures in some Gulf of Mexico sediments (Katahara, 2006), that other stress related mechanisms may also contribute (Lahann et al., 2001). A review of the origin of overpressure is given by Chilingar et al., (2002) and a 'true shale compaction model' for pore pressure prediction, which integrates stress, temperature and chemical processes has been recently proposed by (Krushin, 2013).

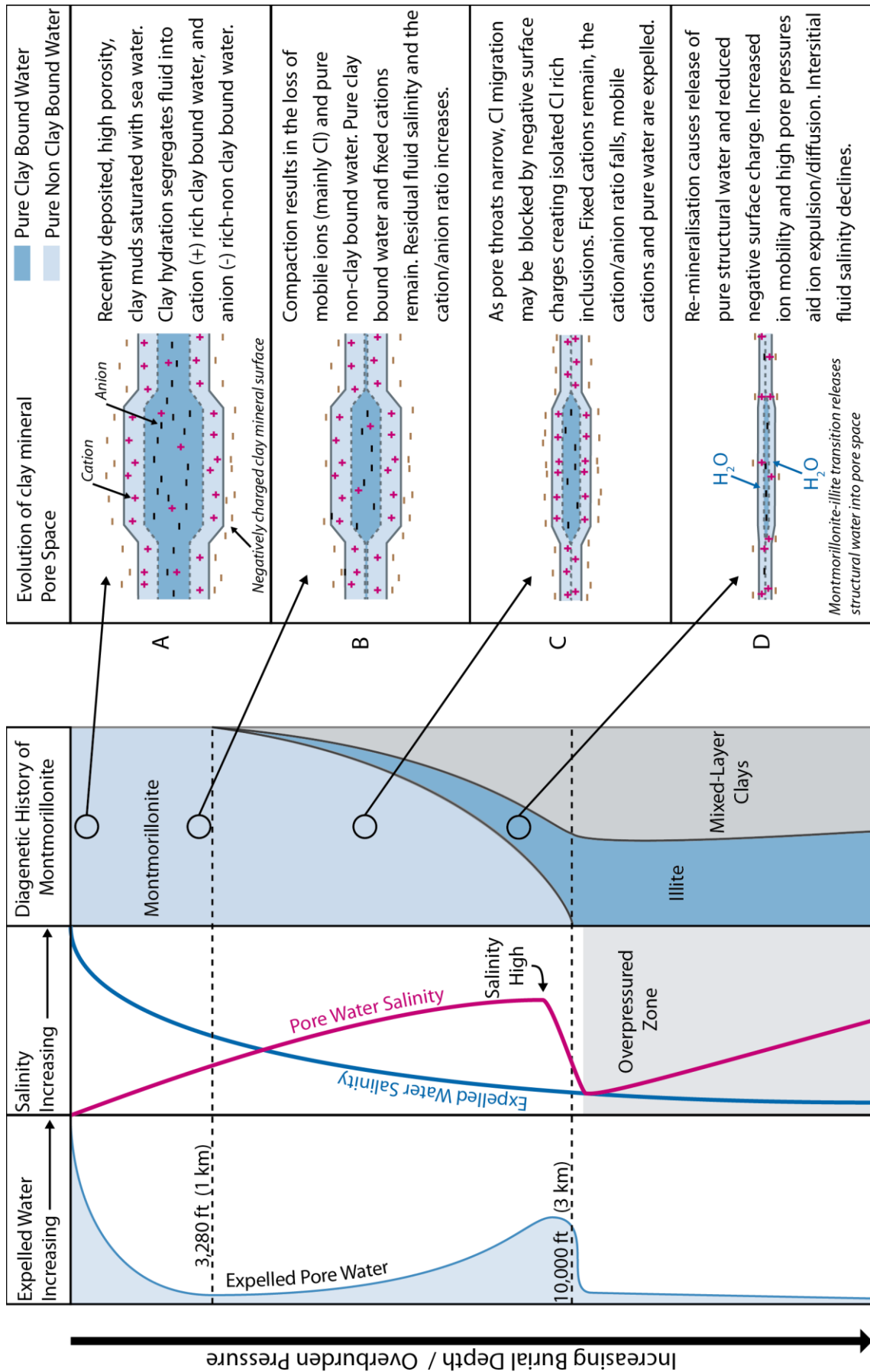


Figure 7.11. Schematic illustration of the effects of compaction on pore fluid salinity

Expelled Water and diagenetic history adapted from (Powers, 1967), pore water salinity and overpressure inferred from (Overton and Zanier, 1970) and (Fertl and Timko, 1971), and notional depiction of clay pore evolution based on descriptions by Von Engelhardt and Gaida (1963) and Chilingar et al., (1969).

The depth related changes described above are schematically depicted in Figure 7.11. This integrates a compaction model (Powers, 1967) with pore water and expelled salinity changes described by Overton and Zanier, (1970) and Fertl and Timko, (1971), with pore ion exchange mechanisms described by Von Engelhardt and Gaida (1963) and Chilingar et al., (1969). The schematic includes two highlighted depths: (A) 3,200 ft. (approx. 100°C), below which montmorillonite begins to convert to illite (Powers, 1967), and (B) 10,000 ft. (approx. 300°C), below which no pure montmorillonite was observed in Texan and Louisianan Gulf Coast sediments by Powers (1967). It is however noted that high pore pressures, undercompaction, unusual temperature gradients and heterogeneity in clay chemistry, may also impact transition depths (Chilingar et al., 2002; Freed and Peacor, 1989). Figure 7.11 attempts to schematically depict the evolution of fluid-mineral interactions, diagenesis and overpressures with increasing depth, and can be split into three general zones:

Zone 1 (0-3,200 ft.): This depicts the initial clay sediment deposition (A), where clay hydration results in the development of a pure water and cation rich electrical double layer (CBW). The anions are actively repelled from the negative surface charge and CBW resulting in respective cation and anion rich fluid components. As compaction progresses (B) the CBW and fixed cations are retained and the anion rich free waters are preferentially expelled with a net increase in the overall salinity of the remaining pore fluids which have elevated cation/anion ratios. This is somewhat validated in a study of the thermodynamics of salinity change accompanying compaction by (Smith, 1977), who finds that the concentration of anions in compaction expelled fluids decreases monotonically with reductions in clay sediment porosity whilst the cations in the residual pore fluids increase monotonically. Within this zone pore-fluid salinity increases with depth and the expelled water volume (analogous to porosity and permeability trends) declines rapidly.

Zone 2 (3,200-10,000 ft.): With continuing burial, (C) the negative surface charge of clays in narrow pore throats may inhibit chlorine migration. This prevents further expulsion of anions at the expense of pure water and more mobile cations, possibly resulting in the development of local anion rich fluidic inclusions. In addition, increasing pressures drive off outer-layers of pure clay-bound water (Burst, 1969). As a result, pore water salinity increases and the cation/anion ratio may fall (Chilingar et al., 1969). Additionally, below 3,200 ft. thermobarometric conditions allow for the illitisation of montmorillonite. As montmorillonite begins to remineralise, illitic sheets develop creating an intermediary illite-smectite (I/S) mixed-layer clay, which, with increasing temperature and pressure becomes increasingly crystalline and illitic (Potter, 2005). During this transformation interlayer potassium becomes fixed in the clay structure, whilst silica and interlayer hydration water are expelled into the pore space (Chilingar et al., 2002; Potter, 2005). As a result, with progressive illitisation (D) and a reduction in bulk CEC, ion mobility, pore water expulsion and pore water pressures are all increased. With increasing depth pressure and temperature approaching 10,000 ft. the rate of illitisation increases (Powers, 1967). As a consequence of the influx of structural pure water, pore water salinity drops below the salinity maximum, and pore pressures and porosity rise (Fertl and Timko, 1971; Fowler Jr, 1970; Overton and Zanier, 1970). As pore fluids begin to accommodate the lithostatic load, the formation becomes over-pressured.

Zone 3 (below 10,000 ft.): Below 10,000 ft. no pure montmorillonite remains. Progressive illitisation of the mixed-layer clay continues at a reduced rate, pore pressures remain high and pore fluid salinities again begin to increase as the structural pure water is progressively expelled.

The schematic presented in Figure 7.11 incorporates observations from multiple sources in attempting to accommodate regional trends observed in the GOM basin. It is intended to highlight pore water chemistry and its evolution as a complex function of diagenetic history and clay mineralogy. Within this framework, core data for the BSR-HY, which are: (A) overpressured, (B) sampled below 10,000 ft., (C) contain no

smectite, and (D) have low volumes of mixed layer clays (Figure 7.4), fit within Zone 3. It is therefore suggested that the clay-pore fluid interactions responsible for regional GOM trends also result in highly heterogeneous pore fluid salinities at the core scale as a function of clay volume and distribution. This extends the conclusion of Chilingar et al., (1969) that '*the salinity of interstitial fluid solutions in shale should be lower than those in associated sandstones*' to: the salinity of clay rich shale should be less than that of associated clay poor, more permeable shales. For instance, within the BSR-HY a heterogeneous mixture of at least four types of pore fluid regimes can be visualised: (1) non-clay bound, (2) illite dominated, (3) mixed-layer clay dominated, and (4) chlorite dominated, each with different pore water chemistries. Given the preceding discussions, and as a consequence of ion exclusion, it is suggested that the non-clay bound fluids will have greater salinities, such that overall pore water salinity is dependent on ratio of non-CBW : CBW and is thus relative to V_{Clay} . This is demonstrated in Figure 7.12 below, where above approximately 28% V_{Clay} , the pore fluid becomes increasingly CBW dominated, heterogeneous and generally fresher (Figure 7.10), such that compensatory increases in R_{we} from R_t relationships (e.g. Figure 4.15), can allow for the calculation of S_{wR} with reduced residual MAE (Figure 0.3). Moreover, it is notable that only those wells where samples have generally less than approximately 28% V_{Clay} does S_{wR} fail to improve upon standard 3D optimisation (W4).

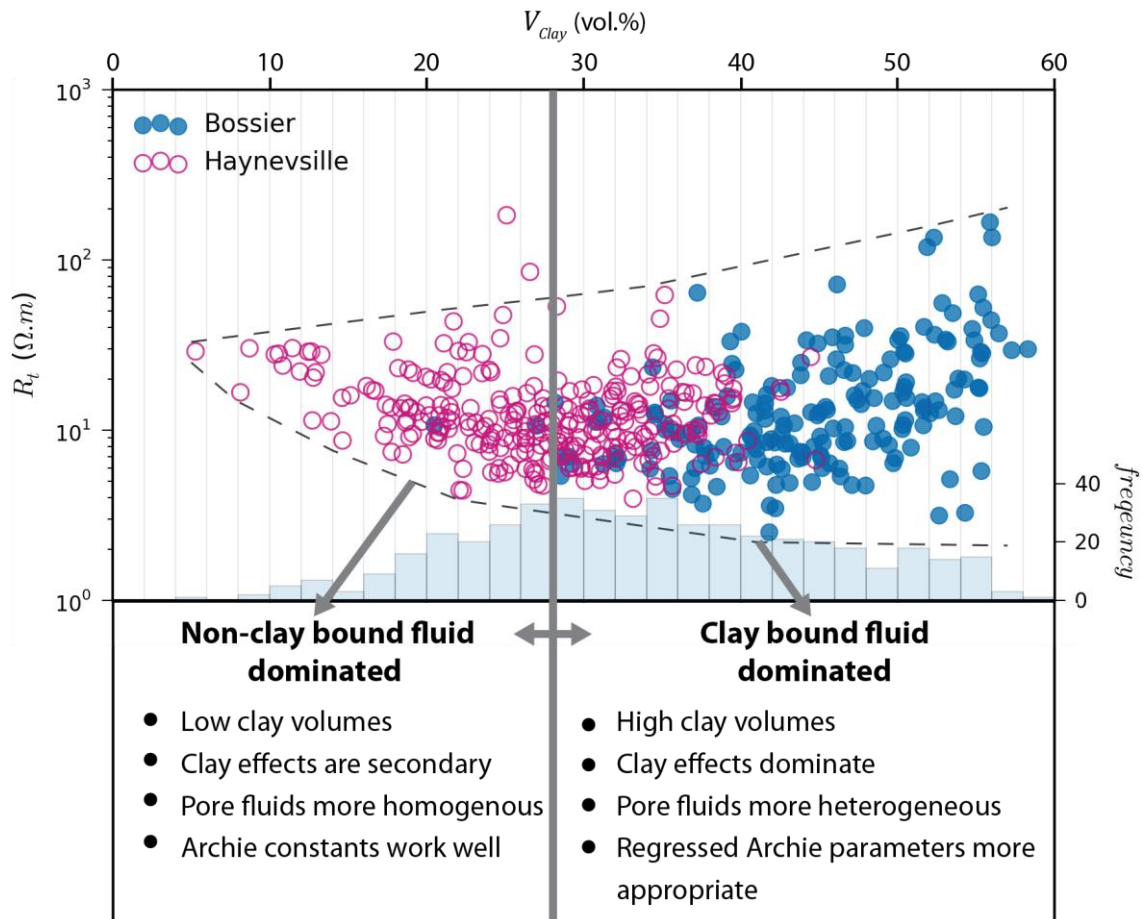


Figure 7.12. Key change in petrophysical behaviour with V_{clay}

5.3.4 A mechanism for increased pore-complexity

The effects of authigenic pore-lining chlorite, though not fully understood, are well documented in 'low resistivity pay' (Worthington, 2000). In this setting chlorite effects are considered to be less a product of surface area and CEC (Motealleh et al., 2007), but as a result of their effect on the amount and distribution of microporosity (Durand et al., 2001; Tudge, 2010). Where hydrous chlorite coatings preserve conduction pathways on grain surfaces, maintaining depressed R_t values that mask and undervalue hydrocarbon saturation. This necessitates compensatory reductions in m and n values (e.g. parameter trade-offs Figure 0.6) that have been demonstrated experimentally, with m values shown to be less than 2 and n values of around 1.5 (Durand et al., 2001; Edmundson, 1988b). Chlorite minerals can therefore be said to exert indirect electrical influence on ion conduction pathways (m and n) as a consequence of their distribution within the pore space. Whilst the direct intrinsic electrical effects of chlorite, which

have generally low CECs (2-14 meq/100g (Ellis and Singer, 2007)), on bulk fluid resistivity (R_{we}) are likely to be minimal.

In the example given by a 'low resistivity pay' analogue, the principal porosity is invaded by hydrocarbons whilst the secondary chlorite micro-porosity provides a CBW or capillary bound water-wet conductive membrane on the grain surface. Yet unlike 'low resistivity pay', and particularly in the BSR, the chlorite and other CBWs constitute the **primary** porous network. Such that additional chlorite and associated reduced ϕ_{tC} , k relationships (Figure 7.9) will add to m^* . This is witnessed in all optimiser models and core modelled parameter values, where the BSR consistently necessitate higher m^* or m values than the clay poor HY (Figure 4.8). Additionally, the BSR data, which have generally low hydrocarbon saturations, indicates a reliance on optimising m in model W4 (Figure 0.17). By contrast, the HY, which has generally significant hydrocarbon saturations, demonstrates greater emphasis on n . This is taken to suggest that pore surface wettability in the BSR is not particularly variable, being dominated by water wet clays whose distribution, in particular that of chlorite, primarily impacts m . It is therefore appropriate that the HY, which has lower clay contents, higher oil wet TOC fraction and related porosity, and a potentially more homogenous and saline free pore fluid, demonstrates an increased importance and thus a reasonable probability distribution for n .

Other impacts on m may result from clay grain orientation. Where illitisation and mechanical compaction may contribute to the re-mineralisation or re-orientation of clays perpendicular to the principle stress, potentially increasing clay alignment and creating a more elongate and regular pore space (Alpin and MacQuaker, 2010; Alpin et al., 2003; Day-Stirrat et al., 2012; Dewhurst et al., 1999; Esemé et al., 2006; Fawad et al., 2010). This might infer lower m values for increasingly aligned or fissile mudstones that have more capillary like pore-spaces, though there is no evidence in the literature to support or refute this. In any case, should illitisation result in increased planar alignment and a reduction in m , chlorite and illite precipitated in matrix supported pores and thus less influenced by vertical stress, are likely to counteract any such reduction. This argument may be overly simplistic, but it highlights the prospect of

highly heterogeneous pore geometries coincident with diverse electrical effects as noted in Figure 7.12 above 28% V_{Clay} .

Overall, it is likely that the variability in m and n exponents are intrinsically linked to both R_{we} and clay content. This is indirectly suggested by Yu and Aguilera (2011), who note that m values are typically lower than 2 in shales, as interconnected clays combined with formation water provides more paths for electric current flow. Such that if R_{we} is influenced by clay, then so must m and n . This sentiment is echoed by Bust et al., (2011) who also suggest that R_w exerts a major influence over pseudo-Archie exponent m and n . In addition, Wu and Aguilera (2012) suggest that m changes continuously in response to the variability in fracture and Kerogen porosity, which would again require like changes in R_{we} .

5.3.5 Summary and conclusions

In summary, two general petrophysical regimes can be proposed for the BSR and HY:

BSR: Dominated by CBW with non-clay bound fluid as a secondary contributor to BVW . This manifests as a freshening of pore fluids (increase in R_{we}) with increasing clay content. As the non-clay bound water volume is a secondary contributor to BVW , the addition of CBW electrical conduction pathways, and associated decreases in m , are limited. Moreover, the increased presence of chlorite and associated reductions in ϕ_{tC} and k further reduce the influence of non-clay bound fluids at higher V_{Clay} values and result in increases in m above 2.

HY: Dominated by non-clay bound fluid, CBW is a secondary contributor to BVW . This manifests in more homogenous R_{we} values and limited freshening of pore fluids with increasing clay content. As the non-clay bound water is the bulk contributor to BVW , the addition of CBW electrical conduction pathways results in reductions in m below 2, aided by higher ϕ_{tC} and k values.

The BSR and HY demonstrate markedly different petrophysical relationships and associated pseudo-Archie exponents that reflect the volume and effect of clay minerals. A boundary between the two petrophysical regimes falls qualitatively at

approximately 28% V_{Clay} (Figure 7.12). Above this limit (predominantly in the BSR), clay and chlorite volumes and clay dilution effects act to increase R_{we} , m and n . This model fits well with the generated parameters and explains the observed petrophysical heterogeneity and anomalously high BSR resistivities. In addition, an empirical method is demonstrated that increases the accuracy of S_w estimates by modifying either R_{we} or m^* as regressed from R_t relationships (Figure 0.2). Below 28% V_{Clay} the predominantly HY data are more Archie-like in their behaviour, more homogenous petrophysically, and have lower R_{we} , m and n values.

5.4 Composite core data summary

The following section integrates the relationships described in Chapter 4 and sections 7.11 and 7.12 within a single display (Figure 7.13), highlighting the relationships between mineralogy (XRD), R_t , BVW , saturation data, and the relative error (RE) in S_{wA} for each well. First the relationships, as depicted in Figure 7.13, are summarised; this is followed by a qualitative review of thin section images so as to relate mineralogical and petrophysical variations to accompanying differences in formation fabric, where discernable.

5.4.1 Petrophysical and mineralogical relationships

The preceding discussion and relationships can be largely reconciled within a single summary display. Core summary panels are provided for the BSR and HY Shales in Figure 7.13 and integrate RE , XRD, R_t , BVW and S_w data. Figure 7.13 includes five tracks:

- Track 1 (far left), RE : Includes the RE generated by all optimiser models arranged in rank order from -1 (S_{wA} underestimated by 100%) to +1 (S_{wA} overestimated by 100%) for each well. The relative error generated by optimiser model W4 is highlighted in bold, with a shaded zone denoting samples where the error is within $\pm 10\%$ (i.e. where S_{wA} is within 10% of S_{wC}). The remaining tracks are arranged in this order.
- Track 2, XRD: Includes core XRD data, highlighting a generally upward increasing V_{Clay} trend which coincides with increasingly negative RE (track 1) and underestimated S_{wA} (track 4). Likewise carbonate contents ($V_{Calcite} + V_{Dolomite}$) are highest where RE is positive and S_{wA} is overestimated.
- Track 3, BVW and R_t : Indicates a consistent increases in BVW with R_t , linked to an increase in V_{Clay} (track 2) and negative RE (track 1). Likewise, R_t and BVW are lowest where V_{Clay} is minimal, carbonate contents are high and S_{wA} overestimated (track 4).

- Track 4 saturation data: The bars represent S_{wC} , the red line is S_{wA} generated by optimiser model W4, and the blue line is S_{wR} . S_{wR} demonstrates improved performance and correlation with S_{wC} for a number of wells, particularly in the BSR.
- Track 5, R_t vs. BVW cross plots: Highlights BVW vs R_t relationships for each Well. The data is divided into three groups based on the magnitude of relative error (RE) for model W4 as defined by the light grey shaded region:

Pink: $-1.0 < RE < -0.1$: links to high R_t , BVW and V_{Clay} samples

Grey: $-0.1 < RE < 0.1$: S_w estimates accurate to $\pm 10\%$

Blue: $0.1 < RE < 1.0$: links to low R_t , BVW and V_{Clay} samples

Figure 7.13 highlights the petrophysical trends discussed in sections 7.11 and 7.12. In addition, it demonstrates that the $BVW : R_t$ relationships highlighted in track 3 of Figure 7.13 can be loosely segregated into a series of more Archie like sample groups by arbitrarily partitioning RE (see cross plots in track 5). This zoning is found to frequently coincide, particularly in the BSR, with distinctions in V_{Clay} and R_t values. This suggests a means of petrophysically zoning the formation based on singular or combined V_{Clay} or R_t cut-offs into smaller optimised groups, which may further improve S_w estimates. This is shown in rudimentary fashion by shading the baseline region of R_t in track 3 for the BSR (Figure 7.13, plot A), though in practise, a more complex multivariate means of data segregation including V_{Clay} and R_t may prove useful. Moreover, data points within any one group (Pink, Grey or Blue) form relatively linear $BVW : R_t$ relationships implying a narrower range of Archie parameters. I.e. if R_t vs. BVW are linearly related then R_{we} , m and n should remain nearer to constant.

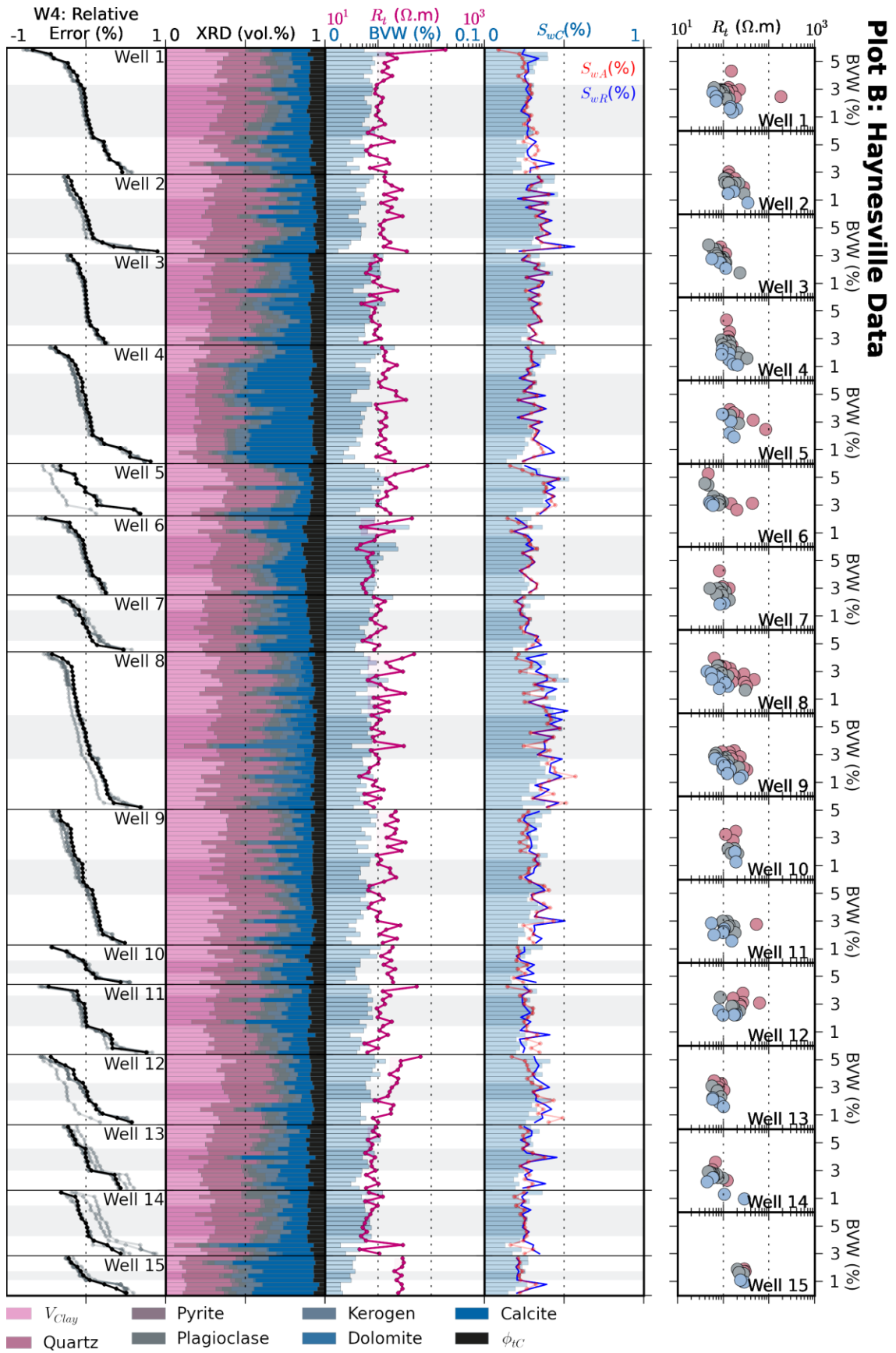


Figure 7.13. Composite core summary panels.

Track 1 (far left), Relative Error (RE): Includes the RE generated by all optimiser models arranged in rank order from -1 (S_{wA} underestimated by 100%) to +1 (S_{wA} overestimated by 100%) for each well. The RE generated by optimiser model W4 is highlighted in bold, with a shaded zone denoting samples where the error is within $\pm 10\%$ (i.e. where S_{wA} is within 10% of S_{wC}). The remaining tracks are arranged in this order. **Track 2, XRD:** Includes core XRD data, highlighting a generally upward increasing V_{Clay} trend which coincides with increasingly negative RE (track 1) and underestimated S_{wA} (track 4). Likewise carbonate contents ($V_{Calcite} + V_{Dolomite}$) are highest where RE is positive and S_{wA} is overestimated. **Track 3, BVW and R_t :** Indicates a consistent increases in BVW with R_t , linked to an increase in V_{Clay} (track 2) and negative RE (track 1). Likewise, R_t and BVW are lowest where V_{Clay} is minimal, carbonate contents are high and S_{wA} overestimated (track 4). **Track 4 saturation data:** The bars represent S_{wC} , the red line is S_{wA} generated by optimiser model W4, and the blue line is S_{wR} . S_{wR} demonstrates improved performance and correlation with S_{wC} for a number of wells, particularly in the BSR. **Track 5, R_t vs. BVW cross plots:** Highlights BVW vs R_t relationships for each Well. Data is divided into three groups based on RE for model W4 as defined by the light grey shaded region. Note; see electronic version of Figure 5.13 for a large, expandable plot.

5.4.2 Linking mineralogy and petrophysics to formation fabric

The marked change in mineralogical and petrophysical properties with RE as highlighted in Figure 7.13, combined with the large variation in m^* or R_{we} values generated in deriving S_{wR} (see section 4.4.3.1) suggest that there should be a corresponding and discernable change in sediment fabric. As such, the available thin section imagery was reviewed for each core sample. It should however be noted that comparisons between available thin section images and other core data is extremely limited, as the thin sections are not available for viewing in their entirety. For each core sample four thin section images are available, taken at the same location at different magnifications and light conditions as summarised in Figure 7.14. The first image for each core sample captures an area of 12.8 mm^2 in plane light, the second is taken at the same magnification but in epifluorescent light, the third zooms in on a selected area of the first image covering 0.512 mm^2 , with the fourth image displaying a magnified area of the third image covering 0.128 mm^2 .

Summary of thin section images available for each core sample (scale 1:1)

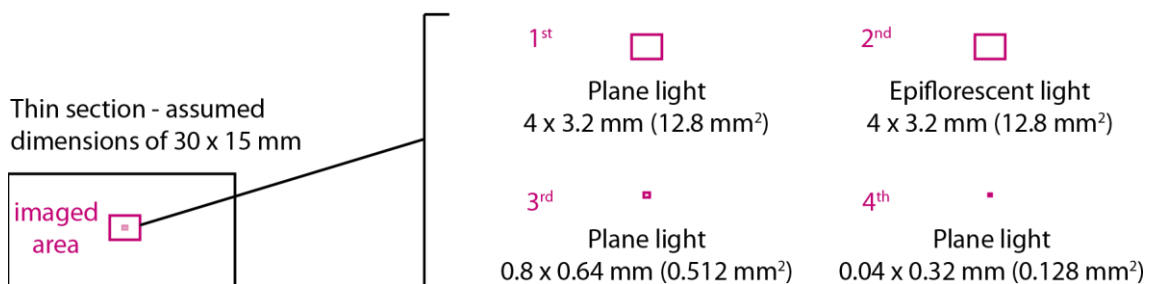


Figure 7.14. Summary of available thin section imagery

As depicted in Figure 7.14, only a single thin section image capturing a very small fraction of the entire thin section is available for any one core sample, such that little can be deduced of overall sediment fabric at any one sampling location. Whilst mudstones are highly heterogeneous with complex fabrics occurring at the centimetre to millimetre scale, sediment fabric (grading, lamina sets etc., see section 2.1.3) is generally not discernable at scales represented within the available images, particularly in the absence of context provided by the remainder of the thin section. Moreover, the rationale for the selection and inclusion of these images within the RAPID database is likely to have been dependant on the individual responsible for collating and compiling database information. In other words, links between fabric displayed in thin section images and core data are at best qualitative.

Considering the limitations discussed above, thin section images were arranged and reviewed in order of RE for optimiser model W4, in kind with the data displayed in Figure 7.13. In general, for the BSR data, as the change in V_{Clay} with RE (RE decreases as V_{Clay} increases) is both marked and consistent, variations in sediment fabric linked to grain size and clay content can be observed in the majority of wells. An example is displayed in Figure 7.15 for well 10, where, as V_{Clay} increases the thin section photographs display increasingly planar / anisotropic, fine grained and burrowed fabrics. Though within the HY, whilst variations in mineralogy follows similar trends to the BSR, they are contrastingly subtle, and no systematic variation in fabric was found. Examples are displayed for BSR well 10 and HY well 8 in Figure 7.15 and Figure 7.16 respectively.

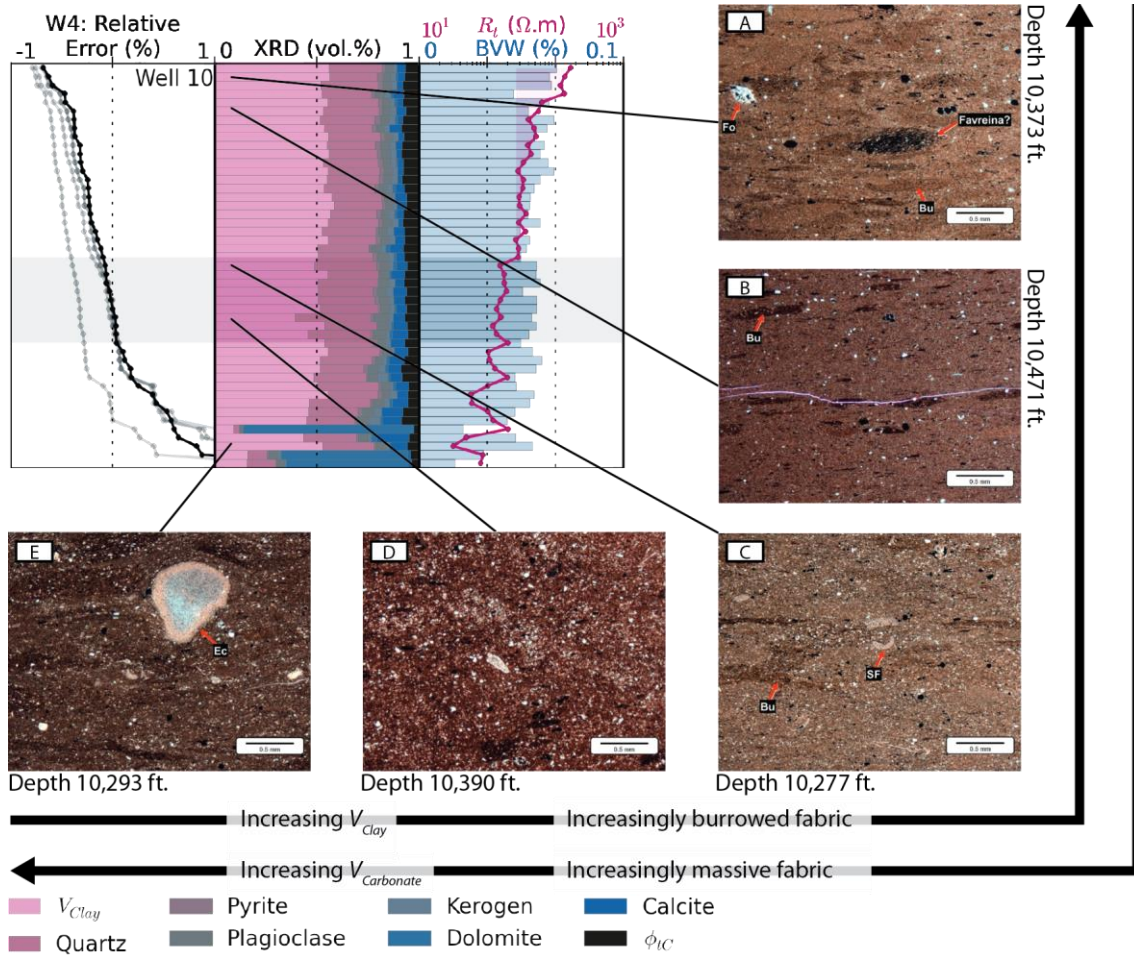


Figure 7.15. Thin section images: BSR well 10

Exert of Figure 7.13 highlighting BSR well 10, displaying changes in thin section fabric with RE and clay content. Note, the apparent decrease in grain size and increasingly burrowed fabric with increasing V_{Clay} . Thin section photographs descriptions as taken from Core Laboratories: **(A)** Burrowed (Bu), weakly calcareous and dolomitic, siliceous, slightly silty shale (claystone) with scattered benthic foraminifers (Fo). Pyrite appears as replacement mineral in some microfossils (SF). Favreina burrows are distinguished. The high quartz content (24%) is mostly due to microquartz (authigenic?) mixed with the matrix. Silt-sized siliciclastics occur dispersed throughout the sample. The larger quartz grain size is 70 micron (average grain size: 20 micron). Framboidal pyrite is common. **(B)** Burrowed (Bu), calcareous, siliceous, slightly silty shale (claystone) with scattered undifferentiated carbonate filaments (SF?). The high quartz content (29%) is mostly microquartz (authigenic?). Silt-sized siliciclastics occur dispersed throughout the sample. Framboidal pyrite is common. Microfractures are clearly visible. **(C)** Burrowed (Bu), calcareous, weakly dolomitic, siliceous, slightly silty shale (claystone) with scattered skeletal fragments (e.g.: echinoderms; SF). Benthic foraminifers are minor constituents. The high quartz content (32%) is probably due mainly to microquartz (authigenic?) mixed with the matrix. Silt-sized siliciclastics occur dispersed throughout the sample. The larger quartz grain size is 80 micron (average grain size: 10 micron). Pyrite (Py), and micas (Mi) are common. **(D)** Burrowed, calcareous, argillaceous siltstone to highly silty shale (claystone) with scattered benthic foraminifers (Fo). Some skeletal fragments from mollusks are distinguished. Silt-sized siliciclastics (e.g.: quartz, Q) occur dispersed throughout the sample. The larger quartz grain size is 110 micron (average grain size: 20 micron). Framboidal pyrite (Py) and micas (Mi) are common. **(E)** Highly calcareous, weakly dolomitic, siliceous, silty shale (claystone) with scattered skeletal fragments (e.g.: echinoderms [Ec], and benthic foraminifers [Fo]). The high quartz content (27%) is probably due mainly to microquartz (authigenic?) mixed with the matrix. Silt-sized siliciclastics occur dispersed throughout the sample. The larger quartz grain size is 100 micron (average grain size: 20 micron). Pyrite is common.

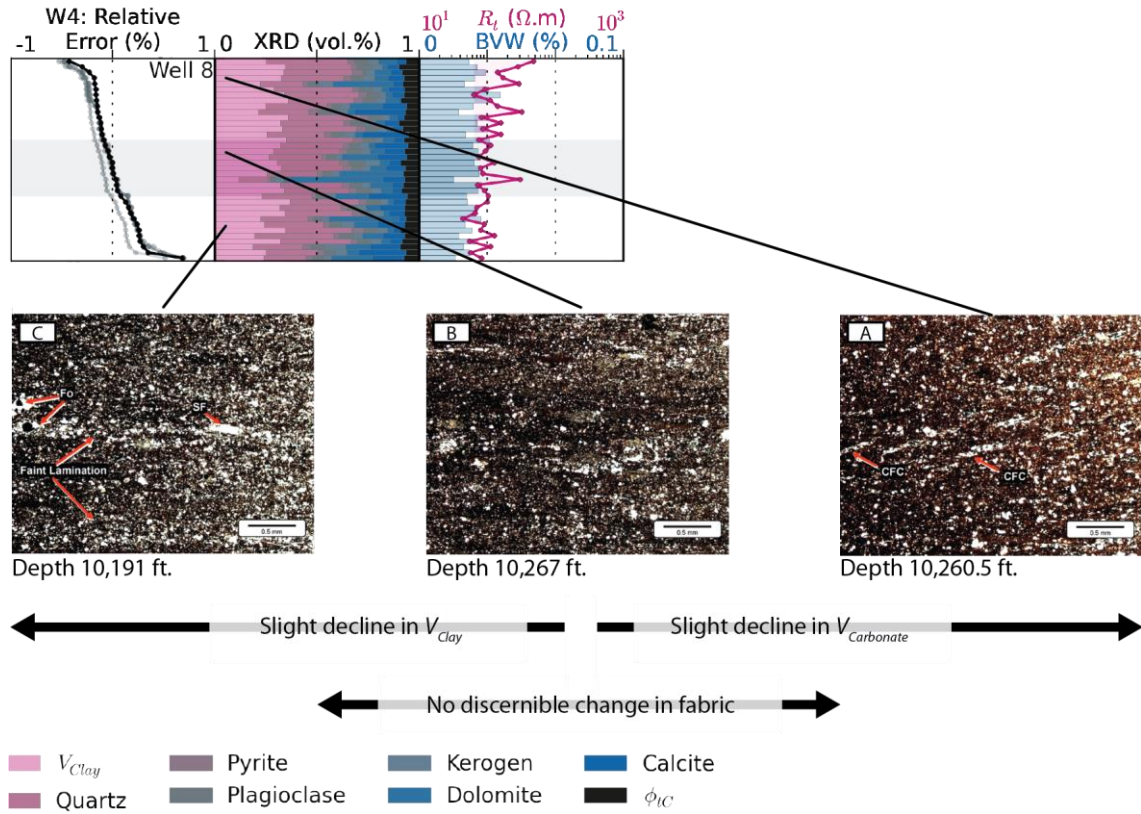


Figure 7.16. Thin section images: HY well 8

Exert of Figure 7.13 highlighting HY well 8, displaying changes in thin section fabric with RE and clay content. Note, slight variations in clay and carbonate with no discernablke change in fabric. Thin section photograph descriptions presented as taken from Core Laboratories: **(A)** Calcareous, micaceous, pyritic, quartzose (Q), silty shale with calcite-filled cracks (CFC). Carbonate particles include calcispheres (Csp). Predominant clay is illite. Calcite volume is 8.3%, dolomite volume is 7.1%, clay volume is 34.8%. **(B)** Calcareous, slightly burrow ed (Bu), faintly laminated, pyritic (Py), quartzose (Q), silty shale. Micas (Mi) are common. Burrows appear filled by dolomite crystals. Intergranular replacements (IR) are minor constituents. Predominant clay is illite. Microfractures are clearly visible in epifluorescent light. Calcite volume is 11%, dolomite volume is 7.2%, clay volume is 30.7%. **(C)** Calcareous, faintly laminated, pyritic, micaceous, quartzose, silty shale with carbonate particles, and undifferentiated plates (UP). Skeletal fragments (SF) and Foraminifers (Fo) are common. Predominant clay is illite. Microfractures are clearly visible in epifluorescent light. Calcite volume is 14.6%, dolomite volume is 12.3%, clay volume is 25.9%.

5.4.3 Summary and conclusions

The petrophysical and mineralogical relationships discussed in Chapter 4 and sections 7.11 and 7.12 are summarised in Figure 7.13. This highlights consistency in BVW, R_t and V_{Clay} particularly in the BSR, though with similar subtle trends evident for much of the HY data (e.g. wells 1, 5, 6, 8, 12, 14). Comparison of thin section images reveals qualitative variation in fabric related to V_{Clay} in the BSR, but, as a result of subtle mineralogical variations, no systematic change could be identified in the HY. This qualitative review and comparison of thin section images with RE is however extremely limited in the absence of core material and the inability to observe wider variations in

sediment fabric. This highlights the obvious limitations and a miss-match in scales where attempting to compare log data (with a vertical resolution of $\sim 30\text{cm}$), with core data (which utilises $\sim 1\text{-}2\text{ cm}$ core plug) and thin section images (where only 12mm^2 of core material can be viewed). As a consequence of data limitations, the interplay of depositional processes, resultant sediment fabric and associated petrophysical properties cannot be adequately evaluated. Despite this however, it is clear, particularly in the BSR, that clastic dilution (increased V_{Clay}) is linked to elevated BVW and R_t , greater sediment anisotropy and burrow intensity. This latter point, increased burrow intensity, is discussed in section 2.13, where in other formations burrowed fabrics are found to form permeable burrow networks. This contradicts BSR data, and the association of very low k values, high V_{Clay} and burrowed fabrics in the BSR. One possible explanation is that burrowed fabrics, at some early stage of burial, did contribute to higher permeability, and perhaps enabled fluid migration and escape. This would provide a mechanism for the expulsion of unrequired ions and double layer water as discussed in section 7.12.3, allowing for pore water freshening in high V_{Clay} regions where the majority fluid is CBW. Following fluid expulsion, the permeable burrow network, may then have been progressively clogged by authigenic chlorite mineral growth. This is supported by the positive association between $V_{Chlorite}$, V_{Clay} , k , and an increased incidence of burrowed fabrics. Moreover, authigenic chlorite formation can occur during, and is linked to the later, higher temperature/pressure, stages of the smectite-illite transition at (e.g. Burton, 1987; Davarcioglu, 2012). $V_{Chlorite}$ distribution is however unknown, though the availability of core for thin section and SEM analysis, particularly of burrowed clay rich fabrics, would be helpful in strengthening this hypothesis. In any case, it is demonstrable, that formation mineralogy and associated fabric can be linked to accompanying petrophysical properties and consistent trends in optimised Archie parameters.

5.5 Predicted pseudo-Archie parameters

The average pseudo-Archie parameters predicted by the optimiser models (H1 and W1-W4) and associated core modelled parameters are summarised below in Table 7.2 and in Figure 4.8. It has been demonstrated that the parameter trends of all the generated Archie parameters can be geologically rationalised within the context of the preceding discussion; $BVW/V_{clay}/R_t$ relationships and formation petrophysical heterogeneity. The following section compares the predicted parameters with those generated by other studies and discusses the manipulation of some parameters noted in the sensitivity analysis and parameter trade-offs.

<i>Optimised parameters</i>						
	<i>BSR</i>			<i>HY</i>		
	<i>m</i>	<i>n</i>	<i>R_{we} (Ω.m)</i>	<i>M</i>	<i>n</i>	<i>R_{we} (Ω.m)</i>
W1			0.0277 ± 0.0183			0.00784 ± 0.00298
W2	2.18 ± 0.23	*		1.82 ± 0.09	*	
W3	2.45 ± 0.24	*	0.0061 ± 0.0001	2.02 ± 0.13	*	0.00710 ± 0.00248
W4	1.79 ± 0.41	3.86 ± 0.31	0.0332 ± 0.0385	1.24 ± 0.31	3.39 ± 0.68	0.01177 ± 0.01375

<i>Core modelled parameters</i>						
	<i>BSR</i>			<i>HY</i>		
	<i>m</i>	<i>n</i>	<i>R_{we} (Ω.m)</i>	<i>M</i>	<i>n</i>	<i>R_{we} (Ω.m)</i>
W1			0.0546 ± 0.0871			0.00943 ± 0.00935
W2	2.28 ± 0.34	*		1.84 ± 0.16	*	
W3	2.17 ± 0.45	*	0.0286 ± 0.0260	1.75 ± 0.27	*	0.02874 ± 0.02603
W4	1.98 ± 0.58	2.79 ± 0.83	0.0327 ± 0.0267	1.48 ± 0.39	2.42 ± 0.78	0.02459 ± 0.02165

Note: * refers to m^* and $m=n$

Table 7.2. Mean predicted Archie parameters ± standard deviation

5.5.1 Comparison with previous works

As discussed in section 4.2 and displayed in Table 7.2, the generated parameters are consistently higher in the BSR than in the HY. In addition, the parameters generally decrease with increasing parameter freedom from model W1 to W4, with a corresponding increase in their variation. For instance, the average BSR core modelled parameter m for model W4 is lower (1.98), but has a higher standard deviation (0.58)

than m^* for W3 (2.14 ± 0.45). In general however, these figures fall within the ranges discussed in section 2.4.2 and compare well with the limited literature resources available on the subject.

In particular, the m^* values produced for all HY models compare well with those presented by Luffel et al., (1992), who assumes $m=n$ (m^*) for core Dean Stark S_w estimates in Devonian Shales and found $m=n=1.7$. It should be noted that the Devonian Shales included within the study are more comparable in petrophysical/mineralogical terms to the HY than the BSR. Kruschwitz and Yaramanci, (2004) found fitted m and n values for electrical measurements made on dried and re-saturated samples of Opalinus clay from Mont Terry, Switzerland where $m=1.29$ to 1.46 and $n=1.49$ to 1.93 . These figures agree well with the HY core modelled parameters for model W4, though it is noted that sample drying irrevocably alters the pore space (Jougnot and Revil 2010). Similar findings on oven dried and partially re-saturated clay-rocks of the Callovo-Oxfordian Formation by Jougnot and Revil (2010) also found $m=1.37$ to 1.54 and $n=1.99$ to 2.16 , though they suggest that oven-drying results in the formation of micro-cracks that reduce m upon saturation. This assertion is supported by analyses by Revil (2005) and Jougnot et al., (2009) on the conductivity of undisturbed saturated clay-rocks from Callovo-Oxfordian Formation where fitted $m=1.95 \pm 0.04$ and $m=2.0$ respectively. Additional work on the Mancos Shale in eastern Utah by Leroy and Revil (2009), which has a similar carbonate content, but a higher clay content than the HY, found fitted values of $m=2.2$. Yu and Aguilera (2011) combined Pickett plots with empirical TOC relationships to find m values in the HY of between 1.45 to 1.85 , provided a , n and R_w are kept constant. These values are similar to most of the predicted W1-W4 predicted m and m^* values. In addition, a case study on formation evaluation in the HY by Ramirez et al., (2011) notes that Archie's equation with $m=n=1.9$ 'works well'. In summary, the range in m and n values reported in the literature largely agree with those presented in Table 7.2.

5.5.2 Optimiser models and parameter manipulation

5.5.2.1 One dimensional models (W1 and W2)

In investigating models W1 and W2, it is clear that the sensitivity of m^* (W2) is higher than R_{we} , such that W2 is a preferable optimisation tool providing improved *MAE* reduction. In addition, the variable and parameter relationships established can be reconciled by the mineralogical / petrophysical relationships established in section 5.3, and thus have a reasoned geological footing. Moreover, these relationships allow for the calculation of S_{wR} , and a significant reduction in *MAE* for the majority of wells where V_{Clay} is generally above 28%.

Within models W1 and W2 the only parameter that can be manipulated are the fixed parameter inputs R_{we} and m^* respectively. It is noted in Figure 4.12, that increasing either fixed parameter value shifts the range and alters the sensitivity of the optimised parameter.

5.5.2.2 Two dimensional models (W3)

The disparity in the sensitivity of *MAE* to changes in m^* and R_{we} established in W1 and W2 investigations is highlighted as a significant flaw when utilising model W3. Where the optimiser consistently favours reducing R_{we} to or very close to the minimum bound (0.006 $\Omega.m$). This occurs as a by-product of least error optimisation, where reducing R_{we} effectively reduces the sensitivity of m^* , increasing the m^* parameter range within which a least *MAE* solution can be selected. This is manifest by uniformly inclined R_{we} parameter distributions, yielding an increase in the number of low error solutions at low R_{we} values (Figure 0.8 and Figure 0.9). As a consequence, other than that R_{we} values are likely to be relatively low, no geological meaning can be attributed to R_{we} output. If prior information were available, and allowed for greater constraints to be placed on R_{we} bounds, it is still likely that the lower bound would always be selected. On this basis it considered more appropriate to fix R_{we} at a reasoned value, based on available information, or other selection methods. Despite this, the resultant m^* output is very similar to that of model W2 (Table 7.2) and reflects the same trends:

generally higher m^* values coupled with increased heterogeneity in BSR as related to clay volume and clay effects on formation resistivity (Figure 4.8).

The manipulation of R_{we} so as to alter the range and sensitivity of m^* has been demonstrated within the grid-search algorithm. There is however, limited literature available examining the optimisation of Archie exponents in conventional or unconventional formations. That said, a study by Chen et al., (1995) investigated the efficacy of the simplex method in optimising a , m and n for S_w prediction using benchmark core S_w (observed) data in sandstones. They find, that for some samples, optimised a could be quite high ($a=6.3$) or low ($a=0.6$), but did not necessarily yield a significant improvement in fit. In other words, a was determined to have a low sensitivity and thus fixed at unity for some samples. This draws some parallels with this study, where R_{we} , which assumes $a=1$, also demonstrates low sensitivity and is thus preferably manipulated so as to alter the range in the more sensitive m^* . Likewise studies of the uncertainty and error propagation within multiple shaly sand models by Mahgoub et al., (2008) also find R_w and a to be the least, and m and n to be the most sensitive parameters.

5.5.2.3 Three dimensional models (W4)

Similar to model W2, increased parameter freedom appears to result in more extensive parameter manipulation. Where, in addition to a reduction in R_{we} , n is also artificially inflated to further refine the selection of m . Thus parameter manipulation appears to occur in order of least sensitivity or R_{we} , n and m . This is particularly true in the BSR which displays a flat uniform distribution of R_{we} and inclined distribution of n , suggesting insensitivity to R_{we} and an increased number of low error solutions at high n values. Unlike optimised model data however, core modelled parameters in the HY exert greater preference and whilst the probability distributions for R_{we} remains flat, n peaks at ~ 2.25 and m at ~ 1.3 (Figure 0.16 and Figure 0.17). As discussed previously (section 7.14.1), these values are not without precedence in the literature, and would likely be higher if R_{we} were fixed at some value above the saline saturation limit (0.006 $\Omega.m$).

5.5.3 Summary and conclusions

The predicted pseudo-Archie parameters and their sensitivities agree with those presented in the literature. The data supports m and n values of less than 2 in the HY and values greater than or equal to 2 in the BSR. It is notable that the preceding discussion makes little mention of the predicted R_{we} values. This is in part due to uncertainty in the predicted parameter and its manipulation in models W2 and W3. R_{we} is therefore difficult to rationalise, such that preference is given to fixing R_{we} for a given formation zone. This is compounded by a lack of literature documenting BSR and HY R_{we} values. It is however possible to say that R_{we} is likely to be higher and more variable in the BSR than in the HY (Figure 4.13).

It is also demonstrated that whilst multi-dimensional models (W2, W3 and W4) may yield an improved fit, that they generate greater uncertainty in output parameters and thus hamper the prospect of their prediction based on geological interpretation. In kind, simplistic one-dimensional models (W1 & W2) are shown to generate more constrained parameter outputs that can be placed within a geological framework. In this instance, this has yielded empirical relationships (S_{wR}) that reduce residual MAE beyond the capability of 3D optimisation (W4) methods.

Chapter 6

Conclusions and recommendations for further work

The main aim of this project has been to improve our understanding of the application of Archie's equation in shale gas systems, linking formation attributes, such as mineralogy and fabric, to measured petrophysical properties and generated pseudo-Archie parameters. This chapter presents the main conclusions of this work and considers the original aims and objectives as presented in section 1.2. It is divided into a series of research questions that are discussed in turn, followed by a summary of additional findings, an overall summary of the main conclusions and suggestions for further work.

6.1 Research question I:

Premise: Variability in optimiser model output must be linked to the heterogeneity and inter-relationships of the petrophysical inputs (ϕ_{tC} , R_t , S_{wC}). In turn, the petrophysical inputs express the interaction and distribution of formation mineral and fluid components as determined by depositional and diagenetic processes.

Question: *How does variability in the error of S_w optimiser model outputs for Bossier (BSR) and Haynesville (HY) data link to the variability in formation mineralogical and petrophysical properties as represented within the wireline and core data? What are the principal geological controls on model accuracy?*

This was investigated by evaluating mineralogical and petrophysical variability and interrelationships as related to the variability in the residual mean absolute error (MAE) of optimiser model outputs. Findings indicate:

- The HY, though mineralogically heterogeneous, is relatively homogenous petrophysically, yielding low residual MAEs of between 1.03 to 5.59% and a restricted range of generated Archie parameters where m and n are typically below 2 (1.24 to 2.02). As a consequence of formation homogeneity, there is limited difference in MAE between the results of 1D and 3D optimiser models.
- The BSR, which is comparatively mineralogically homogenous, is markedly more heterogeneous petrophysically, with a larger residual MAE of 5.32 to 17.34% and a correspondingly wider range in generated Archie parameters, with m and n values typically above 2 (1.79 to 2.45). This petrophysical heterogeneity is reflected by a marked decrease in MAE with increases in optimiser model dimensionality, i.e. model W4 is significantly more accurate than W1.
- Petrophysical heterogeneity in the BSR can be directly linked to high V_{clay} and in particular the chlorite clay fraction, which is associated with a generally higher, though more variable resistivity response. In other words, results suggest that greater quantities of clay contribute to electrical variability and a typically 'excess resistivity,' not an 'excess conductivity' as might be conventionally expected. The

heteroskedastic relationship and increased variance in R_t at high V_{Clay} is likely to reflect varying distribution and interaction of clay minerals with the pore space and thus electrical properties. As a consequence, despite highly variable fluid distribution characteristics (BVW and S_{wC}) it is the effect of clay minerals in generating a variable resistivity response that in turn generates a large variation in model MAE and Archie parameter outputs. This is evident, in that the generated Archie parameters for the BSR typically demonstrate a positive linear relationship with R_t for all optimisation models considered. In addition, it explains why the S_{wR} regression method is more accurate than least error optimisation, as it allows Archie parameters to be selected with greater fidelity, where they can be modulated by and vary in accordance with R_t . Thus V_{Clay} , and not mineralogical heterogeneity, is the primary control on petrophysical variability and optimiser model accuracy. Where, if porosity-fluid relationships are the primary mechanism determining formation electrical properties, then the effects of clay minerals and thus R_{we} , m and n parameters must be extremely variable.

6.2 Research question II:

Premise: The modelled results are based on a modified Archie's equation (equation 4.1), for which the principal underlying petrophysical mechanism is the negative relationship between the volume of the saturating electrolyte and formation resistivity (Archie, 1942). Clay minerals are known to affect this relationship by reducing the resistivity, or inversely, by providing a source of excess conductivity (Hill and Milburn, 1956; Patnode and Wyllie, 1950; Winsauer and McCardell, 1953; Wyllie and Southwick, 1954). If uncorrected, this can overestimate S_w and contribute to an undervaluation of the reservoir.

Question: *How does core data for clay volume and the volume of the saturating electrolyte (BVW) relate to measured R_t , what is the geological basis for these relationships, and are they reflected by predicted Archie parameters values (m , n and R_w)?*

This was approached by investigating petrophysical relationships related to the clay mineral fractions in combination with a review of published literature trends and Archie parameters generated using log and core data. This confirms that high V_{Clay} core samples are consistently associated with greater ϕ_{tC} , BVW , R_t and lower k , particularly in the BSR. Whilst it is not surprising that clay dominated samples contain a high proportion of water, with low permeability, their link to increased formation resistivity is in stark contrast with conventional wisdom. A geologically consistent mechanism is proposed to explain the noted anomalous increase in R_t with V_{Clay} :

- A system of pore water freshening (increase in R_{we}) in clay rich regions resulting from pore water and ion expulsion linked to compaction, diagenesis (smectite-illite transition) and associated reduction in clay CEC, with fluid mobility aided in earlier stages of burial by permeable burrow networks prior to later authigenic mineral (primarily chlorite) growth and reduced permeability. In addition, latter stages of authigenic mineral growth may also result in an increase in pore geometrical complexity and m and n .

This proposed model explains the observed petrophysical heterogeneity and anomalously high BSR resistivities. Moreover, it serves to divide a continuum of HY and BSR data into two distinct, 'Archie like' and 'non-Archie like' petrophysical regimes:

- **Non-Archie like (largely BSR data):** Dominated by CBW with non-clay bound fluid as a secondary contributor to BVW . Pore fluids freshen (increase in R_{we}) with increasing clay content. As the non-clay bound water volume is a secondary contributor to BVW , the addition of CBW conduction pathways, and associated decreases in m , are limited. Moreover, the increased presence of chlorite and associated reductions in ϕ_{tC} and k further reduce the influence of non-clay bound fluids at higher V_{Clay} values and result in increases in m above 2.
- **Archie like (largely HY data):** Dominated by non-clay bound fluid, CBW is a secondary contributor to BVW . This manifests in more homogenous R_{we} values and limited freshening of pore fluids with increasing clay content. As the non-clay bound water is the bulk contributor to BVW , the addition of CBW electrical conduction pathways results in reductions in m below 2, aided by higher ϕ_{tC} and k values.

The boundary between the two petrophysical regimes is shown to fall qualitatively at approximately 28% V_{Clay} (Figure 7.12). Above this limit (predominantly in the BSR), it is suggested that clay and chlorite volumes and clay dilution effects act to increase R_{we} , m and n . This is supported by the empirical relationship for calculating S_{wR} , which increases the accuracy of S_w estimates by modifying either R_{we} or m^* as regressed from R_t relationships in wells where V_{Clay} is typically above 28% (Figure 0.2). Below 28% V_{Clay} , the predominantly HY data are more Archie-like in their behaviour, more homogenous petrophysically, and have lower R_{we} , m and n values.

6.3 Research question III:

Premise: The efficacy of a core calibrated optimised Archie approach and thus the geological validity of the Archie parameter values generated, has not been tested and the geological interpretation of these values have not been explored in shale gas systems.

Question: *What are the mechanics of an optimised Archie approach, what controls the value of generated Archie parameters, what can we infer of their validity from sensitivity analyses and parameter trade-offs, and how do modelled Archie parameter values compare with those predicted by other studies?*

This was approached by evaluating the output of the optimisation models and examining the change in MAE with variations in parameter values. This highlighted the following:

- In examining 1D optimisation models W1 and W2, MAE is shown to be more sensitive to changes in m^* than R_{we} , such that W2 and optimising m^* provides greater potential for MAE reduction. Moreover, models W1 and W2 reveal a linear empirical relationship between the optimised parameter and R_t , which allows for the calculation of S_{wR} , and a further improvement in the accuracy of S_w estimates.
- The 2D optimisation model, W3, is shown to consistently bias the parameter outputs, where R_{we} is generally minimised so as to modify the sensitivity and

parameter value range of m^* to a preferable least *MAE* solution. As such, limited geological meaning can be attributed to generated R_{we} values within model W3.

- The 3D optimisation model, W4, is shown to consistently bias parameter outputs, where, in addition to a reduction in R_{we} , n is artificially inflated so as to further refine the selection of m . Thus parameter manipulation appears to occur in order of least sensitivity or R_{we} , n and m . This is particularly true of the BSR, where the generated parameters can be ascribed limited geological meaning. Though in the HY, whilst generated R_{we} values remain questionable, the distributions for n and m peak at ~ 2.25 and ~ 1.3 respectively. Interestingly m and n appear to have different roles in the BSR and HY which are consistent with formation petrophysical properties:
 - The BSR, which generally has low gas saturations and high V_{clay} and CBW volume, demonstrates an inclined uniform n distribution and appears reliant on optimising m .
 - The HY, which has relatively high gas saturations, has very low and constrained m values, and appears reliant on optimising n .

Across all optimisation models, the generated parameters typically form a linear relationship with R_t , particularly in the BSR, suggesting that *BVW* and thus traditional Archie relationships are of limited importance in forcing parameter selection.

In general, the predicted pseudo-Archie parameters and their sensitivities agree with those presented in the literature. The data supports m and n values of less than 2 in the HY and values greater than or equal to 2 in the BSR. By contrast, R_{we} , which is systematically biased by optimisation models W2, W3 and W4 so as to preferentially adjust m and n parameter values, cannot be geologically rationalised. Indeed, where using optimisation models, it may be preferable to fix R_{we} for a given formation zone. This is compounded by a lack of literature documenting BSR and HY R_{we} values. It is however, possible to say that R_{we} is likely to be higher and more variable in the BSR than in the HY (Figure 4.13).

It is also demonstrated that whilst multi-dimensional models (W2, W3 and W4) may yield an improved fit over arbitrary Archie exponent value selection, they generate

greater uncertainty in output parameters and thus hamper the prospect of their prediction based on geological interpretation. In kind, simplistic one-dimensional models (W1 & W2) are shown to generate more constrained parameter outputs that can be placed within a geological framework. In this instance, this has demonstrated empirical relationships (S_{wR}) that reduce residual MAE beyond the capability of optimisation methods.

6.4 Research applications

The findings of this work present no complete solution to the conundrum that is the application of Archie based saturation equations to shale gas systems in the exploration and production sector. They do however highlight the potential for complex least error multi parameter optimisers (a commonly used industry method) to contain significant model error, and so produce Archie parameters with little geological meaning. Findings also highlight that whilst optimisation models that solve for only a single Archie parameter have relatively high MAE 's (i.e. they generate a poor fit between core and calculated S_w values), they produce useful and potentially geologically meaningful empirical relationships. Moreover, the combined application of 1D solver models with the resulting empirical relationships are shown to be more effective in reducing MAE than higher dimensional solvers. These empirical observations support additional findings revealed in exploring the interrelationship between clay volume and resistivity that run contrary to the currently accepted doctrine. Where, as opposed to adding 'extra' conductivity, clay minerals are shown to add 'extra' resistivity in the Bossier and Haynesville shales when clay volume exceeds 28%. This highlights both the need for extra caution in applying solver models and the need to further our understanding of the role of clay minerals in contributing to formation resistivity.

6.5 Additional findings

- Well data indicate (Figure 3.12 and Figure 3.13) a predominantly northern to north westerly origin of clastic sediments. This contrasts a north-eastern origin linked to the ancestral Mississippi River delta suggested by Hammes and Frébourg (2012). It is however recognised that Hammes and Frébourg (2012) utilised a far larger data set covering a wider region. It is therefore possible that data within this study identifies localised trends in sediment provenance within a region dominated by sediment sourced to the north and east.
- Empirical models developed in a near identical region of the BSR-HY for the prediction of TOC based on W_{pyrite} are noted to be highly inaccurate and no consistent link between pyrite and organic matter is observed. This highlights either laboratory or reservoir inconsistencies that renders the application of empirical models problematic, at least at the local level.
- Analysis indicates $\rho_{Kerogen}$ values for the BSR and HY data of between 1.23 to 1.77 g/cc. This range is far higher than the constant value of $\rho_{Kerogen}=1.17$ g/cc thought to be used by Core Laboratories. This is likely to result in an overestimation of $V_{Kerogen}$ by approximately 20% when converting from wt. to vol. %, causing the remaining mineral volumes to be subtly overestimated.

6.6 Summary

- Optimisation models can be used with good effect in calculating S_w , though the greater the freedom of the optimisation model, the greater the likelihood that Archie parameters produced are biased, limiting their geological interpretation.
- One dimensional optimisation models are less accurate in calculating S_w , but reveal empirical relationships which are demonstrated to increase the accuracy of S_w estimates beyond the capability of higher dimensional optimisation models.
- Optimiser generated Archie parameters often have linear relationships with formation R_t , but not BVW in the BSR. This indicates that formation fluids (BVW) in the BSR play a reduced role in controlling the formation R_t response. By contrast,

the HY is more Archie-like with a typically negative linear relationship between BVW and R_t .

- Though mineralogically heterogeneous, the HY is relatively homogenous petrophysically. This is reflected by a typically narrow range in generated Archie parameters.
- Though relatively homogenous mineralogically, the BSR is relatively heterogeneous petrophysically. This is reflected by a wider, more varied range in generated Archie parameters.
- Increased resistivity and variability in the resistivity responses are shown to correlate linearly with residual MAE in the BSR.
- In contrast to typical relationships, clay content, particularly the chlorite fraction, is linked to an increase in R_t , and an increase in the heterogeneity of the R_t response.
- It is proposed that that the anomalously high BSR resistivity response could be accounted for burial diagenesis driven ion expulsion and bound water freshening, particularly in clay rich bioturbated regions, in combination with authigenic chlorite mineral growth and increased pore complexity. In general, it is suggested that the salinity of clay rich mudstone should be less than that of associated clay poor, more permeable mudstone.

6.7 Recommendations for further work

There are numerous avenues available for further work in investigating the relationships between formation fabric, mineralogy, geochemistry and petrophysical properties, particularly in regards to formation electrical properties of shale gas systems.

Access to core with additional core analysis, specifically XRD and clay mineralogy, calculated CEC, or core measured CEC values, would help validate the suggestion that fluid resistivity may contribute to increased resistivity in clay rich areas. Moreover, analysis of variations in formation fabric in areas of contrasting resistivity response in the BSR would help determine the role of clay mineral distribution and formation fabric in determining formation electrical properties. Specifically, thin section studies of BSR bioturbated fabric could confirm the qualitative association made in this study between bioturbation and authigenic clay mineral growth, particularly chlorite.

Core material in shale plays, particularly in relatively thin productive successions such as the HY, are often fully cored. Multi-sensor core logging of newly retrieved core, with particular reference to infrared spectrophotometry, which measures light reflection and transmission properties of a material to identify mineral constituents, can be measured with a high sampling rate (less than 1cm). In conjunction with additional MSCL tools such as X-Ray fluorescence, and core sampling and XRD analysis, a robust and high resolution mineralogy log could be created. This would serve a number of purposes, firstly as a means to calibrate and validate log multi-mineral solver tools, but also in evaluating the links between changes in mineralogy with observable differences in formation fabric and any inherent systematic patterns or cyclicity that may fall within a sequence stratigraphic framework. Integration with typically available wireline data would help determine mineralogical and fabric effects on upscaled log characteristics, but also lend greater predictive capability in nearby wells that share similar log characteristics in the absence of detailed core data.

Within this study, it is suggested that due to ion exclusion, that clay rich shales should have a lower salinity than adjacent clay poor shales, which have a greater proportion of non-clay bound water. Moreover, it is suggested that, in more plastic clay rich regions which lack grain support, the bound water between clay grains will be at a hydrostatic minimum, whereas bound water affiliated with similar clays but supported by granular material may retain more water. On this basis, the volume of clay bound water and fluid salinity should be a function of composition and fabric. A study utilising thermo gravimetric analysis of regions of contrasting fabric and mineralogy within shale, provided it is possible to distinguish between clay bound and non-clay bound fluids, would be useful in indicating the variability in fluid characteristics and heterogeneity associated with fabric and mineralogy.

Within this study, the Archie type equation used draws parallels with Archie's original equation and the Dual water and Waxman Smitt methods. A wider sensitivity analysis encompassing other popular saturation equations, such as Simandoux and Indonesian methods, including recently proposed models by Herrick and Kennedy (2009) and Iheanacho (2013), would further aid the informed selection and choice of appropriate saturation models in shale systems. Moreover, these analyses could be applied to a wider range of shale sequences, so as to further link Archie parameter behaviour to changes in formation geological properties.

Appendices

Appendix A

GRI method laboratory protocol

LABORATORY PROCEDURES

Sample Preparation

Approximately 300g of sample is removed from each preserved core section by making a longitudinal slice with a band saw, using chilled nitrogen as the blade lubricant. Each sample is weighed to $\pm 0.001\text{g}$ and the bulk volume by mercury immersion is measured to $\pm 0.01\text{cc}$. These initial measurements are performed to determine natural sample density (Bulk Density). The samples are then wrapped in saran and placed in sealed vials pending further sample preparation.

Each 300g sample is processed using a mechanical rock crusher and sieved through 20 and 35 US mesh sieve screens. The material retained on the 35-mesh screen is separated into a Dean Stark sub-sample (~100g) and a permeability sub-sample (~50g). These procedures are performed while minimizing exposure time and evaporative losses. These sample splits are sealed in airtight vials pending further analysis. Any sample remnants are collected and maintained in airtight vials as well.

Measurements

Matrix Permeability:

Matrix permeability is determined by monitoring pressure decay as defined in the "Advances in Shale Analyses Report, D.L. Luffel, 1993 ". The permeability sub-sample is placed into a sealed sample chamber and approximate 30 cc of helium gas at ~200 psig is injected into the sample chamber system. Pressure decay is recorded in 0.25 sec increments to a maximum time of 4000 sec. Pressure versus time data are used to calculate matrix permeability.

Fluid Saturations – Dean Stark Technique:

Reagent grade toluene is conditioned to remove excess water and used for the extraction. The Dean Stark sub-samples are placed in glass thimbles to eliminate grain loss and weighed to $\pm 0.001\text{g}$. The samples are loaded into the Dean-Stark apparatus under an argon bath and refluxed for 8 days. Water volumes are recorded twice daily to ensure complete water extraction. The extraction solvent discoloration is noted to validate removal of trace quantities of mobile hydrocarbon.

Sample Drying:

Samples are dried in a vacuum oven at 110°C until weight equilibrium is achieved ($\pm 0.001\text{ g}$). The minimum drying time is 1 week. After weight stabilization, samples are stored in a desiccator pending further analysis.

Porosity and Grain Density:

Porosity is determined by measuring grain volume at ambient conditions using the Boyle's Law double-cell technique with helium as the expansion gas (API RP-40, Sec 5.3.2.1). Sample bulk volume is calculated using the weight of the sample before extraction and the bulk density of the original core piece. Grain density values are calculated by direct measurement of grain volume and weight on dried crushed samples.

Appendix B

Grid search optimiser: example Python
code for optimiser model W4

W4.Grid.Search (example).py 1Printed on 28/05/2014, 14:45:13 1Page 1

```

1 import csv
2 from numpy import genfromtxt
3 from numpy import savetxt
4 from numpy import array
5 import numpy as np
6
7 def grid_search(step,Formation,Label):
8     #data input
9     my data = genfromtxt('data.file.csv', delimiter=',', skip header=2)
10    #output data
11    outfile0 = csv.writer(open('W4.GS '+Label+'.OUT.csv', 'ab'))
12    outfile0.writerow(['well/F','m','n','Rwe','Swcalc','Sqdiff','RMSE','MAE','Ndata'])
13    outfile1 = csv.writer(open('W4.GS '+Label+'.OPT.csv', 'ab'))
14    outfile1.writerow(['well/F','m','n','Rwe','Swcalc','Sqdiff','RMSE','MAE','Ndata'])
15    #Variable Range
16    Mmin, Mmax, Mstep = 1, 3.1, step #Porosity Exponent M
17    Nmin, Nmax, Nstep = 1, 4.1, step #Saturation Exponent N
18    RWmin, RWmax, RWlogstep = 0.006, 0.1, step #Fluid Resistivity Rw
19    #Element input positions in input CSV file
20    #RT: deep resistivity, PHIT: tcore otal porosity, Sw Core: core water saturation
21    RT, PHIT, SW Core = 20, 22, 32
22    #Create list of wells in input file (two formation options: 1=Bossier, 2=Hayneville)
23    Ref=np.unique([i[2] for i in my_data if i[1] == Formation])
24    #Cycle through well (Ref) list for selected formation
25    for R in Ref:
26        MAE_opt = 1
27        #Cycle through the range of M
28        M = Mmin
29        while M < Mmax:
30            #Cycle through the range of N
31            N = Nmin
32            while N < Nmax:
33                #Cycle through the range of Rw
34                RW = np.log10(RWmin)
35                while RW < np.log10(RWmax):
36                    AE,Sqdiff_culm,Ndata = 0,0,0
37                    for i in my data:
38                        if i[2] == R:
39                            #Calculate Archie SW (SWcalc)
40                            SWcalc = np.power(((np.power(10,RW))/
41                                (np.power(i[PHIT]/100,M) * i[RT])),(1/N))
42                            #Count the data
43                            Ndata += 1
44                            #Add up the squared difference
45                            Sqdiff = np.power( (SWcalc - i[SW Core]), 2)
46                            #Cumulative error
47                            Sqdiff_culm += Sqdiff
48                            AE += np.sqrt(Sqdiff)
49                            #Calculate the root mean square error(RMSE)
50                            RMSE = np.sqrt(Sqdiff_culm/Ndata)
51                            #Calculate the absolute mean error(MAE)
52                            MAE = AE/Ndata
53                            #output optimum value only
54                            if MAE <= MAE_opt:
55                                MAE_opt=MAE
56                                OPTOUT = array([i[2],M , N, np.power(10,RW), SWcalc,
57                                    Sqdiff, RMSE, MAE, Ndata])
58                            #output all other values if error less than 100%
59                            if 0 < RMSE < 1 or 0 < MAE < 1:
60                                Vals = array([i[2],M , N, np.power(10,RW), SWcalc,
61                                    Sqdiff, RMSE, MAE, Ndata])
62                                outfile0.writerow(Vals)
63                            #close loops
64                                RW += RWlogstep
65                                N += Nstep
66                                M += Mstep
67                                outfile1.writerow(OPTOUT)
68    #function call: specify:#1:define step value,#2:formation,#3:file label
69    grid_search(0.01,1,'OUT')

```

G:\PHD15.THESIS\Chapter 4\Data_CSvsW4.Grid.Search (example).py JFile date: 28/05/2014 JFile time: 14:45:04

Appendix C

Multi-sensory core logger: a summary of work undertaken

Core material for well 11 was made available by BG Group for a period of 6 months in 2011. The cored section spanned the entire depth of the Haynesville Formation, equivalent to 18.63 meters or 61.1220 ft in well 11. The core was photographed and examined using a multi-sensor core logger (MSCL) provided by Geotek and sampled at selected locations for thin section analysis. The MSCL tool included an infrared spectrophotometer, magnetic susceptibility tool non-contact resistivity, density and natural gamma ray detectors, with measurements taken at intervals of between 1 and 5cm. The core had however been stored in an open uncontrolled environment at room temperature in typical UK office conditions. During this time, significant moisture loss and drying, in combination with vibration and movement linked to repeated transport between laboratory and office environments, is likely to have contributed significantly to the degradation of core quality. As a consequence the data generated by the MSCL tool was significantly impaired. This arose principally from the drying and movement related 'biscuiting' of friable core material, where biscuiting refers to the separation of largely continuous core material along bedding and cleavage planes to form numerous disk or biscuit shaped core sections. The sections of core therefore comprised many

hundreds of biscuit fragments, with each containing many more incomplete bedding/cleavage partings. The void space between core fragments and incomplete partings affects the density, magnetic susceptibility and natural gamma response, causing significant noise that negatively impacts tool response and cannot be easily corrected. Moreover, the MSCL resistivity tool is designed for saturated material, where core biscuiting and desiccation will likely significantly impact tool response, as such the tool could not be adequately calibrated and only a relative resistivity output could be generated. The infrared spectrophotometry tool, which is likely the most reliable data generated, requires specialist software for which funding was not available. As a consequence of these data quality issues, the investigation of the data was not pursued.

For further information and access to core MSCL data please contact Professor Mike Lovell at the University of Leicester (mike.lovell@le.ac.uk)

Appendix D

Example petrophysical workflow

Example petrophysical workflow

Below is an example petrophysical workflow after Bust et al., 2011. This highlights the evaluation of water saturation as one of five components critical to determining the gas in place in shale systems.

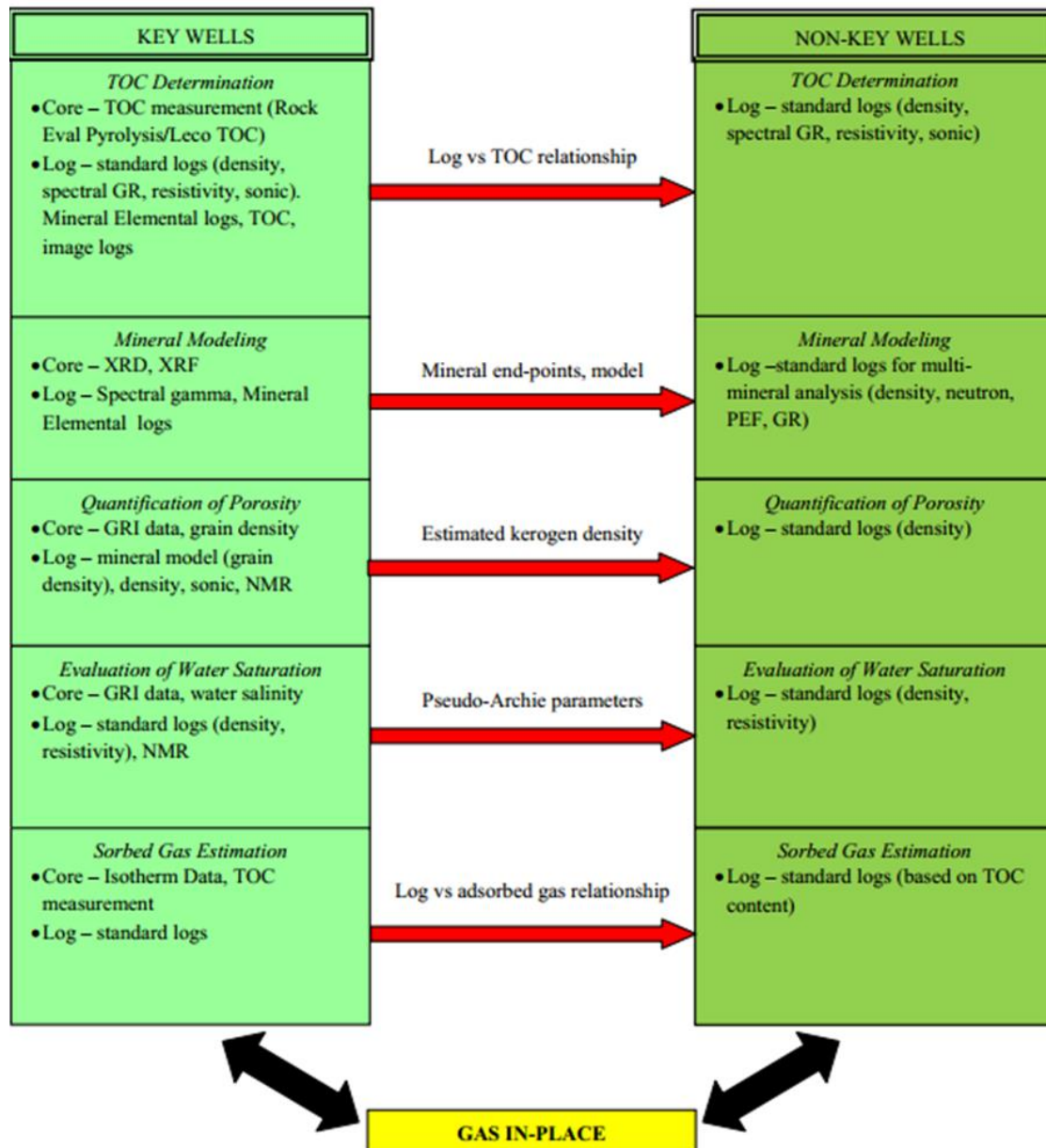


Figure D.1. Example petrophysical workflow. Firstly, this shows that S_{WA} (W4) is relatively accurate in the HY, and less so in the BSR as per Figure 4.4. Secondly, S_{WR} estimates demonstrate a marked improvement over S_{WA} (W4), particularly in the BSR, with little observable difference between S_{WR} and S_{WA} (W4) estimates in the HY.

Average MAE values for S_{WA} (W4) and S_{WR} are directly compared for each well in Figure 0.2, where it is clear that errors in S_{WR} estimates are significantly lower than those for

S_{WA} . This is particularly true of the BSR, with more subtle benefits in error reduction in the HY for the majority of wells.

The relative benefits in using S_{WR} over S_{WA} are presented in Figure 0.3, where S_{WR} estimates are shown to reduce mean MAE in 18 of 26 wells, or 69% of the time. In the BSR, 9 of 10 wells show a reduction in MAE of between 7% and 78%, whilst in the HY, 8 of 14 wells show a reduction in MAE of between 7% and 36%.

It should be noted however, that S_{WR} estimates are not universally effective in reducing MAE , having a marginally negative overall impact in some HY wells (Figure 0.3).

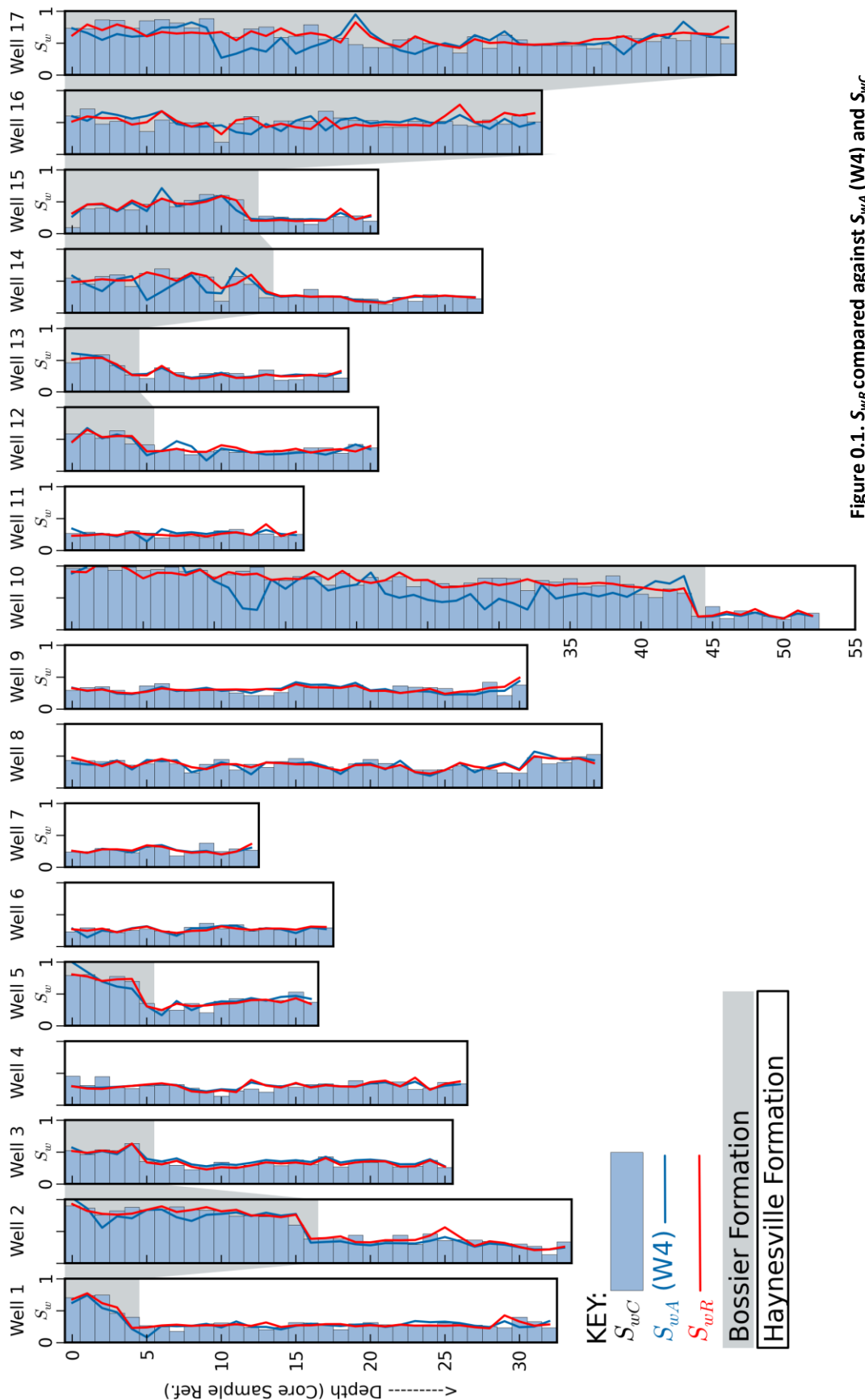


Figure 0.1. S_{wR} compared against S_{wA} (W4) and S_{wC}
 Log comparison of fractional S_{wC} , S_{wA} (W4) and S_{wR}
 values for BSR (grey) and HY (white).

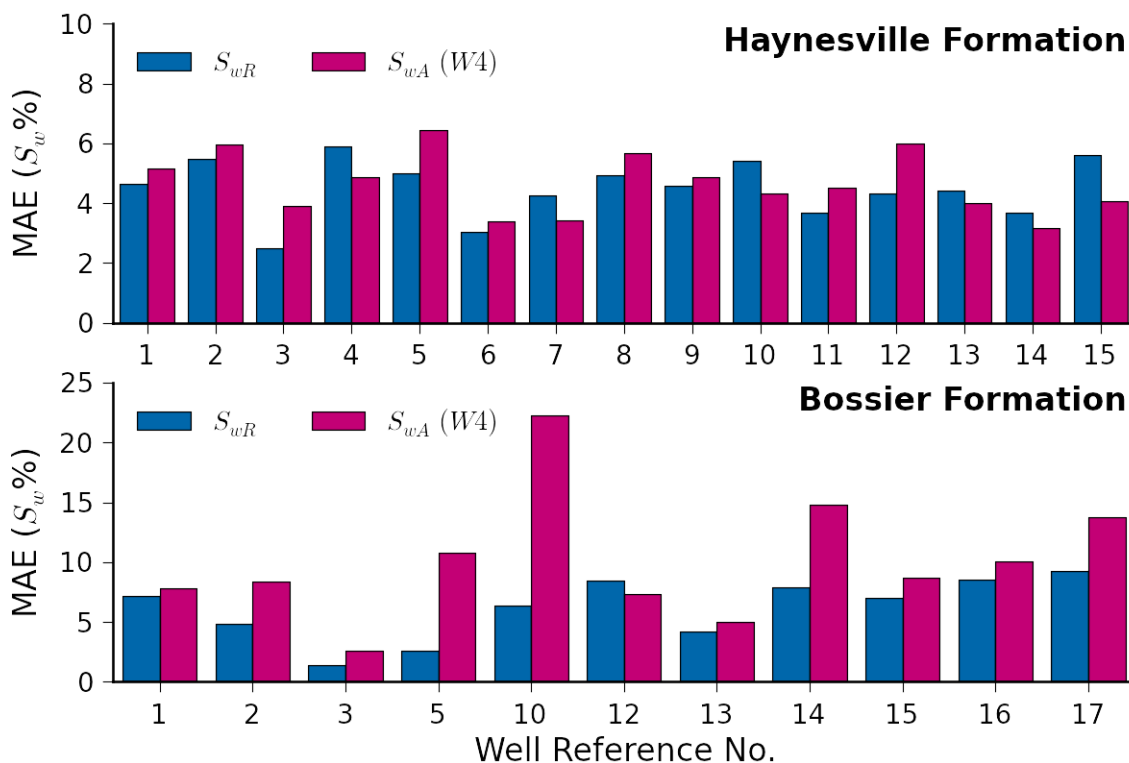


Figure 0.2. Comparison of MAE between S_{wA} (W4) and S_{wR}
 Comparison of MAE (S_w %) between S_{wA} (W4) and S_{wR} estimates.

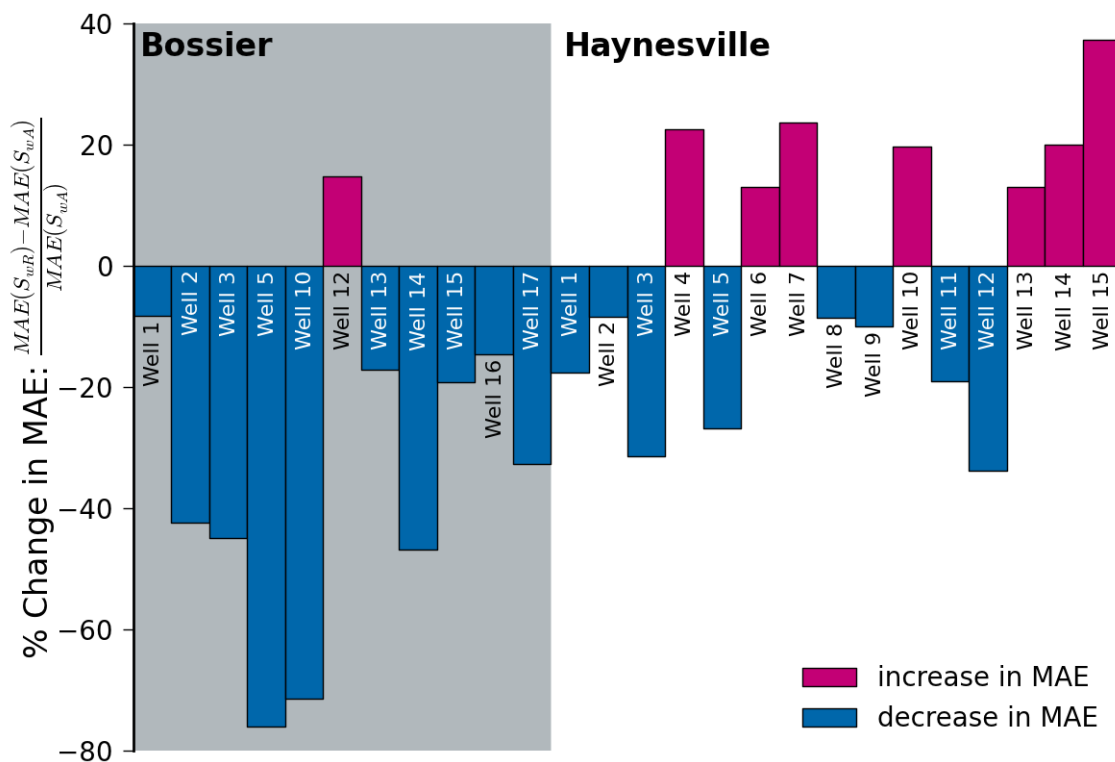


Figure 0.3. % Change in MAE when using S_{wR} as opposed to S_{wA} (W4)
 The % change in MAE when using S_{wR} as opposed to S_{wA} (W4) for the BSR and HY data.

6.7.1 Summary

6.7.1.1 Sensitivity analysis

- Residual *MAE* is more sensitive to changes in m^* than R_{we} (Figure 4.9).
- The HY displays relatively consistent and higher sensitivity profiles. In contrast the BSR data displays a wider variety of parameter values and sensitivities suggestive of a more petrophysically heterogeneous formation (Figure 4.9).

6.7.1.2 Parameter trade-offs

- It is suggested that the primary variable forcing parameter selection in both models W1 and W2 is R_t . This effect is shown to be more dominant in the BSR, where data indicates that sample *BVW* exerts lesser control on parameter forcing. By contrast, variation in HY *BVW* appears to exert a larger impact on optimised parameter values (Figure 4.10 and Figure 4.11).
- The effects of changing static model assumptions for W1 ($R_{we}=0.014$) and W2 ($m^*=2$) are demonstrated:
 - model W1; reducing m^* increases the sensitivity of R_{we} and shifts the *BVW* range away from the saline saturation limit,
 - model W2; reducing R_{we} slightly decreases the sensitivity of m^* , thus increasing the range of possible m^* values (Figure 4.12).

6.7.1.3 Core sample parameter modelling

- The HY displays relatively consistent and higher sensitivity profiles. In contrast the BSR data displays a wider variety of parameter values and sensitivities suggestive of a more petrophysically heterogeneous formation (Figure 4.9).
- Directly solving for parameter values suggests that the BSR is far less sensitive to variations in *BVW* than the HY (Figure 4.13).
- The correlation between R_t and the calculated parameter (m^* or R_{we}) allows for parameter prediction using standard regression analysis (Figure 4.13). For a large number of wells the resulting S_{wR} estimates demonstrate a significant

improvement over optimised S_{WA} (W4), with reductions in error as high as 78% in the BSR and 36% in the HY (**Error! Not a valid bookmark self-reference.**, Figure 0.2 and Figure 0.3).

6.8 Results: 2D parameter optimisation

This section details the analysis of the 2D optimisation model (W3) and aims to highlight the nature of any model limitations, parameter interactions, parameter forcing linked to geological/petrophysical properties, and any predictive capabilities the investigation of these relationships might reveal.

The following sections include:

- 4.5.4 The sensitivity of *MAE* across the range of possible parameter values.
- 4.5.5 The trade-offs between parameters and input variables in Archie's equation.
- 4.5.6 The range of parameters produced by direct optimisation for each core sample.

6.8.1 Sensitivity analysis

The sensitivity data for model W3 is displayed in Figure 0.4 and plots the change in *MAE* between S_{wA} and S_{wC} for every R_{we} and m^* parameter combination. Wells 3 and 10 are displayed as examples of characteristic BSR and HY relationships, highlighting a typical linear association between m^* and R_{we} . That m^* is a power function is also evident, such that *MAE* is more sensitive to increases rather than decreases in m^* from the optimum value. It also highlights, as in Figure 4.4, the tendency for R_{we} values to remain at or very near to the lowest bound. This is a compensatory effect, where reductions in R_{we} act to reduce the sensitivity of and thus expand the range of possible m^* values and so generate a preferred least error solution, though this reduction in parameter sensitivity is most likely linked to an increase in model error. In other words, high R_{we} increases the sensitivity of *MAE* to small changes in m^* . It should be noted that the reference to model error refers to the least error optimisation modelling approach, not specific *MAE* values.

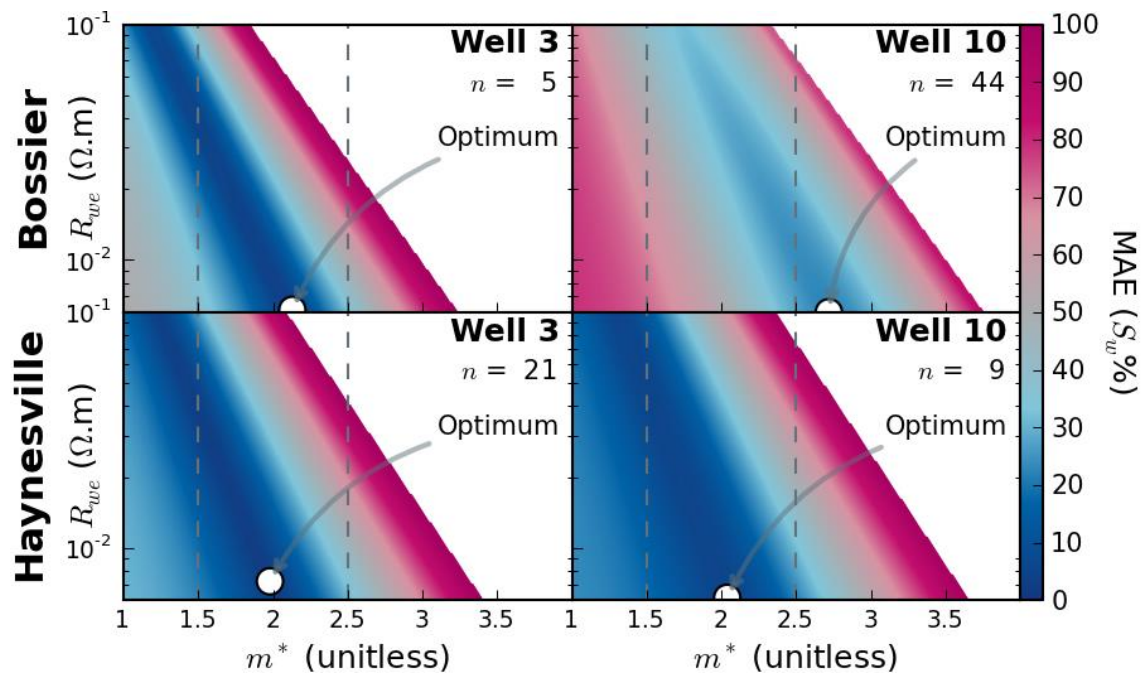


Figure 0.4. Sensitivity analysis (Model W3)

MAE sensitivity plot for model W3: R_{we} vs. m^ for the BSR (top) and HY (bottom). Two representative wells are displayed for each formation. The optimum values (white marker), corresponds with the least MAE, n refers to the number of samples within the optimised well. Note the decrease in m^* sensitivity as R_{we} decreases.*

The R_{we} , m^* relationships discussed above (Figure 0.4) are summarised for all wells (1 to 17) in Figure 0.5. This displays the parameter distributions for the lowest 5% of MAE values for each well, highlighting the optimum parameter values associated with global least MAE. Here, the R_{we} distributions show an increase in the number of low error solutions available at low R_{we} values. In all but three instances (HY wells 2, 3 and 13) the optimal R_{we} value is at or very close to the lower bound.

The m^* distributions depicted in Figure 0.5, whilst showing variation in parameter range, show a consistent distribution style. As discussed, MAE is more sensitive to higher m^* as opposed to lower values (m^* is a power function), as such each distribution is skewed with fewer high error solutions available to the right of the modal value than to the left. It should also be noted that the optimal m^* value rarely coincides with, and usually occurs to the right of the modal value. Those instances where the optimal m^* is to the left of the modal value also coincides with optimal R_{we} values that are above the lower bound (HY wells 2, 3 and 13).

Whilst these observations may reflect genuinely high fluid salinities (low R_{we}), it is clearly implied for the majority of wells, that optimiser model W3 simply minimises R_{we}

so as to refine m^* value selection, thus rendering the optimised values highly questionable in physical terms. The only exceptions to this trend are for HY wells 2, 3 and 13, whose optimal parameters may be of greater geological/physical significance.

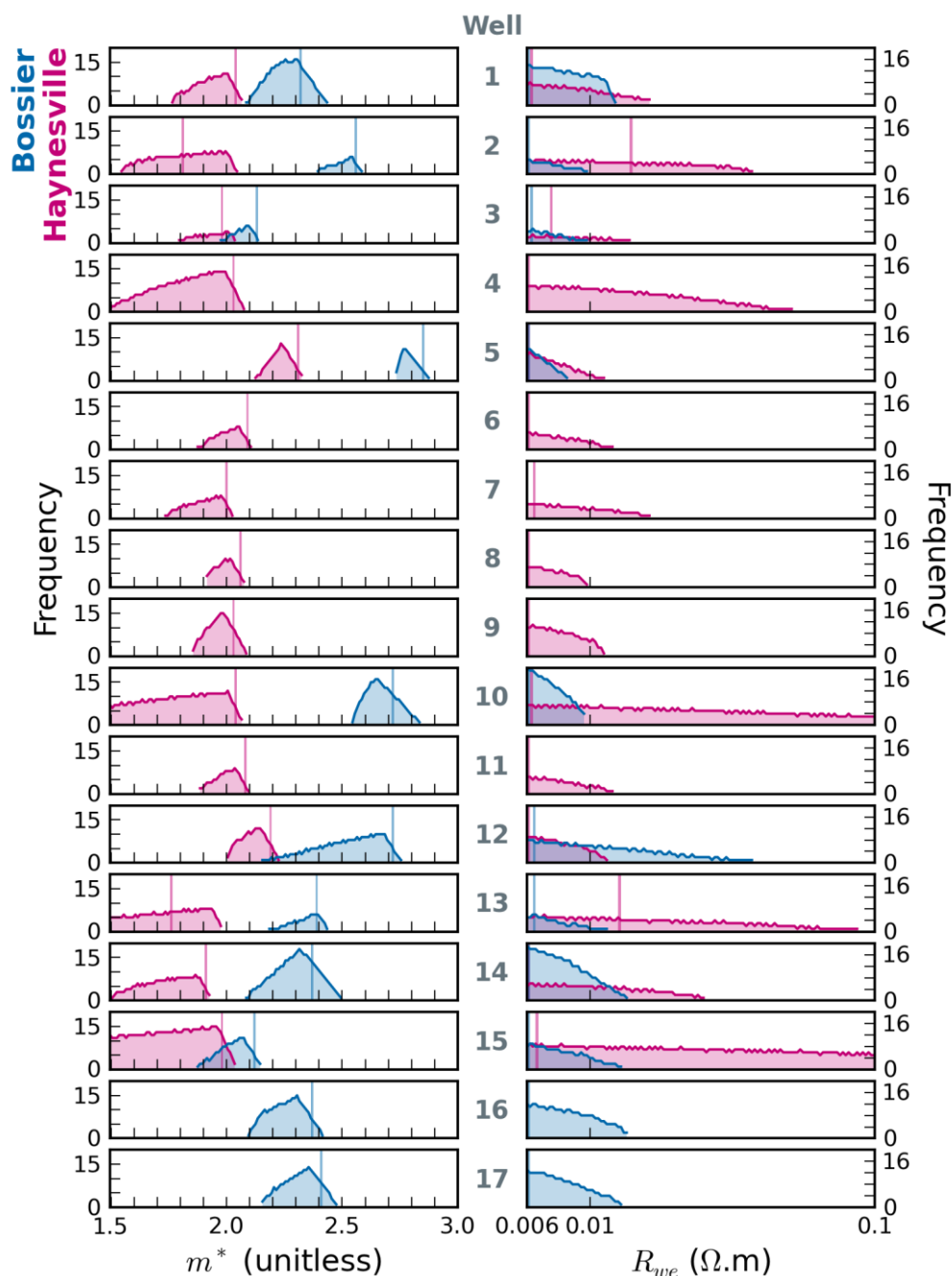


Figure 0.5. Parameter distributions, sensitivity analysis (model W3)

Plot of BSR (blue) HY (red) model W3 parameter distributions for the lowest 5% of MAE values. The faded bars indicate the optimal parameter value for each well and formation.

6.8.2 Parameter trade-offs

The parameter trade-offs in optimiser model W3 were modelled using equation 4.9 in the same manner as those for model W2. The approach was however modified to reflect the optimised R_{we} values reported in Figure 4.7, where 19 of 26 R_{we} values equal 0.006 $\Omega.m$. The R_{we} constant was therefore changed from 0.014 to 0.006 $\Omega.m$.

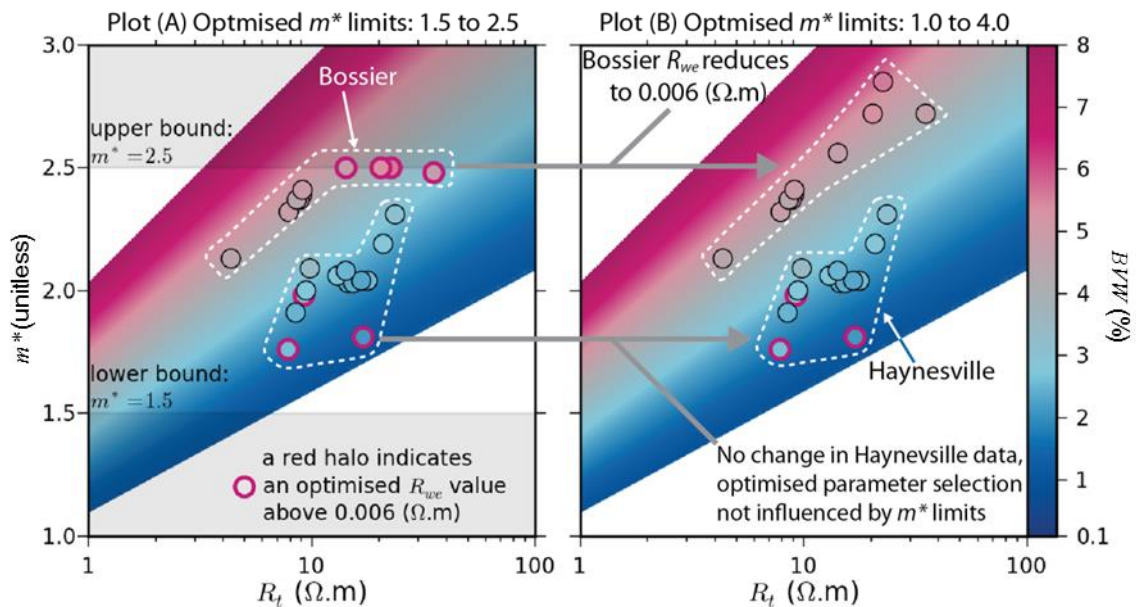


Figure 0.6. Parameter trade-offs (model W3)

Calculated m^* (at $R_{we}=0.006$, Equation 4.9) vs. average R_t for a BVW range (colour bar) representative of HY and BSR core data (Equation 4.7). Overlain are W3 optimised m^* vs. mean R_t values for each well, with marker colour a function of mean well BVW (colour bar right). Plot (A) shows overlain W3 optimised values where m^* is limited between 1.5 and 2.5 (conceptual limits). Plot (B) overlays W3 optimised data with expanded m^* limits of 1.0 to 4.0. *Note: consistent minimisation of R_{we} and good linear relationship for BSR data in plot (B).*

The parameter trade-offs depicted in Figure 0.6 are very similar in character to those described for model W2 (section 4.4.2.2), with a clear linear trend between optimised m^* vs. R_t values. The only exceptions to this linear relationship are the highlighted markers, representing wells whose R_{we} values optimise to in excess of 0.006 $\Omega.m$, for the BSR core data, these highlighted wells plot on the m^* upper bound ($m^*=2.5$). If the optimiser is allowed to exceed the m^* upper bound (as depicted), this results in slightly higher m^* values and R_{we} values of 0.006 $\Omega.m$, and a much improved linear $m^* : R_t$ relationship. In other words, as discussed in the sensitivity analysis, R_{we} appears to be simply modified so as to exploit a preferred range in m^* . The same is not however true for the HY data, where R_{we} values exceed 0.006 $\Omega.m$ for three wells (2, 3 and 13). This

reiterates previous observations that *BVW* in the BSR may not be the dominant factor in controlling R_t , the primary variable forcing optimised parameter selection.

6.8.3 Core sample parameter modelling

R_{we} and m^* values were generated iteratively for each core sample to further explore any parameter forcing. This was achieved using the Grid Search methodology outlined in section 4.2.2, applied to each individual core sample with a parameter step increment of 0.01.

The optimum parameter combinations generated for each core sample are given in Figure 0.7. Here the results are displayed as R_{we} vs. m^* for both the BSR (left) and HY (right), with marker colour and size as a function of R_t and *BVW* respectively. This plot indicates a linear trend between R_{we} and m^* , which can be further linked to perpendicular relationships with both *BVW* and R_t , such that R_t and *BVW* increase with increases in R_{we} and m^* . The distributions of the optimum parameters are also plotted alongside each axis, indicating a near uniform distribution in R_{we} for both formations, though there is a slight increase in frequency for the lowermost R_{we} values. By contrast, both formations have more normally distributed m^* parameters (Figure 0.7) of similar distribution and range to those calculated for model W2. That there should be a uniform distribution across the entire range of R_{we} in both formations is dubious, and similar to previous findings, it is probable that R_{we} values are selected principally to allow for a preferred selection of m^* .

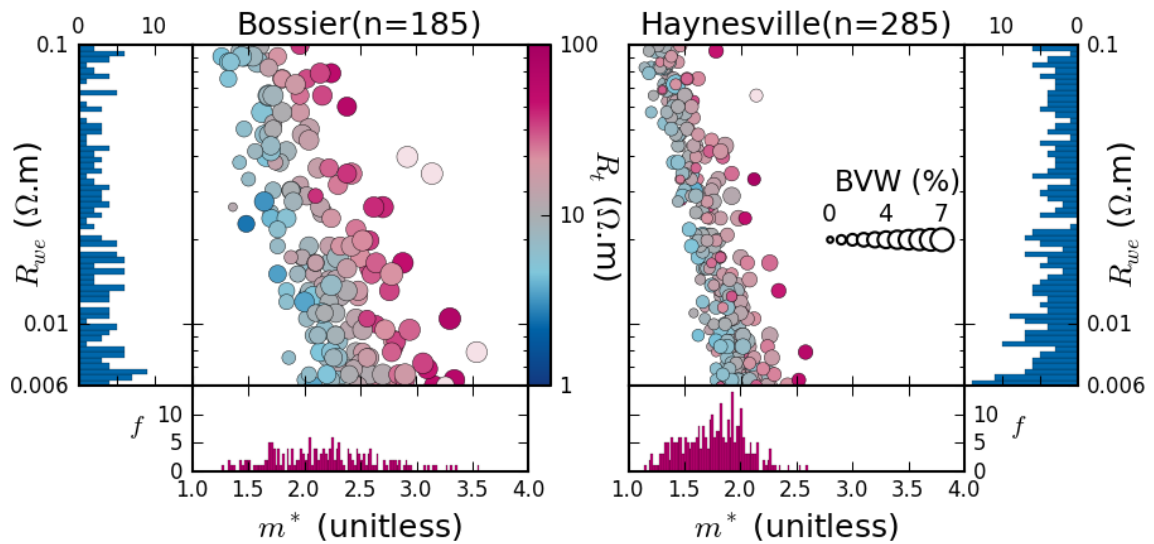


Figure 0.7. Core sample optimised parameters (model W3)

Grid search optimised R_{we} and m^* parameters for BSR and HY data. Marker colour and size are a function of R_t and BVW . Parameter distributions are provided on axis. Note linear R_{we} - m^* relationship with perpendicular R_t trend. In the BSR, and to a reduced extent in the HY, trends in R_t are linked to BVW .

The optimal parameters generated for each core sample and displayed in Figure 0.7 have least MAE values varying from between 0.000023% to 0.16% for the 470 BSR and HY core samples. These are however ‘least’ MAE solutions, with between 377 to 1487 alternative solutions within $\pm 5\%$ error of S_{wC} benchmark values for each core sample (at a 0.01 parameter spacing). Furthermore, given that the experimental error in core data measurements are poorly constrained (see section 2.3), what error bounds are appropriate: 5%, 10%, 15%, or more? If there is a geologically meaningful parameter combination, is it possible to identify it without tighter parameter constraints? This problem is explored in Figure 0.8 which displays the parameter distributions for S_{wA} estimates within $\pm 5\%$ of the benchmark S_{wC} values.

Figure 0.8, similar to previous results, depicts a relatively tight series of m^* distributions for the HY with a much wider and variable range in sample m^* distributions for the BSR. For both formations the range in m^* can be linked to BVW , with parameter distributions moving to lower m^* values at lower BVW . Furthermore, there is a consistent uniform though inclined distribution of near identical character for R_{we} in all core samples. This demonstrates a general increase in the availability of low error solutions at lower R_{we} values but ultimately fails to define a probabilistic value range. This suggests that identifying R_{we} by optimiser methods may not be

feasible and that a constant R_{we} may be more suitable. These results are summarised in Figure 0.9 by totalling the frequency in occurrence of each parameter for each formation. This highlights: a) the contrast in m^* parameter distributions, and b) identical distributions in R_{we} for the BSR and HY.

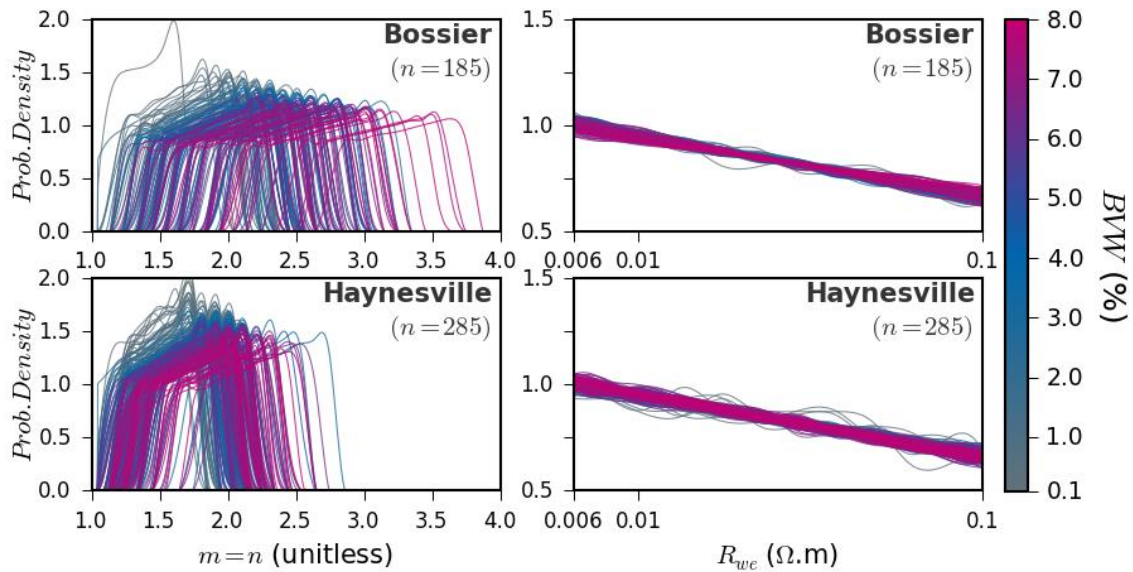


Figure 0.8. Optimised parameter distributions for S_{wA} within +/-5% of S_{wc} (model W3)

Grid search optimised R_{we} and m^* parameters distributions for S_{wA} estimates within +/- 5% of benchmark S_{wc} values for BSR (top) and HY (bottom) data. Line colour is a function of sample BVW.

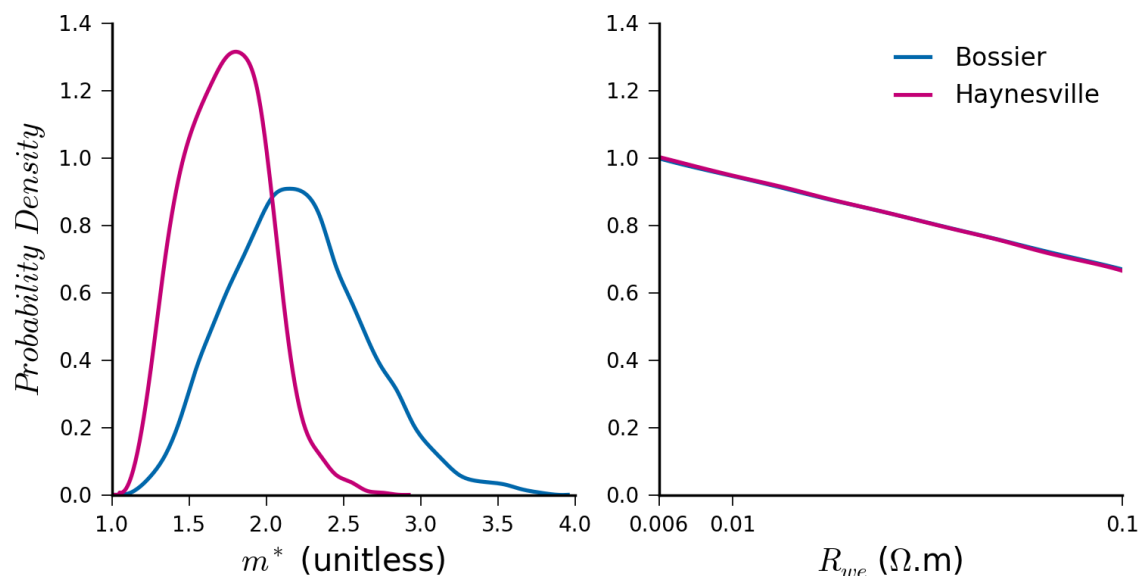


Figure 0.9. Totalled parameter distributions for S_{wA} estimates within +/-5% of S_{wc} (model W3)

Grid search optimised m^* (left) and R_{we} (right) parameter distributions for S_{wA} estimates within +/- 5% of benchmark S_{wc} values for BSR and HY data. Probability density is calculated from the total frequency of all core samples at each parameter value at a parameter spacing of 0.01.

6.8.4 Summary

6.8.4.1 Sensitivity analysis

- Results are demonstrated to favour minimised R_{we} values that reduce the sensitivity of, and expands the viable range of m^* values, therefore allowing for a preferred least error solution though at the expense of a likely increase in model error. The consistent manipulation of R_{we} values prevents a reasoned geological interpretation of the optimised value (Figure 0.4).

6.8.4.2 Parameter trade-offs

- Similar to the 1D models considered, analysis of the 2D model indicates a linear relationship between the optimised parameters and R_t , suggesting that BVW is of limited importance in forcing parameter selection (Figure 0.6).

6.8.4.3 Parameter modelling

- Model W2 predicted m^* and R_{we} can be shown to consistently relate to R_t and BVW (Figure 0.7).
- Results show consistent parameter distributions for the HY with diverse and heterogeneous distributions in the BSR (Figure 0.8).
- Distributions for m^* are noted to be consistent with those generated for 1D models.
- The lack of any parameter distribution for R_{we} stresses the tendency for this parameter to be minimised so as to increase the frequency of low error solutions (Figure 0.9).

6.9 Results: 3D parameter optimisation

This section details the analysis of 3D optimisation model (W4) and aims to highlight the nature of any model limitations, parameter interactions, parameter forcing linked to geological/petrophysical properties, and any predictive capabilities the investigation of these relationships might reveal.

The following sections investigate:

- 4.6.4 The sensitivity of *MAE* across the range of possible parameter values.
- 4.6.5 The trade-offs between parameters and input variables in Archie's equation.
- 4.6.6 The range of parameters produced by direct optimisation for each core sample.

6.9.1 Sensitivity analysis

The sensitivity data for model W4 is displayed in Figure 0.10, illustrating characteristic relationships between parameter modifications and their effects on *MAE* for wells 3 and 10 of the HY and BSR respectively. The plots on the left of Figure 0.10 present all the available data where *MAE* is less than 100%, with plots on the right presenting only those parameters for the lowest 5% of *MAE* values.

All plots in Figure 0.10 depict steep linear relationships between R_{we} and m and between m and n , with a shallower linear trend between R_{we} and n for both wells 3 and 10. The combination of these trends creates a distinct least error plane which remains broadly similar between all wells. As per model W3, it is evident that changing certain parameter values can be beneficial in modifying the sensitivity and effective value range of another. For instance, in BSR well 10, maximising n to $n=4$ decreases the sensitivity of both R_{we} and m , increasing the precision with which the later parameter can be selected.

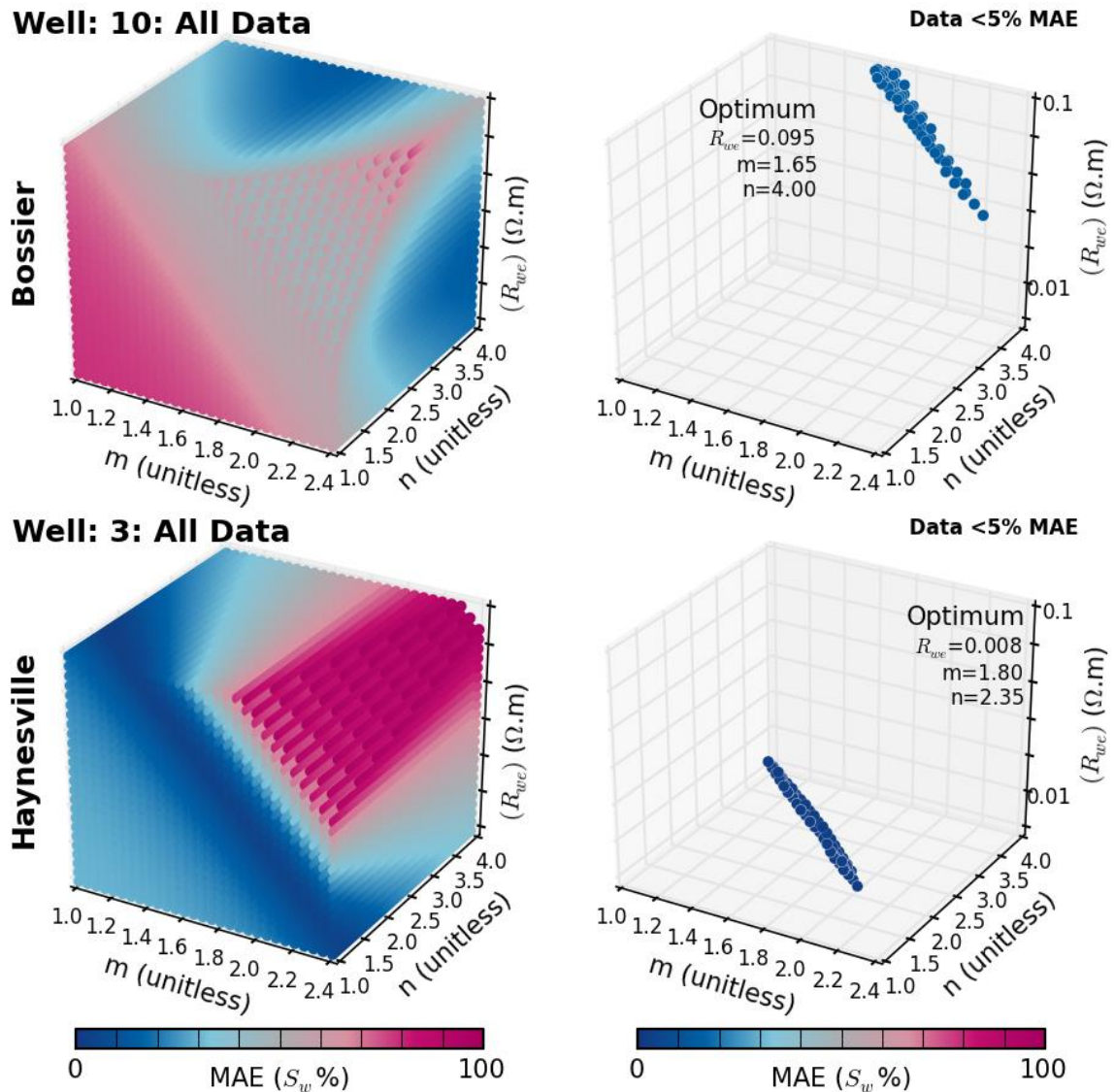


Figure 0.10. Sensitivity analysis (model W4)

MAE sensitivity plot for model W4: R_{we} vs. m and n for BSR (top) and HY (bottom) data. Plots Left: Parameter values for MAE $\leq 100\%$. Plots right: parameter values for the lowest 5% of MAE values.

Unlike well 10 however, HY well 3 is one of few wells where all of the generated parameters sit away from an upper or lower bound. Well 3 also has the best (least error) S_{wA} vs. S_{wC} correlation of any well. Though this may be linked to geological forcing, this cannot be confirmed, and it remains possible that R_{we} is only so low as to maximise the choice and selection of m and n .

The parameter relationships depicted in Figure 0.10 are summarised in Figure 0.11, which depicts parameter distributions for the lowest 5% of MAE values for each well in the BSR and HY. Here, with the exception of well 3 and 13, every well has at least one, often two, globally optimised parameters fixed at an upper or lower bound. The fixed

parameters are often minimum bound R_{we} or m or maximum bound n values, a feature coincident with an inclined parameter distribution.

Individual parameter distributions in Figure 0.10 are broadly similar to those described for model W3, though with some important distinctions. In model W3, m^* distributions for both formations are generally similar in form. Though where m^* is partitioned into individual optimised m and n parameters, it is clear that they each play a different role within the BSR and HY:

- In the BSR, which has relatively low gas saturations (Figure 4.5), m has a dominant role, exhibits a relatively normal distribution, and has optimal values which sit away from the parameter bound. This is coincident with n and R_{we} distributions that are generally inclined to their respective upper and lower bounds.
- In the HY, which has relatively high gas saturations (Figure 4.5), n has a dominant role, exhibits a relatively normal distribution, and has optimal values which sit away from the parameter bounds. This is coincident with m and R_{we} distributions that are generally inclined to their respective lower bounds.

The sensitivity analysis also highlights the impact of changing parameter bounds on the generated parameters. For instance, in Figure 4.7, model W4 optimised parameters were limited to conceptual upper and lower bounds (m and $n=1.5-2.5$) and appear reliant on modifying R_{we} values with m and n often fixed at their minimum and maximum respective bounds. Here, with m and n parameter bounds expanded to between 1 and 4, HY optimisation appears reliant on modifying n , showing little consistency between the two sets of optimised parameters.

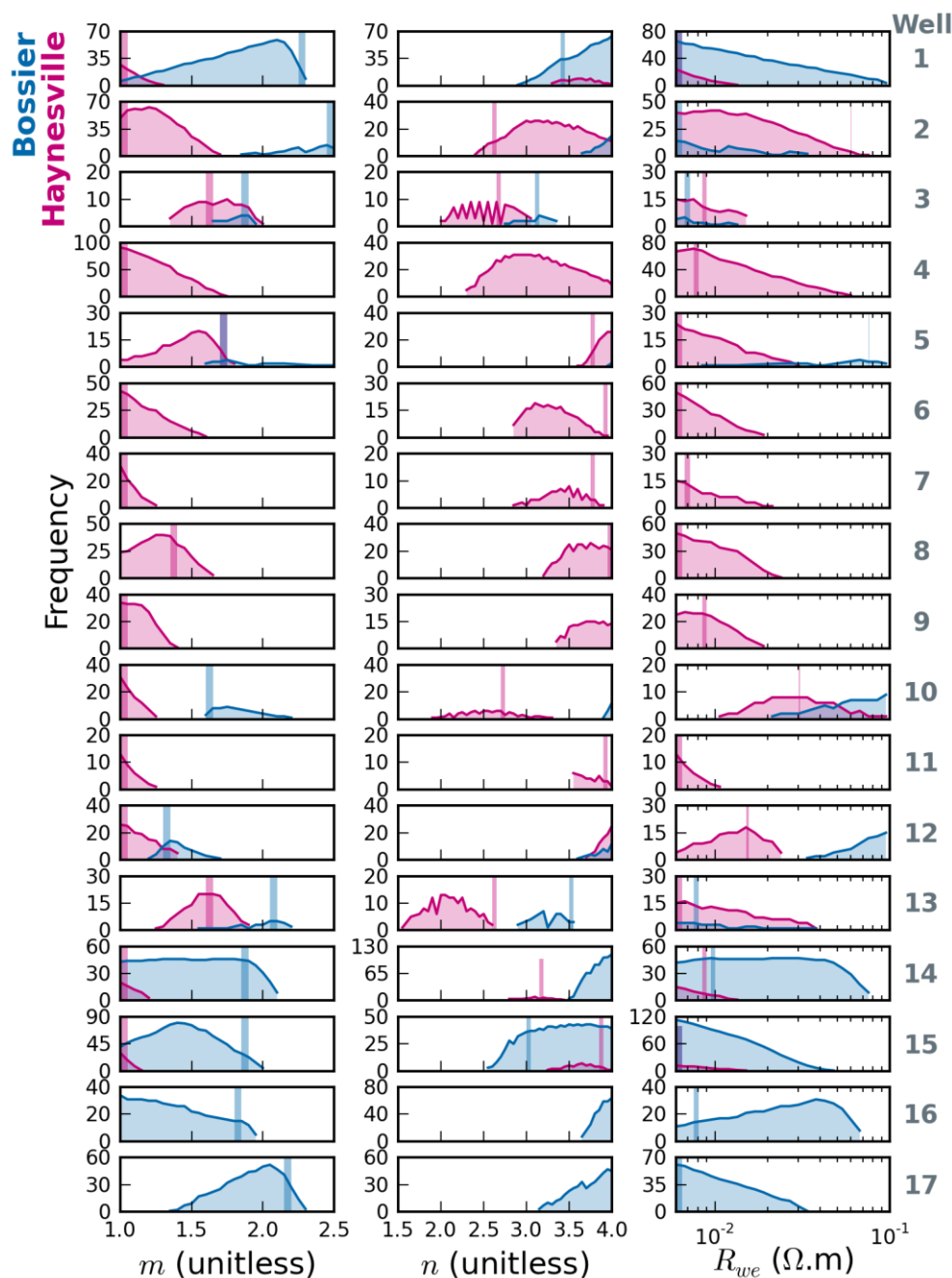


Figure 0.11. Parameter distributions, sensitivity analysis (model W4)

Plot of Haynesville model W4 parameter distributions for the lowest 5% of MAE values. Only parameter combinations which yield MAE values \leq (optimum MAE + (optimum MAE*0.05)). The faded red (HY) and blue (BSR) bars indicate the optimal parameter value for each well.

Furthermore, sensitivity data for model W3 demonstrate a clear tendency for R_{we} values to be manipulated so as to achieve a greater flexibility in m^* selection. Model W4 shows similar though more varied evidence of parameter manipulation, which, without a much improved understanding of the pore network and fluid salinity conditions, cannot be dissociated from the optimisation process. As a result, 3D optimised parameters offer limited prospect of accurate geological interpretation.

6.9.2 Parameter trade-offs

The parameter trade-offs in model W4 are illustrated in Figure 0.12 using equation 4.8 at $n=1$ (left) and $n=4$ (right) for a representative range of R_t , ϕ_{tc} and S_{wc} variables across the parameter range for m and R_{we} . This confirms prior observations that higher n values decrease the sensitivity of m and R_{we} , but also reveals a reduction in the sensitivity of all other input variables (R_t and BVW). It is therefore preferable for any optimised solution to favour higher n values and a reduced sensitivity and an increase in the possible range of other equation inputs.

Derived using: $R_{we} = R_t \cdot \phi_{tc}^m \cdot S_w^n$

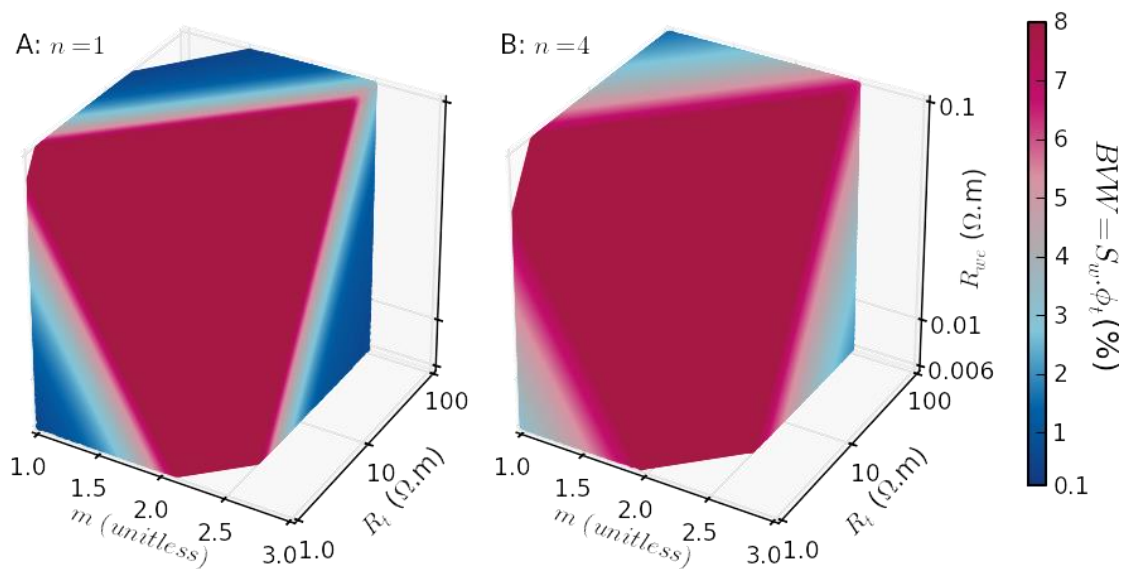


Figure 0.12. Parameter trade-offs (model W4)

Calculated R_{we} at $n=1$ (left) and $n=4$ (right) for a range of m , R_{we} , ϕ_{tc} and R_t values.

The relationship between model W4 optimised parameters and the parameter trade-offs are illustrated in Figure 0.13 for the BSR and in Figure 0.14 for the HY. In the BSR, the optimised parameters (all with n values of 2.5) sit on a plane. This is made clear on the rotated insert, with all points plotting on a plain equivalent to a near constant BVW of 3% (Figure 0.13).

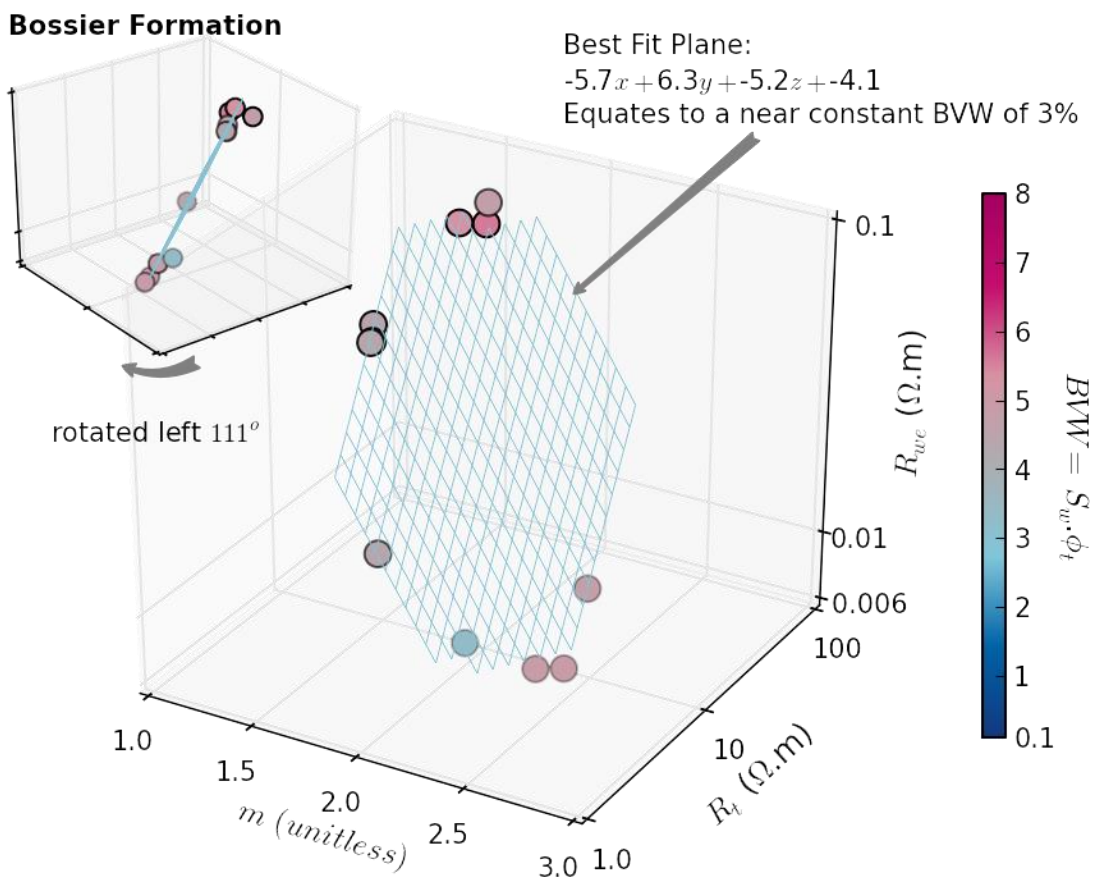


Figure 0.13. Optimised BSR parameters (model W4)

Model W4 optimised parameters and mean R_t and BW values for all wells.

Similarly, the HY (Figure 0.14) optimised parameters also fit a plane highlighted by the rotated insert. This plane also indicates a near constant BW of 1%, though not all HY wells optimise to $n=2.5$ (highlighted in red).

Haynesville Formation

Best Fit Plane:

$$-5.4x + 7.6y + -9.1z + -17.$$

Equates to a near constant BVW of ~1%

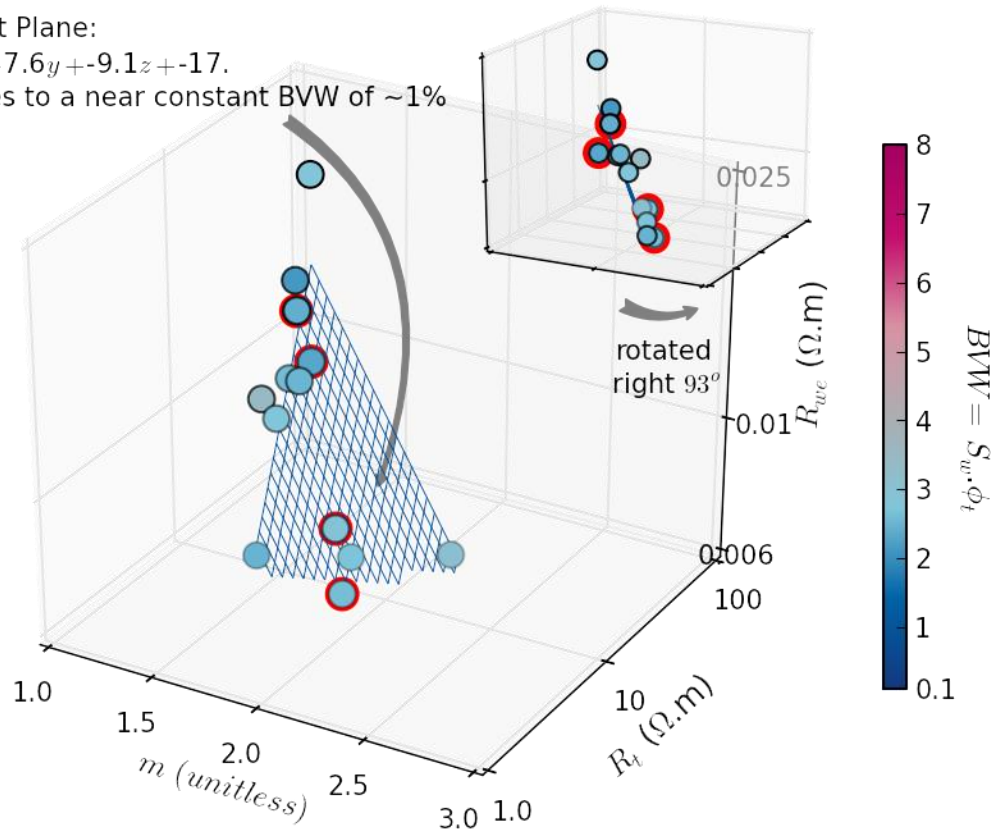


Figure 0.14. Optimised Haynesville parameters (model W4)

Model W4 optimised parameters and mean R_t and BVW values for all wells.

As with observations for models W2 and W3, the optimised W4 parameters are consistent in fitting to a specific BVW plane with limited movement across the BVW range. This combined with a good linear relationship with R_t , again suggests that pore water volume (BVW) is of secondary importance in forcing parameter selection. For the volume of fluid to have reduced importance, then either the fluid salinity or electrical properties must be highly variable, or other geological factors must be influencing R_t .

6.9.3 Core sample parameter modelling

R_{we} , m and n parameters were modelled with a parameter grid spacing of 0.05 using the same method outlined for model W3. The optimum parameter combinations generated are displayed in Figure 0.15 with marker colour controlled by n (y axis), so as to help judge depth within each 3D plot. For both the BSR and HY, no clear links could

be established between the generated parameters and wider formation mineralogical/petrophysical properties.

Both 3D scatter plots in Figure 0.15 are orientated 'edge on' to a plane defined by the optimum parameters. For the BSR, this plane is weakly defined by data with near uniform distributions, though there is a slight increase in the frequency of high n values linked to a decrease in m , with R_{we} remaining more or less uniform. By contrast, the HY occupies a distinctive plane in parameter space, with a distinct increase in the frequency of low R_{we} and m values, and n values that remain relatively uniform. These results support previous observations that the HY has a more constrained range of optimal Archie parameters than the BSR. Furthermore, the lack of defined parameter distributions in both formations combined with unreasonably oil wet (high n) or low salinity (high R_{we}) suggests that the generated parameters are 'not' geologically representative, and it was not possible to link observed parameters with wider geological/petrophysical data.

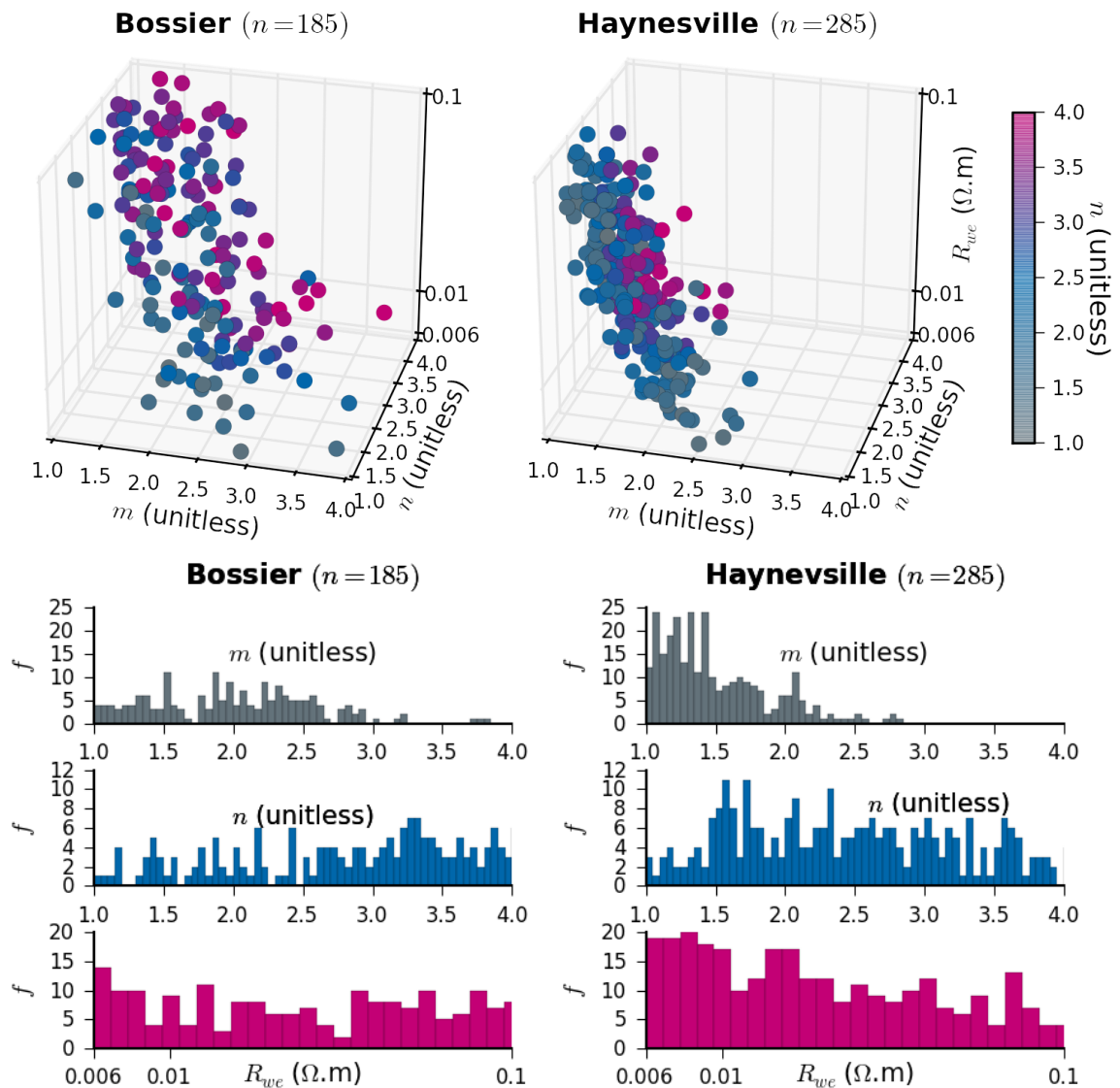


Figure 0.15. Individual core sample optimised parameters (model W4)

Grid search optimised R_{we} , m and n parameters for the BSR (left) and HY (right). Parameter distributions are included.

As with model W3, numerous alternative parameter combinations exist within a 5% MAE margin of benchmark S_{WC} values. The parameter distributions within $\pm 5\%$ error are displayed in Figure 0.16.

The BSR in Figure 0.16 shows significant variation in m , with an increase in m values at higher BVW. In addition, the n value distributions are consistently sloped, indicating a larger number of viable S_{WA} solutions at higher n values. Whilst the R_{we} values remain near uniform for the majority of samples, but similar to n , also indicate an increase in the number of viable solutions at low R_{we} for some low BVW values. Both R_{we} and n fail to define probabilistic parameter value ranges, representing solely least MAE solutions

with limited geological merit. By contrast the wide variations in m , which are significantly more variable than those observed for the HY, are analogous to variations observed for m^* in models W2 and W3 and may be linked to a greater degree of formation heterogeneity in BSR data.

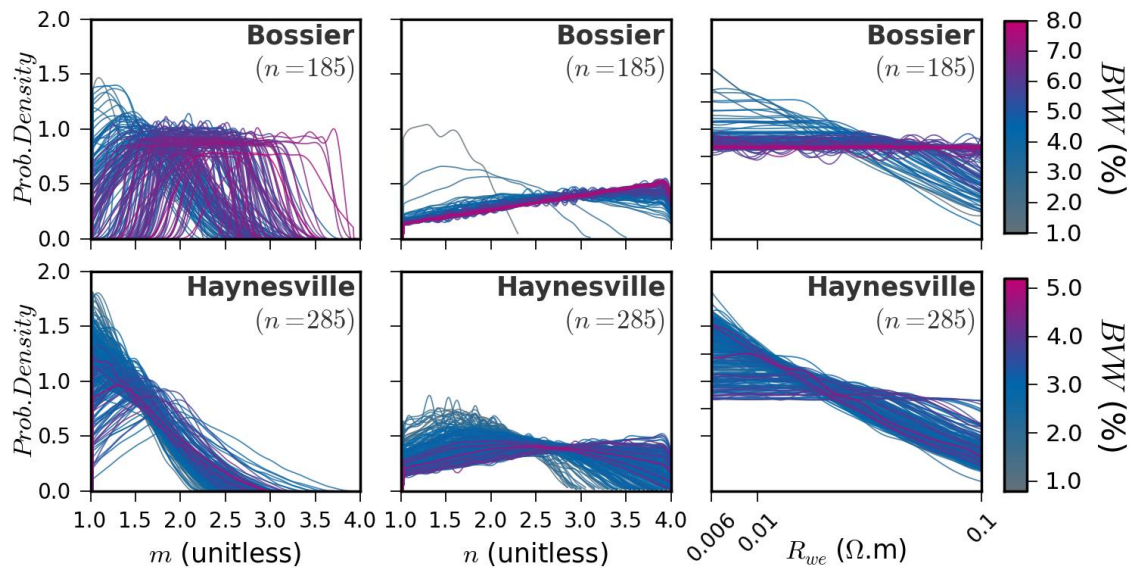


Figure 0.16. Optimised parameter distributions for S_{wa} within +/-5% of S_{wc} (model W4)

Grid search optimised R_{we} and m and n parameter distributions for S_{wa} estimates within +/- 5% of benchmark S_{wc} values for the BSR (top) and HY (bottom). Line colour is a function of sample BVW .

The parameter distributions generated for the HY differ significantly from those described for the BSR. Firstly, similar to m^* in model W3 and W2, m is consistently constrained to a relatively low value range. Secondly, there is significantly more character in n distributions which can be linked to BVW , i.e. higher BVW links to higher n values and vice a versa. Thirdly, though R_{we} distributions are broadly similar to those for the BSR, there is no apparent link to BVW .

These results are summarised in Figure 0.17 by totalling the frequency in occurrence of each parameter for each formation. Taken into consideration with Figure 0.16, this has a number of implications:

- e) the contrast in m parameter distributions may be representative of greater heterogeneity in formation petrophysical properties in the BSR as opposed to the HY,

- f) for the BSR, porosity and m is far more significant in controlling Archie's equation than formation fluid/pore wall interactions and n .
- g) for the HY, which has a far lower BVW range and a higher gas filled porosity, it suggests that formation fluid/pore wall interactions and hence n is a more significant factor in Archie's equation.
- h) for both formations, data generated for R_{we} provides little information that can be placed within a geological context, revealing only that lower values carry an increased chance of a low MAE solution.

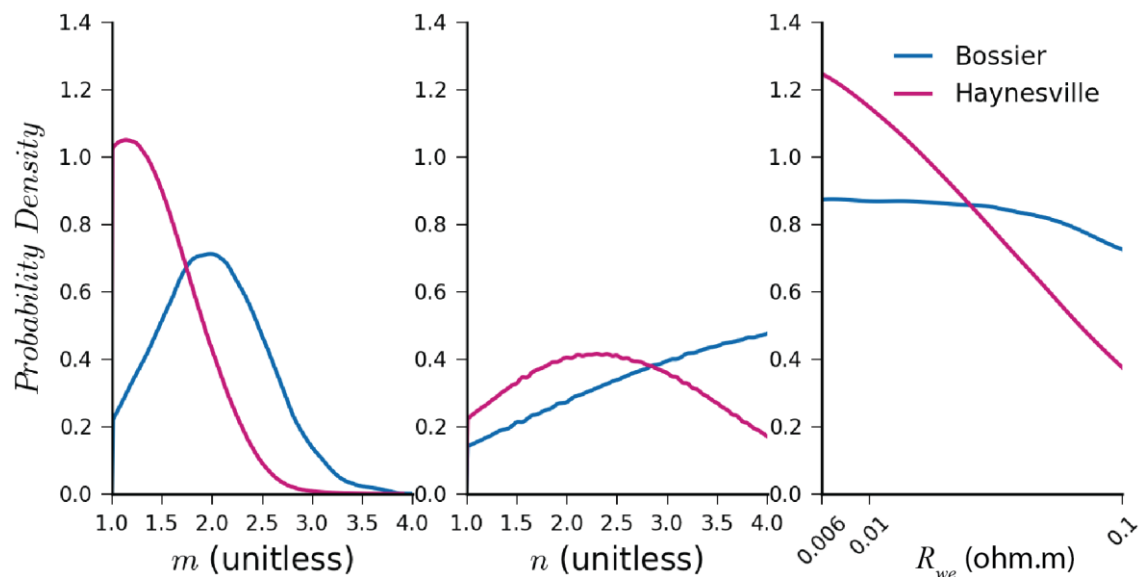


Figure 0.17. Totalled parameter distributions for S_{wA} estimates within +/-5% of S_{wC} (model W4)
Grid search optimised R_{we} and m and n parameter distributions for S_{wA} estimates within +/- 5% of benchmark S_{wC} values for the BSR (top) and HY (bottom). Line colour is a function of sample BVW .

6.9.4 Summary

6.9.4.1 Sensitivity analysis

- In the BSR, n is routinely maximised and R_{we} minimised so as to reduce the sensitivity and increase the range in possible m values. This allows for a least MAE solution, but at the likely expense of an increase in model error (Figure 0.11).
- In the BSR, n is routinely maximised and R_{we} minimised so as to reduce the sensitivity and increase the range in possible m values. This allows for a least

MAE solution, but at the likely expense of an increase in model error (Figure 0.11).

6.9.4.2 Parameter trade-offs

- Analysis indicates, similar to the 1D and 2D models, a linear relationship between the optimised parameters and R_t , suggesting that *BVW* is of limited importance in forcing parameter selection (Figure 0.12).

6.9.4.3 Parameter modelling

- Similar to model W3, it is notable that parameter distributions in the BSR are notably more constrained than in the HY.
- m and n parameters are shown to have different roles in the BSR and HY (Figure 0.16 and Figure 0.17):
 - The BSR, which generally has low gas saturations and high V_{Clay} and CBW volume, demonstrates inclined uniform n distribution and appears reliant on optimising m .
 - The HY, which has relatively high gas saturations, has very low m values and distributions and appears reliant on optimising n .

Chapter 7

Unconventional applications of Archie's equation: does geology matter?

This chapter incorporates the results of the error analysis in Chapter 4 with log and core geological/petrophysical data presented in Chapter 3. This aims to provide a geological interpretation and rationale for optimised Archie parameters and associated petrophysical and mineralogical relationships and is broadly divided into four sections:

- 5.5 *Formation heterogeneity*: explores the links between mineralogical and petrophysical heterogeneity, and effects on optimiser model and Archie parameter outputs.
- 5.6 *BVW, R_t and V_{clay} relationships*: these relationships are explored and a model accounting for their behaviour proposed.
- 5.7 *Composite core data summary*: key core data are presented, highlighting mineralogical / petrophysical trends linked to variations in formation fabric.
- 5.8 *Predicted pseudo-Archie parameters*: the range and behaviour of predicted Archie parameters are discussed and compared with values reported in the literature.

7.10 Introduction

Following Archie's seminal 1942 paper, the terms 'Archie rock', 'Archie like' or 'non-Archie' (Herrick and Kennedy, 1996) have come to prominent use as describing 'clean' (clay free) formations with regular pore geometries described by petrophysical constants within Archie's equation. Nevertheless, though the BSR and HY might be considered to fail in meeting this 'clean' criterion (Glorioso and Rattia, 2012; Worthington, 2011b), results (Chapter 4) indicate that a modified Archie equation can work satisfactorily in some wells, particularly in the HY, despite significant mineralogical/petrophysical complexity. Understanding the geological controls on the accuracy and validity of Archie-based methods for a given shale gas prospect is therefore critical to the informed use of existing resistivity based methods and for the development of novel saturation modelling techniques.

7.11 Formation heterogeneity

The analysis of multiple optimisation models (sections 4.3 to 6.9) indicate that their residual *MAEs*, generated parameters and parameter sensitivities, are consistently more heterogeneous in the BSR than in the HY. The term heterogeneity is used here synonymously with variability, and variability in model outputs must be linked to the heterogeneity and inter-relationships of the petrophysical inputs (ϕ_{tC} , R_t , S_{wC}). In turn, the petrophysical inputs express the interaction and distribution of formation mineralogy and fluid components as determined by depositional and diagenetic processes. This section aims to link the separation of BSR and HY results to wider underlying formation geological properties as represented within the log and core data discussed in Chapter 3.

7.11.1 Heterogeneity in optimiser model response

Residual *MAEs* for the HY wells are both consistently low and of limited variability when compared to those for the BSR. This is depicted in Figure 4.4 and Figure 4.6 and summarised in Table 7.1, where the substantially higher range and variability in BSR *MAE* suggests that optimised Archie parameter constants are less able to characterise a wider range in BSR core sample characteristics. This is supported by the large reduction in mean BSR *MAE* between optimiser model H1 to W1 (Figure 4.6, Table 7.1), equivalent to a relative reduction in *MAE* of 31%. This constitutes the single largest decrease in *MAE* between optimiser models in the BSR and is accompanied by an increase in the number of optimised sample populations from one in H1 to 11 in W1. In other words, the largest reduction in *MAE* for the BSR is attained in considering it as a heterogeneous as opposed to homogenous petrophysical system. By contrast, reductions in mean *MAE* in the HY between H1 to W1 are slight, and equivalent to a relative reduction in *MAE* of 3%. In other words, the HY is not particularly sensitive to changes in the style of sample binning and can be adequately represented as an homogenous petrophysical system. This assertion is supported by Popielski et al., (2012), whose study of rock typing using k-means cluster analysis of conventional well

data suggested a 'vertically-homogenous Haynesville Formation' in their study well, which corresponded with low variability in petrophysical log and core properties (R_t , ρ_b , ϕ_n , S_{wc} , TOC , and ϕ_{tc}).

MAE (S_w %)	H1	W1	W2	W3	W4
BSR	17.64 ± 7.92	12.15 ± 6.62	11.31 ± 5.56	10.84 ± 5.44	10.14 ± 5.32
HY	5.59 ± 2.40	5.42 ± 1.28	5.37 ± 1.40	5.19 ± 1.25	4.66 ± 1.03

Table 7.1: Mean residual MAE per optimisation model (Figure 4.4)

Mean MAE taken as the mean of the residual MAE per Well (Figure 4.4) ± the average standard deviation in residual MAE.

Contrasts in the heterogeneity of residual MAE between the BSR and HY are mirrored by similar differences in modelled parameter sensitivity. Figure 4.9 (models W1 and W2) is a good example, where the sensitivity of MAE to changes in R_{we} and m^* is on average 30% lower and more variable in the BSR than in the HY, which displays very tight and consistent sensitivity curves. In addition, the optimised BSR parameters occupy a wider more variable m^* range (2.175±0.233) compared to more constrained HY m^* values (1.822±0.089). This trend is again emphasised for modelled core sample parameters, and is succinctly displayed in Figure 0.9 for model W3. Where the probability distribution in BSR m^* values is significantly wider than that for the HY data, equating to mean core modelled m^* values of 2.187±0.441 for the BSR and $m^*=1.735±0.273$ for the HY. It should be noted that generated core parameters are displayed to three decimal places to avoid rounding.

7.11.2 Heterogeneity in mineralogical / petrophysical properties

The mineralogical/petrophysical log and core data for the BSR and HY are characterised in Chapter 3. This includes plots of variable distributions highlighting key descriptive statistics, but does not explicitly attempt to categorise one formation as being petrophysically or mineralogically more heterogeneous than the other. This is in part because there is no universally accepted measure of variability that allows for direct comparison of variables with multiple parent units and underlying normal, log-normal and non-normal distributions. For example, σ provides a measure of the dispersion about the mean (μ), and is therefore ideally suited to normal or log-normal

distributions. For skewed distributions, where the mean may be influenced by extreme values, the interquartile range ($IQR=Q_3-Q_1$) may be a more suitable measure of variability. Other measures of variability such as median or mean absolute deviation (MAD), or normalised measures of error such as the co-efficient of variation ($CV=(\sigma/u)*100$) are equally dependant on assumptions regarding the underlying variable distribution. It is however, not the intention of this section to present a detailed review of the statistical measures of variability/heterogeneity, only to emphasise that it is a nontrivial and sometimes inexact process which should not be dissociated from the underlying distribution. With this in mind, a comparison of variability calculated simply as σ and IQR is presented for principal mineralogical/petrophysical components in Figure 7.1, though the reader is encouraged to refer back to the variable distributions presented in Chapter 3.

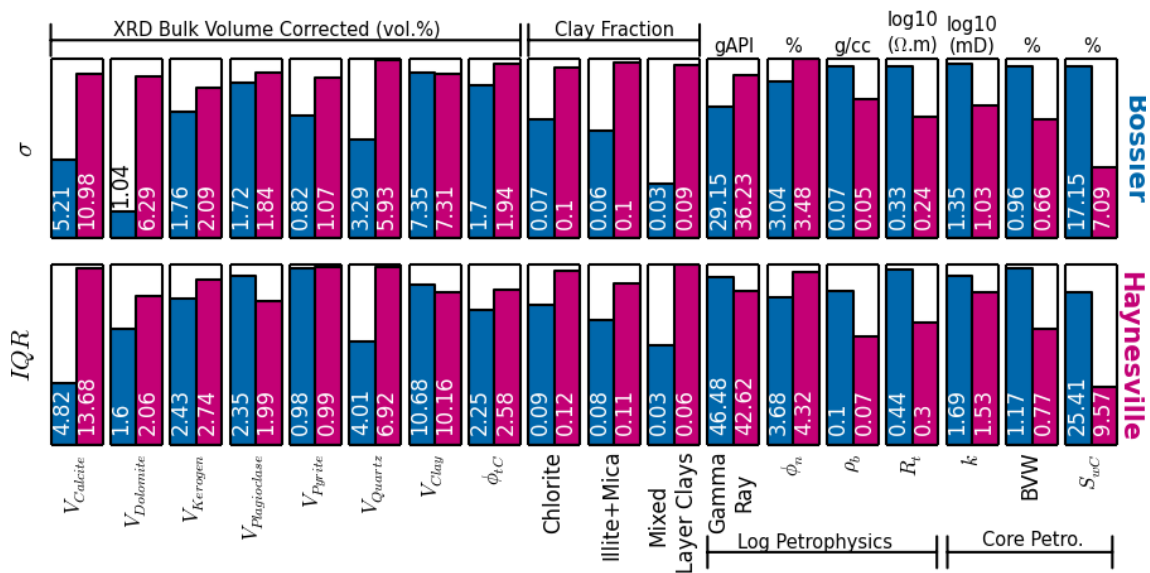


Figure 7.1. Comparison of mineralogical / petrophysical variability

σ (standard deviation) and IQR (interquartile range) calculated for bulk volume corrected XRD volumes and petrophysical log and core data.

Both measures of variability displayed in Figure 7.1 are in general agreement, though there are some variations, most notably for GR and $V_{Dolomite}$ and $V_{Plagioclase}$. In general however, two broad trends are evident: a) the HY is mineralogically more heterogeneous than the BSR, particularly with regard to $V_{Calcite}$, $V_{Dolomite}$ and V_{Quartz} , and b) the BSR is petrophysically more heterogeneous than the HY, with the exception of ϕ_{tC} , GR and ϕ_n .

Of the three principal input parameters (R_t , S_{wC} , and ϕ_{tC}) in an optimised Archie model, R_t , S_{wC} (and therefore BVW) are significantly more heterogeneous in the BSR. It therefore follows that the optimiser response (residual MAE , generated parameters and parameter sensitivities) should mirror this heterogeneity. In plotting mean residual MAE vs. σ for each of the three principal variables R_t , S_{wC} , and ϕ_{tC} , it is possible to further define which of the three variable inputs is most influential in determining the degree of variation and magnitude in MAE (Figure 7.2). Figure 7.2 indicates that as much as 94% of the variation in BSR residual MAE can be attributed to variability in formation resistivity, with little impact from S_{wC} and even less from ϕ_{tC} . This is supported by Wu and Aguilera (2012) who also suggest that saturation estimates are more sensitive to R_t than ϕ_{tC} . In contrast, HY residual MAE (model W4) is only weakly linked to R_t , with variability in S_{wC} and ϕ_{tC} playing a greater role in determining MAE . In other words, heterogeneity in BSR R_t , which is paradoxically not clearly linked to either porosity or saturation (i.e. ϕ_{tC} and/or S_{wC} often increase at higher resistivities), accounts for the observed variation in residual MAE and thus selected parameters and their sensitivity. For the HY, which exhibits low residual MAE s of limited variability, the source of error cannot be attributed to one, but a combination of all three inputs.

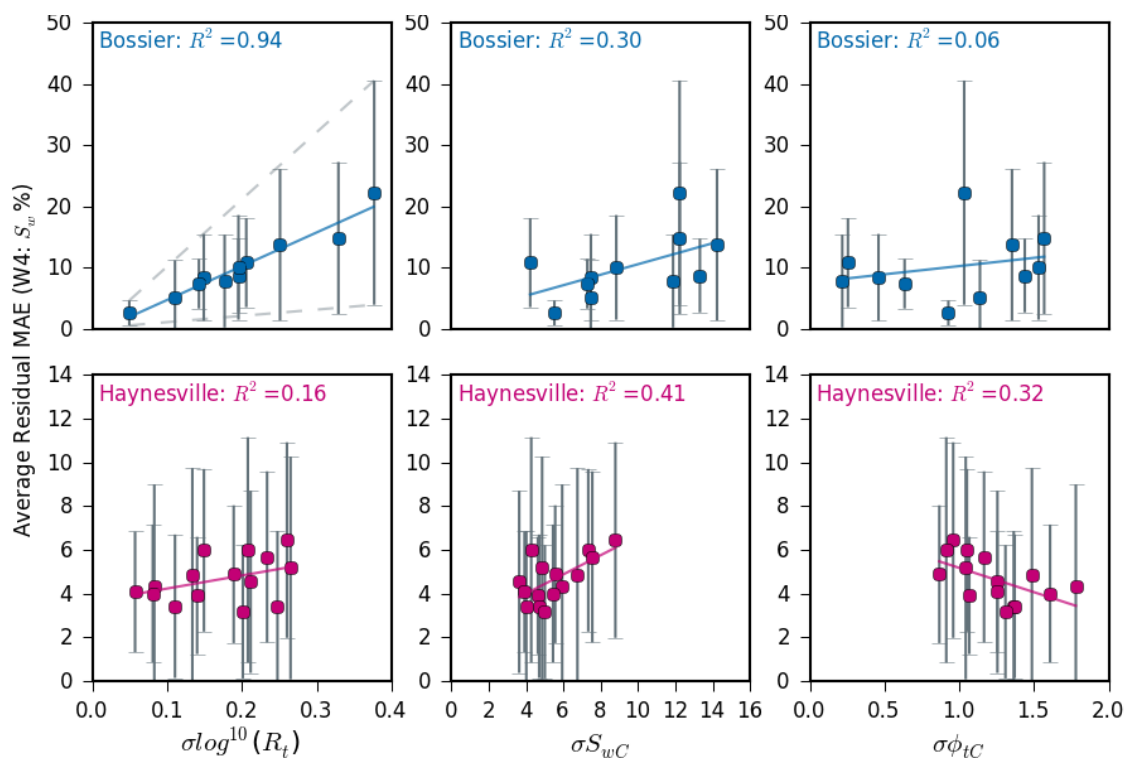


Figure 7.2. Average residual MAE (model W4) vs. key petrophysical inputs

Average residual MAE for each well vs. σ (standard deviation) in: R_t (left), S_{wC} (middle) and ϕ_{tC} (right). Average taken as the sample mean, limited difference found between median and mean MAE values.

The observation that R_t is the primary variable controlling error and the generated Archie parameters is supported by the results of the parameter trade-offs for models W1 to W4 (Figure 4.10, Figure 4.11, Figure 0.6, Figure 0.12), where, for each model, the predicted Archie parameters for the BSR increase linearly with R_t , with limited deviation attributable to BVW ($S_{wC} * \phi_{tC}$). By contrast parameter trade-offs analysed for the HY, show that parameters are selected in response to both R_t and BVW (Figure 7.2).

7.11.3 Mineralogical controls on petrophysical heterogeneity

That variability in mineralogical composition does not coincide with petrophysical heterogeneity (Figure 7.1) is not surprising. Complex textural effects, variations in mineral distributions and other factors (e.g. depositional style and environment) are likely to play a significant role in determining petrophysical variability in mudstones. Whilst there are undoubtedly multivariate textural/mineralogical relationships controlling the petrophysical properties, a significant portion of the observed variability can be linked to the presence and effects of clay minerals (see section 2.3.3.1). This is supported in comparing XRD mineral volumes with petrophysical properties, where V_{clay} consistently stands out as displaying heteroskedastic tendencies (heteroskedasticity refers to a systematic inconsistency in variance, where variance is not homogenous (Schwartzman, 1994)). An example is given as R_t vs. V_{clay} in Figure 7.3, where σR_t increases with increasing V_{clay} in the BSR. In other words, heterogeneity in R_t increases in core samples with higher V_{clay} .

That elevated R_t and/or σR_t should be linked to increased V_{clay} contradicts the long held consensus that clay effects typically act to reduce resistivity, or inversely, provide a source of excess conductivity (Hill and Milburn, 1956; Patnode and Wyllie, 1950; Winsauer and McCardell, 1953; Wyllie and Southwick, 1954). This relationship is absent in the HY (Figure 7.3), where there is no consistent relationship between R_t and V_{clay} .

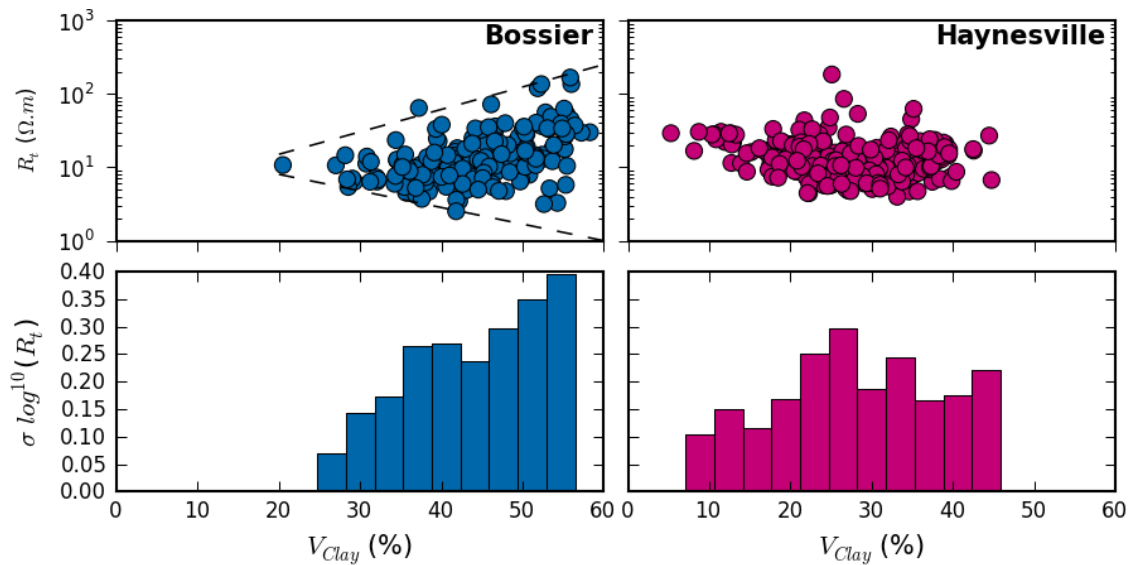


Figure 7.3. R_t vs. V_{clay} and heteroskedasity

R_t vs. V_{clay} cross-plots (top) for the BSR and HY coupled with bar charts of the $\sigma \log^{10}(R_t)$ for binned V_{clay} intervals (bottom).

It is notable however, that in combining HY and BSR data (Figure 7.4) a continuum is formed where R_t is shown to initially decline to a V_{clay} of $\sim 28\%$, and then increases with σR_t . This observation can be linked to clay mineralogy for which the following trends are noted:

- e) the chlorite fraction increases with increases in R_t and variability in R_t (σR_t) in the BSR,
- f) high variability in the chlorite fraction coincides with high σR_t in the HY,
- g) the illite+mica fraction increases at higher V_{clay} in parallel with increased σR_t ,
- h) the mixed-layer clay fraction shows little variability in the BSR, but significant variability in the HY where σR_t is more pronounced,

Taken together, the mixed-layer clays appear to have the least impact and the chlorite fraction the most impact on σR_t , with the illite+mica fraction (the dominant clay type) sitting somewhere in between. Significant control over electrical character can therefore be linked to the chlorite fraction or variations in other structural/mineralogical components concurrent with higher chlorite volumes.

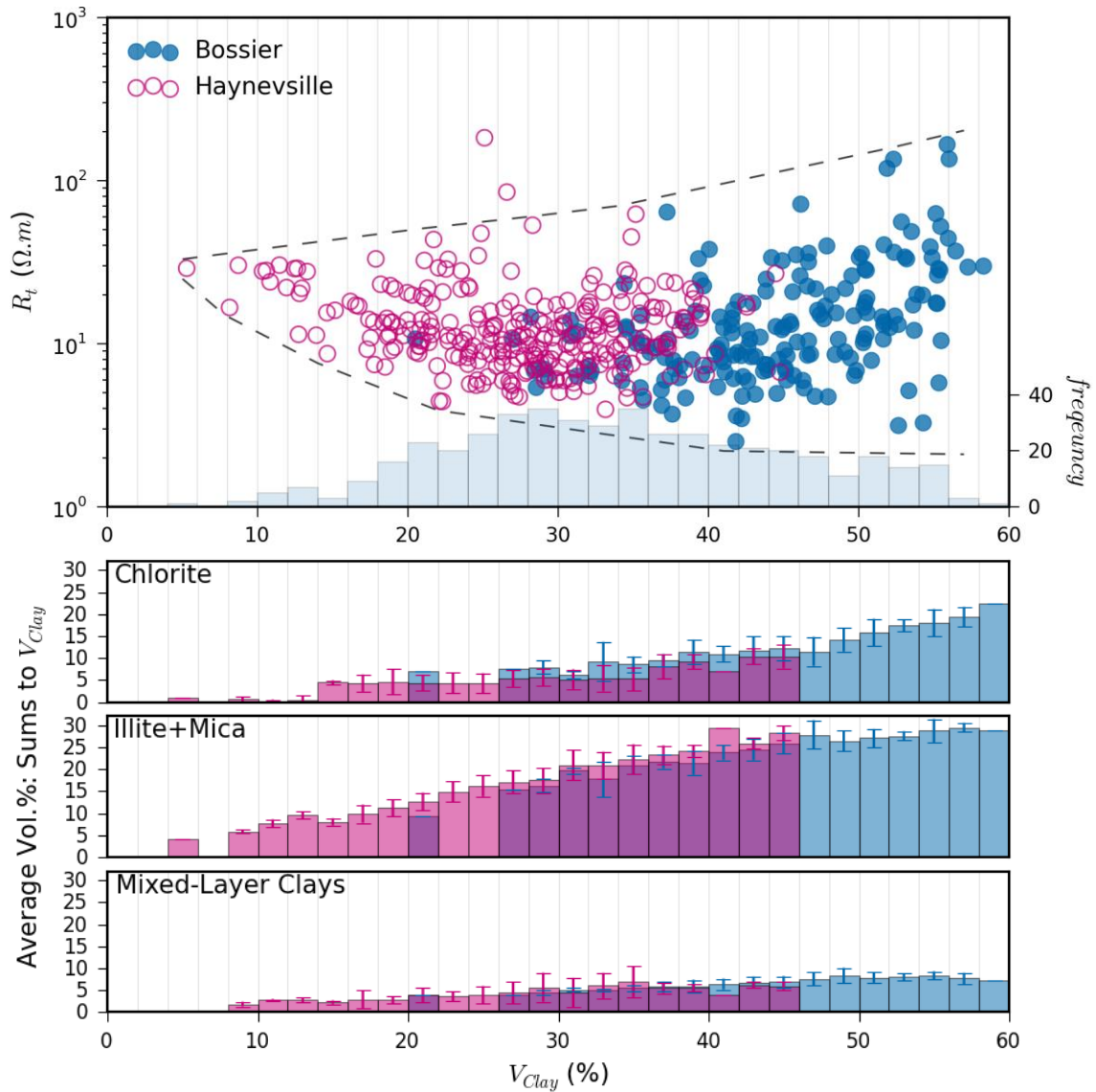


Figure 7.4. R_t vs. V_{Clay} and clay fractions

R_t vs. V_{Clay} cross-plot (top) for the combined BSR and HY data with integrated histogram. V_{Clay} represents the total of the chlorite, illite+mica and mixed-layer clay volumes, given here as a fraction of V_{Clay} which sum to 1 for every 2% V_{Clay} interval. Y axis error bars are a function of the standard deviation.

Just as an increase in V_{Clay} can be shown to coincide with an increase in σR_t , similar heteroskedastic relationships are noted in the BSR for V_{Clay} vs. σk (Figure 7.5) and fluid distribution (S_{wC} and ϕ_{tC}) in Figure 7.6. For k , elevated V_{Clay} is associated with an increase in σk at low matrix permeabilities. For S_{wC} and ϕ_{tC} , it is evident that high V_{Clay} is generally associated with low ϕ_{tC} and high S_{wC} and that $\sigma \phi_{tC}$ increases with decreases in V_{Clay} . Or put another way, σS_{wC} increases at higher porosities coincident with a decrease in V_{Clay} . Despite relatively high clay volumes (average = 44%), no such relationships are however observed in the HY.

These observations have the following implications:

- v. that V_{Clay} plays a dominant role in controlling fluid distribution and poro-perm relationships, and their respective heterogeneities in the BSR,
- vi. that the wide variability in k or R_t at a given high V_{Clay} value in the BSR, necessitates either a highly variable fluid chemistry or a difference in texture / grain partitioning and thus a potentially observable litho-facies distinction.
- vii. that clay minerals play a reduced role in controlling fluid distributions in the HY,
- viii. that V_{Clay} has a consistently limited impact on petrophysical variability in the HY suggests either a) homogeneity in clay distribution and/or pore fluid chemistry, or b) that clay volumes of below 28% are insufficiently high to dominate formation petrophysical properties.

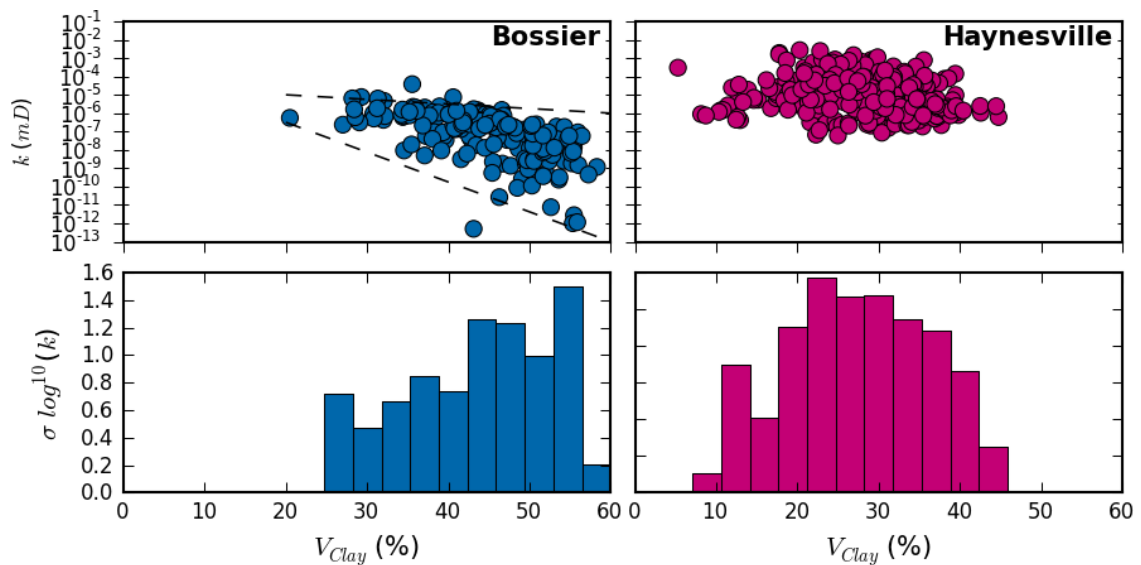


Figure 7.5. k vs. V_{Clay} and heteroskedasticity

k vs. V_{Clay} cross-plots (top) for the BSR and HY coupled with bar charts of the $\sigma \log^{10}(k)$ for binned V_{Clay} intervals (bottom).

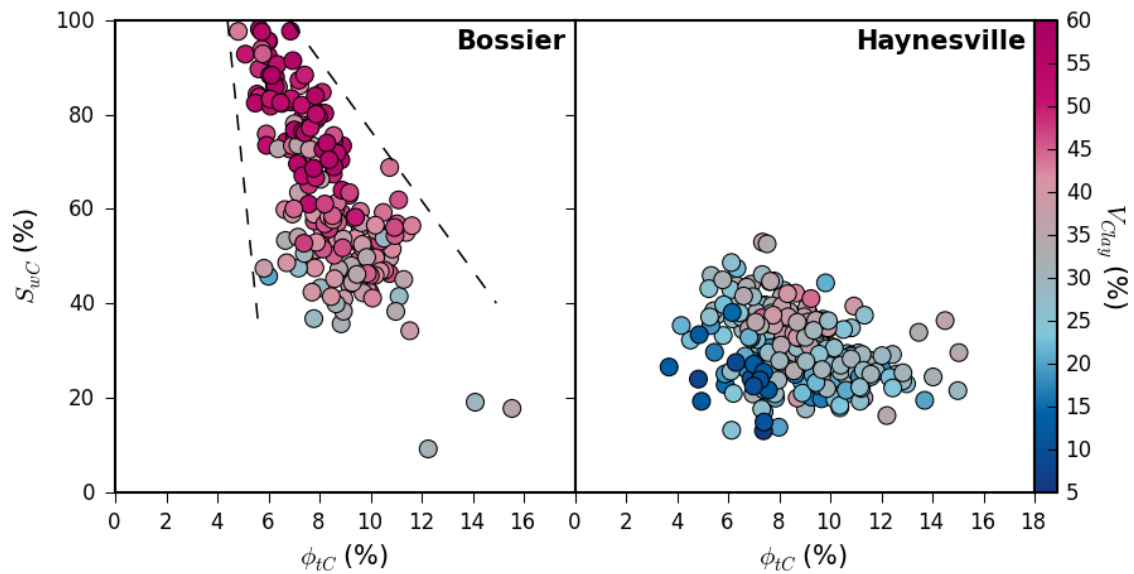


Figure 7.6. S_{wc} vs. ϕ_{tC}

S_{wc} vs. ϕ_{tC} cross-plots for the BSR (left) and HY (right), markers coloured by V_{Clay} .

7.11.4 Summary and conclusions

- Though mineralogically heterogeneous, the HY is relatively homogenous petrophysically, resulting in low, well constrained residual MAE and well constrained Archie generated parameters and sensitivities.
- The BSR is homogenous mineralogically when compared to the HY, but is petrophysically heterogeneous.
- Elevated V_{Clay} and in particular the chlorite clay fraction are associated with increased variability in R_t in the BSR.
- The role of clay minerals, their interaction with formation pore space and their influence over formation electrical properties varies significantly between the BSR and HY.
- Despite highly variable fluid distribution characteristics (BVW and S_{wc}) it is variability in R_t which is principally responsible for determining heterogeneity in MAE . As a consequence, generated Archie parameters for the BSR have a positive linear relationship with average R_t for all optimisation models considered. Thus, for porosity-fluid relationships to be the primary mechanism determining formation electrical properties, then R_{we} , m and n parameters are required to be extremely variable. Or, additional mineral or other textural

relationships must contribute to electrical characteristics, undermining and limiting the use of traditional Archie approaches to saturation modelling.

The relationships underlying the disparity in BSR-HY petrophysical heterogeneity and its links to error in S_w estimation are explored in the following section.

7.12 Water, resistivity and clay relationships

The negative relationship between the volume of the saturating electrolyte (BVW) and formation resistivity (Archie, 1942) is the principal petrophysical mechanism underlying Archie's equation. In the presence of a saline pore fluid, clay minerals and their electrical properties are considered detrimental to this relationship by contributing 'excess conductivity,' which if not corrected for, may result in reservoir undervaluation (Hardwick, 1989). Despite well documented clay effects (Hamada et al., 2001; Worthington, 2000), the results of the error analysis (sections 4.3 to 6.9) and core data petrophysical relationships (Figure 7.4), repeatedly highlight an unexpected and positive co-dependency between BVW , V_{clay} and R_t (Figure 4.8, Figure 0.7), but with very different trends for the BSR and HY. In effect, contrary to providing 'excess conductivity,' high clay volumes are coincident with an 'excess resistivity' and an overestimation of reservoir potential (Figure 4.2). As a consequence, unlike 'low resistivity pay' reservoirs where clay effects often require a compensatory **decrease** in m and n parameter values (Durand et al., 2001), the BSR-HY core modelled (e.g. Figure 4.13 or Figure 0.7) and optimised (e.g. Figure 0.6) R_{we} , m or n parameters are required to **increase** so as to compensate for the anomalously high BVW and R_t . The following section aims to elucidate key core petrophysical relationships and attempts to rationalise these observations within a geological framework. This discussion is divided into three parts:

- iv. A review of the key core petrophysical relationships, their links with clay mineralogy and impact on Archie based saturation models.
- v. A brief review of literature documenting and attempting to account for the unusually high resistivities observed in the BSR.
- vi. A proposed mechanism that integrates mineralogical and petrophysical relationships with burial and diagenetic processes, that can both account for the unusually high resistivities and the trends in optimised Archie parameters.

7.12.1 Key core petrophysical relationships

Clay minerals, their grain size and grain shape, are key factors in defining fabric and form a primary control on pore size distribution, fluid flow and thus permeability (Dewhurst et al., 1999). In addition, pore lining clay minerals can contribute significant microporosity and are often associated with high water saturations (Hamada et al., 2001; Herrick and Kennedy, 1996). These relationships are clearly observed in the BSR (Figure 4.2, Figure 7.7 and Figure 7.8), with BSR core samples exhibiting a quintuple association of increasing V_{Clay} linked to high S_{wC} , BVW , and low ϕ_{tC} and K . In other words, BSR poro-perm relationships and fluid distribution appears to be linked to, or even controlled by V_{Clay} . By contrast, the HY displays an even distribution of V_{Clay} from low to high ϕ_{tC} (Figure 7.7), inferring that V_{Clay} has limited impact on fluid distribution, though it is still observed to negatively impact k (Figure 7.8).

The effects of clay minerals on fluid distribution and poro-perm relationships can in part be attributed to the chlorite clay fraction, where, if authigenic in origin, and occurring predominantly in the style of grain coatings or interstitial growths, is likely to impact ϕ_{tC} and k (Rushing et al., 2008). This assertion is supported by the negative impact of chlorite on K and ϕ_{tC} depicted in Figure 7.9. Where chlorite contributes to microporosity (hence the BSR has a similar ϕ_{tC} range to the HY) but acts to narrow the pore-throats resulting in a lower k range (Figure 7.9).

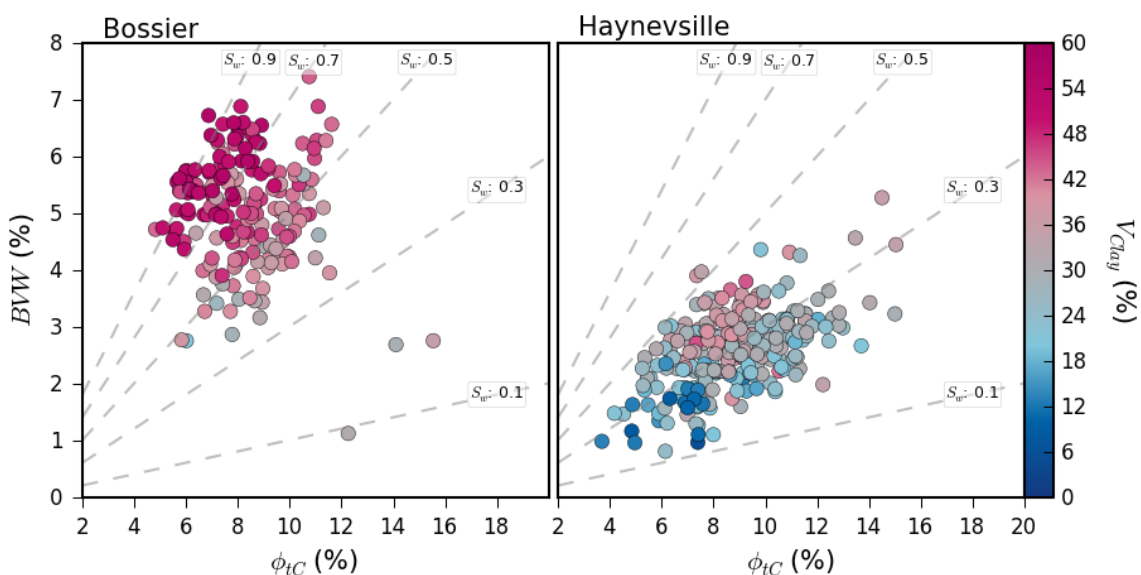


Figure 7.7. BVW vs. ϕ_{tC}
 BVW vs. ϕ_{tC} for the BSR (left) and HY (right). Marker colour is a function of V_{Clay} . Dashed grey lines depict S_w based on BVW / ϕ_{tC} .

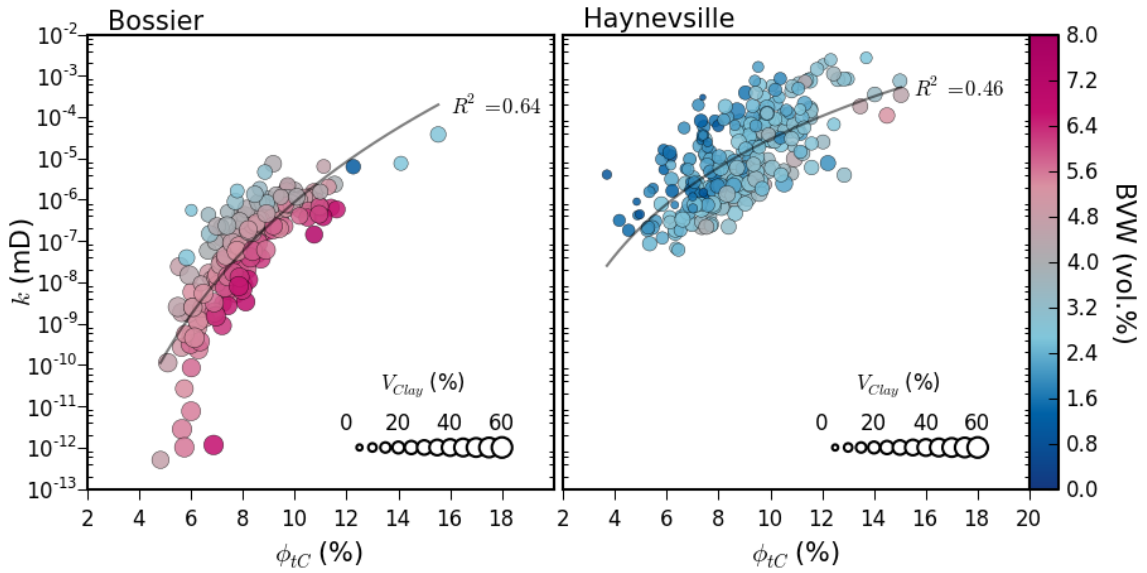


Figure 7.8. Matrix permeability (k) vs. ϕ_{tc} (coloured by BVW)
 Matrix permeability (k) vs. ϕ_{tc} for the BSR (left) and HY (right) Formations. Marker colour is a function of $V_{Chlorite}$ and marker size a function of V_{Clay} .

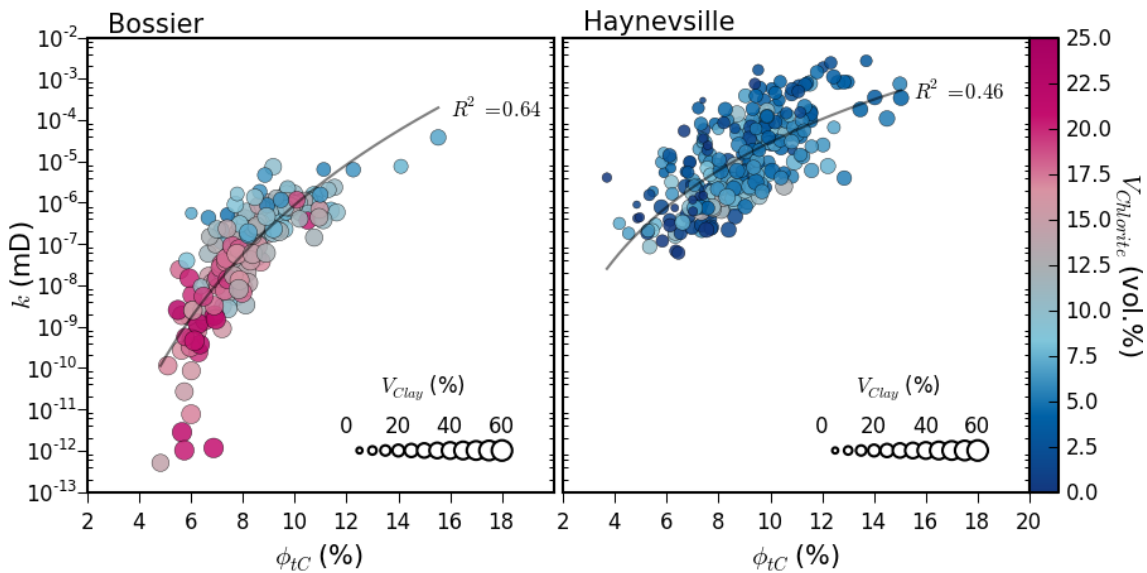


Figure 7.9: Matrix permeability (k) vs. ϕ_{tc} (coloured by chlorite)
 Matrix permeability (k) vs. ϕ_{tc} for the BSR (left) and HY (right). Marker colour is a function of $V_{Chlorite}$ and marker size a function of V_{Clay} .

As a consequence of the impact of clay minerals on formation poro-perm and fluid distributional relationships, it follows that V_{Clay} should also impact formation electrical properties, where, as discussed, clay minerals are typically expected to increase rock conductivity by increasing the conductivity of bulk water in the pore spaces (Hamada 2001). Thus BVW might be expected to form a negative relationship with R_t , though Figure 7.10 shows that this is not entirely evident. So whilst the HY broadly complies with Archie's equation (a negative $BVW : R_t$ relationship) the BSR shows a significant

departure and an increase in R_t coincident with an increase in V_{Clay} . In addition, overlain on Figure 7.10 are the calculated R_t values for either fixed m^* (left) or fixed R_{we} (right). The BSR plot (left), shows good agreement between calculated R_t (at $m^*=2$) and V_{Clay} with incremental increases in R_{we} . Likewise, the HY plot (right) shows good agreement between calculated R_t (at $R_{we}=0.014$) and V_{Clay} with incremental increases in m^* . This demonstrates that either parameter (an increase in either fluid conductivity or pore complexity) can be utilised to compensate for the observed increase in R_t with V_{Clay} . This observation is identical to that made for W1 and W2 modelled core parameters (Figure 4.13), where either R_{we} or m^* can be directly regressed from R_t relationships, allowing for a significant reduction in MAE for S_{wR} estimates (Figure 0.3).

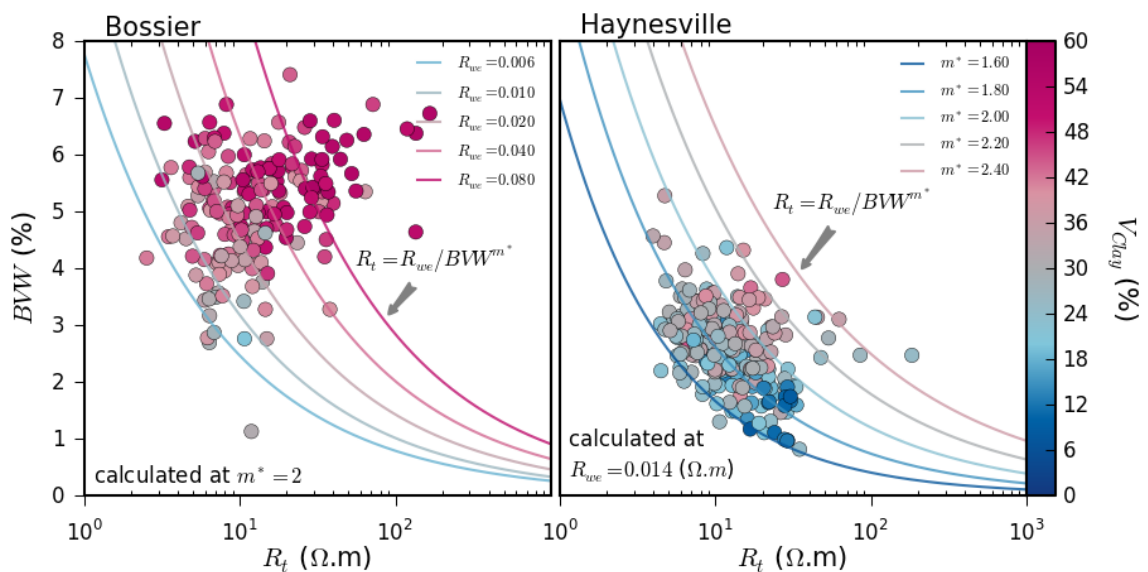


Figure 7.10. BVW vs. R_t
 BVW vs. R_t for the BSR (left) and HY (right). Marker colour is a function of V_{Clay} .

These observations suggest that V_{Clay} controls fluid distribution and formation electrical properties in the BSR and implies that free and capillary fluids contribute minimally to BVW. In addition, Figure 7.10 suggests that CBW is a net contributor to electrical resistance, either by a consequence of CEC effects and/or pore geometrical complexity. Similar observations are made for the HY, though in tandem with significantly lower V_{Clay} , far less influence over fluid distribution is observed. This raises the question: *what mechanism(s) might allow for clay minerals to add to bulk fluid resistivity and/or pore complexity, and so contribute to formation resistivity?*

7.12.2 Anomalously high resistivities in the BSR

Unexpectedly high resistivity tool responses have been previously reported in the BSR (Corley et al., 2010; Le et al., 2011) and in other northern Gulf of Mexico shales (Anderson et al., 2006). The unusual response manifests as both generally high deep resistivities and an unexpected separation in resistivity profiles with depth of investigation. This observation might normally be indicative of invasion by conductive fluids, but in this instance the extremely low BSR permeabilities (Figure 7.9), which show a similar response in oil or water based muds, make such an explanation physically untenable (Corley et al., 2010). In addition, the response does not correlate with organic content or gas production (e.g. high S_w and V_{Clay} in Figure 7.7) and neither are they unique to resistivity tool type (Corley et al., 2010).

These unusual effects were first noted on array induction logs in Oklahoma and Texas in the 1980's and were recently re-examined by Anderson et al., (2006), whose study suggests that the petrophysical complexity of shale microstructure might cause large dielectric permittivity resulting from a large internal polarisation due to the size and structure of clay minerals combined with disseminated pyrite. This mechanism requires that some dielectric permittivity be generated by the polarisation of the counter-ions in the double layer surrounding clay minerals, with the bulk of the permittivity generated by surface oxidation-reduction reactions on the surface of pyrite grains. Further investigation was undertaken by Corley et al.,(2010) using multiple tools with varying array spacings and frequencies of between 30 Hz to 200 MHz. This later study demonstrated a similar curve separation with depth of investigation for all tool types, but noted that the model proposed by Anderson et al (2006) (i.e., high dielectric permittivity caused by clay and pyrite and a single set of resistivity and dielectric permittivity parameters), could not reconcile the response for multiple tool types. In addition, the parameters were required to vary in X, Y and Z directions, and suggested exceptionally high horizontal resistivity anisotropy with exceptionally low (less than 1) vertical resistivity anisotropy. These conditions were felt to be physically unrealistic by Corley et al., (2010), who suggests that dielectric effects in isolation fail to account for the unusual log response. In order to explain the log

response Corley et al., (2010) suggests that a hypothetical series of vertical fractures filled with resistive material could satisfy the required conditions. This suggestion was tested by Le et al., (2011), who concludes that a series of vertical fractures filled with resistive material coupled with ultra-high permittivity parallel to bedding is required to explain the unusual log responses. Though in the absence of any geological evidence to support the presence of a series of vertical resistive fractures, a geological explanation remains enigmatic.

7.12.3 A mechanism for clay mineral freshening

In this study, anomalously high resistivities are highlighted as the cause of significant underestimation of S_{wA} (Figure 4.2). This is coincident with elevated V_{Clay} (Figure 4.2) and can be demonstrably corrected (**Error! Not a valid bookmark self-reference.**) by compensatory increases in either m^* or R_{we} (Figure 4.15). Furthermore, as depicted in Figure 7.10, increases in V_{Clay} correspond well with calculated R_t over a range of potential R_{we} values, implying an effective freshening of bulk formation fluid with increasing clay content. It can therefore be argued that the higher than expected resistivity response in the BSR may be a result of high V_{Clay} and clay dilution effects. Where, if BVW is principally formed from CBW , ions in addition to those required to satisfy the clay mineral surface charge will migrate away by diffusion along electrochemical gradients. In order to develop this hypothesis, it is first necessary to review the mechanisms related to changes in pore fluid chemistry and salinity with depth.

7.12.3.1 Changes in pore fluid chemistry and salinity with depth

The BSR-HY have a combined average porosity of 8%. Recently deposited clay rich muds have porosities as high as 90% (Velde, 1996), requiring the expulsion of large volumes of pore fluid over their burial history. The decline in porosity with burial and depth is well established (Hedberg, 1936; Mackey and Bridge, 1995). During this process, the sediment undergoes significant physical change (e.g. porosity, permeability, density) related to increased vertical stress, and chemical change (e.g.,

re-mineralisation reactions and thermal maturation of organic matter) in response to temperature and diagenetic processes (Boggs, 2009; Potter, 2005; Wignall, 1994). As a consequence, the pore water chemistry and its electrical resistivity also evolve typically from that of sea water at the time of deposition, to the saturating pore fluid present at the time of investigation. It is also generally accepted that pore fluid salinity increases with depth (Chilingar et al., 2002; Rieke and Chilingarian, 1974), and in the case of the Gulf of Mexico Basin, depth-salinity relationships are both well established and linked to formation overpressure (Fertl and Timko, 1971; Fowler Jr, 1970; Overton and Zanier, 1970; Sharp et al., 2001; Smith, 1977).

The effects of compaction on the pore fluid chemistry of clay rich muds and pure clays was widely investigated in the 1960's and 70's. Von Engelhardt and Gaida (1963) studied the effects of compaction on the pore solution chemistry on montmorillonite and kaolinite clay over a pressure range of 440 psi to 47,027 psi (*BSR-HY core were sampled at 10,000 ft. to 14,000 ft., equating to an approximate pressure range of 15,000 psi to 20,000 psi based on pore and overburden pressures from Rocha and Bourgoyne, (1996)*). This experiment applied instantaneous loads to clays saturated in a saline solution. Compaction was demonstrated to have no effect on the pore water chemistry of kaolinite clays, which have a near neutral surface charge and low CECs of 2-5 meq/100g (Ellis and Singer, 2007). Whilst the montmorillonite clays, which have high CECs of 5 to 40 meq/100g (Ellis and Singer, 2007), showed an decrease in pore fluid salinity up to pressures of 11,756 psi, after which salinity was noted to increase.

Later investigations by Chilingar et al., (1969) applied gradual loads to 'marine muds' from the Santa Cruz Basin (off-shore southern California), observing a decrease in the salinity of expelled fluids with increasing over-burden pressure. Implying both an increase in the salinity of the residual pore fluid, and that compaction rates can significantly impact pore fluid evolution. From these experiments Chilingar et al., (1969) concludes (A) that the salinity of expelled fluid decreases with increasing overburden pressure and (B), that the salinity of shale pore fluids should be lower than those of associated sandstones. The latter conclusion was reasoned on the basis of work by Fowler (1968), who found a correlation between high salinity and abnormally

high overpressures in the Bayou Field, Texas, where the salinity of produced water decreased with time. From this, as the freshest water was found in sands (which received their water from associated over-pressured shales) it was concluded that shale fluid salinity must be less than that of the associated sands. This was validated by Fertl and Timko, (1971), who found that the pore water chlorinity (indicative of salinity) of sands was consistently higher than that of associated shale's at similar depth. In addition, field examples presented by Overton and Zanier, (1970), Fertl and Timko, (1971) and Fowler Jr, (1970) highlight a decrease in shale resistivity with an increase in formation overpressure and a decrease in fluid salinity at approximately 10,000 ft., 11,300 ft. and 12,000 ft. respectively. In all three instances these observations can be explained by shale compaction models suggested by Powers, (1967) and modified by Burst, (1969). This advocates the release of structural pure water into the pore space during the remineralisation of smectite to illite at 3,200 to 16,000 ft., resulting in an increase in pore pressure (leading to formation overpressure) and a decrease in interstitial fluid salinity. Moreover, Krushin (2013), notes a loss in CEC (exchangeable ions and thus bound water salinity) with smectite to illite conversion, which correspond with observations by Dewhurst et al. (2008) and Dewhurst et al. (2013) that shale CEC decreases within increased compressive strength, consolidation and dewatering. It should however be noted, that whilst illitisation reactions may account for observed salinity changes and overpressures in some Gulf of Mexico sediments (Katahara, 2006), that other stress related mechanisms may also contribute (Lahann et al., 2001). A review of the origin of overpressure is given by Chilingar et al., (2002) and a 'true shale compaction model' for pore pressure prediction, which integrates stress, temperature and chemical processes has been recently proposed by (Krushin, 2013).

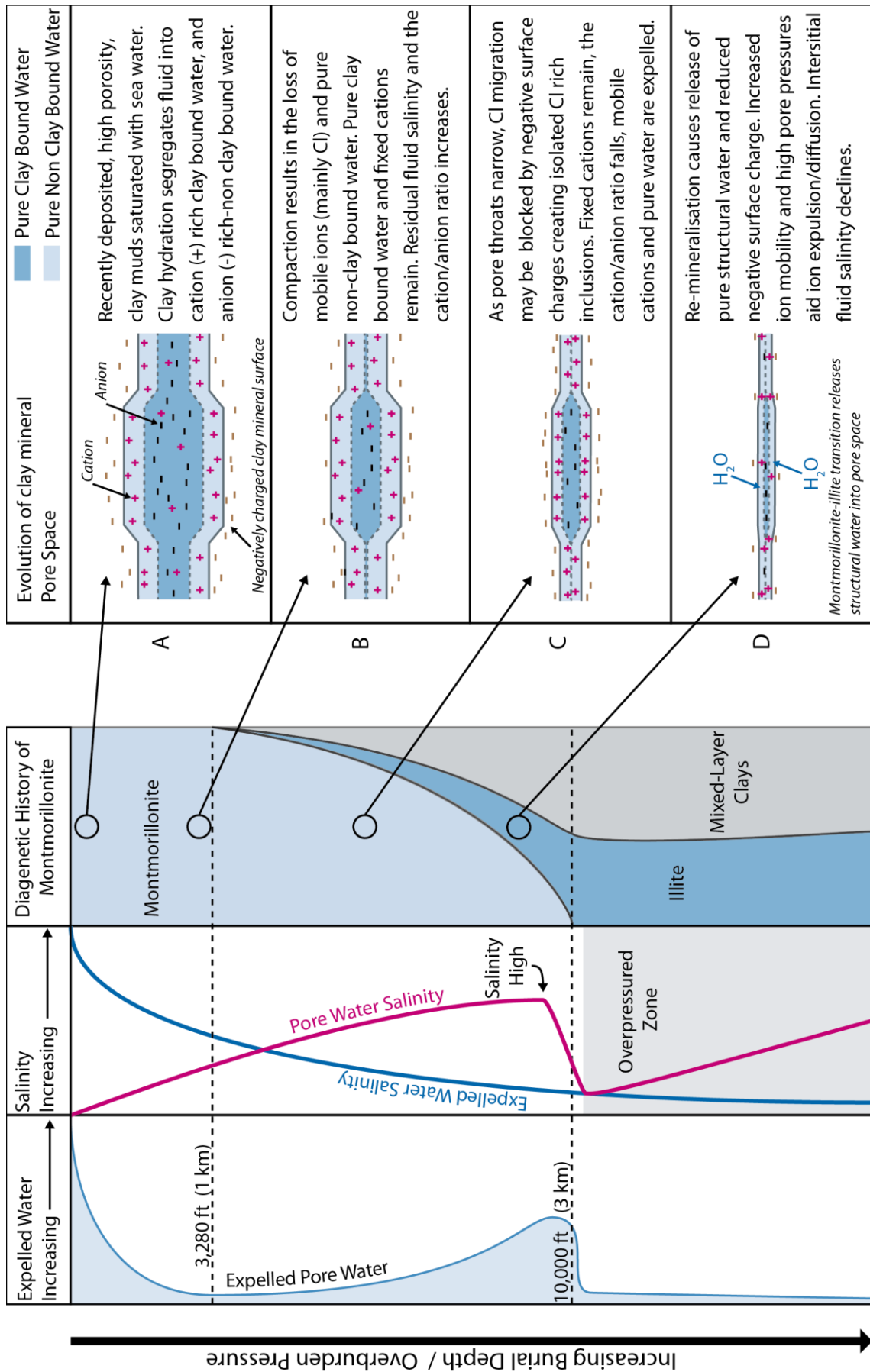


Figure 7.11. Schematic illustration of the effects of compaction on pore fluid salinity

Expelled Water and diagenetic history adapted from (Powers, 1967), pore water salinity and overpressure inferred from (Overton and Zanier, 1970) and (Fertl and Timko, 1971), and notional depiction of clay pore evolution based on descriptions by Von Engelhardt and Gaida (1963) and Chilingar et al., (1969).

The depth related changes described above are schematically depicted in Figure 7.11. This integrates a compaction model (Powers, 1967) with pore water and expelled salinity changes described by Overton and Zanier, (1970) and Fertl and Timko, (1971), with pore ion exchange mechanisms described by Von Engelhardt and Gaida (1963) and Chilingar et al., (1969). The schematic includes two highlighted depths: (A) 3,200 ft. (approx. 100°C), below which montmorillonite begins to convert to illite (Powers, 1967), and (B) 10,000 ft. (approx. 300°C), below which no pure montmorillonite was observed in Texan and Louisianan Gulf Coast sediments by Powers (1967). It is however noted that high pore pressures, undercompaction, unusual temperature gradients and heterogeneity in clay chemistry, may also impact transition depths (Chilingar et al., 2002; Freed and Peacor, 1989). Figure 7.11 attempts to schematically depict the evolution of fluid-mineral interactions, diagenesis and overpressures with increasing depth, and can be split into three general zones:

Zone 1 (0-3,200 ft.): This depicts the initial clay sediment deposition (A), where clay hydration results in the development of a pure water and cation rich electrical double layer (CBW). The anions are actively repelled from the negative surface charge and CBW resulting in respective cation and anion rich fluid components. As compaction progresses (B) the CBW and fixed cations are retained and the anion rich free waters are preferentially expelled with a net increase in the overall salinity of the remaining pore fluids which have elevated cation/anion ratios. This is somewhat validated in a study of the thermodynamics of salinity change accompanying compaction by (Smith, 1977), who finds that the concentration of anions in compaction expelled fluids decreases monotonically with reductions in clay sediment porosity whilst the cations in the residual pore fluids increase monotonically. Within this zone pore-fluid salinity increases with depth and the expelled water volume (analogous to porosity and permeability trends) declines rapidly.

Zone 2 (3,200-10,000 ft.): With continuing burial, (C) the negative surface charge of clays in narrow pore throats may inhibit chlorine migration. This prevents further expulsion of anions at the expense of pure water and more mobile cations, possibly resulting in the development of local anion rich fluidic inclusions. In addition, increasing pressures drive off outer-layers of pure clay-bound water (Burst, 1969). As a result, pore water salinity increases and the cation/anion ratio may fall (Chilingar et al., 1969). Additionally, below 3,200 ft. thermobarometric conditions allow for the illitisation of montmorillonite. As montmorillonite begins to remineralise, illitic sheets develop creating an intermediary illite-smectite (I/S) mixed-layer clay, which, with increasing temperature and pressure becomes increasingly crystalline and illitic (Potter, 2005). During this transformation interlayer potassium becomes fixed in the clay structure, whilst silica and interlayer hydration water are expelled into the pore space (Chilingar et al., 2002; Potter, 2005). As a result, with progressive illitisation (D) and a reduction in bulk CEC, ion mobility, pore water expulsion and pore water pressures are all increased. With increasing depth pressure and temperature approaching 10,000 ft. the rate of illitisation increases (Powers, 1967). As a consequence of the influx of structural pure water, pore water salinity drops below the salinity maximum, and pore pressures and porosity rise (Fertl and Timko, 1971; Fowler Jr, 1970; Overton and Zanier, 1970). As pore fluids begin to accommodate the lithostatic load, the formation becomes over-pressured.

Zone 3 (below 10,000 ft.): Below 10,000 ft. no pure montmorillonite remains. Progressive illitisation of the mixed-layer clay continues at a reduced rate, pore pressures remain high and pore fluid salinities again begin to increase as the structural pure water is progressively expelled.

The schematic presented in Figure 7.11 incorporates observations from multiple sources in attempting to accommodate regional trends observed in the GOM basin. It is intended to highlight pore water chemistry and its evolution as a complex function of diagenetic history and clay mineralogy. Within this framework, core data for the BSR-HY, which are: (A) overpressured, (B) sampled below 10,000 ft., (C) contain no

smectite, and (D) have low volumes of mixed layer clays (Figure 7.4), fit within Zone 3. It is therefore suggested that the clay-pore fluid interactions responsible for regional GOM trends also result in highly heterogeneous pore fluid salinities at the core scale as a function of clay volume and distribution. This extends the conclusion of Chilingar et al., (1969) that '*the salinity of interstitial fluid solutions in shale should be lower than those in associated sandstones*' to: the salinity of clay rich shale should be less than that of associated clay poor, more permeable shales. For instance, within the BSR-HY a heterogeneous mixture of at least four types of pore fluid regimes can be visualised: (1) non-clay bound, (2) illite dominated, (3) mixed-layer clay dominated, and (4) chlorite dominated, each with different pore water chemistries. Given the preceding discussions, and as a consequence of ion exclusion, it is suggested that the non-clay bound fluids will have greater salinities, such that overall pore water salinity is dependent on ratio of non-CBW : CBW and is thus relative to V_{Clay} . This is demonstrated in Figure 7.12 below, where above approximately 28% V_{Clay} , the pore fluid becomes increasingly CBW dominated, heterogeneous and generally fresher (Figure 7.10), such that compensatory increases in R_{we} from R_t relationships (e.g. Figure 4.15), can allow for the calculation of S_{wR} with reduced residual MAE (Figure 0.3). Moreover, it is notable that only those wells where samples have generally less than approximately 28% V_{Clay} does S_{wR} fail to improve upon standard 3D optimisation (W4).

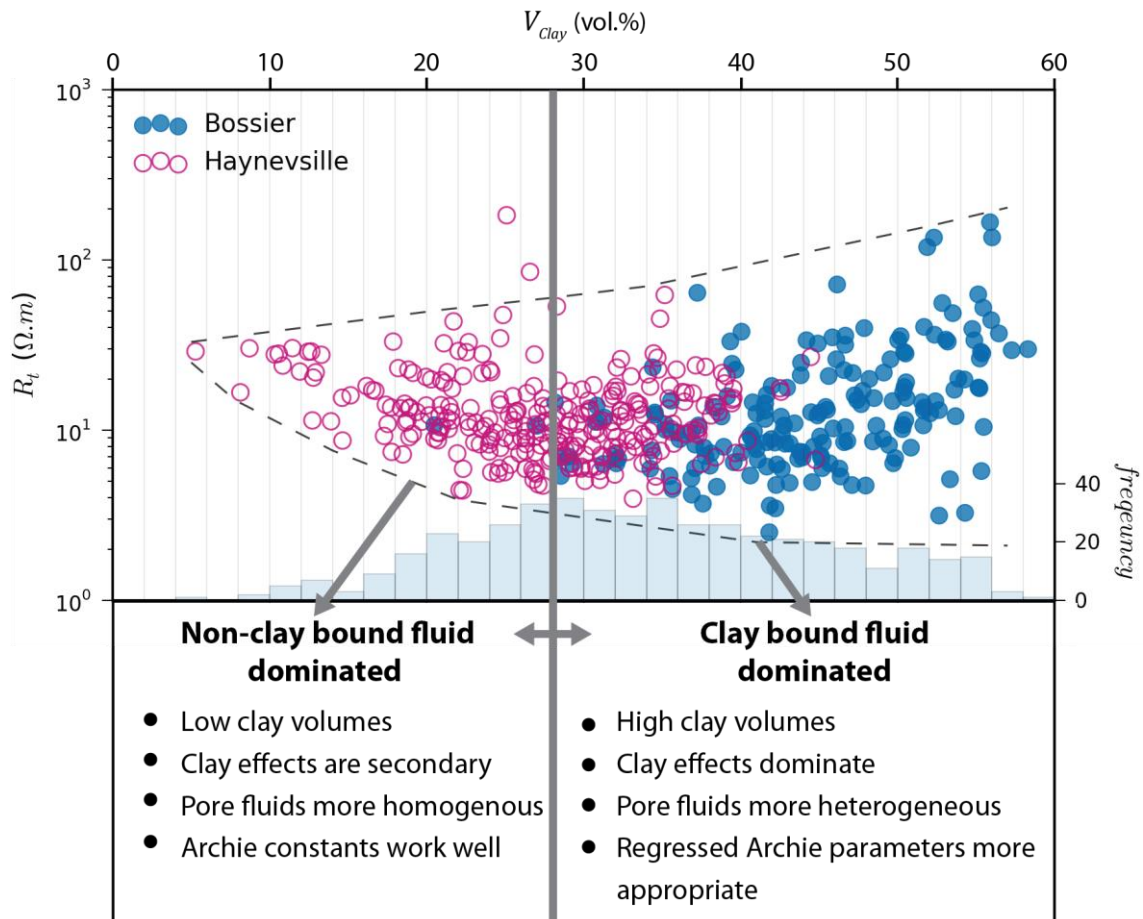


Figure 7.12. Key change in petrophysical behaviour with V_{clay}

7.12.4 A mechanism for increased pore-complexity

The effects of authigenic pore-lining chlorite, though not fully understood, are well documented in 'low resistivity pay' (Worthington, 2000). In this setting chlorite effects are considered to be less a product of surface area and CEC (Motealleh et al., 2007), but as a result of their effect on the amount and distribution of microporosity (Durand et al., 2001; Tudge, 2010). Where hydrous chlorite coatings preserve conduction pathways on grain surfaces, maintaining depressed R_t values that mask and undervalue hydrocarbon saturation. This necessitates compensatory reductions in m and n values (e.g. parameter trade-offs Figure 0.6) that have been demonstrated experimentally, with m values shown to be less than 2 and n values of around 1.5 (Durand et al., 2001; Edmundson, 1988b). Chlorite minerals can therefore be said to exert indirect electrical influence on ion conduction pathways (m and n) as a consequence of their distribution within the pore space. Whilst the direct intrinsic electrical effects of chlorite, which

have generally low CECs (2-14 meq/100g (Ellis and Singer, 2007)), on bulk fluid resistivity (R_{we}) are likely to be minimal.

In the example given by a 'low resistivity pay' analogue, the principal porosity is invaded by hydrocarbons whilst the secondary chlorite micro-porosity provides a CBW or capillary bound water-wet conductive membrane on the grain surface. Yet unlike 'low resistivity pay', and particularly in the BSR, the chlorite and other CBWs constitute the **primary** porous network. Such that additional chlorite and associated reduced ϕ_{tC} , k relationships (Figure 7.9) will add to m^* . This is witnessed in all optimiser models and core modelled parameter values, where the BSR consistently necessitate higher m^* or m values than the clay poor HY (Figure 4.8). Additionally, the BSR data, which have generally low hydrocarbon saturations, indicates a reliance on optimising m in model W4 (Figure 0.17). By contrast, the HY, which has generally significant hydrocarbon saturations, demonstrates greater emphasis on n . This is taken to suggest that pore surface wettability in the BSR is not particularly variable, being dominated by water wet clays whose distribution, in particular that of chlorite, primarily impacts m . It is therefore appropriate that the HY, which has lower clay contents, higher oil wet TOC fraction and related porosity, and a potentially more homogenous and saline free pore fluid, demonstrates an increased importance and thus a reasonable probability distribution for n .

Other impacts on m may result from clay grain orientation. Where illitisation and mechanical compaction may contribute to the re-mineralisation or re-orientation of clays perpendicular to the principle stress, potentially increasing clay alignment and creating a more elongate and regular pore space (Alpin and MacQuaker, 2010; Alpin et al., 2003; Day-Stirrat et al., 2012; Dewhurst et al., 1999; Esemé et al., 2006; Fawad et al., 2010). This might infer lower m values for increasingly aligned or fissile mudstones that have more capillary like pore-spaces, though there is no evidence in the literature to support or refute this. In any case, should illitisation result in increased planar alignment and a reduction in m , chlorite and illite precipitated in matrix supported pores and thus less influenced by vertical stress, are likely to counteract any such reduction. This argument may be overly simplistic, but it highlights the prospect of

highly heterogeneous pore geometries coincident with diverse electrical effects as noted in Figure 7.12 above 28% V_{Clay} .

Overall, it is likely that the variability in m and n exponents are intrinsically linked to both R_{we} and clay content. This is indirectly suggested by Yu and Aguilera (2011), who note that m values are typically lower than 2 in shales, as interconnected clays combined with formation water provides more paths for electric current flow. Such that if R_{we} is influenced by clay, then so must m and n . This sentiment is echoed by Bust et al., (2011) who also suggest that R_w exerts a major influence over pseudo-Archie exponent m and n . In addition, Wu and Aguilera (2012) suggest that m changes continuously in response to the variability in fracture and Kerogen porosity, which would again require like changes in R_{we} .

7.12.5 Summary and conclusions

In summary, two general petrophysical regimes can be proposed for the BSR and HY:

BSR: Dominated by CBW with non-clay bound fluid as a secondary contributor to BVW . This manifests as a freshening of pore fluids (increase in R_{we}) with increasing clay content. As the non-clay bound water volume is a secondary contributor to BVW , the addition of CBW electrical conduction pathways, and associated decreases in m , are limited. Moreover, the increased presence of chlorite and associated reductions in ϕ_{tC} and k further reduce the influence of non-clay bound fluids at higher V_{Clay} values and result in increases in m above 2.

HY: Dominated by non-clay bound fluid, CBW is a secondary contributor to BVW . This manifests in more homogenous R_{we} values and limited freshening of pore fluids with increasing clay content. As the non-clay bound water is the bulk contributor to BVW , the addition of CBW electrical conduction pathways results in reductions in m below 2, aided by higher ϕ_{tC} and k values.

The BSR and HY demonstrate markedly different petrophysical relationships and associated pseudo-Archie exponents that reflect the volume and effect of clay minerals. A boundary between the two petrophysical regimes falls qualitatively at

approximately 28% V_{Clay} (Figure 7.12). Above this limit (predominantly in the BSR), clay and chlorite volumes and clay dilution effects act to increase R_{we} , m and n . This model fits well with the generated parameters and explains the observed petrophysical heterogeneity and anomalously high BSR resistivities. In addition, an empirical method is demonstrated that increases the accuracy of S_w estimates by modifying either R_{we} or m^* as regressed from R_t relationships (Figure 0.2). Below 28% V_{Clay} the predominantly HY data are more Archie-like in their behaviour, more homogenous petrophysically, and have lower R_{we} , m and n values.

7.13 Composite core data summary

The following section integrates the relationships described in Chapter 4 and sections 7.11 and 7.12 within a single display (Figure 7.13), highlighting the relationships between mineralogy (XRD), R_t , BVW , saturation data, and the relative error (RE) in S_{wA} for each well. First the relationships, as depicted in Figure 7.13, are summarised; this is followed by a qualitative review of thin section images so as to relate mineralogical and petrophysical variations to accompanying differences in formation fabric, where discernable.

7.13.1 Petrophysical and mineralogical relationships

The preceding discussion and relationships can be largely reconciled within a single summary display. Core summary panels are provided for the BSR and HY Shales in Figure 7.13 and integrate RE , XRD, R_t , BVW and S_w data. Figure 7.13 includes five tracks:

- Track 1 (far left), RE : Includes the RE generated by all optimiser models arranged in rank order from -1 (S_{wA} underestimated by 100%) to +1 (S_{wA} overestimated by 100%) for each well. The relative error generated by optimiser model W4 is highlighted in bold, with a shaded zone denoting samples where the error is within $\pm 10\%$ (i.e. where S_{wA} is within 10% of S_{wC}). The remaining tracks are arranged in this order.
- Track 2, XRD: Includes core XRD data, highlighting a generally upward increasing V_{Clay} trend which coincides with increasingly negative RE (track 1) and underestimated S_{wA} (track 4). Likewise carbonate contents ($V_{Calcite} + V_{Dolomite}$) are highest where RE is positive and S_{wA} is overestimated.
- Track 3, BVW and R_t : Indicates a consistent increases in BVW with R_t , linked to an increase in V_{Clay} (track 2) and negative RE (track 1). Likewise, R_t and BVW are lowest where V_{Clay} is minimal, carbonate contents are high and S_{wA} overestimated (track 4).

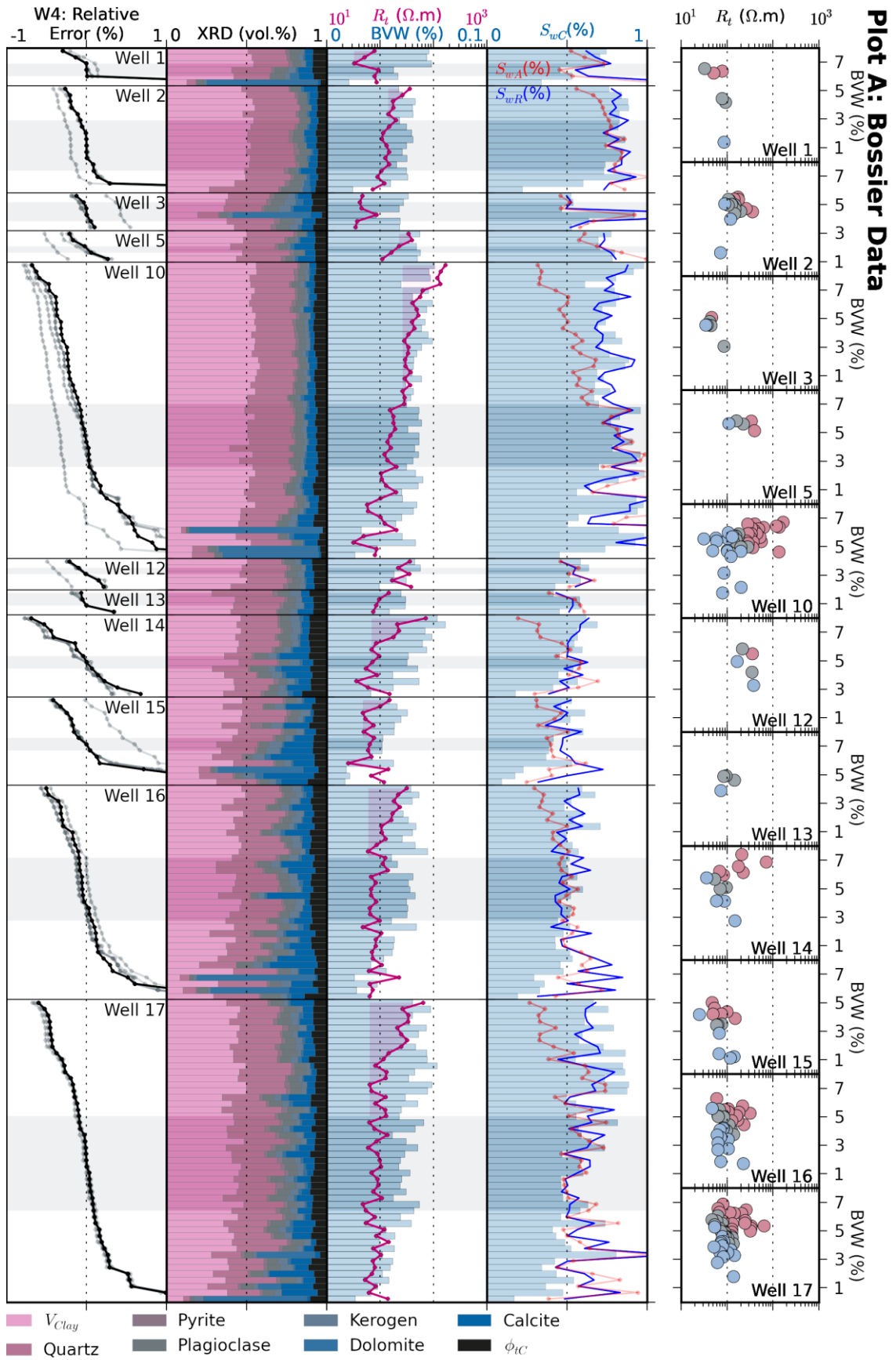
- Track 4 saturation data: The bars represent S_{wC} , the red line is S_{wA} generated by optimiser model W4, and the blue line is S_{wR} . S_{wR} demonstrates improved performance and correlation with S_{wC} for a number of wells, particularly in the BSR.
- Track 5, R_t vs. BVW cross plots: Highlights BVW vs R_t relationships for each Well. The data is divided into three groups based on the magnitude of relative error (RE) for model W4 as defined by the light grey shaded region:

Pink: $-1.0 < RE < -0.1$: links to high R_t , BVW and V_{Clay} samples

Grey: $-0.1 < RE < 0.1$: S_w estimates accurate to $\pm 10\%$

Blue: $0.1 < RE < 1.0$: links to low R_t , BVW and V_{Clay} samples

Figure 7.13 highlights the petrophysical trends discussed in sections 7.11 and 7.12. In addition, it demonstrates that the $BVW : R_t$ relationships highlighted in track 3 of Figure 7.13 can be loosely segregated into a series of more Archie like sample groups by arbitrarily partitioning RE (see cross plots in track 5). This zoning is found to frequently coincide, particularly in the BSR, with distinctions in V_{Clay} and R_t values. This suggests a means of petrophysically zoning the formation based on singular or combined V_{Clay} or R_t cut-offs into smaller optimised groups, which may further improve S_w estimates. This is shown in rudimentary fashion by shading the baseline region of R_t in track 3 for the BSR (Figure 7.13, plot A), though in practise, a more complex multivariate means of data segregation including V_{Clay} and R_t may prove useful. Moreover, data points within any one group (Pink, Grey or Blue) form relatively linear $BVW : R_t$ relationships implying a narrower range of Archie parameters. I.e. if R_t vs. BVW are linearly related then R_{we} , m and n should remain nearer to constant.



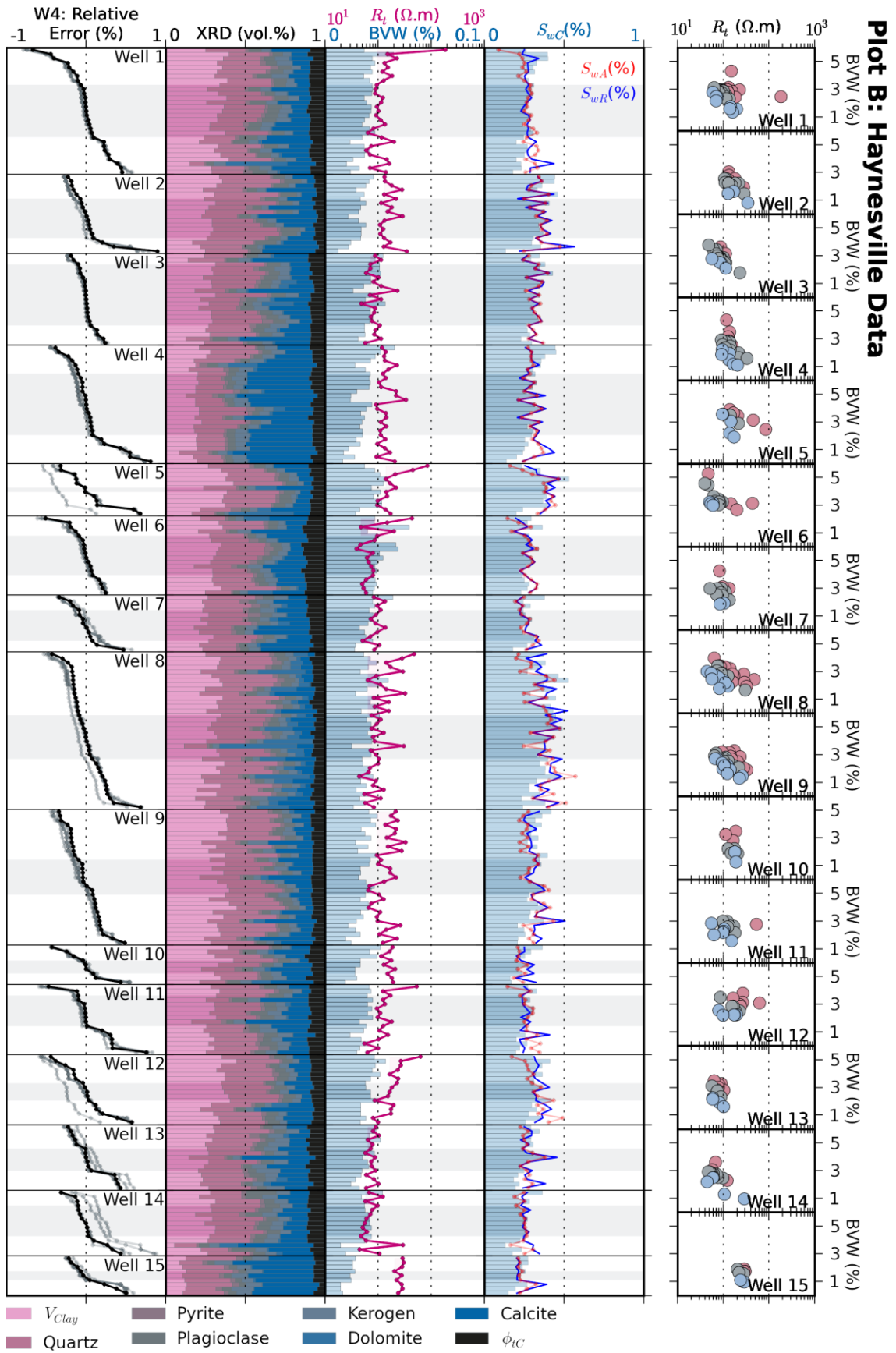


Figure 7.13. Composite core summary panels.

Track 1 (far left), Relative Error (RE): Includes the RE generated by all optimiser models arranged in rank order from -1 (S_{wA} underestimated by 100%) to +1 (S_{wA} overestimated by 100%) for each well. The RE generated by optimiser model W4 is highlighted in bold, with a shaded zone denoting samples where the error is within $\pm 10\%$ (i.e. where S_{wA} is within 10% of S_{wC}). The remaining tracks are arranged in this order. **Track 2, XRD:** Includes core XRD data, highlighting a generally upward increasing V_{Clay} trend which coincides with increasingly negative RE (track 1) and underestimated S_{wA} (track 4). Likewise carbonate contents ($V_{Calcite} + V_{Dolomite}$) are highest where RE is positive and S_{wA} is overestimated. **Track 3, BVW and R_t :** Indicates a consistent increases in BVW with R_t , linked to an increase in V_{Clay} (track 2) and negative RE (track 1). Likewise, R_t and BVW are lowest where V_{Clay} is minimal, carbonate contents are high and S_{wA} overestimated (track 4). **Track 4 saturation data:** The bars represent S_{wC} , the red line is S_{wA} generated by optimiser model W4, and the blue line is S_{wR} . S_{wR} demonstrates improved performance and correlation with S_{wC} for a number of wells, particularly in the BSR. **Track 5, R_t vs. BVW cross plots:** Highlights BVW vs R_t relationships for each Well. Data is divided into three groups based on RE for model W4 as defined by the light grey shaded region. Note; see electronic version of Figure 5.13 for a large, expandable plot.

7.13.2 Linking mineralogy and petrophysics to formation fabric

The marked change in mineralogical and petrophysical properties with RE as highlighted in Figure 7.13, combined with the large variation in m^* or R_{we} values generated in deriving S_{wR} (see section 4.4.3.1) suggest that there should be a corresponding and discernable change in sediment fabric. As such, the available thin section imagery was reviewed for each core sample. It should however be noted that comparisons between available thin section images and other core data is extremely limited, as the thin sections are not available for viewing in their entirety. For each core sample four thin section images are available, taken at the same location at different magnifications and light conditions as summarised in Figure 7.14. The first image for each core sample captures an area of 12.8 mm^2 in plane light, the second is taken at the same magnification but in epifluorescent light, the third zooms in on a selected area of the first image covering 0.512 mm^2 , with the fourth image displaying a magnified area of the third image covering 0.128 mm^2 .

Summary of thin section images available for each core sample (scale 1:1)

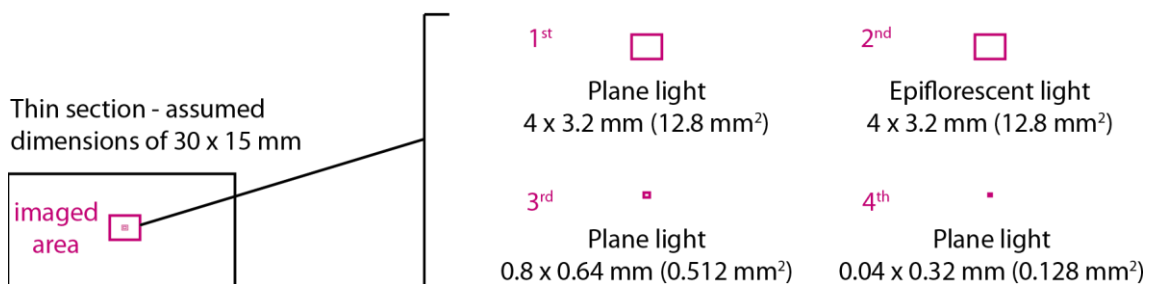


Figure 7.14. Summary of available thin section imagery

As depicted in Figure 7.14, only a single thin section image capturing a very small fraction of the entire thin section is available for any one core sample, such that little can be deduced of overall sediment fabric at any one sampling location. Whilst mudstones are highly heterogeneous with complex fabrics occurring at the centimetre to millimetre scale, sediment fabric (grading, lamina sets etc., see section 2.1.3) is generally not discernable at scales represented within the available images, particularly in the absence of context provided by the remainder of the thin section. Moreover, the rationale for the selection and inclusion of these images within the RAPID database is likely to have been dependant on the individual responsible for collating and compiling database information. In other words, links between fabric displayed in thin section images and core data are at best qualitative.

Considering the limitations discussed above, thin section images were arranged and reviewed in order of RE for optimiser model W4, in kind with the data displayed in Figure 7.13. In general, for the BSR data, as the change in V_{Clay} with RE (RE decreases as V_{Clay} increases) is both marked and consistent, variations in sediment fabric linked to grain size and clay content can be observed in the majority of wells. An example is displayed in Figure 7.15 for well 10, where, as V_{Clay} increases the thin section photographs display increasingly planar / anisotropic, fine grained and burrowed fabrics. Though within the HY, whilst variations in mineralogy follows similar trends to the BSR, they are contrastingly subtle, and no systematic variation in fabric was found. Examples are displayed for BSR well 10 and HY well 8 in Figure 7.15 and Figure 7.16 respectively.

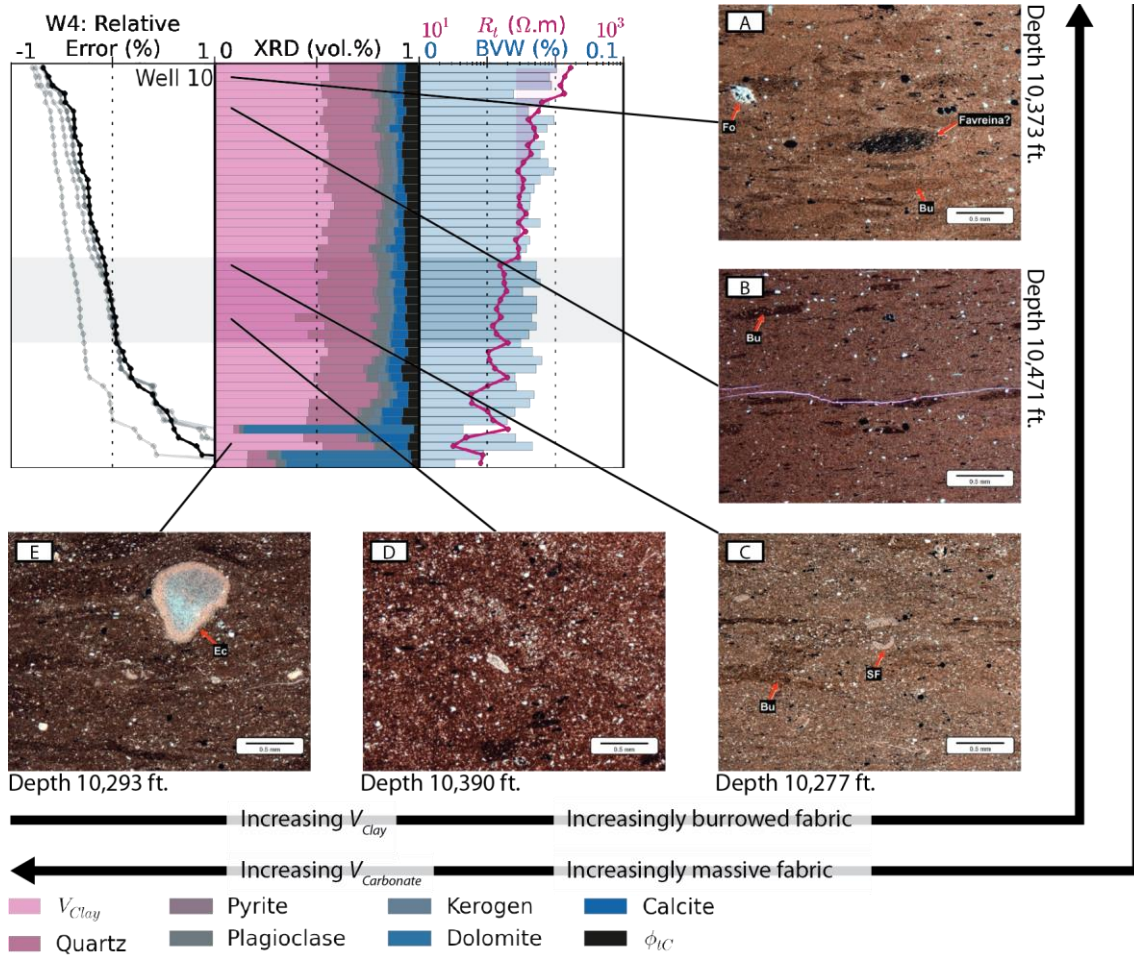


Figure 7.15. Thin section images: BSR well 10

Exert of Figure 7.13 highlighting BSR well 10, displaying changes in thin section fabric with RE and clay content. Note, the apparent decrease in grain size and increasingly burrowed fabric with increasing V_{Clay} . Thin section photographs descriptions as taken from Core Laboratories: **(A)** Burrowed (Bu), weakly calcareous and dolomitic, siliceous, slightly silty shale (claystone) with scattered benthic foraminifers (Fo). Pyrite appears as replacement mineral in some microfossils (SF). Favreina burrows are distinguished. The high quartz content (24%) is mostly due to microquartz (authigenic?) mixed with the matrix. Silt-sized siliciclastics occur dispersed throughout the sample. The larger quartz grain size is 70 micron (average grain size: 20 micron). Framboidal pyrite is common. **(B)** Burrowed (Bu), calcareous, siliceous, slightly silty shale (claystone) with scattered undifferentiated carbonate filaments (SF?). The high quartz content (29%) is mostly microquartz (authigenic?). Silt-sized siliciclastics occur dispersed throughout the sample. Framboidal pyrite is common. Microfractures are clearly visible. **(C)** Burrowed (Bu), calcareous, weakly dolomitic, siliceous, slightly silty shale (claystone) with scattered skeletal fragments (e.g.: echinoderms; SF). Benthic foraminifers are minor constituents. The high quartz content (32%) is probably due mainly to microquartz (authigenic?) mixed with the matrix. Silt-sized siliciclastics occur dispersed throughout the sample. The larger quartz grain size is 80 micron (average grain size: 10 micron). Pyrite (Py), and micas (Mi) are common. **(D)** Burrowed, calcareous, argillaceous siltstone to highly silty shale (claystone) with scattered benthic foraminifers (Fo). Some skeletal fragments from mollusks are distinguished. Silt-sized siliciclastics (e.g.: quartz, Q) occur dispersed throughout the sample. The larger quartz grain size is 110 micron (average grain size: 20 micron). Framboidal pyrite (Py) and micas (Mi) are common. **(E)** Highly calcareous, weakly dolomitic, siliceous, silty shale (claystone) with scattered skeletal fragments (e.g.: echinoderms [Ec], and benthic foraminifers [Fo]). The high quartz content (27%) is probably due mainly to microquartz (authigenic?) mixed with the matrix. Silt-sized siliciclastics occur dispersed throughout the sample. The larger quartz grain size is 100 micron (average grain size: 20 micron). Pyrite is common.

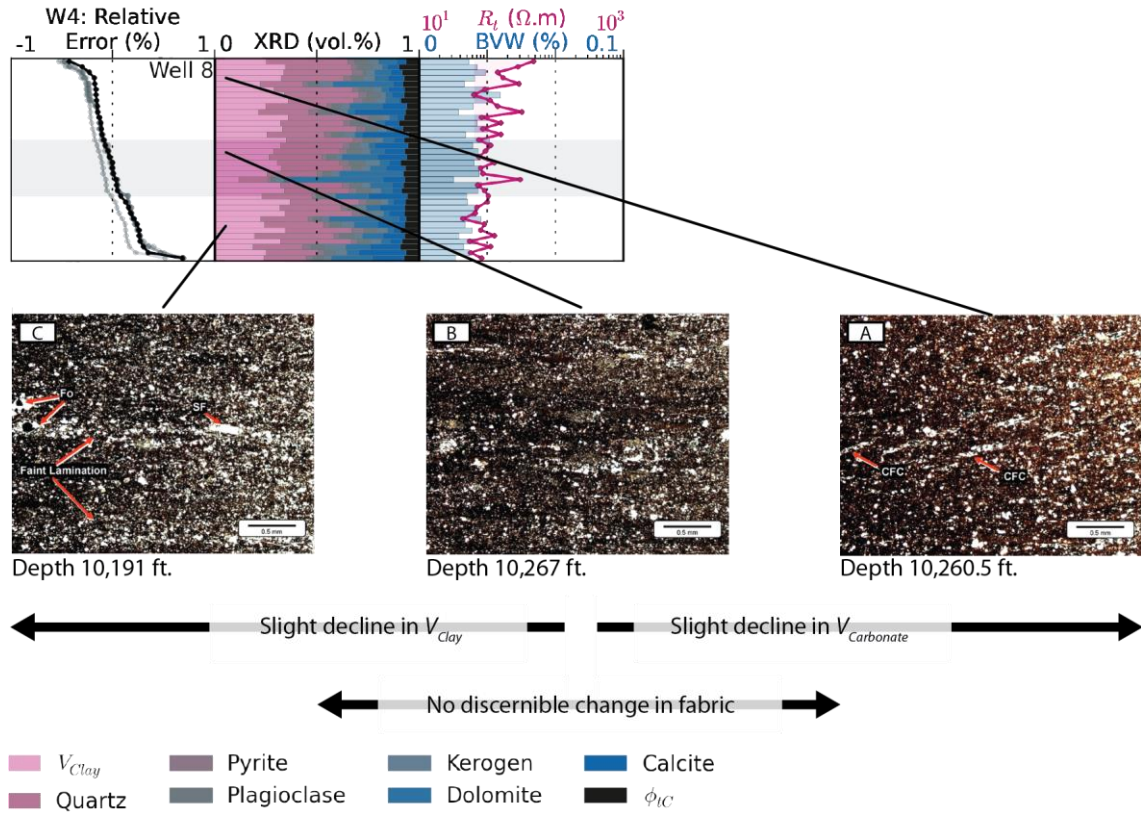


Figure 7.16. Thin section images: HY well 8

Exert of Figure 7.13 highlighting HY well 8, displaying changes in thin section fabric with R_t and clay content. Note, slight variations in clay and carbonate with no discernablke change in fabric. Thin section photograph descriptions presented as taken from Core Laboratories: **(A)** Calcareous, micaceous, pyritic, quartzose (Q), silty shale with calcite-filled cracks (CFC). Carbonate particles include calcispheres (Csp). Predominant clay is illite. Calcite volume is 8.3%, dolomite volume is 7.1%, clay volume is 34.8%. **(B)** Calcareous, slightly burrow ed (Bu), faintly laminated, pyritic (Py), quartzose (Q), silty shale. Micas (Mi) are common. Burrows appear filled by dolomite crystals. Intergranular replacements (IR) are minor constituents. Predominant clay is illite. Microfractures are clearly visible in epifluorescent light. Calcite volume is 11%, dolomite volume is 7.2%, clay volume is 30.7%. **(C)** Calcareous, faintly laminated, pyritic, micaceous, quartzose, silty shale with carbonate particles, and undifferentiated plates (UP). Skeletal fragments (SF) and Foraminifers (Fo) are common. Predominant clay is illite. Microfractures are clearly visible in epifluorescent light. Calcite volume is 14.6%, dolomite volume is 12.3%, clay volume is 25.9%.

7.13.3 Summary and conclusions

The petrophysical and mineralogical relationships discussed in Chapter 4 and sections 7.11 and 7.12 are summarised in Figure 7.13. This highlights consistency in BVW, R_t and V_{Clay} particularly in the BSR, though with similar subtle trends evident for much of the HY data (e.g. wells 1, 5, 6, 8, 12, 14). Comparison of thin section images reveals qualitative variation in fabric related to V_{Clay} in the BSR, but, as a result of subtle mineralogical variations, no systematic change could be identified in the HY. This qualitative review and comparison of thin section images with R_t is however extremely limited in the absence of core material and the inability to observe wider variations in

sediment fabric. This highlights the obvious limitations and a miss-match in scales where attempting to compare log data (with a vertical resolution of $\sim 30\text{cm}$), with core data (which utilises $\sim 1\text{-}2\text{ cm}$ core plug) and thin section images (where only 12mm^2 of core material can be viewed). As a consequence of data limitations, the interplay of depositional processes, resultant sediment fabric and associated petrophysical properties cannot be adequately evaluated. Despite this however, it is clear, particularly in the BSR, that clastic dilution (increased V_{Clay}) is linked to elevated BVW and R_t , greater sediment anisotropy and burrow intensity. This latter point, increased burrow intensity, is discussed in section 2.13, where in other formations burrowed fabrics are found to form permeable burrow networks. This contradicts BSR data, and the association of very low k values, high V_{Clay} and burrowed fabrics in the BSR. One possible explanation is that burrowed fabrics, at some early stage of burial, did contribute to higher permeability, and perhaps enabled fluid migration and escape. This would provide a mechanism for the expulsion of unrequired ions and double layer water as discussed in section 7.12.3, allowing for pore water freshening in high V_{Clay} regions where the majority fluid is CBW. Following fluid expulsion, the permeable burrow network, may then have been progressively clogged by authigenic chlorite mineral growth. This is supported by the positive association between $V_{Chlorite}$, V_{Clay} , k , and an increased incidence of burrowed fabrics. Moreover, authigenic chlorite formation can occur during, and is linked to the later, higher temperature/pressure, stages of the smectite-illite transition at (e.g. Burton, 1987; Davarcioglu, 2012). $V_{Chlorite}$ distribution is however unknown, though the availability of core for thin section and SEM analysis, particularly of burrowed clay rich fabrics, would be helpful in strengthening this hypothesis. In any case, it is demonstrable, that formation mineralogy and associated fabric can be linked to accompanying petrophysical properties and consistent trends in optimised Archie parameters.

7.14 Predicted pseudo-Archie parameters

The average pseudo-Archie parameters predicted by the optimiser models (H1 and W1-W4) and associated core modelled parameters are summarised below in Table 7.2 and in Figure 4.8. It has been demonstrated that the parameter trends of all the generated Archie parameters can be geologically rationalised within the context of the preceding discussion; $BVW/V_{clay}/R_t$ relationships and formation petrophysical heterogeneity. The following section compares the predicted parameters with those generated by other studies and discusses the manipulation of some parameters noted in the sensitivity analysis and parameter trade-offs.

<i>Optimised parameters</i>						
	<i>BSR</i>			<i>HY</i>		
	<i>m</i>	<i>n</i>	<i>R_{we} (Ω.m)</i>	<i>M</i>	<i>n</i>	<i>R_{we} (Ω.m)</i>
W1			0.0277 ± 0.0183			0.00784 ± 0.00298
W2	2.18 ± 0.23	*		1.82 ± 0.09	*	
W3	2.45 ± 0.24	*	0.0061 ± 0.0001	2.02 ± 0.13	*	0.00710 ± 0.00248
W4	1.79 ± 0.41	3.86 ± 0.31	0.0332 ± 0.0385	1.24 ± 0.31	3.39 ± 0.68	0.01177 ± 0.01375

<i>Core modelled parameters</i>						
	<i>BSR</i>			<i>HY</i>		
	<i>m</i>	<i>n</i>	<i>R_{we} (Ω.m)</i>	<i>M</i>	<i>n</i>	<i>R_{we} (Ω.m)</i>
W1			0.0546 ± 0.0871			0.00943 ± 0.00935
W2	2.28 ± 0.34	*		1.84 ± 0.16	*	
W3	2.17 ± 0.45	*	0.0286 ± 0.0260	1.75 ± 0.27	*	0.02874 ± 0.02603
W4	1.98 ± 0.58	2.79 ± 0.83	0.0327 ± 0.0267	1.48 ± 0.39	2.42 ± 0.78	0.02459 ± 0.02165

Note: * refers to m^* and $m=n$

Table 7.2. Mean predicted Archie parameters ± standard deviation

7.14.1 Comparison with previous works

As discussed in section 4.2 and displayed in Table 7.2, the generated parameters are consistently higher in the BSR than in the HY. In addition, the parameters generally decrease with increasing parameter freedom from model W1 to W4, with a corresponding increase in their variation. For instance, the average BSR core modelled parameter m for model W4 is lower (1.98), but has a higher standard deviation (0.58)

than m^* for W3 (2.14 ± 0.45). In general however, these figures fall within the ranges discussed in section 2.4.2 and compare well with the limited literature resources available on the subject.

In particular, the m^* values produced for all HY models compare well with those presented by Luffel et al., (1992), who assumes $m=n$ (m^*) for core Dean Stark S_w estimates in Devonian Shales and found $m=n=1.7$. It should be noted that the Devonian Shales included within the study are more comparable in petrophysical/mineralogical terms to the HY than the BSR. Kruschwitz and Yaramanci, (2004) found fitted m and n values for electrical measurements made on dried and re-saturated samples of Opalinus clay from Mont Terry, Switzerland where $m=1.29$ to 1.46 and $n=1.49$ to 1.93 . These figures agree well with the HY core modelled parameters for model W4, though it is noted that sample drying irrevocably alters the pore space (Jougnot and Revil 2010). Similar findings on oven dried and partially re-saturated clay-rocks of the Callovo-Oxfordian Formation by Jougnot and Revil (2010) also found $m=1.37$ to 1.54 and $n=1.99$ to 2.16 , though they suggest that oven-drying results in the formation of micro-cracks that reduce m upon saturation. This assertion is supported by analyses by Revil (2005) and Jougnot et al., (2009) on the conductivity of undisturbed saturated clay-rocks from Callovo-Oxfordian Formation where fitted $m=1.95 \pm 0.04$ and $m=2.0$ respectively. Additional work on the Mancos Shale in eastern Utah by Leroy and Revil (2009), which has a similar carbonate content, but a higher clay content than the HY, found fitted values of $m=2.2$. Yu and Aguilera (2011) combined Pickett plots with empirical TOC relationships to find m values in the HY of between 1.45 to 1.85 , provided a , n and R_w are kept constant. These values are similar to most of the predicted W1-W4 predicted m and m^* values. In addition, a case study on formation evaluation in the HY by Ramirez et al., (2011) notes that Archie's equation with $m=n=1.9$ 'works well'. In summary, the range in m and n values reported in the literature largely agree with those presented in Table 7.2.

7.14.2 Optimiser models and parameter manipulation

7.14.2.1 One dimensional models (W1 and W2)

In investigating models W1 and W2, it is clear that the sensitivity of m^* (W2) is higher than R_{we} , such that W2 is a preferable optimisation tool providing improved *MAE* reduction. In addition, the variable and parameter relationships established can be reconciled by the mineralogical / petrophysical relationships established in section 5.3, and thus have a reasoned geological footing. Moreover, these relationships allow for the calculation of S_{wR} , and a significant reduction in *MAE* for the majority of wells where V_{Clay} is generally above 28%.

Within models W1 and W2 the only parameter that can be manipulated are the fixed parameter inputs R_{we} and m^* respectively. It is noted in Figure 4.12, that increasing either fixed parameter value shifts the range and alters the sensitivity of the optimised parameter.

7.14.2.2 Two dimensional models (W3)

The disparity in the sensitivity of *MAE* to changes in m^* and R_{we} established in W1 and W2 investigations is highlighted as a significant flaw when utilising model W3. Where the optimiser consistently favours reducing R_{we} to or very close to the minimum bound (0.006 $\Omega.m$). This occurs as a by-product of least error optimisation, where reducing R_{we} effectively reduces the sensitivity of m^* , increasing the m^* parameter range within which a least *MAE* solution can be selected. This is manifest by uniformly inclined R_{we} parameter distributions, yielding an increase in the number of low error solutions at low R_{we} values (Figure 0.8 and Figure 0.9). As a consequence, other than that R_{we} values are likely to be relatively low, no geological meaning can be attributed to R_{we} output. If prior information were available, and allowed for greater constraints to be placed on R_{we} bounds, it is still likely that the lower bound would always be selected. On this basis it considered more appropriate to fix R_{we} at a reasoned value, based on available information, or other selection methods. Despite this, the resultant m^* output is very similar to that of model W2 (Table 7.2) and reflects the same trends:

generally higher m^* values coupled with increased heterogeneity in BSR as related to clay volume and clay effects on formation resistivity (Figure 4.8).

The manipulation of R_{we} so as to alter the range and sensitivity of m^* has been demonstrated within the grid-search algorithm. There is however, limited literature available examining the optimisation of Archie exponents in conventional or unconventional formations. That said, a study by Chen et al., (1995) investigated the efficacy of the simplex method in optimising a , m and n for S_w prediction using benchmark core S_w (observed) data in sandstones. They find, that for some samples, optimised a could be quite high ($a=6.3$) or low ($a=0.6$), but did not necessarily yield a significant improvement in fit. In other words, a was determined to have a low sensitivity and thus fixed at unity for some samples. This draws some parallels with this study, where R_{we} , which assumes $a=1$, also demonstrates low sensitivity and is thus preferably manipulated so as to alter the range in the more sensitive m^* . Likewise studies of the uncertainty and error propagation within multiple shaly sand models by Mahgoub et al., (2008) also find R_w and a to be the least, and m and n to be the most sensitive parameters.

7.14.2.3 Three dimensional models (W4)

Similar to model W2, increased parameter freedom appears to result in more extensive parameter manipulation. Where, in addition to a reduction in R_{we} , n is also artificially inflated to further refine the selection of m . Thus parameter manipulation appears to occur in order of least sensitivity or R_{we} , n and m . This is particularly true in the BSR which displays a flat uniform distribution of R_{we} and inclined distribution of n , suggesting insensitivity to R_{we} and an increased number of low error solutions at high n values. Unlike optimised model data however, core modelled parameters in the HY exert greater preference and whilst the probability distributions for R_{we} remains flat, n peaks at ~ 2.25 and m at ~ 1.3 (Figure 0.16 and Figure 0.17). As discussed previously (section 7.14.1), these values are not without precedence in the literature, and would likely be higher if R_{we} were fixed at some value above the saline saturation limit (0.006 $\Omega.m$).

7.14.3 Summary and conclusions

The predicted pseudo-Archie parameters and their sensitivities agree with those presented in the literature. The data supports m and n values of less than 2 in the HY and values greater than or equal to 2 in the BSR. It is notable that the preceding discussion makes little mention of the predicted R_{we} values. This is in part due to uncertainty in the predicted parameter and its manipulation in models W2 and W3. R_{we} is therefore difficult to rationalise, such that preference is given to fixing R_{we} for a given formation zone. This is compounded by a lack of literature documenting BSR and HY R_{we} values. It is however possible to say that R_{we} is likely to be higher and more variable in the BSR than in the HY (Figure 4.13).

It is also demonstrated that whilst multi-dimensional models (W2, W3 and W4) may yield an improved fit, that they generate greater uncertainty in output parameters and thus hamper the prospect of their prediction based on geological interpretation. In kind, simplistic one-dimensional models (W1 & W2) are shown to generate more constrained parameter outputs that can be placed within a geological framework. In this instance, this has yielded empirical relationships (S_{wR}) that reduce residual MAE beyond the capability of 3D optimisation (W4) methods.

Chapter 8

Conclusions and recommendations for further work

The main aim of this project has been to improve our understanding of the application of Archie's equation in shale gas systems, linking formation attributes, such as mineralogy and fabric, to measured petrophysical properties and generated pseudo-Archie parameters. This chapter presents the main conclusions of this work and considers the original aims and objectives as presented in section 1.2. It is divided into a series of research questions that are discussed in turn, followed by a summary of additional findings, an overall summary of the main conclusions and suggestions for further work.

8.15 Research question I:

Premise: Variability in optimiser model output must be linked to the heterogeneity and inter-relationships of the petrophysical inputs (ϕ_{tC} , R_{tr} , S_{wC}). In turn, the petrophysical inputs express the interaction and distribution of formation mineral and fluid components as determined by depositional and diagenetic processes.

Question: *How does variability in the error of S_w optimiser model outputs for Bossier (BSR) and Haynesville (HY) data link to the variability in formation mineralogical and petrophysical properties as represented within the wireline and core data? What are the principal geological controls on model accuracy?*

This was investigated by evaluating mineralogical and petrophysical variability and interrelationships as related to the variability in the residual mean absolute error (MAE) of optimiser model outputs. Findings indicate:

- The HY, though mineralogically heterogeneous, is relatively homogenous petrophysically, yielding low residual MAEs of between 1.03 to 5.59% and a restricted range of generated Archie parameters where m and n are typically below 2 (1.24 to 2.02). As a consequence of formation homogeneity, there is limited difference in MAE between the results of 1D and 3D optimiser models.
- The BSR, which is comparatively mineralogically homogenous, is markedly more heterogeneous petrophysically, with a larger residual MAE of 5.32 to 17.34% and a correspondingly wider range in generated Archie parameters, with m and n values typically above 2 (1.79 to 2.45). This petrophysical heterogeneity is reflected by a marked decrease in MAE with increases in optimiser model dimensionality, i.e. model W4 is significantly more accurate than W1.
- Petrophysical heterogeneity in the BSR can be directly linked to high V_{clay} and in particular the chlorite clay fraction, which is associated with a generally higher, though more variable resistivity response. In other words, results suggest that greater quantities of clay contribute to electrical variability and a typically 'excess resistivity,' not an 'excess conductivity' as might be conventionally expected. The

heteroskedastic relationship and increased variance in R_t at high V_{Clay} is likely to reflect varying distribution and interaction of clay minerals with the pore space and thus electrical properties. As a consequence, despite highly variable fluid distribution characteristics (BVW and S_{wC}) it is the effect of clay minerals in generating a variable resistivity response that in turn generates a large variation in model MAE and Archie parameter outputs. This is evident, in that the generated Archie parameters for the BSR typically demonstrate a positive linear relationship with R_t for all optimisation models considered. In addition, it explains why the S_{wR} regression method is more accurate than least error optimisation, as it allows Archie parameters to be selected with greater fidelity, where they can be modulated by and vary in accordance with R_t . Thus V_{Clay} , and not mineralogical heterogeneity, is the primary control on petrophysical variability and optimiser model accuracy. Where, if porosity-fluid relationships are the primary mechanism determining formation electrical properties, then the effects of clay minerals and thus R_{we} , m and n parameters must be extremely variable.

8.16 Research question II:

Premise: The modelled results are based on a modified Archie's equation (equation 4.1), for which the principal underlying petrophysical mechanism is the negative relationship between the volume of the saturating electrolyte and formation resistivity (Archie, 1942). Clay minerals are known to affect this relationship by reducing the resistivity, or inversely, by providing a source of excess conductivity (Hill and Milburn, 1956; Patnode and Wyllie, 1950; Winsauer and McCardell, 1953; Wyllie and Southwick, 1954). If uncorrected, this can overestimate S_w and contribute to an undervaluation of the reservoir.

Question: *How does core data for clay volume and the volume of the saturating electrolyte (BVW) relate to measured R_t , what is the geological basis for these relationships, and are they reflected by predicted Archie parameters values (m , n and R_w)?*

This was approached by investigating petrophysical relationships related to the clay mineral fractions in combination with a review of published literature trends and Archie parameters generated using log and core data. This confirms that high V_{Clay} core samples are consistently associated with greater ϕ_{tC} , BVW , R_t and lower k , particularly in the BSR. Whilst it is not surprising that clay dominated samples contain a high proportion of water, with low permeability, their link to increased formation resistivity is in stark contrast with conventional wisdom. A geologically consistent mechanism is proposed to explain the noted anomalous increase in R_t with V_{Clay} :

- A system of pore water freshening (increase in R_{we}) in clay rich regions resulting from pore water and ion expulsion linked to compaction, diagenesis (smectite-illite transition) and associated reduction in clay CEC, with fluid mobility aided in earlier stages of burial by permeable burrow networks prior to later authigenic mineral (primarily chlorite) growth and reduced permeability. In addition, latter stages of authigenic mineral growth may also result in an increase in pore geometrical complexity and m and n .

This proposed model explains the observed petrophysical heterogeneity and anomalously high BSR resistivities. Moreover, it serves to divide a continuum of HY and BSR data into two distinct, 'Archie like' and 'non-Archie like' petrophysical regimes:

- **Non-Archie like (largely BSR data):** Dominated by CBW with non-clay bound fluid as a secondary contributor to BVW . Pore fluids freshen (increase in R_{we}) with increasing clay content. As the non-clay bound water volume is a secondary contributor to BVW , the addition of CBW conduction pathways, and associated decreases in m , are limited. Moreover, the increased presence of chlorite and associated reductions in ϕ_{tC} and k further reduce the influence of non-clay bound fluids at higher V_{Clay} values and result in increases in m above 2.
- **Archie like (largely HY data):** Dominated by non-clay bound fluid, CBW is a secondary contributor to BVW . This manifests in more homogenous R_{we} values and limited freshening of pore fluids with increasing clay content. As the non-clay bound water is the bulk contributor to BVW , the addition of CBW electrical conduction pathways results in reductions in m below 2, aided by higher ϕ_{tC} and k values.

The boundary between the two petrophysical regimes is shown to fall qualitatively at approximately 28% V_{Clay} (Figure 7.12). Above this limit (predominantly in the BSR), it is suggested that clay and chlorite volumes and clay dilution effects act to increase R_{we} , m and n . This is supported by the empirical relationship for calculating S_{wR} , which increases the accuracy of S_w estimates by modifying either R_{we} or m^* as regressed from R_t relationships in wells where V_{Clay} is typically above 28% (Figure 0.2). Below 28% V_{Clay} , the predominantly HY data are more Archie-like in their behaviour, more homogenous petrophysically, and have lower R_{we} , m and n values.

8.17 Research question III:

Premise: The efficacy of a core calibrated optimised Archie approach and thus the geological validity of the Archie parameter values generated, has not been tested and the geological interpretation of these values have not been explored in shale gas systems.

Question: *What are the mechanics of an optimised Archie approach, what controls the value of generated Archie parameters, what can we infer of their validity from sensitivity analyses and parameter trade-offs, and how do modelled Archie parameter values compare with those predicted by other studies?*

This was approached by evaluating the output of the optimisation models and examining the change in MAE with variations in parameter values. This highlighted the following:

- In examining 1D optimisation models W1 and W2, MAE is shown to be more sensitive to changes in m^* than R_{we} , such that W2 and optimising m^* provides greater potential for MAE reduction. Moreover, models W1 and W2 reveal a linear empirical relationship between the optimised parameter and R_t , which allows for the calculation of S_{wR} , and a further improvement in the accuracy of S_w estimates.
- The 2D optimisation model, W3, is shown to consistently bias the parameter outputs, where R_{we} is generally minimised so as to modify the sensitivity and

parameter value range of m^* to a preferable least *MAE* solution. As such, limited geological meaning can be attributed to generated R_{we} values within model W3.

- The 3D optimisation model, W4, is shown to consistently bias parameter outputs, where, in addition to a reduction in R_{we} , n is artificially inflated so as to further refine the selection of m . Thus parameter manipulation appears to occur in order of least sensitivity or R_{we} , n and m . This is particularly true of the BSR, where the generated parameters can be ascribed limited geological meaning. Though in the HY, whilst generated R_{we} values remain questionable, the distributions for n and m peak at ~ 2.25 and ~ 1.3 respectively. Interestingly m and n appear to have different roles in the BSR and HY which are consistent with formation petrophysical properties:
 - The BSR, which generally has low gas saturations and high V_{clay} and CBW volume, demonstrates an inclined uniform n distribution and appears reliant on optimising m .
 - The HY, which has relatively high gas saturations, has very low and constrained m values, and appears reliant on optimising n .

Across all optimisation models, the generated parameters typically form a linear relationship with R_t , particularly in the BSR, suggesting that *BVW* and thus traditional Archie relationships are of limited importance in forcing parameter selection.

In general, the predicted pseudo-Archie parameters and their sensitivities agree with those presented in the literature. The data supports m and n values of less than 2 in the HY and values greater than or equal to 2 in the BSR. By contrast, R_{we} , which is systematically biased by optimisation models W2, W3 and W4 so as to preferentially adjust m and n parameter values, cannot be geologically rationalised. Indeed, where using optimisation models, it may be preferable to fix R_{we} for a given formation zone. This is compounded by a lack of literature documenting BSR and HY R_{we} values. It is however, possible to say that R_{we} is likely to be higher and more variable in the BSR than in the HY (Figure 4.13).

It is also demonstrated that whilst multi-dimensional models (W2, W3 and W4) may yield an improved fit over arbitrary Archie exponent value selection, they generate

greater uncertainty in output parameters and thus hamper the prospect of their prediction based on geological interpretation. In kind, simplistic one-dimensional models (W1 & W2) are shown to generate more constrained parameter outputs that can be placed within a geological framework. In this instance, this has demonstrated empirical relationships (S_{wR}) that reduce residual MAE beyond the capability of optimisation methods.

8.18 Research applications

The findings of this work present no complete solution to the conundrum that is the application of Archie based saturation equations to shale gas systems in the exploration and production sector. They do however highlight the potential for complex least error multi parameter optimisers (a commonly used industry method) to contain significant model error, and so produce Archie parameters with little geological meaning. Findings also highlight that whilst optimisation models that solve for only a single Archie parameter have relatively high MAE 's (i.e. they generate a poor fit between core and calculated S_w values), they produce useful and potentially geologically meaningful empirical relationships. Moreover, the combined application of 1D solver models with the resulting empirical relationships are shown to be more effective in reducing MAE than higher dimensional solvers. These empirical observations support additional findings revealed in exploring the interrelationship between clay volume and resistivity that run contrary to the currently accepted doctrine. Where, as opposed to adding 'extra' conductivity, clay minerals are shown to add 'extra' resistivity in the Bossier and Haynesville shales when clay volume exceeds 28%. This highlights both the need for extra caution in applying solver models and the need to further our understanding of the role of clay minerals in contributing to formation resistivity.

8.19 Additional findings

- Well data indicate (Figure 3.12 and Figure 3.13) a predominantly northern to north westerly origin of clastic sediments. This contrasts a north-eastern origin linked to the ancestral Mississippi River delta suggested by Hammes and Frébourg (2012). It is however recognised that Hammes and Frébourg (2012) utilised a far larger data set covering a wider region. It is therefore possible that data within this study identifies localised trends in sediment provenance within a region dominated by sediment sourced to the north and east.
- Empirical models developed in a near identical region of the BSR-HY for the prediction of TOC based on W_{pyrite} are noted to be highly inaccurate and no consistent link between pyrite and organic matter is observed. This highlights either laboratory or reservoir inconsistencies that renders the application of empirical models problematic, at least at the local level.
- Analysis indicates $\rho_{Kerogen}$ values for the BSR and HY data of between 1.23 to 1.77 g/cc. This range is far higher than the constant value of $\rho_{Kerogen}=1.17$ g/cc thought to be used by Core Laboratories. This is likely to result in an overestimation of $V_{Kerogen}$ by approximately 20% when converting from wt. to vol. %, causing the remaining mineral volumes to be subtly overestimated.

8.20 Summary

- Optimisation models can be used with good effect in calculating S_w , though the greater the freedom of the optimisation model, the greater the likelihood that Archie parameters produced are biased, limiting their geological interpretation.
- One dimensional optimisation models are less accurate in calculating S_w , but reveal empirical relationships which are demonstrated to increase the accuracy of S_w estimates beyond the capability of higher dimensional optimisation models.
- Optimiser generated Archie parameters often have linear relationships with formation R_t , but not BVW in the BSR. This indicates that formation fluids (BVW) in the BSR play a reduced role in controlling the formation R_t response. By contrast,

the HY is more Archie-like with a typically negative linear relationship between BVW and R_t .

- Though mineralogically heterogeneous, the HY is relatively homogenous petrophysically. This is reflected by a typically narrow range in generated Archie parameters.
- Though relatively homogenous mineralogically, the BSR is relatively heterogeneous petrophysically. This is reflected by a wider, more varied range in generated Archie parameters.
- Increased resistivity and variability in the resistivity responses are shown to correlate linearly with residual MAE in the BSR.
- In contrast to typical relationships, clay content, particularly the chlorite fraction, is linked to an increase in R_t , and an increase in the heterogeneity of the R_t response.
- It is proposed that that the anomalously high BSR resistivity response could be accounted for burial diagenesis driven ion expulsion and bound water freshening, particularly in clay rich bioturbated regions, in combination with authigenic chlorite mineral growth and increased pore complexity. In general, it is suggested that the salinity of clay rich mudstone should be less than that of associated clay poor, more permeable mudstone.

8.21 Recommendations for further work

There are numerous avenues available for further work in investigating the relationships between formation fabric, mineralogy, geochemistry and petrophysical properties, particularly in regards to formation electrical properties of shale gas systems.

Access to core with additional core analysis, specifically XRD and clay mineralogy, calculated CEC, or core measured CEC values, would help validate the suggestion that fluid resistivity may contribute to increased resistivity in clay rich areas. Moreover, analysis of variations in formation fabric in areas of contrasting resistivity response in the BSR would help determine the role of clay mineral distribution and formation fabric in determining formation electrical properties. Specifically, thin section studies of BSR bioturbated fabric could confirm the qualitative association made in this study between bioturbation and authigenic clay mineral growth, particularly chlorite.

Core material in shale plays, particularly in relatively thin productive successions such as the HY, are often fully cored. Multi-sensor core logging of newly retrieved core, with particular reference to infrared spectrophotometry, which measures light reflection and transmission properties of a material to identify mineral constituents, can be measured with a high sampling rate (less than 1cm). In conjunction with additional MSCL tools such as X-Ray fluorescence, and core sampling and XRD analysis, a robust and high resolution mineralogy log could be created. This would serve a number of purposes, firstly as a means to calibrate and validate log multi-mineral solver tools, but also in evaluating the links between changes in mineralogy with observable differences in formation fabric and any inherent systematic patterns or cyclicity that may fall within a sequence stratigraphic framework. Integration with typically available wireline data would help determine mineralogical and fabric effects on upscaled log characteristics, but also lend greater predictive capability in nearby wells that share similar log characteristics in the absence of detailed core data.

Within this study, it is suggested that due to ion exclusion, that clay rich shales should have a lower salinity than adjacent clay poor shales, which have a greater proportion of non-clay bound water. Moreover, it is suggested that, in more plastic clay rich regions which lack grain support, the bound water between clay grains will be at a hydrostatic minimum, whereas bound water affiliated with similar clays but supported by granular material may retain more water. On this basis, the volume of clay bound water and fluid salinity should be a function of composition and fabric. A study utilising thermo gravimetric analysis of regions of contrasting fabric and mineralogy within shale, provided it is possible to distinguish between clay bound and non-clay bound fluids, would be useful in indicating the variability in fluid characteristics and heterogeneity associated with fabric and mineralogy.

Within this study, the Archie type equation used draws parallels with Archie's original equation and the Dual water and Waxman Smitt methods. A wider sensitivity analysis encompassing other popular saturation equations, such as Simandoux and Indonesian methods, including recently proposed models by Herrick and Kennedy (2009) and Iheanacho (2013), would further aid the informed selection and choice of appropriate saturation models in shale systems. Moreover, these analyses could be applied to a wider range of shale sequences, so as to further link Archie parameter behaviour to changes in formation geological properties.

Appendices

Appendix A

GRI method laboratory protocol

LABORATORY PROCEDURES

Sample Preparation

Approximately 300g of sample is removed from each preserved core section by making a longitudinal slice with a band saw, using chilled nitrogen as the blade lubricant. Each sample is weighed to $\pm 0.001\text{g}$ and the bulk volume by mercury immersion is measured to $\pm 0.01\text{cc}$. These initial measurements are performed to determine natural sample density (Bulk Density). The samples are then wrapped in saran and placed in sealed vials pending further sample preparation.

Each 300g sample is processed using a mechanical rock crusher and sieved through 20 and 35 US mesh sieve screens. The material retained on the 35-mesh screen is separated into a Dean Stark sub-sample (~100g) and a permeability sub-sample (~50g). These procedures are performed while minimizing exposure time and evaporative losses. These sample splits are sealed in airtight vials pending further analysis. Any sample remnants are collected and maintained in airtight vials as well.

Measurements

Matrix Permeability:

Matrix permeability is determined by monitoring pressure decay as defined in the "Advances in Shale Analyses Report, D.L. Luffel, 1993". The permeability sub-sample is placed into a sealed sample chamber and approximate 30 cc of helium gas at ~200 psig is injected into the sample chamber system. Pressure decay is recorded in 0.25 sec increments to a maximum time of 4000 sec. Pressure versus time data are used to calculate matrix permeability.

Fluid Saturations – Dean Stark Technique:

Reagent grade toluene is conditioned to remove excess water and used for the extraction. The Dean Stark sub-samples are placed in glass thimbles to eliminate grain loss and weighed to $\pm 0.001\text{g}$. The samples are loaded into the Dean-Stark apparatus under an argon bath and refluxed for 8 days. Water volumes are recorded twice daily to ensure complete water extraction. The extraction solvent discoloration is noted to validate removal of trace quantities of mobile hydrocarbon.

Sample Drying:

Samples are dried in a vacuum oven at 110°C until weight equilibrium is achieved ($\pm 0.001\text{ g}$). The minimum drying time is 1 week. After weight stabilization, samples are stored in a desiccator pending further analysis.

Porosity and Grain Density:

Porosity is determined by measuring grain volume at ambient conditions using the Boyle's Law double-cell technique with helium as the expansion gas (API RP-40, Sec 5.3.2.1). Sample bulk volume is calculated using the weight of the sample before extraction and the bulk density of the original core piece. Grain density values are calculated by direct measurement of grain volume and weight on dried crushed samples.

Appendix B

Grid search optimiser: example Python
code for optimiser model W4

W4.Grid.Search (example).py 1Printed on 28/05/2014, 14:45:13 1Page 1

```

1 import csv
2 from numpy import genfromtxt
3 from numpy import savetxt
4 from numpy import array
5 import numpy as np
6
7 def grid_search(step,Formation,Label):
8     #data input
9     my data = genfromtxt('data.file.csv', delimiter=',', skip header=2)
10    #output data
11    outfile0 = csv.writer(open('W4.GS '+Label+'.OUT.csv', 'ab'))
12    outfile0.writerow(['well/F','m','n','Rwe','Swcalc','Sqdiff','RMSE','MAE','Ndata'])
13    outfile1 = csv.writer(open('W4.GS '+Label+'.OPT.csv', 'ab'))
14    outfile1.writerow(['well/F','m','n','Rwe','Swcalc','Sqdiff','RMSE','MAE','Ndata'])
15    #Variable Range
16    Mmin, Mmax, Mstep = 1, 3.1, step #Porosity Exponent M
17    Nmin, Nmax, Nstep = 1, 4.1, step #Saturation Exponent N
18    RWmin, RWmax, RWlogstep = 0.006, 0.1, step #Fluid Resistivity Rw
19    #Element input positions in input CSV file
20    #RT: deep resistivity, PHIT: tcore otal porosity, Sw Core: core water saturation
21    RT, PHIT, SW Core = 20, 22, 32
22    #Create list of wells in input file (two formation options: 1=Bossier, 2=Haynesville)
23    Ref=np.unique([i[2] for i in my_data if i[1] == Formation])
24    #Cycle through well (Ref) list for selected formation
25    for R in Ref:
26        MAE_opt = 1
27        #Cycle through the range of M
28        M = Mmin
29        while M < Mmax:
30            #Cycle through the range of N
31            N = Nmin
32            while N < Nmax:
33                #Cycle through the range of Rw
34                RW = np.log10(RWmin)
35                while RW < np.log10(RWmax):
36                    AE,Sqdiff_culm,Ndata = 0,0,0
37                    for i in my data:
38                        if i[2] == R:
39                            #Calculate Archie SW (SWcalc)
40                            SWcalc = np.power(((np.power(10,RW))/
41                            (np.power(i[PHIT]/100,M) * i[RT])),(1/N))
42                            #Count the data
43                            Ndata += 1
44                            #Add up the squared difference
45                            Sqdiff = np.power( (SWcalc - i[SW Core]), 2)
46                            #Cumulative error
47                            Sqdiff_culm += Sqdiff
48                            AE += np.sqrt(Sqdiff)
49                            #Calculate the root mean square error(RMSE)
50                            RMSE = np.sqrt(Sqdiff_culm/Ndata)
51                            #Calculate the absolute mean error(MAE)
52                            MAE = AE/Ndata
53                            #output optimum value only
54                            if MAE <= MAE_opt:
55                                MAE_opt=MAE
56                                OPTOUT = array([i[2],M , N, np.power(10,RW), SWcalc,
57                                Sqdiff, RMSE, MAE, Ndata])
58                            #output all other values if error less than 100%
59                            if 0 < RMSE < 1 or 0 < MAE < 1:
60                                Vals = array([i[2],M , N, np.power(10,RW), SWcalc,
61                                Sqdiff, RMSE, MAE, Ndata])
62                                outfile0.writerow(Vals)
63                            #close loops
64                                RW += RWlogstep
65                                N += Nstep
66                                M += Mstep
67                                outfile1.writerow(OPTOUT)
68    #function call: specify:#1:define step value,#2:formation,#3:file label
69    grid_search(0.01,1,'OUT')

```

G:\PHD15.THESIS\Chapter 4\Data_CSvsW4.Grid.Search (example).py JFile date: 28/05/2014 JFile time: 14:45:04

Appendix C

Multi-sensory core logger: a summary of work undertaken

Core material for well 11 was made available by BG Group for a period of 6 months in 2011. The cored section spanned the entire depth of the Haynesville Formation, equivalent to 18.63 meters or 61.1220 ft in well 11. The core was photographed and examined using a multi-sensor core logger (MSCL) provided by Geotek and sampled at selected locations for thin section analysis. The MSCL tool included an infrared spectrophotometer, magnetic susceptibility tool non-contact resistivity, density and natural gamma ray detectors, with measurements taken at intervals of between 1 and 5cm. The core had however been stored in an open uncontrolled environment at room temperature in typical UK office conditions. During this time, significant moisture loss and drying, in combination with vibration and movement linked to repeated transport between laboratory and office environments, is likely to have contributed significantly to the degradation of core quality. As a consequence the data generated by the MSCL tool was significantly impaired. This arose principally from the drying and movement related 'biscuiting' of friable core material, where biscuiting refers to the separation of largely continuous core material along bedding and cleavage planes to form numerous disk or biscuit shaped core sections. The sections of core therefore comprised many

hundreds of biscuit fragments, with each containing many more incomplete bedding/cleavage partings. The void space between core fragments and incomplete partings affects the density, magnetic susceptibility and natural gamma response, causing significant noise that negatively impacts tool response and cannot be easily corrected. Moreover, the MSCL resistivity tool is designed for saturated material, where core biscuiting and desiccation will likely significantly impact tool response, as such the tool could not be adequately calibrated and only a relative resistivity output could be generated. The infrared spectrophotometry tool, which is likely the most reliable data generated, requires specialist software for which funding was not available. As a consequence of these data quality issues, the investigation of the data was not pursued.

For further information and access to core MSCL data please contact Professor Mike Lovell at the University of Leicester (mike.lovell@le.ac.uk)

Appendix D

Example petrophysical workflow

Example petrophysical workflow

Below is an example petrophysical workflow after Bust et al., 2011. This highlights the evaluation of water saturation as one of five components critical to determining the gas in place in shale systems.

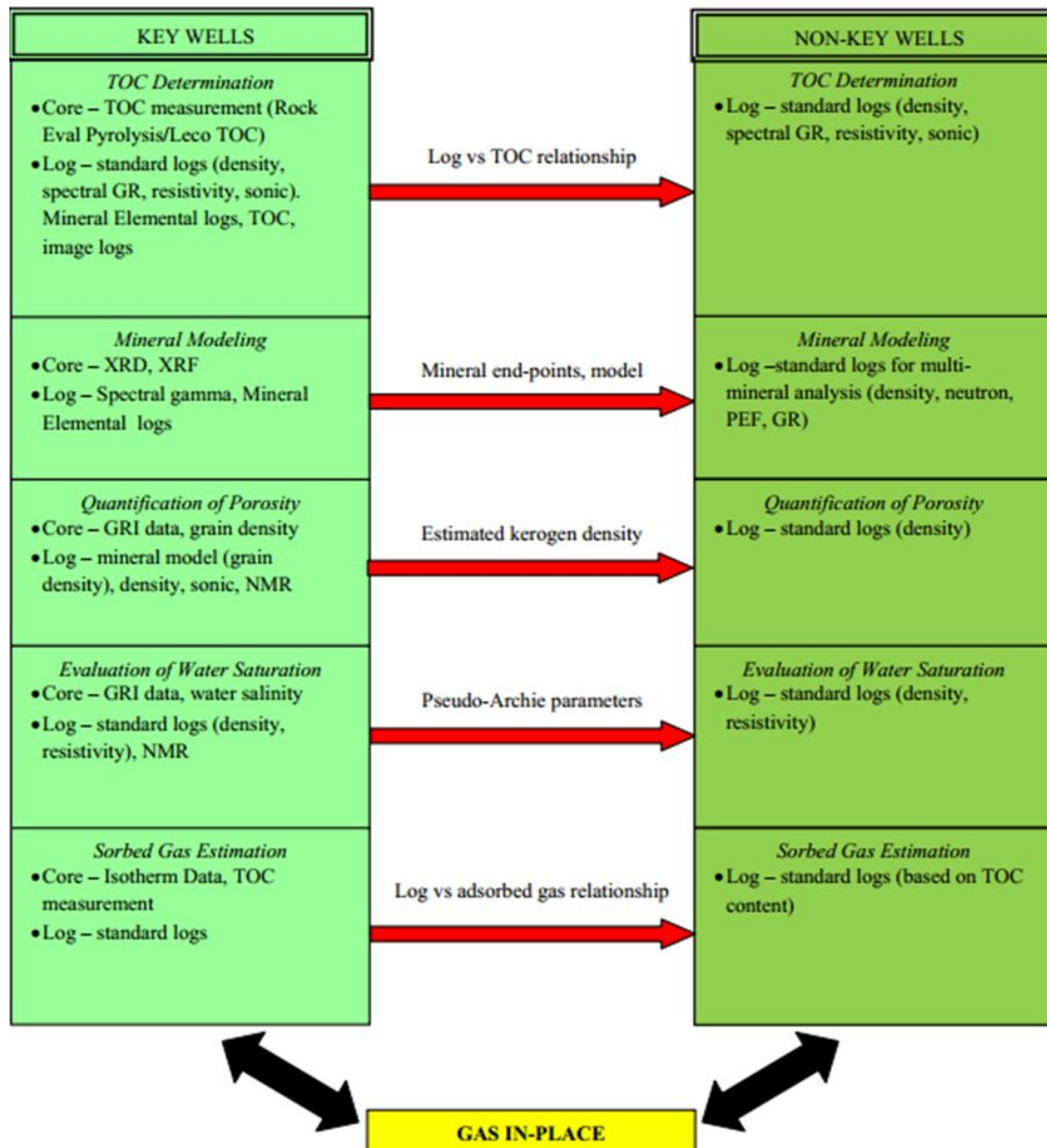


Figure D.1. Example petrophysical workflow

Example petrophysical workflow, reproduced from Bust et al., 2011.

Appendix E

Electronic thesis

References

- Abouelresh, M.O., Slatt, R.M., 2011. Shale depositional processes: Example from the Paleozoic Barnett Shale, Fort Worth Basin, Texas, USA. *Central European Journal of Geosciences* 3, 398–409. doi:10.2478/s13533-011-0037-z
- Abouelresh, M.O., Slatt, R.M., 2012. Lithofacies and sequence stratigraphy of the Barnett Shale in east-central Fort Worth Basin, Texas. *AAPG Bulletin* 96, 1–22
- Adams, R.L., 2009. Basement Tectonics and Origin of the Sabine Uplift; *GCAGS Transactions*, v. 59, p. 3-19
- Adiguna, H., 2012. Comparative Study for the Interpretation of Mineral Concentrations, Total Porosity, and TOC in Hydrocarbon-bearing Shale from Conventional Well Logs. *SPE Annual Technical Conference and Exhibition*, 30 September-2 October, New Orleans, Louisiana, USA. SPE-166139-MS
- Adisoemarta, P., Anderson, G., Frailey, S., Asquith, G., 2001. Saturation Exponent n in Well Log Interpretation: Another Look at the Permissible Range. *SPE Permian Basin Oil and Gas Recovery Conference*, 15-17 May, Midland, Texas. SPE-70043-MS. doi:10.2118/70043-MS
- Adisoemarta, P.S., Anderson, G.A., Frailey, S.M., Asquith, G.B., 2000. Historical use of m and a in well log interpretation: is conventional wisdom backwards?, in: *SPE Permian Basin Oil and Gas Recovery Conference*, 21-23 March, Midland, Texas. SPE-59699-MS. doi; 10.2118/59699-MS
- Ahmad, M., Haghghi, M., 2012. Mineralogy and Petrophysical Evaluation of Roseneath and Murteree Shale Formations, Cooper Basin, Australia Using QEMSCAN and CT-Scanning. *SPE Asia Pacific Oil and Gas Conference and Exhibition*, 22-24 October, Perth, Australia. SPE-158461-MS. doi; 10.2118/158461-MS
- Al-Marzoug, A.M., Al-Ghamdi, T.M., Sassi, K.H., Badri, M., 2013. Characterization of Shale Gas Rocks Using Dielectric Dispersion and Nuclear Magnetic Resonance.

- SPE Saudi Arabia Section Technical Symposium and Exhibition, 19-22 May, Al-Khobar, Saudi Arabia. SPE-168081-MS. doi; 10.2118/168081-MS
- Alfred, D., Vernik, L., 2013. A new petrophysical model for organic shales. *Petrophysics* 54, 240–247
- Algeo, T.J., Maynard, J.B., 2004. Trace-element behavior and redox facies in core shales of Upper Pennsylvanian Kansas-type cyclothems. *Chemical Geology* 206, 289–318
- Allaby, M., 2008. *A dictionary of earth sciences*. Oxford University Press, Oxford
- Allix, P., Burnham, A., Fowler, T., Herron, M., Symington, B., 2010. Coaxing Oil from Shale. *Oilfield Review* 22
- Alpin, A.C., MacQuaker, J., 2010. *Getting Started In Shales*. AAPG/Datapages
- Alpin, A.C., Matenaar, I.F., van der Pluijm, B., 2003. Influence of mechanical compaction and chemical diagenesis on the microfabric and fluid flow properties of Gulf of Mexico mudstones. *Journal of Geochemical Exploration* 78-79, 449–451. doi:10.1016/S0375-6742(03)00035-9
- Ambrose, R., Hartman, R., diaz campos, mery, Akkutlu, I.Y., Sondergeld, C., 2010. New Pore-scale Considerations for Shale Gas in Place Calculations, in: *Proceedings of SPE Unconventional Gas Conference*. Presented at the SPE Unconventional Gas Conference. doi:10.2118/131772-MS
- Anderson, B.I., Barber, T., Luling, M., 2006. Observations of Large Dielectric Effects on Induction Logs, or Can Source Rocks Be Detected with Induction Measurements. Presented at the SPWLA 47th Annual Logging Symposium, 2006
- Andrews, I.J., 2013. *The Carboniferous Bowland Shale gas study: geology and resource estimation*. British Geological Survey
- Angulo, S., Buatois, L.A., 2012. Integrating depositional models, ichnology, and sequence stratigraphy in reservoir characterization: The middle member of the Devonian–Carboniferous Bakken Formation of subsurface southeastern Saskatchewan revisited. *AAPG Bulletin* 96, 1017–1043. doi:10.1306/11021111045
- Aplin, A.C., Macquaker, J.H.S., 2011. Mudstone diversity: Origin and implications for source, seal, and reservoir properties in petroleum systems. *AAPG Bulletin* 95, 2031–2059. doi:10.1306/03281110162
- Archie, G.E., 1942. The Electrical Resistivity Log as an Aid in Determining Some Reservoir Characteristics. *Petroleum Transactions, AIME* 146, 54–62

- Awolusi, F., Fasesan, O., Adisoemarta, P., Heinze, L., 2005. Analysis of Errors in Historical Use of Archie's Parameters, in: Canadian International Petroleum Conference, 7-9 June, Calgary, Alberta. PETSOC-2005-202. doi; 10.2118/2005-202
- Baihly, J., Altman, R., Malpani, R., Luo, F., 2010. Shale Gas Production Decline Trend Comparison Over Time and Basins. SPE Annual Technical Conference and Exhibition, 19-22 September, Florence, Italy. SPE-135555-MS. doi; 10.2118/135555-MS
- Bardon, C., Pied, B., 1969. Formation Water Saturation In Shaly Sands. SPWLA 10th Annual Logging Symposium, 25-28 May, Houston, Texas. SPWLA-1969-Z
- Bauluz, B., Yuste, A., Mayayo, M.J., Rodríguez-Navarro, A.B., González-López, J.M., 2012. Microtexture and genesis of clay minerals from a turbiditic sequence in a Southern Pyrenees foreland basin (Jaca basin, Eocene). *Clay Minerals* 47, 303–318. doi:10.1180/claymin.2012.047.3.02
- Bergstra, J., Bengio, Y., 2012. Random search for hyper-parameter optimization. *The Journal of Machine Learning Research* 13, 281–305
- Bhuyan, K., Passey, Q.R., 1994. Clay Estimation from GR and Neutron-Density Porosity Logs," in: SPWLA 35th Annual Logging Symposium
- Blakey, R.C., Peterson, F., Kocurek, G., 1988. Synthesis of late Paleozoic and Mesozoic eolian deposits of the Western Interior of the United States. *Sedimentary Geology* 56, 3–125. doi:10.1016/0037-0738(88)90050-4
- Boggs, S., 2009. Petrology of sedimentary rocks. Cambridge University Press.
- Bohacs, K., Passey, Q., Rudnicki, M., Esch, W., 2013. The Spectrum of Fine-Grained Reservoirs from "Shale Gas" to "Shale Oil"/ Tight Liquids: Essential Attributes, Key Controls, Practical Characterization. Society of Petroleum Engineers - International Petroleum Technology Conference 2013,. doi:10.2523/16676-MS
- Bohacs, K.M., Grabowski, G.J., Carroll, A.R., Mankiewicz, P.J., Miskell-Gerhardt, K.J., Schwalbach, J.R., Wegner, M.B., Simo, J.A., 2005. Production, destruction, and dilution-the many paths to source-rock development. *SPECIAL PUBLICATION-SEPM* 82, 61
- Bona, N., Bam, B., Rossi, E., 2014. Ultrafast Determination of Archie and Indonesia m&n Exponents for Electric Log Interpretation: a Tight Gas Example. Society of Petroleum Engineers. doi:10.2523/17446-MS
- Boonen, P., Liu, Z., Xu, L., Huiszoon, C., Schultz, W., 2010. Applications of Triple Neutron Porosity Measurements In Gas Shales And Shaly Sands. SPWLA 51st Annual Logging Symposium, 19-23 June, Perth, Australia. SPWLA-2010-53450.

- Boyce, M.L., Carr, T.R., 2009. Lithostratigraphy and Petrophysics of the Devonian Marcellus Interval in West Virginia and Southwestern Pennsylvania. AAPG Search and Discover Article #90113©2010
- Boyer, C., Kieschnick, J., Lewis, R., Waters, G., 2006. Producing Gas from Its Source. Schlumberger
- Brown, G.A., 1986. A mathematical comparison of common saturation equations, in: SPWLA 27th Annual Logging Symposium. pp. 1–24. SPWLA-1986-T
- Burst, J.F., 1969. Diagenesis of Gulf Coast Clayey Sediments and Its Possible Relation to Petroleum Migration. AAPG Bulletin 53, 73–93
- Burton, J.H., 1987. Authigenesis of Kaolinite and Chlorite in Texas Gulf Coast Sediments. Clays and Clay Minerals 35, 291–296. doi:10.1346/CCMN.1987.0350406
- Bust, V.K., Majid, A.A., Oletu, J.U., Worthington, P.F., 2011. The Petrophysics of Shale Gas Reservoirs: Technical Challenges and Pragmatic Solutions. International Petroleum Technology Conference, 15-17 November, Bangkok, Thailand. International Petroleum Technology Conference. doi:10.2523/14631-MS
- Bustin, A., Bustin, R., Cui, X., 2008. Importance of Fabric on the Production of Gas Shales. SPE Unconventional Reservoirs Conference, 10-12 February, Keystone, Colorado, USA. doi:10.2118/114167-MS
- Canfield, D.E., 1994. Factors influencing organic carbon preservation in marine sediments. Chemical Geology 114, 315–329. doi:10.1016/0009-2541(94)90061-2
- Carman, P., 1937. Fluid flow through granular beds. Transactions of the Institution of Chemical Engineers 15, 150–166
- Chalmers, G.R., Bustin, R.M., Power, I.M., 2012. Characterization of gas shale pore systems by porosimetry, pycnometry, surface area, and field emission scanning electron microscopy/transmission electron microscopy image analyses: Examples from the Barnett, Woodford, Haynesville, Marcellus, and Doig units. AAPG Bulletin 96, 1099–1119. doi:10.1306/10171111052
- Chen, D.S., Fang, J.H., Kortright, M.E., Chen, H.C., 1995. Novel Approaches to the Determination of Archie Parameters I: Simplex Method. SPE Advanced Technology Series 3, 39–43
- Chen, H.C., Fang, J.H., Kortright, M.E., Chen, D.S., 1995. Novel approaches to the determination of archie parameters II: Fuzzy regression analysis. SPE Advanced technology series 3, 44–52.
- Chen, X., Kuang, L.C., Sun, Z.C., 2002. Archie Parameter Determination By Analysis Of Saturation Data. Petrophysics 43

- Chiaromonte, J.M., Ellis, D.V., 2000. Interpreting Neutron Logs In Horizontal Wells: A Forward Modeling Tutorial. *Petrophysics* 41
- Chilingar, G., Rieke III, H., Sawabini, S., 1969. Chemistry of interstitial solutions in shales versus that in associated sandstones, in: Fall Meeting of the Society of Petroleum Engineers of AIME, 28 September-1 October, Denver, Colorado. doi; 10.2118/2527-MS
- Chilingar, G.V., Serebryakov, V.A., Robertson, J.O., 2002. Origin and prediction of abnormal formation pressures. Elsevier
- Clarkson, C.R., Jensen, J.L., Pedersen, P.K., Freeman, M., 2012. Innovative Methods for Flow-Unit and Pore-Structure Analyses in a Tight Siltstone and Shale Gas Reservoir. *AAPG Bulletin* 96, 355–374. doi:10.1306/05181110171
- Clavier, C., Coates, G., Dumanoir, J., 1984. Theoretical and Experimental Bases for the Dual-Water Model for Interpretation of Shaly Sands. *Society of Petroleum Engineers Journal* 24. doi:10.2118/6859-PA
- Clennell, M.B., 1997. Tortuosity: a guide through the maze. Geological Society, London, Special Publications 122, 299 –344. doi:10.1144/GSL.SP.1997.122.01.18
- Clennell, M.B., Dewhurst, D.N., Raven, M., 2006. Shale petrophysics: electrical dielectric and nuclear magnetic resonance studies of shales and clays. SPWLA 47th Annual Logging Symposium, 4-7 June, Veracruz, Mexico
- Cluff, B., 2012. How to assess shales from well logs. Presentation given at IOGA 66th Annual Meeting, Evansville, Indiana, March 2012. http://www.discovery-group.com/resources_recent.htm
- Condon, S.M., Dyman, T.S., Klett, T.R., Le, P.A., Geological Survey (U. S.), National Assessment of Oil and Gas Project (U. S.), USGS Gulf Coast Region Assessment Team, 2006. Petroleum systems and geologic assessment of undiscovered oil and gas, Cotton Valley Group and Travis Peak-Hosston Formations, East Texas Basin and Louisiana-Mississippi Salt Basins Provinces of the Northern Gulf Coast Region, U.S. Geological Survey digital data series ; DDS-69-E. U.S. Geological Survey.
- Corley, B., Garcia, A., Maurer, H.-M., Rabinovich, M., Zhou, Z., DuBois, P., Shaw Jr., N., 2010. Study of Unusual Responses From Multiple Resistivity Tools in the Bossier Formation of the Haynesville Shale Play. SPE Annual Technical Conference and Exhibition, 19-22 September, Florence, Italy. doi; 10.2118/134494-MS.
- Couzens-Schultz, B., Axon, A., Jiang, L., Azbel, K., 2013. Pore Pressure Prediction in Unconventional Resources. Presented at the 6th International Petroleum Technology Conference, Mar 26 - 28, 2013 2013, Beijing, China, Society of Petroleum Engineers. doi:10.2523/16849-MS
- Craig, R.F., 2004. *Craig's soil mechanics*. Taylor & Francis.

- Cui, X., Bustin, A.M.M., Bustin, R.M., 2009. Measurements of gas permeability and diffusivity of tight reservoir rocks: different approaches and their applications. *Geofluids* 9, 208–223
- Curtis, M., Ambrose, R., Sondergeld, C., Rai, C., 2011. Investigation of the Relationship Between Organic Porosity and Thermal Maturity in The Marcellus Shale. North American Unconventional Gas Conference and Exhibition, 14-16 June, The Woodlands, Texas, USA. Society of Petroleum Engineers. doi:10.2118/144370-MS
- Curtis, M., Ambrose, R., Sondergeld, C., Sondergeld, C., 2010. Structural Characterization of Gas Shales on the Micro- and Nano-Scales. Canadian Unconventional Resources and International Petroleum Conference, 19-21 October, Calgary, Alberta, Canada. Society of Petroleum Engineers. doi:10.2118/137693-MS
- Curtis, M.E., Sondergeld, C.H., Ambrose, R.J., Rai, C.S., 2012. Microstructural Investigation of Gas Shales in Two and Three Dimensions Using Nanometer-Scale Resolution Imaging. *AAPG Bulletin* 96, 665–677. doi:10.1306/08151110188
- Das, B.M., 2008. *Advanced soil mechanics*. Routledge
- Davarcioglu, B., 2012. Kolsuz-Ulukisla-Nigde Clays, Central Anatolian Region - Turkey and Petroleum Exploration, in: Valaskova, M. (Ed.), *Clay Minerals in Nature - Their Characterization, Modification and Application*. InTech.
- Day-Stirrat, R.J., Flemings, P.B., You, Y., Aplin, A.C., van der Pluijm, B.A., 2012. The fabric of consolidation in Gulf of Mexico mudstones. *Marine Geology* 295-298, 77–85. doi:10.1016/j.margeo.2011.12.003
- Demaison, G.J., Moore, G.T., 1980. Anoxic environments and oil source bed genesis. *Organic Geochemistry* 2, 9–31. doi:10.1016/0146-6380(80)90017-0
- Denham, M.E., Tieh, T.T., 1991. Occurrence of Uranium in the Upper Smackover Limestones of the North Louisiana Salt Basin. *GCAGS Transactions*. Vol. 41 (1991), Pages 175-183
- Derkowski, A., Bristow, T.F., 2012. On the Problems of Total Specific Surface Area and Cation Exchange Capacity Measurements in Organic-Rich Sedimentary Rocks. *Clays and Clay Minerals* 60, 348–362. doi:10.1346/CCMN.2012.0600402
- Dewhurst, D.N., Bungler, A., Josh, M., Sarout, J., Delle Piane, C., Esteban, L., Clennell, M.B., 2013. Mechanics Physics Chemistry and Shale Rock Properties. 47th U.S. Rock Mechanics/Geomechanics Symposium, 23-26 June, San Francisco, California.. American Rock Mechanics Association
- Dewhurst, D.N., Siggins, A.F., Kuila, U., Clennell, M.B., Raven, M.D., Nordgard-Bolas, H.M., 2008. Elastic Geomechanical and Petrophysical Properties of Shales. The

- 42nd U.S. Rock Mechanics Symposium (USRMS), 29 June-2 July, San Francisco, California. American Rock Mechanics Association
- Dewhurst, D.N., Yang, Y., Aplin, A.C., 1999. Permeability and fluid flow in natural mudstones. Geological Society London Special Publications 158, 23
- Diaz De Souza, O., Sharp, A., Martinez, R., Foster, R., Piekenbrock, E., Reeves Simpson, M., Abou-Sayed, I., Abou-Sayed, I., 2012. Integrated Unconventional Shale Gas Reservoir Modeling: A Worked Example From the Haynesville Shale, De Soto Parish, North Louisiana. SPE Americas Unconventional Resources Conference, 5-7 June, Pittsburgh, Pennsylvania USA. doi:10.2118/154692-MS
- Diederix, K.M., 1982. Anomalous relationships between resistivity index and water saturations in the Rotliegend sandstone (The Netherlands), in: SPWLA 23rd Annual Logging Symposium, 6-9 July, Corpus Christi, Texas. Society of Petrophysicists and Well-Log Analysts
- Dix, M.C., Spain, D., Walling, C., Sano, J., Casarta, N., Richardson, A., 2010. Stratigraphy and Depositional Dynamics of the Haynesville-Bossier Sequence: Inferences from Whole-Rock Elemental Data. Search and Discovery Article #10298 (2011)
- Donaldson, E.C., Siddiqui, T.K., 1989. Relationship between the Archie saturation exponent and wettability. SPE formation evaluation 4, 359–362
- Donaldson, E.C., Tiab, D., 2003. Petrophysics, Second Edition: Theory and Practice of Measuring Reservoir Rock and Fluid Transport Properties, 2nd ed. Gulf Professional Publishing
- Dooley, T.P., Jackson, M.P.A., Hudec, M.R., 2013. Coeval extension and shortening above and below salt canopies on an uplifted, continental margin: Application to the northern Gulf of Mexico. AAPG Bulletin 97, 1737–1764. doi:10.1306/03271312072
- Doveton, J.H., 1994. The Spectral Gamma-Ray Log. SEPM SpecialPublication (SC29)
- Doveton, J.H., 2001. All Models Are Wrong, but Some Models Are Useful: “Solving” the Simandoux Equation. IAMG Cancun 2001 Conference
- Durand, C., Brosse, E., Cerepi, A., 2001. Effect of pore-lining chlorite on petrophysical properties of low-resistivity sandstone reservoirs. SPE Reservoir Evaluation & Engineering 4, 231–239
- Eastwood, R.L., Hammes, U., 2011. Log Model Development For the Bossier And Haynesville Shales. Presented at the SPWLA 52nd Annual Logging Symposium, May 14 - 18, 2011 , Colorado Springs, Colorado
- Edmundson, H., 1988a. Archie’s Law: Electrical Conduction in Clean Water-Bearing Rock. The Technical Review 36, 4–13

- Edmundson, H., 1988b. Archie II: Electrical Conduction in Hydrocarbon-Bearing Rock. *The Technical Review* 36, 12–21
- El Mahgoub, S., Daoud, A., El-Tayeb, E.-S., 2008. Development of Water Saturation Error Analysis Charts for Different Shaly Sand Models for Uncertainty Quantification of Volumetric In-Place Estimate. SPE Russian Oil and Gas Technical Conference and Exhibition, 28-30 October, Moscow, Russia. doi:10.2118/116591-MS
- Ellis, D.V., Case, C.R., Chiaramonte, J.M., 2003. Tutorial - Porosity from Neutron Logs I - Measurement. *Petrophysics* 44
- Ellis, D.V., Case, C.R., Chiaramonte, J.M., 2004. Porosity from Neutron Logs II: Interpretation. *Petrophysics* 45
- Ellis, D.V., Singer, J.M., 2007. *Well logging for earth scientists*. Springer
- Emery, D., Myers, K., 2009. *Sequence Stratigraphy*. John Wiley & Sons
- Eseme, E., Littke, R., Krooss, B.M., 2006. Factors controlling the thermo-mechanical deformation of oil shales: Implications for compaction of mudstones and exploitation. *Marine and Petroleum Geology* 23, 715–734. doi:10.1016/j.marpetgeo.2006.02.007
- Etherington, J., McDonald, I., 2004. Is Bitumen a Petroleum Reserve? Society of Petroleum Engineers. SPE Annual Technical Conference and Exhibition, 26-29 September, Houston, Texas. doi:10.2118/90242-MS
- Etherington, J., Ritter, J., 2007. The 2007 SPE/AAPG/WPC/SPEE Reserves and Resources Classification, Definitions, and Guidelines: Defining the Standard! Hydrocarbon Economics and Evaluation Symposium, 1-3 April, Dallas, Texas, U.S.A.. Society of Petroleum Engineers. doi:10.2118/107693-MS
- Fan, L., Thompson, J., Robinson, J., 2010. Understanding Gas Production Mechanism and Effectiveness of Well Stimulation in the Haynesville Shale Through Reservoir Simulation. Canadian Unconventional Resources and International Petroleum Conference, 19-21 October, Calgary, Alberta, Canada Society of Petroleum Engineers. doi:10.2118/136696-MS
- Fawad, M., Mondol, N.H., Jahren, J., Bjørlykke, K., 2010. Microfabric and rock properties of experimentally compressed silt-clay mixtures. *Marine and Petroleum Geology* 27, 1698–1712. doi:10.1016/j.marpetgeo.2009.10.002
- Fertl, W., Timko, D., 1971. Association of Salinity Variations and Geopressures in Soft and Hard Rock. *The Log Analyst* 12
- Fowler Jr, W., 1970. Pressures, Hydrocarbon Accumulation, and Salinities Chocolate Bayou Field, Brazoria County, Texas. *Journal of Petroleum Technology* 22, 411–423

- Franquet, J., Bratovich, M., Glass, R., 2012. State-of-the-Art Openhole Shale Gas Logging. SPE Saudi Arabia Section Technical Symposium and Exhibition, 8-11 April, Al-Khobar, Saudi Arabia. doi:10.2118/160862-MS
- Freed, R.L., Peacor, D.R., 1989. Variability in temperature of the smectite/illite reaction in Gulf Coast sediments. *Clay Minerals* 24, 171–180
- Gamero Diaz, H., Lewis, R., Miller, C.K., 2013. sCore: A Mineralogy Based Classification Scheme for Organic Mudstones, in: SPE Annual Technical Conference and Exhibition, 30 September-2 October, New Orleans, Louisiana, USA. doi; 10.2118/166284-MS
- Ghadeer, S.G., Macquaker, J.H.S., 2011. Sediment transport processes in an ancient mud-dominated succession: a comparison of processes operating in marine offshore settings and anoxic basinal environments. *Journal of the Geological Society* 168, 1121–1132. doi:10.1144/0016-76492010-016
- Gilchrist, W.A., 2009. Compensated Neutron Log Response Issues. *Petrophysics* 50
- Glorioso, J., Rattia, A., 2012. Unconventional Reservoirs: Basic Petrophysical Concepts for Shale Gas. SPE/EAGE European Unconventional Resources Conference and Exhibition, 20-22 March, Vienna, Austria. doi:10.2118/153004-MS
- Glover, P., 2009. What is the cementation exponent? A new interpretation. *The Leading Edge* 28, 82
- Gribble, C.D., Hall, A.J., 1992. *Optical mineralogy: principles and practice*. UCL Press, London
- Guidry, F.K., Luffel, D.L., Olszewski, A.J., Scheper, R.J., 1996. Devonian Shale Formation Evaluation Model Based on Logs, New Core Analysis Methods, and Production Tests. SPE REPRINT SERIES 101–120
- Gupta, N., Rai, C.S., Sondergeld, C.H., 2012. Integrated Petrophysical Characterization of the Woodford Shale In Oklahoma. SPWLA 53rd Annual Logging Symposium, 16-20 June, Cartagena, Colombia. Society of Petrophysicists and Well-Log Analysts
- Haghighi, M., Ahmad, M., 2013. Water Saturation Evaluation of Murteree and Roseneath Shale Gas Reservoirs, Cooper Basin, Australia Using Wire-line Logs, Focused Ion Beam Milling and Scanning Electron Microscopy. SPE Unconventional Resources Conference and Exhibition-Asia Pacific, 11-13 November, Brisbane, Australia. doi:10.2118/167080-MS
- Hamada, G.M., Al-Awad, M.N.J., Almalik, M.S., 2001. Log Evaluation of Low - Resistivity Sandstone Reservoirs. SPE Permian Basin Oil and Gas Recovery Conference, 15-17 May, Midland, Texas. doi:10.2118/70040-MS

- Hammes, U., 2009. Sequence Stratigraphy and Core Facies of the Haynesville Mudstone, East Texas Ursula Hammes. Gulf Coast Association of Geological Societies Transactions 59, 321–324
- Hammes, U., 2012. Depositional Environment, Stratigraphy, Geochemical, and Reservoir Characteristics of the Haynesville and Bossier Shale-Gas Plays of East Texas and Northwest Louisiana. Search and Discovery Article #10434 (2012)
- Hammes, U., Frébourg, G., 2012. Haynesville and Bossier mudrocks: A facies and sequence stratigraphic investigation, East Texas and Louisiana, USA. Marine and Petroleum Geology 31, 8–26. doi:10.1016/j.marpetgeo.2011.10.001
- Hammes, U., Hamlin, H.S., Ewing, T.E., 2011. Geological analysis of the Upper Jurassic Haynesville Shale in east Texas and west Louisiana. AAPG Bulletin V. 95, 1643–1666
- Han, M., Tariel, V., Youssef, S., Rosenberg, E., 2008. The Effect Of The Porous Structure On Resistivity Index Curves. An Experimental And Numerical Study. Presented at the 49th Annual Logging Symposium, May 25 - 28, 2008 , Austin, Texas, Society of Petrophysicists and Well-Log Analysts
- Hancock, N.J., 1992. Quick-Look Lithology from Logs: Part 4. Wireline Methods 95, 174–179
- Handwerger, D., Keller, J., Vaughn, K., Keller, J., 2011. Improved Petrophysical Core Measurements on Tight Shale Reservoirs Using Retort and Crushed Samples. SPE Annual Technical Conference and Exhibition, 30 October-2 November, Denver, Colorado, USA. doi:10.2118/147456-MS
- Handwerger, D., Willberg, D., Pagels, M., Rowland, B., Keller, J., 2012. Reconciling Retort versus Dean Stark Measurements on Tight Shales. SPE Annual Technical Conference and Exhibition, 8-10 October, San Antonio, Texas, USA. doi:10.2118/159976-MS
- Hardwick, A., 1989. X Is: A New Shale Parameter for Resistivity Log Evaluation. Presented at the SPE Annual Technical Conference and Exhibition, 8-11 October 1989, San Antonio, Texas. doi; 10.2118/19576-MS
- Haro, C., 2009. The Equations Archie Forgot: Anisotropy of the Rocks. SPE Annual Technical Conference and Exhibition, 4-7 October, New Orleans, Louisiana. doi:10.2118/123913-MS
- Haro, C.F., 2008. Advanced Petrophysical Modelling. Correcting Shaly-sand Theory, in: 49th Annual Logging Symposium, 25-28 May, Austin, Texas. Society of Petrophysicists and Well-Log Analysts.
- Harrington, J.F., Horseman, S.T., 1999. Gas transport properties of clays and mudrocks. Geological Society London Special Publications 158, 107.

- Hart, B.S., Macquaker, J.H.S., Taylor, K.G., 2013. Mudstone (“shale”) depositional and diagenetic processes: Implications for seismic analyses of source-rock reservoirs. *Interpretation* 1, B7–B26. doi:10.1190/INT-2013-0003.1
- Haskett, W., Brown, P., 2005. Evaluation of Unconventional Resource Plays, in: *Proceedings of SPE Annual Technical Conference and Exhibition*. Presented at the SPE Annual Technical Conference and Exhibition. doi:10.2118/96879-MS
- Heath, J.E., Dewers, T.A., McPherson, B.J.O.L., Petrusak, R., Chidsey, T.C., Rinehart, A.J., Mozley, P.S., 2011. Pore networks in continental and marine mudstones: Characteristics and controls on sealing behavior. *Geosphere* 7, 429–454. doi:10.1130/GES00619.1
- Hedberg, H.D., 1936. Gravitational compaction of clays and shales. *American Journal of Science* s5-31, 241–287. doi:10.2475/ajs.s5-31.184.241
- Hedges, J.I., Keil, R.G., 1995. Sedimentary organic matter preservation: an assessment and speculative synthesis. *Marine Chemistry* 49, 81–115.
- Heidari, Z., Torres-Verdin, C., Preeg, W.E., 2011. Quantitative Method for Estimating Total Organic Carbon and Porosity, and for Diagnosing Mineral Constituents from Well Logs in Shale-Gas Formations, in: *Colorado Springs: SPWLA 52nd Annual Logging Symposium, 14-18 May, Colorado Springs, Colorado*. The Society of Petrophysicists and Well Log Analysts.
- Herrick, D.C., Kennedy, W.D., 1996. Electrical properties of rocks: effects of secondary porosity, laminations, and thin beds, in: *SPWLA 37th Annual Logging Symposium, 16-19 June, New Orleans, Louisiana*. Society of Petrophysicists and Well-Log Analysts
- Herrick, D.C., Kennedy, W.D., 2009. A New Look at Electrical Conduction in Porous Media: A Physical Description of Rock Conductivity, in: *SPWLA 50th Annual Logging Symposium, 21-24 June, The Woodlands, Texas*. Society of Petrophysicists and Well-Log Analysts
- Heslop, A., 1974. Gamma-ray Log Response Of Shaly Sandstones. *The Log Analyst* 15.
- Hill, H., Milburn, J., 1956. Effect of Clay and Water Salinity on the Electrochemical Behavior of Reservoir Rocks. *SPE Reprint Series* 401
- Howard, J.J., 1991. Porosimetry measurement of shale fabric and its relationship to illite/smectite diagenesis. *Clays and Clay Minerals* 39, 355–361
- Hudec, M.R., Jackson, M.P.A., Peel, F.J., 2013a. Influence of deep Louann structure on the evolution of the northern Gulf of Mexico. *AAPG Bulletin* 97, 1711–1735. doi:10.1306/04011312074

- Hudec, M.R., Norton, I.O., Jackson, M.P.A., Peel, F.J., 2013b. Jurassic evolution of the Gulf of Mexico salt basin. *AAPG Bulletin* 97, 1683–1710. doi:10.1306/04011312073
- Hurst, A., 1990. Natural gamma-ray spectrometry in hydrocarbon-bearing sandstones from the Norwegian Continental Shelf. Geological Society, London, Special Publications 48, 211–222. doi:10.1144/GSL.SP.1990.048.01.18
- Hyndman, R.J., Koehler, A.B., 2006. Another look at measures of forecast accuracy. *International Journal of Forecasting* 22, 679–688. doi:10.1016/j.ijforecast.2006.03.001
- Iheanacho, P., 2013. Formation Resistivity Theory: How Archie Equations, Shaly Reservoir Models, Conductive Rock Matrix Model and Dual/Triple Porosity Models Are Related, in: SPE Nigeria Annual International Conference and Exhibition, 5-7 August, Lagos, Nigeria. doi; 10.2118/167507-MS
- Ingall, E.D., Bustin, R.M., Van Cappellen, P., 1993. Influence of water column anoxia on the burial and preservation of carbon and phosphorus in marine shales. *Geochimica et Cosmochimica Acta* 57, 303–316. doi:10.1016/0016-7037(93)90433-
- Jackson, P.D., 1978. Resistivity-porosity-particle shape relationships for marine sands. *Geophysics* 43, 1250. doi:10.1190/1.1440891
- Jacobi, D., Gladkikh, M., LeCompte, B., Hursan, G., Mendez, F., Longo, J., Ong, S., Bratovich, M., Patton, G., Shoemaker, P., 2008. Integrated Petrophysical Evaluation of Shale Gas Reservoirs. CIPC/SPE Gas Technology Symposium 2008 Joint Conference, 16-19 June, Calgary, Alberta, Canada. Society of Petroleum Engineers. doi:10.2118/114925-MS
- Jarvie, D.M., Hill, R.J., Ruble, T.E., Pollastro, R.M., 2007. Unconventional shale-gas systems: The Mississippian Barnett Shale of north-central Texas as one model for thermogenic shale-gas assessment. *AAPG Bulletin* 91, 475–499. doi:10.1306/12190606068
- Jones, E., Oliphant, T., Peterson, P., 2001. SciPy: Open Source Scientific Tools for Python. SciPy.org. URL <http://www.scipy.org>
- Jougnot, D., Revil, A., 2010. Thermal conductivity of unsaturated clay-rocks. *Hydrology and Earth System Sciences* 14, 91–98
- Jougnot, D., Revil, A., Leroy, P., 2009. Diffusion of ionic tracers in the Callovo-Oxfordian clay-rock using the Donnan equilibrium model and the formation factor. *Geochimica et Cosmochimica Acta* 73, 2712–2726. doi:10.1016/j.gca.2009.01.035
- Juhasz, I., 1981. Normalized Qv-the key to shaly sand evaluation using the Waxman-Smits equation in the absence of core data, in: SPWLA 22nd Annual Logging

- Symposium, 23-26 June, Mexico City, Mexico. Society of Petrophysicists and Well-Log Analysts
- Karastathis, A., 2007. Petrophysical Measurements on Tight Gas Shales. Thesis. University of Oklahoma.
- Katahara, K., 2006. Overpressure and shale properties: Stress unloading or smectite-illite transformation?, in: 2006 SEG Annual Meeting, 1-6 October, New Orleans, Louisiana. Society of Exploration Geophysicists.
- Katahara, K.W., 1995. Gamma Ray Log Response In Shaly Sands. *The Log Analyst* 36.
- Kearey, P., 2001. *The new Penguin dictionary of geology*. Penguin, London.
- Kennedy, W.D., Herrick, D.C., 2012. Conductivity models for Archie rocks. *Geophysics* 77, WA109–WA128. doi:10.1190/geo2011-0297.1
- Khairy, H., Harith, Z.Z.T., 2011. Influence of pore geometry, pressure and partial water saturation to electrical properties of reservoir rock: Measurement and model development. *Journal of Petroleum Science and Engineering*. V 78, 3-4, p687-704
- Klein, G., Chaivre, K., 2003. Sequence and Seismic Stratigraphy of the Bossier Play (Tithonian), western East Texas Basin. *Search and Discovery Article #10045 (2003)*
- Knackstedt, M.A., Arns, C.H., Sheppard, A.P., Senden, T.J., Sok, R.M., Cinar, Y.A., Pinczewski, W.V., Ioannidis, M.A., Padhy, G.S., 2007. Archie's exponents in complex lithologies derived from 3D digital core analysis, in: 48th Annual Logging Symposium, 3-6 June, Austin, Texas. Society of Petrophysicists and Well-Log Analysts
- Krushin, J., 2013. A True Shale Compaction Model with Pore Pressure Prediction. The Offshore Technology Conference, 6-9 May, Houston, Texas, USA. Offshore Technology Conference. doi:10.4043/23954-MS
- Kumar, M., Senden, T.J., Sheppard, A.P., Arns, C.H., Knackstedt, M.A., 2011. Probing the Archie's Exponent under Variable Saturation Conditions. *Petrophysics* 52, 124–134
- Kurniawan, B., Bassiouni, Z., 2007. Use Of CEC-Dependent Cementation And Saturation Exponents In Shaly Sand Resistivity Models, in: 48th Annual Logging Symposium, 3-6 June, Austin, Texas. Society of Petrophysicists and Well-Log Analysts.
- Kurniawan, B., White, C., Bassiouni, Z., 2007. Experimental and Statistical Analysis of Shaly Sand Evaluation Using CEC-Dependent Parameters. SPE Annual Technical Conference and Exhibition, 11-14 November, Anaheim, California, U.S.A. Society of Petroleum Engineers . doi:10.2118/110986-MS

- Kwon, O., Kronenberg, A.K., Gangi, A.F., Johnson, B., Herbert, B.E., 2004. Permeability of illite-bearing shale: 1. Anisotropy and effects of clay content and loading. *J. Geophys. Res.* 109, B10205. doi:10.1029/2004JB003052
- La Croix, A.D., Gingras, M.K., Dashtgard, S.E., Pemberton, S.G., 2012. Computer Modeling Bioturbation: The Creation of Porous and Permeable Fluid-Flow Pathways. *AAPG Bulletin* 96, 545–556. doi:10.1306/07141111038
- Lahann, R., Lahann, C., McCarty, D., Hsieh, J., 2001. Influence of clay diagenesis on shale velocities and fluid-pressure, in: *Offshore Technology Conference*, 4/30/2001, Houston, Texas. doi: 10.4043/13046-MS
- Lauer-Leredde, C., Pezard, P.A., Robert, C., Dekeyser, I., 1998. Mineralogical association and physical properties of sediments with palaeoclimatic implications (ODP Site 798B, Japan Sea): a comparative study from core and downhole measurements. *Marine geology* 150, 73–98
- Le, F., Zhou, Z., Maurer, H.-M., 2011. 3-D Study of Resistivity Tool Responses In Formations With Vertical Fractures Or Horizontal Transverse Isotropy. Presented at the SPWLA 52nd Annual Logging Symposium, May 14 - 18, 2011 , Colorado Springs, Colorado
- LeCompte, B., Franquet, J., Jacobi, D., 2009. Evaluation of Haynesville Shale Vertical Well Completions With a Mineralogy Based Approach to Reservoir Geomechanics. *Society of Petroleum Engineers*. doi:10.2118/124227-MS
- Leeder, M.R., 1999. *Sedimentology and sedimentary basins: from turbulence to tectonics*. Wiley-Blackwell
- Leroy, P., Revil, A., 2009. A mechanistic model for the spectral induced polarization of clay materials. *Journal of Geophysical Research: Solid Earth* 114, n/a–n/a. doi:10.1029/2008JB006114
- Lock, G.A., Hoyer, W.A., 1971. *Natural Gamma-Ray Spectral Logging*. SPWLA 12th Annual Logging Symposium, 2-5 May, Dallas, Texas. Society of Petrophysicists and Well-Log Analysts
- Loucks, R.G., Reed, R.M., Ruppel, S.C., Hammes, U., 2012. Spectrum of pore types and networks in mudrocks and a descriptive classification for matrix-related mudrock pores. *AAPG Bulletin* 96, 1071–1098. doi:10.1306/08171111061
- Loucks, R.G., Ruppel, S.C., 2007. Mississippian Barnett Shale: Lithofacies and depositional setting of a deep-water shale-gas succession in the Fort Worth Basin, Texas. *AAPG bulletin* 91, 579
- Luffel, D.L., Guidry, F.K., 1992. New Core Analysis Methods for Measuring Reservoir Rock Properties of Devonian Shale. *Journal of Petroleum Technology* 44. doi:10.2118/20571-PA

- Luffel, D.L., Guidry, F.K., Curtis, J.B., 1992. Evaluation of Devonian shale with new core and log analysis methods. *Journal of Petroleum Technology* 44, 1192–1197
- Lüning, S., Kolonic, S., 2003. Uranium spectral gamma-ray response as a proxy for organic richness in black shales: applicability and limitations. *Journal of petroleum geology* 26, 153–174
- Mackey, S.D., Bridge, J.S., 1995. Three-dimensional model of alluvial stratigraphy; theory and applications. *Journal of Sedimentary Research* 65, 7–31
- Macquaker, J.H., Adams, A.E., 2003. Maximizing information from fine-grained sedimentary rocks: an inclusive nomenclature for mudstones. *Journal of Sedimentary Research* 73, 735
- Macquaker, J.H.S., Bentley, S.J., Bohacs, K.M., 2010a. Wave-enhanced sediment-gravity flows and mud dispersal across continental shelves: Reappraising sediment transport processes operating in ancient mudstone successions. *Geology* 38, 947–950. doi:10.1130/G31093.1
- Macquaker, J.H.S., Bohacs, K.M., 2007. *GEOLOGY: On the Accumulation of Mud*. *Science* 318, 1734–1735. doi:10.1126/science.1151980
- Macquaker, J.H.S., Keller, M.A., Davies, S.J., 2010b. Algal Blooms and “Marine Snow”: Mechanisms That Enhance Preservation of Organic Carbon in Ancient Fine-Grained Sediments. *Journal of Sedimentary Research* 80, 934–942. doi:10.2110/jsr.2010.085
- Macquaker, J.H.S., Taylor, K.G., 1996. A sequence-stratigraphic interpretation of a mudstone-dominated succession: the Lower Jurassic Cleveland Ironstone Formation, UK. *Journal of the Geological Society* 153, 759–770. doi:10.1144/gsjgs.153.5.0759
- Macquaker, J.H.S., Taylor, K.G., Gawthorpe, R.L., 2007. High-Resolution Facies Analyses of Mudstones: Implications for Paleoenvironmental and Sequence Stratigraphic Interpretations of Offshore Ancient Mud-Dominated Successions. *Journal of Sedimentary Research* 77, 324–339. doi:10.2110/jsr.2007.029
- Macquaker, J.H.S., Taylor, K.G., Keller, M., Polya, D., 2014. Compositional controls on early diagenetic pathways in fine-grained sedimentary rocks: Implications for predicting unconventional reservoir attributes of mudstones. *AAPG Bulletin* 98, 587–603. doi:10.1306/08201311176
- Mancini, E.A., 2010. Jurassic Depositional Systems, Facies, and Reservoirs of the Northern Gulf of Mexico
- Mancini, E.A., Mink, R.M., Bearden, B.L., Wilkerson, R.P., 1985. Norphlet Formation (Upper Jurassic) of southwestern and offshore Alabama: environments of deposition and petroleum geology. *AAPG Bulletin* 69, 881–898

- Mastalerz, M., Schimmelmann, A., Drobniak, A., Chen, Y., 2013. Porosity of Devonian and Mississippian New Albany Shale across a maturation gradient: Insights from organic petrology, gas adsorption, and mercury intrusion. *AAPG Bulletin* 97, 1621–1643. doi:10.1306/04011312194
- Maute, R.E., Lyle, W.D., Sprunt, E., 1992. Improved Data-Analysis Method Determines Archie Parameters From Core Data (includes associated paper 24964). *Journal of Petroleum Technology* 44, 103–107
- McClain, T., Wang, G., Carr, T., 2013. Petrophysical Analysis and Sequence Stratigraphy of the Utica Shale and Marcellus Shale, Appalachian Basin, USA. *International Petroleum Technology Conference*, 26–28 March, Beijing, China. Society of Petroleum Engineers. doi:10.2523/16935-Abstract
- Michael, G.E., Packwood, J., Holba, A., 2013. Determination of In-Situ Hydrocarbon Volumes in Liquid Rich Shale Plays. Society of Exploration Geophysicists, American Association of Petroleum Geologists, Society of Petroleum Engineers, pp. 2037–2043. doi:10.1190/urtec2013-211
- Milliken, K.L., Esch, W.L., Reed, R.M., Zhang, T., 2012. Grain assemblages and strong diagenetic overprinting in siliceous mudrocks, Barnett Shale (Mississippian), Fort Worth Basin, Texas. *AAPG Bulletin* 96, 1553–1578. doi:10.1306/12011111129
- Milner, M., McLin, R., Petriello, J., 2010. Imaging Texture and Porosity in Mudstones and Shales: Comparison of Secondary and Ion-Milled Backscatter SEM Methods. *Canadian Unconventional Resources and International Petroleum Conference*, 19–21 October, Calgary, Alberta, Canada. Society of Petroleum Engineers. doi:10.2118/138975-MS
- Mitchell, J.K., Soga, K., 2005. *Fundamentals of soil behavior*. John Wiley & Sons
- Modica, C.J., Lapierre, S.G., 2012. Estimation of kerogen porosity in source rocks as a function of thermal transformation: Example from the Mowry Shale in the Powder River Basin of Wyoming. *AAPG Bulletin* 96, 87–108
- Moon, C.F., Hurst, C.W., 1984. *Fabric of muds and shales: an overview*. Geological Society London Special Publications 15, 579
- Moore, G.T., Sloan, L.C., Hayashida, D.N., Umrigar, N.P., 1992. Paleoclimate of the Kimmeridgian/Tithonian (Late Jurassic) world: II. Sensitivity tests comparing three different paleotopographic settings. *Palaeogeography, Palaeoclimatology, Palaeoecology* 95, 229–252. doi:10.1016/0031-0182(92)90143-S
- Motealleh, S., Bryant, S.L., Gladkikh, M., Besspalov, A., Herrick, D.C., 2007. Grain-Scale Modeling of Electrical Resistivity of 'Shaly Sands', in: *48th Annual Logging Symposium*, 3–6 June, Austin, Texas, Society of Petrophysicists and Well-Log Analysts

- Mungan, N., Moore, E., 1968. Certain wettability effects on electrical resistivity in porous media. *Journal of Canadian Petroleum Technology* 7, 20–25
- Murphy, E., Praznik, G., Quirein, J., Galford, J., Witkowsky, J., Chen, S., 2013. A Workflow to Evaluate Mineralogy, Porosity, TOC, and Hydrocarbon Volume in the Eagle Ford Shale. SPE Unconventional Resources Conference and Exhibition-Asia Pacific, 11-13 November, Brisbane, Australia. Society of Petroleum Engineers. doi:10.2118/167012-MS
- Nieto, J., Bercha, R., Chan, J., 2009. Shale Gas Petrophysics - Montney and Muskwa Are They Barnett Look-Alikes? SPWLA 50th Annual Logging Symposium, 21-24 June, The Woodlands, Texas. Society of Petrophysicists and Well-Log Analysts
- Orlandi, M., Bartelucci, P., Chelini, V., 2011. Unconventional Reservoir Characterisation Methods using Core and Well Logging Data: Shale Gas and Tight Gas Sand Examples. Presented at the Offshore Mediterranean Conference and Exhibition, March 23 - 25, 2011, Ravenna, Italy. *Offshore Mediterranean Conference*
- Overton, H., Zanier, A., 1970. Hydratable Shales and the Salinity High Enigma. Fall Meeting of the Society of Petroleum Engineers of AIME, 4-7 October, Houston, Texas Society of Petroleum Engineers. doi:10.2118/2989-MS
- Ozkan, A., Cumella, S.P., Milliken, K.L., Laubach, S.E., 2011. Prediction of lithofacies and reservoir quality using well logs, Late Cretaceous Williams Fork Formation, Mamm Creek field, Piceance Basin, Colorado. *AAPG Bulletin* 95, 1699–1723
- Parker, M., Buller, D., Petre, J., Dreher, D., 2009. Haynesville Shale-Petrophysical Evaluation. SPE Rocky Mountain Petroleum Technology Conference, 14-16 April, Denver, Colorado. Society of Petroleum Engineers. doi:10.2118/122937-MS
- Passey, Q., Bohacs, K., Esch, W., Klimentidis, R., Sinha, S., 2010. From Oil-Prone Source Rock to Gas-Producing Shale Reservoir – Geologic and Petrophysical Characterization of Unconventional Shale-Gas Reservoirs. International Oil and Gas Conference and Exhibition in China, 8-10 June, Beijing, China. Society of Petroleum Engineers. doi:10.2118/131350-MS
- Passey, Q.R., Creaney, S., Kulla, J.B., Moretti, F.J., Stroud, J.D., 1990. A practical model for organic richness from porosity and resistivity logs. *AAPG Bulletin* 74, 1777–1794
- Patnode, H.W., Wyllie, M.R.J., 1950. The presence of conductive solids in reservoir rocks as a factor in electric log interpretation. *Journal of petroleum technology* 2, 47–52
- Pedersen, T.F., Calvert, S.E., 1990. Anoxia vs productivity; what controls the formation of organic-carbon-rich sediments and sedimentary rocks? *AAPG Bulletin* 74, 454–466

- Pickett, G.R., 1966. A Review of Current Techniques for Determination of Water Saturation From Logs. *Journal of Petroleum Technology* 18, 1425–1433. doi:10.2118/1446-PA
- Pitcher, J., Buller, D., Mellen, M., 2012. Shale Exploration Methodology and Workflow. SPE Middle East Unconventional Gas Conference and Exhibition, 23-25 January, Abu Dhabi, UAE . Society of Petroleum Engineers. doi:10.2118/153681-MS
- Popielski, A., Heidari, Z., Torres-Verdin, C., 2012. Rock Classification from Conventional Well Logs in Hydrocarbon-Bearing Shale. SPE Annual Technical Conference and Exhibition, 8-10 October, San Antonio, Texas, USA. Society of Petroleum Engineers. doi:10.2118/159255-MS
- Potter, P.E., 2005. *Mud and Mudstones: Introduction and Overview*. Springer, Berlin
- Poupon, A., Leveaux, J., 1971. Evaluation Of Water Saturation In Shaly Formations. *The Log Analyst* XII
- Powers, M.C., 1967. Fluid-Release Mechanisms in Compacting Marine Mudrocks and Their Importance in Oil Exploration. *AAPG Bulletin* 51, 1240–125
- Prasad, M., Mukerji, T., Reinstaedler, M., Arnold, W., 2009. Acoustic Signatures, Impedance Microstructure, Textural Scales, and Anisotropy of Kerogen-Rich Shale. SPE Annual Technical Conference and Exhibition, 4-7 October, New Orleans, Louisiana. SPE-124840-MS. doi; 10.2118/124840-MS
- Profice, S., Lasseux, D., Jannot, Y., Jebara, N., Hamon, G., 2011. Permeability, porosity and Klinkenberg coefficient determination on crushed porous media. International Symposium of the Society of Core Analysts held in Austin, Texas, USA 18-21 September, 2011. SCA2010-32
- Quirein, J., Gardner, J., Watson, J., 1982. Combined Natural Gamma Ray Spectral/Litho-Density Measurements Applied to Complex Lithologies. SPE Annual Technical Conference and Exhibition, 26-29 September, New Orleans, Louisiana. SPE-11143-MS. doi:10.2118/11143-MS
- Quirein, J., Murphy, E., Praznik, G., Witkowsky, J., Shannon, S., Buller, D., 2012. A Comparison of Core and Well Log Data to Evaluate Porosity, TOC, and Hydrocarbon Volume in the Eagle Ford Shale. SPE Annual Technical Conference and Exhibition, 8-10 October, San Antonio, Texas, USA. SPE-159904-MS. doi:10.2118/159904-MS
- Quirein, J., Witkowsky, J., Truax, J., Galford, J., Spain, D., Odumosu, T., 2010. Integrating Core Data and Wireline Geochemical Data for Formation Evaluation and Characterization of Shale-Gas Reservoirs, in: SPE Annual Technical Conference and Exhibition, 19-22 September, Florence, Italy. SPE-134559-MS. doi; <http://dx.doi.org/10.2118/134559-MS>

- Ramdhan, A.M., Goult, N.R., 2011. Overpressure and mudrock compaction in the Lower Kutai Basin, Indonesia: A radical reappraisal. *AAPG Bulletin* 95, 1725–1744
- Ramirez, T., Klein, J., Bonnie, R., Howard, J., 2011. Comparative Study of Formation Evaluation Methods for Unconventional Shale Gas Reservoirs: Application to the Haynesville Shale (Texas). North American Unconventional Gas Conference and Exhibition, 14-16 June, The Woodlands, Texas, USA. Society of Petroleum Engineers. doi:10.2118/144062-MS
- Ransom, R.C., 2007. DUAL-WATER ARCHIE, and the IMPORTANCE of WATER GEOMETRY. A MODEL and a DISCUSSION. <http://www.archieparameters.com>
- Reeves, G.M., Sims, I., Cripps, J.C., 2006a. The composition of clay materials. *Geological Society, London, Engineering Geology Special Publications* 2006, v. 21, p. 13-27. doi: 10.1144/GSL.ENG.2006.021.01.02
- Reeves, G.M., Sims, I., Cripps, J.C., 2006b. Formation and alteration of clay materials. *Geological Society, London, Engineering Geology Special Publications* 2006, v. 21, p. 29-71. doi: 10.1144/GSL.ENG.2006.021.01.03
- Revil, A., 2005. Characterization of transport properties of argillaceous sediments: Application to the Callovo-Oxfordian argillite. *Journal of Geophysical Research* 110. doi:10.1029/2004JB003442
- Reynolds, S., Gorsline, D.S., 1992. Clay microfabric of deep-sea, detrital mud (stone) s, California continental borderland. *Journal of Sedimentary Research* 62, 41
- Rezaee, M.R., Motiei, H., Kazemzadeh, E., 2007. A new method to acquire m exponent and tortuosity factor for microscopically heterogeneous carbonates. *Journal of Petroleum Science and Engineering* 56, 241–251. doi:10.1016/j.petrol.2006.09.004
- Rider, M.H., 1986. *The Geological Interpretation of Well Logs*. Blackie
- Rider, M.H., Kennedy, M., 2011. *The geological interpretation of well logs*. Rider-French Consulting Limited, Scotland
- Ritch, H.J., Pennebaker, E.S., 1978. Relationship Between The Conductivities Of Tertiary Water-Bearing Sands And Nearby Shales Offshore Louisiana. SPWLA 19th Annual Logging Symposium, 13-16 June, El Paso, Texas. Society of Petrophysicists and Well-Log Analysts
- Romero, A.M., Philp, R.P., 2012. Organic geochemistry of the Woodford Shale, southeastern Oklahoma: How variable can shales be? *AAPG Bulletin* 96, 493–517. doi:10.1306/08101110194
- Rushing, J., Newsham, K., Blasingame, T., 2008. Rock Typing: Keys to Understanding Productivity in Tight Gas Sands, in: SPE Unconventional Reservoirs Conference,

- 10-12 February, Keystone, Colorado, USA. Society of Petroleum Engineers. doi; 10.2118/114164-MS
- Sageman, B.B., Murphy, A.E., Werne, J.P., Ver Straeten, C.A., Hollander, D.J., Lyons, T.W., 2003. A tale of shales: the relative roles of production, decomposition, and dilution in the accumulation of organic-rich strata, Middle-Upper Devonian, Appalachian basin. *Chemical Geology* 195, 229–273
- Salem, H.S., Chilingarian, G.V., 1999. The cementation factor of Archie's equation for shaly sandstone reservoirs. *Journal of Petroleum Science and Engineering* 23, 83–93. doi:16/S0920-4105(99)00009-1
- Salvador, A., 1987. Late Triassic-Jurassic paleogeography and origin of Gulf of Mexico basin. *Am. Assoc. Pet. Geol., Bull.;*(United States) 71.
- Schieber, J., 1978. Depositional fabric of mudstones, in: *Sedimentology, Encyclopedia of Earth Science*. Springer Berlin Heidelberg, pp. 323–327
- Schieber, J., 1990. Significance of styles of epicontinental shale sedimentation in the Belt basin, Mid-Proterozoic of Montana, U.S.A. *Sedimentary Geology, Processes and Patterns in Epeiric Basins* 69, 297–312. doi:10.1016/0037-0738(90)90055-X
- Schieber, J., 1999. Distribution and deposition of mudstone facies in the Upper Devonian Sonyea Group of New York. *Journal of Sedimentary Research* 69, 909–925
- Schieber, J., 2010. Common Themes in the Formation and Preservation of Intrinsic Porosity in Shales and Mudstones - Illustrated With Examples Across the Phanerozoic. Society of Petroleum Engineers. doi:10.2118/132370-MS
- Schieber, J., 2011. Marcasite in Black Shales--a Mineral Proxy for Oxygenated Bottom Waters and Intermittent Oxidation of Carbonaceous Muds. *Journal of Sedimentary Research* 81, 447–458. doi:10.2110/jsr.2011.41
- Schieber, J., Southard, J., Thaisen, K., 2007. Accretion of Mudstone Beds from Migrating Floccule Ripples. *Science* 318, 1760–1763. doi:10.1126/science.1147001
- Schieber, J., Southard, J.B., Schimmelmann, A., 2010. Lenticular Shale Fabrics Resulting from Intermittent Erosion of Water-Rich Muds--Interpreting the Rock Record in the Light of Recent Flume Experiments. *Journal of Sedimentary Research* 80, 119–128. doi:10.2110/jsr.2010.005
- Schieber, J., Zimmerle, Winfried, Sethi, P.S. (Eds.), 1998. Shales and mudstones. Volume I, Volume I,. E. Schweizerbart, Stuttgart
- Schmoker, J.W., 1979. Determination of organic content of Appalachian Devonian shales from formation-density logs. *AAPG Bulletin* 63, 1504–1509

- Schwartzman, S., 1994. *The Words of Mathematics: An Etymological Dictionary of Mathematical Terms Used in English*. MAA
- Seewald, J.S., 2003. Organic–inorganic interactions in petroleum-producing sedimentary basins. *Nature* 426, 327–333. doi:10.1038/nature02132
- Sharp, J.M., Fenstermaker, T.R., Simmons, C.T., McKenna, T.E., Dickinson, J.K., 2001. Potential Salinity-Driven Free Convection in a Shale-Rich Sedimentary Basin: Example from the Gulf of Mexico Basin in South Texas. *AAPG Bulletin* 85, 2089–2110. doi:10.1306/8626D351-173B-11D7-8645000102C1865D
- Simm, R., 2007. Practical Gassmann fluid substitution in sand/shale sequences. *First Break* 61
- Singh, S., Morgan, N., Qiu, F., Pritchard, T., Nath, G., 2013. Critical Comparative Assessment of a Novel Approach for Multi-mineral Modeling in Shale Gas: Results from an Evaluation Study of Marcellus Shale. *SPE Unconventional Resources Conference and Exhibition-Asia Pacific*, 11-13 November, Brisbane, Australia. Society of Petroleum Engineers. doi:10.2118/167037-MS
- Size, W.B., Geology, I.A. for M., Meeting, G.S. of A., 1987. *Use and abuse of statistical methods in the earth sciences*. Oxford University Press
- Slatt, R.M., 2011. Important geological properties of unconventional resource shales. *Central European Journal of Geosciences* 3, 435–448. doi:10.2478/s13533-011-0042-2
- Slatt, R.M., Rodriguez, N.D., 2012. Comparative sequence stratigraphy and organic geochemistry of gas shales: Commonality or coincidence? *Journal of Natural Gas Science and Engineering, Unconventional Natural Gas* 8, 68–84. doi:10.1016/j.jngse.2012.01.008
- Smith, G., 1990. *Elements of Soil Mechanics - Sixth Edition*. Blackwell Science Publications
- Smith, J.E., 1977. Thermodynamics of salinity changes accompanying compaction of shaly rocks. *Old SPE Journal* 17, 377–386
- Sondergeld, C., Newsham, K., Comisky, J., Rice, M., Rai, C., 2010. Petrophysical Considerations in Evaluating and Producing Shale Gas Resources, in: *Proceedings of SPE Unconventional Gas Conference*. SPE Unconventional Gas Conference, 23-25 February, Pittsburgh, Pennsylvania, USA. Society of Petroleum Engineers. doi:10.2118/131768-MS
- Spears, R.W., Jackson, L., 2009. Development of a Predictive Tool for Estimating Well Performance in Horizontal Shale Gas Wells in the Barnett Shale, North Texas, USA. *Petrophysics* 50, 19–31

- Stabell, C., 2005. Integrated Risk, Resource and Value Assessment of Unconventional Petroleum Assets. SPE Hydrocarbon Economics and Evaluation Symposium, 3-5 April, Dallas, Texas. Society of Petroleum Engineers. doi:10.2118/94667-MS
- Stalheim, S.O., Eidesmo, T., 1995. Is The Saturation Exponent n A Constant? Presented at the SPWLA 36th Annual Logging Symposium, 26-29 June, Paris, France. Society of Petrophysicists and Well-Log Analysts
- Steinhoff, I., Cicero, A., Koepke, K.A., Dezelle, J., McClain, T., Gillet, C., 2011. Understanding the Regional Haynesville and Bossier Shale Depositional Systems in East Texas and Northern Louisiana: An Integrated Structural/Stratigraphic Approach. Search and Discovery Article #50379 (2011)
- Stern, R.J., Dickinson, W.R., 2010. The Gulf of Mexico is a Jurassic backarc basin. *Geosphere* 6, 739–754
- Suarez-Rivera, R., Green, S., McLennan, J., Bai, M., 2006. Effect of Layered Heterogeneity on Fracture Initiation in Tight Gas Shales. SPE Annual Technical Conference and Exhibition, 24-27 September, San Antonio, Texas, USA. Society of Petroleum Engineers. doi:10.2118/103327-MS
- Sullivan, K.L., 1985. Organic Facies Variation of the Woodford Shale in Western Oklahoma. The Shale Shaker Digest XI, Volumes XXXIII-XXXV (1982-1985). Pages 185–198
- Tanner, W.F., 1965. Upper jurassic paleogeography of the four corners region. *Journal of Sedimentary Research* 35, 564–574. doi:10.1306/74D712F3-2B21-11D7-8648000102C1865D
- Taylor, K.G., Macquaker, J.H.S., 2011. Iron minerals in marine sediments record chemical environments. *Elements* 7, 113
- Terzaghi, K., 1996. *Soil Mechanics in Engineering Practice*. John Wiley & Sons
- Tingay, M.R.P., Morley, C.K., Laird, A., Limpornpipat, O., Krisadasima, K., Pabchanda, S., Macintyre, H.R., 2013. Evidence for overpressure generation by kerogen-to-gas maturation in the northern Malay Basin. *AAPG Bulletin* 97, 639–672. doi:10.1306/09041212032
- Tucker, M.E., 1982. *Sedimentary petrology: an introduction to the origin of sedimentary rocks*. Blackwell Science Publications
- Utley, L., 2005. Unconventional Petrophysical Analysis in Unconventional Reservoirs. Presentation, <http://utleypetro.com/shales.htm>
- Vandenbroucke, M., Largeau, C., 2007. Kerogen origin, evolution and structure. *Organic Geochemistry* 38, 719–833. doi:10.1016/j.orggeochem.2007.01.001

- Velde, B., 1996. Compaction trends of clay-rich deep sea sediments. *Marine Geology* 133, 193–201
- Wagoner, J.C.V., Mitchum, R.M., Campion, K.M., Rahmanian, V.D., 1990. Siliciclastic Sequence Stratigraphy in Well Logs, Cores, and Outcrops: Concepts for High-Resolution Correlation of Time and Facies 174, III–55
- Ward, J., 2010. Kerogen Density in the Marcellus Shale. SPE Unconventional Gas Conference, 23-25 February, Pittsburgh, Pennsylvania, USA. Society of Petroleum Engineers. doi:10.2118/131767-MS
- Waxman, M.H., Smits, L.J.M., 1968. Electrical Conductivities in Oil-Bearing Shaly Sands. *Society of Petroleum Engineers Journal* 8. doi:10.2118/1863-A
- Weniger, P., Kalkreuth, W., Busch, A., Krooss, B.M., 2010. High-pressure methane and carbon dioxide sorption on coal and shale samples from the Paraná Basin, Brazil. *International Journal of Coal Geology*. doi:10.1016/j.coal.2010.08.003
- Wignall, P.B., 1994. *Black shales*. Clarendon Press
- Willmott, C.J., Matsuura, K., 2005. Advantages of the mean absolute error (MAE) over the root mean square error (RMSE) in assessing average model performance. *Clim Res* 30, 79–82. doi:10.3354/cr030079
- Winsauer, W.O., 1952. Resistivity of brine-saturated sands in relation to pore geometry. *AAPG Bulletin* 36, 253–277.
- Winsauer, W.O., McCardell, W.M., 1953. Ionic double-layer conductivity in reservoir rock. *Journal of Petroleum Technology* 5, 129–134
- Witkowsky, J., Galford, J., Quirein, J., Truax, J., 2012. Predicting Pyrite and Total Organic Carbon from Well Logs for Enhancing Shale Reservoir Interpretation. SPE Eastern Regional Meeting, 3-5 October, Lexington, Kentucky, USA. Society of Petroleum Engineers. doi:10.2118/161097-MS
- Wood, J., 2012. Water Distribution in the Montney Tight Gas Play of the Western Canadian Sedimentary Basin: Significance for Resource Evaluation. SPE Canadian Unconventional Resources Conference, 30 October-1 November, Calgary, Alberta, Canada. Society of Petroleum Engineers. doi:10.2118/161824-MS
- Worthington, P., 1985. The evolution of shaly-sand concepts in reservoir evaluation. *The Log Analyst* 26, 23–40
- Worthington, P., 2004. Improved Quantification of Fit-for-Purpose Saturation Exponents. *SPE Reservoir Evaluation & Engineering* 7, 270–284

- Worthington, P., 2007. Petrophysical Type Curves for Identifying the Electrical Character of Petroleum Reservoirs. SPE Reservoir Evaluation & Engineering 10. doi:10.2118/96718-PA
- Worthington, P., 2009. Identifying the Potential Upside of Hydrocarbon Saturation From Electric Logs. SPE Reservoir Evaluation & Engineering 12. doi:10.2118/103075-PA
- Worthington, P., 2011a. The Petrophysics of Problematic Reservoirs. Journal of Petroleum Technology 63, 88–97
- Worthington, P., 2011b. Quality-assured evaluation of freshwater-bearing hydrocarbon reservoirs. Journal of Petroleum Science and Engineering 78, 542–551. doi:10.1016/j.petrol.2011.06.008
- Worthington, P.F., 2000. Recognition and evaluation of low-resistivity pay. Petroleum Geoscience 6, 77–92. doi:10.1144/petgeo.6.1.77
- Worthington, P.F., 2001. The influence of formation anisotropy upon resistivity–porosity relationships. Petrophysics 42, 83–92
- Wu, P., Aguilera, R., 2012. Investigation of Gas Shales at Nanoscale Using Scan Electron Microscopy, Transmission Electron Microscopy and Atomic Force Microscopy. SPE Annual Technical Conference and Exhibition, 8-10 October, San Antonio, Texas, USA. Society of Petroleum Engineers. doi:10.2118/159887-MS
- Wu, P., Aguilera, R., 2013. Uncertainty Analysis of Shale Gas Simulation: Consideration of Basic Petrophysical Properties. SPE Unconventional Resources Conference Canada, 5-7 November, Calgary, Alberta, Canada. Society of Petroleum Engineers. doi:10.2118/167236-MS
- Wyllie, M.R.J., Gregory, A.R., 1953. Formation Factors of Unconsolidated Porous Media: Influence of Particle Shape and Effect of Cementation. Journal of Petroleum Technology 5. doi:10.2118/223-G
- Wyllie, M.R.J., Rose, W., 1950. Some Theoretical Considerations Related To The Quantitative Evaluation Of The Physical Characteristics Of Reservoir Rock From Electrical Log Data. Journal of Petroleum Technology 2. doi:10.2118/950105-G
- Wyllie, M.R.J., Southwick, P.F., 1954. An experimental investigation of the SP and resistivity phenomena in dirty sands. Journal of Petroleum Technology 6, 44–57.
- Yeo, T., 2011. Shale gas: fifth report of session 2010-12. The Stationery Office.
- Yu, D., Wang, Y., Zhao, Z.A., 2013. New Integrated Method for Petrophysical Evaluation of Shale Gas: A Case Study in Weiyuan Field. SPE Unconventional Resources Conference and Exhibition-Asia Pacific, 11-13 November, Brisbane, Australia . Society of Petroleum Engineers. doi:10.2118/167061-MS

- Yu, G., Aguilera, R., 2011. Use of Pickett Plots for Evaluation of Shale Gas Formations. SPE Annual Technical Conference and Exhibition, 30 October-2 November, Denver, Colorado, USA. Society of Petroleum Engineers. doi:10.2118/146948-MS
- Zak, A.J., Smith, J.E., 1959. Gamma Ray-Density Logging. Society of Petroleum Engineers. SPE-1253-G
- Zhang, J., Wieseneck, J., 2011. Challenges and Surprises of Abnormal Pore Pressures in the Shale Gas Formations, in: SPE Annual Technical Conference and Exhibition, 30 October-2 November, Denver, Colorado, USA.. Society of Petroleum Engineers. doi; 10.2118/145964-MS
- Zhang, T., Ellis, G., Ruppel, S., Milliken, K., Lewan, M., Sun, X., 2013. Effect of Organic Matter Properties, Clay Mineral Type and Thermal Maturity on Gas Adsorption in Organic-Rich Shale Systems, in: Unconventional Resources Technology Conference, 12-14 August, Denver, Colorado, USA, SPE-168862-MS
- Zhao, H., Givens, N.B., Curtis, B., 2007. Thermal maturity of the Barnett Shale determined from well-log analysis. AAPG Bulletin 91, 535–549. doi:10.1306/10270606060